Transactions of the ASME®

Technical Editor, LEON M. KEER

The Technological Institute
Northwestern University
Evanston, IL 60201

APPLIED MECHANICS DIVISION

Chairman, THOMAS L. GEERS
Secretary, S. LEIBOVICH
Associate Editors,
R. M. CHRISTENSEN
C. O. HORGAN
R. L. HUSTON
D. J. INMAN
W. D. IWAN
W. G. KNAUSS
F. A. LECKIE
J. T. C. LIU
R. M. McMEEKING
A. K. NOOR
J. W. NUNZIATO
R. H. PLAUT
J. W. RUDNICKI
J. G. SIMMONDS
P. D. SPANOS
K. R. SREENIVASAN
Z. WARHAFT
L. T. WHEELER

BOARD ON COMMUNICATIONS
Chairman and Vice-President
R. NICKELL

Members-at-Large
J. LLOYD
R. REDER
F. SCHMIDT
M. FRANKE
M. KUTZ
T. MIN
F. LANDIS
R. ROCKE
W. WINER
R. GENTILE
B. ZIELS
R. MATES

President, E. L. DAMAN
Exec. Dir.
D. L. BELDEN
Treasurer, ROBERT A. BENNETT

PUBLISHING STAFF
Mng. Dir., Publ., JOS. SANSONE
Managing Editor,
CORNELIA MONAHAN
Production Editor, JUDY SIERANT
Prod. Asst., MARISOL ANDINO

Transactions of the ASME, Journal of Applied Mechanics (ISSN 0021-8936) is published quarterly (Mar., June, Sept., Dec.) for $120 per year by The American Society of Mechanical Engineers, 345 East 47th Street, New York, NY 10017. Second class postage paid at New York, NY and additional mailing offices. POSTMASTER: Send address changes to The Journal of Applied Mechanics, c/o THE AMERICAN SOCIETY OF MECHANICAL ENGINEERS, 22 Law Drive, Box 2300, Fairfield, NJ 07007-2300.
CHANGES OF ADDRESS must be received at Society headquarters seven weeks before they are to be effective. Please send old label and new address.

PRICES: *To members, $29.00, annually; to* nonmembers, $120.00.
Add $15.00 for postage to countries outside the United States and Canada.

STATEMENT from By-Laws. The Society shall not be responsible for statements or opinions advanced in papers or . . . printed in its publications (B7.1, Par. 3).

COPYRIGHT © 1988 by the American Society of Mechanical Engineers. Reprints from this publication may be made on condition that full credit be given the TRANSACTIONS OF THE ASME, JOURNAL OF APPLIED MECHANICS, and the author, and date of publication be stated.

INDEXED by Applied Mechanics Reviews and Engineering Information, Inc.

Journal of Applied Mechanics

Published Quarterly by The American Society of Mechanical Engineers

VOLUME 55 • NUMBER 4 • DECEMBER 1988

TECHNICAL PAPERS

755 Penetration of 6061-T651 Aluminum Targets With Rigid Long Rods
M. J. Forrestal, K. Okajima, and V. K. Luk

761 Elastic-Plastic Ring-Loaded Cylindrical Shells (89-APM-20)
G. N. Brooks

767 *Material Compatibility in Interfacial Transient Thermal Fracture of Ceramic-to-Metal Bonds* (88-WA/APM-54)
K. Kokini

773 A Continuum Damage Model for Viscoelastic Materials (89-APM-12)
Y. Weitsman

781 General Image Method in a Plane-Layered Elastostatic Medium (89-APM-14)
N. Fares and V. C. Li

786 A Novel Displacement Gradient Boundary Element Method for Elastic Stress Analysis With High Accuracy (89-APM-21)
H. Okada, H. Rijiyah, and S. N. Atluri

795 A Surface Crack in Shells Under Mixed-Mode Loading Conditions (89-APM-11)
P. F. Joseph and F. Erdogan

805 Three-Dimensional Stress Field Near the Crack Front of a Thin Elastic Plate (88-WA/APM-56)
T. Nakamura and D. M. Parks

814 Small Scale Contact Conditions for the Linear-Elastic Interface Crack (89-APM-16)
P. M. Anderson

818 On a Paradoxical Phenomenon Related to Beams on Elastic Foundation: Could External Compliant Leads Reduce the Strength of a Surface-Mounted Device? (89-APM-5)
E. Suhir

822 Stresses in Dual-Coated Optical Fibers (89-APM-22)
E. Suhir

831 The Differential Geometry of the General Helix as Applied to Mechanical Springs (89-APM-17)
Y. Lin and A. P. Pisano

837 Theory of Elasticity of Filament Wound Anistropic Ellipsoids With Specialization to Torsion or Orthotropic Bars
G. A. Kardomateas

845 The Elastica With End-Load Flip-Over (89-APM-18)
J. F. Wilson and J. M. Snyder

849 Sound Radiation From Beams Under the Action of Moving Line Forces (89-APM-19)
R. F. Keltie and H. Peng

855 Axisymmetric Free Vibrations of a Transversely Isotropic Finite Cylindrical Rod
C. P. Lusher and W. N. Hardy

863 Ultrasonic Wave Reflection From Liquid-Coupled Orthotropic Plates With Application to Fibrous Composites (88-WA/APM-55)
A. H. Nayfeh and D. E. Chimenti

871 Effect of Interface Layers on Scattering of Elastic Waves (89-APM-10)
R. Paskaramoorthy, S. K. Datta, and A. H. Shah

879 The Normal Impact of a Rod-Mass System on a Viscoelastic Layered Half Space
H. A. Downey, Jr. and D. B. Bogy

887 Low Velocity Impact of an Elastic Plate Resting on Sand (89-APM-13)
H. L. Chen, W. Lin, L. M. Keer, and S. P. Shah

895 *A Sufficient Condition for the Stability of Conservative Gyroscopic Systems* (88-WA/APM-76)
D. J. Inman

899 Coordinate Reduction in the Dynamics of Constrained Multibody Systems—A New Approach (89-APM-15)
S. K. Ider and F. M. L. Amirouche

905 Response of Linear Systems to Polynomials of Gaussian Processes
M. Grigoriu and S. T. Ariaratnam

911 Some Observations on the Random Response of an Elasto-Plastic System (88-WA/APM-64)
L. G. Paparizos and W. D. Iwan

918 *Equivalent Stochastic Systems* (88-WA/APM-77)
Y. K. Lin and G. Q. Cai

923 Hopf Bifurcation in the Presence of Both Parametric and External Stochastic Excitations (88-WA/APM-63)
N. Sri Namachchivaya

931 Optimal Control of Nonlinear Structures (88-WA/APM-75)
J. N. Yang, F. X. Long, and D. Wong

939 Trade-Offs Between Identification and Control in Dynamic Systems
F. E. Udwadia and H. Flashner

(Contents continued on Inside Back Cover)

Downloaded 04 May 2010 to 171.66.16.49. Redistribution subject to ASME license or copyright; see http://www.asme.org/terms/Terms_Use.cfm

CONTENTS (Continued)

946 **On the Dynamics of Large Systems with Localized Nonlinearities**
P. Hagedorn and W. Schramm

952 **Chaotic Motions of a Torsional Vibration Absorber**
S. W. Shaw and S. Wiggins

959 **Chaos and Three-Dimensional Horseshoes in Slowly Varying Oscillators**
S. Wiggins and S. W. Shaw

969 **The Thickness of Steady Plane Shear Flows of Circular Disks Driven by Identical Boundaries** (89-APM-8)
D. M. Hanes, J. T. Jenkins, and M. W. Richman

975 **The Meniscus Instability of a Thin Liquid Film**
H. Koguchi, M. Okada, and K. Tamura

981 **An Exact Periodic Solution of a Hydromagnetic Flow in a Horizontal Channel**
K. Vajravelu

BRIEF NOTES

Axisymmetric Divergence of Ring-Stiffened Composite Cylindrical Shells Subject to Axial Compression
V. Birman 984

Comments on Rayleigh's Quotient and Perturbation Theory for the Eigenvalue Problem
C. Pierre 986

Bounds on Harmonically Forced Response of Damped Linear Systems
Z. Liang and T. T. Soong 988

990 Wave Propagation in a Rod With a Varying Cross-Section
D. L. Clements and A. Larsson

992 Structural Decomposition Approach for the Stability of Uncertain Dynamic Systems
Y. H. Chen and C. Hsu

994 On Certain Refined Theories for Plate Bending
K. P. Soldatos

BOOK REVIEWS

996 ***Thermal Stress II*** **edited by R. B. Hetnarski** . . . Reviewed by **L. Y. Bahar**

996 ***Numerical Modelling in Science and Engineering*** **by M. B. Allen III, I. Herrera, and G. F. Pinder** . . . Reviewed by **W. K. Liu**

997 ***Boundary Element Methods in Mechanics*** **by D. E. Beskos** . . . Reviewed by **U. Heise**

997 ***Chaotic Vibrations: An Introduction for Applied Scientists and Engineers*** **by F. C. Moon** . . . Reviewed by **E. Dowell and C. Pezeshki**

752 Books Received by the Office of the Technical Editor

999 Worldwide Mechanics Meeting List

910 Change of Address Form

1002 Tenth ASME Freeman and Scholarship Program in Fluids Engineering

974 Eleventh U.S. National Congress of Applied Mechanics

780 First World Congress of Biomechanics

772 Second International Post-SMiRT Seminar

813 Errata

785, 836, 854, 945, 983 Applied Mechanics Symposium Proceedings

Downloaded 04 May 2010 to 171.66.16.49. Redistribution subject to ASME license or copyright; see http://www.asme.org/terms/Terms_Use.cfm

M. J. Forrestal
Sandia National Laboratories,
Albuquerque, N.M. 87185
Fellow ASME

K. Okajima
University of Dayton Research Institute,
Dayton, Ohio 45469

V. K. Luk
Sandia National Laboratories,
Albuquerque, N.M. 87185
Mem. ASME

Penetration of 6061-T651 Aluminum Targets With Rigid Long Rods

We developed engineering models for forces on rigid, long rods with spherical, ogival, and conical noses that penetrated rate independent, elastic-perfectly plastic targets. The spherical and cylindrical, cavity-expansion approximations simplified the target analyses, so we obtained closed-form penetration equations. To verify our models, we performed terminal-ballistic experiments with 7.1-mm dia., 0.024 kg, marging steel rods and 152-mm dia., 6061-T651 aluminum targets. The models predicted penetration depths that were in reasonable agreement with the data for impact velocities between 0.4-1.4 km/s.

Introduction

Backman and Goldsmith (1978) and Zukas (1982) surveyed the broad field of penetration mechanics. For penetration by long rods into semi-infinite targets, they discuss several penetration mechanisms that depend on the target material, the impact velocity, and geometry and material of the projectile. Because many mechanisms are possible, experimental observations usually precede and guide engineering models. Our study was limited to the observations shown in Fig. 1. This posttest, in-material, X-ray photograph shows a spherical nose, steel rod embedded in an aluminum target. This rod was launched at 1.12 km/s, was not deformed, and produced a tunnel about the size of the shank diameter. For much higher impact velocities, rods are eroded during penetration and produce cavities several times the shank diameter; e.g., see Wright and Frank (1987) and Tate (1969).

Analytical methods for penetration mechanics began with the pioneering paper by Bishop, Hill, and Mott (1945). They developed equations for the quasi-static expansions of cylindrical and spherical cavities from zero, initial radii, and used these equations to estimate forces on conical nose punches. Later, Goodier (1965) developed models to predict the penetration of rigid spheres into metal targets. That problem was dynamic, and Goodier approximated the target response by using results from the spherically symmetric, cavity-expansion solution for an incompressible, elastic-plastic material derived by Hill (1948).

In this study, we developed engineering models that predicted forces on rigid, long rods with spherical, ogival, and conical noses that penetrated rate independent, elastic-perfectly plastic targets. The cavity-expansion approximations (Bishop, Hill, and Mott, 1945) simplified the target analysis, so penetration equations were obtained in closed-form. These penetration equations depend on the impact velocity, geometry and mass of the projectile, the material properties of the target, and the frictional resistance at the projectile-target interface.

To verify our models, we conducted terminal-ballistic experiments with 7.1-mm dia., 0.024 kg, maraging steel projectiles and 152-mm dia., 6061-T651 aluminum targets. Impact velocities ranged from 0.40-1.40 km/s and final penetration depths were measured. Predicted penetration depths were compared with measurements for rods with a spherical nose, a 3.0 CRH (caliber-radius-head) ogival nose, and a conical nose with $l/2a = 1.5$ (nose length-to-diameter ratio).

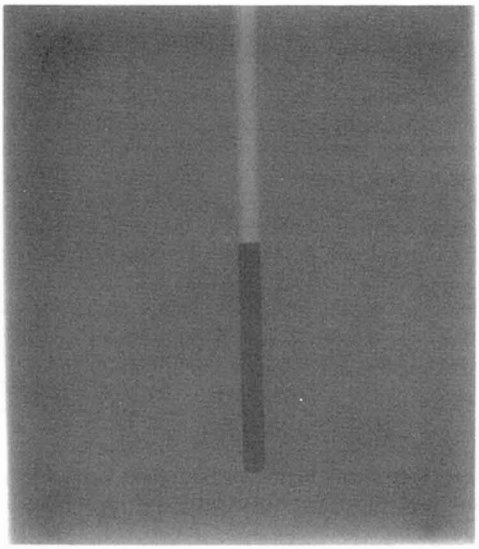

Fig. 1 Posttest, in-material, X-ray photograph for a spherical nose rod with impact velocity 1.12 km/s (Shot No. 6-1362)

Contributed by the Applied Mechanics Division for publication in the JOURNAL OF APPLIED MECHANICS.

Discussion on this paper should be addressed to the Editorial Department, ASME, United Engineering Center, 345 East 47th Street, New York, N.Y. 10017, and will be accepted until two months after final publication of the paper itself in the JOURNAL OF APPLIED MECHANICS. Manuscript received by ASME Applied Mechanics Division, October 13, 1987; final revision, May 15, 1988.

Copyright © 1988 by ASME
Downloaded 03 May 2010 to 171.66.16.21. Redistribution subject to ASME license or copyright; see http://www.asme.org/terms/Terms_Use.cfm

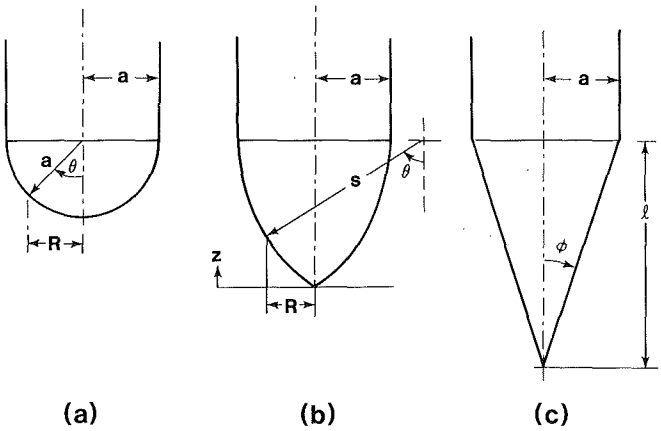

Fig. 2 Projectile geometries: (a) spherical nose, (b) ogival nose, and (c) conical nose

Formulation of the Penetration Models

Rigid projectiles with spherical, ogival, or conical noses impact a uniform target at normal incidence with velocity V_0 and proceed to penetrate at rigid-body velocity V_z. Nose geometries are shown in Fig. 2, and Fig. 2(*b*) shows an ogive is the arc of a circle that is tangent to the projectile shank. It is also common to define the ogive in terms of caliber-radius-head

$$\text{CRH} = s/2a = \psi \tag{1}$$

where s and a are defined in Fig. 2(*b*). For a rigid projectile, motion and final depth can be calculated when forces are known. Thus, we first model target resistance and then calculate motion and depth.

To obtain engineering models, we use the spherical and cylindrical, cavity-expansion approximations. For the spherical approximation, normal stress on the projectile nose is approximated by results from a spherically symmetric, cavity-expansion analysis that relates normal stress at the cavity surface to cavity-expansion velocity (Forrestal and Luk, 1988). In particular, normal stress on the nose is taken as the stress at the cavity surface associated with the distributed expansion velocity at the nose-target interface caused by the projectile penetrating at rigid-body velocity V_z. As explained by Forrestal (1986), the cylindrical, cavity-expansion approximation idealizes the target as thin, independent layers normal to the penetration direction and simplifies the target analysis to one-dimensional motion in the radial direction.

As previously discussed and shown in Fig. 1, the projectiles produce a tunnel in the target about the size of the shank diameter. In addition, photomicrographs of the targets showed that a 5-15 μm layer normal to the tunnel surface had undergone microstructural changes. From this observation we assumed that during penetration there was a thin layer of melted, target material between the nose and target. Thus, penetration resistance consisted of normal pressure on the nose and a tangential, frictional component from the thin, melted layer. For lack of detailed data on frictional resistance at high velocities and large confining pressures, we assume a tangential stress on the nose σ_t proportional to the normal stress σ_n, so

$$\sigma_t = \mu\sigma_n \tag{2}$$

where μ is the sliding-friction coefficient.

Spherical Nose Rods With the Spherical Cavity-Expansion Approximation. From the geometry shown in Fig. 2(*a*), incremental ring forces normal and tangent to the spherical nose are

$$dF_n = 2\pi Ra\sigma_n(V_z,\theta)d\theta \tag{3a}$$

$$dF_t = 2\pi Ra\mu\sigma_n(V_z,\theta)d\theta \tag{3b}$$

where the symbols are defined in Fig. 2(*a*), and $\sigma_n(V_z, \theta)$ is the normal stress on the nose from target resistance that depends on rigid-body velocity V_z. Thus, the axial force is given by

$$F_z = \pi a^2 \int_0^{\pi/2} \sigma_n(V_z,\theta)\left[\sin 2\theta + 2\mu\sin^2\theta\right]d\theta \tag{4}$$

The normal stress $\sigma_n(V_z, \theta)$ will be approximated by results from an elastic-plastic, spherically symmetric, cavity-expansion analysis (Forrestal and Luk, 1988).

Ogival Nose Rods With the Spherical Cavity-Expansion Approximation. From the geometry shown in Fig. 2(*b*), incremental ring forces normal and tangent to the ogival nose are

$$dF_n = 2\pi s^2\left[\sin\theta - \left(\frac{s-a}{s}\right)\right]\sigma_n(V_z,\theta)d\theta \tag{5a}$$

$$dF_t = 2\pi s^2\left[\sin\theta - \left(\frac{s-a}{s}\right)\right]\mu\sigma_n(V_z,\theta)d\theta \tag{5b}$$

where symbols are defined in Fig. 2(*b*), and $\sigma_n(V_z, \theta)$ is the stress normal on the ogival nose from target resistance. The axial force on the ogival nose is

$$F_z = 2\pi s^2 \int_{\theta_0}^{\pi/2} \left\{\left[\sin\theta - \left(\frac{s-a}{s}\right)\right]\right.$$

$$\left.\times\left(\cos\theta + \mu\sin\theta\right)\right\}\sigma_n(V_z,\theta)d\theta \tag{6a}$$

$$\theta_0 = \sin^{-1}\left(\frac{s-a}{s}\right) \tag{6b}$$

Ogival Nose Rod With the Cylindrical Cavity-Expansion Approximation. As previously discussed, the cylindrical, cavity-expansion approximation idealizes the target as thin layers normal to the direction of penetration and simplifies the target analysis to one-dimensional wave propagation in the radial coordinate $R(z)$ (see Fig. 2(*b*)). From Forrestal, Norwood, and Longcope (1981), the axial component of force that neglects sliding frictional resistance is

$$F_{zn} = 2\pi\int_0^l \sigma_r(V_z,z)R(dR/dz)dz \tag{7}$$

where $\sigma_r(V_z, z)$ is the radial, stress component from an elastic-plastic, cylindrical, cavity-expansion analysis (Forrestal, 1986). The equation for an ogive in R, z coordinates is

$$\left[R-(a-s)\right]^2 + (z-l)^2 = s^2 \tag{8}$$

where symbols are defined in Fig. 2(*b*). Using (8), the axial component of force without sliding frictional resistance is

$$F_{zn} = 2\pi\int_0^l \left\{l - z - \frac{(s-a)(l-z)}{\left[s^2-(l-z)^2\right]^{1/2}}\right\}\sigma_r(V_z,z)dz \tag{9}$$

The axial component of force from sliding friction is contained in (6), so the total axial force is given by

$$F_z = F_{zn} + 2\pi s^2\mu\int_{\theta_0}^{\pi/2}\left[\sin\theta - \left(\frac{s-a}{a}\right)\right]\sin\theta\sigma_r(V_z,\theta)d\theta \tag{10}$$

where F_{zn} is given by (9).

Conical Nose Rods With the Spherical and Cylindrical Cavity-Expansion Approximations. As discussed by Bishop, Hill, and Mott (1945), the normal stress on a conical nose is spatially constant for the cavity-expansion approximations. Thus,

Downloaded 03 May 2010 to 171.66.16.21. Redistribution subject to ASME license or copyright; see http://www.asme.org/terms/Terms_Use.cfm

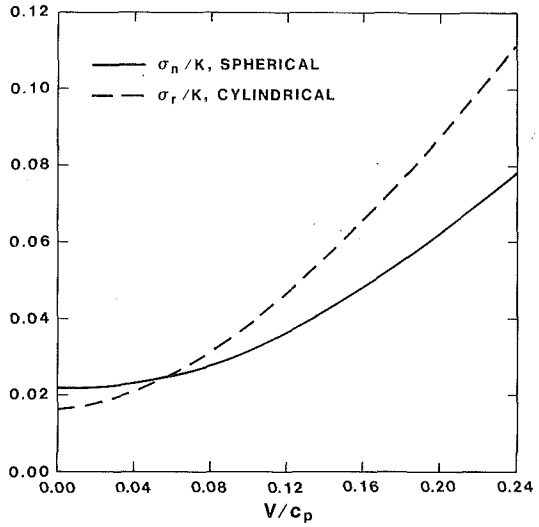

Fig. 3 Radial stress at the cavity surface versus cavity-expansion velocity for spherical and cylindrical symmetry (ν = 1/3, Y = 400 MPa, K = 68,950 MPa and ρ = 2,710 kg/m^3)

$$F_z = \pi a^2 \sigma_n(V_z)(1+\mu/\tan\phi) \tag{11}$$

for the spherical approximation, and

$$F_z = \pi a^2 \sigma_r(V_z)(1+\mu/\tan\phi) \tag{12}$$

for the cylindrical approximation, where ϕ is defined in Fig. 2(*c*). Again, $\sigma_n(V_z)$ and $\sigma_r(V_z)$ are given by results from one-dimensional, symmetric, spherical and cylindrical, cavity-expansion analyses, respectively.

Penetration Equations

Axial forces for the spherical and ogival nose rods are given by the integrals (4) and (6) and (10), respectively; and, forces on the conical nose rods are given by (11) and (12). These equations contain $\sigma_n(V_z, \theta)$ or $\sigma_r(V_z, z)$ that are the normal and radial stresses on the nose from target resistance. We approximate these stresses by results from one-dimensional, symmetric, spherical (Forrestal and Luk, 1988) and cylindrical (Forrestal, 1986), cavity-expansion analyses. Results from those analyses are presented in Fig. 3 and show radial stresses, σ_n and σ_r, at the cavity surface versus cavity-expansion velocity, V. In Fig. 3, K, ν, Y, and ρ are bulk modulus, Poisson's ratio, flow stress, and density of the target, respectively; and $c_p^2 = K/\rho$. To obtain closed-form, penetration equations, we also curve-fit the symmetric, cavity-expansion results with the expressions

$$S_s = \frac{\sigma_n}{K} = A_s + B_s\left(\frac{V}{c_p}\right)^2 \tag{13a}$$

$$A_s = \frac{2Y}{3K}\left\{1 + ln\left[\frac{(1-2\nu)K}{(1-\nu)Y}\right]\right\} \tag{13b}$$

and

$$S_c = \frac{\sigma_r}{K} = A_c + B_c\left(\frac{V}{c_p}\right)^2 \tag{14a}$$

$$A_c = \frac{Y}{2K}\left\{1 + ln\left[\frac{6(1-2\nu)K}{(5-4\nu)Y}\right]\right\} \tag{14b}$$

where subscripts s, c refer to the spherical and cylindrical analyses, respectively. In equations (13) and (14), A_s and A_c are expressions for the quasi-static expansions of spherical and cylindrical cavities from zero, initial radii (Hill, 1950). Therefore, only one term in each of the equations (13*a*) and (14*a*) needs to be adjusted to fit the cavity-expansion results. The symmetric, cavity-expansion results in Fig. 3 are accurately curve-fit with $B_s = 1.041$ and $B_c = 1.837$.

Spherical Nose Rod With Spherical Cavity-Expansion Approximation. From the geometry shown in Fig. 2(*a*), the target particle velocity at the nose-target interface caused by the projectile penetrating at rigid-body velocity V_z is

$$v(V_z,\theta) = V_z\cos\theta \tag{15}$$

We approximate the normal stress distribution on the spherical nose by replacing the spherically symmetric, cavity-expansion velocity V in (13*a*) with the particle velocity v given by (15). Thus, normal stress distribution round the spherical nose is taken as

$$S_s(V_z,\theta) = A_s + B_s\left(\frac{V_z\cos\theta}{c_p}\right)^2 \tag{16}$$

Substitution of (16) into (4) and integrating gives

$$F_z = \alpha_s + \beta_s V_z^2 \tag{17a}$$

$$\alpha_s = \pi a^2 K A_s(1+\mu\pi/2) \tag{17b}$$

$$\beta_s = (\pi a^2\rho/2)B_s(1+\mu\pi/4) \tag{17c}$$

where A_s is given by (13*b*) and $B_s = 1.041$.

Final penetration depth is obtained from

$$m(dV_z/dt) = mV_z(dV_z/dz) = -F_z \tag{18}$$

where m is the projectile mass and z is penetration depth. Substitution of (17) into (18) and integrating gives

$$P = \frac{m}{2\beta_s}\, ln\left[1 + \frac{\beta_s V_o^2}{\alpha_s}\right] \tag{19}$$

where P is final penetration depth and V_o is impact velocity.

Ogival Nose Rods With Spherical Cavity-Expansion Approximation. For the ogival nose (Fig. 2(*b*)) and the spherical, cavity-expansion approximation, axial force is obtained by substituting (16) into (6) and integrating. Thus,

$$F_z = \alpha_s + \beta_s V_z^2 \tag{20a}$$

$$\alpha_s = \pi a^2 K A_s\left[1 + 4\mu\psi^2(\pi/2-\theta_o) - \mu(2\psi-1)(4\psi-1)^{1/2}\right] \tag{20b}$$

$$\beta_s = \pi a^2\rho B_s\left[\frac{(8\psi-1)}{24\psi^2} + \mu\psi^2(\pi/2-\theta_o) - \frac{\mu(2\psi-1)(6\psi^2+4\psi-1)(4\psi-1)^{1/2}}{24\psi^2}\right] \tag{20c}$$

$$\theta_o = \sin^{-1}\left(\frac{2\psi-1}{2\psi}\right) \tag{20d}$$

where ψ is the caliber-radius-head of the ogive given by (1). For $\psi = 1/2$, the ogive degenerates to a sphere, and for this special case (20) reduces to (17).

Final depth of penetration is given by (19) and (20*b*,*c*).

Ogival Nose Rods With Cylindrical Cavity-Expansion Approximation. From the geometry shown in Fig. 2(*b*) and the cylindrical, cavity-expansion approximation, radial stress round the ogival nose is taken as

$$S_c(V_z,z) = A_c + B_c\left(\frac{V_z}{c_p}\cdot\frac{dR}{dz}\right)^2 \tag{21a}$$

$$\frac{dR}{dz} = \frac{l-z}{\left[s^2-(l-z)^2\right]^{1/2}},\quad l = a(4\psi-1)^{1/2} \tag{21b}$$

Downloaded 03 May 2010 to 171.66.16.21. Redistribution subject to ASME license or copyright; see http://www.asme.org/terms/Terms_Use.cfm

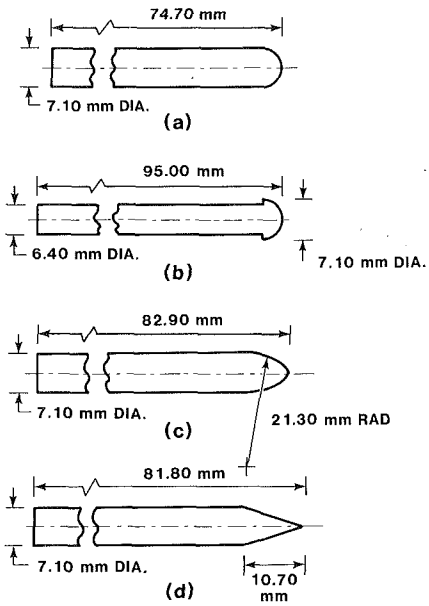

Fig. 4 Dimensioned projectiles used in the experiments: (*a*) spherical nose, (*b*) spherical nose with cut-back shank, (*c*) ogival nose, and (*d*) conical nose

Substitution of (21) into (10) and integrating gives the axial force

$$F_z = \alpha_c + \beta_c V_z^2 \tag{22a}$$

$$\alpha_c = \pi a^2 K A_c \left[1 + 4\mu\psi^2(\pi/2 - \theta_o) - \mu(2\psi - 1)(4\psi - 1)^{1/2}\right] \tag{22b}$$

$$\beta_c = \pi a^2 \rho B_c \left[8\psi^2 ln\left(\frac{2\psi}{2\psi - 1}\right) - (1 + 4\psi) + \mu\psi^2(\pi/2 - \theta_o) - \frac{\mu(2\psi - 1)(6\psi^2 + 4\psi - 1)(4\psi - 1)^{1/2}}{24\psi^2}\right] \tag{22c}$$

Final depth of penetration is obtained from (18) and (22*b*,*c*) and given by

$$P = \frac{m}{2\beta_c} ln\left[1 + \frac{\beta_c V_o^2}{\alpha_c}\right] \tag{23}$$

Conical Nose Rods With Spherical and Cylindrical Cavity-Expansion Approximations. Substitution of (13) into (11) gives the axial force predicted by the spherical, cavity-expansion approximation. Thus,

$$F_z = \alpha_s + \beta_s V_z^2 \tag{24a}$$

$$\alpha_s = \pi a^2 K A_s (1 + \mu/\tan\phi) \tag{24b}$$

$$\beta_s = \pi a^2 \rho B_s (1 + \mu/\tan\phi)\sin^2\phi \tag{24c}$$

Final penetration depth is given by (19) and (24*b*,*c*).

For the cylindrical, cavity-expansion approximation, axial force is obtained from (14) and (12) and given by

$$F_z = \alpha_c + \beta_c V_z^2 \tag{25a}$$

$$\alpha_c = \pi a^2 K A_c (1 + \mu/\tan\phi) \tag{25b}$$

$$\beta_c = \pi a^2 \rho B_c (1 + \mu/\tan\phi)\tan^2\phi \tag{25c}$$

Final penetration depth is given by (23) and (25*b*,*c*).

Experiments

Briefly, a 20-mm, smooth-bore, powder gun launched the rods shown in Fig. 4 to impact velocities between 0.4–1.4 km/s. Impact velocities were determined by the projectile interrupting two continuously monitored laser beams. Penetration depths were measured from posttest, in-material, X-ray photographs (see Fig. 1).

Targets. The targets were cut from 152-mm dia (6.0 in.), 6061-T651 aluminum bars. In addition, samples from this bar stock were machined for dynamic, tensile, stress-strain tests and two tests were conducted for each strain rate. For strain rates of 10^{-2}, 10^{0} and $10^{1}s^{-1}$ the material was nearly strain-rate insensitive and had a yield stress between 350–380 MPa. After the yield, the true stress-true strain curve was nearly linear until fracture at 390–400 MPa with corresponding strains between 0.052–0.059. The dynamic, tensile test has a one-dimensional, stress state prior to necking and fracture, and this stress state allows necking to occur. For this application, no necking occurs in the bulky targets, so we assumed that the flow stress in the targets remained constant at Y = 400 MPa.

Projectiles. The projectiles were machined from T-200 and C-300, maraging steel[1] and had a nominal mass of 0.024 kg. Dimensioned spherical, ogival, and conical nose rods are shown in Fig. 4. Since our models only predict forces on the noses, we also conducted a few experiments with the spherical nose rod shown in Fig. 4(*b*). This projectile has a cut-back shank and was designed to eliminate possible drag on the shank from target rebound. As will be shown later, penetration depths for the rods shown in Figs. 4(*a*) and 4(*b*) were within the data scatter.

Terminal-Ballistic Experiments. A 20-mm, smooth-bore, powder gun launched the rods shown in Fig. 4 to incident velocities between 0.4–1.4 km/s. The rods were encased in two-piece, serrated, plastic sabots. Pusher plates were 15.7-mm dia., 6.35-mm long, titanium discs, and the obturator was made from the same material as the sabot. The sabot fit snugly in the gun barrel, while the slightly oversized obturator was forced into the barrel to provide a gas seal. Air drag stripped the sabot, pusher plate, and obturator from the rod prior to impact (Rosenberg and Forrestal, 1988).

Incident velocity was determined within one percent accuracy by the penetrator interrupting two continuously monitored laser beams. Posttest, penetration depths were measured from in-material, X-ray photographs; one of these photographs is shown in Fig. 1. Tables 1, 2, and 3 summarize the data for the experimental program.

Comparison of Predictions and Measured Penetration Depths

Figures 5, 6, and 7 show predictions from the engineering models and measured, penetration depths. The target material properties were taken as ν = 1/3, Y = 400 MPa, K = 68.9 GPa, and ρ = 2,710 kg/m^3; and projectiles are shown in Fig. 4. In addition, the models require the sliding-interface, friction coefficient μ. Bowden and Tabor (1968) discuss laboratory experiments that determine μ at high, sliding velocities. Unfortunately, values of μ were apparatus dependent and varied between μ = 0.10–0.20. Montgomery (1976) measured sliding frictional resistance on projectile rotating bands during field tests of gun launches. Mean pressures on the rotating bands were about 350 MPa (50,000 psi); whereas, pressures for laboratory experiments did not exceed 96 MPa (14,000 psi). Montgomery suggests a high-velocity, friction coefficient of μ = 0.02. Because of the simple expression for frictional resistance (2) and the uncertain values of μ, we present predicted penetration depths for μ = 0.02 and 0.10.

Figure 5 shows final penetration depth versus impact veloci-

[1] Vasco Pacific, 707 West Olympic Blvd., Montebello, CA 90640. T-200 and C-300 have nominal yield stresses of 200 ksi and 300 ksi, respectively.

Downloaded 03 May 2010 to 171.66.16.21. Redistribution subject to ASME license or copyright; see http://www.asme.org/terms/Terms_Use.cfm

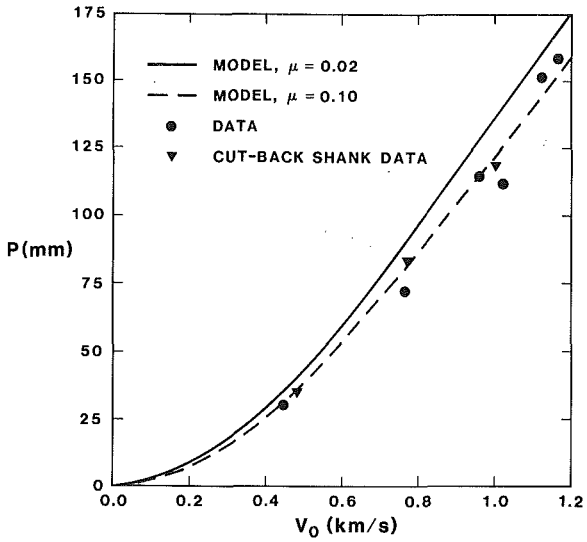

Fig. 5 Depth predictions and measurements versus impact velocity for the spherical nose rods

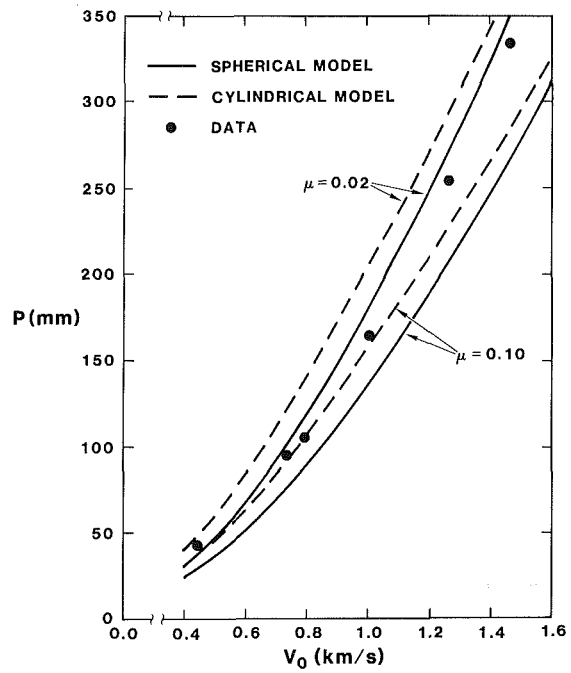

Fig. 6 Depth predictions and measurements versus impact velocity for the ogival nose rods

ty for the spherical nose projectiles shown in Fig. 4(*a*) and 4(*b*). The predictions are not very sensitive to $\mu = 0.02$ or 0.10 for a spherical nose. Also, penetration depths with the cut-back, shank projectile show that possible shank drag is negligible. We also conducted experiments at $V_0 = 1.32$ and 1.57 km/s, but posttest X-ray photographs showed that multiple fractures occurred in the shanks.

Figure 6 shows model predictions and measurements for the 3 CRH, ogival nose projectile shown in Fig. 4(*c*). For a fixed value of friction coefficient, predictions using the cylindrical and spherical, cavity-expansion approximations are in reasonably close agreement. However, unlike the spherical nose predictions, predictions for the ogival nose projectiles are more sensitive to the chosen value of μ.

Figure 7 shows model predictions and measurements for the conical nose projectile shown in Fig 4(*d*) with nose length to

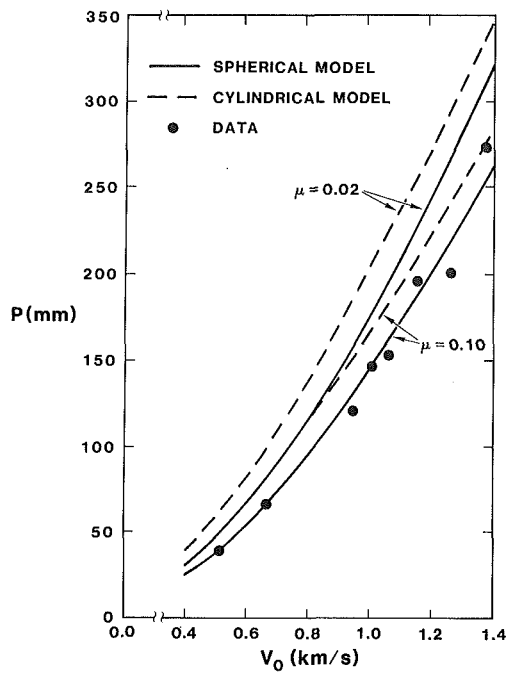

Fig. 7 Depth predictions and measurements versus impact velocity for the conical nose rods

Table 1 Data summary for the C-300 maraging steel, spherical nose rods. Shots 6-1403, 6-1404, and 6-1405 used rods with the cut-back shank.

Shot Number	Mass (*g*)	V_o (km/s)	P (mm)
6-1358	23.3	0.45	30
6-1357	23.3	0.76	72
6-1360	23.3	0.96	115
6-1355	23.3	1.02	112
6-1362	23.3	1.12	152
6-1359	23.3	1.16	159
6-1403	23.7	0.48	36
6-1404	24.0	0.77	84
6-1405	23.7	1.00	119

Table 2 Data summary for the T-200 maraging steel, 3 CRH, ogival nose rods

Shot Number	Mass (*g*)	V_o (km/s)	P (mm)
6-1366	24.9	0.44	44
6-1365	24.9	0.73	94
6-1372	24.7	0.79	105
6-1364	24.7	1.00	163
6-1370	24.7	1.26	253
6-1371	24.8	1.46	333

Table 3 Data summary for the C-300 maraging steel, conical nose rods

Shot Number	Mass (*g*)	V_o (km/s)	P (mm)
6-1342	23.8	0.51	40
6-1329	23.7	0.66	66
6-1344	23.6	0.94	121
6-1334	23.7	1.00	145
6-1564	24.1	1.06	153
6-1561	24.1	1.15	196
6-1336	23.7	1.26	201
6-1353	23.7	1.37	273

diameter ratio, $l/d = 1.5$. Predictions in Fig. 7 exhibit the same trends as those discussed about Fig. 6 for the ogival nose.

In summary, predictions and measurements are in excellent

Downloaded 03 May 2010 to 171.66.16.21. Redistribution subject to ASME license or copyright; see http://www.asme.org/terms/Terms_Use.cfm

agreement for the spherical nose projectiles. For the ogival and conical nose projectiles, predictions are sensitive to the chosen value of μ. However, Figs. 6 and 7 show that predictions are in reasonable agreement with penetration data.

Conclusions

We developed closed-form equations that predicted forces on rigid rods with spherical, ogival, and conical noses that penetrated rate independent, elastic-perfectly plastic targets. To test our models, we conducted terminal-ballistic experiments with maraging steel rods and 6061-T651 aluminum targets for impact velocities between 0.40–1.40 km/s. Predicted and measured final depths of penetration are in excellent agreement for the spherical nose rods. For the ogival and conical nose rods, predictions are in reasonable agreement with the penetration data. Predictions for the ogival and conical nose rods are more sensitive to the high-velocity, friction coefficient than are predictions for the spherical nose rods. Results from Figs. 6 and 7 indicate that a better understanding of interface frictional resistance is required to improve our models.

Acknowledgments

M. J. Forrestal and V. K. Luk were supported by the U. S. Department of Energy. K. Okajima, a visiting scientist at the University of Dayton Research Institute (UDRI), was supported by Mitsubishi Heavy Industries, Ltd. The authors thank Dr. S. J. Bless (UDRI) for many helpful discussions. R. Strong (UDRI) assisted with the experiments.

References

Backman, M. E., and Goldsmith, W., 1978, "The Mechanics of Penetration of Projectiles Into Targets," *International Journal of Engineering Science*, Vol. 16, pp. 1–99.

Bishop, R. F., Hill, R., and Mott, N. F., 1945, "The Theory of Indentation and Hardness Tests," *The Proceedings of the Physical Society*, Vol. 57, Part 3, pp. 147–159.

Bowden, F. P., and Tabor, D., 1968, *The Friction and Lubrication of Solids*, Part 2, Oxford University Press, London, Chap. 22.

Forrestal, M. J., Norwood, F. R., and Longcope, D. B., 1981, "Penetration Into Targets Described by Locked Hydrostats and Shear Strength," *International Journal of Solids and Structures*, Vol. 17, pp. 915–924.

Forrestal, M. J., 1986, "Penetration Into Dry Porous Rock," *International Journal of Solids and Structures*, Vol. 22, No. 12, pp. 1485–1500.

Forestal, M. J., Luk, V. K., 1988, "Dynamic Spherical Cavity-Expansion in a Compressible Elastic-Plastic Solid," ASME JOURNAL OF APPLIED MECHANICS, Vol. 55, pp. 275–279.

Goodier, J. N., 1965, "On the Mechanics of Indentation and Cratering in Solid Targets of Strain-Hardening Metal by Impact of Hard and Soft Spheres," *Proceedings of the 7th Symposium on Hypervelocity Impact*, Vol. III, pp. 215–259.

Hill, R., 1948, "A Theory of Earth Movement Near a Deep Underground Explosion," Memo No. 21-48, Armament Research Establishment, Fort Halstead, Kent, England.

Hill, R., 1950, *The Mathematical Theory of Plasticity*, Oxford University Press, London.

Montgomery, R. S., 1976, "Surface Melting of Rotating Bands," *Wear*, Vol. 38, pp. 235–243.

Rosenberg, Z., and Forrestal, M. J., 1988, "Performance of Aluminum Plates With Conical Nosed Rods—Additional Data and Discussion," ASME JOURNAL OF APPLIED MECHANICS, Vol. 55, pp. 236–238.

Tate, A., 1969, "Further Results in the Theory of Long Rod Penetration," *Journal of the Mechanics and Physics of Solids*, Vol. 17, pp. 141–150.

Wright, T. W., and Frank, K., 1987, "Approaches to Penetration Problems," *SMIRT Symposium*, No. 14, Impact, Lausanne, Switzerland.

Zukas, J. A., 1982, *Impact Dynamics*, Wiley, New York, pp. 202–205.

Downloaded 03 May 2010 to 171.66.16.21. Redistribution subject to ASME license or copyright; see http://www.asme.org/terms/Terms_Use.cfm

Elastic-Plastic Ring-Loaded Cylindrical Shells

Gregory N. Brooks
Assistant Professor.
Department of Engineering Science and Mechanics,
The University of Tennessee,
Knoxville, TN 37996-2030
Assoc. Mem. ASME

The elastic-plastic solution for an infinitely long cylindrical shell with an axisymmetric ring load is presented. Except for the material nonlinearity, the standard assumptions of small deflection shell theory were made. Because the principal directions are known for the axisymmetric problem, the Tresca yield condition was used. This made it possible to obtain closed-form expressions for the elastic-plastic, moment-curvature relations, greatly simplfying the computational task. The actual stress distribution through the thickness was used, making these relations exact. Yielding was contained near the load. Thus, for the analysis the cylinder was divided along its axis into elastic-plastic and purely elastic regions. Solutions were obtained for each region which were then matched at their intersection to give the complete solution. All results are given in dimensionless form so that they may be applied to any shell.

Introduction

The typical pressure vessel is a thin-walled shell of revolution. It is well known that the stress in such a vessel is essentially given by the membrane solution except in the vicinity of stiffening rings, or any other geometric discontinuity, where additional bending stresses occur. A purely elastic design for a vessel made of a ductile material is generally overly conservative. Plastic limit analysis, such as detailed in Hodge (1959, 1963), is useful but does not give any information about residual stresses or about the strains present. Moderately ductile materials may fail before the load predicted by limit analysis.

As a section of a shell becomes plastic, generally one of the surfaces yields first. Then, as the load is increased, the plastic zone spreads through the thickness and the other surface may also begin to yield. To avoid the difficulty of accurately considering the elastic-plastic behavior through the thickness, early investigators, such as Hodge (1963), used approximations to the yield surface in terms of shell stress resultants for rotationally symmetric shells. It was assumed that the entire shell section yields simultaneously, producing an elastic-perfectly plastic relationship between the shell strain measures, that is the curvatures and midsurface strains, and the stress resultants. This is sometimes referred to as the "sandwich" shell approximation since it is similar to the behavior of an idealized shell made of two thin layers of material separated by a constant distance. The yield condition is then a function of the stress resultants of the shell. This is much simpler than considering the state of stress at each material point through the thickness. Hodge also developed a two-moment limited interaction yield condition by neglecting the interaction between orthogonal forces and between orthogonal moments. This approximate yield condition has been used to study plate (Lance and Onat, 1962) and shell (Leckie, 1965) problems.

Brooks (1982) developed a computationally efficient method of elastic-plastic analysis of axisymmetric shell problems that does not depend on approximate yield conditions of the type discussed above. The evolving state of stress and strain through the thickness was taken into account. The Tresca yield condition was used because for axisymmetric problems the principal directions are known and unchanging. Also, it is shown in a following section that for plane stress, with some modest restrictions, the current state of stress can be found as a function of the current applied strains. Assuming that the shell is in a state of plane stress and that the Kirchhoff-Love hypothesis is valid, this solution was integrated through the thickness to give relationships between the total strains and stress resultants. These elastic-plastic constitutive relations were combined with the standard equilibrium and strain-displacement equations of small deflection shell theory to give a complete, computationally efficient description of the elastic-plastic cylinder. The method is applied here to the problem of the ring-loaded, infinitely long cylinder shown in Fig. 1.

All of the equations in this paper are in terms of modified dimensionless quantities. These variables are introduced in the text in the format of the variable followed by brackets containing the parameters which give the variable its standard dimensional definition.

Elastic Solution

The elastic solution of the ring load problem is well known (see Krauss, 1967, or Seide, 1975). Due to symmetry only the region $x \leq 0$ need be considered. The axial and hoop mem-

Contributed by the Applied Mechanics Division of THE AMERICAN SOCIETY OF MECHANICAL ENGINEERS for presentation at the Joint ASCE/ASME Applied Mechanics, Biomechanics, and Fluids Engineering Conference, San Diego, CA, July 9 to 12, 1989.

Discussion of this paper should be addressed to the Editorial Department, ASME, United Engineering Center, 345 East 47th Street, New York, N.Y. 10017, and will be accepted until two months after final publication of the paper itself in the JOURNAL OF APPLIED MECHANICS. Manuscript received by ASME Applied Mechanics Division, September 15, 1987; final revision, May 28, 1988.

Paper No. 89-APM-20.

Copyright © 1988 by ASME
Downloaded 03 May 2010 to 171.66.16.21. Redistribution subject to ASME license or copyright; see http://www.asme.org/terms/Terms_Use.cfm

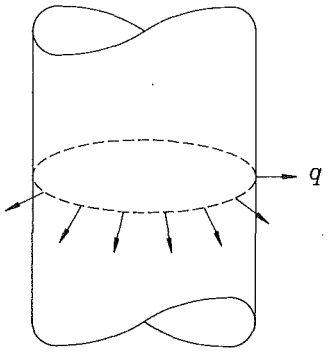

Fig. 1 Infinite cylindrical shell with circumferential line load

brane resultants, N_a and N_h, and the bending stress resultants, M_a and M_h, are

$$N_a = 0 \tag{1}$$

$$N_h = q\sqrt{3(1-\nu^2)}e^x(\cos x - \sin x)/8 \tag{2}$$

$$M_a = qe^x(\cos x + \sin x)/4 \tag{3}$$

$$M_h = \nu M_a. \tag{4}$$

The resultants have been made dimensionless through division by their ultimate fully plastic values. Thus their dimensional values are $N[Yt]$ and $M[Yt^2/4]$, where Y is the yield stress and t the shell thickness. The dimensional axial position is $x[\sqrt{2Rc}\,]$ where R is the radius of the cylinder and $c = t/\sqrt{12(1-\nu^2)}$. The ring load is $q[Yt\sqrt{6c(1-\nu^2)}/4\sqrt{R}]$.

The surface stresses $\sigma[Y]$ are obtained from the formula $\sigma = N \pm 3M/2$. They are plotted in Fig. 2 for $\nu = 0.3$. The highest effective Tresca stress is on the inner surface for all values of ν less than 0.5. For $\nu = 0.5$ both surfaces reach yield simultaneously. The value of the elastic limit load is

$$q_{el} = 8\{\sqrt{3(1-\nu^2)} + 3(1-\nu)\}^{-1}. \tag{5}$$

The horizontal (or radial) displacement $h[YR\sqrt{3(1-\nu^2)}/2E]$ at the ring load is $h = q/4$.

Elastic-Plastic Moment Curvature Relations

The Tresca yield surface for plane stress is defined by $\max(|\sigma_1|, |\sigma_2|, |\sigma_1 - \sigma_2|) = 1$, which gives the well-known, six-sided yield surface (Kachanov, 1974). The subscripts 1 and 2 refer to the principal directions. If the stress state of the yielding material stays on the same side of the yield surface, the plane stress problem can be integrated to give the current stresses as a function of the current strains. The case for yielding by the condition $\sigma_1 - \sigma_2 = 1$ is given next; see Brooks (1982) for the general case.

Combining this elastic-plastic plane stress solution with the assumed linear strain variation gives the stress distribution through the shell. Moment-curvature relations are obtained, in closed-form, by integrating the stresses through the thickness. The effect of transverse shear upon the yield condition is ignored. This is certainly valid initially, since the transverse shear stress is zero at the surfaces of the shell. Because the transverse shear stress generally is much less than the in-plane stresses and is largest near the middle while the yielding occurs near the shell surfaces, this assumption should be reasonable well beyond the elastic limit. This procedure is analogous to what is done to calculate the elastic relationships.

Plane Stress Solution. Consider the problem where all yielding occurs under the condition $\sigma_1 - \sigma_2 = 1$. Let $\epsilon_1[Y/E]$ and $\epsilon_2[Y/E]$ be the true principal strains. Although the true strains are dimensionless by definition, Y/E is a "characteristic" strain for elastic-plastic problems that would appear as a parameter in the equations involving the strains if

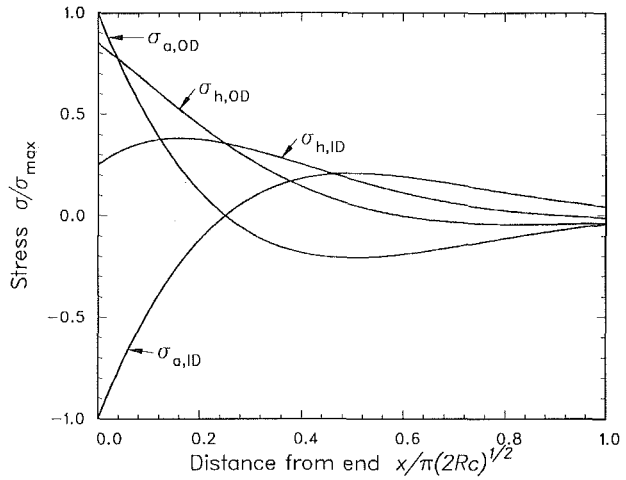

Fig. 2 Hoop and axial stresses on inner and outer diameters of an elastic cylinder with a ring load

not incorporated into the "dimensionless" strain. As the strains increase eventually the material yields, with ϵ_{1_Y} and ϵ_{2_Y} being the values of the principal strains at initial yield. Since the elastic-strain law is still valid at this instant, the yield condition may be expressed as

$$\sigma_1 - \sigma_2 = \frac{1}{1-\nu^2}\left[(\epsilon_{1_Y} + \nu\epsilon_{2_Y}) - (\epsilon_{2_Y} + \nu\epsilon_{1_Y})\right] = 1 \tag{6}$$

or

$$\epsilon_{1_Y} - \epsilon_{2_Y} = (1+\nu). \tag{7}$$

The associated flow rule for the Tresca yield condition (Kachanov, 1974) gives the plastic strain increments

$$d\epsilon_1^p = -d\epsilon_2^p \equiv d\epsilon^p. \tag{8}$$

Since the total strain increments are the sum of the elastic and plastic components (i.e., $d\epsilon_i = d\epsilon_i^e + d\epsilon_i^p$), the incremental stress-strain law gives

$$d\sigma_1 = \frac{d\epsilon_1^e + \nu d\epsilon_2^e}{1-\nu^2} = \frac{d\epsilon_1 - d\epsilon^p + \nu(d\epsilon_2 + d\epsilon^p)}{1-\nu^2}. \tag{9}$$

The expression for $d\sigma_2$ is analogous.

For perfect plasticity $d\sigma_1 - d\sigma_2 = 0$ so that the stress state remains on the yield surface. Substituting the expressions for $d\sigma_1$ and $d\sigma_2$ into this condition gives the plastic strain increment $d\epsilon^p$ in terms of the principal strains:

$$d\epsilon^p = (d\epsilon_1 - d\epsilon_2)/2. \tag{10}$$

Substituting this into (9) and integrating from initial yield (7) to the current state gives σ_1 as a function of the current applied strains. The yield condition (6) then gives σ_2.

$$\sigma_1 = \frac{1}{2(1-\nu)}(\epsilon_1 + \epsilon_2) + \frac{1}{2} \tag{11}$$

$$\sigma_2 = \frac{1}{2(1-\nu)}(\epsilon_1 + \epsilon_2) - \frac{1}{2} \tag{12}$$

For satisfaction of the yield condition with $\sigma_1 = \pm 1$, the same method (Brooks (1982), (1987)) gives

$$\sigma_1 = \pm 1 \tag{13}$$

$$\sigma_2 = \pm 1 + \epsilon_2 \tag{14}$$

The stress is a linear function of the strain after yielding initiates. Since the strain is assumed to vary linearly through the thickness, the stress will vary in a piecewise linear fashion.

Integration into Moment-Curvature Relation. Yielding initiates under the ring load on the inner surface when

Downloaded 03 May 2010 to 171.66.16.21. Redistribution subject to ASME license or copyright; see http://www.asme.org/terms/Terms_Use.cfm

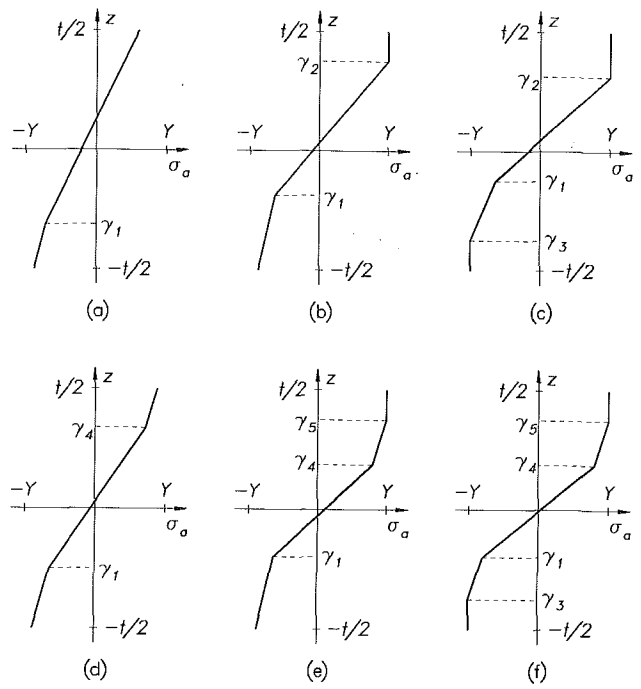

Fig. 3 Axial stress profiles used for elastic-plastic cylinder with ring load: (a) inside yields by $\sigma_h - \sigma_a = Y$; (b) inside by $\sigma_h - \sigma_a = Y$; outside by $\sigma_a = Y$; (c) inside by $\sigma_h - \sigma_a = Y$ or at corner $\sigma_h = 0$, $\sigma_a = -Y$; outside by $\sigma_a = Y$; (d) inside by $\sigma_h - \sigma_a = Y$; outside by $\sigma_h = Y$; (e) inside by $\sigma_h - \sigma_a = Y$; outside by $\sigma_h = Y$ or at corner $\sigma_h = \sigma_a = Y$; (f) inside by $\sigma_h - \sigma_a = Y$ or at corner; outside by $\sigma_h = Y$ or at corner

$\sigma_h - \sigma_a = 1$. It was found that yielding at all positions along the axis started on the inside by this condition. Thus the axial stress profile immediately after yielding begins looks like that in Fig. 3(*a*). The distance from the midsurface is $z[t/2]$, with $z = 1$ at the outer surface and $z = -1$ at the inside. There is a plastic region near the inside while the rest of the cross section remains elastic. This gives the bilinear stress distribution shown. The relations between the stress resultants and the shell strain measures (the axial and hoop midsurface strains $e_a[Y/E]$ and $e_h[Y/E]$, and the axial curvature $\kappa[3Y(1-\nu^2)2Et]$) are

$$M_a = \left[\frac{e_a - e_h}{4(1+\nu)} + \frac{1}{4}\right](1-\gamma_1^2) + (3+\nu-(1-\nu)\gamma_1^3)\frac{\kappa}{8} \tag{15}$$

$$N_h = \frac{1+\gamma_1}{4} + \frac{e_h}{4(1-\nu^2)}(3+\nu-(1-\nu)\gamma_1) + \frac{e_a(1+3\nu+(1-\nu)\gamma_1)}{4(1-\nu^2)} + \frac{3(1-\nu)(\gamma_1^2-1)}{32}\kappa \tag{16}$$

where γ_1 is the value of z at the elastic-plastic boundary

$$\gamma_1 = \frac{4(e_h - e_a - 1 - \nu)}{3(1-\nu^2)\kappa}. \tag{17}$$

The axial midsurface strain can be determined as a function of the hoop strain and curvature from the equilibrium condition $N_a = 0$:

$$e_a = e_h - (1+\nu)\left\{\frac{3(3+\nu)\kappa}{4} + 1 - \sqrt{\frac{9(1+\nu)}{2}\kappa^2 + 6\kappa - 6e_h\kappa}\right\}. \tag{18}$$

As the load increases the outer diameter begins to yield when $\sigma_a = 1$. Plasticity on the inside is still by $\sigma_a - \sigma_h = 1$. Figure 3(*b*) shows the axial stress profile for this situation. For this case the stress resultants are

$$M_a = (\gamma_1^2 + \gamma_1\gamma_2 + \gamma_2^2 - 3)\left\{\frac{e_a + e_h}{12(1-\nu)} - \frac{1}{4}\right\} + \frac{(1+\nu)\kappa}{16}(\gamma_1^2\gamma_2 + \gamma_1\gamma_2^2 + 2) \tag{19}$$

$$N_h = \frac{e_h + e_a + 3(1-\nu^2)(\gamma_1 - 1)\kappa/8}{4(1-\nu)} + \frac{2e_h + 1 + 2\nu}{4} + \frac{\gamma_2}{8}\left(\frac{e_h + e_a + 3(1-\nu^2)\gamma_1\kappa/4}{(1-\nu)} - 2e_h + 1 - 2\nu\right) + \frac{\gamma_1}{8}\left(\frac{e_h + e_a - 3(1-\nu^2)\kappa/4}{(1-\nu)} - 2e_h + 1 - 2\nu\right) \tag{20}$$

where γ_1 is given above and

$$\gamma_2 = \frac{4(1-\nu^2 - e_a - \nu e_h)}{3(1-\nu^2)\kappa} \tag{21}$$

$$e_a = 3(1-\nu) + 3(1-\nu^2)\kappa/4 - e_h - \{2(1-\nu)[e_h^2 + (2-\nu)^2 + 3(1-\nu^2)\kappa - 2(2-\nu)e_h]\}^{1/2} \tag{22}$$

Eventually the stress state of the material on the inside reaches the corner of the yield surface where $\sigma_a = -1$ and $\sigma_h = 0$. The axial stress profile is as shown in Fig. 3(*c*).

$$M_a = \frac{6 - 2\gamma_1^2 - \gamma_2^2 - \gamma_3^2 - \gamma_1\gamma_2 - \gamma_1\gamma_3}{6} + \left(e_a + \nu e_h + \frac{3(1-\nu^2)}{4}\gamma_1\kappa\right)\frac{\gamma_2^2 + \gamma_1\gamma_2 - \gamma_1\gamma_3 - \gamma_3^3}{6(1-\nu^2)} \tag{23}$$

$$N_h = \frac{\nu + e_h}{4}(2 - \gamma_2 - \gamma_3) + \left[\frac{e_h + e_a + 3(1-\nu^2)\gamma_1\kappa/4}{(1-\nu)} + 1\right]\frac{\gamma_2 - \gamma_3}{8} \tag{24}$$

where γ_1 and γ_2 are given above and

$$\gamma_3 = -\frac{4(1 - \nu + e_a + e_h)}{3(1-\nu^2)\kappa} \tag{25}$$

$$e_a = -\frac{(e_h + \nu)^2}{4} \tag{26}$$

At locations far enough away from the load the outer surface yields when $\sigma_h = 1$ rather than $\sigma_a = 1$ because the hoop strain decays slower than the axial strain with distance from the load. The inside always yields first and always initially by $\sigma_h - \sigma_a = 1$. Figure 3(*d*) shows the axial stress profile for this case. The moment-curvature relation becomes

$$M_a = \left[\frac{e_a + e_h - 3(1-\nu^2)\kappa/4}{(1-\nu)} - 1\right]\left[\frac{\gamma_1^2 - \gamma_1 - 2}{12}\right] + \left\{\frac{e_a + e_h + 3(1-\nu^2)\gamma_1\kappa/4}{(1-\nu)} - 1\right\}\left\{\frac{\gamma_4^2 + \gamma_1\gamma_4 + \gamma_1 - 1}{12}\right\} + \left(e_a + \nu + \frac{3(1-\nu^2)\kappa\gamma_4}{4}\right)\left(\frac{1 + \gamma_4 - \gamma_1\gamma_4 - \gamma_1^2}{6}\right) + \left(e_a + \nu + \frac{3(1-\nu^2)\kappa}{4}\right)\left(\frac{2 - \gamma_4 - \gamma_4^2}{6}\right) \tag{27}$$

$$N_h = \frac{6 - \gamma_4 - \gamma_1}{8} + \frac{e_a + e_h}{8(1-\nu)}(2 + \gamma_1 + \gamma_4) + \frac{3(1+\nu)\kappa}{32}(\gamma_1\gamma_4 - 1) \tag{28}$$

where γ_1 is given above and

Downloaded 03 May 2010 to 171.66.16.21. Redistribution subject to ASME license or copyright; see http://www.asme.org/terms/Terms_Use.cfm

$$\gamma_4 = \frac{4(1-\nu^2-\nu e_a - e_h)}{3\nu(1-\nu^2)\kappa} \quad (29)$$

When the yield corner $\sigma_h = \sigma_a = 1$ has been reached on the outside, but the inside is not yet at the corner (Fig. 3(*e*)) the relationships are

$$M_a = \frac{3-\gamma_4^2-\gamma_4\gamma_5-\gamma_5^2}{6} + \left(\frac{e_a+e_h-3(1-\nu^2)\kappa/4}{(1-\nu)}-1\right)\left(\frac{\gamma_1^2-\gamma_1-2}{12}\right) + \left(\frac{e_a+e_h-3(1-\nu^2)\kappa\gamma_1/4}{(1-\nu)}-1\right)\left(\frac{\gamma_4^2+\gamma_4\gamma_1+\gamma_1-1}{12}\right) + \left(e_a+\frac{3(1-\nu^2)\kappa\gamma_4}{4}\nu\right)\left(\frac{\gamma_5^2+\gamma_5\gamma_4-\gamma_4\gamma_1-\gamma_1^2}{6}\right) \quad (30)$$

$$N_h = \frac{1-\gamma_4}{2} + \frac{\gamma_4-\gamma_1}{8}\left[\frac{e_a+e_h+3(1-\nu^2)\kappa\gamma_1/4}{(1-\nu)}+3\right] + \frac{\gamma_1+1}{4}\left[\frac{e_a+e_h+3(1-\nu^2)(\gamma_1-1)\kappa/8}{(1-\nu)}+1\right] \quad (31)$$

where γ_1 and γ_4 are above and

$$\gamma_5 = \frac{4(1-\nu-e_a)}{3(1-\nu^2)\kappa} \quad (32)$$

$$e_a = 3(1-\nu)+3(1-\nu^2)\kappa/4 - e_h - \{2(1-\nu)[3-2\nu+3(1-\nu^2)\kappa-2e_h]\}^{1/2}. \quad (33)$$

Finally, when both the inside and outside have reached their respective yield corners the axial stress profile is as in Fig. 3(*f*). This gives

$$M_a = \frac{6-\gamma_1^2-\gamma_3^2-\gamma_4^2-\gamma_5^2-\gamma_1\gamma_3-\gamma_4\gamma_5}{6} + \left[\frac{e_a+e_h+3(1-\nu^2)\kappa\gamma_1/4}{(1-\nu)}-1\right] \times \left[\frac{\gamma_4^2+\gamma_1\gamma_4-\gamma_1\gamma_3-\gamma_3^2}{12}\right] + \left(e_a+\frac{3(1-\nu^2)\kappa\gamma_4}{4}+\nu\right)\left(\frac{\gamma_5^2+\gamma_5\gamma_4-\gamma_4\gamma_1-\gamma_1^2}{6}\right) \quad (34)$$

$$N_h = \frac{2-\gamma_1-\gamma_3}{4} + \frac{\gamma_4-\gamma_3}{8}\left[\frac{e_a+e_h+3(1-\nu^2)\kappa\gamma_1/4}{(1-\nu)}-1\right] \quad (35)$$

where

$$e_a = (1-2\nu-2e_h)/4. \quad (35)$$

For the general axisymmetric shell, there are many other possible stress states through the thickness. These were the only ones necessary for this problem. It was not possible to invert these relationships to give the curvature in terms of the stress resultants, as it was for the clamped-end, pressurized cylinder (Brooks, 1987). Nevertheless, having the closed-form expressions results in a more efficient computational procedure.

Solution Procedure

The stresses peak sharply near the ring load. Since the load is self-equilibrating, the plasticity is localized near the load. For the analysis, the cylinder is divided into a semi-infinite region that is completely elastic and the region near the load where the shell is yielding. The boundary between the regions was defined to be $x=0$. The length of the plastic zone $\Delta[\sqrt{2Rc}]$ is an unknown. Each section is analyzed independently and the displacement and stress resultants are matched at their intersection. This is similar to the approach of Steele (1968) for the analysis of axisymmetric shells with a bilinear moment-curvature relationship.

The remaining equations needed to describe the shell are: the equilibrium equations

$$\frac{dH}{dx} = \frac{4}{\sqrt{3(1-\nu^2)}} N_h \quad (36)$$

$$\frac{dM_a}{dx} = H \quad (37)$$

where $H[Yt\sqrt{6c(1-\nu^2)}/4\sqrt{R}]$ is the transverse shear, and the strain-displacement relations

$$e_h = h\sqrt{3(1-\nu^2)}/2 \quad (38)$$

$$\chi = -\frac{dh}{dx} \quad (39)$$

$$\kappa = \frac{d\chi}{dx}. \quad (40)$$

It was found that yielding at any axial position always initiated on the inside by the condition $\sigma_h - \sigma_a = 1$. Setting $\gamma_1 = -1$ in (17) and substituting into the moment-curvature relation (15) gives the moment at the intersection of the elastic and plastic regions.

$$M(0) = \frac{2}{3(1-\nu)}[1-e_h(0)]. \quad (41)$$

To make the problem better conditioned when near the limit load, the deflection was prescribed at the ring load rather than the load itself. The first step of the solution procedure is to estimate the radial deflection $h(0)$, and thus $e_h(0)$ by (38), in order to find $M(0)$. The elastic solution gives the remaining quantities of interest at $x=0$.

$$\chi(0) = M(0) - h(0) \quad (42)$$

$$\kappa(0) = 2M(0) \quad (43)$$

$$H(0) = M(0) + h(0) \quad (44)$$

$$N_h(0) = e_h(0). \quad (45)$$

These values are then used as the initial values for the integrations through the plastic zone. Starting at $x=0$, the elastic-plastic boundary, (36)–(40) are integrated, with the appropriate constitutive relation, until $\chi=0$. If h is not equal to the imposed displacement under the load, the estimate of $h(0)$ is changed and the integration repeated until the solution has converged.

Taking increments in x for the numerical integration requires an iteration on the moment-curvature relations after each step to determine the new value of the curvature. To avoid this, increments in κ, which varies monotically in the plastic zone, were taken instead. The new κ plus an estimate of the new e_h were substituted into the constitutive equations to give the values of the stress resultants at the end of the increment. Then the corresponding increment in x was calculated from the equilibrium equations (36), (37). If the value of e_h calculated from (38)–(39) differed much from the estimate used in the constitutive relations, then the estimate was updated and the calculations repeated. This procedure is much more efficient than the more "straightforward" approach of using increments in x.

Because the moment-curvature relations were between the total strains and stress resultants, rather than between increments as usually is the case for elastic-plastic problems, the solution technique was like that for a nonlinear elastic problem. It was not necessary to follow the solution incremen-

Downloaded 03 May 2010 to 171.66.16.21. Redistribution subject to ASME license or copyright; see http://www.asme.org/terms/Terms_Use.cfm

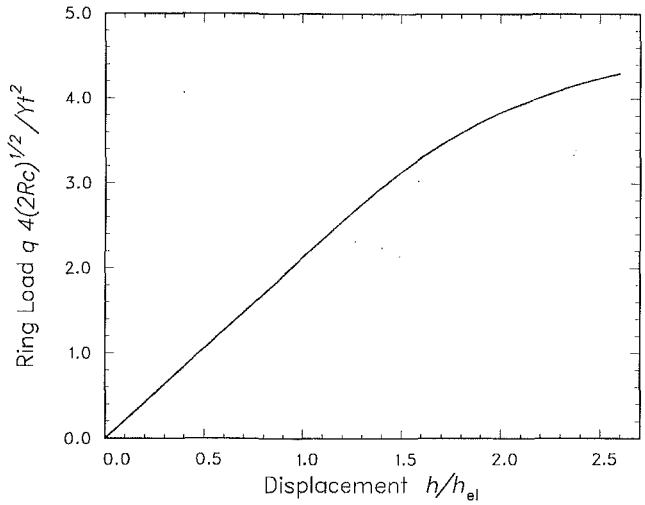

Fig. 4 Magnitude of circumferential line load causing the imposed ring displacement for an elastic-perfectly plastic cylinder

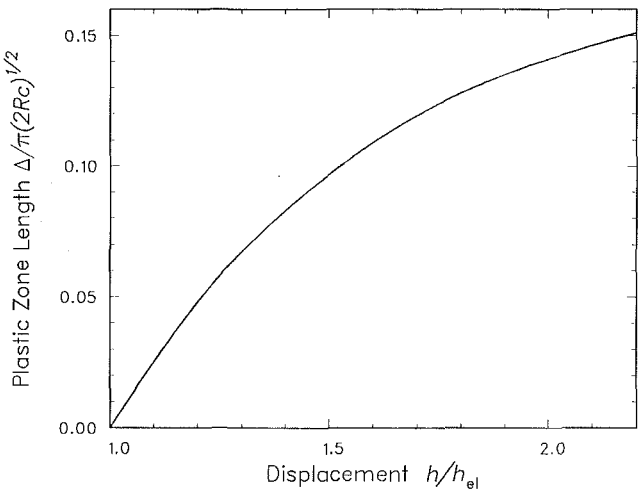

Fig. 7 Growth of the plastic zone

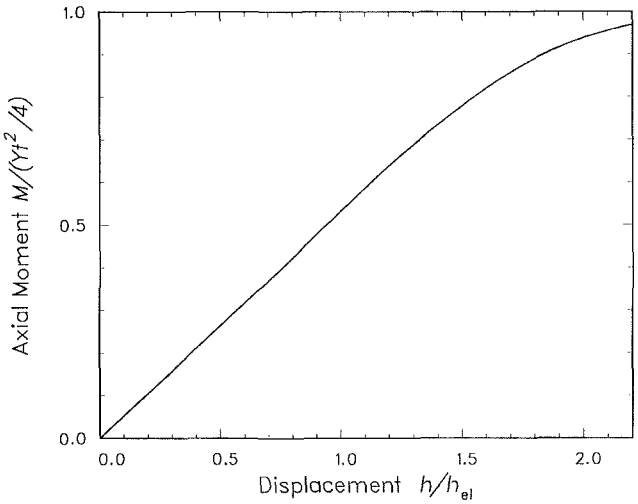

Fig. 5 Axial moment resultant under load

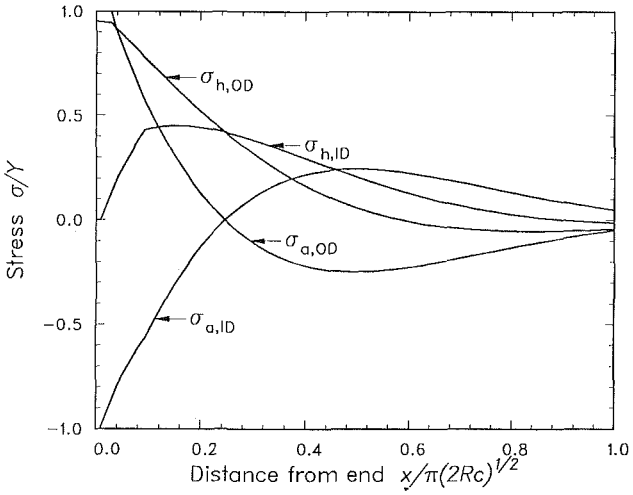

Fig. 8 Axial and hoop stresses on the inner and outer diameters when the ring displacement is 1.5 times that which causes initial yield

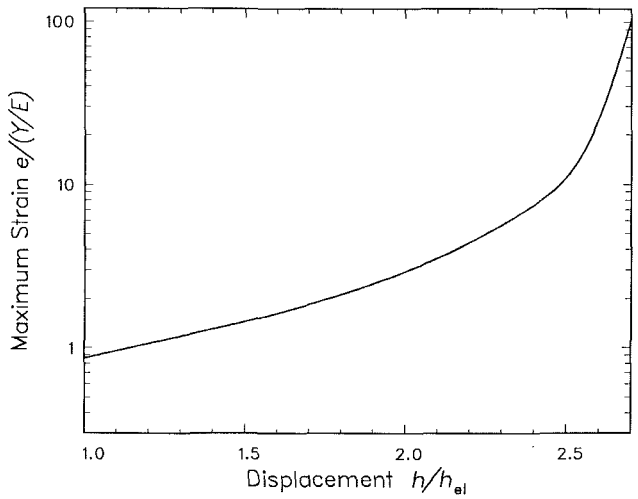

Fig. 6 Axial strain under the circumferential line load on the inner diameter of the cylinder. This is the maximum principal strain.

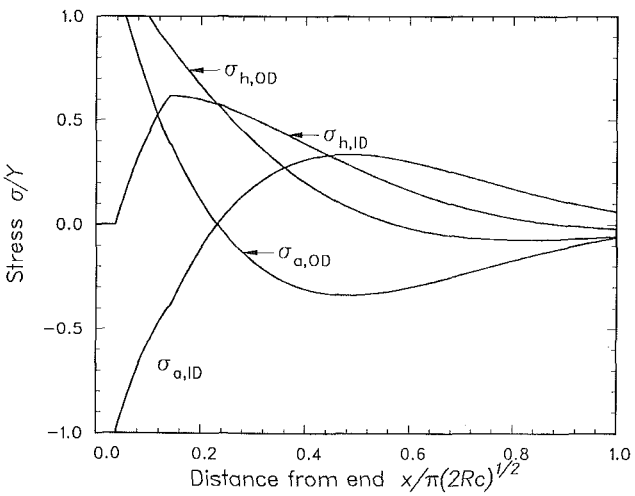

Fig. 9 Axial and hoop stresses on the inner and outer diameters when the ring displacement is twice that which causes initial yield

tally. Any value of the load could be prescribed and the solution found. However, the validity of the moment-curvature relations does depend on the yielding material following an assumed loading path. So calculations were performed for many values of the load to insure that the assumed strain paths were being followed.

Downloaded 03 May 2010 to 171.66.16.21. Redistribution subject to ASME license or copyright; see http://www.asme.org/terms/Terms_Use.cfm

Results

Figures 4 through 9 show the calculation results. Poisson's ratio was set to 0.3 for this analysis.

The magnitude of the ring load as a function of the displacement is given in Fig. 4. The relationship is quite linear well beyond the elastic limit. This is because the plastic zone is short and initially most of the cross-section is not yielding. Figure 5 shows the axial moment under the load, which is also the maximum moment in the cylinder. It was close to the fully plastic value when the calculations were stopped.

The maximum strain component in the cylinder is the axial strain on the inner surface under the point of application of the load. Its variation with increasing displacement is shown in Fig. 6. As with the case of the pressurized cylinder (Brooks, 1987), most materials could withstand loading significantly beyond the elastic limit. The calculations were stopped when the strain growth, with increasing load, became so large as to cause numerical difficulties. Since the strain was two orders of magnitude greater than the yield strain at this point anyway, it seemed like a reasonable place to stop.

Upper and lower bounds from limit analysis for this problem are given in Prager (1959). The load at which computations were stopped happens to be the calculated lower bound. From Fig. 4 it is clear that there is additional load carrying capacity if the material has no strain limit. However, Fig. 6 indicates that many real materials probably could not withstand higher loading. An estimate of a maximum ring load of 5 would seem reasonable by inspection of Fig. 4. This would still fall below the upper bounds given in Prager (1959). Thus the results are consistent with those of limit analysis.

The growth of the plastic zone with load is plotted in Fig. 7. Plasticity is very localized near the ring load, as would be expected by Saint Venat's principle. This means that this analysis is valid for any cylinder long enough to be considered infinite in the elastic case. The movement of the boundaries between the elastic and yielded regions through the thickness and between the various yield conditions was also checked to verify that the assumptions made in the analysis were valid (Brooks, 1982).

Figures 8 and 9 give the axial and hoop surface stresses as a function of distance from the load for imposed ring displacements of 1.5 and twice the elastic limit displacement. The effect of the different yield conditions on the stress components can be seen.

Discussion

Since the results are all given in dimensionless form they can be applied to any cylindrical shell satisfying the assumptions. The numerical solution of the equations can be considered exact, given the standard shell assumptions which were made. The method was so inexpensive that thousands of points were used in the numerical integration through the plastic zone. Thus, these results could be useful for comparison against other numerical methods. The one complication would be that most general methods use the Mises yield condition rather than Tresca, as was used here.

Acknowledgments

The author would like to thank his Ph.D. advisor, Charles R. Steele, for his guidance and encouragement during the time this research was being done. The support of the National Science Foundation with a Graduate Fellowship while the author was a graduate student at Stanford University, and subsequently with grant MEA-8404055, has made this work possible.

References

Brook, G. N., 1982, "Plastic Boundary Layers and Part-Through Cracks in Shells," Ph.D. Thesis, Stanford University, Stanford, CA.

Brooks, G. N., 1987, "Elastic-Plastic Analysis of Pressurized Cylindrical Shells," ASME JOURNAL OF APPLIED MECHANICS, Vol. 54, pp. 597–603.

Hodge, Jr., P. G., 1963, *Limit Analysis of Rotationally Symmetric Plates and Shells*, Prentice-Hall, Englewood Cliffs, N.J.

Hodge, Jr., P. G., 1959, *Plastic Analysis of Structures*, McGraw-Hill, New York.

Kachanov, L. M., 1974, *Fundamentals of the Theory of Plasticity*, Mir Publishers, Moscow.

Krauss, H., 1967, *Thin Elastic Shells*, Wiley, New York.

Lance, R. H., and Onat, E. T., 1962, "A Comparison of Experiments and Theory in the Plastic Bending of Circular Plates," *Journal of the Mechanics and Physics of Solids*, Vol. 10, pp. 301–311.

Leckie, F. A., 1965, "The Plastic Analysis of a Spherical Shell Subjected to a Radial Load Applied Through Rigid Boss," Brown University Report, NSF-GP-1115/23.

Prager, W., 1959, An Introduction of Plasticity, Addison-Wesley Publishing Company, pp. 72–76.

Seide, P., 1975, *Small Elastic Deformations of Thin Shells*, Noordhoff International Publishing, Holland.

Steele, C. R., 1968, "Pressure Vessels with Edge Zone Yielding," *Int. J. Solids and Structures*, Vol. 4, pp. 777–785.

Timoshenko, S. P., 1970, *Theory of Elasticity*, McGraw-Hill, New York.

Downloaded 03 May 2010 to 171.66.16.21. Redistribution subject to ASME license or copyright; see http://www.asme.org/terms/Terms_Use.cfm

Material Compatibility in Interfacial Transient Thermal Fracture of Ceramic-to-Metal Bonds

Klod Kokini

Purdue University,
School of Mechanical Engineering,
West Lafayette, IN 47907

The effect of changing thermal expansion coefficients and thermal properties on the deformations and strain energy release rates of cracks at the interface between a ceramic-to-metal bond subjected to a transient thermal load is examined. The configurations of a two-dimensional edge and center through-cracks are analyzed. The effects of the thickness of the ceramic are considered. The results show that equating the thermal expansion coefficients of the two materials can lead to an increase in the strain energy release rate. A simple two-bar model is used to provide a qualitative explanation for the results.

1 Introduction

Ceramic materials bonded to metal substrates are being developed for high temperature applications where the temperature fluctuates between two extremes. Examples of such applications are ceramic coated parts in heat engines, gas turbines, and ceramic-to-metal bonds in microelectronics.

During heating and cooling, these structures are subjected to transient thermal loads which result in large stresses especially in the interface region between the ceramic and the metal (Fisher, 1984; Hartsock and McLean, 1984). In the case of ceramic thermal barrier coatings, the cracking in the interfacial region leads to debonding and spalling of the coating (Berndt and Miller, 1984). Most of the studies that considered this problem have been in the form of cyclic thermal shock testing. A summary of such studies is given by Liebert and Miller (1984).

The application of fracture mechanics principles provides a fundamental understanding of the effect of a transient thermal load. Until recently, the result of a temperature change on an interfacial crack was analyzed mostly for a steady-state temperature excursion. An exact solution of the problem was obtained by Erdogan (1965) and applied to material compatibility by Suga and Elssner (1986). More recently, Charreyon et al. (1986, 1987) have analyzed such effects for ceramic-to-metal bonds. The problem of an interface penny-shaped crack subjected to a steady heat flux has been considered by Barber and Comninou (1982, 1983) and Martin-Moran et al. (1983).

The problem of a transient thermal load acting on an interfacial crack between a ceramic-to-metal bond has been analyzed by Kokini (1987). The configuration studied is shown in Fig. 1. It was determined that the transient strain energy release rate G due to such a load would be significantly different for edge and center cracks. For the former, under slow cooling conditions, the maximum G occurred at steady-state, while for the latter, a transient maximum G was obtained which would govern the failure behavior by being larger than the steady-state value. The other important difference between an edge and center crack was determined to result from the thickness ratio of the ceramic-to-metal bond. For the edge-cracked structure the largest G occurred when the thicknesses of the ceramic and metal were equal. It was therefore concluded that a thinner coating at the edge would be more resistant to failure than a layer of equal thickness. For a center crack, however, the results showed that the smallest G occurred when the ceramic had an equal thickness to the metal. A subsequent study by Kokini (1987) examined the effect of thermal and mechanical boundary conditions on the interfacial thermal fracture of ceramic-to-metal bonds.

When uniform thermal excursions are considered, the ther-

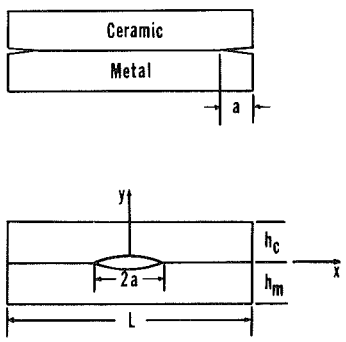

Fig. 1 Model of ceramic-to-metal bond with edge and center cracks

Contributed by the Applied Mechanics Division for presentation at the Winter Annual Meeting, Chicago, IL, November 28 to December 2, 1988, of THE AMERICAN SOCIETY OF MECHANICAL ENGINEERS.

Discussion on this paper should be addressed to the Editorial Department, ASME, United Engineering Center, 345 East 47th Street, New York, N.Y. 10017, and will be accepted until two months after final publication of the paper itself in the JOURNAL OF APPLIED MECHANICS. Manuscript received by ASME Applied Mechanics Division, July 24, 1987; final revision, February 15, 1988.

Paper No. 88-WA/APM-54.

Copyright © 1988 by ASME

Downloaded 03 May 2010 to 171.66.16.21. Redistribution subject to ASME license or copyright; see http://www.asme.org/terms/Terms_Use.cfm

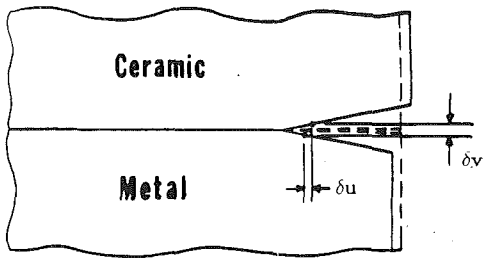

Fig. 2 Schematic representation of the deformation of the crack faces

mal stresses in two dissimilar bonded materials are reduced as the thermal expansion coefficient mismatch is reduced. In this paper, the effect of varying the thermal expansion coefficients of the ceramic and the metal, on the transient strain energy release rate resulting from transient cooling is examined. Similarly, since in the case of a center crack, the largest G corresponded to a transient maximum, this indicated that thermal properties (thermal conductivity, density, and specific heat) should also play an important role in reducing this transient G. Consequently, the effect of changing thermal properties on G is also examined.

A simple uniaxial model is used to explain the behavior of the strain energy release rate as the thermal expansion properties are changed.

Finally, it should be mentioned that while this study considers a ceramic-to-metal bond, the general results apply to any bonded dissimilar material system with similar properties.

2 Theoretical Model

The problem analyzed is schematically shown in Fig. 1. The materials considered are zirconia (ZrO_2) and nodular cast iron. The properties of the materials are listed in the Appendix.

The entire structure shown is initially at a uniform temperature T_0. The ceramic surface is then subjected to a convective cooling while the metal surface is insulated. It is assumed that the crack surfaces do not conduct any heat, thus creating a temperature discontinuity across the crack faces. The equations that govern this heat transfer process are as follows:

In the ceramic

$$k_c \nabla^2 T = \rho_c C_c \frac{\partial T}{\partial t} \tag{1}$$

In the metal

$$k_m \nabla^2 T = \rho_m C_m \frac{\partial T}{\partial t} \tag{2}$$

The initial condition is

$$T(x,y,0) = T_0 \tag{3}$$

The boundary conditions are:

$$k_c \frac{\partial T(x,h_c,t)}{\partial y} = h[T(x,h_c,t) - T_a] \tag{4}$$

$$\frac{\partial T(x,-h_m,t)}{\partial y} = 0 \tag{5}$$

$$\frac{\partial T(x,0,t)}{\partial y} = 0, \quad 0 \le |x| < a \tag{6}$$

$$T(x,0^+,t) = T(x,0^-,t) \quad a < x < \frac{L}{2} \tag{7}$$

$$k_m \frac{\partial T(x,0^-,t)}{\partial y} = k_c \frac{\partial T(x,0^+,t)}{\partial y}, \quad a < x < \frac{L}{2} \tag{8}$$

For symmetry about $x = 0$

$$\frac{\partial T(0,y,t)}{\partial x} = 0 \tag{9}$$

For the edge crack, the boundary $x = L/2$ is also subjected to convective cooling.

$$k_i \frac{\partial T\left(\frac{L}{2},y,t\right)}{\partial x} = h\left[T\left(\frac{L}{2}, y, t\right) - T_a\right],$$

$$\text{with} \begin{cases} i = c \text{ for } 0 < y < h_c \\ i = m \text{ for } -h_m < y < 0 \end{cases} \tag{10}$$

For the center crack, the same boundary is assumed to be insulated

$$\frac{\partial T\left(\frac{L}{2},y,t\right)}{\partial x} = 0, \quad -h_m < y < h_c \tag{11}$$

Equations (1)-(11) were solved using the finite element method[1]. These calculations resulted in the temperature distribution in the ceramic/metal assembly at every increment of time.

The corresponding displacements and stresses were obtained by solving the uncoupled quasi steady-state plane strain thermoelasticity problem. For this purpose, both materials were assumed to be homogeneous, isotropic, and linearly elastic. It was also assumed that no residual stresses were present in the materials and the crack surface were frictionless. The resulting transient displacement configuration was calculated also using the finite element method.

The model used for the solution of the problem was divided into 217 8-node isoparametric quadrilateral elements with a total of 740 nodes. Overlapping of the crack faces were prevented through the use of interface elements. The use of these elements corresponds to the analytical model where the crack tip is assumed to be partially closed, i.e., it represents the Comninou model. However, in order to observe the closing of the crack, the mesh near the crack tip has to be very fine for the cases where the loading is such that, the crack faces away from the tip tend to open.

In order to calculate the strain energy release rate G, the relative displacements of the crack faces at any distance r from the crack tip were first related to the stress intensity factor K_0 by using the following relationship given by Smelser (1979).

$$\frac{|\Delta u|}{r^{1/2}} = \frac{(\mu_m + \mu_c\kappa_m)(\mu_c + \mu_m\kappa_c)}{\mu_m\mu_c(\mu_m + \mu_c + \mu_m\kappa_c + \mu_c\kappa_m)} \frac{\cosh^2 \epsilon\, \pi}{\sqrt{2\pi}\lambda_0} K_0 \tag{12}$$

where for plane strain,

$$\kappa_i = 3 - 4\nu_i \quad i = m,c \tag{13}$$

$$\epsilon = \frac{1}{2\pi} \ln \frac{\mu_m + \mu_c\kappa_m}{\mu_c + \mu_m\kappa_c} \tag{14}$$

$$\lambda_0 = \left[\frac{1}{4} + \epsilon^2\right]^{1/2} \tag{15}$$

$$|\Delta u| = [(\delta u)^2 + (\delta v)^2]^{1/2} \tag{16}$$

and μ_i and ν_i represent, respectively, the shear modulus and Poisson's ratio of each material. In equation (16) δu is the relative sliding of the crack and δv is the relative opening. These deformations are schematically shown in Fig. 2. K_0 is then related to the strain energy release rate G using

[1] A general purpose program called ABAQUS, developed by Hibbitt, Karlsson and Sorensen, Inc., Providence, RI was used for the solution.

Downloaded 03 May 2010 to 171.66.16.21. Redistribution subject to ASME license or copyright; see http://www.asme.org/terms/Terms_Use.cfm

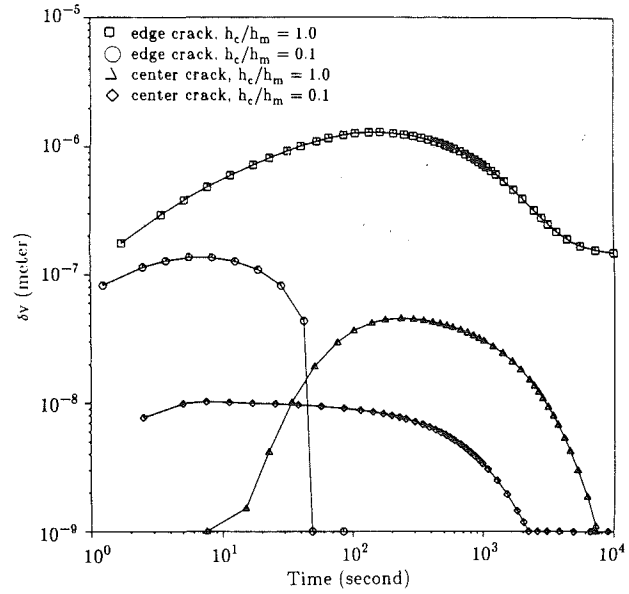

Fig. 3 Opening of the crack faces versus time at distance $r/a = 0.05$ from the crack tip

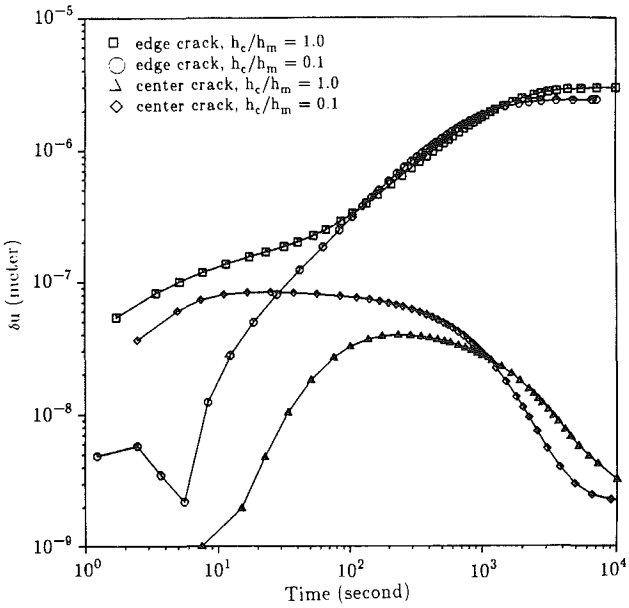

Fig. 4 Sliding of the crack faces versus time at distance $r/a = 0.05$ from the crack tip

$$G = \sum_i \frac{(1-\nu_i)}{4\mu_i} K_0^2 \quad i = m,c \tag{17}$$

This method of calculating G has been applied to the case where an interface crack was subjected to pure tension and the results compared to those presented by Comninou. The details of this study are beyond the scope of this paper. However, it should be mentioned that in order to observe the closing at the crack tip, the smallest element in this region had to be of the same length or smaller than the length of the closed portion predicted by Comninou, i.e., of the order of $(a \times 10^{-4})$. On the other hand, even if closing is not observed because of a coarser mesh, the values of G calculated using the method described above were comparable (within 10 percent difference) to those obtained by Comninou. Therefore, it should be kept in mind that the crack opening shown here represents the qualitative behavior away from crack tip.

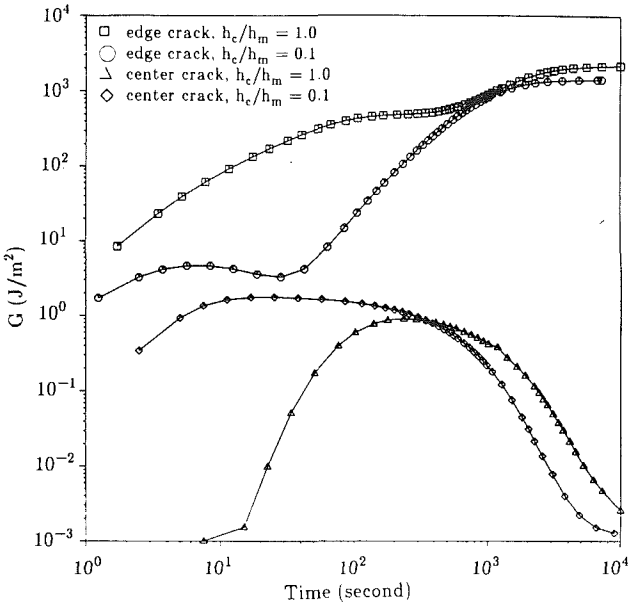

Fig. 5 Strain energy release rate versus time

3 Results

The effect of changing the material properties on the transient cooling of an interface was studied for a center and edge cracks. The comparisons for the different cases are made for one crack length only. However, it should be remembered that the strain energy release rate decreases when the crack gets shorter. In this study the length of the crack was $a = 1.5625$ mm. The total length L in figure 1 was 100 mm. Two thickness configurations were considered. For a "thin coating" of ceramic, the thickness h_c was 1.25 mm while h_m was 12.5 mm, so that the ratio $h_c/h_m = 0.1$. A second case considered had a ratio of $h_c/h_m = 1$. In equation (12), it was shown that the case of $h_c/h_m = 1$ resulted in the largest steady-state G for an edge crack, while for a center crack, the same case yielded the smallest transient maximum G.

The initial uniform temperature was taken to be $T_0 = 1000°C$ with a final temperature of $T_a = 20°C$. The ceramic surface was cooled at a rate of $h = 50\ W/m^2 - °C$ which is a relatively slow rate. It is clear that as h increases, the resulting transient values of G are expected to become larger, thus causing more severe conditions in terms of failure.

3.1 Effect of Thermal Expansion Properties. The thermal expansion coefficients of the particular materials used are $\alpha_c = 10.2 \times 10^{-6}/°C$ and $\alpha_m = 13.7 \times 10^{-6}/°C$. In order to examine the effect of transient cooling and compare it to the steady-state case, first the relative opening and shearing of the crack faces, as well as the strain energy release rate for these cases are presented respectively in Figs. 3 through 5. The results are presented on a log-log plot in order to include the variation in the parameters for all four cases studied and for the entire time interval until steady-state is reached.

The opening δv of the crack faces at a distance $r/a = 0.05$ from the crack tip is plotted in Fig. 3 for the center and edge cracked ceramic-to-metal bonds of two different thickness ratios. It can be noted that in all four cases the opening initially increases, reaches a maximum, and then decreases to reach a smaller steady-state value.

The shearing δu of the crack faces is shown in Fig. 4. In all cases, the actual difference in displacements as defined in Fig. 2 is negative. The only exception is in the case of the edge cracked thin coating $(h_c/h_m = 0.1)$ where, for the first 4 seconds, δu is positive. The sliding behavior of the crack is distinctly different for the center and edge cracked cases. For

Downloaded 03 May 2010 to 171.66.16.21. Redistribution subject to ASME license or copyright; see http://www.asme.org/terms/Terms_Use.cfm

the former, δu first increases, reaches a maximum, then decreases and reaches a smaller steady-state value. In the case of the edge crack, δu increases continuously until it results in a large steady-state value. As a result of this, the strain energy release rate G, plotted in Fig. 5 behaves in a similar fashion as the shearing deformation of the crack faces. It should be remembered that the steady-state behavior is mainly the result of the thermal expansion differential of the two materials since the temperature distribution in this case is uniform. For the transient case, there is an additional load due to nonuniformity of the temperature distribution as well as temperature discontinuity across the crack surfaces. Therefore, the effect of changing the material properties will be analyzed by considering the transient maximum G values obtained and by comparing them to the steady-state results.

First, the thermal expansion properties of the two materials are varied. These influence the steady-state as well as the transient results. Four separate cases are considered:

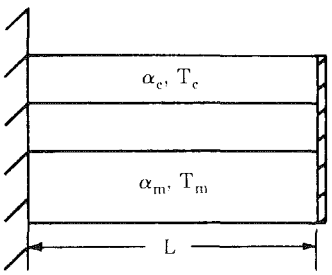

Fig. 6 Schematic representation of the two-bar model

Table 1 Strain energy release rate at steady-state (J/m^2)

	h_c/h_m	$\alpha_m > \alpha_c$	$\alpha_m = \alpha_c$ small	$\alpha_m = \alpha_c$ large	$\alpha_m < \alpha_c$
center crack	1	0.00259	0	0	0.00069
	0.1	0.00128	0	0	0.00045
edge crack	1	2159	0	0	897
	0.1	1421	0	0	728

Table 2 Transient maximum strain energy release rate (J/m^2) [(s.s) represents the value of G at steady-state)]

	h_c/h_m	$\alpha_m > \alpha_c$	$\alpha_m = \alpha_c$ small	$\alpha_m = \alpha_c$ large	$\alpha_m < \alpha_c$
center crack	1	0.945	0.951	1.716	1.724
	0.1	1.793	1.748	3.154	3.097
edge crack	1	2159 (s.s.)	430	775	770
	0.1	4.6	7.5	13.5	728 (s.s.)

(*a*) The metal and ceramic have their actual thermal expansion properties.
(*b*) Both thermal expansion coefficients are made equal to that of the ceramic (the smaller one).
(*c*) Both thermal expansion coefficients are made equal to that of the metal (the larger one).
(*d*) The thermal expansion properties of the two materials are reversed (i.e., $\alpha_c = 13.7 \times 10^{-6}/°C$ and $\alpha_m = 10.2 \times 10^{-6}/°C$).

The steady-state strain energy release rates corresponding to all four cases for the two crack configurations and thickness ratios are presented in Table 1. It should be remembered that these results are due to thermal expansion differential only since the temperature distribution at steady-state is uniform. For the cases where the thermal expansion coefficients are equal, the steady-state G is zero. For the center crack cases a very small G results, while for the edge crack the steady-state G is large. In all cases, the $\alpha_m > \alpha_c$ case results in larger G values than the $\alpha_m < \alpha_c$. Also, the $h_c/h_m = 1$ cases result in larger steady-state strain energy release rate than $h_c/h_m = 0.1$.

The maximum strain energy release rates that occurs during the transient cooling of the two materials are presented in Table 2. A comparison of these results to those obtained in Table 1 shows that for a center crack, the transient maximum G values are larger than the steady-state ones. Therefore, they need to be considered in the determination of the failure of the bond. It is now interesting to note that for $h_c/h_m = 1$, equating the thermal expansion coefficients results in *larger* maximum G values than the $\alpha_m > \alpha_c$ case. The largest G is obtained when α_m and α_c reversed. For $h_c/h_m = 0.1$, the largest G is obtained when both α's are equal to the larger of the two values.

When the two materials contain an edge crack at the interface, nonequal coefficient of thermal expansion values result in a steady-state G which is larger than any transient maximums. The transient maximum values shown for these cases in Table 2 occur because of the temporary opening of the crack which then decreases while the sliding keeps increasing to become largest at steady-state. For the cases where the thermal expansion coefficients are equal, however, significant transient G values are obtained which are due to the nonuniform temperature distribution.

In order to provide a qualitative explanation for the fact that during transient cooling, the transient G values could become larger if α_m and α_c are made equal, a simple two-bar model, shown in Fig. 6 is considered. The two bars are assembled as shown by (a) allowing free thermal expansion to occur and then (b) by applying stresses to equalize the differential expansion. Strain energy is introduced during the second stage and for given cross-sections and elastic moduli, the strain energy, G, is proportional to the square of the differential strain that has to be neutralized. Therefore, equating α_m and α_c will increase the strain energy of the system if this results in a larger absolute value of differential thermal expansion, i.e., if

$$|\alpha_c T_m - \alpha_c T_c| > |\alpha_m T_m - \alpha_c T_c| \tag{18}$$

or

$$|\alpha_m T_m - \alpha_m T_c| > |\alpha_m T_m - \alpha_c T_c| \tag{19}$$

Table 3 Thermal strain differentials obtained using the two-bar model

$\frac{h_c}{h_m}$	T_m (°C)	T_c (°C)	$\lvert\alpha_m T_m - \alpha_c T_c\rvert$	$\lvert\alpha_c(T_m - T_c)\rvert$	$\lvert\alpha_m(T_m - T_c)\rvert$	$\lvert\alpha_c T_m - \alpha_m T_c\rvert$
1	94	183	5.79×10^{-4}	9.08×10^{-4}	12.19×10^{-4}	15.48×10^{-4}
0.1	30	75	3.54×10^{-4}	4.59×10^{-4}	6.165×10^{-4}	7.215×10^{-4}

Downloaded 03 May 2010 to 171.66.16.21. Redistribution subject to ASME license or copyright; see http://www.asme.org/terms/Terms_Use.cfm

Table 4 Transient maximum strain energy release rates for the center crack with different thermal properties

h_c/h_m	$k, \rho c$	$2k, \rho c$	$k, 2\rho c$
1	0.945	0.275	0.427
0.1	1.793	0.521	1.482

In order to make a comparison in the qualitative behavior of the strain energy as the α's are changed, the average temperatures of the ceramic and the metal were calculated from the finite element results at the time when G of the center crack is maximum. These average temperatures were then used to calculate the differential thermal strains of equations (18) and (19). These are presented in Table 3. It can be noted that the behavior of the strain differential is similar to that of Table 1.

It should be remembered, however, that this model does not represent the actual transient behavior of the cracks since no bending is allowed, while in the case of the ceramic-to-metal bond of this study bending does occur. However, the two-bar model is helpful in providing a qualitative explanation for the effect of changing the thermal expansion properties during transient cooling. It also clarifies the concept that during transient thermal loads, equality of thermal expansion coefficients is not enough to reduce the strain energy release rate, but instead, the differential thermal strain needs to be minimized.

3.2 Effect Of Thermal Properties. The discussion presented so far shows that under slow cooling conditions, the center cracked interface experiences a transient maximum G, while the edge crack sustains a maximum G at steady-state when $\alpha_m \neq \alpha_c$. In order for an interface to be more resistant to failure due to transient thermal loads, the strain energy release rate has to be minimized. The transient maximum values of G occur because of transient temperature gradients. For given boundary conditions, these temperature gradients are controlled by the thermal properties of the two materials. In this section, the effect of changing such properties on the transient behavior of G is investigated. This is accomplished only for the case of the center crack when the transient behavior is especially important compared to the steady-state value.

The base material properties are indicated in the Appendix. The thermal expansion coefficients correspond to the real case of $\alpha_m > \alpha_c$. The two thermal properties whose effects are analyzed are the thermal conductivity k and the products of density and specific heat, ρC. For each of these cases, the thermal diffusivity ratio of the two materials are affected. However, each one affects the transient temperature distribution differently. This can be explained by considering the equations that govern the heat transfer process. In equations (1) and (2), the thermal diffusivity $k/\rho C$ of each material governs the rate heat flow in the material. Equation (8), however, shows that the heat flow from one material to the other is governed only by the thermal condutivities of the two materials. Therefore, in order to investigate these effects the thermal material properties were changed by doubling (*i*) the thermal conductivity of the ceramic, (*ii*) the ρC product for the ceramic.

The transient maximum G values calculated in each case are presented in Table 4. In all cases, a reduction in the value of the strain energy release is observed. The most significant reduction occurs when the thermal conductivity of the ceramic is increased twice. The maximum G, in this case, is reduced by a factor of 3.44 for $h_c/h_m = 1$ and for $h_c/h_m = 0.1$. When ρ_C for the ceramic is doubled keeping k at its standard value, the transient G is reduced by 54.8 percent for $h_c/h_m = 1$ and 17.3 percent for $h_c/h_m = 0.1$. It is interesting to note that when k is multiplied by two, the thermal diffusivity is also doubled. On the other hand, when ρC is doubled, the thermal diffusivity is reduced to half its value. In both cases, however, a reduction in G is obtained. This is due to the effect of the interface conditions as described above.

4 Conclusions

The effect of changing expansion and thermal properties on the transient strain energy release rates for an interfacial center and edge cracks has been analyzed.

The results show, that equating the thermal expansion coefficients does not necessarily result in improved resistance to failure under transient thermal loads. For such an improvement to occur, conditions related to the properties of the materials and the temperature distribution need to be satisfied.

A qualitative indication of such conditions can be obtained by using the simplified model of two dissimilar bars subjected to different uniform temperatures.

The transient maximum G can also be decreased by changing the thermal properties of the materials. For the case of a ceramic bonded to a metal, the main purpose is to create an insulation for the metal. Therefore, a drastic increase in the thermal conductivity, for example, would probably be detrimental to this goal. However, these results suggest that an optimization process could be applied which would result in a decrease in the load that the cracks experience and, therefore, would lead to an improved failure resistance.

Acknowledgment

Support for this research by the National Science Foundation, Grant No. MSM-8617455, is gratefully acknowledged.

References

Barber, J. R., and Comninou, M., 1982, "The External Axisymmetric Interface Crack with Heat Flow," *Quarterly Journal of Mechanics and Applied Mathematics*, Vol. 35, pp. 403–417.

Barber, J. R., and Comninou, M., 1983, "The Penny-Shaped Interface Crack with Heat Flow, Part 2: Imperfect Contact," ASME JOURNAL OF APPLIED MECHANICS, Vol. 50, pp. 770–776.

Berndt, C. C., and Miller, R. A., 1984, "Failure Analysis of Plasma-Sprayed Thermal Barrier Coatings," *Thin Solid Films*, Vol. 119, pp. 173–184.

Charreyron, P. O., Bylina, J. J., and Hannoosh, J. G., 1986, "Ceramic-to-Metal Bonding from a Fracture Mechanics Perspective," *Fracture Mechanics of Ceramics*, Vol. 8, Plenum Press, New York, pp. 235–238.

Charreyron, P. O., Patten, D. O., and Miller, B. J., 1987, "Modeling of Ceramic-to-Metal Brazed Joints," presented at the 89th American Ceramic Society Annual Meeting, Pittsburgh, PA.

Erdogan, F., 1965, "Stress Distribution in Bonded Dissimilar Materials with Cracks," ASME JOURNAL OF APPLIED MECHANICS, Vol. 32, p. 403.

Fisher, G., 1984, "Advanced Ceramics Continue Progress to Products," *American Ceramic Society Bulletin*, Vol. 63, No. 2, pp. 249–252.

Hartsock, D. L., and McLean, A. F., 1984, "What the Designer with Ceramic Needs," *American Ceramic Society Bulletin*, Vol. 63, No. 2, pp. 266–270.

Kokini, K., 1987, "Interfacial Cracks in Ceramic-to-Metal Bonds Under Transient Thermal Loads," *Journal of the American Ceramic Society*, Vol. 70, No. 12, pp. 855–859.

Kokini, K., 1987, "Boundary Effects on the Interfacial Transient Thermal Fracture of Ceramic-to-Metal Bonds," *Advances in Ceramics*, in press.

Liebert, C. H., and Miller, R. A., 1984, "Ceramic Thermal Barrier Coatings," *I&EC Product Research and Development*, pp. 344–349.

Martin-Moran, C. J., Barber, J. R., and Comninou, M., 1983, "The Penny-Shaped Interface Crack with Heat Flow, Part I: Perfect Contact," ASME JOURNAL OF APPLIED MECHANICS, Vol. 50, pp. 19–36.

Smelser, R. E., 1979, "Evaluation of Stress Intensity Factors for Bimaterial Bodies Using Numerical Crack Flank Displacement Data," *International Journal of Fracture*, Vol. 15, pp. 135–143.

Suga, T., and Elssner, G., 1986, "Composite Parameters and Mechanical Compatibility of Material Joints," private communications.

Downloaded 03 May 2010 to 171.66.16.21. Redistribution subject to ASME license or copyright; see http://www.asme.org/terms/Terms_Use.cfm

APPENDIX

Material properties of the two components:

Zirconia:

$k_c = 2.2$ W/m – °C
$C_c = 460.6$ J/kg – °C
$\rho_c = 5900$ kg/m^3
$E_c = 200$ GPa
$\alpha_c = 10.2 \times 10^{-6}$/°C
$\nu_c = 0.23$

Nodular cast iron:

$k_m = 48.9$ W/m – °C
$C_m = 418.4$ J/kg – °C
$\rho_m = 7289$ kg/m^3
$E_m = 168$ GPa
$\alpha_m = 13.7 \times 10^{-6}$/°C
$\nu_m = 0.31$

Downloaded 03 May 2010 to 171.66.16.21. Redistribution subject to ASME license or copyright; see http://www.asme.org/terms/Terms_Use.cfm

A Continuum Damage Model for Viscoelastic Materials

Y. Weitsman
Mechanics and Materials Center,
Texas A&M University,
College Station, TX 77843
Mem. ASME

This paper presents a continuum damage model for viscoelastic materials. "Damage" is expressed by two symmetric, second rank tensors which are related to the total areas of "active" and "passive" microcracks within a representative volume element of the multifractured material. Viscoelasticity is introduced through scalar valued internal state variables that represent the internal degrees-of-freedom associated with the motions of long chain polymeric molecules. The constitutive relations are established from basic considerations of continuum mechanics and irreversible thermodynamics, with detailed expressions derived for the case of initially isotropic materials. It is shown that damage causes softening of the material moduli as well as changes in material symmetry. The special cases of uniaxial damage under uniaxial stress and the interaction of damage with moisture diffusion are also considered.

1 Introduction

Continuum damage modelling, pioneered by Kachanov (1958), has become a most active subject of research in the recent decade. A comprehensive review of work in this area was given recently by Krajcinovic (1986).

Thus far, most of the modeling concerned the behavior materials like rock and concrete which exhibit brittle behavior, or metals—which creep upon reaching a plastic range. Very little attention was paid to the modeling of damage in polymeric materials that creep viscoelastically. In a recent works by Schapery (1980, 1981, 1984), viscoelastic stress-strain relations were modified to include the effects of damage. However, since those relations were not derived from a free energy and the tensorial character of the damage variable was not identified, the above approach could not specify the changes in material symmetry which may occur in damaged configurations.

Viscoelastic response in the presence of distributed microflaws occurs in solid propellants and is likely to be encountered in thermoplastic composites. In contrast to rock and metals, polymeric materials absorb various kinds of solvents, which may damage the polymeric composites in a variety of ways. In the case of water absorption by epoxy-based composites, such damage was noted by several investigators (e.g., Ashbee and Wyatt (1969), Shirrell et al. (1979), Drzal et al. (1985), and Jackson and Weitsman (1985)). Coupling between damage and diffusion was modeled by Weitsman (1987b,c) assuming elastic response.

In Section 2 of the present work the choice of internal state variables to model damage is motivated by micromechanical considerations. Consequently "damage" is represented by two symmetric second rank tensors. This representation resembles the form employed by Murakami and Ohno (1981), although their choice derived from different physical and mathematical considerations.

In Section 3, viscoelasticity is introduced by means of scalar valued internal state variables which correspond to the degrees-of-freedom afforded by the motions of molecular chains within the bulk polymer. The thermodynamic theory is then applied when this set of variables is present in addition to the tensor-valued damage state variables.

In Section 4, the special case of an initially isotropic medium is considered. Viscoelastic constitutive relations are formulated, accounting for both damage growth and contraction.

Some specific circumstances are considered in Section 5. These include the case of parallel, unidirectional damage and stress and the interaction between moisture flux and damage in the absence of stresses.

2 Basic Equations, Damage, and Internal State Variables

When a solid body absorbs solvent from the exterior the mass contained within the material volume of the solid is not conserved and the solid-solvent mixture is a thermodynamically *open* system. The basic equations for this circumstance were developed by several researchers, including Prigogine (1968), Biot (1973), Rice and Cleary (1976), and Kestin (1979). A version of these equations was given recently by Weitsman (1987a). Accordingly, the "reduced entropy inequality" is expressed as follows[1]:

Contributed by the Applied Mechanics Division of THE AMERICAN SOCIETY OF MECHANICAL ENGINEERS for presentation at the Joint ASCE/ASME Applied Mechanics, Biomechanics, and Fluids Engineering Conference, San Diego, CA, July 9 to 12, 1989.

Discussion on this paper should be addressed to the Editorial Department, ASME, United Engineering Center, 345 East 47th Street, New York, N.Y. 10017, and will be accepted until two months after final publication of the paper itself in the JOURNAL OF APPLIED MECHANICS. Manuscript received by ASME Applied Mechanics Division, February 8, 1988; final revision, July 20, 1988.

Paper No. 89-APM-12.

[1] Equation (1) follows an earlier expression (Weitsman, 1987a, equation (17)) upon considering infinitesimal deformations and $\rho_s \Phi = \rho_s \psi - \sigma_{ij} \epsilon_{ij}$.

Copyright © 1988 by ASME
Downloaded 03 May 2010 to 171.66.16.21. Redistribution subject to ASME license or copyright; see http://www.asme.org/terms/Terms_Use.cfm

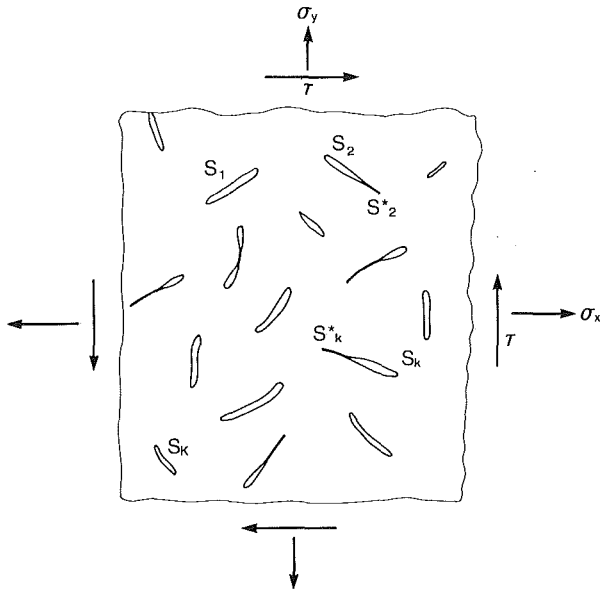

Fig. 1 A sketch of a representative volume element containing K microcracks, with open surfaces S_k and closed portions S_k^*

$$-\rho_s\dot{\Phi}-\epsilon_{ij}\dot{\sigma}_{ij}-\rho_s s\dot{T}-(q_i/T)g_i+\mu\dot{m}-\bar{\mu}_i f_i-g_i\bar{f}_i\bar{s}\geq 0. \quad (1)$$

In equation (1) Φ is the Gibbs free energy, ρ_s—the mass density of the solid, ϵ_{ij}—components of the infinitesimal strain tensor, σ_{ij}—components of Cauchy stress, s—entropy density of the solid-solvent mixture, T—temperature, q_i—components of the heat flux vector, $g_i=\partial T/\partial x_i$, m—solvent mass, f_i—components of the flux of m, μ and $\bar{s}$—the chemical potential and entropy of the solvent in a reservoir in thermodynamic equilibrium with the solid-solvent mixture.

To motivate the choice of damage variables, consider a statistically representative volume element (RVE) containing K microcracks, which may be partially or completely closed. If the material consists of several phases, then consider their equivalent homogeneous properties.

Consider the kth microcrack and denote by S_k its open ("active") part and by S^*_k its closed ("passive") surface, as shown in Fig. 1. Although portions of S_k and S_k^* may switch interchangeably under the effects of stress, temperature and moisture—or with the passage of time—they serve as independent variables that characterize the state of the material at a given instant of time. The "macro"-level stresses and strains are quantities averaged over the volume of the RVE. Assuming infinitesimal deformations, these "macro" quantities are given by the following, well-known expressions:

$$\bar{\sigma}_{ij}=\frac{1}{V}\int_V \sigma_{ij}(\mathbf{x})dV=\frac{1}{2V}\left\{\int_{S_o}(T_i^0 x_j+T_j^0 x_i)dS + \sum_{k=1}^{K}\int_{S_k US_k^*}(T_i^{(k)}x_j+T_j^{(k)}x_i)dS\right\} \quad (2)$$

and

$$\bar{\epsilon}_{ij}=\frac{1}{V}\int_V \epsilon_{ij}(\mathbf{x})dV=\frac{1}{2V}\left\{\int_{S_o}(u_i n_j^o+u_j n_i^o)dS + \sum_{k=1}^{K}\int_{S_k US_k^*}(u_i n_j^{(k)}+u_j n_i^{(k)})dS\right\}. \quad (3)$$

In equations (2) and (3) S_o denotes the outer surface of the RVE, T_i denotes tractions, n_i are components of the outward unit normal, and u_i are displacements.

If the tractions $T_i^{(k)}$ are continuous *across* all surfaces S_k and S_k^*, and T_i^o correspond to a uniform stress field σ_{ij}^o, namely $T_i^o=\sigma_{ij}^o n_j(S_o)$, then it is well known that $\bar{\sigma}_{ij}=\sigma_{ij}^o$.

Let Δu_n and Δu_s denote normal and tangential components of displacement discontinuity at points on some surface S. Then, by hypothesis, on all surfaces S_k^* $\Delta u_n^{(k)}=0$, while $\Delta u_s^{(k)}$ occurs against the resistance of frictional forces. It is therefore reasonable to expect that Δu_s on the surfaces S_k^* are much smaller than Δu_s on surfaces S_k.

Consequently, it is assumed that, instead of equation (3), $\bar{\epsilon}_{ij}$ is given by

$$\bar{\epsilon}_{ij}\simeq\frac{1}{2V}\left\{\int_{S_o}(u_i n_j^o+u_j n_i^o)dS + \sum_{k=1}^{K}\int_{S_k}(u_i n_j^{(k)}+u_j n_i^{(k)})dS\right\}. \quad (3a)$$

Although S_k^* no longer appear explicitly in equation (3*a*), these surfaces of discontinuity still affect $\bar{\epsilon}_{ij}$ through an implicit presence in u_i.

To amplify this point, consider linear elastic response with fixed crack geometry. In this case $\bar{\sigma}_{ij}$ and $\bar{\epsilon}_{ij}$ in the RVE can be constructed by superposition of:

(*a*) $T_i^o=\sigma_{ij}^o n_j(S_o)$ acting on the intact (undamaged) RVE, and

(*b*) $T_i^o=0$ on S_o, $T_i^{(k)}=-\sigma_{ij}^o n_j^{(k)}$ on S_k, while on S_k^* $\Delta T_i^{(k)}=0$, $\Delta u_n^{(k)}=0$, and $\Delta u_s^{(k)}$ are related *linearly* to the tractions. ($k=1,2,\ldots K$).

Since in Part (*b*) all tractions across $S_k U S_k^*$ are continuous, obviously $\bar{\sigma}_{ij}=\sigma_{ij}^o$ for the superposed solution.

In view of the linearity of the problem, all displacements are *proportional to* σ_{ij}^o. Hence, for Part (*a*)

$$u_i^{(a)}(\mathbf{x})=S_{ijkl}^o x_j\sigma_{kl}^o \quad (4a)$$

while for Part (*b*)

$$u_i^{(b)}(\mathbf{x})=P_{ikl}(\mathbf{x}, S_1, S_2, \ldots S_K, S_1^*, S_2^*, \ldots S_K^*)\sigma_{kl}^o. \quad (4b)$$

In (4*a*) S_{ijkl}^o denote the compliances of the undamaged material.

Substitution of equations (4) into equation (3*a*) yields

$$\bar{\epsilon}_{ij}\simeq\left\{S_{ijkl}^o+\frac{1}{2V}\sum_{k=1}^{K}\int_{S_k}(P_{ikl}(\mathbf{x}, S_1, \ldots S_K, S_1^*, \ldots S_K^*)n_j^{(k)} + P_{jkl}(\mathbf{x}, S_1, \ldots S_K, S_1^*, \ldots S_K^*)n_i^{(k)})dS\right\}\bar{\sigma}_{kl}. \quad (5)$$

Equation (5) can be expressed formally as

$$\bar{\epsilon}_{ij}=S_{ijkl}(S_1, \ldots S_K; S_1^*, \ldots S_K^*)\bar{\sigma}_{kl} \quad (6)$$

where S_{ijkl} are the damage affected compliances. However, equation (5) provides an additional insight by implying that changes in material symmetry are mostly due to the configuration of "active" cracks, while both "active" and "passive" cracks contribute to the overall softening. The above assumption simplifies the constitutive expressions developed in Section 4. However, it should be emphasized that the general development of the constitutive formalism does not depend on the assumptions that led to the approximation expressed in equation (5).

It seems that a complete accounting of the response of the RVE requires the incorporation of $2K$ parameters which represent the surfaces S_k and S_k^* ($k=1, \ldots K$). Since the shapes of those surfaces are generally unknown, they may be approximated by some equivalent *flat* surfaces, namely by vectors $\mathbf{D}^{(k)}=D^{(k)}\mathbf{n}^{(k)}$ and $\mathbf{D}^{*(k)}=D^{*(k)}\mathbf{n}^{(k)}$ (no sum on k, $k=1, \ldots K$). However, since each microcrack has two equal and opposite surfaces, the representation should be independent of the sense of $\mathbf{n}^{(k)}$. Following Spencer (1972), this is ac-

Downloaded 03 May 2010 to 171.66.16.21. Redistribution subject to ASME license or copyright; see http://www.asme.org/terms/Terms_Use.cfm

complished by representing each microcrack by the symmetric dyad $\underset{\sim}{\mathbf{A}}^{(k)} = \mathbf{D}^{(k)}\mathbf{D}^{(k)}$. Similarly we have $\underset{\sim}{\mathbf{A}}^{*(k)} = \mathbf{D}^{*(k)}\mathbf{D}^{*(k)}$.

Due to the paucity of detailed information regarding the size and location of the surfaces S_k and $S_k{}^*$ it is proposed to account for their joint effect on P_{ikl} in equation (4*b*) and S_{ijkl} in equation (6) by means of their dyadic sums, namely through

$$\underset{\sim}{\mathbf{A}} = \sum_{k=1}^{K} \mathbf{D}^{(k)}\mathbf{D}^{(k)}$$

and (7)

$$\underset{\sim}{\mathbf{A}}^* = \sum_{k=1}^{K} \mathbf{D}^{*(k)}\mathbf{D}^{*(k)}.$$

Hence, the effects of "damage" are represented by two, "macro"-level, internal state variables that are symmetric, second rank tensors.

The selection of $\underset{\sim}{\mathbf{A}}$ to represent damage was recently employed by Weitsman (1988). It was also alluded to in an earlier work by Kachanov (1980). It is worth noting that this choice corresponds to the second of three terms that were recently selected by Krajcinovic (1987) to represent damage. In that work damage is expressed by a scalar, as well as by tensors of second and fourth ranks.

The tensors $\underset{\sim}{\mathbf{A}}$ and $\underset{\sim}{\mathbf{A}}^*$ can be nondimensionalized through division by a characteristic area Δ, e.g., any one of the "walls" of the RVE. This leads to the nondimensional quantities

$$\underset{\sim}{\mathbf{a}} = \underset{\sim}{\mathbf{A}}/\Delta^2, \quad \underset{\sim}{\mathbf{a}}^* = \underset{\sim}{\mathbf{A}}^*/\Delta^2. \tag{8}$$

Although the present work considers infinitesimal strains ($\epsilon_{ij} \ll 1$), the aforementioned representation of "damage" does not infer small a_{ij} and $a_{ij}{}^*$. Consequently, Taylor series expansions are useful in ϵ_{ij} but not in a_{ij} and $a^*{}_{ij}$.

As mentioned earlier (Weitsman, 1988), the present choice of damage variables yields, in the case of randomly oriented microcracks of equal area, the intuitively appealing result $a_{ij} = a^2\,\delta_{ij}$ in both two and three dimensions. This outcome, which implies that randomly distributed damage affects the material's response as a scalar quantity devoid of orientation, is not borne out when a vectorial representation $\mathbf{D} = D\mathbf{n}$ is chosen for "damage."

Viscoelastic behavior, which occurs most commonly in polymeric materials, has been attributed to the various degrees-of-freedom afforded by the motions of intertwined long chain molecules. Such considerations led Rouse (1953), Bueche (1954), and Zimm (1956), to express the motions of molecular chains consisting of N segments in forms which, upon transformation to principal coordinates and normal modes, resulted in N scalar valued internal state variables. These formulations motivated subsequent researchers (Biot (1954a, b) and Schapery (1964), (1966), (1969)) to derive a theory of viscoelasticity from fundamental concepts of irreversible thermodynamic processes, with irreversibility stemming from N internal state variables whose "growth laws" derived from the motion of chain segments subjected to viscous resistance.

It is worth noting that in the aforementioned works the tensorial character of the internal state variables was not specified the stress-strain relations for viscoelastic materials of various symmetries were inferred from analogies with the elastic case. This procedure will not carry over to the present work, which incorporates "damage" by means of two symmetric second rank tensors. As shown in Sections 3 and 4, the derivation of constitutive expressions and symmetry relations hinges on the identification of the viscoelastic internal state variables as scalars.

3 Constitutive Relations: Thermodynamic Considerations

Consider a viscoelastic material with continuously distributed damage represented by the symmetric second rank tensors a_{ij}, $a_{ij}{}^*$ defined in Section 2. Furthermore, let γ_r ($r = 1, \ldots N$) denote N *scalar valued* internal state variables which represent the internal degrees-of-freedom of molecular motion within the viscoelastic polymer.

The subsequent formulation is based upon the premise that the internal molecular motions, represented by γ_r, occur on a dimensional scale which is much smaller than the microdamage expressed by a_{ij} and $a_{ij}{}^*$. This suggests that the viscoelastic retardation times are unaffected by damage, although damage growth rates are influenced by the inherent viscoelasticity of the material.

To maintain tractability and focus on the effects of damage, we shall assume a common time dependence for all compliances. This assumption is valid for many isotropic polymers which exhibit a constant Poisson's ratio.

Accordingly, consider a Gibbs free energy Φ of the form

$$\Phi = f(\sigma_{ij}, a_{ij}, a^*_{ij}, m, T)\phi(m, T, \gamma_r) \quad (r = 1, \ldots N) \tag{9}$$

Without loss of generality let $f > 0$. Also, let ϕ be dimensionless.

Consider a representative volume element subjected to fixed levels of σ_{ij}, m, and T. Following Coleman and Gurtin (1967), this circumstance will trigger an irreversible thermodynamic process in the material, causing the internal variables a_{ij}, a^*_{ij} and γ_r to drift towards their equilibrium values a^e_{ij}, a^{*e}_{ij} and $\gamma_r{}^e$.

According to the extremum principles of thermodynamics (Callen, 1960) the Gibbs free energy attains a minimum at a^e_{ij}, a^{*e}_{ij} and $\gamma_r{}^e$. Therefore, at those values we have

$$\frac{\partial \Phi}{\partial \gamma_r} = 0, \quad \frac{\partial \Phi}{\partial a_{ij}} = 0, \quad \frac{\partial \Phi}{\partial a^*_{ij}} = 0 \tag{10}$$

and

$$\frac{1}{2}\frac{\partial^2 \Phi}{\partial \gamma_r \partial \gamma_s}\delta\gamma_r\delta\gamma_s + \frac{\partial^2 \Phi}{\partial \gamma_r \partial a_{ij}}\delta\gamma_r\,\delta a_{ij} + \frac{\partial^2 \Phi}{\partial \gamma_r \partial a^*_{ij}}\delta\gamma_r\delta a^*_{ij} + \frac{1}{2}\frac{\partial^2 \Phi}{\partial a_{ij}\partial a_{kl}}\delta a_{ij}\delta a_{kl} + \frac{\partial^2 \Phi}{\partial a_{ij}\partial a^*_{kl}}\delta a_{ij}\delta a^*_{kl} + \frac{1}{2}\frac{\partial^2 \Phi}{\partial a^*_{ij}\partial a^*_{kl}}\delta a^*_{ij}\delta a^*_{kl} > 0 \tag{11}$$

Equation (11) holds at a^e_{ij}, a^{*e}_{ij}, $\gamma_r{}^e$ for all arbitrary variations δa_{ij}, δa^*_{ij} and $\delta\gamma_r$.

Expanding Φ about a^e_{ij}, a^{*e}_{ij}, $\gamma_r{}^e$ employing equations (9) and (10) and assuming $\gamma_r < \gamma_r{}^e \ll 1$ we get

$$\Phi(\sigma_{ij}, m, T, a^e_{ij}, a^{*e}_{ij}, \gamma_r) = \Phi^e + \frac{1}{2} f(\sigma_{ij}, a^e_{ij}, a^{*e}_{ij}, m, T)\frac{\partial^2 \phi}{\partial \gamma_r \partial \gamma_s}(\gamma_r - \gamma_r{}^e)(\gamma_s - \gamma_s{}^e) + \text{higher order terms in } (\gamma_r - \gamma_r{}^e). \tag{12}$$

Alternately, an expansion about $a_{ij} = a^e_{ij}$, $a^*_{ij} = a^{*e}_{ij}$ and $\gamma_r = 0$ gives

$$\Phi(\sigma_{ij}, m, T, a^e_{ij}, a^{*e}_{ij}, \gamma_r) = \Phi(\sigma_{ij}, a^e_{ij}, a^{*e}_{ij} m, T, 0) + f(\sigma_{ij}, a^e_{ij}, a^{*e}_{ij}, m, T)\left.\frac{\partial \phi}{\partial \gamma_r}\right|_{\gamma_r = 0}\gamma_r + \frac{1}{2} f(\sigma_{ij}, a^e_{ij}, a^{*e}_{ij}, m, T)\left.\frac{\partial^2 \phi}{\partial \gamma_r \partial \gamma_s}\right|_{\gamma_p = 0}\gamma_r\gamma_s + \text{higher order terms in } \gamma_r. \tag{13}$$

In view of the assumption that $(\gamma_r, \gamma_r{}^e) \ll 1$ expansions (12) and (13) are equal, therefore

Downloaded 03 May 2010 to 171.66.16.21. Redistribution subject to ASME license or copyright; see http://www.asme.org/terms/Terms_Use.cfm

$$\Phi(\sigma_{ij},\ m,\ T,\ a^e_{ij},\ a^{*e}_{ij};\ 0)=\Phi^e + \frac{1}{2} f(\sigma_{ij},\ a^e_{ij},\ a^{*e}_{ij},\ m,\ T)\ \frac{\partial^2\phi}{\partial\gamma_r\partial\gamma_s}\bigg|_{\gamma_p=\gamma_p{}^e}\gamma^e_r\gamma^e_s \quad (14a)$$

$$\frac{\partial\phi}{\partial\gamma_r}\bigg|_{\gamma_p=0} = -\frac{\partial^2\phi}{\partial\gamma_r\partial\gamma_s}\bigg|_{\gamma_p=\gamma_p{}^e}\gamma^e_s \quad (14b)$$

and, in particular

$$\frac{\partial^2\phi}{\partial\gamma_r\partial\gamma_s}\bigg|_{\gamma_p=0} = \frac{\partial^2\phi}{\partial\gamma_r\partial\gamma_s}\bigg|_{\gamma_p=\gamma_p{}^e}. \quad (14c)$$

Denote $\partial\phi/\partial\gamma_r\ |_{\gamma_r=0}=\phi_r$ and $\partial^2\phi/\partial\gamma_r\partial\gamma_s\ |_{\gamma_p=0}=\phi_{rs}$. It follows from equations (9), (11) and (14*a*) that $\phi_{rs}>0$ *independently of* a_{ij} *and* $a_{ij}{}^*$.

Following the conceptual models of Rouse (1953) and Bueche (1955), and their incorporation into a growth relationship for the internal state variable as proposed by deGroot and Mazur (1962), Biot (1954a,b) and Schapery (1964), assume that $\dot\gamma_s$ depend only on that portion of Φ which concerns the internal processess within the polymer (excluding damage). Thus let

$$\frac{\partial\phi}{\partial\gamma_r} = -b_{rs}\,\dot\gamma_s \quad (r,s=1,\ \ldots\ N). \quad (15)$$

For linear viscoelastic behavior $b_{rs}=b_{rs}(m,T)$. Furthermore, by Onsager's principle $b_{rs}=b_{sr}$.

Expanding $\phi(m,T,\gamma_r)$ in powers of γ_r, truncating after the second power in view of the foregoing assumption that $\gamma_r \ll 1$, we have

$$\phi(m,T,\gamma_r)=\phi(m,T,0)+\phi_r(m,T,0)\gamma_r+\frac{1}{2}\phi_{rs}(m,T,0)\gamma_r\gamma_s. \quad (16)$$

Substitution of (16) in (15) gives

$$\phi_r+\phi_{rs}\gamma_s=-b_{rs}\dot\gamma_s. \quad (17)$$

Substitution of the specific form of Φ, given in equation (9), into equation (1) yields

$$-\rho_s\frac{\partial f}{\partial\sigma_{ij}}\phi\ \dot\sigma_{ij}-\rho_s\frac{\partial f}{\partial a_{ij}}\phi\ \dot a_{ij} -\rho_s\frac{\partial f}{\partial a^*_{ij}}\phi\ \dot a^*_{ij}-\rho_s\frac{\partial\Phi}{\partial m}\dot m-\rho_s\frac{\partial\Phi}{\partial T}\dot T -\rho_s f\,\phi_r\dot\gamma_r-\epsilon_{ij}\dot\sigma_{ij}-\rho_s s\dot T-(q_i/T)g_i+\mu\ \dot m -\mu_{,i}f_i-g_if_i\tilde s\geq 0. \quad (18)$$

Since equation (18) cannot be violated for any process, familiar arguments (e.g., Jaunzemis 1967) give

$$\epsilon_{ij}=-\rho_s\phi\frac{\partial f}{\partial\sigma_{ij}},\ \mu=\rho_s\frac{\partial\Phi}{\partial m},\ s=-\frac{\partial\Phi}{\partial T} \quad (19)$$

and

$$-\rho_s\phi\frac{\partial f}{\partial a_{ij}}\dot a_{ij}-\rho_s\phi\frac{\partial f}{\partial a^*_{ij}}\dot a^*_{ij}-\rho_s f\frac{\partial\phi}{\partial\gamma_r}\dot\gamma_r -(q_i/T)g_i-f_i\mu_{,i}-g_if_i\tilde s\geq 0. \quad (20)$$

In particular, at fixed damage, moisture and temperature

$$-\frac{\partial\phi}{\partial\gamma_r}\dot\gamma_r\geq 0. \quad (20a)$$

Equationis (15) and (20*a*) give $b_{rs}\dot\gamma_r\dot\gamma_s\geq 0$, namely $b_{rs}(m,T)$ are components of a symmetric, semi-positive definite matrix. Since a similar conclusion was reached earlier for ϕ_{rs}, it is possible to diagonalize b_{rs} and ϕ_{rs} simultaneously and rewrite equation (17) in the form

$$B_r\dot\gamma_r+\chi_r\gamma_r=-\phi_r \quad (r=1,2,\ \ldots\ N.\ \text{No sum on } r). \quad (21)$$

The solution of the N, now uncoupled, equations (21) is

$$\gamma_r=K_r(1-e^{-t/Z_r}) \quad (r=1,\ \ldots\ N.\ \text{No sum on } r) \quad (22)$$

where $K_r=-\phi_r/\chi_r$ and $Z_r=B_r/\chi_r>0$. Both K_r and Z_r depend on m and T.

As noted by Schapery (1969), if the dependence of b_{rs} on m and T is *common*, namely

$$b_{rs}(m,\ T)=b(m,\ T)b^o_{rs} \quad (b^o_{rs}\ \text{constants}) \quad (23)$$

then, equation (17) reduces to

$$\phi_r+\phi_{rs}\ \gamma_s+b^o_{rs}\frac{d}{d\psi}\gamma_s=0 \quad (24)$$

and, instead of (22), we have the simpler result

$$\gamma_r=K_r(1-e^{-\psi/Z_r}). \quad (25)$$

In equations (24) and (25) $\psi=t/b(m,T)$ is the "reduced time," and $b(m,\ T)$ is the moisture- and temperature-dependent shift factor.

If, in addition, all $\phi_{rs}=b_G(m,\ T)\phi^\circ_{rs}$, $\phi^\circ_{rs}=$ constants, then equation (17) reads

$$\phi_r+b_G\ \phi^\circ_{rs}\gamma_s+b^o_{rs}\frac{d\gamma_s}{d\psi}=0 \quad (24a)$$

and its solution reduces to

$$\gamma_r=-\frac{\phi_r}{\chi_r^\circ b_G}(1-e^{-\xi/Z^\circ_r}) \quad (26)$$

where $\xi=b_G(m,\ T)\psi=\dfrac{b_G(m,T)}{b(m,T)}\,t.$ (27)

An expansion of $\phi(m,T,\gamma_r)$ in powers of γ_r—truncating after the second power—and employing the expression given in equation (26), yields the form[2]

$$\phi=\sum_r\frac{L_r}{b_G}(1-e^{-\xi/\tau_r}). \quad (28)$$

In the case of a continuous spectrum of retardation times we obtain

$$\phi(m,T,t)=\frac{1}{b_G}\int_o^\infty L(\tau)(1-e^{-\xi/\tau})d\tau=\frac{1}{b_G}D(\xi). \quad (29)$$

To proceed beyond this stage it is necessary to consider material symmetry. Isotropy will be selected, since it applies to particle reinforced polymeric composites and also provides the simplest illustration.

4 Isotropic Constitutive Relations

In the case of isotropy $f(\sigma_{ij},\ a_{ij},\ a^*_{ij})$ depends on the isotropic invariants of these three symmetric, second rank tensors. Following Spencer (1971) these invariants are:

$I_1=\sigma_{kk}$, $I_2=\sigma_{ij}\sigma_{ji}$, $I_3=\sigma_{ij}\sigma_{jk}\sigma_{ki}$, $I_4=a_{kk}$, $I_5=a_{ij}a_{ji}$,
$I_6=a_{ij}a_{jk}a_{ki}$, $I_7=I^*_4$,
$I_8=I^*_5$, $I_9=I^*_6$, $I_{10}=a_{ij}\sigma_{ij}$,
$I_{11}=a_{ij}a_{jk}\sigma_{ki}$, $I_{12}=a_{ij}\sigma_{jk}\sigma_{ki}$,
$I_{13}=a_{ij}a_{jk}\sigma_{kl}\sigma_{li}$, $I_{14}=a_{ij}a^*_{ji}$,
$I_{15}=a_{ij}a_{jk}a^*_{ki}$, $I_{16}=a_{ij}a^*_{jk}a^*_{ki}$, $I_{17}=a_{ij}a_{jk}a^*_{kl}a^*_{li}$

and nine more invariants which include σ_{ij} and a^*_{kl} (with or without a_{mn}). In the above list $I^*=I(a^*_{ij})$. The nine unlisted invariants are discarded in f because it is assumed herein that, while both "active" and "passive" microcracks participate in the softening of the material, only the active cracks affect its

[2] Note that this *form* is retained even for products of γ_r because products like $\prod_{k=1}^{n}(1-e^{-a_kx})$ can be expressed as sums $\sum_{k=1}^{n}(1-e^{-\alpha_kx})$

Downloaded 03 May 2010 to 171.66.16.21. Redistribution subject to ASME license or copyright; see http://www.asme.org/terms/Terms_Use.cfm

symmetry. This assumption is consistent with the earlier premises indicated in equations (3*a*) and (5).

Expanding $f(\sigma_{ij}, a_{ij}, a^*_{ij})$ in powers of σ_{ij}, terminating at the second power, we obtain.:

$$-\rho_s f(\sigma_{ij},a_{ij},a^*_{ij},m,T) = -\rho_s A_o + A_1\sigma_{kk} + A_2 a_{ij}\sigma_{ij} + A_3 a_{ij}a_{jk}\sigma_{ki} + \frac{1}{2}A_4\sigma_{kk}\sigma_{ll} + \frac{1}{2}A_5\sigma_{ij}\sigma_{ji} + A_6 a_{ij}\sigma_{ij}\sigma_{kk} + A_7 a_{ij}a_{jk}\sigma_{ki}\sigma_{ll} + A_8 a_{ij}\sigma_{ij}a_{kl}a_{lm}\sigma_{mk} + \frac{1}{2}A_9 a_{ij}\sigma_{ij}a_{kl}\sigma_{kl} + \frac{1}{2}A_{10}a_{ij}a_{jk}\sigma_{ki}a_{lm}a_{mn}\sigma_{nl} + A_{11}a_{ij}\sigma_{jk}\sigma_{ki} + A_{12}a_{ij}a_{jk}\sigma_{kl}\sigma_{li}. \tag{30}$$

In equation (30) the terms $A_o, A_1, \ldots A_{12}$ are functions of the damage invariants $I_4 - I_9$ and $I_{14} - I_{17}$, m, and T.

Strain-stress relations are obtained from equation $(19)_1$. In view of equation (30) we have

$$\epsilon^{el}_{pq} = -\frac{\partial \rho_s f}{\partial \sigma_{pq}} = A_1\delta_{pq} + A_2 a_{pq} + A_3 a_{qj}a_{jp} + A_4\sigma_{kk}\delta_{pq} + A_5\sigma_{pq} + A_6(a_{ij}\sigma_{ij}\delta_{pq} + a_{pq}\sigma_{kk}) + A_7(a_{qj}a_{jp}\sigma_{kk} + a_{ij}a_{jk}\sigma_{ki}\delta_{pq}) + A_8(a_{pq}a_{ij}a_{jk}\sigma_{ki} + a_{ij}\sigma_{ij}a_{qk}a_{kp}) + A_9 a_{pq}a_{ij}\sigma_{ij} + A_{10}a_{qj}a_{jp}a_{ik}a_{kl}\sigma_{li} + A_{11}(a_{ip}\sigma_{qi} + a_{qi}\sigma_{ip}) + A_{12}(a_{ij}a_{jp}\sigma_{qi} + a_{qj}a_{ji}\sigma_{ip}). \tag{31}$$

The first three terms on the right side of equation (31) are related to hygrothermal expansion in the absence of stress. In addition, A_1, A_4, and A_5 should reduce to $(\alpha\Delta T + \beta\Delta m)$ and to the "classical" compliances J_1 and J_2 in the absence of damage.

It can be noted from equation (31) that $\epsilon^{el}_{pq} = \epsilon^{el}_{qp}$. Furthermore, if all active microcracks are parallel to a common plane it can be shown that equation (31) corresponds to transverse isotropy in that plane. Similarly, if all active microcracks are parallel to two or three mutually perpendicular planes equation (31) corresponds, as expected, to orthotropic symmetry.

For fixed a_{ij}, a^*_{ij}, σ_{ij}, m, and T the viscoelastic strain-strain relations are simply a product of expressions (29) and (31), namely

$$\epsilon_{pq}(t) = \epsilon^{el}_{pq} D(\xi)/b_G. \tag{32}$$

For fixed damage but for fluctuating σ_{ij}, m, and T the straightforward employment of superposition integrals gives

$$b_G(m(t), T(t))\epsilon_{pq}(t) = (\alpha_1\delta_{pq} + \alpha_2 a_{pq} + \alpha_3 a_{qj}a_{jp})\int_o^t D(\xi-\xi')\frac{\partial \Delta T}{\partial \tau}\,d\tau + (\beta_1\delta_{pq} + \beta_2 a_{pq} + \beta_3 a_{qj}a_{jp})\int_o^t D(\xi-\xi')\frac{\partial \Delta m}{\partial \tau}\,d\tau + A_4\delta_{pq}\int_o^t D(\xi-\xi')\frac{\partial \sigma_{kk}}{\partial \tau}\,d\tau + A_5\int_o^t D(\xi-\xi')\frac{\partial \sigma_{pq}}{\partial \tau}\,d\tau + \ldots + A_{12}\left\{a_{ij}a_{jp}\int_o^t D(\xi-\xi')\frac{\partial \sigma_{qi}}{\partial \tau}\,d\tau + a_{qj}a_{ji}\int_o^t D(\xi-\xi')\frac{\partial \sigma_{ip}}{\partial \tau}\,d\tau\right\}. \tag{33}$$

In equation (33), α_i and β_i $(i=1,2,3)$, as well as in all A_j $(j=4, \ldots 12)$, depend on the invariants $I_4 - I_9$, $I_{14} - I_{17}$ and, possibly, on m and T. Also

$$\xi = \xi(t) = \int_o^t \frac{du}{b[m(u), T(u)]} \quad \text{and} \quad \xi' = \xi(\tau).$$

Regarding the case of fluctuating damage, consider first the situation of monotonic growth of all microcracks. Furthermore, assume all $S^*_k = 0$ in equation (6) thus the compliances are $S_{ijkl} = S_{ijkl}\ (S_1(t), S_2(t), \ldots S_K(t))$. In the context of the continuum damage variables employed herein we have $S_{ijkl}(t) = S_{ijkl}\ (a_{mn}(t))$. Under constant σ_{ij}, m, and T, and for the elastic case, equation (6) reads

$$\epsilon_{ij}(t) = S_{ijkl}(a_{pq}(t))\sigma^o_{kl}$$

which can be expressed as

$$\epsilon_{ij}(t) = S_{ijrs}(a_{pq}(0))C_{rsmn}(a_{pq}(0))S_{mnkl}(a_{pq}(t))\sigma^o_{kl}. \tag{34}$$

Equation (34), where $C_{ijkl} = S_{ijkl}{}^{-1}$, shows that the case of growing damage can be viewed formally as that of fixed damage with an appropriately modified, time varying stress.

Upon postulating continuity of S_{ijkl} in a_{pq}, the *entire* history dependence of S_{ijkl} is given by

$$S_{ijkl}(a_{pq}(t)) = S_{ijkl}(a_{pq}(0)) + \int_o^t \frac{\partial S_{ijkl}(a_{pq})}{\partial a_{mn}}(\tau)\frac{\partial a_{mn}(\tau)}{\partial \tau}\,d\tau. \tag{35}$$

Consequently, with $\sigma_{ij} = \sigma_{ij}(t)$, formal employment of Boltzmann's superposition principle leads to the following viscoelastic strain-stress relation

$$b_G(m,T)\epsilon_{ij}(t) = S_{ijkl}(a_{mn}(0))\int_o^t D(\xi-\xi')\frac{\partial \sigma_{kl}}{\partial \tau}\,d\tau + \int_o^t D(\xi-\xi')\frac{\partial}{\partial \tau}\left[\sigma_{kl}(\tau)\int_o^\tau \frac{\partial S_{ijkl}(a_{mn})}{\partial a_{mn}}\frac{\partial a_{mn}(u)}{\partial u}\,du\right]d\tau. \tag{36}$$

Upon identifying $S_{ijkl}\ (a_{pq})$ with the compliances and forms for the intially isotropic case in equation (31), the strain-stress relations, with monotonically growing microcracks, and time-dependent σ_{ij}, m, and T, read

$$\begin{aligned} b_G\epsilon_{pq}(t) = {} & D^*\{\Delta T \circ (\alpha_1\delta_{pq} + \alpha_2 a_{pq} + \alpha_3 a_{qj}a_{jp}) \\ & + \Delta m \circ (\beta_1\delta_{pq} + \beta_2\alpha_{pq} + \beta_3\alpha_{qj}\alpha_{jp}) + (\sigma_{kk} \circ A_4)\delta_{pq} \\ & + (\sigma_{pq} \circ A_5) + [\sigma_{ij} \circ (A_6 a_{ij})]\delta_{pq} + (\sigma_{kk} \circ (A_6 a_{pq})) \\ & + (\sigma_{kk} \circ (A_7 a_{qj}a_{jp})) + (\sigma_{ki} \circ (A_7 a_{ij}a_{jk}))\delta_{pq} \\ & + (\sigma_{ki} \circ (A_8 a_{pq}a_{ij}a_{jk})) + (\sigma_{ij} \circ (A_8 a_{ij}a_{qk}a_{kp})) \\ & + (\sigma_{ij} \circ (A_9 a_{pq}a_{ij})) + (\sigma_{li} \circ (A_{10}a_{qj}a_{jp}a_{ik}a_{kl})) \\ & + (\sigma_{qi} \circ (A_{11}a_{ip})) + (\sigma_{ip} \circ (A_{11}a_{qi})) \\ & + (\sigma_{qi} \circ (A_{12}a_{ij}a_{jp})) \\ & + (\sigma_{ip} \circ (A_{12}a_{qj}a_{ji}))\} \end{aligned} \tag{37}$$

where $D^* f$ denotes $\int_o^t D(\xi-\xi')\frac{\partial f}{\partial \tau}\,d\tau$ and $(g \circ h)\ (\tau)$ denotes

$$g(\tau)\left[h(a_{mn}(0)) + \int_o^\tau \frac{\partial h}{\partial a_{mn}}\frac{\partial a_{mn}}{\partial u}\,du\right]. \tag{38}$$

Obviously, in equation (37) all α_i, β_i and A_j $(i=1,2,3;\ j=4,5, \ldots 12)$ depend only on the invariants I_4, I_5, and I_6 of a_{ij}.

Downloaded 03 May 2010 to 171.66.16.21. Redistribution subject to ASME license or copyright; see http://www.asme.org/terms/Terms_Use.cfm

In particular, if the material is initially undamaged, then $\alpha_1(a_{mn}(0))=\alpha$, $\beta_1(a_{mn}(0))=\beta$, $A_4(a_{mn}(0))=J_1$ and $A_5(a_{mn}(0))=J_2$ which denote the familiar viscoelastic expansional coefficients and compliances. In this case the initial values of all other terms—α_2, α_3, β_2, β_3, $A_6, \ldots A_{12}$—vanish.

In the formal derivation of equation (36) the fact that time-dependent a_{ij} are associated with changing material geometry was not explicitly considered. This fact should be addressed because the elastic-viscoelastic correspondence principle does not apply straightforwardly in this circumstance. A rigorous mathematical derivation of this circumstance was provided by Schapery (1980, 1981, 1984), yielding results of essentially the same form as equation (36). The derivation applied to monotonically growing damage in materials of any symmetry, including the case of stress-strain nonlinearity, but with the restriction that all material compliances possess a common time dependence. The latter restriction prevails also in the present work.

When the microcracks experience both growth and closure the current configuration, as given by $a_{ij}(t)$ and $a^*_{ij}(t)$, may reflect distinct growth and closure histories. The viscoelastic strain-stress relation should distinguish among such histories.

Consider an initially undamaged material. A formal extension of equation (36) to the case of damage growth and closure yields the following expression:

$$
\begin{aligned}
b_G\epsilon_{ij}(t) = S_{ijkl}(0)\int_o^t D(\xi-\xi')\,\frac{\partial\sigma_{kl}}{\partial\tau}\,d\tau \\
+\int_o^t D(\xi-\xi')\,\frac{\partial}{\partial\tau}\Big[\sigma_{kl}(\tau)\int_o^{\tau(g)} \\
\times\frac{\partial S_{ijkl}(a_{mn},a^*_{pq})}{\partial a_{mn}}\,\frac{\partial a_{mn}}{\partial u}\,du\Big]d\tau \\
+\int_o^t D(\xi-\xi')\,\frac{\partial}{\partial\tau}\Big[\sigma_{kl}(\tau)\int_o^{\tau(c)} \\
\times\frac{\partial S_{ijkl}(a_{mn},a^*_{pq})}{\partial a^*_{pq}}\,\frac{\partial a^*_{pq}}{\partial u}\,du\Big]d\tau
\end{aligned}
\tag{39}
$$

where $\tau(g)$ and $\tau(c)$ represent the time intervals for damage growth and closure, respectively. Those intervals may overlap.

Reverting to the initially isotropic case, the result is still given by equation (37), except that expression (38) should be modified to read

$$
\begin{aligned}
(g\circ h)(\tau) = g(\tau)\Big[h(0) \\
+\int_o^{\tau(g)}\frac{\partial h(a_{mn},a^*_{pq})}{\partial a_{mn}}\,\frac{\partial a_{mn}}{\partial u}\,du \\
+\int_o^{\tau(c)}\frac{\partial h(a_{mn},a^*_{pq})}{\partial a^*_{pq}}\,\frac{\partial a^*_{pq}}{\partial u}\,du\Big].
\end{aligned}
\tag{39a}
$$

It should be noted that equation (39) was obtained in a strictly formal manner, without proof based upon considerations of fluctuating material geometry.

5 Some Special Subcases

(a) Unidirectional Damage Under Uniaxial Stress. Let all "active" and "passive" microcracks be in planes normal to the x_3-direction, whereby $a_{ij}=a\,\delta_{3i}\delta_{3j}$ and $a^*_{ij}=a^*\,\delta_{3i}\delta_{3j}$.

In this case equation (31) reduces to the transversely isotropic relation

$$
\begin{aligned}
\epsilon^{el}_{pq} = J_1\sigma_{kk}\delta_{pq}+J_2\sigma_{pq}+A(\sigma_{33}\delta_{pq}+\delta_{3p}\delta_{3q}\sigma_{kk}) \\
+B\,\delta_{3p}\delta_{3q}\sigma_{33}+C(\delta_{3p}\sigma_{3q}+\delta_{3q}\sigma_{3p}).
\end{aligned}
\tag{40}
$$

In equation (40) A, B, and C represent combinations of the seven compliances $A_6, \ldots A_{12}$ of equation (31). Also, all five compliances in equation (40) depend on a and a^*.

Consider the case of uniaxial stress $\sigma_{33}=\sigma_o H(t)$ and, in addition, assume $m=0$ and $\Delta T=0$. In this case the strains are

$$
\begin{aligned}
\epsilon^{el}_{11} &= \epsilon^{el}_{22}=(J_1+A)\sigma_o \\
\epsilon^{el}_{33} &= (J_1+J_2+2A+B+2C)\sigma_o.
\end{aligned}
\tag{41}
$$

In view of equation (39*a*), the corresponding viscoelastic strains are

$$
\begin{aligned}
\epsilon_{11}(t)/\sigma_o=\epsilon_{22}(t)/\sigma_o=J_1(0,0)D(t) \\
+\int_o^t D(t-\tau)\Big[\frac{\partial F_1(a,a^*)}{\partial a}\,\frac{\partial a(\tau(g))}{\partial\tau(g)}\,d\tau(g) \\
+\frac{\partial F_1(a,a^*)}{\partial a^*}\,\frac{\partial a^*(\tau(c))}{\partial\tau(c)}\,d\tau(c)\Big]
\end{aligned}
\tag{42}
$$

$$
\begin{aligned}
\epsilon_{33}(t)/\sigma_o=[J_1(0,0)+J_2(0,0)]D(t) \\
+\int_o^t D(t-\tau)\Big[\frac{\partial F_2(a,a^*)}{\partial a}\,\frac{\partial a(\tau(g))}{\partial\tau(g)}\,d\tau(g) \\
+\frac{\partial F_2(a,a^*)}{\partial a^*}\,\frac{\partial a^*(\tau(c))}{\partial\tau(c)}\,d\tau(c)\Big].
\end{aligned}
$$

In equation (42) $F_1=J_1+A$, $F_2=J_1+J_2+2A+B+2C$, and $\tau(g)$, $\tau(c)$ denote times of crack growth and closure, respectively. These expressions show that Poisson's ratio, as inferred from $-\epsilon_{11}(t)/\epsilon_{33}(t)$, can serve as a measure of the effects of damage on material properties.

(b) Coupling of Damage With Moisture Transport. Consider the flux of moisture f_i in the presence of damage but in the absence of stress. In addition, let the temperature remain constant, i.e., $\Delta T=0$.

The flux f_i will depend on the gradient of the chemical potential $z_i=\partial\mu/\partial x_i$ as well as on a_{ij} and a^*_{ij}.

To derive the flux gradient relationship it is necessary to generate all the isotropic invariants among the two vectors and two symmetric second rank tensors f_i, z_i, a_{ij} and $a_{ij}{}^*$. According to Spencer (1971, page 293) there are seventeen such invariants.[3] To maintain tractability we shall consider only the seven first terms from Spencer's list. Accordingly,

$$
\begin{aligned}
f_i &= F^{(1)}z_i+F^{(2)}a_{ij}z_j+F^{(3)}a_{ik}a_{kj}z_j+F^{(4)}a^*_{ij}z_j \\
&+F^{(5)}a^*_{ik}a^*_{kj}z_j+F^{(6)}(a_{ik}a^*_{kj}+a_{jk}a^*_{ki})z_j \\
&+F^{(7)}(a_{ik}a_{kj}-a_{jk}a^*_{ki})z_j.
\end{aligned}
\tag{43}
$$

In equation (43), all $F^{(i)}$ $(i=1,2,\ldots 7)$ are assumed to depend on the damage invariants I_4-I_9, $I_{14}-I_{17}$ listed in Section 4.

According to equation (43) the flux of moisture is affected by changes in the material symmetry caused by *both* damage parameters a_{ij} and a^*_{ij}. Recall equations $(19)_2$, (29), and (30). Accordingly, in the absence of stress

$$
\begin{aligned}
\mu=\frac{\partial}{\partial m}\{A_o(a_{ij},a^*_{kl},m,T_o)[\phi(m,T_o,0)+\phi_r(m,T_o,0)\gamma_r \\
+1/2\phi_{rs}(m,T_o,0)\gamma_r\gamma_s]\}
\end{aligned}
\tag{44}
$$

which can be expressed in the form

[3] Invariants of the form $U_i(\Pi_\alpha)_{ij}U_j$ are irrelevant for the construction of flux gradient relationships.

Downloaded 03 May 2010 to 171.66.16.21. Redistribution subject to ASME license or copyright; see http://www.asme.org/terms/Terms_Use.cfm

$$\mu = M_o(a_{ij}, a^*_{kl}, m, T_o) + \sum_r M_r(a_{ij}, a^*_{kl}, m, T_o)(1 - e^{-\xi/\tau_r}). \tag{45}$$

Since the boundary condition for the moisture transport process is $\mu(\mathbf{x} \,|\mathbf{x} \in \text{boundary}) = \mu^A$ (Ambient vapor), equation (45) shows that even under constant ambient humidity the boundary condition will be time dependent. A similar conclusion was reached by Long and Richman (1959), Frisch (1964), Jackle and Frisch (1985), and Weitsman (1987a)—even in the absence of damage.

Consider now the gradients $z_i = \partial\mu/\partial x_i$. In view of equation (45) z_i will include gradients of damage, through the dependence of M_o and M_r on the invariants $I_4 - I_9$, $I_{14} - I_{17}$. Obviously, z_i will also contain moisture gradients.

The chain rule of differentiation gives

$$z_i = F_{kl} \frac{\partial a_{kl}}{\partial x_i} + F^*_{kl} \frac{\partial a^*_{kl}}{\partial x_i} + F_m \frac{\partial m}{\partial x_i} \tag{46}$$

where F_{kl} and F^*_{kl} contain partial derivatives of M_o and M_r with respect to a^*_{ij} and a^*_{kl}, respectively. The term F_m contains partial derivatives of M_o and M_r with respect to m, as well as a derivative of ξ with respect to m in view of the moisture-dependent shift factors b and b_G contained in ξ.

Combining equations (43) and (46) it is observed that the flux of moisture is reoriented into directions of increasing damage. Since damage growth can be attributed to moisture (Ashbee and Wyatt (1969), Drzal et al. (1985), Jackson and Weitsman (1985), and Weitsman (1987*c*)), the latter two observations would indicate that moisture absorption and damage may form a synergistic mechanism.

6 Concluding Remarks

This paper presented a continuum damage model for viscoelastic materials under several simplifying assumptions. The distinct microcracks were represented by two continuum level, internal state variables. These variables, which were expressed by nondimensional symmetric, second rank tensors, represented the total areas of "active" and "passive" microcracks contained within a representative volume element of the material. It was further assumed that all viscoelastic material responses follow a common time dependence, and all detailed expressions were derived for materials that were isotropic prior to the onset of damage.

The resulting expressions show that, in the presence of damage, the response of viscoelastic materials contains *two* time dependent phenomena. The first is attributable to the "inherent" viscoelastic behavior of the undamaged material, while the second is due to time-dependent damage growth. In addition, damage induces changes in the global symmetry of the material.

As can be noted from equations (37)–(39), the coupling of damage and viscoelasticity introduces very significant complexities in the material's response and substantial work remains to be done—both experimentally and analytically—to attain a quantitative and practical understanding of the phenomenon.

The most important ingredient which remains missing in the present work concerns the growth relations for the damage parameters $\dot{a}_{ij}$ and $\dot{a}^*_{ij}$. To be meaningful, such relations should be correlated with basic solutions for crack growth and closure in viscoelastic media. Several solutions for viscoelastic crack growth are already available at the present time, as reviewed by Kaminskii (1980) and outlined by Christensen (1982). Additional research into the fundamentals of viscoelastic fracture is necessary.

Acknowledgments

The author thanks Prof. R. A. Schapery for several helpful discussions.

This work was conducted under Contract N00014-82-K-0562 from the Office of Naval Research (ONR). The author is grateful to Dr. Y. Rajapakse of the Mechanics Division, Engineering Sciences Directorate, ONR, for his support and encouragement.

References

Ashbee, K. H. G., and Wyatt, R. C., 1969, "Water Damage in Glass Fiber/Resin Composites," *Proc. Royal Soc. London*, Vol. A312, pp. 553–564.

Biot, M. A., 1954, "Theory of Stress-Strain Relations in Anisotropic Viscoelasticity and Relaxation Phenomena," *Journal of Applied Physics*, Vol. 25, pp. 1385–1391.

Biot, M. A., 1955, "Variational Principles in Irreversible Thermodynamics with Application to Viscoelasticity," *Physical Review*, Vol. 97, No. 6, pp. 1463–1469.

Biot, M. A., 1973, "Nonlinear and Semilinear Rheology of Porous Solids," *Journal of Geophysical Research*, Vol. 78, pp. 4924–4937.

Bueche, F., 1954, "The Viscoelastic Properties of Plastics," *Journal of Chemical Physics*, Vol. 22, No. 4, pp. 603–609.

Callen, H. B., 1960, *Thermodynamics*, John Wiley, New York, (especially p. 106).

Chritensen, R. M., 1982, *Theory of Viscoelasticity*, 2nd Ed., Academic Press, New York, (especially pp. 167–179 and 185).

Coleman, B. D., and Gurtin, M. E., 1967, "Thermodynamics with Internal State Variables," *Journal of Chemical Physics*, Vol. 47, No. 2, pp. 597–613.

Drzal, L. T., Rich, M. J., and Koenig, M. F., 1985, "Adhesion of Graphite Fibers to Epoxy Matrices, III: The Effect of Hygrothermal Exposure," *Journal of Adhesion*, Vol. 18, pp. 49–72.

Frisch, H. L., 1964, "Isothermal Diffusion in Systems with Glasslike Transitions," *Journal of Chemical Physics*, Vol. 41, No. 12, pp. 3679–3683.

deGroot, S. R., and Mazur, P., 1962, *Non-Equilibrium Thermodynamics*, North-Holland (especially pp. 273–284).

Jackle, J., and Frisch, H. L., 1986, "Properties of a Generalized Diffusion Equation with Memory," *Journal of Chemical Physics*, Vol. 85, No. 3, pp. 1621–1627.

Jackson, S. P., and Weitsman, Y., 1985, "Moisture Effects and Moisture Induced Damage in Composites," *Proc. 5th Int. Conference on Composite Materials (ICCMV)*, The Metallurgical Society, pp. 1435–1452.

Jaunzemis, W., 1967, *Continuum Mechanics*, McMillan, New York.

Kachanov, L. M., 1958, "Time of the Rupture Process Under Creep Conditions" (in Russian), *Izv. Akad. Nauk. ANSSR Otd. Tekh, Nauk.*, Vol. 8, pp. 26–31.

Kaminskii, A. A., 1980, "Investigations in the Field of Mechanics of the Fracture of Viscoelastic Bodies," *Prikl. Mekh.*, Vol. 16, No. 9, pp. 3–26.

Kestin, J., 1979, *A Course in Thermodynamics*, Vol. I, McGraw-Hill, New York, (especially pp. 582–585).

Krajcinovic, D., 1986, "Continuum Damage Mechanics," *Applied Mechanics Update*, ASME, New York, pp. 397–406.

Krajcinovic, D., 1987, "Micromechanical Basis of Phenomenological Models," *Continuum Damage Mechanics: Theory and Applications*, Krajcinovic and Lemaitre, eds., Springer-Verlag, pp. 195–206.

Long, F. A., and Richman, D., 1960, "Concentration Gradients for Diffusion of Vapors in Glassy Polymers and their Relation to Time Dependent Diffusion Phenomena," *Journal of the American Chemical Society*, Vol. 82, pp. 513–519.

Murakami, S., and Ohno, N., 1981, "A Continuum Theory of Creep and Creep Damage," *Creep in Structures*, Ponter and Hayhurst, eds., Springer-Verlag, pp. 422–444.

Prigogine, I., 1967, *Thermodynamics of Irreversible Processes*, 3rd Ed., Interscience.

Rice, J. R., and Cleary, M. P., 1976, "Some Basic Stress Diffusion Solutions for Fluid-Saturated Elastic Porous Media with Compressible Constituents," *Rev. Geophysics and Space Physics*, Vol. 14, No. 2, pp. 227–241.

Rouse, P. E., 1953, "A Theory of the Linear Viscoelastic Properties of Diolute Solutions of Coiling Polymers," *Journal of Chemical Physics*, Vol. 21, No. 7, pp. 1272–1280.

Schapery, R. A., 1964, "Application of Thermodynamics to Thermomechanical, Fracture and Birefringent Phenomena in Viscoelastic Media," *Journal of Applied Physics*, Vol. 35, No. 5, pp. 1451–1465.

Schapery, R. A., 1966, "A Theory of Non-Linear Viscoelasticity Based on Irreversible Thermodynamics," *Proc. 5th U.S. National Congress of Applied Mechanics*, pp. 511–530.

Schapery, R. A., 1969, "Further Development of a Thermodynamic Constitutive Theory: Stress Formulation," Purdue Univ., Report AA&ES 69-2. (AFML Contract F 33615-67-C-1412).

Schapery, R. A., 1980, "On Constitutive Equations for Viscoelastic Composite Materials Wtih Damage," *Workshop on a Continuum Mechanics Approach to Damage and Life Prediction*, NSF, pp. 119–133.

Downloaded 03 May 2010 to 171.66.16.21. Redistribution subject to ASME license or copyright; see http://www.asme.org/terms/Terms_Use.cfm

Schapery, R. A., 1981, "On Viscoelastic Deformation and Failure Behavior of Composite Materials with Distributed Flaws," *Advances in Aerospace Structures and Materials*, S. S. Wang and W. J. Renton, eds., ASME, New York, pp. 5–20.

Schapery, R. A., 1984, "Correspondence Principles and a Generalized J Integral for Large Deformation and Fracture Analysis of Viscoelastic Media," *International Journal of Fracture*, Vol. 25, pp. 195–223.

Shirrell, C. D., Leisler, W. H., and Sandow, F. A., 1979, "Moisture-Induced Surface Damage in T300/5208 Graphite Epoxy Laminates," *Nondestructive Evaluation and Flaw Criticality for Composite Materials*, R. B. Pipes, ed., ASTM STP 696, pp. 209–222.

Spencer, A. J. M., 1971, "Theory of Invariants," *Continuum Physics, Vol. I: Mathematics*, A. C. Eringen, ed., Academic Press, New York, pp. 268–293.

Spencer, A. J. M., 1972, *Deformation of Fibre-Reinforced Materials*, Oxford, (especially pp. 79–81).

Weitsman, Y., 1987a, "Stress Assisted Diffusion in Elastic and Viscoelastic Materials," *Journal of the Mechanics and Physics of Solids*, Vol. 35, No. 1, pp. 73–97.

Weitsman, Y., 1987b, "Environmentally Induced Damage in Composites," *Continuum Models of Discrete Systems*, A. J. M. Spencer, ed., Balkema, pp. 187–192.

Weitsman, Y., 1987c, "Coupled Damage and Moisture-Transport in Fiber-Reinforced, Polymeric Composites," *International Journal of Solids and Structures*, Vol. 23, No. 7, pp. 1003–1025.

Weitsman, Y., 1988, "Damage Coupled with Heat Conduction in Uniaxially Reinforced Composites," ASME JOURNAL OF APPLIED MECHANICS, Vol. 55, No. 3, pp. 641–647.

Zimm, B. H., 1956, "Dynamics of Polymer Molecules in Dilute Solution: Viscoelasticity, Flow Birefringence and Dielectric Loss," *Journal of Chemical Physics*, Vol. 24, No. 2, pp. 269–278.

Downloaded 03 May 2010 to 171.66.16.21. Redistribution subject to ASME license or copyright; see http://www.asme.org/terms/Terms_Use.cfm

N. Fares[1]
Research Fellow.
Division of Applied Science,
Harvard University,
Cambridge, Mass.

V. C. Li
Associate Professor of Civil Engineering.
Massachusetts Institute of Technology,
Cambridge, Mass.
Mem. ASME

General Image Method in a Plane-Layered Elastostatic Medium

Introduction

The study of elastic deformation fields in plane-layered media due to localized elastic disturbance (e.g., cracks) is relevant to several areas of applied mechanics. Theses areas include the study of deformations near fault zones in layered earth models and the study of the structural strength and micromechanics of layered composites. When studying such problems it is often important to determine the elastic response due to disturbances localized at a point (e.g., point forces, dilatation sources, and nuclei of strain, hereafter referred to as point sources) or along a line (e.g., line forces and dislocations, hereafter referred to as line sources). These point source and line source solutions often lead to an appropriate theoretical formulation of a variety of problems in the layered media under consideration, which could then be efficiently solved either analytically or numerically.

This paper describes a new general algorithm for obtaining the elastic response to point and line source disturbances in either of two mediums. The first medium consists of two bonded elastic half spaces having different elastic moduli (Fig. 1(*a*)) and the second medium consists of an elastic layer perfectly bonded to two elastic half spaces of different moduli (Fig. 1(*b*)) hereafter referred to as mediums A and B, respectively. When the elastic response due to an antiplane line source disturbance (e.g., a screw dislocation) is required, the algorithm is seen to correspond to the scalar image method. Hence, the present algorithm for obtaining the elastic fields due to point and line sources will be referred to as the generalized image method.

The image method for antiplane and plane strain problems has been applied to obtain the screw dislocation solution (Chou, 1966) in mediums A and B, the edge dislocation solution (Head, 1953) in medium A and (Stagni and Lizzio, 1987) in medium B. Various other researchers have studied the edge dislocation problem in special cases of medium B, where either one or both of the interfaces are either traction-free or frictionless (e.g., Lee and Dundurs, 1973; Nabarro and Kostlan, 1978; Moss and Hoover, 1978; Stagni and Lizzio, 1986).

Other known point and line source elastic fields include the line force parallel to a free surface (special case of medium A (Mellan, 1932)), point force in an elastic half space with a free surface (special case of medium A (Mindlin, 1936)), and point force in medium A (Rongved, 1955).

A systematic formulation for the derivation of point sources in a multilayered medium (medium B being a special case) was presented by Ben-Menahem and Singh (1968a,b) and later refined by Singh (1970) and independently by Sato (1971). Sato and Matsu'ura (1973) and Jovanovich et al. (1974a,b) made use of the Sato and Singh formulations respectively to calculate surface deformations for a variety of nuclei of strain disturbances and a variety of layered media having a free surface. The Ben-Menahem and Singh and the Sato formulations determine the required elastic fields in terms of inverse integral transforms which have to be numerically inverted for specific numerical parameters. Rundle and Jackson (1977) presented an approximate solution (as the sum of an infinite series) corresponding to a shearing nucleus of strain where the shearing plane is parallel to the interfaces in a special case of medium B and where a free surface is substituted for one of the half spaces. It is to be noted that the nuclei of strain elastic fields in medium A (or any elastic medium) can be obtained from the corresponding point force solution by means of differentiations and simple algebraic operations (e.g., Maruyama, 1964).

The scalar image method can be described as follows. Assume that the solution field due to a localized line or point source disturbance is known in an infinite homogeneous medium, and call that solution the fundamental field. The scalar image method (e.g., when dealing with Laplace's equation) applied to plane-layered mediums determines the solution field to a line or point surface disturbance separately for each layer. The solution field in the layer containing the disturbance is equal to the fundamental field plus one (with a single interface) or an infinite series (with multiple interfaces) of some constant factors multiplying fundamental fields located at shifted positions. The shifted positions correspond to (direct or indirect) reflections of the actual position of disturbance source with respect to the interfaces (an analogy is the reflections of an object placed between parallel partially refracting mirrors). The factors multiplying the image fundamental fields are determined from satisfying boundary con-

[1] Formerly graduate student of Civil Engineering, M.I.T.

Contributed by the Applied Mechanics Division of THE AMERICAN SOCIETY OF MECHANICAL ENGINEERS for presentation at the Joint ASCE/ASME Applied Mechanics, Biomechanics, and Fluids Engineering Conference, San Diego, CA, July 9 to 12, 1989.

Discussion on this paper should be addressed to the Editorial Department, ASME, United Engineering Center, 345 East 47th Street, New York, N.Y. 10017, and will be accepted until two months after final publication of the paper itself in the JOURNAL OF APPLIED MECHANICS. Manuscript received by ASME Applied Mechanics Division, January 7, 1988; final revision, April 12, 1988.

Paper No. 89-APM-14.

Copyright © 1988 by ASME
Downloaded 03 May 2010 to 171.66.16.21. Redistribution subject to ASME license or copyright; see http://www.asme.org/terms/Terms_Use.cfm

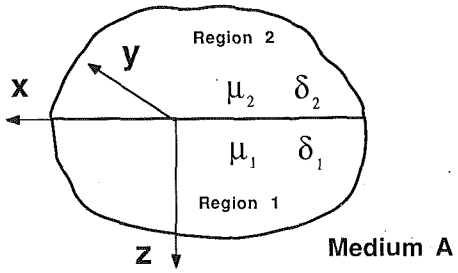

Fig. 1(a)

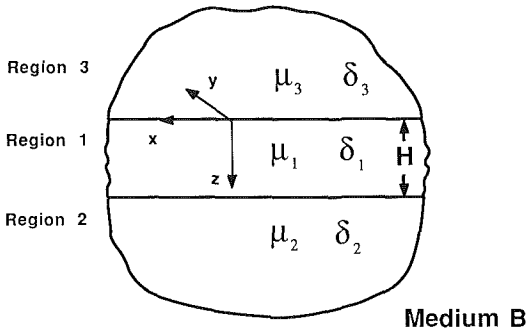

Fig. 1(b)

ditions at the plane interfaces. The solution field in the layers not containing the disturbance is equal to one (with a single interface) or an infinite series (with multiple interfaces) of some constant factors multiplying fundamental fields located at shifted positions. The shifted positions correspond to (direct or indirect) transmission of the actual position of the disturbance source with respect to the interfaces. Figure 2 is a graphical interpretation of the reflection-transmission of the fundamental field.

Stagni and Lizzio (1987) presented a two-dimensional image method in medium B. Since the field equations of two-dimensional elasticity are not scalar, boundary conditions at the interfaces cannot be satisfied by assuming the reflected and transmitted fields are constant factors multiplying shifted fundamental fields. Using Muskhelishvili potentials (Muskhelishvili, 1975), Stagni and Lizzio assumed that there does exist image fields whose potentials are then expanded in a general Laurent's series plus a logarithmic term. By matching boundary conditions at the two interfaces, a recursion relation is obtained which determines the image fields. Finally, Aderogba (1977) presents a three-dimensional method in medium A in terms of Papkovich-Neuber potentials (hereafter referred to as P–N potentials). Although the extension of Aderogba's algorithm to a medium B is in principle possible, the calculation of image P–N potentials involve evaluating multiple indefinite integrals whose multiplicity increases (linearly) with the number of reflections. In general, these indefinite integrals may not be obtained in closed form. The algorithm to be presented is in terms of Hansen potentials (used by Ben-Menahem and Singh, 1968a,b) whose relations to the P–N potentials are described in the next section. The general image algorithm presented in terms of the Hansen potentials does not require the evaluation of indefinite integrals, although multiple partial differentiations with respect to the coordinate perpendicular to the interface are required. The need for multiple partial differentiations (with respect to all coordinates) is required when the image method involves the P–N potentials. The Hansen potentials can be viewed as a linear operation (involving differentiation and integration) on the P–N potentials which obviates the need for indefinite integration when specifying an image algorithm.

In this paper the algorithm of the generalized image method is presented for mediums A and B. Application of this algorithm to a point dilatation source is then illustrated (other examples can be found in Fares, 1987). The present algorithm is suitable for generalization to viscoelastic mediums.

The Algorithm

Any elastic field can be represented in terms of Hansen potentials (Ben-Menahem and Singh, 1968a,b). The Hansen potentials are three harmonic (in the case of no body forces) scalar functions (ϕ_1, ϕ_2 ϕ_3) defined in the region of interest such that the elastic displacement field ($\underline{u}$) is given as:

$$\underline{u} = \nabla\phi_1 + \left(2\hat{e}_z\frac{\partial}{\partial z}\phi_2 - \nabla\phi_2 - 2\delta z\nabla\frac{\partial}{\partial z}\phi_2\right) + \nabla x(\hat{e}_z\phi_3) \qquad (1)$$

where ∇ is the gradient operator, ∇x is the curl operator and $\delta = 1/(3-4\nu)$ (ν is Poisson's ratio, μ is the shear modulus). The P–N potentials (Ω and Ψ) are defined as:

$$\underline{u} = (1/2\mu)\cdot(\nabla\Omega - \frac{1}{\delta}\cdot\underline{\Psi} + \underline{r}\cdot\nabla\Psi) \qquad (2)$$

The Hansen potentials are therefore related to the P–N potentials as:

$$\phi_1 = (1/2\mu)\cdot\Omega$$

$$\frac{\partial^2}{\partial z^2}\phi_2 = -\frac{1}{4\mu\delta}\nabla\cdot\underline{\Psi} \qquad (3)$$

$$\frac{\partial^2}{\partial z^2}\phi_3 = -\frac{1+\delta}{2\mu\delta}e_z\cdot\nabla x\underline{\Psi}$$

In order to derive a general image method for a multilayered medium, it is sufficient to describe an algorithm which derives the reflected and transmitted field of an arbitrary point or line source in a medium with a single interface. The procedure to obtain the elastic field in a multilayered medium would then be formally similar to Chou's method (1966) with image fields obtained by repeated use of the single interface general image algorithm (instead of factors multiplied by the original fundamental field).

Consider the single interface of Fig. 1(*a*) (medium A) with a point or line source located at $x=y=0$ and $z=h$. Let the Hansen potentials of the point or line source (located at $x=y=z=0$) in the absence of region 2 with an infinite extension of region 1 be given by ($\phi_1{}^0$, $\phi_2{}^0$, $\phi_3{}^0$). Assuming the Hansen potentials of the reflected and transmitted elastic fields are scalar multiplies of ($\phi_1{}^0$, $\phi_2{}^0$, $\phi_3{}^0$), ($\partial/\partial z$)($\phi_1{}^0$, $\phi_2{}^0$, $\phi_3{}^0$) and ($\partial^2/\partial z^2$)($\phi_1{}^0$, $\phi_2{}^0$, $\phi_3{}^0$), the algorithm is obtained (after a lot of algebra) by satisfying displacement and traction boundary conditions along the interface $z=0$ (see Fares, 1987, for an alternate derivation). Define the reflected and transmitted potentials by ($\phi_1{}^R$, $\phi_2{}^R$, $\phi_3{}^R$) and ($\phi_1{}^T$, $\phi_2{}^T$, $\phi_3{}^T$), respectively. The reflected and transmitted potentials are then given by:

$$\begin{bmatrix}\phi_1^R\\ \phi_2^R\end{bmatrix} = \underline{\underline{R}}\cdot\begin{bmatrix}\phi_1^{0*}\\ \phi_2^{0*}\end{bmatrix} \qquad \begin{bmatrix}\phi_1^T\\ \phi_2^T\end{bmatrix} = \underline{\underline{T}}\cdot\begin{bmatrix}\phi_1^0\\ \phi_2^0\end{bmatrix}$$

$$\phi_3^R = \left(\frac{1-\gamma}{1+\gamma}\right)\cdot\phi_3^{0*} \qquad \phi_3^T = \left(\frac{2}{1+\gamma}\right)\cdot\phi_3^0 \qquad (4)$$

where: $\phi^*(x,y,z) = \phi(z,y,-z)$ (5)

Downloaded 03 May 2010 to 171.66.16.21. Redistribution subject to ASME license or copyright; see http://www.asme.org/terms/Terms_Use.cfm

$$\underline{\underline{R}} = \begin{bmatrix} 2\cdot\delta_1\cdot\dfrac{\gamma-1}{\delta_1+\gamma}h\cdot\dfrac{\partial}{\partial z} & \dfrac{\gamma\delta_2-\delta_1}{\gamma\delta_2+1} - 4\cdot\delta_1^2\cdot\dfrac{\gamma-1}{\delta_1+\gamma}h^2\cdot\dfrac{\partial^2}{\partial z^2} \\ \dfrac{\gamma-1}{\delta_1+\gamma} & -2\cdot\delta_1\cdot\dfrac{\gamma-1}{\delta_1+\gamma}h\cdot\dfrac{\partial}{\partial z} \end{bmatrix} \tag{6}$$

$$\underline{\underline{T}} = \begin{bmatrix} \dfrac{\delta_1+1}{\delta_1+\gamma} & -2\cdot(\delta_1+1)\cdot\left(\dfrac{\delta_2}{\gamma\delta_2+1} - \dfrac{\delta_1}{\delta_1+\gamma}\right)\cdot h\cdot\dfrac{\partial}{\partial z} \\ 0 & \dfrac{\delta_1+1}{\gamma\delta_2+1} \end{bmatrix} \tag{7}$$

$$\gamma = \mu_2/\mu_1 \tag{8}$$

The Hansen potentials for regions 1 and 2 are then given by $(\phi_1{}^0(x,y,z-h)+\phi_1{}^R(x,y,z+h),\ \phi_2{}^0(x,y,z-h)+\phi_2{}^R(x,y,z+h),\ \phi_3{}^0(x,y,z-h)+\phi_3{}^R(x,y,z+h))$ and $(\phi_1{}^T(x,y,z-h),\ \phi_2{}^T(x,y,z-h),\ \phi_3{}^T(x,y,z-h))$, respectively. Note that **R** and **T** are matrix operators dependent on δ_1, δ_2, γ, and h.

The single interface image algorithm can now be used to obtain an image algorithm for multiple interfaces (Rice, 1985, private communications). Consider medium B (refer to Fig. 1(*b*)) with a point or line source located in region 1 at $x=y=0$ and $z=h$ (the case of the source lying in region 2 is given in Fares, 1987). Let the single interface reflection matrix operator related to the upper and lower interfaces be denoted as $\mathbf{R}^+(h)$ and $\mathbf{R}^-(-H+h)$, respectively (H is the thickness of region 1), and define $\gamma^+=\mu_3/\mu_1$ and $\gamma^-=\mu_2/\mu_1$. An image field reflected by the upper interface will have to be reflected again by the lower interface and vice versa as depicted in Fig. 2. These repeated reflections (in two directions) with the associated transmission of fields will lead to Hansen potentials defined as an infinite series of potentials in each of regions 1, 2, and 3 (in a manner analogous to Chou's results). The Hansen potentials in region 1 (potentials for region 2 are given in Fares, 1987) are then given by:

$$\phi = \begin{bmatrix} \phi_1^1 \\ \phi_2^1 \end{bmatrix}$$

$$\phi = \phi^0(x,y,z-h) + \sum_{m=1}^{\infty} [\phi_{m1}(x,y,z+2(m-1)H+h) + \phi_{m2}(x,y,z-2mH-h) + \phi_{m3}(x,y,z-2mH+h) + \phi_{m4}(x,y,z+2mH-h)] \tag{9}$$

where:

$$\phi_{02} = \phi_{04} = \phi^0$$

$$\phi_{m1}(x,y,z) = \underline{\underline{R}}^+((2m-2)\cdot H+h)\cdot\phi^*_{(m-1)2}(x,y,z)$$

$$\phi_{m2}(x,y,z) = \underline{\underline{R}}^-((-2m+1)\cdot H-h)\cdot\phi^*_{m1}(x,y,z)$$

$$\phi_{m3}(x,y,z) = \underline{\underline{R}}^-((-2m+1)\cdot H+h)\cdot\phi^*_{(m-1)4}(x,y,z)$$

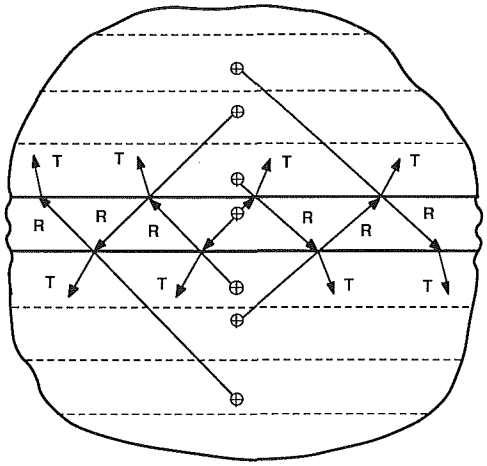

Fig. 2

$$\phi_{m4}(x,y,z) = \underline{\underline{R}}^+(2mH-h)\cdot\phi^*_{m3}(x,y,z) \tag{10}$$

The ϕ_3 potentials are given by (9) with $\phi=\phi_3$ and $\mathbf{R}^+$ and $\mathbf{R}^-$ replaced by $(1-\gamma^+)/(1+\gamma^+)$ and $(1-\gamma^-)/(1+\gamma^-)$, respectively in equation (10). When $\phi_1=\phi_2=0$ the scalar image method used by Chou is obtained, and hence, ϕ_3 can be associated with the antiplane component of an elastic deformation.

The convergence of the displacements or stresses corresponding to the series of potentials given by (9) depends on both the material contrasts between regions 1, 2, and 3 and on the singularity of the point or line source being considered. Given a fixed type of line or point source, the contribution of the farther images (images with higher "m" in equation (9)) decreases to zero as the medium approaches a homogeneous or bimaterial state. In addition, given fixed material properties in regions 1, 2, and 3, the contribution of the farther images decreases algebraically with the location of those images. Limited convergence studies on antiplane line sources (Fares, 1987) suggest that if the singularity of the line source is at least as strong as that corresponding to a dislocation, then the series giving the displacements and stresses converge for a wide range of material contrasts between regions 1, 2, and 3. Specifically, the series corresponding to the displacements due to a screw dislocation converges to the analytic closed form solution given by Tse and Rice (1986).

Example

In this section the elastic field of a dilatation source in a half space with a traction-free surface (special case of medium A), and the elastic field of a dilatation source in an elastic plate with two traction-free surfaces (special case of medium B) will be derived using the general image method. (Examples of several point and line source disturbances in a medium A, and nuclei of strain in a medium B are derived using the general image method in Fares, 1987.)

The P-N potentials for a dilatation source of expansion of net volume "V" are given by:

$$\Omega = \frac{\mu V}{2\pi}\cdot\frac{1}{r}$$

$$\underline{\Psi} = \underline{0} \tag{11}$$

where $r^2 = x^2+y^2+z^2$.

Therefore, by using (3), the Hansen potentials can be obtained as:

$$\phi_1 = \frac{V}{4\pi}\cdot\frac{1}{r}$$

Downloaded 03 May 2010 to 171.66.16.21. Redistribution subject to ASME license or copyright; see http://www.asme.org/terms/Terms_Use.cfm

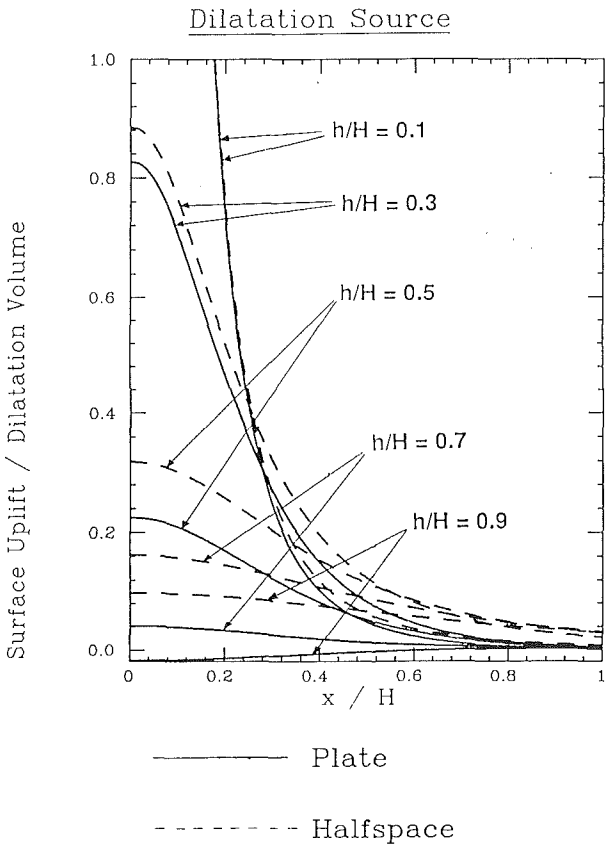

Fig. 3

$$\phi_2 = \phi_3 = 0 \tag{12}$$

Using the general image method relations (4) and (6) with $\gamma = 0$ for a traction-free half space, the reflected image potentials due to a dilatation source located at $x = y = 0$ and $z = h$ are then given by:

$$\phi_1^R = \frac{V}{4\pi} \cdot \left(-2 \cdot h \cdot \frac{z}{r^3} \right)$$

$$\phi_2^R = \frac{V}{4\pi} \cdot \left(\frac{1}{\delta} \cdot \frac{1}{r} \right)$$

$$\phi_3^R = 0 \tag{13}$$

Using both (12) and (13) and relation (1), the displacement field for a dilatation source in a half space is obtained:

$$\underline{u}/(V/4\pi) = e_x \cdot \left[\frac{x}{r^3} + 6 \cdot h \cdot \frac{x \cdot (z+h)}{r_2^5} + \frac{x}{\delta \cdot r_2^3} - 6 \cdot x \cdot \frac{(z+h)^2}{r_2^5} \right] + e_y \cdot \left[\frac{y}{r^3} + 6 \cdot h \cdot \frac{y \cdot (z+h)}{r_2^5} + \frac{y}{\delta \cdot r_2^3} - 6 \cdot y \cdot \frac{(z+h)^2}{r_2^5} \right] + e_z \cdot \left[\frac{(z-h)}{r^3} - 2 \cdot h \cdot \frac{1}{r_2^3} + 6 \cdot h \cdot \frac{(z+h)^2}{r_2^5} + \left(2 - \frac{1}{\delta} \right) \cdot \frac{(z+h)}{r_2^3} - 6 \cdot \frac{(z+h)^3}{r_2^5} \right] \tag{14}$$

where:

$$r^2 = x^2 + y^2 + (z-h)^2$$

$$r_2{}^2 = x^2 + y^2 + (z+h)^2 \tag{15}$$

The Hansen potentials representations for a dilatation source in a plate with two free surfaces has an infinite series representation. The displacement field obtained from these series for points located at finite distances from the dilatation source converges. The convergence is assured because the successive image displacement fields are located successively farther from the plate (with distance growing algebraically as "m" defined in (9) increases) while having functional variations which vary as $1/r^2$ (where "r" is the distance from the image source location to a point in the plate). In practice, however, the infinite series representations of the Hansen potentials have to be truncated. Since the calculation of image Hansen potentials with successively higher "m" in (9) and (10) is time consuming, an extrapolation (using Richardson's extrapolation, e.g., Bender and Orszag, 1978) is used to accelerate the convergence. By extrapolating and using Hansen potentials up to $m = 4$ in (9) and (10), very accurate elastic fields can be obtained at distances within three plate thicknesses from the source disturbance as evidenced by numerical studies based on antiplane deformation fields (Fares, 1987). Figure 3 shows the displacement in the z-direction at $z = 0$ when a dilatation source is located in a plate at $x = y = 0$ and $z/H = 0.1$, 0.3, 0.5, 0.7, and 0.9, (solid line). The corresponding displacement in the z-direction when a dilatation source is located in a half space is also shown (dashed line). Since the displacement field is radially symmetric, only displacements with $y = 0$ and a range of x values (taken to be $0 < x < H$ since the displacement field falls off rapidly with distance) need to be shown.

Referring to Fig. 3, the displacement magnitude above the dilatation source decreases with the depth of the source. Also, the dilatation source is more effective at causing surface uplift when the supporting foundation is more rigid, which explains the higher uplift values in the half space as compared to the plate. Finally, the surface deformations at $z = 0$ in a plate can be negative when the dilatation source is very close to the lower free surface ($z = H$). This can be explained as follows: The dilatation source in the lower portion of the plate causes local compressive stresses which have to be compensated by tensile stresses in the upper portion of the plate. This stress distribution is equivalent to a bending moment in the plate which produces negative surface uplift when the dilatation source is at a depth lower than $0.5H$. In addition to the bending moment effect of the dilatation source, expansion of the dilatation source produces displacements which are pointing away from the source producing positive surface uplift. The net surface deformation is a resultant of these two effects.

Conclusions

A general image method used to obtain elastostatic fields in plane-layered media has been presented. The image method relies on using potentials to represent elastic fields. For the case of a single interface, the image method gives the displacement fields in closed form, and can be applied to antiplane, plane, and three-dimensional problems. For the case of multiple interfaces, the image method gives the displacement fields in terms of infinite series. The convergence of the series can be accelerated which improves the efficiency of the method.

Acknowledgments

The authors wish to thank J. R. Rice for useful discussions and acknowledge support of this work from the crustal dynamics program at the National Aeronautics and Space Administration to the Massachusetts Institute of Technology.

References

Aderogba, K., 1977, "On Eigenstresses in Dissimilar Media," *Phil. Mag.*, Vol. 35, pp. 281-292.

Downloaded 03 May 2010 to 171.66.16.21. Redistribution subject to ASME license or copyright; see http://www.asme.org/terms/Terms_Use.cfm

Bender, C. M., and Orszag, S. A., 1978, *Advanced Mathematical Methods for Scientists and Engineers*, McGraw-Hill, New York.

Ben-Menahem, A., and Singh, S. J., 1968a, "Multipolar Elastic Fields in a Layered Half-space," *Bull. Seism. Soc. Amer.*, Vol. 58, pp. 1519–1572.

Ben-Menahem, A., and Singh, S. J., 1968b, "Eigenvector Expansions of Green's Dyads with Application to Geophysical Theory," *Geophys. J. R. Astr. Soc.*, Vol. 16, pp. 417–452.

Chou, Y. T., 1966, "Screw Dislocations in and Near Lamellar Inclusions," *Phys. Status Solids*, Vol. 17, pp. 509–516.

Fares, N., 1987, "Green's Functions for Plane-layered Elastostatic and Viscoelastic Regions with Application to 3-D Crack Analysis," Ph.D. Thesis, M.I.T.

Head, A. K., 1953, "Edge Dislocations in Inhomogeneous Media," *Proc. Phys. Soc. B*, Vol. 66, p. 793.

Jovanovich, D. B., Husseini, M. I., and Chinnery, M. A., 1974a, "Elastic Dislocations in a Layered Half-space—I. Basic Theory and Numerical Methods," *Geophys. J. R. Astr. Soc.*, Vol. 39, pp. 205–217.

Jovanovich, D. B., Husseini, M. I., and Chinnery, M. A., 1974b, "Elastic Dislocations in a Layered Half-space—II. The Point Source," *Geophys. J. R. Astr. Soc.*, Vol. 39, pp. 219–239.

Lee, M. S., and Dundurs, J., 1973, "Edge Dislocation in a Surface Layer," *Int. J. Engng. Sci.*, Vol. 11, p. 87.

Maruyama, T., 1964, "Statical Elastic Dislocations in an Infinite and Semi-infinite Medium," *Bull. Earthquake Res. Inst.*, Vol. 42, pp. 289–368.

Mellan, E., 1932, "Der Spannungszustand der Durch eine Einzelkraft in Innern Beanspruchten Halbsheibe," *Z. Angew. Math. Mech.*, Vol. 12, pp. 343–346.

Mindlin, R. D., 1936, "Force at a Point in the Interior of a Semi-Infinite Solid," *Physics*, Vol. 7, pp. 195–202.

Moss, W. C., and Hoover, G., 1978, "Edge-Dislocation Displacements in an Elastic Strip," *J. Appl. Phys.*, Vol. 49, p. 5449.

Muskhelishvili, N. I., 1975, *Some Basic Problems of the Mathematical Theory of Elasticity*, 4th ed., Noordhoff, Leiden.

Nabarro, F. R. N., and Kostlan, J., 1978, "The Stress Field of a Dislocation Lying in a Plate," *J. Appl. Phys.*, Vol. 49, p. 5445.

Rongved, L., 1955, "Force Interior to One of Two Joined Semi-infinite Solids," *Proc. of the 2nd Midwestern Conf. on Solid Mech.*, pp. 1–13.

Rundle, J. B., and Jackson, D. D., 1977, "A 3-D Viscoelastic Model of a Strike-slip Fault," *Geophys. J. R. Astr. Soc.*, Vol. 49, pp. 575–591.

Sato, R., 1971, "Crustal Deformation Due to Dislocations in the Multilayered Medium," *J. Phys. Earth*, Vol. 19, pp. 31–46.

Sato, R., and Matsu'ura, M., 1973, "Static Deformations Due to a Fault Spreading over Several Layers in a Multi-layered Medium. Part I: Displacement," *J. Phys. Earth*, Vol. 21, pp. 227–249.

Singh, S. J., 1970, "Static Deformation of a Multi-layered Half-space by Internal Sources," *J. Geophys. Res.*, Vol. 75, pp. 3257–3263.

Stagni, L., and Lizzio, R., 1986, "The Elastic Field within an Internally Stressed Infinite Strip," *Int. J. Engng. Sci.*, Vol. 24, p. 471.

Stagni, L., and Lizzio, R., 1987, "Interaction of an Edge Dislocation with a Lamellar Inhomogeneity," *Mech. of Matls.*, Vol. 6, pp. 17–25.

Tse, S. T., and Rice, J. R., 1986, "Crustal Earthquake Instability in Relation to the Depth Variation of Frictional Slip Properties," *J. Geophys. Res.*, Vol. 91, pp. 9452–9472.

Downloaded 03 May 2010 to 171.66.16.21. Redistribution subject to ASME license or copyright; see http://www.asme.org/terms/Terms_Use.cfm

A Novel Displacement Gradient Boundary Element Method for Elastic Stress Analysis With High Accuracy

H. Okada

H. Rajiyah

S. N. Atluri
Fellow ASME

Center for Advancement of Computational Mechanics,
Georgia Institute of Technology,
Atlanta, GA 30332-0356

The boundary element method (BEM) in current usage, is based on the displacement boundary integral equation. The current practice of computing stresses in the BEM involves the use of a two-tier approach: (i) *numerical differentiation of the displacement field at the boundary, and* (ii) *analytical differentiation of the displacement integral equation at the source point in the interior. A new direct integral equation for the displacement gradient is proposed here, to obviate this two-tier approach. The new direct boundary integral equation for displacement gradients has a lower order singularity than in the standard formulation, and is quite tractable from a numerical view point. Numerical results are presented to illustrate the advantages of the present approach.*

1 Introduction

The boundary element method (BEM) is based upon classical integral equation formulations of boundary value/initial value problems. Although such formulations were originally thought to be primarily of theoretical interest, the engineering applications of this method in linear elastostatics and potential problems can be traced to the works of Jaswon and Symm (1963), Massonnet (1963), and Hess (1967). Later, this method was applied to a wide range of time dependent and vibration problems, and those involving fluid flow and material nonlinearities. Recently, this method has been extended to solve material as well as geometrically nonlinear problems in solid mechanics (see, for example, Zhang and Atluri (1968), O'Donoghue and Atluri (1987), and Im and Atluri (1987)).

Numerical solutions to two-dimensional problems in linear elasticity were obtained by Rizzo (1967) and later for three-dimensional problems by Cruse (1969). The boundary element formulation (as also noted by Brebbia (1978)) can be shown to be based on a weak form of the momentum balance laws in solid mechanics. Here the trial and test function spaces are quite different from each other. The test functions correspond to fundamental solutions (in this case Kelvin's singular solution), in finite space, of the differential operator of the problem, and hence are usually infinitely differentiable except possibly at singular points. On the other hand, the trial functions in BEM are required to be differentiable and continuous to a lessor degree (as compared to the finite element method).

The currently popular BEM is based on displacement boundary integral equations in linear elastic solid mechanics. The stress field in this standard BEM formulation is computed by differentiating the displacement field at the source point, to obtain the strain field and then applying Hooke's law to obtain the stress field. Unfortunately, this method works well in the interior of the body, but at the boundary it gives rise to hypersingular integrals which are intractable from a numerical standpoint. Hence, to circumvent this predicament at the boundary, numerical differentiation of the displacements (Cruse (1969), and Lachat and Watson (1975)) and other ad hoc techniques are used to obtain the displacement derivatives at the boundary. Now, making use of the boundary tractions and the numerically obtained tangential displacement derivatives, the stress field at the boundary is determined.

The hypersingular kernels in the equation for displacement gradients, in the traditional boundary element methods, continue to be of concern to researchers and practitioners in this discipline. In Ghosh et al. (1986), an attempt was made to reduce the order of singularity in the traction kernel in the equation for displacement gradients (see equation (11) to follow later in the present paper), by transferring the derivatives of the traction kernel (i.e., of $\partial t_{ji}^{*}/\partial \xi_l$) to the displacement u_i, thereby introducing the tangential derivatives of u_i. It will be shown later, that the present formulation for displacement gradients is fundamentally different from that of Ghosh et al. (1986). Furthermore, the present formulation *does not* suffer from the following limitations of the approach

Contributed by the Applied Mechanics Division of THE AMERICAN SOCIETY OF MECHANICAL ENGINEERS for presentation at the Joint ASCE/ASME Applied Mechanics, Biomechanics, and Fluids Engineering Conference, San Diego, CA, July 9 to 12, 1989.

Discussion on this paper should be addressed to the Editorial Department, ASME, United Engineering Center, 345 East 47th Street, New York, N.Y. 10017, and will be accepted until two months after final publication of the paper itself in the JOURNAL OF APPLIED MECHANICS. Manuscript received by ASME Applied Mechanics Division, March 14, 1988; final revision, June 23, 1988.

Paper No. 89-APM-21.

Copyright © 1988 by ASME
Downloaded 03 May 2010 to 171.66.16.21. Redistribution subject to ASME license or copyright; see http://www.asme.org/terms/Terms_Use.cfm

of Ghosh et al. (1986): (*i*) when the displacements are prescribed at the boundary, the evaluation of tangential derivatives involve numerical differentiation and, hence, leads to inaccuracies, especially for arbitrary boundaries with discontinuous tangents, (*ii*) their formulation is limited to simply connected domains. For multiply connected regions, the quantities u_i; $(\partial u_i/\partial s)$, and t_i appear as variables and, hence, it is necessary to impose additional equations of constraint between u_i and $(\partial u_i/\partial s)$, and (*iii*) in the case of three-dimensional problems, their formulation is not conducive to numerical implementation.

The directly derived integral equations for the displacement gradients in the presently reported formulation, obtained from a novel weak form of the momentum balance equations, has lower order singularities in the relevant kernels, than in the standard formulation. This makes the singularities to be tractable from a numerical point of view. A detailed numerical treatment of these singularities is given in this paper. The present formulation is more accurate than the standard two-tier approach of evaluating the stress field. This is illustrated through several numerical examples at the end of this paper.

2 The BEM Formulation

Let σ_{ij} be the Cartesian components of the Cauchy stress tensor and let ϵ_{ij} be the corresponding strain components. The equations of linear and angular momentum balance are

$$\sigma_{ij,i} + f_j = 0; \qquad \sigma_{ij} = \sigma_{ji} \tag{1}$$

where $(\ )_i$ denotes differentiation with respect to material coordinates x_i and f_i are the body forces per unit volume. The stress-strain relations for the linear elastic body take the following form

$$\sigma_{ij} = E_{ijmn}\epsilon_{mn} \tag{2}$$

where, for an isotropic solid, E_{ijmn} is defined as

$$E_{ijmn} = \lambda\delta_{ij}\delta_{mn} + \mu(\delta_{im}\delta_{jn} + \delta_{in}\delta_{mj}). \tag{3}$$

We restrict our attention here to the case of isotropy. The strain-displacement relations take the following form

$$\epsilon_{ij} = \frac{1}{2}(u_{i,j} + u_{j,i}). \tag{4}$$

Here, u_i refer to the Cartesian components of displacements. The tractions t_j on the boundary can be expressed as

$$t_j = n_i\sigma_{ij}. \tag{5}$$

Here, n_i are the components of the unit normal to the boundary.

The weak form of the linear momentum balance equation, when a displacement field $(\bar{u}_j)$ is taken as the test function, takes the following form:

$$\int_\Omega (\sigma_{ij,i} + f_j)\bar{u}_j d\Omega = 0. \tag{6}$$

Here, Ω and $\partial\Omega$ refer to the domain and the boundary, respectively, of the problem under consideration. We assume $\bar{u}_j$ to be the solutions, in infinite space, of the equation

$$[E_{ijmn}\bar{u}_{m,n}]_i + \delta(x_m - \xi_m)\delta_{jp}e_p = 0 \tag{7}$$

where e_p is the component of a unit load along the x_p coordinate. Thus, $\bar{u}_p$ are the fundamental solutions of the Navier equations of linear isotropic elasticity. Specifically, $u^*_{il}(x_m, \xi_m)$ is the displacement along the x_i-axis at x_m, due to a unit load along the x_l-axis at ξ_m in an infinite body, of a linear elastic isotropic material. Let $t^*_{il}(x_m, \xi_m)$ be the corresponding traction, i.e., it is the traction along the x_i-axis on an oriented surface at x_m due to a unit load along the x_l-axis at ξ_m in an infinite solid, of a linear isotropic elastic solid. Thus, the test functions $\bar{u}_j$ may be represented as

$$\bar{u}_j = u^*_{jp}e_p \tag{8}$$

and correspondingly,

$$\bar{t}_k \equiv nE_{ijkl}\bar{u}_{j,i} = t^*_{kp}e_p. \tag{9}$$

Integrating equation (6) by parts, applying the divergence theorem twice and making use of equations (2), (3), (4), (5), (7), (8), and (9), the standard BEM equations (in the absence of body forces) can be obtained.

$$C_{ij}u_j(\xi_m) = \int_{\partial\Omega} [u^*_{ji}(x_m, \xi_m)t_j(x_m) - t^*_{ji}(x_m, \xi_m)\, u_j(x_m)]\, d(\partial\Omega) \tag{10a}$$

Here, $C_{ij} = \delta_{ij}$ in the interior and $1/2\ \delta_{ij}$ at a smooth boundary point.

The above equation, when discretized and applied at the boundary, results in the standard boundary element system of equations:

$$\mathbf{Hu} = \mathbf{GT} \tag{10b}$$

where **u** and **T** are displacements and tractions, respectively, at the boundary; and **H** and **G** are the associated matrices.

The standard BEM formulation makes use of equation (10), and obtains the strain field by differentiating it with respect to the load point ξ_l.

Thus,

$$C_{ij}u_{j,l}(\xi_m) = \int_{\partial\Omega} \left[\frac{\partial u^*_{ji}(x_m, \xi_m)}{\partial\xi_l} t_j(x_m) - \frac{\partial t^*_{ji}(x_m, \xi_m)}{\partial\xi_l} u_j(x_m)\right] d(\partial\Omega) \tag{11}$$

This method gives rise to $t^*_{ij,l}$ type kernels, which are hypersingular, when ξ_m tends to a boundary point. Hence, this predicament gives rise to a two-tier system of evaluation for the stress field.

With a view towards developing the present "displacement gradient integral equation," directly from the weak form, we take the test function to be $\bar{u}_{j,k}$ instead of $\bar{u}_j$ as in equation (6). The weak form can now be represented in vector form, rather than in a scalar form as in equation (6), as:

$$\int_\Omega (\sigma_{ij,i} + f_j)\bar{u}_{j,k}\, d\Omega = 0. \tag{12}$$

Let the test functions satisfy the same field equations as those in equation (8) and (9). Integrating equation (12) by parts, applying the divergence theorem three times and making use of equations (4), (5), (7), (8), and (9), we obtain the following direct integral equation (in the absence of body forces) for *displacement gradients*

$$C_{il}u_{i,k}(\xi_m) = \int_{\partial\Omega} [n_k(x_m)\, E_{ijpq}u_{p,q}(x_m)\, u^*_{jl,i}(x_m, \xi_m) - t_j(x_m)u^*_{jl,k}(x_m, \xi_m) - u_{p,k}(x_m)t^*_{pl}(x_m, \xi_m)]\, d(\partial\Omega). \tag{13a}$$

Here, $C_{il} = \delta_{il}$ in the interior and $1/2\ \delta_{il}$ at a smooth boundary point. The kernels $u^*_{jl,k}$ and t^*_{pl} have the same order of singularity and in general are tractable from a numerical point of view. Note also that as ξ_m tends to $\partial\Omega$, the singularities in the new representation, equation (13) are of lower order as compared to those in equation (11).

Equation (13*a*), when discretized and applied at the boundary, results in the following system of equations:

$$\mathbf{H}_d\mathbf{u}_d = \mathbf{G}_d\mathbf{T} \tag{13b}$$

Downloaded 03 May 2010 to 171.66.16.21. Redistribution subject to ASME license or copyright; see http://www.asme.org/terms/Terms_Use.cfm

where $\mathbf{u}_d$ and $\mathbf{T}$ are the displacement gradients, and tractions, respectively, at the boundary; and $\mathbf{H}_d$ and $\mathbf{G}_d$ are the associated matrices. It is interesting to note that *the order of singularity* in $\mathbf{H}_d$ and $\mathbf{G}_d$ terms is the same as that of the terms in $\mathbf{H}$ in equation (10*b*).

A detailed analysis of the numerical implementation of the singular integrals in equation (13) will follow in the next section. Equations (10) and (13) are valid for simple as well as multiply connected domains Ω. The surface $\partial\Omega$ must, of course, include outer as well as inner boundaries of Ω in the latter case. Implicit in the derivation of equation (13) is the assumption that the material is homogeneous, i.e., E_{ijmn} are independent of material coordinates x_m. Further details of the derivation of (13), along with similar results for displacement gradient integral equations, in the cases of (*i*) small strain elasto-plasticity; (*ii*) finite strain elasto-plasticity, and (*iii*) large deformations of semilinear elastic material, are given in Okada, Rajiyah, and Atluri (1987).

The unknown boundary displacements and tractions could be obtained from equation (10*b*) as in the standard BEM approach. Once the complete displacement and traction field is completely ascertained on the boundary, equation (13*b*) could be used to solve for the boundary displacement gradients *evaluated on the boundary*. Finally, the displacement gradients could be evaluated pointwise, in the interior, (using equation (13*a*)), once the displacement gradient on the boundary are known. Hence, the stress field could be determined by Hooke's law in a uniform manner.

3 Numerical Implementation of Singular Integrals in Equation (13)

As in Fig. 1, BOC is the boundary segment where the source point O lies and let P be the field point. The straight line EOD is a tangent to the curve BOC at O and let EC and BD be perpendiculars to the line EOD. The points B and C are the ends of the segment under consideration. Let r be the distance between the source point O and field point P. For illustrative purposes, let us consider the integral

$$I_1 = \int_{\partial\Omega} t_j\,(x_m)\; u^*_{jl,k}\,(x_m,\,\xi_m)\;\mathrm{d}(\partial\Omega) \tag{14}$$

When the traction components t_j are expressed an nodal tractions multiplied by the associated shape functions, the resulting singular integral to come out of I_1, would take the following generic form

$$I_2 = \int_{\partial\Omega} N_o t_j\,(x^o_m)\; u^*_{jl,k}\,(x_m,\,\xi_m)\;\mathrm{d}(\partial\Omega). \tag{15}$$

Here, N_o is the shape function associated with point O, and t_j (x^o_m) corresponds to the nodal traction at the source point, i.e., point O. The singular integral I_2 can also be written in the following form

$$\begin{aligned} I_2 &= t_j\,(x^o_m)\int_{\partial\Omega}\,(N_o-1)\;u^*_{jl,k}\,(x_m,\,\xi_m)\;\mathrm{d}(\partial\Omega)\\ &\quad + t_j\,(x^o_m)\int_{\partial\Omega} u^*_{jl,k}\,(x_m,\,\xi_m)\mathrm{d}(\partial\Omega)\\ &= I_3 + t_j\,(x^o_m) I_4 \end{aligned} \tag{16}$$

For simplicity, the shape function N_o can be taken to be linear. The integral I_3 in the above equation is regular and, hence, tractable from a numerical point of view. From here onwards, we will consider only the integral I_4 which appears to be singular. As per Fig. 1, the integral I_4 would take the following form

$$I_4 = \int_{\mathrm{BOC}} u^*_{jl,k}\mathrm{d}S \tag{17}$$

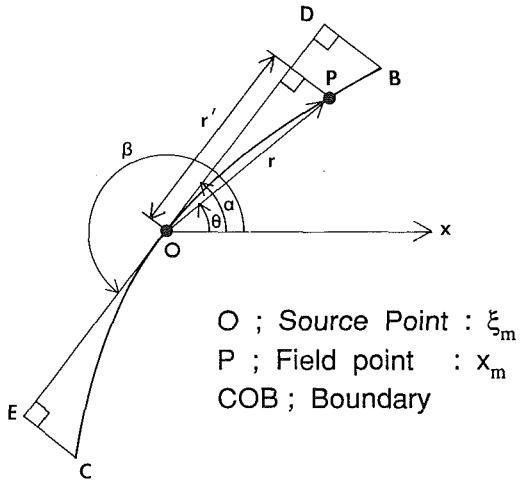

Fig. 1 Numerical implementation of singular integrals

Due to the inherent property of the $u^*_{jl,k}$ kernel, it could be expressed (for two-dimensional problems) in the following form

$$u^*_{jl,k} = \frac{f(\theta)}{r}, \quad f(\theta) = -f(\theta+\pi). \tag{18}$$

Here, r is the distance between the source point and field point. θ is the angle made by the line connecting the source point and field point with the x-axis. Substituting the expression for $u^*_{jl,k}$ in equation (18) into equation (17) we have

$$\begin{aligned} I_4 &= \int_{\mathrm{BOC}} \frac{f(\theta)}{r}\,\mathrm{d}S\\ &= \int_{\mathrm{BO}} \left\{\frac{f(\theta)}{r} - \frac{f(\alpha)}{r'}\left|\frac{\mathrm{d}s'}{\mathrm{d}s}\right|\right\}\mathrm{d}s\\ &\quad + \int_{\mathrm{OC}} \left\{\frac{f(\theta)}{r} - \frac{f(\beta)}{r'}\left|\frac{\mathrm{d}s'}{\mathrm{d}s}\right|\right\}\mathrm{d}s\\ &\quad + \int_{\mathrm{DO}} \frac{f(\theta)}{r}\,\mathrm{d}S' + \int_{\mathrm{OE}} \frac{f(\beta)}{r}\,\mathrm{d}S' \end{aligned} \tag{19}$$

Note here, that the angles α and β are constants and θ varies as the field point moves along the arc (Fig. 1). The integrals along BO and OC in equation (19) are regular and, hence, numerically tractable. Let us define the sum of the integrals over the straight lines DO and OE as I_5. Thus

$$I_5 = \int_{\mathrm{DO}} \frac{f(\alpha)}{r}\,\mathrm{d}S' + \int_{\mathrm{OE}} \frac{f(\beta)}{r}\,\mathrm{d}S' \tag{20}$$

Evaluating I_5 in the sense of Cauchy Principal Value, we have

$$\begin{aligned} I_5 &= \lim_{\epsilon\to 0}\;\{[-\ln|r|f(\alpha)]_D^{\bar{\epsilon}} + [\ln|r|f(\beta)]_{\epsilon}^{E}\} + \mathrm{C.P.V.}\\ &= \lim_{\epsilon\to 0}\;\{-\ln(\epsilon)[f(\alpha)+f(\beta)] + \ln(r_E)f(\beta)\\ &\qquad + \ln(r_D)f(\alpha)\} + \mathrm{C.P.V.} \end{aligned} \tag{21}$$

Here, r_E and r_D are distances between the source point and points E and D, respectively. C.P.V. denotes Cauchy Principal Value terms which arise out of the integral I_5. It so happens that, when equation (13) is considered as a whole, all Cauchy Principal Value terms arising out of the singular kernels $u^*_{jl,i}$ and t^*_{pl} cancel out and hence, in effect, there are no free terms arising out of the integral equation (13). Therefore, it is sufficient to consider equation (21) without the C.P.V. terms.

Since EOD is a straight line (Fig. 1)

Downloaded 03 May 2010 to 171.66.16.21. Redistribution subject to ASME license or copyright; see http://www.asme.org/terms/Terms_Use.cfm

Table 1 Summary of numerical quadratures employed

Case	Type of Integration	Order of Integration Rule
$R>1.2d$	Gauss Numerical Quadrature	3
$R<1.2d$	Gauss Numerical Quadrature Element Sub-divisions: up to 4	6 ~ 10
Log-Singularities	Gauss Numerical Quadrature Element Subdivisions: up to 4 (Quarter Point Coordinate Transformation)	10
$1/r$-Singularities (Cauchy Principal Value Integral)	1) The Use of Rigid Body Motion 2) Dividing the Integral into Two Parts *i*) $1/r$ Singular Integral on the Straight Line *ii*) Non-Singular Integral on the Curved Line	– Analytically 10

(R: distance between the source point and an element); (d: element size)

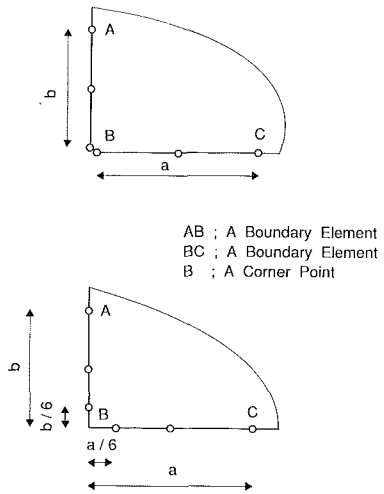

Fig. 2 Use of partially discontinuous boundary elements at a corner point and/or where tractions are discontinuous

$$\beta=\alpha+\pi. \tag{22}$$

Hence, from equations (18) and (21) it is clear that

$$f(\alpha)+f(\beta)=0. \tag{23}$$

There, equation (20) takes the following form

$$I_5=\ln\left(\frac{r_D}{r_E}\right)\cdot f(\alpha) \tag{24}$$

The above-mentioned procedure of regularizing the singular integral is explained in the context of a two-dimensional problem for the $u^*_{jk,l}$ kernels. It should be noted here that the kernels $n_k E_{ijpq} u^*_{jl,i}$ and t^*_{pl} ($=n_q E_{stpq} u^*_{il,s}$) appearing in equation (13) will have a similar procedure of regularizing the singular integrals, since the components of the normal n_k (or n_q) are constant over the straight line EOD (Fig. 1). Without any loss of generality, a similar procedure could be adopted in the context of three-dimensional problems as well.

4 Numerical Results

4.1 Preliminaries. Three-noded (quadratic) boundary elements are employed in the present study. When the given tractions are discontinuous at a boundary point, we use double nodes at the point in question (see Fig. 2). Since the presently derived integral representation for displacement gradients is applicable for points at a smooth boundary, we shift the location of a node such as B (in Fig. 2) from a corner, or from a point where tractions are discontinuous, to a location C (as shown in Fig. 2) where the boundary is smooth and/or where the tractions are continuous.

All the numerical integrations are performed by using Gauss quadrature. The order of numerical quadrature is determined

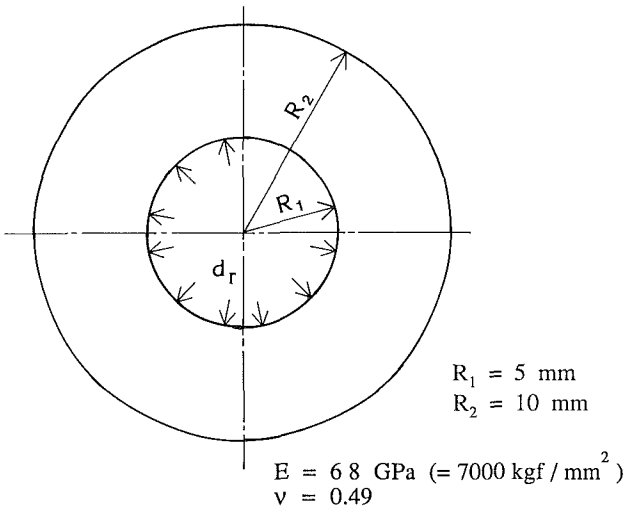

(a) A Problem to be Solved

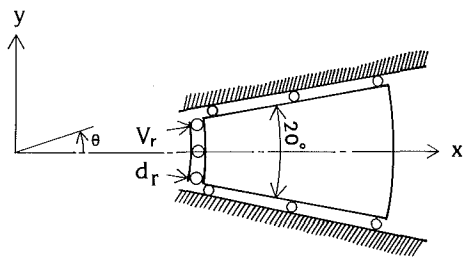

(b) Boundary Conditions for B. E. M.

Fig. 3 Problem of radial expansion of a thick cylinder

by the distance between the source point and nearest nodal point of the element, as shown in Table 1. When this distance is less than roughly the size of the element, an element subdivision technique is employed in the process of numerical quadrature. When logarithmic type singular integrands are involved, a "quarter-point element" type geometric transformations are employed, (leading to Jacobian singularities), and Gauss quadrature is employed in the parent element. When ($1/r$) type singularities are involved in line integrals, integrations are performed as indicated in Table 1.

In the present paper, the designation of "conventional method" implies that all the displacement gradients and stresses at a boundary point are computed from the algebraic equations at the boundary point in question involving the components of traction, and the gradients, along the tangential direction, of the displacements. The gradients of displacements along the tangential direction are evaluated by

Downloaded 03 May 2010 to 171.66.16.21. Redistribution subject to ASME license or copyright; see http://www.asme.org/terms/Terms_Use.cfm

Table 2 Numerical errors in BEM calculations (Present Method, $\theta = 0$ deg)

	Errors in σ_{rr} (percent)			Errors in $\sigma_{\theta\theta}$ (percent)		
$r(mm)$	Mesh 1	Mesh 2	Mesh 3	Mesh 1	Mesh 2	Mesh 3
5.5	0.294	0.136	0.046	−1.156	−0.254	−0.102
6.0	0.829	0.231	0.080	−0.838	−0.194	−0.082
6.5	1.147	0.277	0.102	−0.669	−0.180	−0.074
7.0	1.394	0.338	0.127	−0.640	−0.171	−0.069
7.5	1.708	0.413	0.156	−0.654	−0.166	−0.066
8.0	2.135	0.504	0.192	−0.652	−0.162	−0.063
8.5	2.744	0.613	0.236	−0.608	−0.154	−0.060
9.0	3.877	0.841	0.320	−0.489	−0.126	−0.050
9.5	7.440	1.773	0.662	−0.262	−0.061	−0.026

$$\text{Errors in } \sigma_{rr} \quad (\text{Percent}) = \frac{|\sigma_{rr}(\text{BEM})| - |\sigma_{rr}(\text{exact})|}{|\sigma_{rr}(\text{exact})|} \times 100$$

$$\text{Errors in } \sigma_{\theta\theta} \quad (\text{Percent}) = \frac{|\sigma_{\theta\theta}(\text{BEM})| - |\sigma_{\theta\theta}(\text{exact})|}{|\sigma_{\theta\theta}(\text{exact})|} \times 100$$

Table 3 Numerical errors in BEM calculations (Conventional Method, $\theta = 0$ deg)

	Errors in σ_{rr} (percent)			Errors in $\sigma_{\theta\theta}$ (percent)		
$r(mm)$	Mesh 1	Mesh 2	Mesh 3	Mesh 1	Mesh 2	Mesh 3
5.5	0.698	0.250	0.107	−0.910	−0.195	−0.071
6.0	1.069	0.351	0.127	−1.119	−0.129	−0.058
6.5	1.629	0.349	0.145	−0.819	−0.157	−0.055
7.0	2.295	0.429	0.160	−0.352	−0.145	−0.058
7.5	2.522	0.491	0.185	−0.310	−0.148	−0.059
8.0	2.352	0.521	0.206	−0.602	−0.165	−0.061
8.5	2.354	0.575	0.214	−0.797	−0.157	−0.062
9.0	3.130	0.564	0.220	−0.685	−0.128	−0.050
9.5	6.356	0.781	0.462	−0.305	−0.022	−0.007

$$\text{Errors in } \sigma_{rr} \quad (\text{Percent}) = \frac{|\sigma_{rr}(\text{BEM})| - |\sigma_{rr}(\text{exact})|}{|\sigma_{rr}(\text{exact})|} \times 100$$

$$\text{Errors in } \sigma_{\theta\theta} \quad (\text{Percent}) = \frac{|\sigma_{\theta\theta}(\text{BEM})| - |\sigma_{\theta\theta}(\text{exact})|}{|\sigma_{\theta\theta}(\text{exact})|} \times 100$$

diffentiating the shape functions for displacements in the boundary elements. The stresses at the boundary, computed in this "conventional method" are, in general, discontinuous between the neighboring boundary elements. In such a case, we simply take the average of the two sets of strain and stress components at each interelement nodal point.

4.2 Example Problems.

4.2.1 Radial Expansion of a Thick Cylinder. The geometric and material data for the problem, and the boundary conditions, are shown in Fig. 3. In the boundary element model, a 20-deg segment of the cylinder is considered and displacements are prescribed at the inner surface of the cylinder. Three progressively refined boundary element meshes, as shown in Fig. 4, are considered.

The solid points along the line $\theta = 0$ deg in the Fig. 4 are locations where the computed results for stresses σ_{rr}, and $\sigma_{\theta\theta}$, by the present method are the conventional method, respectively, are given in Tables 2 and 3. Tables 2 and 3 show that the stresses at these *interior points* from both the present method as well as the conventional method, converge to the exact solution, with a progressive refinement of the boundary element mesh.

The solid points along the radius $r = 7.1764$ mm, shown in Fig. 4, are locations where the stresses σ_{rr} computed by the present method and the conventional method, for each of the

Downloaded 03 May 2010 to 171.66.16.21. Redistribution subject to ASME license or copyright; see http://www.asme.org/terms/Terms_Use.cfm

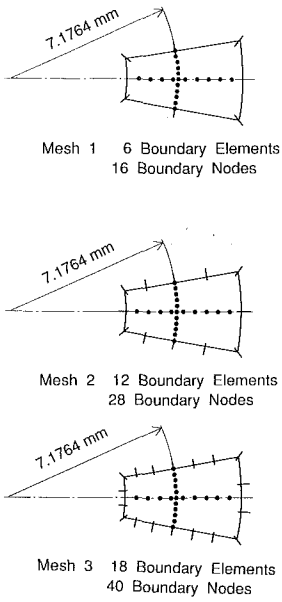

Fig. 4 Boundary element models of a radially expanding thick cylinder

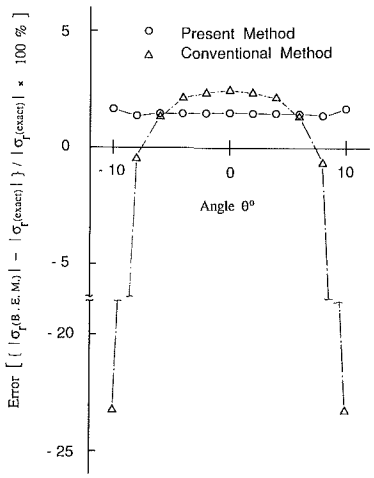

Fig. 5 Stress σ_{rr} at the Section $r = 7.1764$ mm for Mesh 1 (see Fig. 3(*a*))

the three boundary element meshes are shown, respectively, in Figs. 5, 6, and 7. In each of these figures, the locations $r = 7.1764$ mm, and $\theta = \pm 10$ deg are *boundary points* (see Fig. 4). Figures 5, 6, and 7 show clearly that, in spite of the mesh refinement, the stress σ_{rr} computed by the conventional method, is significantly (one order of magnitude) more erroneous at the *boundary point* than at the interior points. On the other hand the stresses σ_{rr} computed by the present method, in all the 3 mesh cases, is of *equal accuracy* at both the boundary points as well as the interior points. It is thus seen that the "boundary layer" type behavior of error in the computed stress that is present in the conventional method is nullified in the present approach.

4.2.2 Problem of a Tension Plate with a Circular Hole. The geometric, material, and load data are shown in Fig. 8. The progressively refined boundary element meshes are shown in Figs. 9(*a*), (*b*), and (*c*), respectively.

Attention is focused on the solution for the direct stress σ_T along the periphery of the hole and at the boundary segments near the hole, as marked by the lines AB – BC – CD in Fig. 8(*b*). Along the segment BC, this direct stress σ_T is the usual $\sigma_{\theta\theta}$. The results for σ_T, computed by the present method as well as the conventional method, by using each of the three

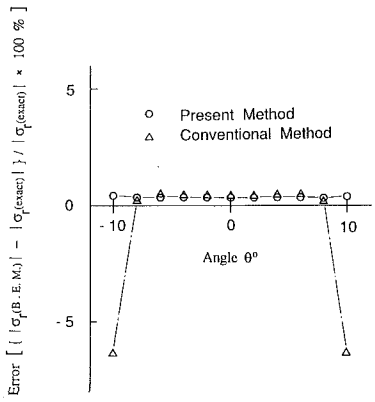

Fig. 6 Stress σ_{rr} at the Section $r = 7.1764$ mm for Mesh 2 (see Fig. 3(*b*))

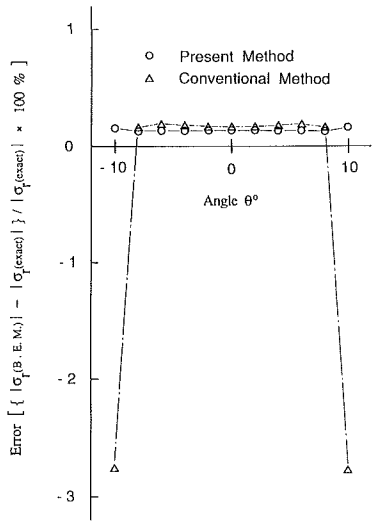

Fig. 7 Stress σ_{rr} at the Section $r = 7.1764$ mm for Mesh 3 (see Fig. 3(c))

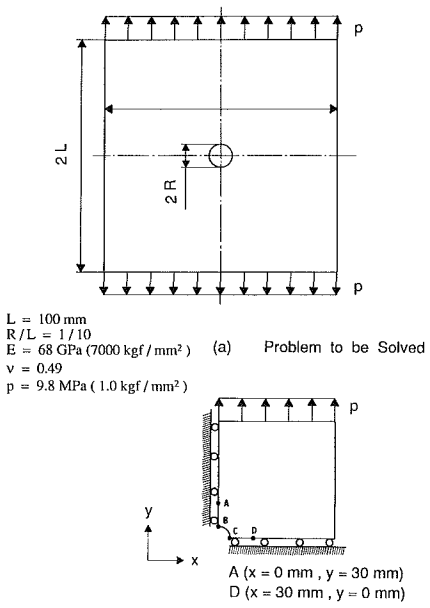

Fig. 8 Problems of a tension plate with a circular hole

Downloaded 03 May 2010 to 171.66.16.21. Redistribution subject to ASME license or copyright; see http://www.asme.org/terms/Terms_Use.cfm

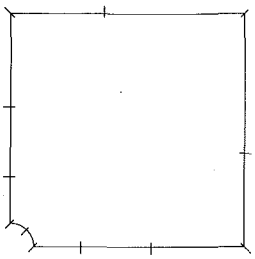

Mesh 1 12 Boundary Elements
29 Boundary Nodes

(*a*)

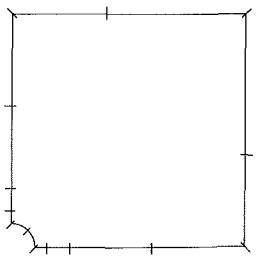

Mesh 2 14 Boundary Elements
33 Boundary Nodes

(*b*)

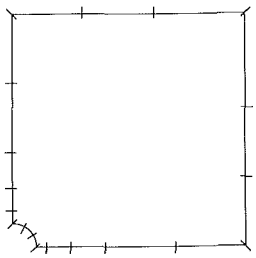

Mesh 3 19 Boundary Elements
43 Boundary Nodes

(*c*)

Fig. 9 Boundary element models of a tension plate with a circular hole

meshes shown in Figs. 9(*a*), (*b*), and (*c*), are shown in Figs. 10, 11, and 12, respectively. The solid lines in Figs. 10, 11, and correspond to the analytical solution for an *infinite* domain subject to remote tension. It is seen that the direct stress along BC converges, in both the present and conventional methods, to the exact solution, with progressive mesh refinement. Along the segments AB and CD the results for the direct stress σ_T from the present method converge to the exact solution with progressive mesh refinement, with the results even for the coarser meshes being quite acceptable. On the other hand, it is seen from Figs. 10, 11, and 12 that the results for σ_T along AB and CD, as computed from the conventional method fail to converge to the exact solution even with mesh refinement, with the results for coarser meshes being unacceptable.

4.2.3 Problem of a Tension Plate With a Square Plate. The geometric, material, and load data are shown in Fig. 13, with progressively refined boundary element meshes being given in Figs. 14(*a*), (*b*), and (*c*), respectively.

Attention is focused here on the direct stress σ_T along the segment QPO of the periphery of the square hole (see Fig. 13).

The results for σ_T along QP, computed by the present method are shown in Fig. 15, while those computed by the conventional method are shown in Fig. 16. From Fig. 15, it is seen that the present method, with mesh refinement, leads to a very smooth data for σ_T and can capture the singularity in σ_T

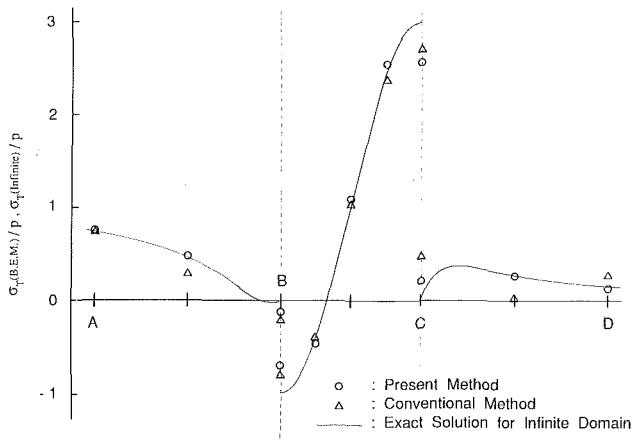

Fig. 10 Direct stress σ_T along the boundary AB-BC-CD (see Fig. 7(*b*)) for Mesh 1 (Fig. 8(*a*))

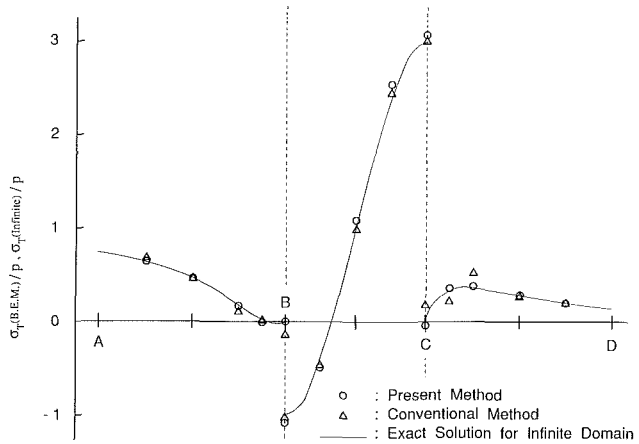

Fig. 11 Direct stress σ_T along the boundary AB-BC-CD (see Fig. 7(*b*)) for Mesh 2 (Fig. 8(*b*))

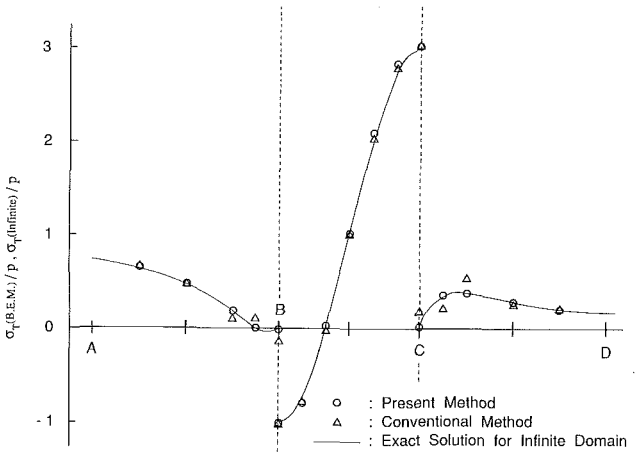

Fig. 12 Direct stress σ_T along the boundary AB-BC-CD (see Fig. 7(*b*)) for Mesh 3 (Fig. 8(*c*))

at the corner point P of the square hole. On the other hand, it is seen for Fig. 16 that in the conventional method, it is difficult to obtain a smooth interpolant function of σ_T for any of the three meshes employed, and convergence to the correct singular solution is unacceptably slow. The results for σ_T along OP, for the present and conventional methods shown in

Downloaded 03 May 2010 to 171.66.16.21. Redistribution subject to ASME license or copyright; see http://www.asme.org/terms/Terms_Use.cfm

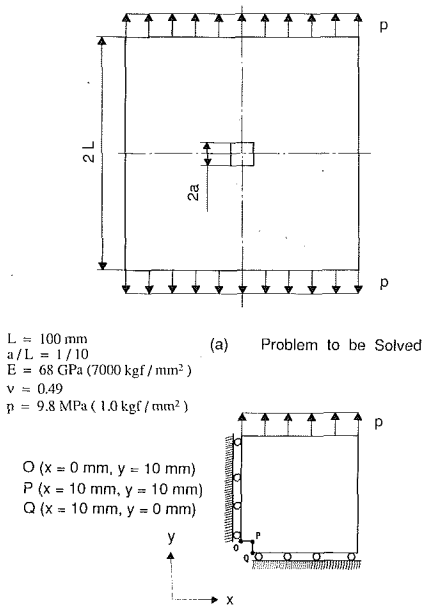

Fig. 13 Problem of a tension plate with a square hole

Figs. 17 and 18 respectively, show similar trends as in Figs. 15 and 16, respectively.

These results clearly demonstrated that the present algorithm yields much better results for stresses and strains at *boundary points*, and can capture stress-strain singularities at such points much better than the conventional method.

5 Closure

The present method, based on a direct integral representation of the displacement gradients, which are of the nonhyper singular type at the boundary, leads to much better numerical results for boundary stresses than the conventional method wherein the integral representation for displacments is differentiated to obtain strains and stresses. This improvement in numerical accuracy of the present method over the conventional method is especially significant for the components of stress and strain along the coordinate tangential to the boundary.

The numerical implementation of the *present novel theoretical formulation* does appear to be inefficient. However, the present formulation and its numerical implementation, do produce continuous, and the most accurate stresses. The evaluation of boundary stresses accurately, is also mandatory in problems such as large strain plasticity, as recently demonstrated by Okada, Rajiyah, and Atluri (1988), who use concepts similar to those in the present paper, to directly develop *non-hyper singular* integral equations for velocity gradients in large strain problems.

Acknowledgments

The support of this work by the U.S. Office of Naval Research, and the encouragement of Drs. Y. Rajapakse and A. Kushner, and gratefully acknowledged. The authors are also indebted to Dr. M. Kikuchi of the Science University of Tokyo for lending his computer program based on the standard BEM approach. It is a pleasure to thank Ms. Deanna Winkler for her assistance in the preparation of this manuscript.

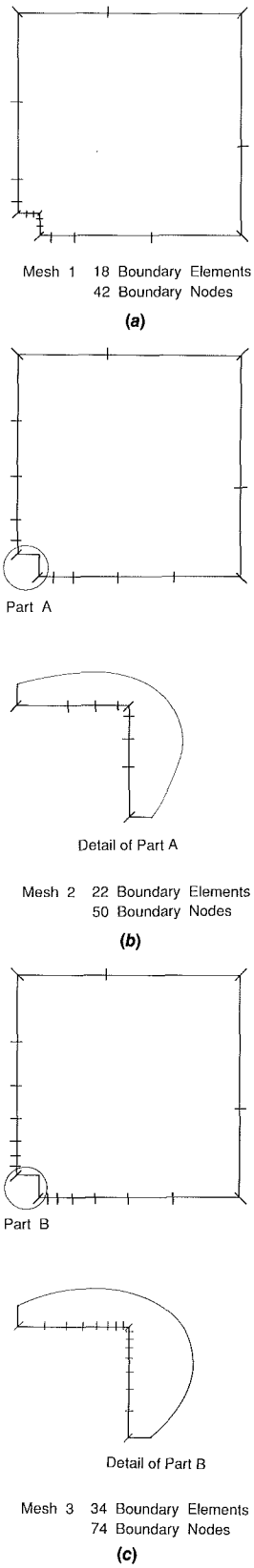

Fig. 14 Boundary element models of a tension plate with a square hole

References

Brebbia, C. A., 1978, "The Boundary Element Method in Engineering," Pentech Press, London.

Cruse, T. A., 1969, "Numerical Solutions in Three-Dimensional Elastostatics," *Int. J. of Solids and Structures*, Vol. 5, pp. 1259–1274.

Ghosh, N, Rajiyah, H., Ghosh, S., and Mukherjee, S., 1986, "A New Boundary Element Method Formulation for Linear Elasticity," ASME JOURNAL OF APPLIED MECHANICS, Vol. 53, pp. 67–76.

Downloaded 03 May 2010 to 171.66.16.21. Redistribution subject to ASME license or copyright; see http://www.asme.org/terms/Terms_Use.cfm

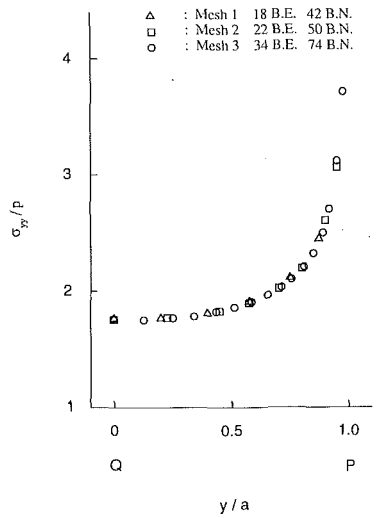

Fig. 15 Stress σ_{yy} along the segment QP (see Fig. 12) of square hole. Results by present method.

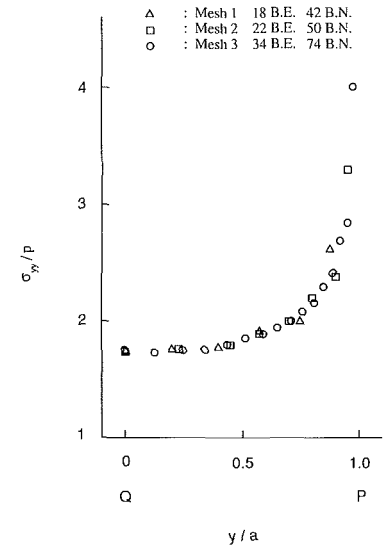

Fig. 16 Stress σ_{yy} along the segment QP (see Fig. 12) of square hole. Results by conventional method.

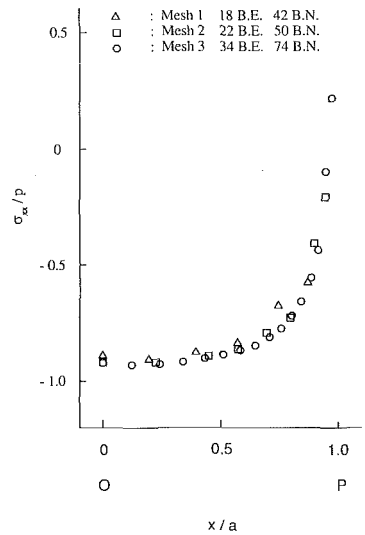

Fig. 17 Stress σ_{xx} along the segment OP (see Fig. 12) of square hole. Results by present method.

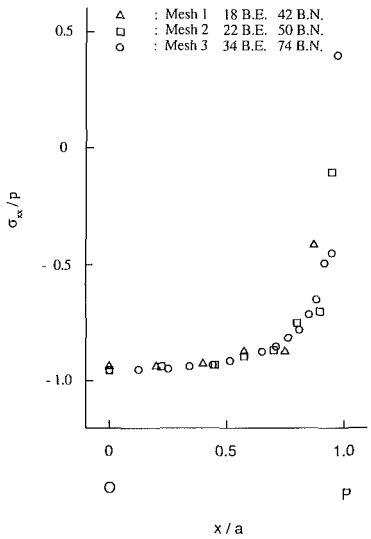

Fig. 18 Stress σ_{xx} along the segment OP (see Fig. 12) of the square hole. Results by the conventional method.

Hess, J. L., and Smith, A. M. O., 1967, "Calculation of Potential Flow About Arbitrary Bodies," *Progress in Aeronautical Sciences*, Vol. 8, D. Küchemann, ed., Pergamon, London.

Im, S., and Atluri, S. N., 1987, "Endochronic Constitutive Modeling of Finite Deformation Plasticity and Creep: A Field-Boundary Element Computational Algorithm," *Recent Advances in Computational Methods for Inelastic Analysis*, S. Nakazawa and K. Williams, eds., ASME New York.

Jaswon, M. A., 1963, "Integral Equation Methods in Potential Theory I," *Proceedings of the Royal Society*, Series A, Vol. 275, pp. 23–32.

Lachat, J. C., and Watson, J. O., 1975, "A Second Generation Boundary Integral Equation Program for 3D Elastic Analysis," *Boundary Integral Equation Method: Computational Applications in Applied Mechanics,* Vol. 11, T. A. Cruse and F. J. Rizzo, eds., ASME, pp. 85–100.

Massonnat, C. E., 1966 "Numerical Use of Integral Procedures, in Stress Analysis," *Stress Analysis*, O. C. Zienkiewicz and G. S. Hollister, eds., Wiley, London.

O'Donoghue, P. E., and Atluri, S. N., 1987, "Field/Boundary Element Approach to the Large Deflections of Thin Plates," *Computer & Structures*, in press.

Okada, H., Rajiyah, H., and Atluri, S. N., 1987, "Non-Hyper-Singular Integral-Representations for Velocity (Displacement) Gradients in Elastic/Plastic Solids (Small or Finite Deformations)," *Computational Mechanics*, in press.

Okada, H., Rijiyah, H., and Alturi, S. N., 1988, "Recent Developments in Finite Strain Elastoplasticity Using the Field Boundary Element Method," *Computers & Structures*, in press.

Rizzo, R., 1967, "An Integral Equation Approach to Boundary Value Problems in Classical Elastostatics," *Quarterly of Applied Mathematics*, Vol. 25, pp. 83–95.

Symm, G. T., 1963, "Integral Equation Methods in Potential Theory, II," *Proceedings of the Royal Society*, Series A, Vol. 275, pp. 33–46.

Zhang, J. D., and Atluri, S. N., 1986, "A Boundary/Interior Element Method for Quasistatic and Transient Response Analysis of Shallow Shells," *Computers & Structures*, Vol. 24, pp. 213–224.

Downloaded 03 May 2010 to 171.66.16.21. Redistribution subject to ASME license or copyright; see http://www.asme.org/terms/Terms_Use.cfm

A Surface Crack in Shells Under Mixed-Mode Loading Conditions[1]

P. F. Joseph

F. Erdogan
Fellow ASME

Department of Mechanical Engineering and Mechanics,
Lehigh University,
Bethlehem, PA 18105

The problem of a shallow shell containing a surface crack and subjected to general loading conditions is considered. It is shown that, as in the three-dimensional elasticity formulation, the mode I state can be separated whereas modes II and III remain coupled. A line spring model is developed to formulate the part-through crack problem under mixed-mode conditions. A shallow shell of arbitrary curvature having a part-through crack located on the outer or the inner surface of the shell is then considered. Reissner's transverse shear theory is used to formulate the problem by assuming that the shell is subjected to all five moment and stress resultants. The uncoupled antisymmetric problem is solved for cylindrical and toroidal shells having a surface crack in various orientations and the primary and the secondary stress intensity factors are given. The results show that, unlike the through crack problems, in surface cracks the effect of shell curvature on the stress intensity factors is relatively insignificant.

1 Introduction

Subcritical growth of surface flaws in plate and shell structures due to cyclic loading and/or corrosive environment is known to be a highly commmon failure mode in engineering materials. In many practical applications as, for example, in nearly all "pressure boundaries" there is usually a symmetry in loading as well as in the geometry of the structure. Consequently, in such structures the surface crack would usually initiate and grow as a mode I crack. Primarily for this reason and also because of the relative analytical and conceptual simplicity of the problem, the previous studies concerning surface cracks have been restricted to mode I problems (see, for example, Rice and Levy (1972); Rice (1972); Delale and Erdogan (1981, 1982); Parks (1981); Erdogan and Boduroglu (1984); Yashi and Erdogan (1985); Erdogan and Yashi (1985) for analytical studies based largely on the line spring model; Newman and Raju (1979); Raju and Newman (1982); Heliot et al. (1979); Nishioka and Atluri (1982); O'Donoghue et al. (1986) for finite element solutions; Joseph and Ergodan (1987) for a comprehensive review). On the other hand in some applications torsion, twisting, and transverse shear components of the external loading may either be the primary loads or be superimposed on the symmetric membrane and bending loads and may thus have a significant effect on the nature and the rate of growth of the surface crack. Pressurized pipes or pipe elbows subjected to cyclic torsion or transverse shear loads may be mentioned as some examples.

In the plate or the shell containing a surface crack if the external load is a fully-reversed antisymmetric load, because of symmetry it is possible that the resulting subcritical crack growth may be coplanar, that is the crack front stress and displacement behavior may remain self-similar as the crack grows. The likelihood of self-similar growth of the surface crack would be higher if a static or cyclic mode I type loading is superimposed on such fully-reversed antisymmetric loads. Under such mixed-mode loading conditions the "smoothness" of the fatigue fracture surface would depend on the relative magnitude of the mode I stress intensity factor. There is indeed some experimental evidence indicating that under fully-reversed in-plane shear (for which the stress state along the crack front is predominantly mode III) macroscopically the surface crack would grow in coplanar fashion with the resulting fatigue crack having factory roof type saw-tooth surfaces of varying degrees of roughness (Tschegg et al., 1983). To model and study the subcritical crack growth process under mixed-mode conditions, the strain energy release rate appears to be the most appropriate correlation parameter representing the nature and the intensity of the external loads and the geometry of the cracked structure. For this it is then clear that the elastic solution of the surface crack problem under mixed-mode conditions will be needed.

For any surface crack geometry the related three-dimensional elasticity problem can always be solved by using a purely numerical technique such as the finite element method. However, one could reduce the computational effort considerably and perform the necessary parametric studies by also using the line spring model with a plate or shell theory to formulate the problem. In this paper the line spring model for surface cracks in shells under mixed-mode conditions will be developed. A number of cylindrical and toroidal shell problems will then be solved as examples.

[1]This work was supported by the NSF under Grant MSM-8613611 and by NASA-Langley under Grant NAG-1-713.

Contributed by the Applied Mechanics Division of THE AMERICAN SOCIETY OF MECHANICAL ENGINEERS for presentation at the Joint ASCE/ASME Applied Mechanics, Biomechanics, and Fluids Engineering Conference, La Jolla, CA, July 9 to 12, 1989.

Discussion on this paper should be addressed to the Editorial Department, ASME, United Engineering Center, 345 East 47th Street, New York, N.Y. 10017, and will be accepted until two months after final publication of the paper itself in the JOURNAL OF APPLIED MECHANICS. Manuscript received by ASME Applied Mechanics Division, January 26, 1988; final revision, May 2, 1988.

Paper No. 89-APM-11.

Copyright © 1988 by ASME
Downloaded 03 May 2010 to 171.66.16.21. Redistribution subject to ASME license or copyright; see http://www.asme.org/terms/Terms_Use.cfm

2 Line Spring Model for Antisymmetric Deformations

Consider a shell having a planar surface crack that is subjected to arbitrary loading. To study the subcritical crack growth process in the shell one would need the details of the solution of the related three-dimensional mixed-mode crack problem. In particular, one would need to determine the stress intensity factors along the crack front in order to do the necessary modeling and the crack path studies. The problem is analytically intractable and numerically highly complicated and costly. On the other hand it has been shown that by using the line spring model to account for the net ligament, surprisingly accurate results can be obtained for surface cracks in plates or shells under mode I conditions (Delale and Erdogan, 1981, 1982; Parks, 1981; Erdogan and Boduroglu, 1984; Yahsi and Erdogan, 1985; Erdogan and Yashi, 1985). See also Joseph and Erdogan (1987) for comparison with finite element results. It is then natural to attempt extending the technique to mixed-mode crack problems.

The problem under consideration is described in Fig. 1. In the usual shallow shell notation let u_1, u_2, u_3 refer to the components of the displacement vector (on the neutral surface), β_1, β_2 to the rotation of the normal to the neutral surface in x_3x_3 and x_2x_3 planes, respectively, and N_{ij}, M_{ij}, and V_i $(i, j=1,2)$ to the membrane, moment and transverse shear resultants. For a shell with arbitrary curvature containing an arbitrarily oriented through crack, the formulation of the problem was given by Yashi and Erdogan (1983) where Reissner's theory was used to reduce the corresponding mixed boundary value problem to a coupled system of five singular integral equations. In their study, as in most similar investigations, derivatives of the displacement quantities on the crack surfaces u_1, u_2, u_3, β_1 and β_2 were used as the unknown functions and stress resultants applied to the crack surfaces as the input. In problems involving the line spring model, it is somewhat more convenient to use directly the displacement quantities as the unknowns. In this paper, the integral equations will, therefore, be expressed in terms of "displacements." The derivation, however, is quite similar to that given by Yashi and Erdogan (1983) and will be omitted here (see Joseph and Erdogan (1987) for details).

For a through crack located on $(x_1=0,\ |x_2|<a,\ |x_3|\le h/2)$ in a shallow shell, the integral equations may be expressed as (Joseph and Erdogan, 1987)

$$\frac{b_i}{2\pi}\int_{-a}^{a}\frac{g_i(t_2)}{(t_2-x_2)^2}dt_2+\int_{-a}^{a}\sum_{j=1}^{5}k_{ij}(x_2,\ t_2)g_j(t_2)dt_2$$

$$=f_{i0}(x_2),\ (i=1,\ \ldots,\ 5),\ (-a<x_2<a), \tag{1}$$

where

$$g_1(x_2) = \frac{1}{2}[u_1(+0,x_2)-u_1(-0,x_2)],$$

$$g_2(x_2) = \frac{1}{2}[\beta_1(+0,x_2)-\beta_1(-0,x_2)],$$

$$g_3(x_2) = \frac{1}{2}[u_3(+0,x_2)-u_3(-0,x_2)],$$

$$g_4(x_2) = \frac{1}{2}[u_2(+0,x_2)-u_2(-0,x_2)] - \frac{x_2}{2R_2}[u_3(+0,x_2)-u_3(-0,x_2)],$$

$$g_5(x_2) = \frac{1}{2}[\beta_2(+0,x_2)-\beta_2(-0,x_2)], \tag{2a-e}$$

$$f_{10}(x_2) = \frac{1}{Eh}N_{11}^0(0,x_2),$$

$$f_{20}(x_2) = \frac{1}{Eh^2}M_{11}^0(0,x_2),$$

$$f_{30}(x_2) = \frac{12(1+\nu)}{5Eh}V_1^0(0,x_2),$$

$$f_{40}(x_2) = \frac{1}{Eh}N_{12}^0(0,x_2),$$

$$f_{50}(x_2) = \frac{1}{Eh^2}M_{12}^0(0,x_2),\ (-a<x_2<a), \tag{3a-e}$$

$$b_1=1,\ b_2=\frac{h}{12},\ b_3=2,\ b_4=1,\ b_5=\frac{h}{12}. \tag{4a-e}$$

Here, h is the shell thickness and R_2 is the radius of curvature in the x_2x_3 plane (Fig. 1). In equation (1) the strongly singular integral should be interpreted in the Hadamard sense (Kaya and Erdogan, 1987). In the usual manner it is assumed that the shell problem has been solved under given applied loads in the absence of the crack and (1) represents the formulation of the perturbation problem in which the stress resultants f_{i0}, $(i=1,\ \ldots,5)$ are the equal and opposite of those obtained from the solution without the crack on the $x_1=0$ plane.

As in the study by Yashi and Erdogan (1983), k_{ij}, $(i, j=1,\ \ldots,5)$ is a full matrix if the crack is arbitrarily oriented with respect to the principal planes of curvatures of the shell. However, it has been shown that if the crack lies in one of the principal planes of curvature, the kernals k_{ij}, k_{2j}, $(j=3, 4, 5)$ and k_{i1}, k_{i2}, $(i=3, 4, 5)$ vanish and the problem is decoupled into a symmetric $(i, j=1, 2)$ and an antisymmetric $(i, j=3, 4, 5)$ component (Joseph and Erdogan, 1987; Yashi and Erdogan, 1983). The symmetric problem involves only mode I stresses and deformations whereas modes II and III remain coupled in the antisymmetric problem.

In this paper, as in previous studies, the compliance functions for the line spring model will be obtained from a flat edge cracked strip under the plane strain and antiplane shear conditions. The consequence of this is that the contribution coming to the integral equations from the line spring is always

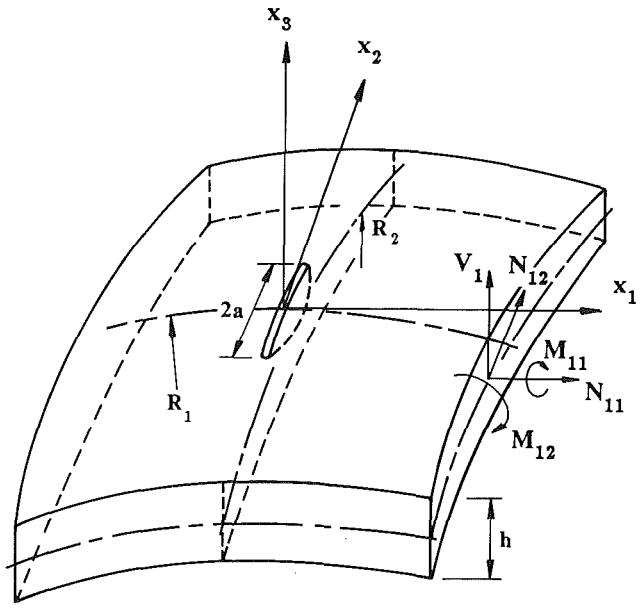

Fig. 1 The shell geometry

Downloaded 03 May 2010 to 171.66.16.21. Redistribution subject to ASME license or copyright; see http://www.asme.org/terms/Terms_Use.cfm

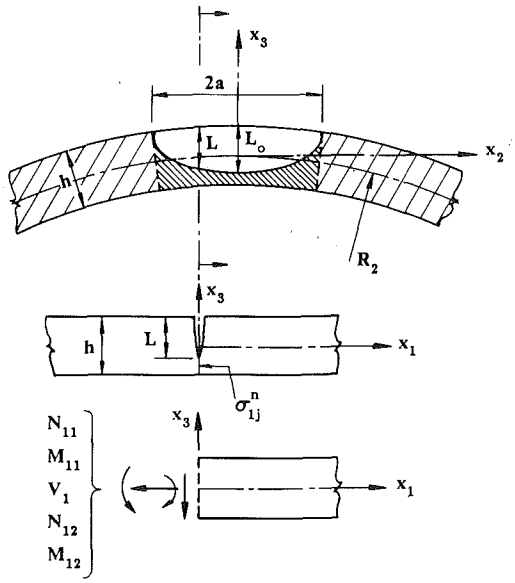

Fig. 2 The notation for a surface crack in shells

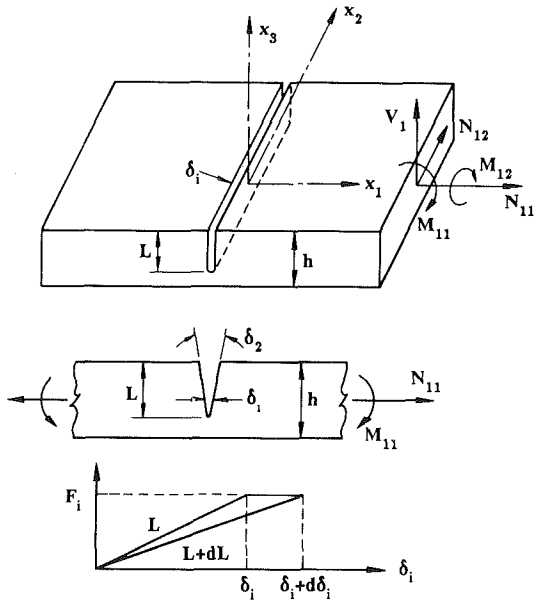

Fig. 3 Development of the line spring model for a part-through crack

decoupled. Thus, even though the primary interest in this paper is in the antisymmetric problem, the line spring model developed is equally applicable to the most general surface crack problem in shells.

Consider now the local geometry of the surface crack shown in Fig. 2. Let $\sigma^n_{ij}(0, x_2, x_3)$, $(j=1, 2, 3)$ be the stresses acting on the net ligament $(x_1=0, \ -a<x_2<a, \ -h/2<x_3<[h/2-L(x_2)])$. Let the net ligament stresses σ^n_{ij} be statically equivalent to the resultants N_{11} $(0, x_2)$, $M_{11}(0, x_2)$, $V_1(0, x_2)$, $N_{12}(0, x_2)$, $M_{12}(0, x_2)$ acting on the neutral surface $x_3=0$ along $(x_1=0, \ -a<x_2<a)$. Note that in expressing the boundary conditions for the three-dimensional surface crack problem the conditions of zero displacements on the uncracked part of the boundary $x_1=0$ may be replaced by the traction boundary conditions $\sigma_{ij}(0, x_2, x_3)=\sigma^n_{ij}(0, x_2, x_3)$, provided σ^n_{ij} are known. One of the major assumptions in developing the line spring model is that the net ligament tractions σ^n_{ij} (which are unknown functions of x_2 and x_3) may be replaced by their statically equivalent resultants N_{11}, M_{11}, V_1, N_{12}, and M_{12} which are now functions of only one variable, x_2. This assumption also implies that, for the purpose of determining the unknown resultants, the part-through crack problem may be replaced by a through crack problem. If we define the matrix

$$\{f_i(x_2)\}^T=\left\{\frac{N_{11}}{Eh}, \frac{M_{11}}{Eh^2}, \frac{12(1+\nu)}{5Eh}V_1, \frac{N_{12}}{Eh}, \frac{M_{12}}{Eh^2}\right\}, \quad (i=1, \ldots, 5), \tag{5}$$

by taking into consideration the contribution coming from the net ligament stresses, the system of integral equations (1) for a through crack may now be modified as

$$\frac{b_i}{2\pi}\oint_{-a}^{a}\frac{g_i(t_2)}{(t_2-x_2)^2}dt_2+\int_{-a}^{a}\sum_{j=1}^{5}k_{ij}(x_2, t_2)g_j(t_2)dt_2 = f_{i0}(x_2)+f_i(x_2), \ (i=1, \ldots, 5), \ (-a<x_2<a). \tag{6}$$

To solve the integral equations (6), the two sets of unknown functions g_i and f_i, $(i=1, \ldots, 5)$ must somehow be related. The key to this relationship is another important assumption made in developing the model to the effect that the stress intensity factors at a location x_2 along the crack front (Fig. 1) may be approximated by the corresponding modes I, II, and III values obtained from the plane elasticity solution of a strip containing an edge crack of depth $L(x_2)$ and subjected to stress and moment resultants ($[N_{11}(x_2), M_{11}(x_2)]$, $V_1(x_2)$ and $[N_{12}(x_2), M_{12}(x_2)]$) away from the crack region. To obtain the relationship between the functions $g_i(x_2)$ and $f_i(x_2)$, $(i=1, \ldots, 5)$, the energy G available for fracture along the crack front is expressed in two ways. First, we note that for coplanar crack growth G is equivalent to the crack closure energy per unit thickness which may be expressed in terms of the stress intensity factors as follows:

$$G=\frac{\partial}{\partial L}(U-V)=\frac{\pi(1-\nu^2)}{E}\left[k_1^2+k_2^2+\frac{1}{1-\nu}k_3^2\right], \tag{7}$$

where U is the work done by the external loads, V is the strain energy, and k_1, k_2, and k_3 are, respectively, the modes I, II, and III stress intensity factors defined by (see Fig. 3)

$$k_1 = \lim_{r\to 0}\sqrt{2r}\sigma_{11}(0, x_2, x_3),$$
$$k_2 = \lim_{r\to 0}\sqrt{2r}\sigma_{13}(0, x_2, x_3),$$
$$k_3 = \lim_{r\to 0}\sqrt{2r}\sigma_{12}(0, x_2, x_3), \ (r=h/2-L-x_3). \tag{8a-c}$$

Referring now to Fig. 3, let δ_i be the relative crack surface displacements and rotations corresponding to the resultants F_i, $(i=1, \ldots, 5)$ defined by

$$\{F_i\}^T = \{N_{11}, M_{11}, V_1, N_{12}, M_{12}\} = \left\{Ehf_1, Eh^2f_2, \frac{5Eh}{12(1+\nu)}f_3, Ehf_4, Eh^2f_5\right\}, \quad (i=1, \ldots, 5), \tag{9}$$

$$\{\delta_i\}^T = \{u_1^+-u_1^-, \beta_1^+-\beta_1^-, u_3^+-u_3^-, u_2^+-u_2^-, \beta_2^+-\beta_2^-\}, \ (i=1, \ldots, 5). \tag{10}$$

Also, let $d\delta_i$ be the change in δ_i, $(i=1, \ldots, 5)$ as the crack length increases from L to $L+dL$ under "fixed load" conditions. From Fig. 3 it may then be seen that the changes in U and V may be expressed as

Downloaded 03 May 2010 to 171.66.16.21. Redistribution subject to ASME license or copyright; see http://www.asme.org/terms/Terms_Use.cfm

$$dU=\sum_{i=1}^{5}F_i d\delta_i, \tag{11}$$

$$dV=\sum_{i=1}^{5}\left[\frac{1}{2}F_i(\delta_i+d\delta_i)-\frac{1}{2}F_i\delta_i\right]=\frac{1}{2}\sum_{i=1}^{5}F_i d\delta_i, \tag{12}$$

giving the energy available for crack growth dL as

$$d(U-V)=\frac{1}{2}\sum_{i=1}^{5}F_i d\delta_i. \tag{13}$$

By observing that under constant loads

$$d\delta_i=\frac{\partial\delta_i}{\partial L}dL,\ (i=1,\ \ldots,\ 5) \tag{14}$$

from (7), (13), and (14) it follows that

$$G=\frac{\partial}{\partial L}(U-V)=\frac{1}{2}\sum_{i=1}^{5}F_i\frac{\partial\delta_i}{\partial L}, \tag{15}$$

and

$$\frac{1}{2}\sum_{i=1}^{5}F_i\frac{\partial\delta_i}{\partial L}=\frac{\pi(1-\nu^2)}{E}\left[k_1^2+k_2^2+\frac{1}{1-\nu}k_3^2\right]. \tag{16}$$

We will now assume that the plane edge crack problem under (uniform) resultants F_i (see (9)) away from the crack region shown in Fig. 3 has been solved and the stress intensity factors are known as fuctions of L/h. Defining the stress amplitudes in the shell by

$$\{\sigma_i\}^T=\left\{\frac{N_{11}}{h},\ \frac{6M_{11}}{h^2},\ \frac{3V_1}{2h},\ \frac{N_{12}}{h},\ \frac{6M_{12}}{h^2}\right\},$$

$$=\left\{\frac{F_1}{h},\ \frac{6F_2}{h^2},\ \frac{3F_3}{2h},\ \frac{F_4}{h},\ \frac{6F_5}{h^2}\right\},\ (i=1,\ \ldots,\ 5), \tag{17}$$

we express the stress intensity factors as

$$k_1 = \sqrt{h}[\sigma_1 p_1(\xi)+\sigma_2 p_2(\xi)],$$

$$k_2 = \sqrt{h}\sigma_3 p_3(\xi),$$

$$k_3 = \sqrt{h}[\sigma_4 p_4(\xi)+\sigma_5 p_5(\xi)],\ (\xi=L/h) \tag{18a-c}$$

where $p_1,\ \ldots,\ p_5$ are known functions given in the Appendix. From (7) and (18) it is seen that

$$G=\frac{\pi h(1-\nu^2)}{E}\left[\sigma_1^2p_1^2+2\sigma_1\sigma_2p_1p_2+\sigma_2^2p_2^2+\sigma_3^2p_3^2\right.$$

$$\left.+\frac{1}{1-\nu}\left(\sigma_4^2p_4^2+2\sigma_4\sigma_5p_4p_5+\sigma_5^2p_5^2\right)\right]=\{\sigma\}^T[\mathbf{P}]\{\sigma\}. \tag{19}$$

The matrix $\{\sigma\}$ is given by (17) and the square matrix $[\mathbf{P}]$ is defined by

$$[\mathbf{P}]=\frac{\pi h(1-\nu^2)}{E}$$

$$\times\begin{bmatrix} p_1^2 & p_1p_2 & 0 & 0 & 0 \\ p_1p_2 & p_2^2 & 0 & 0 & 0 \\ 0 & 0 & p_3^2 & 0 & 0 \\ 0 & 0 & 0 & \frac{1}{1-\nu}p_4^2 & \frac{1}{1-\nu}p_4p_5 \\ 0 & 0 & 0 & \frac{1}{1-\nu}p_4p_5 & \frac{1}{1-\nu}p_5^2 \end{bmatrix}. \tag{20}$$

In terms of the matrices $\{\delta\}$ and $\{\sigma\}$ defined by (9) and (17) from (15), G may also be expressed as

$$G=\frac{1}{2}\{\mathbf{F}\}^T\frac{\partial}{\partial L}\{\delta\}=\{\sigma\}^T\frac{1}{2}[\mathbf{c}]\frac{\partial}{\partial L}\{\delta\}, \tag{21}$$

where the diagonal matrix $[\mathbf{c}]$ is given by

$$[\mathbf{c}]=\text{diag}\ \{h,\ h^2/6,\ 2h/3,\ h,\ h^2/6\}. \tag{22}$$

From (19) and (21) it now follows that

$$\frac{1}{2}[\mathbf{c}]\frac{\partial}{\partial L}\{\delta\}=[\mathbf{P}]\{\sigma\}. \tag{23}$$

By observing that $[\mathbf{c}]$ is constant, $\{\delta\}=0$ for $L=0$, $[\mathbf{P}]$ is a function of L and $\{\sigma\}$ is independent of L, from (23) we obtain

$$\frac{1}{2}[\mathbf{c}]\{\delta\}=\left(\int_0^L[\mathbf{P}]dL\right)\{\sigma\}=h\left(\int_0^\xi[\mathbf{P}(\xi)]d\xi\right)\{\sigma\},$$

$$\xi=L/h. \tag{24}$$

From (20) if we define the matrix

$$[\mathbf{A}] = [\alpha_{ij}]=\frac{E}{\pi h(1-\nu^2)}\int_0^\xi[\mathbf{P}(\xi)]d\xi,$$

$$\alpha_{ij} = \int_0^\xi p_ip_jd\xi,\ (i,j=1,2)\text{ and }(i=j=3),$$

$$\alpha_{ij} = \frac{1}{1-\nu}\int_0^\xi p_ip_jd\xi,\ (i,j=4,5), \tag{25a-c}$$

equation (24) becomes

$$\frac{E}{\pi h^2(1-\nu^2)}[\mathbf{A}]^{-1}\frac{1}{2}[\mathbf{c}]\{\delta\}=\{\sigma\}, \tag{26}$$

which, considering the definitions of $\{\sigma\}$ and $\{\mathbf{f}\}$ given by (17) and (5) and $\{\delta\}$ and $\{\mathbf{g}\}$ given by (10) and (2), provides the needed relationship between $\{\mathbf{f}\}$ and $\{\mathbf{g}\}$.

If the crack lies in a principal plane of curvature of the shell, then the symmetric and antisymmetric components of the problem can be uncoupled, considering only the $x_1>0$ half of the shell, the crack opening displacements and rotations become

$$\delta_1=2u_1(x_2),\ \delta_2=2\beta_1(x_2),\ \delta_3=2u_3(x_2),$$

$$\delta_4=2u_2(x_2),\ \delta_5=2\beta_2(x_2). \tag{27}$$

From (23)–(27) we find

$$u_1(x_2) = \frac{\pi h(1-\nu^2)}{E}(\alpha_{11}\sigma_1+\alpha_{12}\sigma_2),$$

$$\beta_1(x_2) = \frac{6\pi(1-\nu^2)}{E}(\alpha_{21}\sigma_1+\alpha_{22}\sigma_2),$$

$$u_3(x_2) = \frac{3\pi h(1-\nu^2)}{2E}\alpha_{33}\sigma_3,$$

$$u_2(x_2) = \frac{\pi h(1-\nu^2)}{E}(\alpha_{44}\sigma_4+\alpha_{45}\sigma_5),$$

$$\beta_2(x_2) = \frac{6\pi(1-\nu^2)}{E}(\alpha_{54}\sigma_4+\alpha_{55}\sigma_5). \tag{28a-e}$$

Similarily, it may be shown that

$$\sigma_1 = \frac{E}{\pi h(1-\nu^2)}\left(\gamma_{11}u_1+\gamma_{12}\frac{h}{6}\beta_1\right),$$

$$\sigma_2 = \frac{E}{\pi h(1-\nu^2)}\left(\gamma_{21}u_1+\gamma_{22}\frac{h}{6}\beta_1\right),$$

Downloaded 03 May 2010 to 171.66.16.21. Redistribution subject to ASME license or copyright; see http://www.asme.org/terms/Terms_Use.cfm

$$\sigma_3 = \frac{E}{\pi h(1-\nu^2)}\gamma_{33}\frac{2}{3}u_3,$$

$$\sigma_4 = \frac{E}{\pi h(1-\nu^2)}\left(\gamma_{44}u_2+\gamma_{45}\frac{h}{6}\beta_2\right),$$

$$\sigma_5 = \frac{E}{\pi h(1-\nu^2)}\left(\gamma_{54}u_2+\gamma_{55}\frac{h}{6}\beta_2\right), \qquad (29a\text{-}e)$$

where

$$\gamma_{11} = \frac{\alpha_{22}}{\Delta_1},\ \gamma_{12}=-\frac{\alpha_{12}}{\Delta_1}=\gamma_{21},\ \gamma_{22}=\frac{\alpha_{11}}{\Delta_1},$$

$$\gamma_{33} = -\frac{1}{\alpha_{33}},$$

$$\gamma_{44} = \frac{\alpha_{55}}{\Delta_2},\ \gamma_{45}=-\frac{\alpha_{45}}{\Delta_2}=\gamma_{54},\ \gamma_{55}=\frac{\alpha_{44}}{\Delta_2},$$

$$\Delta_1 = \alpha_{11}\alpha_{22}-\alpha_{12}^2,\ \Delta_2=\alpha_{44}\alpha_{55}-\alpha_{45}^2. \qquad (30)$$

The final form of the system of integral equations is obtained by substituting from (9), (17), (29), and (2) into (6). Once the fuctions g_i are determined by solving (6), the stress intensity factors may be obtained as functions of x_2 by substituting from (29) and (2) into (18).

3 Shells Under Antisymmetric Loading.

Consider the shell shown in Fig. 2 that has a part-through crack and is subjected to (modes II and III) antisymmetric loading. Let $\overset{\infty}{V}_1$, $\overset{\infty}{N}_{12}$ and $\overset{\infty}{M}_{12}$ applied to the shell away from the crack region be the only external loads. Defining

$$\overset{\infty}{\sigma}_3=\frac{3\overset{\infty}{V}_1}{2h},\ \overset{\infty}{\sigma}_4=\frac{\overset{\infty}{N}_{12}}{h},\ \overset{\infty}{\sigma}_5=\frac{6\overset{\infty}{M}_{12}}{h^2}, \qquad (31)$$

the integral equations of the problem may be expressed as[1] (the rather lengthy derivation may be found in the report by Joseph and Erdogan (1987))

$$\frac{1}{\pi}\fint_{-a}^{a}\frac{g_3(t_2)}{(t_2-x_2)^2}dt_2$$

$$-\frac{3(1+\nu)h}{10\pi}\left(\frac{1}{R_1}+\frac{3}{R_2}\right)\int_{-a}^{a}\frac{g_4(t_2)}{(t_2-x_2)}dt_2$$

$$+\frac{1}{\pi}\sum_{i=3}^{5}\int_{-a}^{a}k_{3i}(x_2,t_2)g_i(t_2)dt_2-\frac{16\gamma_{33}}{15\pi h(1-\nu)}g_3(x_2)$$

$$=\frac{-8(1+\nu)}{5E}\overset{\infty}{\sigma}_3,\ (-a<x_2<a), \qquad (32)$$

$$\frac{1}{2\pi}\fint_{-a}^{a}\frac{g_4(t_2)}{(t_2-x_2)^2}dt_2+\frac{1}{\pi}\sum_{i=3}^{5}\int_{-a}^{a}k_{4i}(x_2,t_2)g_i(t_2)dt_2$$

$$-\frac{1}{\pi h(1-\nu^2)}\left[\gamma_{44}g_4(x_2)+\gamma_{44}\frac{x_2}{R_2}g_3(x_2)+\gamma_{45}\frac{h}{6}g_5(x_2)\right]$$

$$=\frac{-1}{E}\overset{\infty}{\sigma}_4,\ (-a<x_2<a), \qquad (33)$$

$$\frac{1}{24\pi}\fint_{-a}^{a}\frac{g_5(t_2)}{(t_2-x_2)^2}dt_2+\frac{h}{8\pi}\left(\frac{1}{R_1}+\frac{3}{R_2}\right)\fint_{-a}^{a}\frac{g_3(t_2)}{(t_2-x_2)}dt_2$$

$$+\frac{1}{\pi}\sum_{i=3}^{5}\int_{-a}^{a}k_{5i}(x_2,t_2)g_i(t_2)dt_2$$

$$-\frac{1}{\pi h(1-\nu^2)}\left[\gamma_{54}g_4(x_2)+\gamma_{54}\frac{x_2}{R_2}g_3(x_2)+\gamma_{55}\frac{h}{6}g_5(x_2)\right]$$

$$=\frac{-1}{6E}\overset{\infty}{\sigma}_5,\ (-a<x_2<a), \qquad (34)$$

where the Fredholm kernels k_{ij}, $(i, j=3, 4, 5)$ are given by Joseph and Erdogan (1987).

By using an asymptotic analysis similar to that given by, for example, Yashi and Erdogan (1983) and Delale and Erdogan (1979), it can be shown that for the through crack under consideration the dominant part of the integral equations would give the solution in the following form (Joseph and Erdogan, 1987; Kaya and Erdogan, 1987):

$$g_i(x_2)=G_i(x_2)\sqrt{a^2-x_2^2},\ -a<x_2<a,\ (i=3,4,5) \qquad (35)$$

with G_i being bounded in $-a\le x_2\le a$ and nonzero at $x_2=\pm a$. The asymptotic analysis also shows that the crack tip behavior of modes II and III stress states given by the transverse shear theory of shells is identical to that obtained from the plane and antiplane shear elasticity solutions (Yashi and Erdogan, 1983).

The system of integral equations may be solved by normalizing the interval $(-a, a)$ and by substituting

$$g_i(x_2)=g_{in}(y)=G_{in}(y)\sqrt{1-y^2},\ y=x_2/a,\ t=t_2/a$$

$$G_{in}(y)=\sum_{j=0}^{\infty}A_{ij}U_j(y),\ -1<y<1,\ (i=3,4,5) \qquad (36a,b)$$

where U_j is the Chebychev polynomial of the second kind and A_{ij} are unknown coefficients. First, we observe that (Kaya and Erdogan, 1987 and Joseph and Erdogan, 1987)

$$\frac{1}{\pi}\int_{-1}^{1}\frac{U_j(t)(1-t^2)^{1/2}}{(t-y)^2}dt$$

$$=\begin{cases}-(j+1)U_j(y),\ |y|<1,\ j\ge 0,\\ -(j+1)[y-(y^2-1)^{1/2}]^j\left[1-\dfrac{y}{(y^2-1)^{1/2}}\right],\\ \qquad |y|>1,\ j\ge 0,\end{cases} \qquad (37)$$

$$\frac{1}{\pi}\int_{-1}^{1}\frac{U_j(t)(1-t^2)^{1/2}}{(t-y)}dt$$

$$=\begin{cases}-T_{j+1}(y),\ |y|<1,\ j\ge 0,\\ [y-(y^2-1)^{1/2}]^{j+1},\ |y|>1,\ j\ge 0.\end{cases} \qquad (38)$$

Thus, from (37) and (38) it is seen that by substituting from (36) into (32)–(34), all singularities are removed and the integral equations are reduced to an infinite system of linear algebraic equations in A_{ij}, $(i=3, 4, 5; j=0, 1, 2, \ldots)$. After solving (32)–(34) for g_3, g_4 and g_5 the crack surface displacements and rotation are obtained from (see (2))

$$u_3(x_2) = g_3(x_2),$$

$$u_2(x_2) = g_4(x_2)+\frac{x_2}{R_2}g_3(x_2),$$

$$\beta_2(x_2) = g_5(x_2),\ -a>x_2<a. \qquad (39a\text{-}c)$$

[1] In (32)–(34), the integrals with double bars should be interpreted in Hadamard sense and those with single bars in the Cauchy principal value sense.

Downloaded 03 May 2010 to 171.66.16.21. Redistribution subject to ASME license or copyright; see http://www.asme.org/terms/Terms_Use.cfm

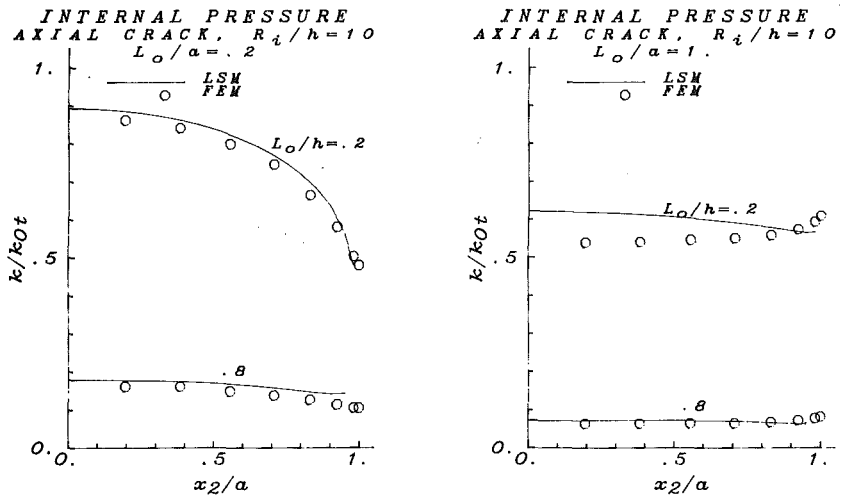

Fig. 4 Comparison of mode I stress intensity factors obtained from the line spring model (full lines) and the finite element solution (Raju and Newman, 1982) (open circles) for an axial semi-elliptic surface crack located on the inside of a pressurized cylinder, ν–0.3 (external loads include the crack surface pressure p_0 in addition to the membrane resultant $\overset{\infty}{N}_{11}=\pi\Delta R_i p_o$)

The stress intensity factors k_2 and k_3 at the location x_2 along the crack front may then be obtained by substituting from (39) and (29*c–e*) into (18*b,c*).

4 Results and Discussion

Since there are no other solutions available in the literature on part-through cracks in plates or shells under mixed-mode loading conditions, to give some idea about the kind of accuracy that may be obtained from line spring model/shell theory solutions, Figs. 4 and 5 show the comparison of the finite element and line spring results calculated under mode I loading conditions. The figures show the stress intensity factor in a pressurized cylinder containing a semi-elliptic axial surface crack on the inner boundary. The finite element results are from Raju and Newman (1982) and O'Donoghue et al. (1986). Note that the only case where the agreement is rather poor is the shallow semi-circular crack ($L_0/a=1$, $L_0/h=0.2$) for which clearly the line spring model is not expected to be representative.

Tables 3–5 show the calculated stress intensity factors k_2 and k_3 for a cylindrical shell with a surface crack under antisymmetric loading (Figs. 1 and 2). Even though any crack geometry can be used in the model, for the examples given in this paper, the crack profile is assumed to be semi-elliptic, that is

$$L(x_2)=L_o\sqrt{1-x_2^2/a^2},\ -a<x_2<a. \tag{40}$$

The normalizing stress intensity factors are obtained from the elasticity solution of the corresponding edge cracked strip shown in Fig. 3 under the same specified perturbation load as for the shell. That is, these results correspond to the exact solution of the problem for $R_1\to\infty$, $R_2\to\infty$, $a\to\infty$ and $L=L_0$ (Figs. 1 and 2). Specifically, the normalizing stress intensity factors k_{3I}, k_{20} and k_{3T} corresponding to in-plane shear $\overset{\infty}{N}_{12}$, out-of-plane shear $\overset{\infty}{V}_1$ and twisting moment $\overset{\infty}{M}_{12}$, respectively, are defined by (see (17), (18), (31)–(34), and Appendix[2])

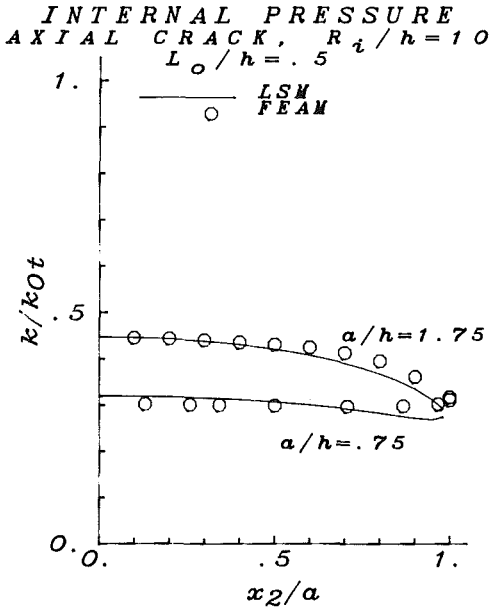

Fig. 5 Same as Fig. 4, finite element alternating method results are from O'Donoghue et al. (1986) and the effect of crack surface pressure is not included, that is $\overset{\infty}{N}_{11}$ is the only external load

$$k_{3I} = \overset{\infty}{\sigma}_4\sqrt{h}p_4(\xi_0),$$
$$k_{2O} = \overset{\infty}{\sigma}_3\sqrt{h}p_3(\xi_0),$$
$$k_{3T} = \overset{\infty}{\sigma}_5\sqrt{h}p_5(\xi_0),\ \xi_o=L_o/h. \tag{41a–c}$$

Table 3 shows some sample results for a cylindrical shell subjected to uniform membrane shear loading $\overset{\infty}{N}_{12}$ away from the crack region. This represents by far the most important antisymmetric loading in practice as in, for example, cylinders subjected to torsion. The table shows only the primary (in this case mode III) stress intensity factor k_3 at the center of the crack where, due to symmetry, stress intensity factor k_2 is zero. In this case the normalizing stress intensity factor k_{3I} is

[2] Equations (41*a*) and (41*c*) are equivalent to (*A*-13) and (*A*-14), and (41*b*) is calculated from (*A*-2) and (*A*-12).

Downloaded 03 May 2010 to 171.66.16.21. Redistribution subject to ASME license or copyright; see http://www.asme.org/terms/Terms_Use.cfm

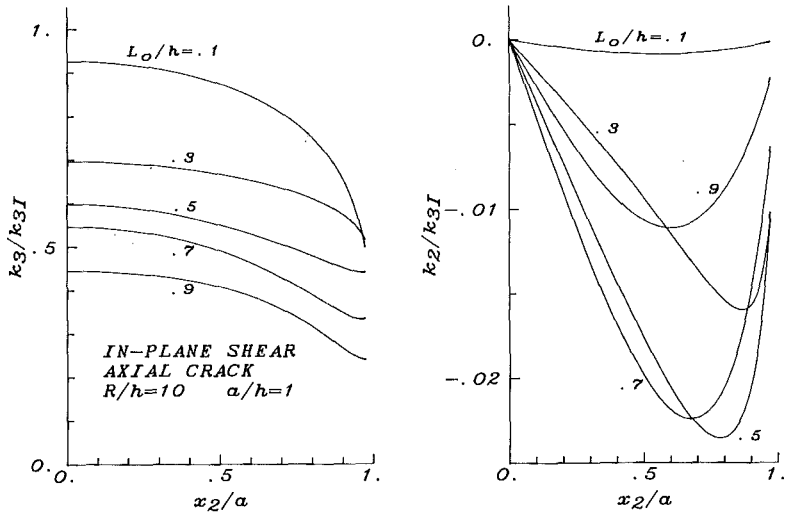

Fig. 6 The variation of the primary (mode III) and the secondary (mode II) stress intensity factors along the crack front for an axial semi-elliptical surface crack on the outside of a cylinder subjected to membrane shear loading $\overset{\infty}{N}_{12}$; $\nu = 0.3$, $R/h = 10$, $a/h = 1$ (Fig. 1)

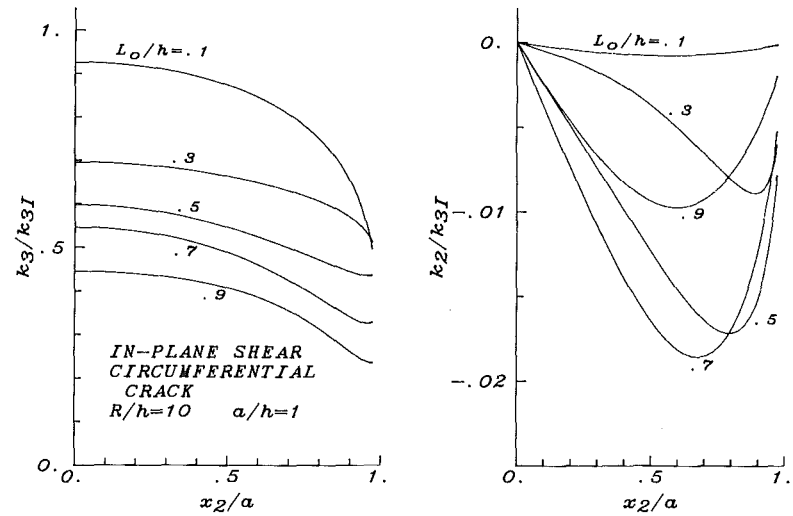

Fig. 7 Same as Fig. 6 for a circumferential semi-elliptic surface crack

the corresponding antiplane shear value given by (41*a*) or (*A*-13). Thus, the deviation of the tabulated values from unity shows the effect of the crack geometry (primarily the length $2a$) and the shell curvature. The limiting values given for $R/h \to \infty$ correspond to the flat plate results (Joseph and Erdogan, 1987). From the results given in this table as well as the more extensive results given by Joseph and Erdogan (1987) for cylindrical and torodial shells, it is clear that the part-through crack results are not very sensitive to shell curvature. Consequently, the difference between the stress intensity factors located inside or outside the shell in the axial or circumferential directions is not very significant. Among the variables R/h, a/h, L_o/h, and ν, the most important parameters appear to be L_o/h and a/h.

Some sample results showing the variation of the primary and secondary stress intensity factors k_3 and k_2 (as functions of x_2) along the crack front are given in Figs. 6 and 7. The results are for a cylindrical shell under in-plane shear $\overset{\infty}{N}_{12}$ and containing an axial or a circumferential semi-elliptic surface crack located on the outside wall. Note that the secondary stress intensity factor k_2 is rather small compared to k_3. Also note that $k_2(x_2) \to 0$ for $x_2 \to 0$, $x_2 \to a$ and $L_o(x_2) \to 0$. The variation of the stress intensity factors along the crack front in shells is also quite similar to that found for surface cracks in plates. Thus, the so-called curvature effect that was found to be rather significant in shells containing a through crack does not seem to be all that significant for part-through cracks. Tables 4 and 5 show further results in cylindrical shells containing a surface crack at various locations and orientations and subjected to uniform antisymmetric loads $\overset{\infty}{N}_{12}$, $\overset{\infty}{M}_{12}$ and $\overset{\infty}{V}_1$.

Some results for a toroidal shell are given in Tables 6 and 7. The notation for crack dimensions R, R_i, R_o and h and the crack locations and orientations A, B, C, and D are shown in Fig. 8. The tables show the stress intensity factors only at the center of surface cracks considered. The distribution of k_2 and k_3 along the crack front is nearly the same as that given for a surface crack of the same length parameters L_o and a in a cylindrical shell (see Joseph and Erdogan (1987) for further results). From these tables too it is seen that in part-through cracks the effect of shell curvature on the stress intensity factors is rather insignificant.

Downloaded 03 May 2010 to 171.66.16.21. Redistribution subject to ASME license or copyright; see http://www.asme.org/terms/Terms_Use.cfm

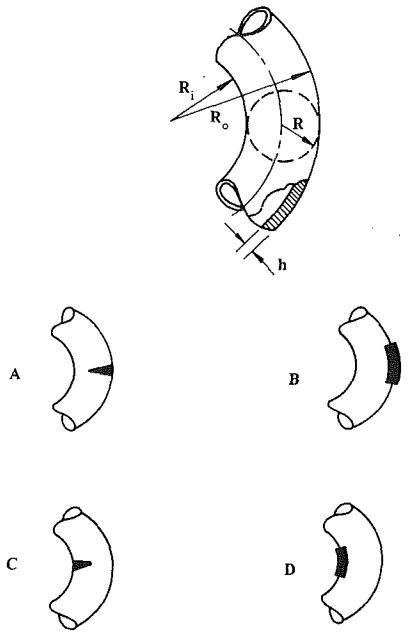

Fig. 8 Notation and crack locations in toroidal shells

Table 1 Normalized stress intensity factors in a strip of thickness h containing an edge crack of depth L and subjected to certain simple loading conditions (see equations (A-11)-(A-14))

ξ=L/h	$\frac{k_1}{\sigma_1\sqrt{L}}$	$\frac{k_1}{\sigma_2\sqrt{L}}$	$\frac{k_2}{\sigma_3\sqrt{L}}$	$\frac{k_3}{\sigma_4\sqrt{L}}$	$\frac{k_3}{\sigma_5\sqrt{L}}$	$\frac{k_2}{\sigma_6\sqrt{L}}$
→0	1.1215	1.1215	0.	1.	1.	1.1215
.025	1.1264	1.0921	0.0670	1.0003	0.9684	1.1215
.05	1.1399	1.0708	0.1313	1.0010	0.9373	1.12155
.1	1.1892	1.0472	0.2522	1.0041	0.8765	1.1219
.15	1.2652	1.0432	0.3628	1.0094	0.8172	1.1233
.2	1.3673	1.0553	0.4638	1.0170	0.7594	1.1264
.25	1.4975	1.0822	0.5556	1.0270	0.7030	1.1323
.3	1.6599	1.1241	0.6392	1.0398	0.6477	1.1419
.35	1.8612	1.1826	0.7156	1.0558	0.5935	1.1562
.4	2.1114	1.2606	0.7859	1.0753	0.5403	1.1763
.45	2.4253	1.3630	0.8512	1.0992	0.4881	1.2034
.5	2.8246	1.4972	0.9131	1.1284	0.4368	1.2391
.55	3.3428	1.6747	0.9733	1.1642	0.3864	1.2854
.6	4.0332	1.9140	1.0339	1.2085	0.3369	1.3450
.65	4.9843	2.2459	1.0980	1.2642	0.2883	1.4221
.7	6.3549	2.7252	1.1700	1.3360	0.2408	1.5229
.725	7.2838	3.0500	1.2111	1.3801	0.2174	1.5852
.75	8.4532	3.4582	1.2572	1.4315	0.1943	1.6578
.775	9.9596	3.9830	1.3102	1.4922	0.1715	1.7435
.8	11.955	4.6764	1.3726	1.5650	0.1491	1.8459
.825	14.694	5.6248	1.4482	1.6541	0.1272	1.9708
.85	18.628	6.9817	1.5429	1.7663	0.1057	2.1269
.875	24.634	9.0444	1.6664	1.9125	0.0848	2.3289
.9	34.632	12.462	1.8368	2.1133	0.0646	2.6037
.91	40.659	14.515	1.9251			2.7448
.92	48.632	17.225	2.0304			2.9116
.925			2.0911	2.4114	0.0453	3.0074
.93	59.559	20.932	2.1584			3.1132
.94	75.23	26.236	2.3185			3.3634
.95	99.14	34.306	2.5260	2.9180	0.0273	3.6854

Table 2 The coefficients C_{ik} for the stress intensity factor shape functions p_i, ($i=1,\ldots,6$)

k	C_{1k}	C_{2k}	C_{3k}	C_{4k}	C_{5k}	C_{6k}
0	1.12152	1.12152	0.0	1.0	1.0	1.12152
1	-1.67890	-3.04507	2.73069	-0.4999949	-1.773760	-0.55939
2	8.43058	10.49184	-3.44019	0.2860705	0.937496	-0.18069
3	-29.46644	-36.66780	0.33305	-0.2661996	-0.602894	0.39478
4	84.43442	110.09900	2.80514	0.2193511	1.176914	2.07787
5	-182.95329	-255.68184	-2.94406	-0.1731221	-2.183231	-5.40893
6	274.45012	421.97167	0.74775	0.1047768	2.906943	5.82745
7	-252.12029	-440.50866	0.63860	-0.0418068	-2.121964	-3.11784
8	92.30672	199.37326	-0.32028	0.0075456	0.659759	0.67088
9	62.66657	123.93056				
10	-88.30652	-237.97164				
11	37.54045	136.17068				
12	-5.30201	-28.91005				

References

Benthem, J. P., and Koiter, W. T., 1973, "Asymptotic Approximations to Cracks Problems," *Methods of Analysis and Solutions of Crack Problems*, G. C. Sih, ed., Noordhoff International Publishing, Leyden, The Netherlands.

Delale, F., and Ergodan, F., 1979, "Transverse Shear Effect in a Circumferentially Cracked Cylindrical Shell," *Quarterly of Applied Mathematics*, Vol. 37, pp. 239-257.

Delale, F., and Erdogan, F., 1981, "Line-Spring Model for Surface Cracks in a Reissner Plate," *International Journal of Engineering Science*, Vol. 19, pp. 1331-1340.

Delale, F., and Erodogan, F., 1982, "Application of the Line-Spring Model to a Cylindrical Shell Containing a Circumferential or Axial Part-Through Crack," ASME JOURNAL OF APPLIED MECHANICS, Vol. 49, pp. 97-102.

Erdogan, F., 1978, "Mixed Boundary-Value Problems in Mechanics," *Mechanics Today*, S. Nemat-Nasser, ed., Vol. 4, Pergamon Press, Oxford, pp. 1-86.

Erdogan, F., and Boduroglu, H., 1984, "Surface Cracks in a Plate of Finite Width Under Extension or Bending," *Theoretical and Applied Fracture Mechanics*, Vol. 2, pp. 197-216.

Erdogan, F., and Yashi, O. S., 1985, "A Cylindrical Shell With a Stress-Free End Which Contains an Axial Part-Through or a Through Crack," *International Journal of Engineering Science*, Vol. 23, pp. 1215-1237.

Heliot, J., Labbens, R. C., and Pellisier-Tanon, A., 1979, "Semi-Elliptical Cracks in a Cylinder Subjected to Stress Gradients," *Fracture Mechanics*, ASTM, STP 677, pp. 341-364.

Joseph, P. F., and Ergodan, F., 1987, "Plates and Shells Containing a Surface Crack Under General Loading Conditions," NASA Contractor Report 178328, NASA Langley Research Center.

Kaya, A. C., and Erdogan, F., 1987, "On the Solution of Integral Equations with Strongly Singular Kernels," *Quarterly of Applied Mathematics*, Vol. 45, No. 1, pp. 105-122.

Newman, Jr., J. C., and Raju, I. S., 1979, "Analysis of Surface Cracks in Finite Plates Under Tension or Bending Loads," NASA Technical Paper 1578.

Nishioka, T., and Atluri, S. N., 1982, "Analysis of Surface Flaw in Pressure Vessels by a New 3-Dimensional Alternating Method," ASME *Journal of Pressure Vessel Technology*, Vol. 104, pp. 299-307.

O'Donoghue, P. E., Nishioka, T., and Atluri, S. N., 1986, "Analysis of Interaction Behavior of Surface Flaws in Pressure Vessels," ASME *Journal of Pressure Vessel Technology*, Vol. 108, pp. 24-32.

Parks, D. M., 1981, "The Inelastic Line-Spring: Estimates of Elastic-Plastic Fracture Mechanics Parameters for Surface-Cracked Plates and Shells," ASME *Journal of Pressure Vessel Technology*, Vol. 103, pp. 246-254.

Raju, I. S., and Newman, Jr., J. C., 1982, "Stress-Intensity Factors for Internal and External Surface Cracks in Cylindrical Vessels," ASME *Journal of Pressure Vessel Technology*, Vol. 104, pp. 293-298.

Rice, J. R., and Levy, N., 1972, "The Part-Through Surface Crack in an Elastic Plate," ASME JOURNAL OF APPLIED MECHANICS, Vol. 39, pp. 185-194.

Rice, J. R., 1972, "The Line Spring Model for Surface Flaws," *The Surface Crack: Physical Problems and Computational Solutions*, J. L. Swedlow, ed., ASME, New York, pp. 171-186.

Tschegg, E. K., Ritchie, R. O., and McClintock, F. A. 1983, "On the Influence of Rubbing Fracture Surfaces on Fatigue Crack Propagation in Mode III," *International Journal of Fatigue*, pp. 29-35.

Yashi, O. S., and Erdogan, F., 1983, "A Cylindrical Shell With an Arbitrarily Oriented Crack," *International Journal of Solids and Structures*, Vol. 19, pp. 955-972.

Yashi, O. S., and Erdogan, F., 1985, "A Pressurized Cylindrical Shell With a Fixed End Which Contains an Axial Part-Through or a Through Crack," *International Journal of Fracture*, Vol. 28, pp. 161-187.

APPENDIX

The Compliance Functions $p_i(\xi)$. Consider a strip $0<x_1=x<h$, $-\infty<x_2=y<\infty$ containing a crack along $a<x<b$, $y=0$ and subjected to in-plane crack surface tractions

$$\sigma_{22}(x,0)=f_1(x),\sigma_{12}(x,0)=f_2(x),\ a<x<b. \qquad (A\text{-}1)$$

In terms of strongly singular kernels the integral equations of the problem may be expressed as (Joseph and Erdogan, 1987 and Kaya and Erdogan, 1987)

$$\frac{1}{\pi}\int_a^b\left\{\frac{1}{(t-x)^2}+K_s(x,t)\right\}u_i(t)dt+\frac{1}{\pi}\int_a^b K_i(x,t)u_i(t)dt$$

$$=\frac{(1+\kappa)}{4\mu}f_i(x),\ a<x<b,\ (i=1,2) \qquad (A\text{-}2)$$

where $i=1$, 2 corresponds to mode I and mode II deformations, respectively, μ and κ are the elastic constants, u_1 and u_2

Downloaded 03 May 2010 to 171.66.16.21. Redistribution subject to ASME license or copyright; see http://www.asme.org/terms/Terms_Use.cfm

are the crack surface displacements $(u_i(x) = u_i(x, +0),\ i = 1, 2)$, and

$$K_s(x,t) = \frac{-1}{(t+x)^2} + \frac{12xt}{(t+x)^4} - \frac{1}{(2h-x-t)^2} + \frac{12(h-x)(h-t)}{(2h-x-t)^4}, \quad (A\text{-}3)$$

$$K_1(x,t) = \int_0^\infty [S_1(x,t,\alpha) + S_1(h-x,h-t,\alpha) + S_2(x,t,\alpha) + S_2(h-x,h-t,\alpha)]d\alpha, \quad (A\text{-}4)$$

$$S_1(x,t,\alpha) = \frac{e^{-(x+t)\alpha}}{\Delta(\alpha)}\{e^{-2\alpha h}[-2\alpha^3 xt + \alpha^2(3x+3t) - 5\alpha] + 8\alpha^5 h^2 xt - 12\alpha^4 h^2(x+t) + \alpha^3[2hx + 18h^2 + 2xt + 2ht] + \alpha^2[-3x-3t-6h] + 5\alpha\}, \quad (A\text{-}5)$$

$$S_2(x,t,\alpha) = \frac{\alpha e^{(x-t)\alpha}}{\Delta(\alpha)}\{e^{-2\alpha h}[-\alpha(x-t) - 3] + \alpha^3[-4h^2 t + 4hxt] + \alpha^2[6h^2 - 6hx + 6ht] + \alpha[x-t-10h] + 3\}, \quad (A\text{-}6)$$

$$\Delta(\alpha) = e^{2\alpha h} - (4\alpha^2 h^2 + 2) + e^{-2\alpha h}, \quad (A\text{-}7)$$

$$K_2(x,t) = \int_0^\infty [S_3(x,t,\alpha) + S_3(h-x,h-t,\alpha) + S_4(x,t,\alpha) + S_4(h-x,h-t,\alpha)]d\alpha, \quad (A\text{-}8)$$

$$S_3(x,t,\alpha) = \frac{e^{-(x+t)\alpha}}{\Delta(\alpha)}\{e^{-2\alpha h}[-2\alpha^3 xt + \alpha^2(x+t) - \alpha] + 8\alpha^5 h^2 xt - 4\alpha^4 h^2(x+t) + \alpha^3[2hx + 2h^2 + 2xt + 2ht] - \alpha^2[x+t+2h] + \alpha\}, \quad (A\text{-}9)$$

Table 3 Normalized stress intensity factor $k_3(0)/k_{3|}$ at the center of a semi-elliptic surface crack in a cylindrical shell under in-plane shear loading $\overset{\infty}{N}_{12}$; $\nu = 0.3$

	a/h=1					a/h=4				
L_o/h R/h	0.2	0.4	0.6	0.8	0.95	0.2	0.4	0.6	0.8	0.95
Outer axial crack										
5	.797	.632	.576	.492	.304	.837	.709	.712	.745	.625
10	.798	.633	.576	.490	.301	.838	.709	.709	.737	.610
20	.799	.634	.576	.489	.300	.838	.709	.708	.732	.601
50	.799	.635	.576	.489	.299	.839	.710	.708	.729	.594
$\to\infty$	.800	.635	.577	.489	.299	.840	.712	.709	.728	.590
Inner axial crack										
5	.803	.641	.585	.496	.303	.843	.720	.726	.757	.627
10	.802	.639	.581	.493	.301	.843	.718	.721	.747	.613
20	.801	.637	.579	.491	.300	.842	.716	.717	.740	.604
50	.800	.636	.578	.490	.299	.841	.714	.713	.734	.597
$\to\infty$	.800	.635	.577	.489	.299	.840	.712	.709	.728	.590
Outer circumferential crack										
5	.797	.631	.575	.492	.305	.836	.707	.711	.750	.643
10	.798	.633	.575	.490	.302	.837	.707	.708	.737	.616
20	.799	.634	.576	.489	.300	.838	.708	.707	.731	.602
50	.799	.634	.576	.489	.299	.839	.710	.707	.728	.594
$\to\infty$	.800	.635	.577	.489	.299	.840	.712	.709	.728	.590
Inner circumferential crack										
5	.803	.642	.586	.498	.304	.845	.725	.733	.771	.645
10	.802	.639	.582	.494	.301	.844	.721	.725	.754	.620
20	.801	.638	.580	.491	.300	.843	.718	.719	.743	.606
50	.800	.636	.578	.490	.299	.841	.715	.714	.735	.597
$\to\infty$	.800	.635	.577	.489	.299	.840	.712	.709	.728	.590

Table 4 Normalized stress intensity factor $k_3(0)/k_{3|}$ at the center of a semi-elliptic surface crack in a cylindrical shell under in-plane shear loading $\overset{\infty}{N}_{12}$ and twisting moment $\overset{\infty}{M}_{12}$; $\nu = 0.3$

	In-Plane Shear					Twisting Moment $\overset{\infty}{M}_{12}$			
L_o/h a/h	0.2	0.4	0.6	0.8	0.95	0.2	0.4	0.6	0.8
Outer axial crack									
0.5	.737	.546	.466	.350	.185	.711	.409	.102	-.637
1	.798	.633	.576	.490	.301	.777	.520	.274	-.337
2	.827	.684	.658	.626	.449	.808	.583	.397	-.018
4	.838	.709	.709	.737	.601	.819	.611	.469	.229
Inner axial crack									
0.5	.739	.549	.468	.351	.184	.713	.413	.107	-.630
1	.802	.639	.581	.493	.301	.781	.528	.286	-.314
2	.832	.693	.668	.633	.451	.813	.594	.417	.027
4	.843	.718	.721	.747	.613	.825	.623	.491	.284
Outer circumferential crack									
0.5	.737	.546	.466	.350	.185	.711	.409	.102	-.638
1	.798	.633	.575	.490	.302	.777	.519	.273	-.339
2	.827	.683	.657	.626	.451	.807	.581	.395	-.022
4	.837	.707	.708	.737	.616	.818	.609	.466	.227
Inner circumferential crack									
0.5	.739	.549	.468	.351	.185	.713	.413	.107	-.629
1	.802	.639	.582	.494	.301	.782	.529	.287	-.310
2	.832	.694	.670	.636	.452	.814	.596	.422	.039
4	.844	.721	.725	.754	.620	.826	.627	.499	.311

Table 5 Normalized stress intensity factor $k_2(0)/k_{2O}$ at the center of a semi-elliptic surface crack in a cylindrical shell under transverse shear loading $\overset{\infty}{N}_1$; $\nu = 0.3$, $R/h = 10$ (Fig. 1)

L_o/h a/h	0.2	0.4	0.6	0.8	0.95
Outer axial crack					
0.5	.988	.883	.685	.467	.277
1	.996	.953	.851	.692	.486
2	.999	.986	.950	.874	.720
4	1.000	.996	.987	.962	.884
Inner axial crack					
0.5	.988	.883	.685	.467	.277
1	.996	.953	.851	.693	.487
2	.999	.986	.950	.876	.723
4	1.000	.997	.988	.965	.888
Outer circumferential crack					
0.5	.988	.883	.684	.466	.276
1	.996	.953	.849	.688	.482
2	.999	.985	.946	.865	.707
4	1.000	.995	.981	.947	.858
Inner circumferential crack					
0.5	.988	.883	.684	.466	.277
1	.996	.953	.850	.691	.485
2	.999	.985	.948	.872	.716
4	1.000	.995	.984	.955	.872

Table 6 Normalized stress intensity factor $k_3(0)/k_{3|}$ at the center of a semi-elliptic surface crack in a toroidal shell subjected to in-plane shear loading $\overset{\infty}{N}_{12}$; $\nu = 0.3$, $R/h = 10$ $a/h = 1$ (Fig. 8)

		$R_i/R=5$					$R_i/R=1$				
	L_o/h	0.2	0.4	0.6	0.8	0.95	0.2	0.4	0.6	0.8	0.95
	Crack Position										
A	inner	.802	.640	.583	.494	.302	.802	.640	.583	.495	.302
	outer	.798	.632	.575	.490	.302	.798	.632	.575	.490	.303
B	inner	.802	.639	.582	.494	.301	.802	.640	.583	.494	.302
	outer	.798	.633	.575	.490	.302	.798	.632	.575	.490	.302
C	inner	.802	.639	.581	.493	.301	.800	.636	.579	.492	.301
	outer	.798	.633	.575	.490	.301	.800	.635	.578	.491	.301
D	inner	.801	.638	.580	.492	.301	.800	.635	.578	.491	.301
	outer	.799	.634	.576	.490	.301	.800	.636	.579	.492	.301

Downloaded 03 May 2010 to 171.66.16.21. Redistribution subject to ASME license or copyright; see http://www.asme.org/terms/Terms_Use.cfm

Table 7 Normalized stress intensity factor $k_3(0)/k_{3I}$ and $k_2(0)k_{2O}$ at the center of a semi-elliptic surface crack in a toroidal shell subjected to in-plane shear loading $\overset{\infty}{N}_{12}$ and transverse shear $\overset{\infty}{V}_1$ loadings; $\nu = 0.3$, $R/h = 10$, $a/h = 2$, crack position A (Fig. 8)

Crack Position	$L_o/h \approx$ / R_i/R	0.2	0.4	0.6	0.8	0.95
		In-Plane Shear $\overset{\infty}{N}_{12}$: $k_3(0)/k_{3I}$				
outer	1	.826	.683	.657	.627	.454
	4	.826	.683	.656	.626	.453
	7	.826	.683	.656	.626	.452
	$\to\infty$	.827	.683	.657	.626	.451
inner	1	.833	.696	.672	.639	.455
	4	.833	.695	.671	.638	.454
	7	.833	.695	.670	.637	.453
	$\to\infty$	.832	.694	.670	.636	.452
		Transverse Shear V_1: $k_2(0)/k_{2O}$				
outer	1	.999	.985	.945	.864	.706
	4	.999	.985	.945	.865	.706
	7	.999	.985	.945	.865	.707
	$\to\infty$	.999	.985	.945	.865	.707
inner	1	.999	.985	.948	.872	.716
	4	.999	.985	.948	.872	.716
	7	.999	.985	.948	.872	.716
	$\to\infty$	.999	.985	.948	.872	.716

$$S_4(x,t,\alpha)=\frac{\alpha e^{(t-x)\alpha}}{\Delta(\alpha)}\{e^{-2\alpha h}[\alpha(t-x)+1]+\alpha^3[4h^2x-4hxt]$$

$$+\alpha^2[-2h^2-2hx+2ht]+\alpha[-t+x+2h]-1\}. \quad (A\text{-}10)$$

The integral equations (A-2) are solved for the edge crack ($a\to\infty$) by using the technique described by Kaya and Erdogan (1987) (see also Joseph and Erdogan (1987)). For an edge crack of length L the normalized stress intensity factors k_1 and k_2 are given in Table 1 for the following loading conditions (corresponding to membrane resultant N, bending resultant M, transverse shear resultant V away from the crack region and uniform transverse shear stress $-\sigma_6$ applied to the crack surfaces, see equation (17))

$$f_1(x) = \begin{cases} -\sigma_1 = -N/h, \\ \sigma_2(2x/h-1)=6M/h^2(2x/h-1), \end{cases} \quad (A\text{-}11)$$

$$f_2(x) = \begin{cases} \sigma_3 x(x-h)(2/h)^2=\dfrac{3V}{2h}x(x-h)(2/h)^2, \\ -\sigma_6 \end{cases} \quad (A\text{-}12)$$

The last column of Table 1 which corresponds to σ_6 is not needed in the line spring model and is provided for completeness.

The solution of the antiplane shear problem for the strip containing an edge crack of length L and subjected crack surface traction σ_{23} $(x, +0)$ is known in closed form, (Erdogan, 1978; and Joseph and Erdogan, 1987). For a membrane shear resultant $h\sigma_4$ and twisting moments $h^2\sigma_5/6$ applied to the strip away from the crack region (see equation (17) and Fig. 3) the crack surface tractions and the corresponding mode III stress intensity factors are

$$\sigma_{23}(x,+0)=-\sigma_4, \frac{k_3}{\sigma_4\sqrt{L}}=\sqrt{\frac{2}{\pi\xi}\tan\left(\frac{\pi\xi}{2}\right)}, \ \xi=L/h, \quad (A\text{-}13)$$

$$\sigma_{23}(x,+0)=\sigma_5(2x/h-1),$$

$$\frac{k_3}{\sigma_4\sqrt{L}}=\sqrt{\frac{2}{\pi\xi}\tan\left(\frac{\pi\xi}{2}\right)}$$

$$\times\left\{1-\frac{8}{\pi^2}\int_0^1\frac{\sin^{-1}\left[t\sin\left(\frac{\pi\xi}{2}\right)\right]}{\sqrt{1-t^2}}dt\right\}, \ \xi=L/h. \quad (A\text{-}14)$$

With $L=h\xi$, from Table 1 it may be seen that for small values of ξ we have $k_i\sim\sqrt{\xi}$, $(i=1, 2, 3)$. Also, from (A-13) and asymptotic results given by Benthem and Koiter (1973), one may conclude that for small values of $(1-\xi)$ we have $k_1\sim(1-\xi)^{-3/2}$, $k_j\sim(1-\xi)^{-1/2}$, $(j=2, 3)$. Thus, for the evaluation of α_{ij} defined by (25), since it would be highly desirable to have relatively simple analytical expressions for $p_1, \ldots, p_5$ we let

$$p_i(\xi)=\frac{\sqrt{\xi}}{(1-\xi)^{3/2}}\sum_{k=0}^{12}C_{ik}\xi^k, \ (i=1,2), \quad (A\text{-}15)$$

$$p_i(\xi)=\frac{\sqrt{\xi}}{\sqrt{1-\xi}}\sum_{k=0}^{8}C_{ik}\xi^k, \ (i=3,4,5,6), \ \xi=L/h. \quad (A\text{-}16)$$

From (18) and Table 1 it is seen that the tabulated results are $k_j/\sigma_i\sqrt{\xi}h=p_i/\sqrt{\xi}$, $(i=1, 2$ for $j=1$; $i=3, 6$ for $j=2$; $i=4, 5$ for $j=3)$. Thus, the coefficients C_{ik} defining p_i $(i=1, \ldots, 5)$ can be obtained from the tabulated results by a simple least squares curve fit. Table 2 shows the calculated results. Particularly for deep cracks, Table 1 or equation (18) with (A-15), (A-16), and Table 2 provide perhaps the most accurate known values for the stress intensity factors.

Downloaded 03 May 2010 to 171.66.16.21. Redistribution subject to ASME license or copyright; see http://www.asme.org/terms/Terms_Use.cfm

Three-Dimensional Stress Field Near the Crack Front of a Thin Elastic Plate

T. Nakamura[1]
Assoc. Mem. ASME
D. M. Parks
Mem. ASME

Department of Mechanical Engineering,
Massachusetts Institute of Technology,
Cambridge, MA 02139

Based on very detailed full-field finite element analysis of the near tip region of a thin isotropic elastic plate, the three-dimensional stress state in the vicinity of a through-crack front is characterized. The computed stress field reveals strong three-dimensional effects within a radial distance of about one-half thickness from the crack-tip. Further away from the tip, through-thickess variation of field quantities decreases and, at the radial distance of approximately 1.5 times the thickness, in-plane stresses merge with the dominant two-dimensional plane stress solutions. These "two-dimensional-three-dimensional" transition distances are essentially independent of the material Poisson's ratio, yet the amplitude of variation is greatly affected by its value. The influence of Poisson's ratio is clearly illustrated by local J along the crack front, which shows much higher variation through the thickness for nearly incompressible solids. At points very close to the crack front, relative magnitudes of out-of-plane strain components become very small, and asymptotic plane strain conditions prevail locally. On the mid-plane of the plate, the crack tip field converges to that given by the local plane strain stress intensity factor solution within a radial distance from the tip of less than 0.5 percent of thickness. In addition, it is found that the field near the intersection of crack front and free surface may be characterized by the corner singularity of a quarter infinite crack in a half space. The size of this domain is inferred from the gradient of local stress intensity factor with respect to distance from the free surface, and it appears that the corner singularity region extends up to a spherical radius of about 3 percent of plate thickness away from the intersection. Also the amplitude of the corner singularity field is described by a corner stress intensity factor, and its magnitude is determined for thin plates of various Poisson's ratios.

1 Introduction

In a thin plate containing a through-crack, a plane stress condition exists everywhere except in regions near the crack front, where the state of stress is three-dimensional. A number of investigations have been carried out to determine the size of the three-dimensional state in a cracked elastic plate (Cruse, 1970; Cruse and Vanburen, 1971; Levy et al., 1971; Burton et al., 1984; Yang and Freund, 1985; Parsons et al., 1986; Rosakis and Ravi-Chandar, 1986). Levy, Marcal, and Rice (1971) presented finite element results which show the three-dimensional near-tip stresses to coincide with the plane stress solution at a distance of twice the thickness away from the crack tip along the mid-plane of a thin plate. Though detailed results were not given, their work was one of the first analyses to present quantitative results of three-dimensional fields near a crack tip. More recent three-dimensional finite element analyses of through-cracked plates have been presented by Burton et al. (1984) and Parsons et al. (1986), who considered cases of center-cracked and edge-cracked panels, respectively. An approximate analytical solution which employed a boundary layer approach was given by Yang and Freund (1985). Their model assumed the crack front to be surrounded by a plane stress field controlled by a remote stress intensity factor. They found the out-of-plane displacement on the free surface to be identical with the corresponding plane stress solution at radial distances from the front greater than one-half to three-fourths of the plate thickness. A similar result was reported in the experimental work of Rosakis and Ravi-Chandar (1986), whose shadow spot method showed the "two-dimensional-three-dimensional" transition to take place at a radial distance near half-thickness away from the front.

Here, geometry similar to that used by Levy et al. (1971) is adopted to study the region near a through-crack front in a thin elastic plate. We define *thin plate* as a cracked plate which, under arbitrary remote loading, contains a region of

[1]Currently at State University of New York, Stony Brook, N.Y. 11794.

Contributed by the Applied Mechanics Division for presentation at the Winter Annual Meeting, Chicago, IL, November 28 to December 2, 1988, of THE AMERICAN SOCIETY OF MECHANICAL ENGINEERS.

Discussion on this paper should be addressed to the Editorial Department, ASME, United Engineering Center, 345 East 47th Street, New York, N.Y. 10017, and will be accepted until two months after final publication of the paper itself in the JOURNAL OF APPLIED MECHANICS. Manuscript received by ASME Applied Mechanics Division, September 30, 1987; final revision, February 13, 1988.

Paper No. 88-WA/APM-56.

Copyright © 1988 by ASME
Downloaded 03 May 2010 to 171.66.16.21. Redistribution subject to ASME license or copyright; see http://www.asme.org/terms/Terms_Use.cfm

essentially two-dimensional plane stress K-field outside a near crack front three-dimensional field. In order to obtain such conditions, the plate thickness must be sufficiently small compared with characteristic in-plane dimensions of the plate. We assume that the near tip region of a thin plate can be represented by a circular disk which contains a crack front at its center. The model has sufficiently large radial extent relative to the plate thickness, and its external strip of boundary is subjected to the traction of an assumed surrounding plane stress mode I stress intensity field. Under these conditions, the "three-dimensional effects" should be confined well within the model so that the plate thickness is the only characteristic dimension of the analysis. The purpose of this study is to assess the size of this three-dimensional field with respect to the physical scale and to determine characteristic features of the field, including the variation of *local* J (and K) along the crack front for various Poisson's ratios.

We also investigate the deformation field in the vicinity of the crack front to determine the degree of plane strain as the crack front is approached. For this purpose, we construct a finer mesh which models a cylindrical region closer to the crack front. The computed angular distributions of stress are compared with plane strain K-field solutions whose amplitudes are given by the local stress intensity factor.

Attention is also given to the field near the intersection of the crack front and free surface. From the results of a finer mesh, we study the existence and size of the domain which is influenced by the corner singularity. Extensive works have been presented on the analysis of the singular stress field near the normal intersection/vertex of a crack and free surface. These investigations are based on both analytical and numerical methods (Benthem, 1975, 1977, 1980; Bazant and Estenssoro 1979; Burton et al., 1984). A discussion of the corner field has been recently given by Riedel (1987). We compare the solutions given by Benthem (1975, 1977) with our numerical results. Benthem's analysis considers a quarter infinite crack in a half space, and the solutions are obtained using a separation of variables technique. His exponents of stress singularity are in agreement with solutions presented in later investigations (Bazant and Estenssoro, 1979; Benthem, 1980; Burton et al., 1984). Finally, a corner stress intensity factor representing the amplitude of singularity field near the intersection is introduced, and its value is given for thin elastic plates with various Poisson's ratios.

2 Procedure

2.1 Computational Model. A circular disk (cylinder) is used to model the near tip region of a thin plate with thickness t, as shown in Fig. 1(a). The straight crack front is located at the center of the disk along the x_3-axis (x_1, $x_2 = 0$). The maximum radial extent of the disk is five times the thickness ($r_{max}/t = 5$), which should be large enough to contain three-dimensional aspects of the fields within the outer boundary. The external strip of boundary is subjected to the traction of an assumed far field mode I stress intensity solution.

For the finite element analysis, only a quarter of the circular disk (region $0 \le \theta \le \pi$, $0 \le x_3/t \le 1/2$, where $\theta = \tan^{-1}(x_2/x_1)$) needs to be modeled since the problem has reflective symmetry with respect to the mid-plane ($x_3 = 0$) and the crack and ligament plane ($x_2 = 0$). The finite element mesh of this geometry is constructed with 8-node trilinear hexahedron (brick) elements as shown in Fig. 1(b). In the plane perpendicular to the crack front ($x_1 - x_2$ plane), the element size is gradually increased with radial distance r (where $r = \sqrt{x_1^2 + x_2^2}$) from the crack tip, while the angular increment of each element is kept constant, $\Delta\theta = \pi/36$, throughout the mesh. The identical planar mesh is repeated along the x_3-axis from the symmetry plane ($x_3 = 0$) to the free surface ($x_3/t = 1/2$). To accommodate the strong variations of field quantities with respect to the x_3-axis, the thickness of successive element layers is gradually reduced toward the free surface.

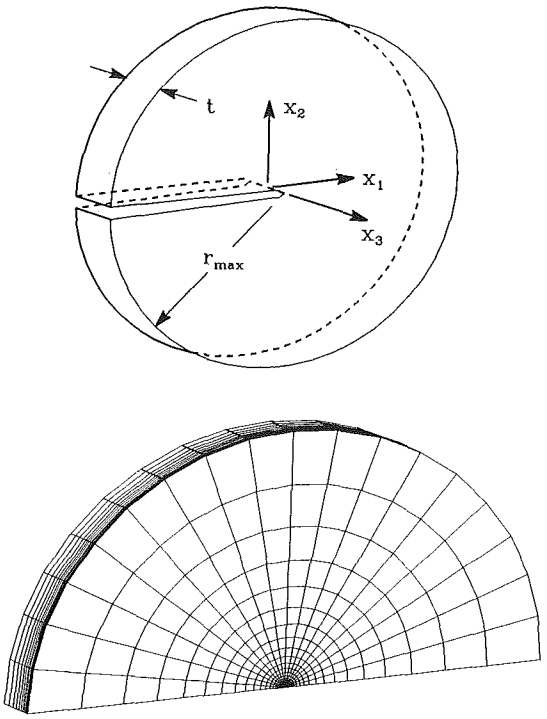

Fig. 1 (*a*) Schematic of a cracked circular disk which represents the near crack front region of a thin plate, (*b*) finite element mesh of the quarter-model

In carrying out the present analyses, two finite element meshes are employed for each Poisson's ratio considered. The first mesh models the entire disk, with the plane stress traction boundary condition applied on the outer perimeter (Fig. 1(b)). The second mesh has the same thickness and a similar element arrangement, but the radial extent is a fraction of the first mesh. Within that radius, elements of even smaller radial extent are contained. This finer mesh is used to obtain more accurate solutions near the crack front and near the intersection of the crack front and the free surface. To prescribe the boundary condition of the finer mesh, the computed displacements from the coarser mesh are interpolated to the nodal points on the outer perimeter. The coarser mesh has a total of 5400 elements (18 circumferential × 25 radial in-plane; 12 layers through half thickness) and 6422 nodes. The finer mesh has 4860 elements (18 × 18 in-plane; 15 layers through half thickness) and 5776 nodes. For the second mesh, the radial extent of the outermost nodes is .181 t, the crack-tip elements have a radial extent of .001 t, and the thickness of the element layer adjoining the free surface is .002 t.

To apply the traction boundary condition on the first mesh, we computed consistent nodal forces by integrating the K-field tractions over each element's surface. The stress distribution on the outer boundary is given by

$$\sigma_{ij} = \frac{K^{far}}{\sqrt{2\pi r}} f_{ij}(\theta). \tag{2.1}$$

Here, K^{far} is the assumed far field (remote) stress intensity factor, $r = r_{max}$ on the boundary, and $f_{ij}(\theta)$ are the cartesian components of angular distributions of stress for a mode I plane stress crack tip region, given as

$$f_{11}(\theta) = \cos\frac{\theta}{2}\left(1 - \sin\frac{\theta}{2}\sin\frac{3\theta}{2}\right)$$

$$f_{22}(\theta) = \cos\frac{\theta}{2}\left(1 + \sin\frac{\theta}{2}\sin\frac{3\theta}{2}\right)$$

Downloaded 03 May 2010 to 171.66.16.21. Redistribution subject to ASME license or copyright; see http://www.asme.org/terms/Terms_Use.cfm

$$f_{12}(\theta) = \sin\frac{\theta}{2}\cos\frac{\theta}{2}\cos\frac{3\theta}{2}$$

$$f_{33}(\theta) = f_{13}(\theta) = f_{23}(\theta) = 0. \qquad (2.2)$$

The material behavior of the plate is taken to be isotropic linear elastic. In our computations, Poisson's ratio of $\nu = 0$, .15, .30, .40, and .499 are chosen.

Two-dimensional "plane stress" solutions in elasticity implicitly assume that (*a*) out-of-plane stress components σ_{3i} vanish identically, and (*b*) the in-plane stress components $\sigma_{\alpha\beta}$ (Greek subscripts range from 1 to 2) are independent of position through the thickness, x_3. Within the context of a three-dimensional formulation, these assumptions are strictly consistent only if the hydrostatic stress, $\sigma_{\alpha\alpha}$, is at most a linear function of x_1 and x_2. As this is not the case for the crack tip field (2.2), it is evident that some degree of approximation is involved in applying the traction derived from them to represent that in a three-dimensional thin plate. However, an approximate three-dimensional stress field can be generated from a standard two-dimensional plane stress analysis by retaining assumption (*a*), but permitting the nonzero $\sigma_{\alpha\beta}$ to vary with x_3. Timoshenko and Goodier (1970) demonstrate that, for problems with symmetry about the plane $x_3 = 0$, a stress field of the latter kind can be obtained from an Airy-type stress function

$$\Phi(x_\gamma; x_3) = \Phi_0(x_\gamma) - \frac{1}{2}\frac{\nu}{1+\nu}(x_3)^2\nabla^2\Phi_0(x_\gamma). \qquad (2.3)$$

Here, $\Phi_0(x_\gamma)$ is the corresponding planar Airy stress function satisfying $\nabla^4\Phi_0 = 0$. Nonzero $\sigma_{\alpha\beta}(x_\gamma; x_3)$ are obtained from Φ in the "standard" way; e.g., $\sigma_{11} = \partial^2\Phi/\partial x_2^2$. They further argue that the thickness-varying part of the field thus generated, while in considerable error within distances from the boundary of order t, nonetheless decays rapidly to negligible values with increasing distance from the boundary. This approach has been carried out in the Appendix, where it is demonstrated that at $r = 5t$, the resulting traction differs from that obtained from (2.2) by less than 1 percent. Furthermore, our numerical solutions are in good agreement with the approximate stress field in the region $r/t > \sim 1$.

2.2 *J*-Integral in 3D Problems. The *J*-integral is a useful parameter in characterizing crack tip fields. It is equivalent to the energy release rate and relates to the amplitude of an assumed plane strain stress intensity factor field at material points very near the crack tip. A mathematical expression for the local energy release rate J in terms of near tip fields for three-dimensional problems is

$$J^{\text{local}}(s) = \lim_{\Gamma\to 0}\mu_k(s)\int_\Gamma\left(Wn_k - \sigma_{ij}n_j\frac{\partial u_i}{\partial x_k}\right)d\Gamma. \qquad (2.4)$$

Here the superscript "local" distinguishes J for a *pointwise* value along a three-dimensional crack front, and s is a parameter which represents the location of the crack tip on the crack front. Also W is the strain energy density, σ_{ij} and u_i are the cartesian components of stress and displacement, and n_i are the components of a unit vector normal to Γ and to the crack front tangent vector of s. A path Γ where the integral is evaluated surrounds the crack front at s and lies in the plane perpendicular to crack front. The unit vector $\mu_k(s)$ denotes the local direction of crack advance. The above integral defines a local energy release rate along any curvilinear crack front in three-dimensional space. In general, an equivalent path-independent integral does not exist in three-dimensional problems, though the shape of path Γ may be arbitrary as it collapses onto the crack tip.

It is apparent that from a discrete computational point of view, equation (2.4) is not suitable for evaluating $J^{\text{local}}(s)$, since accurate calculation of fields near the crack front is difficult. Alternate forms that are better suited for numerical calculations have been given by Parks (1977), Li et al. (1985) and Nakamura et al. (1986). In the present analysis, we employ the domain integral method, where the line integral form of J (2.4) is expressed in terms of a volume/domain integral. A detailed discussion of the formulation and implementation of the domain integral is given by Nakamura et al. We also note that nearly identical values are obtained using the virtual crack extension method (Parks, 1977; ABAQUS, 1987).

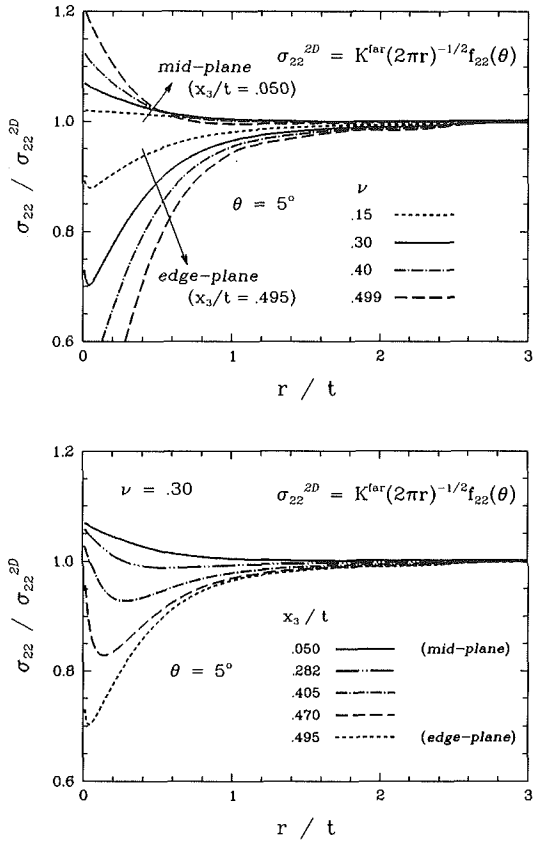

Fig 2 Opening stress ahead of crack front normalized by corresponding two-dimensional *K*-field solution; (*a*) for various Poisson's ratios at mid-plane and edge-plane, (*b*) for $\nu = .30$ at different depths. (Note zero suppression on ordinate axis.)

3 Computational Results

All the finite element results were obtained using the finite element code ABAQUS (1987); the calculations were carried out on an Alliant FX-8 computer. To alleviate the potential numerical difficulties associated with the nearly incompressible solid ($\nu = .499$), the **B**-bar method (Nagtegaal et al., 1974; Hughes, 1980) was implemented in the program for the formulation of the element stiffness matrices. In the case of the 8-node trilinear hexahedron element, the volumetic components of the strain/displacement (**B**) matrix are obtained by 1-point quadrature, while the deviatoric components are obtained by the $2\times2\times2$ quadrature rule. The former integration results in a uniform hydrostatic pressure throughout the element. As a safeguard against spurious pressure modes, we employed the modified **B**-bar method discussed in Nakamura et al. (1986). A small weighting factor of .0001 was chosen for our analyses. This method was employed for all the Poisson's ratios in order to obtain consistency in the computations.

3.1 Three-Dimensional Field of Thin Plate. The deformation field in a thin plate is nearly uniform through thickness, except in the region near the crack front. The transition to the

Downloaded 03 May 2010 to 171.66.16.21. Redistribution subject to ASME license or copyright; see http://www.asme.org/terms/Terms_Use.cfm

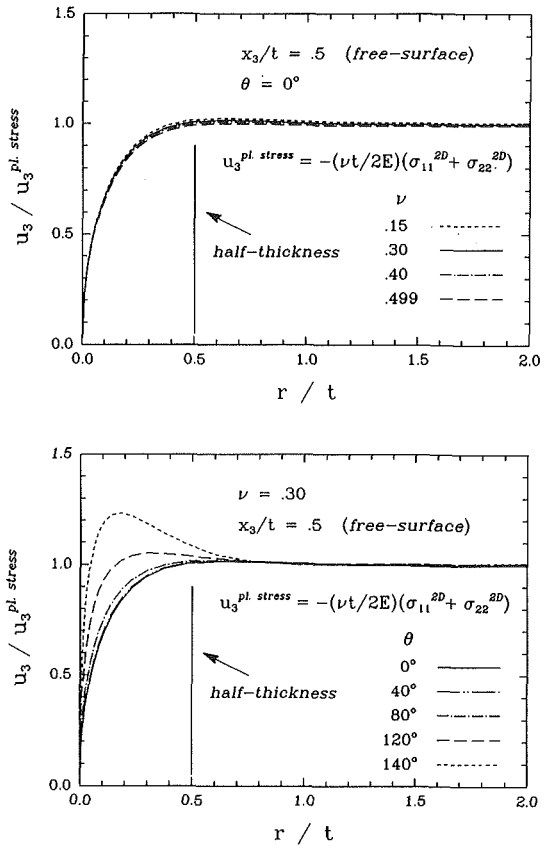

Fig .3 Out-of-plane displacement on the free surface normalized by the corresponding plane stress *K*-field solution; (*a*) for various Poisson's ratios ahead of crack, (*b*) for $\nu = .30$ at different angles. The position of half-thickness is shown.

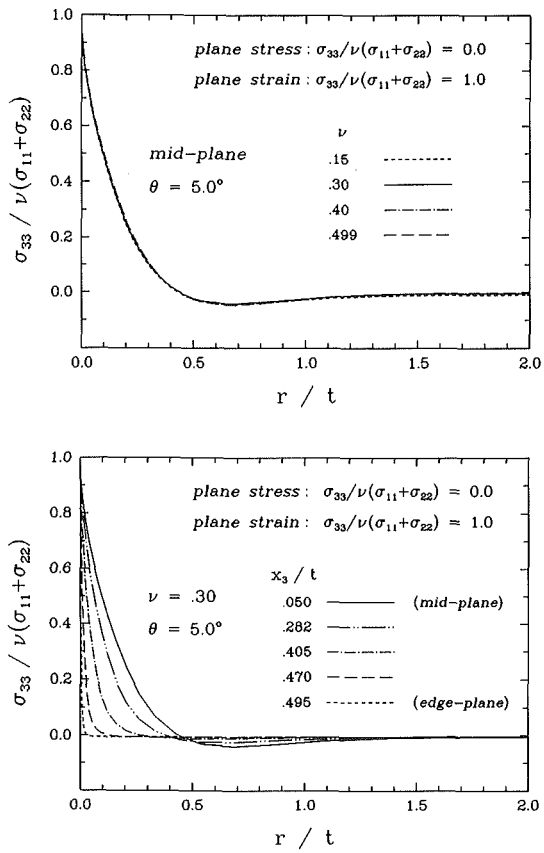

Fig. 4 The degree of plane strain ahead of crack front as a function of radial distance; (*a*) for various Poisson's ratios at mid-plane, (*b*) for $\nu = .30$ at different depths

three-dimensional state occurs within a radial distance from the crack front of order the plate thickness. The opening stress ahead of crack front ($\theta = 5°$) for each Poisson's ratio is plotted as a function of radial distance in Fig. 2. The stress is normalized by the corresponding two-dimensional near-tip value under the far field stress intensity factor, K^{far} (equation (2.1)). In this figure, *mid-plane* and *edge-plane* denote the element layer closest to the mid-plane or symmetry-plane ($x_3 = 0$) and the element layer adjoining the free surface ($x_3/t = 1/2$), respectively. The stress output is given at the centroid of each element. The curves in Fig. 2(*a*) show the computed stress to be nearly identical with the plane stress value for all Poisson's ratios at large r/t. The differences between complete and two-dimensional solutions are greater on the edge-plane than at mid-plane for each Poisson's ratio. The results for higher Poisson's ratios have a larger amplitude of variation through the thickness, and, within the region $r/t \geq 1$, the results agree well with the approximate solution given in the Appendix. The stress at different depths in the plate for $\nu = .30$ is plotted in Fig. 2(*b*). The thickness gradient is largest near the free surface at all radial distances, and in the region $r/t \geq 1$, the thickness variation is also in good agreement with the solution in the Appendix.

The out-of-plane displacement or lateral contraction on the free surface ahead of crack, normalized by the corresponding plane stress solution, is shown in Fig. 3(*a*). The normalized values for different Poisson's ratios are almost indistinguishable from one another. The results along rays at different angles from the crack plane are plotted in Fig. 3(*b*) for $\nu = .30$. The normalized surface displacement along various rays for other Poisson's ratios are also very close to the corresponding result for $\nu = .30$. Both figures show the out-of-plane displacement to match almost exactly with the plane stress solution for $r/t > 0.5$. Along any ray, the value of displacement decreases monotonically for decreasing r/t, but the limiting value at the crack tip is bounded. This value is approximately $u_3^{tip}/\xi = -2.3$, where $\xi = \sqrt{t/2\pi}(\nu/E)K^{far}$ (E is Young's modulus), for all the nonzero Poisson's ratios (within ± 1 percent).

In Fig. 4, the parameter $\sigma_{33}/\nu(\sigma_{11} + \sigma_{22})$ on the mid-plane at angle $\theta = 5°$ from the crack plane is plotted against radial distance from the crack tip. This parameter is called "degree of plane strain," since its value is one under a plane strain condition and is zero when a plane stress condition exists. Figure 4(*a*) shows this parameter to be zero for larger r/t where a plane stress condition exists and the field is two-dimensional. As r/t decreases, it dips slightly below zero between $0.5 < r/t < 1.5$, and, within $r/t < 0.5$, it increases monotonically to unity. This behavior is also nearly identical for all the nonzero Poisson's ratios we examined. Values at different depths for $\nu = .30$ are shown in Fig. 4(*b*). On the edge-plane, the degree of plane strain remains zero up to a point very close to the crack tip. The near tip results of this parameter are described in detail in the next section.

The behavior of the three-dimensional field was also investigated from other components of stress and displacement at various locations. All of these results confirm the characteristics of near crack from three-dimensional field described earlier—a gradual change from the far field plane stress condition near the radial distance of $1.5t$ from the crack tip, and significant through-thickness variation of field quantities within $r/t \leq 0.5$. These transition distances to the three-dimensional field appear to be independent of Poisson's ratio (except $\nu = 0$), and some variables show very weak dependence on Poisson's ratio when they are appropriately normalized (e.g., Figs. 3 & 4).

The *J*-integral along the crack front is obtained using the

Downloaded 03 May 2010 to 171.66.16.21. Redistribution subject to ASME license or copyright; see http://www.asme.org/terms/Terms_Use.cfm

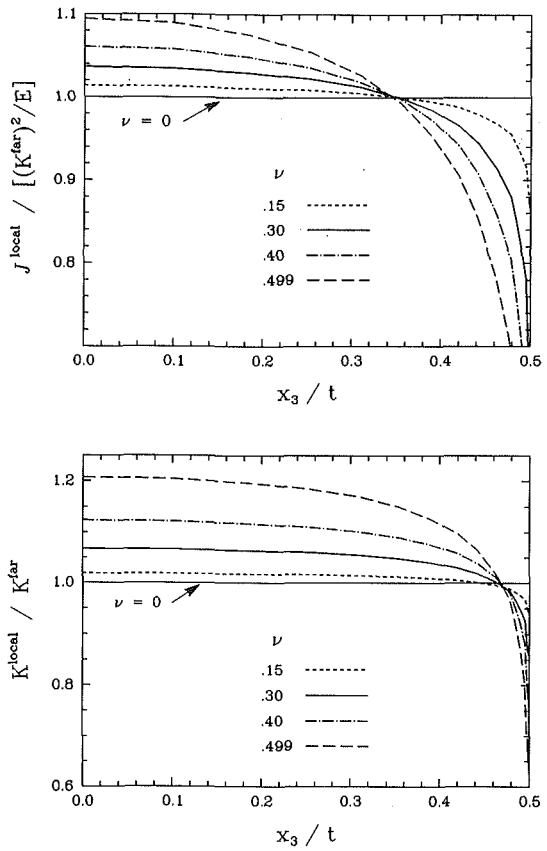

Fig. 5 (*a*) Normalized local J along the half-crack front for various Poisson's ratios, (*b*) normalized local K obtained via (3.1) along the half-crack front for various Poisson's ratios. (Note zero suppression of ordinate axis.)

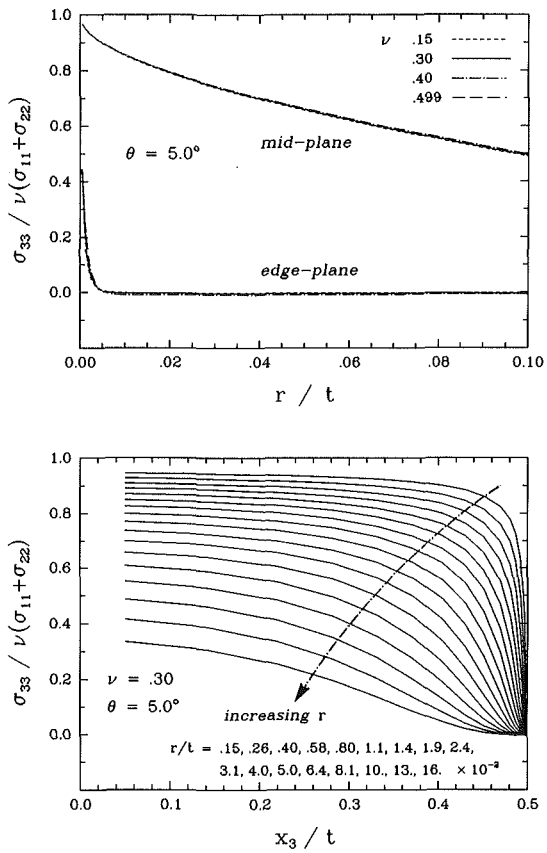

Fig. 6 The degree of plane strain very near crack front; (*a*) for various Poisson's ratios as a function of radial distance at mid-plane and edge-plane, (*b*) for $\nu = .30$ as a function of location on crack front for different radial distances

domain integral method. The values of local J from different domains are generally within 0.5 percent of the mean value at each nodal location along the crack front, except for the node on the free surface, where the domain dependence is somewhat larger. At each location, the mean J value over the domains is denoted as J^{local}. The variation of J^{local} along the crack front is shown in Fig. 5(*a*) for different Poisson's ratios. The local J is normalized by $(K^{\text{far}})^2/E$, which is also the value of the average J for the entire crack front. The figure shows the maximum and minimum values to be located at the points on the centerline and free surface, respectively, for all the nonzero Poisson's ratios. The result for $\nu = 0$ is identical to the two-dimensional solution with the same Poisson's ratio. The difference between the maximum and minimum of each curve increases for larger Poisson's ratios. All of the curves pass through (near) a point located at $x_3/t = .35$ and $J^{\text{local}}/[(K^{\text{far}})^2/E] = 1$. Figure 5(*b*) shows the variations through the thickness of local stress intensity factor. These values are obtained from the local J using the plane strain conversion equation

$$K^{\text{local}} = \sqrt{\frac{EJ^{\text{local}}}{(1-\nu^2)}} \,. \tag{3.1}$$

All the curves shown in Fig. 5(*b*) (except that for $\nu = 0$) cross one another near $x_3/t = .47$ and $K^{\text{local}}/K^{\text{far}} = .99$. The behavior of local stress intensity factor close to the intersection of the crack front and the free surface is discussed in Section 3.3.

3.2 Near Tip Plane Strain Condition. If the out-of-plane strain components are bounded at the crack front, asymptotically a plane strain condition should prevail as the crack front is approached. The degree of plane strain very near the crack front is plotted in Fig. 6. These results are obtained from the finer mesh described in Section 2.1. The parameter approaches unity on the mid-plane layer of elements in an almost identical manner for all the nonzero Poisson's ratios (Fig. 6(*a*)). However, at centroids of elements in the edge-plane layer, it remains zero except very near the crack tip. If an accurate value were obtained *on the free surface*, this parameter would be identically zero, since the traction free condition must exist there. For the case of $\nu = .30$, the through-thickness variation in the degree of plane strain is shown at various radial distances is shown in Fig. 6(*b*). At the radial distance closest to the crack front ($r/t = .15 \times 10^{-2}$), the parameter is nearly uniform through-thickness except between $.47 < x_3/t < 1/2$, where its value drops rapidly to zero.

The complete stress field very near the crack tip is examined in Fig. 7(*a*). The components of computed stress are nomalized by the local stress intensity factor obtained from (3.1) on the mid-plane location and are plotted over the angular range $0 < \theta < \pi$ for $\nu = .30$. The angular distribution of *plane strain* K-field solution (same as $f_{ij}(\theta)$ in (2.2) except for $f_{33} = \nu(f_{11} + f_{22})$) is shown with dashed lines. The agreement of computed stress and f_{ij} for each component is striking. These results confirm that the near tip field of a three-dimensional crack front can be characterized by a plane strain square root singular K-field with its amplitude given by K^{local}. For larger r/t, the agreement of the two solutions deteriorates, as can be seen from Fig. 7(*b*), where mid-plane σ_{33} is plotted for different r/t values. With increasing r/t, there is a monotonic decrease in normalized stress from the asymptotic value $f_{33}(\theta)$ over the entire angular range, $0 < \theta < \pi$. We note that normalized in-plane components of stress differ from the corresponding $f_{ij}(\theta)$ by only as much as $K^{\text{local}}/K^{\text{far}}$ (in ratio) at very large radial distance ($r/t > 1.5$), since an assumed plane

Downloaded 03 May 2010 to 171.66.16.21. Redistribution subject to ASME license or copyright; see http://www.asme.org/terms/Terms_Use.cfm

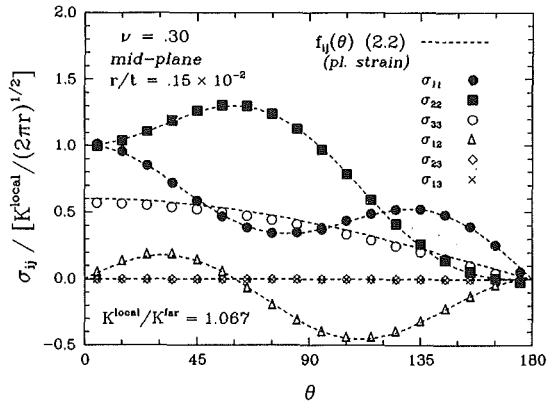

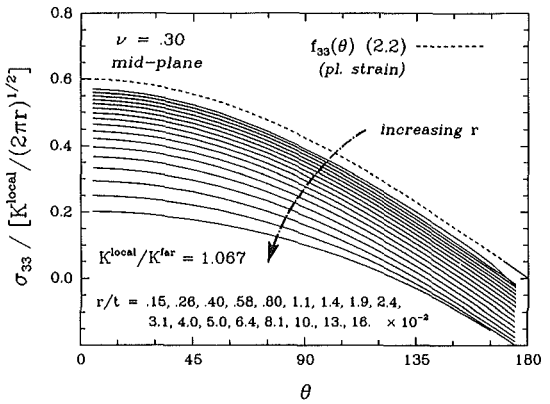

Fig. 7 *(a)* **Angular distributions of stress components very near crack front normalized by K^{local} (Fig. 5(*b*)) at mid-plane, (*b*) normalized angular distribution of σ_{33} at mid-plane for different radial distances. In both figures, corresponding plane strain f_{ij} (2.2) are shown with dashed lines for comparison.**

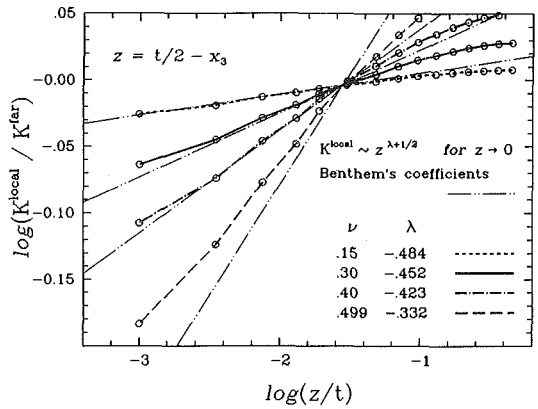

Fig. 8 Normalized K^{local} for various Poisson's ratios plotted against distance from the intersection in a log-log scale. Small circles represent the mid-location of element layers along crack front. Benthem's singularity exponents are shown in inset. Also slopes of straight lines correspond to the corner singularity field solutions.

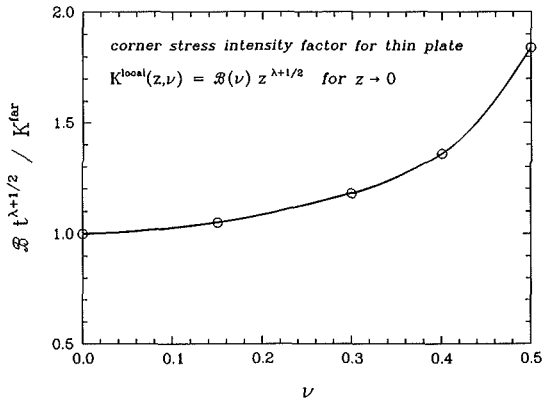

Fig. 9 The corner stress intensity factor for a thin plate, normalized with K^{far} and shown as a function of Poisson's ratio

stress K-field holds there. We have also compared the near-tip stresses with the corresponding plane strain K-field solutions at the same radial distance but different x_3-locations. The results are almost identical to that of mid-plane Fig. 7(*a*)) except at $x_3/t > .45$, where the agreement of stress components, especially σ_{33}, deteriorates.

3.3 Corner Singularity Field. At a point sufficiently close to the normal intersection of crack front and free surface, the deformation field should be characterized by the corner singularity field of a quarter infinite crack plane in a half space. According to Benthem, the stress tensor in the corner singularity field may be expressed in a separable form (Benthem, 1975, 1977) as

$$\sigma_{ij} \propto \rho^{\lambda} g_{ij}(\lambda;\theta,\phi), \tag{3.2}$$

where g_{ij} is a dimensionless function, and spherical coordinates centered at the vertex are

$$\rho = \sqrt{r^2+z^2}, \quad \phi = \tan^{-1}\left(\frac{r}{z}\right), \quad z = \frac{t}{2} - x_3. \tag{3.3}$$

This asymptotic form was also obtained by Bazant and Estenssoro (1979) and Burton et al. (1984).

The eigenvalue λ depends on the Poisson's ratio, and the leading root ranges from $-0.5 \le \lambda \le -.332$ for $0 \le \nu \le 1/2$, respectivley. Suppose the local stress intensity factor along the crack front is defined as

$$K^{local}(z) = \lim_{r \to 0} (\sigma_{22}(r,\theta=0,z) \cdot \sqrt{2\pi r}). \tag{3.4}$$

Then, with the aid of asymptotic form (3.2), Benthem argued that for small z,

$$K^{local}(z) = Bz^{\lambda+1/2}. \tag{3.5}$$

Here B is a constant which represents the intensity of corner singularity field (3.2) and has the dimension of $[\sigma \cdot l^{-\lambda}]$ (σ: stress, l: length dimensions). We may call B the *corner stress intensity factor*, and its value depends on the geometry and the load acting on the crack. A replot of local stress intensity factor versus the distance away from the intersection, z, is shown in Fig. 8. In order to determine the coefficient of power, $\lambda + 1/2$, they are shown in a log-log scale. The small circles in the figure indicate the mid-locations of element layers along the crack front, and the slopes of curves should correspond to the coefficients. As earlier observed in Fig. 5(*b*), all curves appear to intersect the single point $z/t \simeq .03$ and $K^{local}/K^{far} \simeq .99$, and they are nearly straight for $z/t < .03$. Also shown in the figure are straight lines which pass through this point and have slopes of $\lambda + 1/2$ for the respective Poisson's ratios. The values of λ given by Benthem are depicted in the inset. The results for $\nu \le .40$ agree very well with Benthem's exponents for $z/t \le .03$. This implies that the corner singularity field exists within the spherical radius of $\rho/t \simeq .03$. For $\nu = .499$, the agreement is not as good, but this may be attributed to the numerical difficulty associated with the nearly incompressible solid. We also note that the value of local K at the element layer adjoining the free surface (leftmost circle in each curve) is somewhat in error, since obtaining an accurate value of J^{local} in this region is rather difficult.

From the values of computed local stress intensity factor very near the intersection ($z/t < .03$), we can determine the amplitude of corner stress intensity factor for a thin plate. The normalized values of B are plotted as a function of Poisson's ratio in Fig. 9. These values are universal for *any* sufficiently

Downloaded 03 May 2010 to 171.66.16.21. Redistribution subject to ASME license or copyright; see http://www.asme.org/terms/Terms_Use.cfm

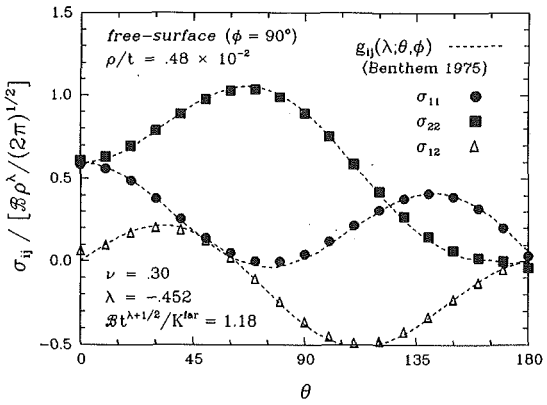

Fig. 10 Angular distributions of nonzero stress components normalized by B very near the intersection on free surface for $\nu = .30$. For comparison, corresponding g_{ij}(Benthem, 1975) are shown with dashed lines.

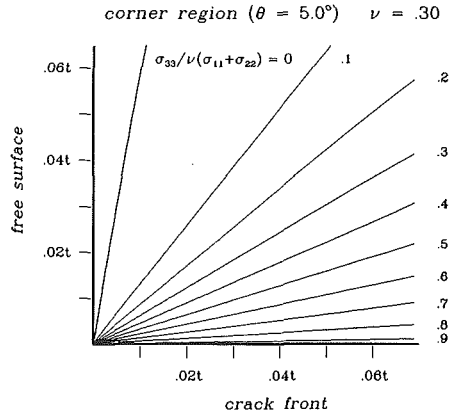

Fig. 11 Contours of the degree of plane strain in the near corner region. Distances away from the intersection are indicated along crack front and free surface.

thin elastic plate under Mode I loading condition. The figure shows monotonically increasing B for larger ν. From (3.2) and (3.5), one may express the stress tensor for the corner singularity field as

$$\sigma_{ij} = \frac{B}{\sqrt{2\pi}} \rho^{\lambda} g_{ij}(\lambda;\theta,\phi). \tag{3.6}$$

A similar notation for the stress near the corner was recently given by Riedel (1987) (his form does not include the factor $1/\sqrt{2\pi}$). From (2.1) and (3.5)–(3.6), the dimensionless function g_{ij} must behave as

$$f_{ij}(\theta) = \lim_{\phi \to 0} \sqrt{\phi} g_{ij}(\lambda;\theta,\phi), \tag{3.7}$$

where the in-plane components of $f_{ij}(\theta)$ are given in (2.2) and the asymptotic plane strain condition is $f_{33} = \nu(f_{11} + f_{22})$.

The corner singularity field is also evident in Fig. 10, where angular distributions of nonzero stresses on the free surface are plotted. The stresses are extrapolated to the free surface and normalized with B for a thin plate with $\nu = .30$. These values are compared with the angular distributions of corner singularity stress, g_{ij}, obtained by Benthem (1985) (dashed lines). The figure shows excellent agreement at the spherical radius of $\rho/t = .48 \times 10^{-2}$. As expected, the agreement deteriorates at larger ρ/t locations. Figure 11 shows contours of the degree of plane strain near the corner on the $\theta = 5°$ plane. This plot is similar to the one shown by Cruse (1970) except considerably more detail can be observed here. In the vicinity of the corner, the contour lines apppear to be straight rays emanating from the intersection of the crack front and free surface (constant ϕ for each ray). This behavior of contours is in agreement with the corner singularity field (3.6), since the degree of plane strain can be expressed as a function of only θ and ϕ.

4 Discussion

Our analysis shows strong three-dimensional effects up to a radial distance of approximately half the plate thickness from the crack front and somewhat weaker variations of field quantities between $.5 < r/t < 1.5$. Since the dominance of the K-field in a two-dimensional plate is typically observed within a radial distance from the tip of ~10 percent of the smallest characteristic in-plane length (such as crack length, uncracked ligament, or distance to a point of load application), this result suggests that the thickness of three-dimensional plate may be no more than 1/5, or more strictly, 1/15 of the smallest in-plane dimensions in order that the plate may be a *thin plate*. The present study also shows the size of the three-dimensional field region to be essentially independent of the Poisson's ratio. In addition, when some variables are appropriately normalized (e.g., surface out-of-plane displacment, degree of plane strain), the values for different Poisson's ratios (except for $\nu = 0$), at the same location are nearly identical, showing at most only very weak dependence on ν. (We have also performed calculations with $\nu = .01$, and the computed results for normalized surface displacement and degree of plane strain are essentially identical with those for $\nu \geq .15$.)

Curiously, we have observed that, for all the Poisson's ratios, the normalized local J in a thin plate attains the value of unity near the crack front location, $x_3/t = .35$. Similar behavior is also shown for local K, which passes through (near) a point, $K^{local}/K^{far} \simeq .99$ and $x_3/t \simeq .47$, for all the nonzero Poisson's ratios we tested.

In the region very near the crack front, the stress field can be characterized by a *plane strain* stress intensity factor solution with K^{local} as the amplitude. The degree of plane strain becomes unity only in the limit of $r \to 0$, since ϵ_{33} remains nonzero at the crack front. If $\sigma_{33}/\nu(\sigma_{11} + \sigma_{22}) > 0.9$ is used as the criterion for the plane strain condition, the boundary of the plane strain region lies near a radial distance of $0.005t$ from the front at the mid-plane (Fig. 6). This value is nearly uniform throughout the thickness except between $.47 < x_3/t < 1/2$, where the contour of $\sigma_{33}/\nu(\sigma_{11} + \sigma_{22}) = 0.9$ heads toward the intersection ($x_3/t = 1/2$, $r/t = 0$) along a straight ray at an angle from the crack front of $\phi \simeq 1°$, as shown in Fig. 11.

The computed values of stress near the intersection of the crack front and free surface closely follow Benthem's corner singularity field for a quarter infinite crack in a half space. The asymptotic behavior of stress near the intersection is expressed explicitly as

$$\sigma_{ij} = \frac{B}{\sqrt{2\pi}} \rho^{\lambda} g_{ij}(\lambda;\theta,\phi) \quad \text{as} \quad \rho/t \to 0. \tag{4.1}$$

Here λ is the singularity exponent, which depends on the Poisson's ratio, and B is the corner stress intensity factor representing the magnitude of singularity field. The universal values of B in thin elastic plates of various Poisson's ratios are shown in Fig. 9. The size of the corner singularity field in a thin plate appears to be about 3 percent of the thickness in spherical radius and depends very little on the Poisson's ratio. The same order of magnitude is expected to hold for somewhat thicker plates.

The above equation also suggests that the local stress intensity factor within this domain behaves as $K^{local} = Bz^{\lambda+1/2}$, implying that K vanishes on the free surface. This does not mean that the stress is finite on the free surface, but means only that its singularity is weaker than $1/\sqrt{r}$. We emphasize that K^{local}

Downloaded 03 May 2010 to 171.66.16.21. Redistribution subject to ASME license or copyright; see http://www.asme.org/terms/Terms_Use.cfm

drops to zero within a thin boundary layer region, whose width is less than 3 percent of thickness, for any nonzero Poisson's ratio (Fig. 5(*b*)). We also note that preliminary results for three-dimensional thin plates under far field mode II loading condition show an *increasing* local stress intensity factor as the intersection is approached, and K^{local} appears to be infinite on the free surface (Nakamura and Parks, 1988). This behavior is consistent with analyses by Bazant and Estenssoro (1979) and Benthem (1980) that show stronger singularity near the vertex ($\lambda < -.5$) under antisymmetry conditions. As Bazant and Estenssoro have emphasized, the corner singularity also depends on the angle made by the tangent to the crack front and the surface normal, and for each Poisson's ratio, an angle can be determined such that the corner singularity exponent is $-1/2$. In order to avoid the parametric complications of additional length scales which would arise in a study of nonnormal intersection in a finite thickness plate, we have ignored this feature. However, further study of such intersections may be warranted.

We tentatively generalize these results to other crack configurations possessing a crack front normally intersecting a free surface. For example, Raju and Newman (1979) have presented numerical and approximate closed form results for the variation of the local K along a part-through semi-elliptical crack front in a finite thickness ($=t$) plate. For each projected surface length, $2c$, and maximum penetration depth, a, they characterize the K distribution in terms of its value at deepest penetration, and a value "at the surface." The grids used by Raju and Newman and by other investigators were insufficiently refined to capture near corner effects, and the actual stress intensity factor distribution presumably drops rapidly from reported "surface" values to zero within a boundary layer. A length scale characterizing a semi-elliptical crack front at its intersection with the free surface is the local crack radius of curvature, given by $\rho_{\text{crack front}} = a^2/c$. We expect the corner singularity to dominate only over a small fraction of this length scale, say, $.03\ \rho_{\text{crack front}} = (a/t) \cdot (a/c) \cdot t/33$.

We believe that our computations have accurately quantified several "universal" three-dimensional aspects of near crack front linear elastic fracture mechanics in thin plates. For materials such as metals which exhibit at least some crack tip ductility, the direct interpretation of these results must, in general, be tempered by consideration of crack front and corner plasticity, resulting zones of dominant plane strain, local J and dominant HRR fields (Hutchinson, 1968; Rice and Rosengren, 1969). Such studies are underway and will be reported shortly.

Acknowledgments

The authors gratefully acknowledge the support of D.O.E. through the joint project with Idaho National Engineering Laboratories under Grant DE-FR02-85ER13331. Computations were performed on an Alliant FX-8 computer obtained under DARPA Grant # N00014-86-K-0768 and on a Data General MV10000 computer denoted to M.I.T. by the Data Gerenal Corporation. The ABAQUS finite element code was made available under academic license from Hibbitt, Karlsson, and Sorensen, Inc., Providence, Rhode Island.

References

ABAQUS, 1987, Version 4.6, Hibbitt, Karlsson and Sorensen, Inc., Providence, R.I.

Bazant, Z. P., and Estenssoro, L. F., 1979, "Surface Singularity and Crack Propagation," *International Journal of Solids and Structures*, Vol. 15, pp. 405-426.

Benthem, J. P., 1975, "Three-Dimensional State of Stress at the Vertex of a Quarter-Infinite Crack in a Half-Space," Report WTHD Nr. 74, Department of Mechanical Engineering, Delft University of Technology.

Benthem, J. P., 1977, "State of Stress at the Vertex of a Quarter-Infinite Crack in a Half-Space," *International Journal of Solids and Structures*, Vol. 13, pp. 479-492.

Benthem, J. P., 1980, "The Quarter-Infinite Crack in a Half Space; Alternative and Additional Solutions," *International Journal of Solids and Structures*, Vol. 16, pp. 119-130.

Burton, W. S., Sinclair, G. B., Solecki, J. S., and Swedlow, J. L., 1984, "On the Implications for LEFM of the Three-Dimensional Aspects in some Crack/Surface Intersection Problems," *International Journal of Fracture*, Vol. 25, pp. 3-32.

Cruse, T. A., 1970, Lateral Constraint in a Cracked, Three Dimensional Elastic Body," *International Journal of Fracture*, Vol. 6, pp. 326-328.

Cruse, T. A., and Vanburen, W., 1971, "Three-Dimensional Elastic Stress Analysis of a Fracture Specimen with an Edge Crack" *International Journal of Fracture*, Vol. 7, pp. 1-15.

Hughes, T. J. R., 1980, "Generalization of Selective Integration Procedures to Anisotropic and Nonlinear Media," *International Journal for Numerical Methods in Engineering*, Vol. 16, pp. 1413-1418.

Hutchinson, J. W., 1968, "Singular Behavior at the End of a Tensile Crack in a Hardening Material," *Journal of the Mechanics and Physics of Solids*, Vol. 16, pp. 13-31.

Levy, N., Marcal, P. V., and Rice, J. R., 1971, "Progress in Three-Dimensional Elastic-Plastic Stress Analysis for Fracture Mechanics," *Nuclear Engineering and Design*, Vol. 17, pp. 64-75.

Li, F. Z., Shih, C. F., and Needleman, A., 1985, "A Comparison of Methods for Calculating Energy Release Rate," *Engineering Fracture Mechanics*, Vol. 21, pp. 405-421.

Nagtegaal, J. C., Parks, D. M., and Rice, J. R., 1974, "On Numerically Accurate Finite Element Solutions in the Fully Plastic Range," *Computer Methods in Applied Mechanics and Engineering*, Vol. 4, pp. 153-178.

Nakamura, T. and Parks, D. M., 1988, "Anti-Symmetrical 3D Stress Field Near the Crack Front of a Thin Elastic Plate," submitted to *International Journal of Solids and Structures*.

Nakamura, T., Shih, C. F., and Freund, L. B., 1986, "Three-Dimensional Transient Analysis of a Dynamically Loaded Three-Point-Bend Ductile Fracture Specimen," Brown University Report ONR0365/3, to appear in ASTM STP on Nonlinear Fracture Mechanics.

Parks, D. M., 1977, "The Virtual Crack Extension Method for Nonlinear Material Behavior," *Computer Methods in Applied Mechanics and Engineering*, Vol. 12, pp. 353-364.

Parsons, I. D., Hall, J. F., and Rosakis, A. J., 1986, "A Finite Element Investigation of the Elastostatic State Near a Three Dimensional Edge Crack," SM Report 86-29, California Institute of Technology.

Raju, I. S., and Newman, J. C., Jr., 1979, "Stress-Intensity Factors for a Wide Variety of Semi-Elliptical Surface Cracks in Finite Thickness Plates," *Engineering Fracture Mechanics*, Vol. 11, pp. 817-829.

Rice, J. R., and Rosengren, G. F., 1968, "Plane Strain Deformation Near a Crack Tip in a Power-Law Hardening Material," *Journal of the Mechanics and Physics of Solids*, Vol. 16, pp. 1-12.

Riedel, H., 1987, *Fracture at High Temperature*, Springer-Verlag, Berlin, Chap. 22.

Rosakis, A., and Ravi-Chandar, K., 1986, "On the Crack-Tip Stress State: an Experimental Evaluation of Three-Dimensional Effects," *International Journal of Solids and Structures*, Vol. 22, pp. 121-134.

Timoshenko, S., and Goodier, J. N., 1970, *Theory of Elasticity*, McGraw-Hill, New York, Sec. 98.

Yang, W., and Freund, L. B., 1985, "Transverse Shear Effects For Through-Cracks in an Elastic Plate," *International Journal of Solids and Structures*, Vol. 21, pp. 977-994.

APPENDIX

The Airy stress function corresponding to the far field Mode I crack tip field is

$$\Phi(r,\theta) = \frac{K^{\text{far}}}{\sqrt{2\pi}}\, r^{3/2}\left(\cos\frac{\theta}{2} + \frac{1}{3}\cos\frac{3\theta}{2}\right), \qquad (A.1)$$

where in-plane polar coordinates are r and θ. The in-plane stress components derivable from this stress function are most conveniently expressed in polar coordinates:

$$\sigma_{\theta\theta} = \frac{\partial^2\Phi}{\partial r^2}$$

$$\sigma_{r\theta} = -\frac{\partial}{\partial r}\left(\frac{1}{r}\frac{\partial\Phi}{\partial\theta}\right) \qquad (A.2)$$

$$\sigma_{rr} = \frac{1}{r}\frac{\partial\Phi}{\partial r} + \frac{1}{r^2}\frac{\partial^2\Phi}{\partial\theta^2}\,.$$

From this field, we obtain

Downloaded 03 May 2010 to 171.66.16.21. Redistribution subject to ASME license or copyright; see http://www.asme.org/terms/Terms_Use.cfm

$$\nabla^2\Phi = \sigma_{rr} + \sigma_{\theta\theta} = \frac{2K^{\text{far}}}{\sqrt{2\pi r}} \cos\frac{\theta}{2} . \qquad (A.3)$$

When (A.1) and A.3) are inserted into (2.3), and the operations indicated in (A.2) are performed, the resulting approximate three-dimensional plane stress fields are

$$\sigma_{\theta\theta}(r,\theta,x_3) = \frac{K^{\text{far}}}{\sqrt{2\pi r}} \frac{1}{4}\left(\left[3 - \frac{3\nu}{1+\nu}\left(\frac{x_3}{r}\right)^2\right]\cos\frac{\theta}{2} + \cos\frac{3\theta}{2}\right)$$

$$\sigma_{r\theta}(r,\theta,x_3) = \frac{K^{\text{far}}}{\sqrt{2\pi r}} \frac{1}{4}\left(\left[1 - \frac{3\nu}{1+\nu}\left(\frac{x_3}{r}\right)^2\right]\sin\frac{\theta}{2} + \sin\frac{3\theta}{2}\right)$$

$$\sigma_{rr}(r,\theta,x_3) = \frac{K^{\text{far}}}{\sqrt{2\pi r}} \frac{1}{4}\left(\left[5 + \frac{3\nu}{1+\nu}\left(\frac{x_3}{r}\right)^2\right]\cos\frac{\theta}{2} - \cos\frac{3\theta}{2}\right) \qquad (A.4)$$

Several observations may be made regarding the approximate fields (A.4). First, it is clear that they are inapplicable as $r \to 0$, since the leading terms are singular as $r^{-5/2}$. On the other hand, it is also clear that the additional terms diminish rapidly with increasing r. The maximum deviation from the uniform plane stress solutions occurs on the free surfaces, $|x_3| = t/2$, and further, the maximum difference also occurs for incompressibility ($\nu = 1/2$), in which case the common term, $3\nu/(1+\nu)$, equals one. We see, then, that at $r = 5t$, where the boundary conditions were applied, the maximum possible magnitude of the thickness varying term has a relative value of order .01 compared to unity and, in fact, the actual values are generally even less affected. Thus this field lends support to the contention that the traction obtained from (2.2) is an acceptably accurate representation of the actual traction transmitted to the crack tip region in a thin plate.

A special case of (A.4) is the normal stress across the plane $\theta = 0$. For this orientation, $\sigma_{\theta\theta} = \sigma_{22}$, and the two-dimensional result is $\sigma_{22}^{2D} = K^{\text{far}}/\sqrt{2\pi r}$. Thus

$$\frac{\sigma_{22}(r,0,x_3)}{\sigma_{22}^{2D}} = 1 - \frac{3\nu}{4(1+\nu)}\left(\frac{x_3}{r}\right)^2 . \qquad (A.5)$$

Equation (A.5) is in good quantitative agreement with the numerical results shown in Figs. 2(*a*) and 2(*b*) in the region $r/t \geq \sim 1$. The trends with respect to Poisson's ratio and with respect to position through the thickness are both followed. These and other quantitative comparisons lead us to conclude that the approximate three-dimensional stress fields given by the closed form expressions (A.4) very accurately represent the complete fields of the (near) crack tip vicinity in a thin plate.

Downloaded 03 May 2010 to 171.66.16.21. Redistribution subject to ASME license or copyright; see http://www.asme.org/terms/Terms_Use.cfm

Small Scale Contact Conditions for the Linear-Elastic Interface Crack

Peter M. Anderson
Department of Materials Science and Engineering,
The Ohio State University,
Columbus, Ohio 43210-1179

Conditions are discussed for which the contact zone at the tip of a two-dimensional interface crack between anisotropic elastic materials is small. For such "small scale contact" conditions combined with small scale yielding conditions, a stress concentration vector uniquely characterizes *the near tip field, and may be used as a crack growth parameter. Representative calculations for an interface crack on a representative Cu grain boundary show small contact conditions to prevail, except possibly under large shearing loads.*

Introduction

It is well known that linear-elastic analysis of the interface crack predicts in general rapid oscillation of stresses and strains in a region near the crack tip. A physically unreasonable consequence of such oscillations is that interpenetration of the crack surfaces is predicted near the crack tip. Solutions involving sliding near-tip contact zones, analyzed within the linear theory, have been devised by Comninou (1977, 1978), and extended for the case of tensile loading by Gautesen and Dundurs (1987). Knowles and Sternberg (1983) note that these oscillations may sometimes be a feature of a linearized analysis, as their use of nonlinear-elastic theory for an interface crack between two semi-infinite Neo-Hookean sheets reveals no such region.

The size of the contact zone is a function of the elastic material constants, the characteristic length scale L in the problem (i.e., crack length, specimen dimension, location of applied tractions, etc.), and the type of applied load. The contact zone, as with the nonlinear region at the crack tip, is frequently seen to be very much smaller than L. For such conditions, Rice (1987) notes that the actual field in the small scale nonlinear or contact zone is uniquely *characterized* by a (complex) elastic stress intensity factor, even though the elastic solution is not correct in that zone. Our particular interest is to formulate conditions for which the small scale contact approach is justified, for the two-dimensional problem of an interface crack bounded by arbitrarily oriented anisotropic materials. The primary application is to grain boundary fracture in polycrystalline materials, and the interface crack between isotropic materials is included as a special case.

The analysis of interface cracks has been treated by several investigators, the first among them appearing to have been Williams (1959), Cherepanov (1962), and Erdogan (1963), who found the stresses near an interface crack in plane strain between two isotropic elastic bodies. This problem was further addressed by England (1965), Erdogan (1965), Rice and Sih (1965), and Malyshev and Salganik (1965). Extensions to anisotropic elasticity have been made by Gotoh (1967), Clements (1971), Willis (1971), and Wang and Choi (1983), the last of whom extend the idea of a sliding near-tip contact zone to the anisotropic case, and propose an approximate model which removes the oscillatory crack tip behavior. In particular, we use the results of an elegant treatment by Willis (1971) of the two-dimensional interface crack bounded by two generally anisotropic half spaces. Included in this treatment is the elastic energy release rate for extension of the crack along the interface.

A related feature to this oscillatory behavior is that the opening and relative in-plane and out-of-plane displacements of the crack surfaces are coupled, in general, and may not be separated into counterparts for the classical Mode I, Mode II, and Mode III crack. There are special cases in this mixed boundary value problem where this "coupling" does not exist. For these cases, the size of the oscillatory region shrinks to zero, and one recovers smooth crack tip stress and strain fields with the characteristic inverse square root dependence on radial distance ρ from the crack tip. One is then able to define the stress intensity factors K_i in the traditional manner,

$$K_i = \lim_{\rho \to 0} [\sqrt{2\pi\rho}\ \sigma_{2i}(\rho, \theta = 0)] \tag{1}$$

where $\theta = 0$ denotes the $x_1 - x_3$ plane ahead of the crack.

In addition to the plane strain problem for which the materials are incompressible (Knowles and Sternberg, 1983), we find the two-dimensional interface crack geometry shown in Fig. 1 for which (*i*) the adjoining materials are the same, and (*ii*) the $x_1 - x_2$ plane is a crystallographic mirror plane, and (*iii*) the materials are oriented relative to one another by a rotation about the x_3-axis, is another case where a singularity of $\rho^{-1/2}$ type, without oscillation, is obtained. These restrictions satisfy the conditions of the general proof by Qu and Bassini (1988) that non-oscillatory behavior occurs for tilt boundaries in which (*i*) the x_3-axis is the tilt axis, and (*ii*) the in-plane and out-of-plane deformations are uncoupled. In such cases, one may then proceed by calculating the crack-tip stresses σ_{ij} in a form given by

Contributed by the Applied Mechanics Division of THE AMERICAN SOCIETY OF MECHANICAL ENGINEERS for presentation at the ASCE/ASME Applied Mechanics, Biomechanics, and Fluids Engineering Conference, San Diego, CA, July 9 to 12, 1989.

Discussion on this paper should be addressed to the Editorial Department, ASME, United Engineering Center, 345 East 47th Street, New York, N.Y. 10017, and will be accepted until two months after final publication of the paper itself in the JOURNAL OF APPLIED MECHANICS. Manuscript received by ASME Applied Mechanics Division, August 17, 1987; final revision, May 26, 1988.

Paper No. 89-APM-16.

Copyright © 1988 by ASME
Downloaded 03 May 2010 to 171.66.16.21. Redistribution subject to ASME license or copyright; see http://www.asme.org/terms/Terms_Use.cfm

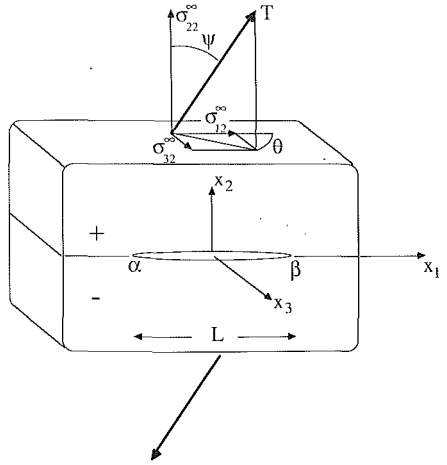

Fig. 1 Geometry for the two-dimensional interface crack of length L, situated on $x_2 = 0$, $\alpha < x_1 < \beta$, with a remote loading described by $\sigma^{\infty}_{12} = T \sin\psi \cos\theta$; $\sigma^{\infty}_{22} = T \cos\psi$; $\sigma^{\infty}_{32} = T \sin\psi \sin\theta$

$$\sigma_{ij} = K_\alpha F^{\alpha}_{ij}(\theta)/\sqrt{\rho} \tag{2}$$

where α sums over the crack loading modes. Further, the elastic energy release rate may be calculated as

$$G = (8\pi)^{-1}\mathbf{K}^T\mathbf{A}^{-1}\mathbf{K} \tag{3}$$

where $\mathbf{A}^{-1}$ is the inverse of $\mathbf{A}$, which appears in the prelogarithmic energy factor $\mathbf{b}^T\mathbf{A}\,\mathbf{b}$ for a straight dislocation line of Burgers vector, $\mathbf{b}$, lying on the interface in a direction parallel to the crack front.

Calculation of $\mathbf{A}$ is straightforward and has been described in the literature (e.g., see Clements, 1971; Willis, 1971; Barnett and Loethe, 1974; Bacon et al., 1979). In general, $\mathbf{A}$ is a 3×3 Hermitian matrix so that $\mathbf{A}^T = \bar{\mathbf{A}}$. However, for the special interface crack geometry with non-oscillatory behavior discussed above, Qu and Bassani (1988) show that $\mathbf{A}$ degenerates to a real matrix in which the components A_{13}, A_{31}, A_{23}, A_{32} referred to the crack tip coordinate system in Fig. 1 all vanish. Thus, the in-plane and out-of-plane loadings are decoupled, and using (3), G takes the form of a quadratic in K_i, in which K_1K_2 is the only cross product term.

Development

We proceed by using the two-dimensional infinite body solution given by Willis (1971). Here, the two-dimensional interface crack is represented by a continuous distribution of dislocation density, $d\mathbf{b}/dx_1$, along the crack, located on the plane $x_2 = 0$ and lying between $x_1 = \alpha$ and $x_1 = \beta$ as shown in Fig. 1. Loads on the cracks are applied by the tractions $\mathbf{t}(x_1)$ and $-\mathbf{t}(x_1)$ on the lower and upper crack surfaces, respectively. In this development, a solution is obtained for the positive definite, Hermitian matrix $\mathbf{A}$ that appears in the expression $\mathbf{b}^T\mathbf{A}\,\mathbf{b}$ for the prelogarithmic energy term of the two-dimensional interface dislocation. The crack problem is expressed in terms of the Hilbert problem, using $\mathbf{A}$ as defined above, and denoting $\mathbf{b}(x_1) = \mathbf{u}(x_1, 0^+) - \mathbf{u}(x_1, 0^-)$ as the relative displacement of the crack tip surfaces.

For distances r very near the crack tip at $x_1 = \beta$,

$$\mathbf{b} \sim \left(\frac{2}{\pi}\right)^{1/2} r^{1/2} \sum_{\xi=0,+,-} \left\{ \bar{\mathbf{v}}_\xi \frac{\cosh(\pi\lambda_\xi)}{1-2i\lambda_\xi} r^{-i\lambda_\xi} k_\xi \right\}. \tag{4}$$

The loading and crack geometry (i.e., dependence on the length scale L in the problem) is contained in the "stress concentration vector," defined here as

$$k_\xi = -e^{-\pi\lambda_\xi} L^{-(1/2-i\lambda_\xi)} \int_\alpha^\beta \left(\frac{x_1-\alpha}{\beta-x_1}\right)^{1/2-i\lambda_\xi} \mathbf{v}_\xi^T \mathbf{t}(x_1)\,dx_1, \tag{5}$$

and as shown by Willis (1971), the application of the Irwin crack closure work argument leads to a simple expression for the elastic energy release rate,

$$G = \bar{\mathbf{k}}^T \Lambda \mathbf{k} \tag{6}$$

where the diagonal matrix Λ has components $\Lambda_{\xi\xi} = (1 + \exp(2\pi\lambda_\xi))/\sqrt{8\pi}$.

The oscillatory behavior arises through the positional dependence on $i\lambda_\xi$ shown in (4). Here, the complex vectors $\mathbf{v}_\xi = \mathbf{v}_0, \mathbf{v}_+, \mathbf{v}_-$ and real scalars $\lambda_\xi = 0, +\kappa, -\kappa$ are determined from the condition that each of three functions (denoted by $0, +, -$) which comprise the solution to the problem satisfy the homogeneous version of the Hilbert Arc problem:

$$(\mathbf{A}^T - e^{2\pi\lambda_\xi}\mathbf{A})\mathbf{v}_\xi = \mathbf{0}, \ (\xi = 0, +, -). \tag{7}$$

Each of the vectors $\mathbf{v}_\xi$ may be normalized such that $\mathbf{v}_\xi^H\,\mathbf{A}\mathbf{v}_\eta = \delta_{\xi\eta}(\xi, \eta = 0, +, -$, and "H" denotes the Hermitian operator). Thus, the nature of the oscillatory behavior (i.e., the values of λ_ξ, $\mathbf{v}_\xi$) depends directly on $\mathbf{A}$. Clearly, all three roots λ_ξ degenerate to zero when $\mathbf{A}$ becomes real, since for that case, $\mathbf{A}$ equals $\mathbf{A}^T$ and may be factored out of the parenthesis in (7). For such cases, the stress intensity factors defined in (1) are given by the traditional expression,

$$K_i = -\left(\frac{2}{\pi L}\right)^{1/2} \int_\alpha^\beta \left(\frac{x_1-\alpha}{\beta-x_1}\right)^{1/2} t_i(x_1)\,dx_1. \tag{8}$$

A useful observation made by Ting (1986) is that κ is invariant to a rotation of the interface, crack, and attached coordinate system about the x_3-axis, relative to the materials. Further, under such rotations, the components of $\mathbf{v}_\xi$ transform according to the standard rules for first order tensors. These properties can be easily shown using (7) and an observation by Barnett and Loethe (1974) and Ting (1986) that for rotations of the crack, interface, and coordinate system about the x_3-axis relative to the materials, the components A_{ij} obey the standard rules of transformation for a second order tensor.

For the two-dimensional geometry of the tunnel crack of length L, loaded on the upper and lower surfaces by uniform tractions $\mathbf{T}$ and $-\mathbf{T}$, we find

$$k_\xi = \pi L^{1/2+i\lambda_\xi} e^{-\pi\lambda_\xi} \frac{1-2i\lambda_\xi}{2\cosh(\pi\lambda_\xi)} \mathbf{v}_\xi^T \mathbf{T}. \tag{9}$$

By a linear superposition, this is equivalently the k_ξ obtained for the tunnel crack loaded by uniform tractions $\mathbf{T}$ at infinity as shown in Fig. 1.

Equation (9) shows that the k_ξ will only be the same for two cracks of length L_a and L_b along the same interface if $\mathbf{T}_a$ and $\mathbf{T}_b$ change according to

$$L_a^{1/2-i\lambda_\xi} \mathbf{v}_\xi^T \mathbf{T}_a = L_b^{1/2-i\lambda_\xi} \mathbf{v}_\xi^T \mathbf{T}_b \tag{10}$$

As emphasized by Rice (1987) for the isotropic case and as displayed above, the *direction* as well as the magnitude of $\mathbf{T}$ must change with crack length if the k_ξ are to be held constant.

A simple estimate of the contact zone size, assuming it is small compared to L, is obtained by finding the largest r for which $b_2 < 0$. For the tunnel crack geometry assumed above, the relative displacement of the crack surfaces near the end $x_1 = \beta$ is

$$\mathbf{b} \sim (2\pi)^{1/2} r^{1/2} L^{1/2} \{\mathbf{c}^0 + \mathbf{c}^+ \bar{f} + \mathbf{c}^- f\}, \tag{11}$$

where the details of the loading are contained in the parameters $\mathbf{c}^\xi = \bar{\mathbf{v}}_\xi e^{-\pi\lambda_\xi} \mathbf{v}_\xi^T \mathbf{T}$, and $f = (r/L)^{-i\kappa}$ is a complex number of magnitude unity with phase dependent on position (r/L). It can be shown that $\mathbf{c}^0$ is a real quantity for all loading and material geometries. Since $\mathbf{b}$ is a real quantity as well, we may rewrite the near-tip expression for $\mathbf{b}$ as

$$\mathbf{b} \sim (2\pi)^{1/2} r^{1/2} L^{1/2} [\mathbf{c}^0 + 2\Re\{\mathbf{c}^- f\}]. \tag{12}$$

Downloaded 03 May 2010 to 171.66.16.21. Redistribution subject to ASME license or copyright; see http://www.asme.org/terms/Terms_Use.cfm

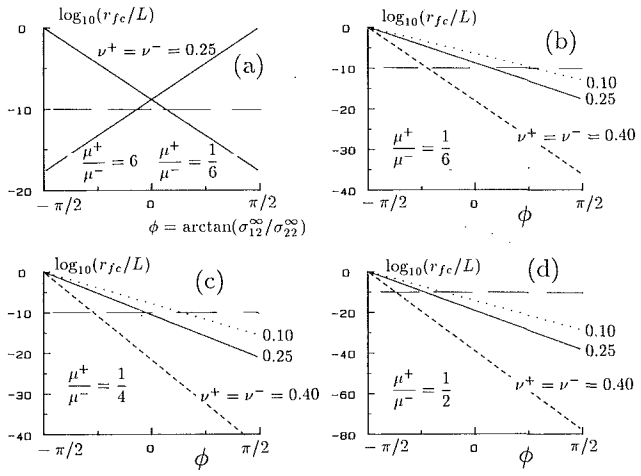

Fig. 2 Ratio (r_{fc}/L) of contact zone size to crack length versus remote in-plane loading described by $\phi = \arctan(\sigma^{\infty}_{12}/\sigma^{\infty}_{22})$, for isotropic materials. The horizontal line $\log_{10}(r_{fc}/L) = -10$ represents a maximum acceptable limit for atomistic crack tip studies.

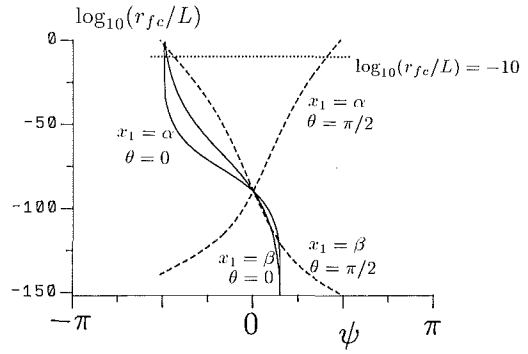

Fig. 3 Ratio (r_{fc}/L) of contact zone size to crack length at opposite ends, $x_1 = \alpha$ and $x_1 = \beta$, of an interface crack, as a function of remote loading $T(\psi,\theta)$ defined in Fig. 1. The Cu grain boundary is formed by joining the (552) and (311) faces of the upper and lower crystals, respectively, such that the (110) and (121) faces of the upper and lower crystals are parallel to the $x_1 - x_2$ plane. $\theta = 0$ represents in-plane loading and $\theta = \pi/2$ denotes out-of-plane shear. The horizontal line $\log_{10}(r_{fc}/L) = -10$ represents a maximum acceptable limit for atomistic crack tip studies.

From the expression for **b**, interpenetration is predicted for values of (r/L) which yield $b_2 < 0$, or for which

$$\Re\{c_2^- f\} < -\frac{c_2^0}{2}, \tag{13}$$

or equivalently, for which

$$\kappa \ln\left(\frac{r}{L}\right) < \arccos\left[-\frac{c_2^0}{2|c_2^-|}\right] - \arg\{c_2^-\} \pm 2n\pi. \tag{14}$$

The size of the contact zone is given by the largest value of (r/L) in the interval $0 < (r/L) < 1$ for which the above equation is satisfied, or equivalently, by the least negative value of $\arg\{f\}$, $-2\pi < \arg\{f\} < 0$, for which equality in (13) is satisfied. For each loaded interface, one must choose the proper branch (positive or negative) of arccos and integer value n as to yield the least negative value of $\kappa \ln(r/L)$ in the range -2π to 0.

The relative displacement of the surfaces at the opposite end of the crack, $x_1 = \alpha$, is given by (11) and (12), except that the vectors $\mathbf{c}^{\xi}$ $(\xi = 0, +, -)$ must be replaced by $\mathbf{R}\bar{\mathbf{c}}^{\xi}$, where $\mathbf{R}$ is a rotation matrix with nonzero components $R_{11} = R_{33} = -1$, $R_{22} = 1$. In the particular case where pure tension σ^{∞}_{22} is applied, so that $\sigma^{\infty}_{12} = \sigma^{\infty}_{32} = 0$, the components c_2^{ξ} are clearly all real and therefore are indentical at each end of the crack. Using this observation with (13) and (14), the contact zones at each end of the crack are always the same size under pure tension.

Results

As a special and more familiar case, consider an interface crack between two isotropic materials, the upper one described by shear modulus μ^+ and Poisson's ratio ν^+, and the lower one by μ^- and ν^-. Here, the $\mathbf{v}_{\xi}$ and κ can be found explicitly, the latter given by

$$\kappa = \frac{1}{2\pi} \ln\left[\left(\frac{3-4\nu^+}{\mu^+} + \frac{1}{\mu^-}\right)\Big/\left(\frac{3-4\nu^-}{\mu^-} + \frac{1}{\mu^+}\right)\right]$$

(isotropic case). (15)

For the isotropic case, $c_2^0 = 0$ and $\arg\{c_2^-\} = \arg\{1 + i\sigma^{\infty}_{12}/\sigma^{\infty}_{22}\} \equiv \phi$. Using these values in (14), and noting $\arccos\{0\} = -\pi/2$ as the proper branch, it is found as shown by Rice (1987) that

$$\frac{r_{fc}}{L} = \exp\left[-\left(\frac{\pi}{2} + \phi\right)/\kappa\right], \quad -\frac{\pi}{2} < \phi < \frac{\pi}{2}. \tag{16}$$

Due to the linearity of this problem, we must restrict ϕ to a range $-\pi/2 < \phi < \pi/2$ within which crack opening is predicted. Presumably, the sign of the relative crack displacement changes in the range $-3\pi/2 < \phi < -\pi/2$, and the criterion used for interpenetration is not meaningful for such closure loads.

Figure 2 presents the ratio r_{fc} (first contact) to crack length L for several interface cracks bounded by isotropic materials. In all cases, the size of the contact zone varies rapidly with the nature of the loading through ϕ, and with the properties of the adjoining materials through dependence on κ. In general, the addition of a positive shear component of loading, σ^{∞}_{12}, so that $\phi > 0$, will decrease r_{fc} at $x_1 = \beta$ if the lower material is of higher shear modulus $(\mu^-/\mu^+ > 1)$. Further, the contact zone size at $x_1 = \alpha$, or instead, that at $x_1 = \beta$ but with the $(+)$ and $(-)$ materials exchanged, is simply given by replacing ϕ by $-\phi$ in Fig. 2. Under pure tension $(\phi = 0)$, r_{fc} is therefore the same at both crack tips, but when a shearing component σ^{∞}_{12} is applied, a decrease in r_{fc} at one crack tip is accompanied by an increase in r_{fc} at the other end. The application of an out-of-plane shearing load, σ^{∞}_{32}, does not affect r_{fc} for isotropic materials, as the $x_1 - x_2$ plane is a mirror plane in this case.

Certainly, the asymptotic analysis performed here is valid only over distances r from the crack tip much less than L; thus, predictions of (r_{fc}/L) which are not $\ll 1$ violate small scale contact conditions and are outside the range of validity. Since the elastic solution is also unacceptable within the contact region, any detailed study of the fracture process zone should be confined to regions $r_{fc}/L \ll r/L \ll 1$. In particular, for atomistic studies of dislocation nucleation from crack tips (e.g., Rice and Thomson, 1974; Mason, 1979; Lin and Thomson, 1986; Anderson and Rice, 1986; Anderson, 1986; Wang et al, 1986), a reasonable condition is that the contact zone size should be less than a lattice spacing. Shown then in each figure is a horizontal line, drawn for $(r_{fc}/L) = 10^{-10}$, below which the solution is expected to be useful for such crack dislocation studies. This assumes a rather extreme case that the crack length L is less than 2 m. In reality, for application to microcracks on grain boundary facets, we might use 100 μm as an upper limit to L, and then $r_{fc}/L = 10^{-6}$ or smaller suffices.

Clearly, for the isotropic materials presented where $\mu^+/\mu^- = 6$ or $1/6$ (see Fig. 2(*b*)), only the case $\nu^+ = \nu^- = 0.4$ is physically acceptable with $L = 2$ m and $\phi = 0$. For materials which have more closely matched elastic shear moduli (e.g., $\mu^+ = \mu^- = 1/4$, $1/2$ in Figs. 2(*c*), (*d*)), the range of loadings over which the solution is physically acceptable increases substantially.

The primary application of interest is to grain boundary

Downloaded 03 May 2010 to 171.66.16.21. Redistribution subject to ASME license or copyright; see http://www.asme.org/terms/Terms_Use.cfm

fracture. As a representative example, Fig. 3 presents (r_{fc}/L) at both ends of a crack on a Cu grain boundary, as a function of the remote tensile, in-plane, and out-of-plane loading shown in Fig. 1 and described here by

$$\sigma_{12}^{\infty} = \mathbf{T} \sin \psi \cos \theta;\ \sigma_{22}^{\infty} = \mathbf{T} \cos \psi;\ \sigma_{32}^{\infty} = \mathbf{T} \sin \psi \sin \theta; \quad (17)$$

Two values of θ are chosen in order to apply a tensile load with either in-plane shear ($\theta = 0$) or out-of-plane shear ($\theta = \pi/2$). In each case, $\psi = 0$ corresponds to pure tension and $\psi = \pm\pi/2$ corresponds to pure shear. An apparent feature is that the relationship between $\log_{10}(r_{fc}/L)$ and ψ is not linear. Further, the range of ψ which corresponds to crack opening does not necessarily coincide with $-\pi/2 < \psi < \pi/2$. Most important, $(r_{fc}/L) < 10^{-10}$ over the bulk of the loading range.

The particular boundary chosen is formed by joining the $(\bar{5}5\bar{2})$ and $(\bar{3}11)$ crystallographic planes of the upper and lower materials, respectively, such that the (110) crystallographic plane of the upper material and the (121) plane of the lower material are parallel to the $x_1 - x_2$ plane. A full Hermitian matrix **A** was obtained here, indicating that any single tensile, in-plane, or out-of-plane loading produces relative shearing and opening displacements of the crack surfaces. A value of $\kappa \approx 0.01$ was obtained, which is within estimates cited for several practical metallic and nonmetallic interfaces based on the isotropic relation (15) (Hutchinson et al., 1987), and for a high modulus graphite-epoxy composite (Wang and Choi, 1983). Cu is moderately anisotropic compared to many f.c.c. and b.c.c. materials, and thus is expected to have a relatively large variation in κ for grain boundary cracks.

Figure 3 provides some additional comparisons between the anisotropic and isotropic cases. When a pure tensile load is applied, the contact zone size is always the same at each crack end, regardless of the crystal anisotropy and orientation. However, when a shear component is applied, r_{fc} at opposite ends of the crack may behave similarly by both growing or shrinking (e.g., Fig. 3 with $\theta = 0$), or may behave oppositely by growing at one end and shrinking at the other (e.g., Fig. 3 with $\theta = \pi/2$).

An interesting feature seen for some interface cracks is that (13) cannot be satisfied for certain loadings, as $c_2^0/2 > |c_2^-|$. This implies that $b_2 = 0$ only at the crack tip, and that a zone of interpenetration does not exist for this loading, even though $\kappa \neq 0$. This is the case shown for the $\theta = 0$ curves in Fig. 3, where at $\psi \approx 25°$, $r_{fc} \to 0$ at each end of the crack.

For tensile loading ($\psi = 0$) of Cu boundaries, a general observation is that the region of predicted interpenetration is small enough compared to an atomic spacing to be neglected. In cases where the applied loading involves a considerable shear component (i.e., $\psi > 60°$), an explicit verification of the contact zone size is warranted to insure that the crack tip loading is uniquely characterized by the stress concentration vector (5) or rather the energy release rate (6). As Cu is a moderately anisotropic material, these observations are expected to be valid for interface cracks in many other cubic materials as well.

Acknowledgment

This study was supported by the NSF Materials Research Laboratory at Harvard University, under grant NSF-DMR-83-16979, and by the Office of Naval Research through subcontract VB38639-0 to Harvard University, based on contract N00014-86-K-0753 with the University of California. J. R. Rice was quite helpful in suggesting and contributing to this work. Discussions with P. M. Mataga were quite useful, and the assistance of J. Qu and J. Bassani in correcting an earlier version of this work is gratefully acknowledged.

References

Anderson, P. M., 1986, "Ductile and Brittle Crack Tip Response," Ph.D. thesis, Harvard University, Cambridge, MA.

Anderson, P. M., and Rice, J. R., 1986, "Dislocation Emission from Cracks in Crystals or Along Crystal Interfaces," *Scripta metall.*, Vol. 20, pp. 1467–1472.

Bacon, D. J., Barnett, D. M., and Scattergood, R. O., 1979, "Anisotropic Theory of Lattice Defects," *Progress in Materials Science*, Vol. 23, pp. 51–262.

Barnett, D. M., and Lothe, J., 1974, "An Image Force Theorem for Dislocations in Anisotropic Bicrystals," *J. Phys. F: Metal Phys.*, Vol. 4, pp. 1618–1635.

Cherepanov, G. P., 1962, "The Stress State in a Heterogeneous Plate with Slits," (in Russian), Izvestia AN SSSR, OTN, *Mekhan. i Mashin.*, Vol. 1, pp. 131–137.

Clements, D. L., 1971, "A Crack Between Dissimilar Anisotropic Media," *Int. J. Eng. Sci.*, Vol. 9, pp. 256–265.

Comninou, M., 1977, "The Interface Crack," ASME JOURNAL OF APPLIED MECHANICS, Vol. 44, pp. 631–636.

Comninou, M., 1978, "The Interface Crack in a Shear Field," ASME JOURNAL OF APPLIED MECHANICS, Vol. 45, pp. 287–290.

England, A. H., 1965, "A Crack Between Dissimilar Media," ASME JOURNAL OF APPLIED MECHANICS, Vol. 32, pp. 400–402.

Erdogan, F., 1963, "Stress Distribution in a Nonhomogeneous Elastic Plane with Cracks," ASME JOURNAL OF APPLIED MECHANICS, Vol. 30, pp. 232–236.

Erdogan, F., 1965, "Stress Distribution in Bonded Dissimilar Materials with Cracks," ASME JOURNAL OF APPLIED MECHANICS, Vol. 32, pp. 403–410.

Gautesen, A. K., and Dundurs, J., 1987, "The Interface Crack in a Tension Field," ASME JOURNAL OF APPLIED MECHANICS, Vol. 54, pp. 93–98.

Gotoh, H., 1967, "Some Problems of Bonded Anisotropic Plates with Cracks Along the Bond," *Int. J. Fract. Mech.*, Vol. 3, pp. 253–265.

Hutchinson, J. W., Mear, M., and Rice, J. R., 1987, "Crack Paralleling an Interface Between Dissimilar Materials," ASME JOURNAL OF APPLIED MECHANICS, Vol. 54, pp. 828–832.

Knowles, J. K., and Sternberg, E., 1983, "Large Deformation Near a Tip of an Interface-Crack Between Two Neo-Hookean Sheets," *J. Elast.*, Vol. 13, pp. 257–293.

Lin, I. H., and Thomson, R., 1986, "Cleavage, Dislocation Emission, and Shielding for Cracks Under General Loading," *Acta Metall.*, Vol. 34, pp. 187–206.

Mason, D. D., 1979, "Segregation-induced Embrittlement of Grain Boundaries," *Phil Mag.*, Vol. 39, pp. 455–468.

Malyshev, B. M., and Salganik, R. L., 1965, "The Strength of Adhesive Joints Using the Theory of Cracks," *Int. J. Fract. Mech.*, Vol. 1, pp. 114–128.

Muskhelishvili, N. I., 1963, "Some Basic Problems of the Mathematical Theory of Elasticity," Martinus Noordhoff, Amsterdam, The Netherlands.

Qu, J., and Bassani, J. L., 1988, "Cracks on Bimaterial and Bicrystal Interfaces," (in preparation).

Rice, J. R., 1987, "Elastic Fracture Mechanics Concepts for Interfacial Cracks," ASME JOURNAL OF APPLIED MECHANICS, Vol. 55, pp. 98–103.

Rice, J. R., and Sih, G. C., 1965, "Plane Problems of Cracks in Dissimilar Media," ASME JOURNAL OF APPLIED MECHANICS, Vol. 32, pp. 418–423.

Rice, J. R., and Thomson, R., 1974, "Ductile versus Brittle Behaviour of Crystals," *Phil. Mag.*, Vol. 29, pp. 73–97.

Ting, T. C. T., 1986, "Explicit Solution and Invariance of the Singularities at an Interface Crack in Anisotropic Composites," *Int. J. Solids Structures*, Vol. 22, pp. 965–983.

Wang, J.-S., Anderson, P. M., and Rice, J. R., 1987, "Micromechanics of the Embrittlement of Crystal Interfaces," *Proc. Fifth Int. Conf. on Mechanical Behaviour of Materials ICM-5*, Beijing, China, June 3–6, 1987, Pergamon Press.

Wang, S. S., and Choi, I., 1983, "The Interface Crack Between Dissimilar Anisotropic Composite Materials," ASME JOURNAL OF APPLIED MECHANICS, Vol. 50, pp. 169–178; "The Interface Crack Behavior in Dissimilar Anisotropic Composites Under Mixed-mode Loading," ibid, pp. 179–183.

Williams, M. L., 1959, "The Stresses Around a Fault or Crack in Dissimilar Media," *Bull. Seismol. Soc. America*, Vol. 49, pp. 199–204.

Willis, J. R., 1971, "Fracture Mechanics of Interfacial Cracks," *J. Mech. Phys. Solids*, Vol. 19, pp. 353–368.

Downloaded 03 May 2010 to 171.66.16.21. Redistribution subject to ASME license or copyright; see http://www.asme.org/terms/Terms_Use.cfm

On a Paradoxical Phenomenon Related to Beams on Elastic Foundation: Could External Compliant Leads Reduce the Strength of a Surface-Mounted Device?

E. Suhir
AT&T Bell Laboratories,
Murray Hill, NJ 07974
Mem. ASME

Compliant external electrical leads are often utilized as strain buffers in surface-mounted device technology to provide the necessary stress relief for the device, when the substrate is subjected to bending. A paradoxical situation was observed, however, during testing of compliant leaded hybrid integrated circuits (HIC): In some tests the bending moment, applied to the printed wire board (PWB) and causing HIC fracture, turned out smaller (not greater), when leads of greater compliance were installed. We show that such a paradoxical situation is due to the redistribution of lead reactions at certain combinations of HIC length, HIC and PWB flexural rigidity, and spring constant of the elastic attachment. Our analysis has indicated, that only sufficiently compliant leads can essentially reduce the stresses, while leads of moderate compliance can result in even greater stresses in the HIC than stiff leads. We suggest an easy-to-calculate governing parameter, which characterizes the mechanical behavior of HIC/PWB and similar assemblies with compliant attachments.

Introduction

T. F. Marinis, R. C. Reinert, and W. M. Sherry (1984) observed a paradoxical situation during testing of compliant leaded hybrid integrated circuits (HIC): In some tests the bending moment, applied to the printed wire board (PWB) and causing HIC fracture, turned out smaller, when leads of greater compliance were installed. The authors indicated that they did not find an adequate explanation to this observation. In order to find an explanation to the observed phenomenon, we develop a simplified analytical model of HIC/PWB assembly bending. The HIC and the PWB are treated as long-and-narrow rectangular plates, connected by a continuous elastic attachment, and the following major assumptions are used: (*1*) compliant leads transmit axial forces only; (*2*) the number of leads is sufficiently great to be substituted in the analysis by a continuous elastic attachment; (*3*) the displacements are small enough, so that the elastic behavior of leads is never compromised; and (*4*) lead reactions never exceed the lead strength.

Analysis

The structure in question is schematically shown in Fig. 1. We proceed from the following equations of bending for long-and-narrow plates (see, for instance, Timoshenko and Woinowski-Kreiger, 1959):

$$D_1 w_1^{IV}(x) = -p(x),\ D_2 w_2^{IV}(x) = p(x). \tag{1}$$

Here $w_1(x)$ and $w_2(x)$ are deflection functions for the HIC and the PWB, respectively,

$$p(x) = k[w_1(x) - w_2(x)] \tag{2}$$

are lead reactions per unit assembly length,

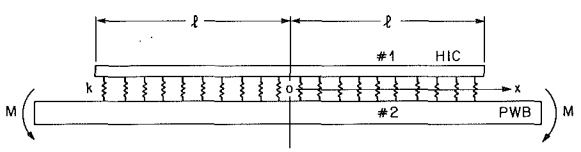

Fig. 1 Hybrid Integrated Circuit (HIC)/Printed Wire Board (PWB) assembly subjected to bending

Contributed by the Applied Mechanics Division for presentation at the Joint ASCE/ASME Applied Mechanics, Biomechanics, and Fluids Engineering Conference, La Jolla, CA, July 9–12, 1989.

Discussion on this paper should be addressed to the Editorial Department, ASME, United Engineering Center, 345 East 47th Street, New York, N.Y. 10017, and will be accepted until two months after final publication of the paper itself in the JOURNAL OF APPLIED MECHANICS. Manuscript received by ASME Applied Mechanics Division, October 7, 1987; final revision, June 8, 1988.

Paper No. 89-APM-5.

Copyright © 1988 by ASME
Downloaded 03 May 2010 to 171.66.16.21. Redistribution subject to ASME license or copyright; see http://www.asme.org/terms/Terms_Use.cfm

Table 1

u	$\phi_1(u)$	$\chi_1(u)$	$\chi_2(u)$	$\rho(u)$	x_*/l
0	1.000	1.000	1.000	1.000	
0.1	1.000	1.000	1.000	1.000	
0.2	1.000	1.000	1.000	1.000	
0.3	0.999	0.999	0.999	0.999	
0.4	0.996	0.996	0.997	0.997	
0.5	0.990	0.991	0.993	0.993	
0.6	0.979	0.982	0.985	0.985	
0.7	0.961	0.967	0.973	0.973	
0.8	0.935	0.946	0.956	0.956	
0.9	0.899	0.917	0.931	0.931	
1.0	0.852	0.878	0.899	0.899	
1.1	0.795	0.830	0.859	0.859	
1.2	0.728	0.774	0.813	0.813	
1.3	0.653	0.712	0.761	0.761	
1.4	0.573	0.645	0.705	0.705	
1.5	0.492	0.576	0.648	0.618	
1.6	0.411	0.509	0.591	0.591	
1.7	0.335	0.444	0.537	0.537	
1.8	0.264	0.384	0.483	0.483	
1.9	0.201	0.328	0.439	0.439	
2.0	0.144	0.279	0.397	0.387	
2.2	0.054	0.197	0.325	0.325	
2.37	0.000	0.147	0.279	0.410	0
2.4	−0.009	0.136	0.269	0.392	0.137
2.6	−0.051	0.092	0.226	0.352	0.330
2.8	−0.074	0.060	0.193	0.327	0.400
3.0	−0.085	0.038	0.167	0.302	0.470
3.2	−0.087	0.023	0.146	0.300	0.500
3.4	−0.082	0.012	0.129	0.299	0.530
3.6	−0.073	0.006	0.115	0.303	0.507
3.8	−0.063	0.002	0.104	0.312	0.509
4.0	−0.052	−0.001	0.094	0.332	0.607
4.2	−0.041	−0.002	0.085	0.320	0.626
4.4	−0.031	−0.003	0.078	0.318	0.643
4.6	−0.022	−0.003	0.071	0.315	0.658
4.8	−0.015	−0.002	0.065	0.313	0.673
5.0	−0.009	−0.002	0.060	0.311	0.686

$$D_1=\frac{E_1h_1^3}{12(1-\nu_1^2)},\quad D_2=\frac{E_2h_2^3}{12(1-\nu_2^2)} \tag{3}$$

are flexural rigidities of the HIC and the PWB, and k is the spring constant of the attachment. The relationships (1) and (2) result in the following equation for the reaction function $p(x)$:

$$p^{IV}(x)+4\alpha^4p(x)=0, \tag{4}$$

where

$$\alpha=\sqrt[4]{k\,\frac{D}{4D_1D_2}}, \tag{5}$$

and $D=D_1+D_2$ is the total rigidity of the assembly.

We seek the solution to the equation (4) in the form:

$$p(x)=C_0V_0(\alpha x)+C_2V_2(\alpha x), \tag{6}$$

where the functions $V_0(\alpha x)$ and $V_2(\alpha x)$ are given by the equations

$$V_0(\alpha x)=\cosh\alpha x\cos\alpha x,\quad V_2(\alpha x)=\sinh\alpha x\sin\alpha x, \tag{7}$$

and C_0 and C_2 are constants of integration. These constants can be determined from the boundary conditions

$$p''(l)=-k\,\frac{M}{D_2},\quad p'''(l)=0, \tag{8}$$

where M are external moments applied to the PWB. The conditions (8) can be easily derived from the obvious conditions $w_1'(l)=0$, $w_2''(l)=M/D_2$, $w_1'''(l)=w_2'''(l)=0$ for the deflection functions. Introducing the solution (6) in the conditions (8) and solving the system of two algebraic equations for the unknowns C_0 and C_2, we obtain the following formulas for the constants of integration:

$$C_0=\frac{kMl^2}{6D_2}\,\chi_1(u),\quad C_2=-\frac{kMl^2}{2D_2}\,\frac{\phi_1(u)}{u^2}. \tag{9}$$

Here

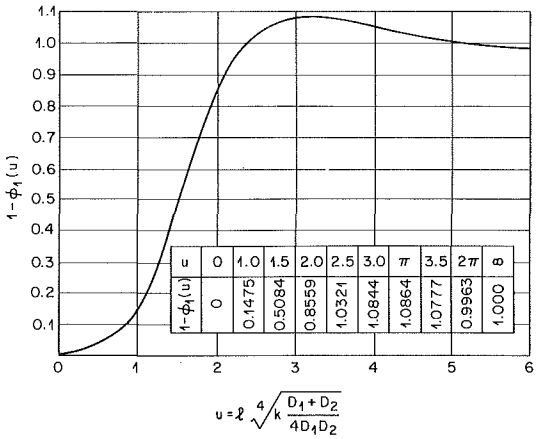

Fig. 2 Effect of lead compliance on maximum bending moment in the HIC

$$u=\alpha l=l\sqrt[4]{k\,\frac{D}{4D_1D_2}}$$

is the governing parameter of the mechanical behavior of the assembly, and the functions

$$\left.\begin{aligned}\chi_1(u)&=\frac{6}{u^2}\,\frac{\cosh u\sin u-\sinh u\cos u}{\sinh 2u+\sin 2u}\\ \phi_1(u)&=\frac{\cosh u\sin u+\sinh u\cos u}{\sinh 2u+\sin 2u}\end{aligned}\right\} \tag{11}$$

are introduced in such a way, that they are equal to unity in the case of an ideally compliant attachment ($u=0$) and tend to zero for absolutely stiff leads ($u\to\infty$). The tabulated values of these functions are given in Table 1. Thus, the reaction function $p(x)$ is as follows:

$$p(x)=2M_\infty\left(\frac{u}{l}\right)^2\left[\frac{u^2\chi_1(u)}{3}\,V_0(\alpha x)-\phi_1(u)\,V_2(\alpha x)\right], \tag{12}$$

where $M_\infty=\dfrac{D_1}{D}$ is the bending moment for a stiff leaded HIC.

After substituting (12) into the first equation in (1) and integrating this equation twice, we obtain the following expression for the bending moment acting over HIC cross-sections:

$$M_1(x)=M_\infty\left[1-\frac{u^2\chi_1(x)}{3}\,V_2(\alpha x)-\phi_1(u)\,V_0(\alpha x)\right]. \tag{13}$$

For the PWB we have:

$$\begin{aligned}M_2(x)&=M-M_1(x)\\&=M_\infty\left[\frac{D_2}{D_1}+\frac{u^2\chi_1(u)}{3}\,V_2(\alpha x)+\phi_1(u)\,V_0(\alpha x)\right].\end{aligned} \tag{14}$$

The maximum bending moment in the HIC is

$$M_{\max}=M_1(0)=M_\infty[1-\phi_1(u)], \tag{15}$$

where the function $1-\phi_1(u)$ reflects the effect of lead compliance (Fig. 2). The maxima of this function occur in the region of relatively great u values ($u>2$), and can be determined by a simplified formula:

$$(1-\phi_1)_{\max}=1+2e^{-m\pi},\quad m=1,3,5,\ldots \tag{16}$$

As evident from this formula, only the first maximum $(1-\phi_1)_{\max}=1.0864$ is essentially different from unity. This maximum takes place for $u=\pi$ and is located between the first two zeros of the function $\phi_1(u)$:

Downloaded 03 May 2010 to 171.66.16.21. Redistribution subject to ASME license or copyright; see http://www.asme.org/terms/Terms_Use.cfm

$$u_1 = \frac{3}{4}\pi = 2.3562, \quad u_2 = \frac{7}{4}\pi = 5.4978. \tag{17}$$

Thus, when the combination of different factors affecting the mechanical behavior of the assembly is such that the u value falls within the above range, the maximum bending moment in the HIC exceeds the moment M_∞ for absolutely stiff leads. Note, that in the Marinis et al., (1984) tests the calculated u values were $u \cong 3.2$ for the BMPM type of PWB with "rigid" (NAS) leads, and $u \cong 2.7$ for "compliant" (Mod1) leads. Fortunately, as has been shown above, the adverse effect of inappropriately chosen leads does not exceed 8.7 percent.

In the range $\pi < u < 7/4\ \pi$ the increase in the attachment compliance results in greater (not smaller) bending moments in the HIC. For $u > 7/4\ \pi$ the strength of the "compliant leaded" HIC is in effect not different from the strength of the HIC with absolutely stiff leads. Therefore, in order to achieve an essential reduction in the HIC bending moment due to application of compliant leads, one has to make the spring constant sufficiently small, so that the u value be smaller than $\frac{3}{4}\pi$.

Shearing forces can be determined from (13) or (14) by differentiation:

$$N(x) = \sqrt{2} M_\infty \frac{u}{l}\left[\frac{u^2 \chi_1(u)}{3} V_1(\alpha x) - \phi_1(u) V_3(\alpha x)\right], \tag{18}$$

where the functions $V_1(\alpha x)$ and $V_3(\alpha x)$ are as follows:

$$\left.\begin{aligned} V_1(\alpha x) &= \frac{1}{\sqrt{2}}(\cosh \alpha x \sin \alpha x + \sinh \alpha x \cos \alpha x) \\ V_3(\alpha x) &= \frac{1}{\sqrt{2}}(\cosh \alpha x \sin \alpha x - \sinh \alpha x \cos \alpha x) \end{aligned}\right\}. \tag{19}$$

The deflection functions $w_1(x)$ and $w_2(x)$ can be found by integrating the equations (13) and (14) twice:

$$\left.\begin{aligned} w_1(x) &= \frac{Ml^2}{2D}\left[\frac{x^2}{l^2} + \frac{\chi_1(u)}{3} V_0(\alpha x) - \frac{\phi_1(u)}{u^2} V_2(\alpha x)\right] \\ w_2(x) &= \frac{Ml^2}{2D}\left[\frac{x^2}{l^2} - \frac{D_1}{D_2}\left(\frac{\chi_1(u)}{3} V_0(\alpha x) - \frac{\phi_1(u)}{u^2} V_2(\alpha x)\right)\right] \end{aligned}\right\}. \tag{20}$$

Here the rigid body motion terms are omitted. The differences in deflections define the bow of each component as follows:

$$\left.\begin{aligned} f_1(0) &= w_1(l) - w_1(0) = \frac{Ml^2}{6D}[3 - \chi_1(u) - 2\chi_2(u)] \\ f_2(0) &= w_2(l) - w_2(0) = \frac{Ml^2}{6D}\left[3 + \frac{D_1}{D_2}(\chi_1(u) + 2\chi_2(u))\right] \end{aligned}\right\}, \tag{21}$$

where the function $\chi_1(u)$ is given by the first formula in (11) and the function

$$\chi_2(u) = \frac{3}{2u^2}\frac{\sinh 2u - \sin 2u}{\sinh 2u + \sin 2u} \tag{22}$$

is also equal to unity for $u = 0$ and tends to zero for $u \to \infty$ (Table 1). Obviously, for ideally compliant leads ($u = 0$) the HIC bow $f_1(0)$ is zero, and the PWB bow $f_2(0)$ is the greatest and is expressed by the formula

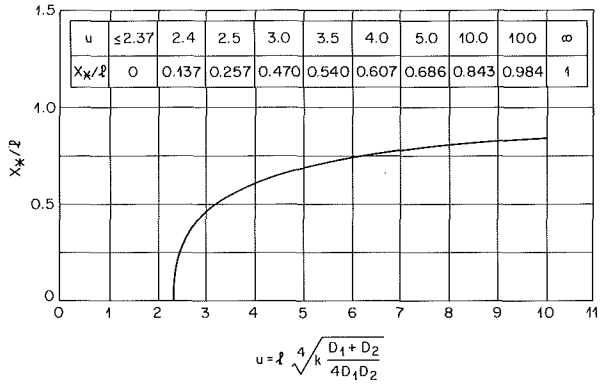

Fig. 3 Longitudinal location of maximum lead reaction as a function of lead compliance parameter

$$f_2(0) = \frac{Ml^2}{2D_2}. \tag{23}$$

For absolutely stiff leads ($u \to \infty$) both maximum bows coincide:

$$f_1(0) = f_2(0) = \frac{Ml^2}{2D}. \tag{24}$$

As evident from equation (12), the lead reactions $p(x)$ have the following values in the middle ($x = 0$) and at the ends ($x = l$) of the assembly:

$$p(0) = M_\infty \left(\frac{2u}{l}\right)^2 \frac{\chi_1(u)}{6}, \quad p(l) = -M_\infty \left(\frac{2u}{l}\right)^2 \frac{\chi_2(u)}{3}. \tag{25}$$

For sufficiently great u values (say, greater than 2), the functions $\chi_1(u)$ and $\chi_2(u)$ can be evaluated by the simplified formulas:

$$\chi_1(u) = \frac{6}{u^2} e^{-u}(\sin u - \cos u), \quad \chi_2(u) = \frac{3}{2u^2}. \tag{26}$$

In this case the formulas (25) yield:

$$p(0) = 4\frac{M_\infty}{l^2} e^{-u}(\sin u - \cos u), \quad p(l) = -2\frac{M_\infty}{l^2}. \tag{27}$$

Hence, when the attachment is sufficiently stiff, its reactions in the middle of the assembly rapidly decrease with the further increase in the stiffness, while the end reactions remain more or less constant.

In order to find out whether the function $p(x)$ has internal extrema, other than in the middle of the assembly, we use the formula for the "curvature"

$$p''(0) = -M_\infty \left(\frac{2u^2}{l^2}\right)^2 \phi_1(u). \tag{28}$$

For $\eta < 3/4\ \pi$ the function $\phi_1(u)$ is positive (see Table 1), $p''(0)$ is negative, and therefore $p(0)$ represents the only internal maximum. For greater u values, when $\phi_1(u)$ becomes negative, the first formula in (25) defines a local minimum, while the maxima of the attachment reactions occur in such a case at the locations $x = x_*$, that can be determined from the condition $p'(x)|_{x=x_*} = 0$. This condition results in the following transcendental equation:

$$\tanh\left(u\frac{x_*}{l}\right)\tanh u + \tanh\left(u\frac{x_*}{l}\right)\tan u = 0. \tag{29}$$

The numerical solution to this equation is plotted in Fig. 3. For great enough u values (say, greater than 3) equation (29) can be simplified:

$$\tan\left(u\frac{x_*}{l}\right)\tan u = -1. \tag{30}$$

The smallest root of the above equation is

Downloaded 03 May 2010 to 171.66.16.21. Redistribution subject to ASME license or copyright; see http://www.asme.org/terms/Terms_Use.cfm

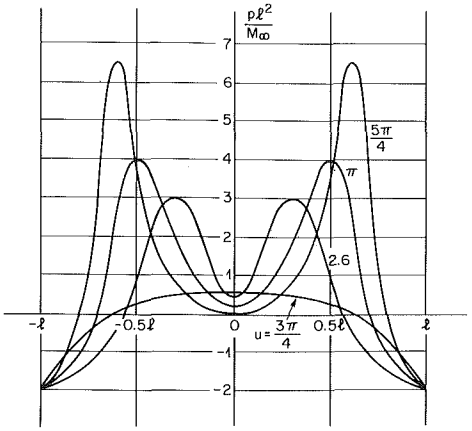

Fig. 4 Distribution of lead reactions along the assembly

$$\frac{x_*}{l}=1-\frac{\pi}{2u}\,. \tag{31}$$

The latter formula indicates that in assemblies with stiff attachments the internal maxima of the reaction forces shift towards the assembly ends with a further increase in the attachment stiffness. These maxima can be determined from the formula (12) and are as follows:

$$p(x_*)=M_\infty\left(\frac{2u}{l}\right)^2\frac{\rho(u)}{3}\,. \tag{32}$$

The tabulated values of the function

$$\rho(u)=\frac{3}{2}\left[\frac{u^2\chi_1(u)}{3}V_0\left(u\frac{x_*}{l}\right)-\phi_1(u)V_2\left(u\frac{x_*}{l}\right)\right] \tag{33}$$

are given in Table 1. For sufficiently stiff attachments the equations (32) and (33) result in the following formula for the maximum reaction force:

$$p(x_*)=2e^{-\pi/2}M_\infty\left(\frac{u}{l}\right)^2\cong 0.416M_\infty\left(\frac{u}{l}\right)^2$$

$$=0.208\,M_\infty\sqrt{k\frac{D}{D_1D_2}}\,. \tag{34}$$

As evident from this formula, in assemblies with stiff attachments the maxima of the reaction forces increase with a further increase in the attachment stiffness (Fig. 4). Note, that these maxima are assembly size independent.

Conclusions

The following major conclusions can be drawn from the above analysis:

- An experimentally observed paradoxical phenomenon, when the ultimate external bending moments turned out in some cases smaller for attachments of greater compliance, is due to the redistribution of lead reactions at certain combinations of the assembly length, HIC and PWB flexural rigidities, and lead compliance. Our analysis has indicated that only sufficiently compliant attachments can essentially reduce the stresses in the HIC, while leads of moderate compliance could result in even greater stress than absolutely stiff leads. Fortunately, such an adverse effect does not exceed 8.7 percent.
- The parameter u can be used as a governing parameter when assessing the mechanical behavior of a surface mounted device with compliant external leads. When the u value is smaller than $3\pi/4$, application of compliant leads indeed results in smaller stresses in the HIC. On the other hand, if this value is greater than $7\pi/4$, then "compliant" leads do not practically affect the mechanical behavior of the assembly, compared to absolutely stiff leads. However, if the calculated u value falls within the range between $3\pi/4$ and $7\pi/4$, then the application of compliant leads adversely affects the HIC strength.
- The obtained results can be utilized as guidance for choosing an appropriate compliant attachment design for the given assembly. They can also be of help in experimental planning.

Acknowledgment

The author is thankful to C. J. Bartlett, J. M. Segelken, and P. M. Hall for valuable comments.

References

Marinis, T. F., Reinert, R. C., and Sherry, W. M. (1984), "Impact of External Lead Design on the Fracture of HIC-PWB Assemblies Subjected to Bending," *Proceedings of the 34th Electronic Component Conference*, New Orleans, LA, pp. 281–193.

Timoshenko, S. P., and Woinowski-Krieger, S. (1979), *Theory of Plates and Shells*, McGraw-Hill, New York.

Downloaded 03 May 2010 to 171.66.16.21. Redistribution subject to ASME license or copyright; see http://www.asme.org/terms/Terms_Use.cfm

Stresses in Dual-Coated Optical Fibers

E. Suhir
AT&T Bell Laboratories,
Murray Hill, N.J. 07974

We examine several problems related to the mechanical behavior of dual-coated optical fibers: low temperature microbending, evaluation of spring constant due to coating layers, strength of the end portions of fibers clamped in termination fixtures, and prediction of stresses caused by the misalignment of the openings in the frame and the termination fixture. The developed formulas are simple, easy-to-use and clearly indicate the role of the major factors affecting the mechanical behavior of the fibers. The obtained results can be of help in physical design of dual-coated fibers and optical interconnections.

1 Introduction

In this analysis we examine several problems, related to the mechanical behavior of dual coated optical fibers.

The first problem has to do with the evaluation of the low temperature microbending. The emphasis is on the effect of initial local curvatures, that inevitably exist in any real fiber. In particular, we determine whether these curvatures can cause appreciable deflections at moderately low temperatures, thereby resulting in added transmission losses. As is known, transmission losses increase at low temperatures, which is attributed by many investigators to fiber microbending (Gloge, 1972 and 1975; Marcuse, 1973 and 1974; Gardner, 1975; Naruse et al., 1977; Sakai and Kimura, 1979; Turuya and Suematsu, 1980; Hanson, 1980; Katsuyama et al., 1980; Blyler, Jr. et al., 1982 and 1983; Yabuta et al., 1983; Vangheluwe, 1984; Lenahan, 1985).

The second problem concerns the spring constant in the buckling of dual coated fibers. This parameter has a strong impact on the buckling force and both the pre- and post-buckling behavior of the fiber. Early work (Katsuyama et al., 1980; Yabuta et al., 1983) assumed that the spring constant is simply equal to Young's modulus of the primary coating material. D. C. L. Vangheluwe (1984), however, showed that this constant depends not only on the elastic properties of the primary coating material, but also on the ratio of the radii of the primary coating and the glass fiber. Calculations executed for a coating with elastic constants $E_1 = 2.00$ MPa, $\nu_1 = 0.5$, have indicated, that when the above ratio is about 2, the spring constant is 45 times greater than Young's modulus of the material. On the other hand, the spring constant in the formula, obtained by Vangheluwe, tends to infinity when the thickness of the primary coating tends to zero. This is an indication that Vangheluwe's formula could result in an overestimation of the actual spring constant for thin primary coatings, especially when the ratio of Young's moduli of the primary and the secondary coatings is not very small. In this case it is important to account for the finite rigidity of the secondary coating. A numerical evaluation carried out by T. A. Lenahan (1985) indicated that the compliance of the secondary coating can substantially reduce the spring constant. In this connection we obtain an exact formula for the spring constant, with consideration of the finite rigidity of the secondary coating. This formula could be of help when the assumption of an absolutely rigid secondary coating is not acceptable.

The third problem is associated with the thermally induced stresses, which could arise in the end portions of dual-coated fibers located within a metal frame. When the device is subjected to low or elevated temperatures, these stresses could result in added transmission losses because of fiber microbending, or even in the failure of the fiber.

The fourth problem deals with bending stresses which arise because of the misalignment of the openings in the frame and the termination fixture. The purpose of the analysis is to develop easy-to-use formulas, which would enable one to determine the minimum allowable length of the clamped portion of the fiber for the given misalignment.

2 Low Temperature Microbending of Dual-Coated Fibers

Let a dual-coated optical fiber (Fig. 1) be cooled down by the temperature Δt. The axial strains in the fiber and the coatings (components #1 and #2) can be expressed as follows:

$$\epsilon_0 = f_0 + \lambda_0 T_0, \quad \epsilon_1 = f_1 - \lambda_1 (T_0 - T_1), \quad \epsilon_2 - \lambda_2 T_1, \qquad (1)$$

where f_i, $i = 0, 1, 2$ are unrestricted thermal strains, with $i = 0$ referring to the glass fiber, λ_i, $i = 0, 1, 2$, are axial compliances of the fiber components, and T_i, $i = 0, 1$, are interfacial forces, with $i = 0$ referring to the interface between the

Contributed by the Applied Mechanics Division of THE AMERICAN SOCIETY OF MECHANICAL ENGINEERS for presentation at the Joint ASCE/ASME Applied Mechancis, Biomechanics, and Fluids Engineering Conference, San Diego, CA, July 9 to 12, 1989.

Discussion on this paper should be addressed to the Editorial Department, ASME, United Engineering Center, 345 East 47th Street, New York, N.Y. 10017, and will be accepted until two months after final publication of the paper itself in the JOURNAL OF APPLIED MECHANICS. Manuscript received by ASME Applied Mechanics Division, November 16, 1987; final revision, May 15, 1988.
Paper No. 89-APM-22.

Copyright © 1988 by ASME
Downloaded 03 May 2010 to 171.66.16.21. Redistribution subject to ASME license or copyright; see http://www.asme.org/terms/Terms_Use.cfm

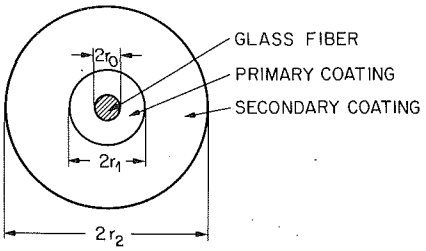

Fig. 1

fiber and the primary coating, and $i = 1$ referring to the interface between the coatings. For the glass fiber the unrestricted thermal strain is

$$f_0 = \alpha_0 \Delta t, \tag{2}$$

where α_0 is the coefficient of linear thermal expansion. For the coating materials, however, the coefficients of thermal expansion could be temperature dependent and therefore the formula

$$f_i = \int_0^{\Delta t} \alpha_i(t)dt, \quad i = 1,2 \tag{3}$$

should be used to evaluate the unrestricted thermal strains. The compliances λ_i can be determined by the obvious formulas:

$$\lambda_0 = \frac{1}{\pi E_0 r_0^2}, \quad \lambda_1 = \frac{1}{\pi E_1 (r_1^2 - r_0^2)}, \quad \lambda_2 = \frac{1}{\pi E_2 (r_2^2 - r_1^2)}, \tag{4}$$

where E_i, $i = 0, 1, 2$, are Young's moduli of the materials, and r_i, $i = 0, 1, 2$, are radii of the fiber and the coating layers.

The forces T_0 and T_1 can be determined on the basis of the conditions of strain compatibility $\epsilon_0 = \epsilon_1 = \epsilon_2$, which result in the following equations for the unknowns T_0 and T_1:

$$\begin{aligned}(\lambda_0 + \lambda_1)T_0 - \lambda_1 T_1 &= f_1 - f_0,\\ -\lambda_1 T_0 + (\lambda_1 + \lambda_2)T_1 &= f_2 - f_1.\end{aligned} \tag{5}$$

These equations yield:

$$T_0 = \frac{\lambda_1(f_2 - f_0) + \lambda_2(f_1 - f_2)}{\lambda_0\lambda_1 + \lambda_1\lambda_2 + \lambda_2\lambda_0}, \quad T_1 = \frac{\lambda_1(f_2 - f_0) + \lambda_0(f_2 - f_1)}{\lambda_0\lambda_1 + \lambda_1\lambda_2 + \lambda_2\lambda_0}. \tag{6}$$

Usually Young's modulus of the primary coating is significantly smaller than Young's modulus of the secondary, not to mention the fiber itself. Therefore the compliance λ_1 is substantially greater than the compliances λ_0 and λ_2. This enables one to simplify the formulas (6) as follows:

$$T_0 = T_1 = \frac{f_2 - f_0}{\lambda_0 + \lambda_2}. \tag{7}$$

Note that the strain f_0 is significantly smaller than the strain f_2 and needs not be taken into account.

The coefficient of thermal expansion and Young's modulus of the primary coating do not enter the expression (7) and therefore do not affect the thermally-induced forces. In addition, since the compressive force T_0 in the fiber is equal to the tensile force T_1 in the secondary coating, then the primary coating is subjected to shear only and does not experience any normal stresses at all. The formula (7) indicates also that it is the secondary coating which plays the major role, as far as the stresses are concerned. Hence, in order to minimize them one should use low expansion and, as far as possible, low modulus materials for the secondary coating and to keep its thickness sufficiently small.

Suppose now that the glass fiber has an initial local curvature

$$w_1(x) = w_0 \cos^2 \frac{\pi x}{l_d}, \tag{8}$$

where l_d is the length of the deflected area and w_0 is the maximum initial deflection. The equation of bending for an initially deflected glass fiber is as follows:

$$E_0 I_0 \frac{\partial^4 w}{\partial x^4} + T_0\left(\frac{\partial^2 w}{\partial x^2} + \frac{\partial^2 w_1}{\partial x^2}\right) + Kw = 0, \tag{9}$$

where $w(x)$ is the deflection function, $E_0 I_0 = \frac{\pi}{4} E_0 r_0^4$ is the flexural rigidity of the glass fiber, T_0 is the compressive force, and K is the spring constant of the elastic foundation. After substituting (8) in (9) we have:

$$E_0 I_0 \frac{\partial^4 w}{\partial x^4} + T_0 \frac{\partial^2 w}{\partial x^2} + Kw = \frac{2\pi^2}{l_d^2} w_0 T_0 \cos \frac{2\pi x}{l_d}. \tag{10}$$

We seek the solution to this equation in the form

$$w(x) = C \cos \frac{2\pi x}{l_d}. \tag{11}$$

Substituting (11) in (10) we obtain:

$$C = \frac{w_0}{2\left(\frac{T_c}{T_0} - 1\right)}, \tag{12}$$

where

$$T_c = \frac{4\pi^2 E_0 I_0}{l_d^2}\left(1 + \frac{l_d^4}{l_c^4}\right) \tag{13}$$

is the critical force and

$$l_c = 2\pi \sqrt[4]{\frac{E_0 I_0}{K}}. \tag{14}$$

As evident from (13), the minimum value of the force T_c takes place when $l_d = l_c$ and is as follows:

$$T_c = 2\sqrt{KE_0 I_0} = r_0^2 \sqrt{\pi K E_0}. \tag{15}$$

This formula coincides with the formula for the critical force in the case of an initially straight long uniform bar on an elastic foundation (Timoshenko, 1959). Hence, an initial curvature did not change the critical force value.

Using (12) we present the thermally induced deflections (11) as follows:

$$w(x) = \frac{w_0}{2\left(\frac{T_c}{T_0} - 1\right)} \cos \frac{2\pi x}{l_d}. \tag{16}$$

As evident from this formula, the initial curvature essentially affects the pre-buckling behavior of the fiber: The deflections in an initially deflected fiber increase gradually with an increase in the compressive force, while an initially straight fiber remains straight up to the very moment of buckling.

Note, that the "critical" length l_c of the initial curvature is twice as great as the "pitch" in the case of an initially straight fiber. This is thought to have an adverse effect on thermally-induced deflections, since longer initially curved areas are usually associated with greater initial deflections.

The total deflection is due to both the initial and the thermally induced deflections and is as follows:

$$w_t(x) = w_1(x) + w(x) = \frac{w_0}{2}\left(1 + \frac{1}{1 - \frac{T_0}{T_c}} \cos \frac{2\pi x}{l_d}\right). \tag{17}$$

We suppose that the maximum total curvature could be

Downloaded 03 May 2010 to 171.66.16.21. Redistribution subject to ASME license or copyright; see http://www.asme.org/terms/Terms_Use.cfm

Table 1

Input Data	Katsuyama	Yabuta	
		First Design	Second Design
Wire (Katsuyama) and fiber (Yabuta):			
• radius r_0, μm (mils)	75(2.953)	62.5(2.5)	62.5(2.5)
• Young modulus, E_0, MPa	162150	73830	73830
• coefficient of thermal expansion, α_0 1/°C	16.0×10^{-6}	0.5×10^{-6}	0.5×10^{-6}
Primary coating (silicon)			
• radius r_1, μm (mils)	175(6.890)	250(9.84)	100(3.94)
• Young's modulus, E_1, MPa (at −40°C)	18.2	18.2	18.2
• Posson's ratio, ν_1	0.5	0.5	0.5
Secondary coating (nylon)			
• radius r_2, μm (mils)	600(23.622)	471(18.54)	448(17.64)
• Young's modulus, E_2, MPa (at −40°C)	2139	2139	2139
• coefficient of thermal expansion, α_2, 1/°C	100×10^{-6}	100×10^{-6}	100×10^{-6}
Buckling temperature, t_b,°C	-70°	—	—
Calculated Data			
Spring constant, K, MPa	48.4	15.1	240.0
Critical force, T_c, N	27.9	7.55	30.1
Compressive force per degree, $T_0/\Delta t=\frac{\alpha_2-\alpha_0}{\lambda}$, N/°C	0.105	0.050	0.054
Critical temperature diff. $\Delta t=T_c\div(T_0/\Delta t)$, °C	266	152	558
Reference (zero stress) temperature, $t_r=t_b+\Delta t$,°C	196	(196)	(196)
Temperature diff. at -50°C, Δt_{50},°C	246	(246)	(246)
Compressive force at -50°C, T_{50}, N	25.8	12.2	13.2
Critical spring constant, $K_*=T_{50}^2/E_0I_0$, MPa	166	159	186
Spring constant/critical spring constant ratio, K/K_*	0.2923	(0.0949)	(1.288)
Total/initial curvature ratio, $\kappa/\kappa_0=(1-T_{50}/T_c)^{-1}$	13.311	—	(1.788)
Total/minimum curvature ratio κ/κ_*	3.5955	—	(1.014)
Pitch of an initially straight fiber, s, μm	1686	1570	787
Critical length of an initially deflected area, l_c, μm	3378	3139	1572

chosen as a suitable criterion of added transmission losses, associated with microbending. The expression for this curvature can be obtained from (17) by differentiation:

$$\kappa=\frac{\kappa_0}{1-\frac{T_0}{T_c}}, \tag{18}$$

where

$$\kappa_0=\frac{2\pi w_0}{l_d^2} \tag{19}$$

is the initial curvature. The formula (18) indicates that if the initial curvature κ_0 is not zero, the total curvature gradually increases with an increase in the compressive force T_0. This could be responsible for the observed added optical losses at moderately low temperatures, well above the temperature of buckling. At the same time, it should be emphasized that the value of the buckling force has a strong impact on thermally-induced curvatures even for relatively small temperature differentials. For this reason thicker glass fibers (great E_0I_0 values) with stiffer coatings (great K values) are expected to have smaller transmission losses because of microbending.

It is natural to assume that a fiber, subjected to compression at low temperature conditions, behaves like a "narrow-band" filter, which amplifies primarily the initial local curvatures whose lengths are equal to the critical length l_c. With this supposition the formula (19) yields:

$$\kappa_0=\frac{w_0}{2}\frac{\sqrt{K}}{E_0I_0}, \tag{20}$$

and the formula (18) can be presented as follows:

$$\kappa=\kappa_*\frac{K/K_*}{2\sqrt{K/K_*}-1}. \tag{21}$$

Downloaded 03 May 2010 to 171.66.16.21. Redistribution subject to ASME license or copyright; see http://www.asme.org/terms/Terms_Use.cfm

Here

$$\kappa_* = \frac{w_0 T_0}{E_0 I_0}, \quad K_* = \frac{T_0^2}{E_0 I_0}. \tag{22}$$

As evident from the formula (20), greater spring constant values result in greater initial curvatures, thereby increasing the total curvature as well. On the other hand, as one could see from (15), greater spring constant values result in greater critical force. This, in accordance with (18), reduces the total curvature. Therefore there must exist a spring constant value K which makes the total curvature κ minimal. Indeed, the analysis of the formula (21) indicates that this minimum total curvature is equal to κ_* and takes place when the spring constant K is equal to K_* (Fig. 2). In the region $K > K_*$ the curvature κ gradually increases with an increase in K, while for $K < K_*$ this curvature increases very rapidly, and tends to infinity, when the K/K_* ratio approaches 0.25. In our analysis this corresponds to buckling conditions.

Hence, in order to minimize the total curvatures, one should design the coating system in such a way, that the spring constant at low temperature conditions would be close to the K_* value. Because of the inevitable uncertainties in predicting both the K and the K_* values, the K value should be preferably somewhat greater than K_*, since in the region $K < K_*$ the curvatures are very sensitive to the variations in K.

We compare our theoretical results with experimental data of Katsuyama (1980) and Yabuta (1983) discussed in detail by Lenahan (1985). Silicone/nylon coating systems were employed in the tested designs. The input and the calculated data are shown in Table 1. The spring constant K was evaluated by the Vangheluwe formula (1984) which, for the case in question, when Poisson's ratio for the primary coating material is close to 0.5, can be simplified as follows:

$$K = \frac{4\pi E_1}{3\left(\ln \frac{r_1}{r_0} - \frac{r_1^2 - r_0^2}{r_1^2 + r_0^2}\right)}. \tag{23}$$

One of the designs of Yabuta, with a relatively thick primary ($r_1 = 250$ μm), had a substantial added loss, while another design, with a thinner primary ($r_1 = 100$ μ), had a negligible loss, even though the secondary coating in this case had a somewhat greater cross-sectional area. Buckling in the Katsuyama tests occurred at -70°C. The buckling temperature of Yabuta fibers was not reported.

Using the buckling temperature value $t_C = -70$°C measured in the Katsuyama tests, we conclude that the reference (zero stress) temperature in these tests was 196°C. Note that this temperature could be different from the actual application temperature for the coatings because of the additional, temperature-differential-independent stresses, caused by the polymerization shrinkage resulting in higher stresses, and by stress relaxation, leading to lower stresses.

Assuming that the lowest temperature possible in operation is, say, -50°C, we determine the compressive force and the critical spring constant at this temperature. In the Katsuyama design the calculated ratio of the actual spring constant to the above initial value is 0.292, which is well below the optimal K/K_* ratio that is equal to unity. Therefore the maximum total curvature in this design is about 3.6 times greater than the minimum curvature, and the added transmission losses are essentially greater than necessary.

In order to evaluate the designs of Yabuta where the buckling temperature was not reported, we assume that the reference temperature in these designs was the same as for the Katsuyama wire. This assumption results in a very small critical temperature differential in the case of the first Yabuta design ($\Delta t = 152$°C), and in a very large temperature differential for the second design, with a thinner primary coating ($\Delta t = 558$°C). Because of this, buckling occurred in the first Yabuta design at the temperatures, which were well above -50°C, while the calculated buckling temperature for the design with a thinner primary is -362°C. Obviously buckling could never occur in this design. It should be emphasized that the second design of Yabuta is in effect an optimal one, since the actual value of the spring constant in this design is close and is somewhat greater than its critical value. Because of this, the actual total curvature at low temperatures practically coincides with the theoretical minimum curvature. It is noteworthy that, as evident from the Table 1 data, pitch does not seem to be an acceptable criterion of the added transmission losses.

As follows from the above analysis, in order to avoid appreciable temperature induced curvatures one should keep the spring constant at a sufficiently high level. This could be achieved by the application of a relatively thin and/or not very compliant primary layer. Obviously, such a primary coating will be relatively stiff in the lateral direction as well. Could this have an adverse effect on the lateral pressures in the glass fiber?

To evaluate these pressures we proceed from the following Lamé formula for the radial displacements in a flat disk subjected to internal p_0 and external p_1 pressures (Timoshenko, 1959):

$$u = \frac{1+\nu}{E} \frac{1}{1-\gamma^2}\left[(1-2\nu)(p_0\gamma^2 - p_1)r + \frac{r_0^2}{r}(p_1 - p_0)\right]. \tag{24}$$

Here r is the current radius and $\gamma = r_0/r_1$. The conditions of the displacement compatibility require that the thermally induced interfacial radial displacements for the glass fiber be equal to the inner displacements of the primary coating, and that the outer interfacial displacements of this coating be equal to the inner displacements of the secondary coating. This results in the following equations for the pressures:

$$c_{11}p_0 + c_{12}p_1 = f_1 - f_0, \quad c_{21}p_0 + c_{22}p_1 = f_2 - f_1, \tag{25}$$

where

$$\left.\begin{aligned} c_{11} &= \frac{(1+\nu_0)(1-2\nu_0)}{E_0} \\ &\quad + \frac{1+\nu_1}{E_1}\frac{(1-2\nu_1)\gamma^2 - 1}{1-\gamma^2} \cong -\frac{1+\nu_1}{E_1}\frac{1}{1-\gamma^2}, \\ c_{12} &= \frac{2\nu_1(1+\nu_1)}{E_1}\frac{1}{1-\gamma^2}, \quad c_{21} = -\frac{2\nu_1(1+\nu_1)}{E_1}\frac{\gamma^2}{1-\gamma^2}, \\ c_{22} &= \frac{1+\nu_1}{E_1}\frac{1-2\nu_1-\gamma^2}{1-\gamma^2} \\ &\quad - \frac{1+\nu_2}{E_2}\frac{(1-2\nu_2)\frac{r_1^2}{r_2^2} - 1}{1-\frac{r_1^2}{r_2^2}} \cong -\frac{1+\nu_1}{E_1}\frac{\gamma^2}{1-\gamma^2} \end{aligned}\right\} \tag{26}$$

The simplifications for the coefficients c_{11} and c_{22} are due to the fact that Young's modulus E_1 of the primary coating material is significantly smaller than Young's moduli E_0 and E_2, and that Poisson's ratio ν_1 is close to 0.5. Then the equations (25) yield:

$$\left.\begin{aligned} p_0 &= -\frac{E_1}{2(1+\nu_1)}(1-\gamma^2)\left(f_1 - f_0 + \frac{f_2 - f_1}{\gamma^2}\right) \\ p_1 &= \frac{E_1}{2(1+\nu_1)}(1-\gamma^2)\left(f_1 - f_0 - \frac{f_2 - f_1}{\gamma^2}\right) \end{aligned}\right\}. \tag{27}$$

Downloaded 03 May 2010 to 171.66.16.21. Redistribution subject to ASME license or copyright; see http://www.asme.org/terms/Terms_Use.cfm

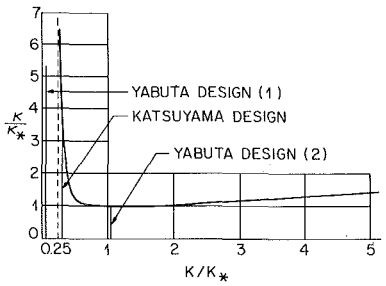

Fig. 2

The first of these formulas indicates that the pressure on the glass fiber could be made very small, if the ratio γ is related to the mismatch strains as follows:

$$\gamma=\sqrt{\frac{f_1-f_2}{f_1-f_0}}\cong\sqrt{1-\frac{f_2}{f_1}}\cong\sqrt{1-\frac{\alpha_2}{\alpha_1}}\,. \tag{28}$$

Then the pressure p_1 is expressed by the formula:

$$p_1=\frac{E_1}{1+\nu_1}\,(f_2-f_0)\cong\frac{E_1}{1+\nu_1}\,f_2\cong\frac{E_1}{1+\nu_1}\,\alpha_2\Delta t. \tag{29}$$

For the examples examined above, assuming $\alpha_1 = 300 \times 10^{-6}$ 1°C we obtain $\gamma = 0.816$. The actual ratios of the wire (fiber) radius to the radius of the primary coating are $\gamma = 0.429$ in the case of Katsuyama design, $\gamma = 0.250$ for the first design of Yabuta, and $\gamma = 0.625$ for the second design of Yabuta. Hence, the latter design is the best and the first design of Yabuta is the worst not only from the standpoint of the axial stresses, but from the standpoint of the lateral pressure as well.

As follows from the above analysis, the expected performance of an optical fiber at low temperatures can be optimized, if the coatings are designed in such a way that the condition (28) and the second formula in (22), are fulfilled.

The optimal coating thicknesses can be determined for the given materials on the basis of the following two step procedure. At the first step we assume that the primary coating is significantly more compliant than the secondary coating, and therefore the simplified formulas (7) and (32) can be used to evaluate the compressive force and the spring constant. This results in the following formula for the ratio $\gamma_2 = r_2/r_0$:

$$\gamma_2=\frac{E_0/E_2}{\sqrt{(f_2-f_0)\sqrt{\dfrac{E_0}{E_1}}\,\eta(\gamma_1)-1}}+\gamma_1{}^2, \tag{30}$$

where $\gamma_1 = \gamma_1/r_0$ and

$$\eta(\gamma_1)=\frac{(1+\nu_1)[(3-4\gamma_1)^2\ln\gamma_1-(\gamma_1{}^2-1)/(\gamma_1{}^2+1)]}{(1-\gamma_1)(3-4\gamma_1)}\,.$$

Thus, at the first step one has to calculate the strains f_1 and f_2, and then the ratios $\gamma_1 = 1/\gamma$ and γ_2 by the formulas (28) and (30), respectively. Obviously, the corresponding coating thicknesses are

$$\tau_1=r_1-r_0=r_0(\gamma_1-1),\quad \tau_2=r_2-r_1=r_0(\gamma_2-\gamma_1). \tag{31}$$

At the second step the more accurate formulas (6) and (35) should be used. If the spring constant calculated on the basis of the formula (35) is somewhat greater than the critical value given by the second formula in (22), then the selected thicknesses are satisfactory, otherwise the actual spring constant must be increased. This can be done, for instance, by reducing the thickness of the primary coating.

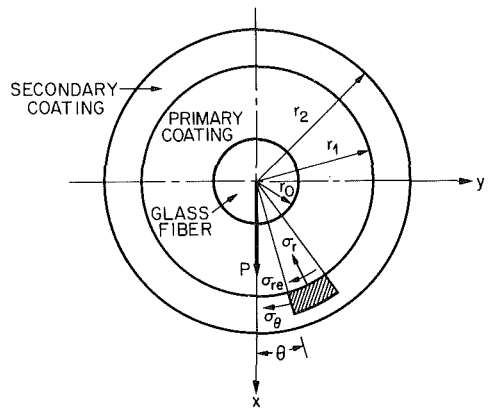

Fig. 3

3 Spring Constant

In this section we obtain an exact formula for the spring constant in dual-coated optical fibers. This formula is a generalization of Vangheluwe's solution for the case when the finite compliance of the secondary coating must be taken into consideration. Our approach is also based on a two-dimensional theory of elasticity (Timoshenko, 1959) but is different from the Muskhelishvili method (1977) applied by Vangheluwe.

We proceed from the following general formulas for the stresses and displacements in a circular ring (Fig. 3):

$$\left.\begin{aligned}
\sigma_r&=\left[\frac{3-2\nu}{4(1-\nu)}\,ar^{-1}+2br-2cr^{-3}\right]\cos\theta\\
\sigma_\theta&=\left[-\frac{1-2\nu}{4(1-\nu)}\,ar^{-1}+6br+2cr^{-3}\right]\cos\theta\\
\tau_{r\theta}&=\left[\frac{1-2\nu}{4(1-\nu)}\,ar^{-1}+2br-2cr^{-3}\right]\sin\theta
\end{aligned}\right\}, \tag{32}$$

$$\left.\begin{aligned}
u&=\frac{1+\nu}{E}\left[\frac{3-4\nu}{4(1-\nu)}\,a\ln r+(1-4\nu)br^2+cr^{-2}\right]\cos\theta\\
&\quad+A\cos\theta-B\sin\theta\\
v&=\frac{1+\nu}{E}\left[-\frac{1}{4(1-\nu)}a-\frac{3-4\nu}{4(1-\nu)}\,a\ln r+(5-4\nu)br^2\right.\\
&\quad\left.+cr^{-2}\right]\sin\theta-A\sin\theta-B\cos\theta+Cr
\end{aligned}\right\}. \tag{33}$$

If the secondary coating can be assumed absolutely rigid, then the spring constant, defined as the ratio of the applied force to the corresponding lateral displacement of the fiber in the soft primary layer, can be calculated by the Vangheluwe (1984) formula

$$K=-\frac{4\pi E(1-\nu_1)(3-4\nu_1)(1+\gamma^2)}{(1+\nu_1)[1-\gamma^2+(3-4\nu_1)^2(1+\gamma^2)\ln\gamma]}\,. \tag{34}$$

However, when the finite rigidity of the secondary coating is important, the boundary problem becomes more complicated.

To obtain a solution to this problem we write down the formulas (32) and (33) for the glass fiber, the primary and the secondary coatings, and use the compatibility conditions, which require that the normal stresses and the displacements

Downloaded 03 May 2010 to 171.66.16.21. Redistribution subject to ASME license or copyright; see http://www.asme.org/terms/Terms_Use.cfm

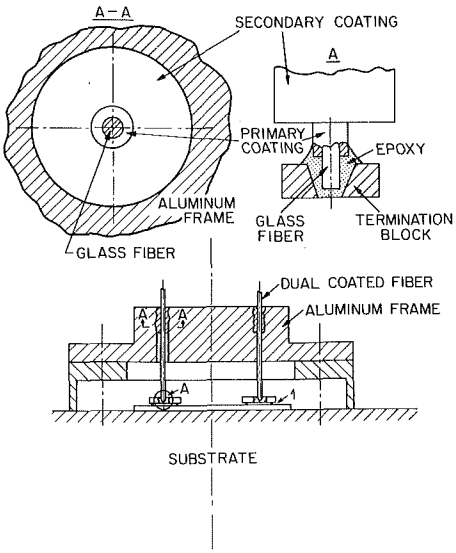

Fig. 4

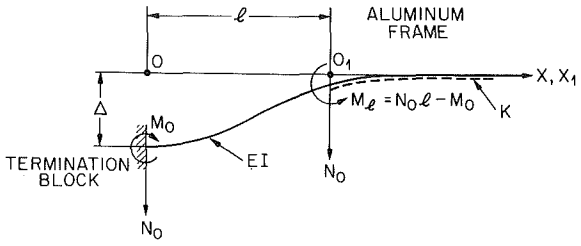

Fig. 5

in the interfaces be the same for the connected components. This results in the following formula for the spring constant:

$$K=\frac{4\pi E_1E_2(1-\nu_1)(1-\nu_2)}{C_{11}\beta_1-C_{21}\beta_2-C_{31}}, \tag{35}$$

where:

$$\left.\begin{aligned}
C_{11}&=r_2^2-r_0^2-\nu_1(r_2^2-r_1^2)-\nu_2(r_1^2-r_0^2),\\
C_{21}&=E_1(1-\nu_1)(1+\nu_2)(r_2^2-r_1^2)\\
&\quad+E_2(1+\nu_1)(1-\nu_2)(r_1^2-r_0^2),\\
C_{31}&=E_1(1-\nu_1)(1+\nu_2)(3-4\nu_2)\ln\frac{r_1}{r_2}\\
&\quad+E_2(1+\nu_1)(1-\nu_2)(3-4\nu_1)\ln\frac{r_0}{r_1},\\
\beta_1&=\frac{C_{23}C_{32}-C_{22}C_{33}}{C_{12}C_{23}+C_{22}C_{13}},\quad \beta_2=\frac{C_{12}C_{33}+C_{13}C_{32}}{C_{12}C_{23}+C_{22}C_{13}},\\
C_{12}&=8(1-\nu_1)(1-\nu_2)[r_1^4+(3-4\nu_1)r_0^4],\\
C_{13}&=8(1-\nu_1)(1-\nu_2)[r_1^4+(3-4\nu_2)r_2^4],\\
C_{22}&=8E_2(1-\nu_1^2)(1-\nu_2)(3-4\nu_1)(r_1^4-r_0^4),\\
C_{23}&=8E_1(1-\nu_1)(1-\nu_2^2)(3-4\nu_2)(r_2^4-r_1^4),\\
C_{32}&=8E_2(1-\nu_1^2)(1-\nu_2)(r_1^2-r_0^2),\\
C_{33}&=8E_1(1-\nu_1)(1-\nu_2^2)(r_2^2-r_1^2).
\end{aligned}\right\} \tag{36}$$

In a special case of a rigid secondary ($r_1 = r_2$) the formula (35) coincides with (34).

If, for instance, a Desolite/Borden coating system is applied ($r_0 = 63.5$ μm, $r_1 = 101.6$ μm, $r_2 = 444.5$ μm, $E_1 = 63.1$ MPa, $\nu_1 = 0.495$, $E_2 = 355.2$ MPa, $\nu_2 = 0.30$), then the calculated spring constant value is $K = 3050$ MPa. If the Vangheluwe formula were used, then the calculated K value would be $K = 5381$ MPa, i.e., 1.76 times greater. Note, that the K value determined on the basis of the formula (35) is greater than Young's modulus E_1 of the primary coating material by the factor of 48.3, while the Vangheluwe formula results in a K value, which is 85.2 times greater than above Young's modulus. Therefore the buckling force, predicted by using Vangheluwe's formula for the spring constant, is about 33 percent greater than its actual value.

Reexamine now the example given in the original Vangheluwe's paper, considering the effect of the finite rigidity of the secondary coating. Assuming, for instance, that it is fabricated of nylon, we use the following input data: $r_0 = 63.5$ μm, $r_1 = 127.0$ μm, $r_2 = 444.5$ μm, $E_1 = 2.00$ MPa, $\nu_1 = 0.5$, $E_2 = 2139$ MPa, $\nu_2 = 0.33$. Then the calculated spring constant is $K = 88.17$ MPa $= 44\,E_1$. The Vangheluwe formula predicts $K = 90.25$ MPa $= 45\,E_1$, so that in this case the error is only 2 percent.

Thus, the formula obtained by Vangheluwe assuming absolutely rigid secondary can be used for the evaluation of spring constant only for sufficiently compliant (thick and low modulus) primary coatings. For moderately compliant primary coatings, especially when the secondary coatings are not very stiff, Vangheluwe's solution results in an overestimation of the spring constant and, hence, in the overestimation of the critical force as well. In this case the more general formula (35) should be applied.

4 Strength and Buckling of a Clamped Fiber

Let the lower end of a dual-coated fiber be adhesively bonded in a pyramid-shaped aperture of a block, attached to a substrate, while its upper part is clamped in an aluminum frame (Fig. 4). We evaluate the stresses which arise in the free (nonclamped) portion of the fiber, when the structure is cooled down by the temperature Δt. We use the following conservative assumptions:

- The fiber does not affect the displacements in the aluminum frame, whose stiffness is supposed to be significantly greater than that of the fiber;
- The buffering effect of the coating is due only to that portion of the coating material, which is in the direct contact with the frame;
- The effect of the thermal contraction of the coating material is not taken into account. As has been shown in Section 2 for a similar situation, this is justified, as long as Young's moduli of the coating materials are significantly smaller, compared to Young's moduli of the aluminum and the glass.

With the first of these assumptions, the vertical displacement in the cross-section 1-1 of the frame is as follows:

$$\Delta l_a=\alpha_a l_a\Delta t, \tag{37}$$

where α_a is the coefficient of thermal expansion for the aluminum, l_a is the height of the cross-section in question above the substrate, and Δt is the temperature change.

If the force T acting on the fiber were known, then the axial displacement of the fiber tip, assuming that no buckling occurs, could be evaluated by the formula:

$$\Delta l_0=\alpha_0 l_0\Delta t+\frac{Tl_0}{\pi E_0 r_0^2}, \tag{38}$$

Downloaded 03 May 2010 to 171.66.16.21. Redistribution subject to ASME license or copyright; see http://www.asme.org/terms/Terms_Use.cfm

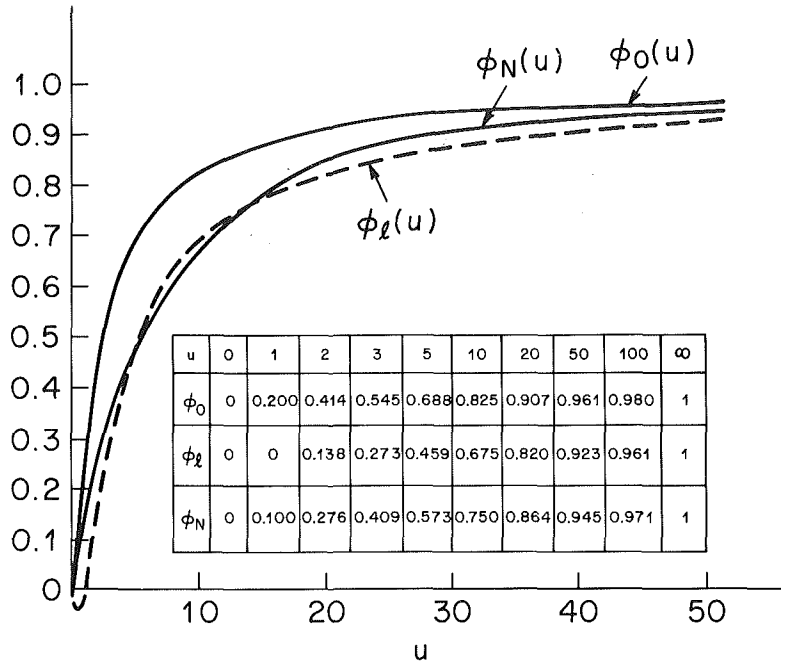

u	0	1	2	3	5	10	20	50	100	∞
ϕ_0	0	0.200	0.414	0.545	0.688	0.825	0.907	0.961	0.980	1
ϕ_ℓ	0	0	0.138	0.273	0.459	0.675	0.820	0.923	0.961	1
ϕ_N	0	0.100	0.276	0.409	0.573	0.750	0.864	0.945	0.971	1

Fig. 6

where α_0 is the coefficient of thermal expansion (contraction) for the glass, l_0 is the height of the cross-section 1-1 above the block, E_0 is Young's modulus of glass, and r_0 is the glass fiber radius. The condition of the compatibility of displacements requires that the displacements Δl_a and Δl_0 are related as follows:

$$\Delta l_a = \Delta l_0 + \xi T, \tag{39}$$

where ξ is the coefficient of compliance. For a dual-coated fiber this coefficient can be calculated by the formula (whose derivation we do not present here):

$$\xi = \frac{1}{\pi l_c}\left(\frac{1+\nu_1}{E_1}\ln\frac{r_1}{r_0} + \frac{1+\nu_2}{E_2}\ln\frac{r_2}{r_1}\right). \tag{40}$$

Here, l_c is the length of the clamped portion. The formula (39) simply states that because of the axial compliance of the coating, the thermal displacements of the aluminum frame and those of the glass fiber differ by a value, which is proportional to the magnitude of the applied force.

After substituting (37) and (38) in the condition (39) we obtain the following formula for the thermally-induced force T:

$$T = \frac{\alpha_a l_a - \alpha_0 l_0}{\dfrac{l_0}{\pi E_0 r_0^2} + \xi}\,\Delta t. \tag{41}$$

Then the stress acting over the cross-section of the glass fiber is

$$\sigma_0 = \frac{T}{\pi r_0^2} = \frac{\alpha_a l_a - \alpha_0 l_0}{\dfrac{l_0}{E_0} + \pi\xi r_0^2}\,\Delta t. \tag{42}$$

As an example, we calculate the stress in a glass fiber at low (−40°C) and elevated (120°C) temperatures, assuming that the structure is fabricated at the room temperature and that the stresses at this temperature are zero. We use the following input data: $r_0 = 63.5\ \mu$m, $E_1 = 2.07$ MPa at −40°C, $E_1 = 1.03$ MPa at 120°C, $\nu_1 = 0.5$; $r_2 = 444.5\ \mu$m, $E_2 = 2898$ MPa at −40°C, $E_2 = 1.9$ MPa at 120°C, $\nu_2 = 0.45$; $l_a = 6.1\ \mu$m, $\alpha_a = 23.6 \times 10^{-6}$ 1°C. With this input data we find that the compressive force at −40°C is $T = 0.131$ N and the tensile force at 120°C is $T = 0.052$ N. The corresponding stresses in the glass fiber are $\sigma_0 = 10.3$ MPa and $\sigma_0 = 4.1$ MPa, respectively. These stresses are considerably smaller than the ultimate strength of glass both in compression and in tension.

As far as the elastic stability of the fiber is concerned, we consider the following two potential buckling modes:

(1) buckling of the dual-coated fiber as a whole, and

(2) microbending of the glass fiber within the soft primary coating.

In the first case we treat the fiber as a clamped-clamped bar, so that the critical (buckling) force is

$$T_c = \frac{4\pi^2 EI}{l_0^2}, \tag{43}$$

where

$$EI = \frac{\pi}{4}\left[E_0 r_0^4 + E_1(r_1^4 - r_0^4) + E_2(r_2^4 - r_1^4)\right] \tag{44}$$

is the flexural rigidity of the dual-coated fiber.

In the second case we treat the glass fiber as a simply-supported bar on an elastic foundation, provided by the coating materials. Then the critical force is determined by the formula (Timoshenko, 1961):

$$T_c = \frac{\pi^2 E_0 I_0}{l_0^2}\left(i^2 + \frac{i_*^4}{i^2}\right) = \frac{\pi^3 E_0 r_0^4}{4 l_0^2}\left(i^2 + \frac{i_*^4}{i^2}\right), \tag{45}$$

where

$$i_*^2 = \left(\frac{l_0}{\pi}\right)^2\sqrt{\frac{K}{E_0 I_0}} = \left(\frac{l_0}{\pi r_0}\right)^2\sqrt{\frac{4K}{\pi E_0}}, \tag{46}$$

and the relationship between the number i of the "half-waves" and the i_* value is as follows:

$$(i-1)i < i_*^2 < i(i+1). \tag{47}$$

Hence, $i = 1$ when $i_*^2 < 2$, $i = 2$ when $2 < i_*^2 < 6$, $i = 3$ when $6 < i_*^2 < 12$, and so on. When the unclamped (free) portion of the fiber within the frame is long, and the number i of "half-waves" in a buckled glass fiber is considerably

Downloaded 03 May 2010 to 171.66.16.21. Redistribution subject to ASME license or copyright; see http://www.asme.org/terms/Terms_Use.cfm

greater than unity, the unequality (47) yields $i_* = i$, and the formula (45) reduces to the formula (15).

Obviously, in order to avoid buckling, one has to make sure that both the critical forces evaluated by the formulas (43) and (45) are smaller than the actual compressive force.

Using the same input data as in the previous example, we find $T_c = 136.6$ N. The spring constant in the formula (46) can be calculated by using the formula (23), which results in the following K value: $K = 93.1$ MPa. Then the formula (46) yields: $i_*^2 = 26.0$. Utilizing the unequality (47), we have: $i = 5$, and the formula (45) yields: $T_c = 99.7$ N. Since both the calculated critical force values are significantly greater than the actual compressive force, no buckling can occur.

5 Stresses Due to the End Off-Set

Let the ends of the internal portion of a fiber, located within an aluminum frame, have an off-set due to the misalignment of the opening in the frame and the aperture in the lower block as schematically shown in Fig. 5.

The equation of bending of the "free" portion $0 \le x \le l$ of the fiber is as follows:

$$E_0 I_0 \frac{\partial^2 w}{\partial x^2} = -M_0 + N_0 x, \tag{48}$$

where M_0 and N_0 are the bending moment and the shearing force, respectively, at the cross-section $x = 0$, and $E_0 I_0$ is the flexural rigidity of the glass fiber. From (48) we obtain the following equation for the angles of rotation:

$$\frac{\partial w}{\partial x} = -\frac{M_0}{E_0 I_0} x + \frac{N_0}{2E_0 I_0} x^2. \tag{49}$$

The next integration yields:

$$w(x) = -\frac{M_0}{2E_0 I_0} x^2 + \frac{N_0}{6E_0 I_0} x^3 + \Delta, \tag{50}$$

where $w(0) = \Delta$ is the end off-set. The equations (49) and (50) result in the following formulas for the rotation angle and the lateral displacement at the end $x = l$:

$$\left.\begin{aligned} w_l' &= -\frac{M_0 l}{E_0 I_0} + \frac{N_0 l^2}{2E_0 I_0} \\ w_l &= \frac{M_0 l^2}{2E_0 I_0} + \frac{N_0 l^3}{2E_0 I_0} + \Delta \end{aligned}\right\}. \tag{51}$$

We examine now the portion $x > l$. When evaluating the bending performance of this portion of the fiber, we treat the latter as an infinitely long beam on an elastic foundation. This beam is loaded at its end by a concentrated force $N_l = N_0$ and a bending moment $M_l = N_0 l - M_0$. The differential equation of bending is as follows:

$$E_0 I_0 \frac{\partial^4 w}{\partial x_1^4} + Kw = 0, \tag{52}$$

where the spring constant of the foundation can be determined on the basis of the formulas (34) or (35). The equation (52) has the following solution:

$$w(x_1) = e^{-\alpha x_1}(C_1 \cos\alpha x_1 + C_2 \sin\alpha x_1), \tag{53}$$

where $x_1 = x - l$, and the parameter α is expressed by the formula:

$$\alpha = \sqrt[4]{\frac{K}{4E_0 I_0}} = \frac{l}{r_0}\sqrt[4]{\frac{K}{\pi E_0}}. \tag{54}$$

The two other constants of integration are put equal to zero to make the deflections $w(x_1)$ fade with an increase in x_1. By substituting (51) into the boundary conditions

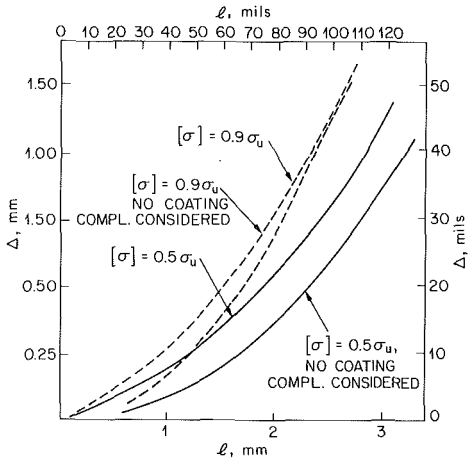

Fig. 7

$$w''(0) = \frac{M_l}{E_0 I_0}, \quad w'''(0) = \frac{N_l}{E_0 I_0} \tag{55}$$

we obtain the following formulas for the constants of integration:

$$C_1 = \frac{N_l + \alpha M_l}{2\alpha^3 E_0 I_0}, \quad C_2 = -\frac{M_l}{2\alpha^2 E_0 I_0}. \tag{56}$$

Using these formulas and having in mind that $N_l = N_0$ and $M_l = N_0 l - M_0$, we obtain the following equations for the angle of rotation and the deflection at $x_1 = 0$:

$$w'(0) = \frac{2\alpha M_0 - (1+2u)N_0}{2\alpha^3 E_0 I_0}, \quad w(0) = -\frac{\alpha M_0 - (1+u)N_0}{2\alpha^3 E_0 I_0}, \tag{57}$$

where

$$u = \alpha l = \frac{l}{r_0}\sqrt[4]{\frac{K}{\pi E_0}} \tag{58}$$

is a dimensionless parameter of bending.

The conditions of compatibility for the angles of rotation and the displacements require that $w_l' = w'(0)$ and $w_l = w(0)$. This results in the following equations for the unknowns M_0 and N_0:

$$\left.\begin{aligned} -3u(1-u^2)M_0 + (3+3u-u^3)lN_0 &= \frac{6\Delta E_0 I_0}{l^2} u^3 \\ 2uM_0 - (1+u)lN_0 &= 0 \end{aligned}\right\}. \tag{59}$$

By solving these equations we find:

$$M_0 = \frac{6\Delta E_0 I_0}{l^2}\Phi_0(u), \quad N_0 = \frac{12\Delta E_0 I_0}{l^3}\Phi_N(u), \tag{60}$$

where the functions

$$\Phi_0(u) = \frac{(1+u)u^2}{u^3+3u^2+3u+3}, \quad \Phi_N(u) = \frac{u^3}{u^3+3u^2+3u+3} \tag{61}$$

reflect the effect of the finite stiffness of the support at $x = l$. The functions (61) tend to unity when the spring constant K (and the u value) tends to infinity. The moment M_c at the end $x = l$ is

$$M_c = N_0 l - M_0 = \frac{6\Delta E_0 I_0}{C^2}\Phi_l(u), \tag{62}$$

where

$$\Phi_l(u) = \frac{(1-u)u^2}{u^3+3u^2+3u+3}. \tag{63}$$

Downloaded 03 May 2010 to 171.66.16.21. Redistribution subject to ASME license or copyright; see http://www.asme.org/terms/Terms_Use.cfm

The functions $\Phi_0(u)$, $\Phi_l(u)$ and $\Phi_N(u)$ are plotted in Fig. 6.

As evident from the formulas (61) and (63), and Fig. 6, the maximum bending moment occurs at the fiber end $x = 0$. The stress due to this moment is as follows:

$$\sigma_0 = \frac{6E_0\Delta r_0}{l^2}\Phi_0(u) = \frac{6}{\sqrt{\pi}}\frac{\Delta}{r_0}\sqrt{KE_0}\Psi_0(u), \tag{64}$$

where

$$\Psi_0(u) = \frac{\Phi_0(u)}{u^2} = \frac{1+u}{u^3+3u^2+3u+3}. \tag{65}$$

Equation (64) results in the following formula for the allowable misalignment:

$$\Delta = \frac{\sqrt{\pi}}{6}\frac{[\sigma]}{\sqrt{KE_0}}\frac{r_0}{\Psi_0(u)}, \tag{66}$$

where $[\sigma]$ is the allowable bending stress in the glass fiber. If we assume that the $[\sigma]$ value is 50 percent of the ultimate tensile stress $\sigma_u = 5520$ MPa (see, Blyler 1987) for the glass fiber material, i.e., $[\sigma] = 2760$ MPa, and calculate the spring constant value for $r_1/r_0 = 1.8$ with $E_1 = 2.1$ MPa (the calculated K value is $K = 145.7$ MPa), then the formula (66) yields:

$$\Delta = \frac{0.6214}{\Psi_0(u)} \text{ mils},$$

where $u = 0.06331$, and l is also in mils. The calculated Δ values are plotted in Fig. 7 (curve 1). When the misalignment is as great as two glass fiber diameters, i.e., equals to 10 mils (0.25 mm), then the clamped length of the fiber should not be smaller than 47 mils (1.2 mm). Obviously, the increase in the allowable stress results in smaller fiber lengths for the given misalignment. When this strength becomes 90 percent of the ultimate tensile strength value, then the minimum allowable lengths decrease by a factor of 1.4 (curve 2). In this case the minimum allowable fiber length for a 10 mil (0.25 mm) misalignment is only 37 mils (0.94 mm). If the finite stiffness of the fiber coating were not considered, then the equation (62) would result in the following formula for the minimum length:

$$l = \sqrt{6\frac{E_0}{[\sigma]}\Delta r_0}. \tag{67}$$

This relationship is plotted in Fig. 7 for the cases $[\sigma] = 0.5\,\sigma_u$ (curve 3) and $[\sigma] = 0.9\,\sigma_u$ (curve 4). Thus, consideration of the favorable effect due to the finite stiffness of the fiber coating has resulted for the fiber in question in about 25 percent smaller minimum length of the fiber.

6 Conclusion

Simple and easy-to-use analytical models have been developed to understand and evaluate the mechanical performance of dual-coated optical fibers. These models can be utilized for stress/deflection evaluation and rational physical design of dual-coated fibers and interconnections, operated, shipped or stored at low temperatures. The developed formulas can also be used as guidance for experimental planning. All the calculations can be done manually and no computerization is necessary. While the overwhelming majority of studies dealing with mechanical performance of optical fibers are experimental, it is the author's belief that a theoretical and, in particular, an analytical approach must always be considered as an important part of any stress-related analysis in this area of engineering.

References

Blyler, Jr., L. L., 1987, private communications.

Blyler, Jr., L. L., et al., 1982, "A New Dual-Coating System for Optical Fibers," *Eighth European Conference on Optical Communications*, Cannes, France.

Blyler, Jr., L. L., et al., 1983, "Buckling of Optical Fibers Within Elastomers Used in an Embedded-Core Cable Structure," *Int. Wire Cable Symposium*.

Gardner, W. B., 1975, "Microbending Loss in Optical Fibers," *Bell System Techn. Journal*, Vol. 54, No. 2, Feb.

Gloge, D., 1972, "Bending Loss in Multimode Fibers With Graded and Ungraded Core Index," *Applied Opt.*, Vol. 11, No. 11, Nov.

Gloge, D., 1975, "Optical Fiber Packaging and its Influence on Fiber Straightness and Loss," *Bell System Techn. Journal*, Vol. 54, No. 2, Feb.

Hanson, E., 1980, "Origin of Temperature Dependence of Microbending Attenuation in Fiber Optic Cables," *Fiber and Integrated Optics*, Vol. 3.

Katsuyama, Y., et al., 1980, "Transmission Loss of Crated Single-Mode Fiber at Low Temperatures," *Appl. Opt.*, Vol. 19, No. 24, Dec.

Lenahan, T. A., 1985, "Thermal Buckling of a Dual-Coated Fiber," *AT&T Techn. Journal*, Vol. 64, No. 7, Sept.

Marcuse, D., 1973, "Losses and Impulse Response of a Parabolic Index Fiber With Random Bends," *Bell System Tech. Journal*, Vol. 52, No. 8, Oct.

Marcuse, D., 1974, "Bent Optical Waveguide With Lossy Jacket," *Bell System Tech. Journal*, Vol. 53, No. 6, July-Aug.

Muskhelishvili, N. I., 1977, *Same Basic Problems of the Mathematical Theory of Elasticity*, Noozdhof, Leyden.

Naruse, I., et al., 1977, "Nylon Jacketed Optical Fiber With Silicone Buffer," *Electronic Letters*, Vol. 13, No. 6.

Sakai, T., and Kimura, I., 1979, "Practial Microbending Loss Formula for Single Mode Optical Fibers," *IEEE Journal on Quant. Electronics*, EQ-15, June.

Timoshenko, S. P., 1959, *Theory of Elasticity*, McGraw-Hill, New York.

Timoshenko, S. P., 1961, *Theory of Elastic Stability*, McGraw-Hill, New York.

Turuya, K., and Suematsu, Y., 1980, "Random-Bend Loss in Single-Mode and Parabolic-Index Multimode Optical Fiber Cables," *Appl. Opt.*, Vol. 19, May.

Vangheluwe, D. C. L., 1984, "Exact Calculations of the Spring Constant in the Buckling of Optical Fibers," *Appl. Opt.*, Vol. 23, No. 13, July.

Yabuta, T., et al., 1983, "Excess Loss of Single-Mode Jacketed Optical Fiber at Low Temperature," *Appl. Opt.*, Vol. 22, No. 15, Aug.

Downloaded 03 May 2010 to 171.66.16.21. Redistribution subject to ASME license or copyright; see http://www.asme.org/terms/Terms_Use.cfm

The Differential Geometry of the General Helix as Applied to Mechanical Springs

Yuyi Lin
Research Assistant.
Albert P. Pisano
Associate Professor.
Assoc. Mem. ASME

Mechanical Engineering Department,
University of California,
Berkeley, CA 94720

In order to improve the performance of helical springs, such as increasing the fatigue life and suppressing resonance, variable pitch angle and variable helix radius may be incorporated into the helical spring geometry. Employing the tool of differential geometry, new and complete formulae of curvature, torsion, and spring force are derived. It is shown that these formulae are more general and accurate than Kelvin's curvature and torsion formulae, than commonly used force formulae (Wahl, 1963). Possible simplifications to the complete formulae and the corresponding errors introduced are both discussed and compared with experimental data.

Introduction

Modern study and research concerning helical springs dates back at least a century (Thomson and Tait, 1883) and some dated assumptions about helical spring geometry, no matter how impractical, are still being applied in modern day analyses. For example, helical springs usually are assumed to have constant pitch angle throughout the spring. However, for stably seating the spring between two parallel end surfaces in practical applications, the pitch angle at the two ends of spring is usually made smaller in order to "close" the coils. Hence, to assume constant pitch angle is to assume an infinite helix length, or a spring without stable and parallel seating ends, and to ignore all end effects. Similarly, some fundamental formulae concerning the geometry of the helix, based on historically made assumptions, are still applied without awareness of the error introduced. For instance, the formulae dating from early work (Thomson and Tait, 1883) expressing curvature, κ, and torsion, τ, in terms of pitch angle, p, and helix radius, r,

$$\kappa = \frac{\cos^2 p}{r} \tag{1}$$

$$\tau = \frac{\sin p \cos p}{r} \tag{2}$$

are still widely used (Love, 1927; Wahl, 1963; Wittrick, 1966; Stokes, 1974; Pearson, 1982; Velinsky, 1987).

In searching for higher performance, springs with large variations from traditional geometries have been manufactured and tested (Fig. 1). However, there is no accurate mathematical description of this new type of spring in the open literature. The purpose of this paper is to utilize differential geometry to derive more accurate and more general formulae for curvature, torsion, and spring force and apply these to the helical spring. The errors introduced using old or simplified formulae are discussed and compared both to the formulae derived herein and to experimental data. It is hoped this paper can contribute an analytical tool to the study of helical spring dynamics, and offer some constructive ideas for a new class of designs of helical springs.

Description of the General Helical Spring

It is a common assumption (Fig. 2), that the helical spring

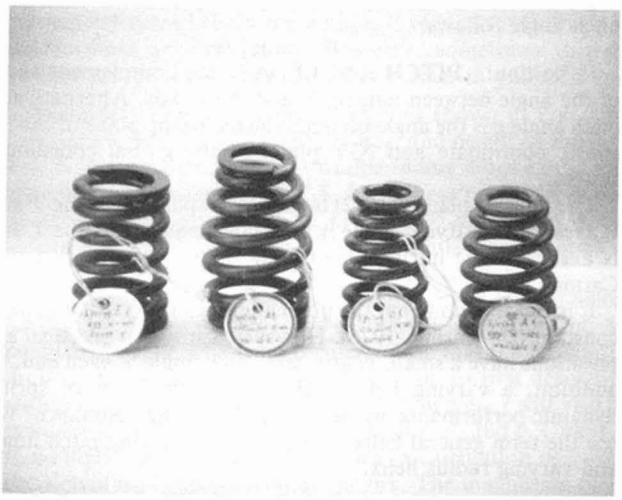

Fig. 1 Helical springs with large variations in radius and pitch angle

Contributed by the Applied Mechanics Division of THE AMERICAN SOCIETY OF MECHANICAL ENGINEERS for presentation at the Joint ASCE/ASME Applied Mechanics, Biomechanics, and Fluids Engineering Conference, San Diego, CA, July 9 to 12, 1989.

Discussion on this paper should be addressed to the Editorial Department, ASME, United Engineering Center, 345 East 47th Street, New York, N.Y. 10017, and will be accepted until two months after final publication of the paper itself in the JOURNAL OF APPLIED MECHANICS. Manuscript received by ASME Applied Mechanics Division, January 1, 1988; final revision, April 29, 1988.

Paper No. 89-APM-17.

Copyright © 1988 by ASME
Downloaded 03 May 2010 to 171.66.16.21. Redistribution subject to ASME license or copyright; see http://www.asme.org/terms/Terms_Use.cfm

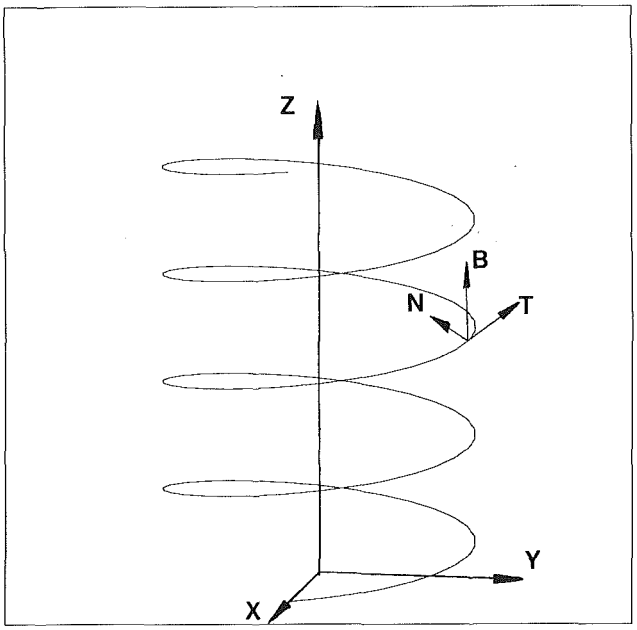

Fig. 2 Circular helix and local-global coordinate systems

can be described to sufficient accuracy by a circular helix (Eisenhart, 1940), which can be considered the trace of a curve, X, in R^3 space, such that:

$$X{:}I \rightarrow R^3 \tag{3}$$

where a parametrization of X is such:

$$X(t) = (r \cos at, r \sin at, bt) \tag{4}$$

where the parameter $t \epsilon I$, I is a subset of R, and r, a, and b are constants.

For the idealized helix treated in general textbooks (Darboux, 1887; Vaisman, 1984), this description is clear and simple. However, even if a commonly used helical spring (where end effects are small due to design) is described in this fashion, the error in predicted spring force for a given, imposed spring displacement can be as much as 5 percent in simple static compression (Lin and Pisano, 1987). An even greater error is introduced when the pitch angle is assumed to be constant throughout the spring in the analysis, but the physical implementation of the spring includes not only closed coils at each end, but a deliberately varying pitch angle in the body of the spring. Since spring technology has been moving toward variable pitch angle designs, an accurate description of pitch angle is both useful and necessary. A precise definition of pitch angle follows:

Definition: PITCH ANGLE, p, is the complement angle of the angle between tangent T and the Z axis. Alternatively, pitch angle p is the angle between the rectifying plane of the intrinsic coordinate and X-Y plane of the global coordinate system.

The tangent plane (Fig. 2) is the plane spanned by the T and B axes, the rectifying plane is the plane spanned by the T and N axes, and the intrinsic coordinate is the Frenet Triad (Do Carmo, 1976).

It is easy to show that the pitch angle for the circular helix is constant (Do Carmo, 1976). However, springs in practical applications have a small, nearly zero pitch angle at each end. In addition, a varying helix radius may help improve spring dynamic performance by de-tuning the spring resonance. We use the term general helix to describe the varying pitch angle and varying radius helix.

Definition: GENERAL HELIX is the trace of a curve

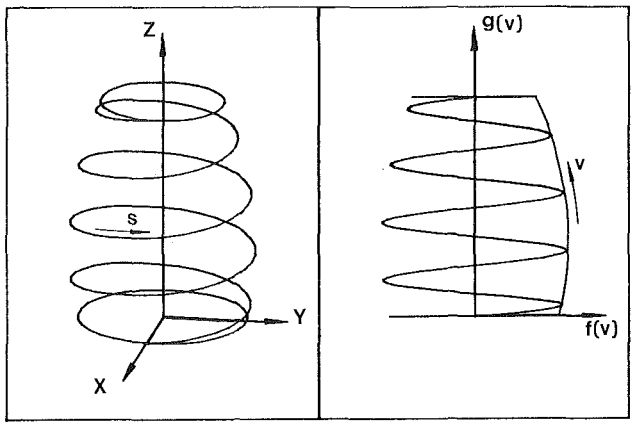

Fig. 3 Describing a general helix

$\alpha(s){:}I \rightarrow R^3$, such that α can be embedded on a surface of revolution, with pitch angle a non-negative function of the parameter, s.

Compared with the circular helix, equation (4), a parametrization of a general helix can be:

$$X(s) = (r(s)\cos\theta(s), r(s)\sin\theta(s), h(s)) \tag{5}$$

The surface of revolution mentioned in the above definition can be parametrized as:

$$Y(u,v) = (f(v)\cos u, f(v)\sin u, g(v)) \tag{6}$$

where f, g are known functions of v, a parameter preferably taken as the arc length, s, because the arc length of a regular curve is an invariant with respect to transformations of the parameter used to define the curve (Stoker, 1969). This is reasonable since in practice spring wire can usually be assumed to be inextensible. A curve, shown in Fig. 3, on Y(u, v) can be determined by either of the following relations:

$$u = u(t), \qquad v = v(t) \tag{7a}$$

or

$$u = u(v) \tag{7b}$$

If equation (7a) is chosen and t is the arc length parameter, then the general helix is described by equation (5). If equation (7b) is chosen, then the curve has the parametrization:

$$X(v) = (f(v)\cos u(v), f(v)\sin(v), g(v)) \tag{8}$$

Although equation (5) and equation (8) have similar forms, parameters v and s have different meanings. Intuitively, it is seen that v is arc length of the helix on the Y-Z plane, and s is the actual wire length (Fig. 3). They can be related by:

$$ds^2 = [E(u_v')^2 + G]dv^2 \tag{9}$$

where E and G are coefficients of first fundamental form (Do Carmo, 1976) of the surface Y(u,v). Using the first fundamental form here enables us to measure arc length in terms of surface coordinates without referring back to the ambient R^3 space where the surface lies (Do Carmo, 1976). In the discussion to follow, the general helix will be represented by equation (5) for convenience.

New Formulae for Curvature and Torsion

Many researchers and engineers have been using the formulae for curvature, κ, and torsion, τ, from the Treatise on Natural Philosophy (Lord Kelvin and Tait, 1883). The formulae state:

$$\kappa = \frac{\cos^2 p}{r} \tag{1}$$

and

Downloaded 03 May 2010 to 171.66.16.21. Redistribution subject to ASME license or copyright; see http://www.asme.org/terms/Terms_Use.cfm

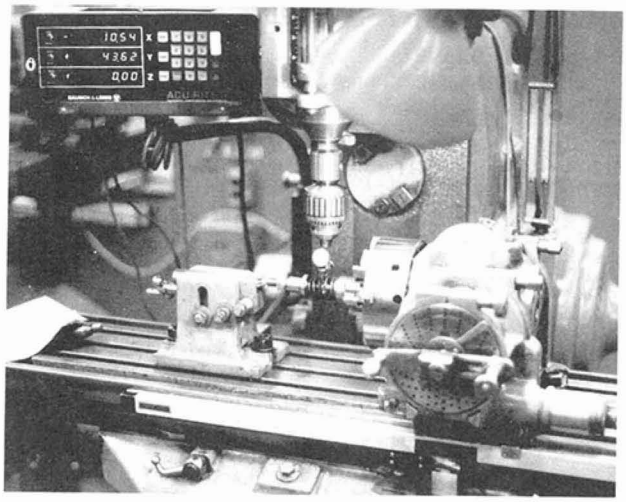

Fig. 4 Measuring radii on a milling machine

$$\tau = \frac{\sin p \cos p}{r} \tag{2}$$

where p is the pitch angle, and r the radius, of the helix. These formulae were derived intuitively (Thomson and Tait, 1883).

Many researchers use the above formulae for a constant radius helix spring even though they realize the pitch angle is a function of helix length. Note that even if the radius is still constant, varying pitch has made the helix not a circular helix in the strict sense of Eisenhart (1940). In addition, if a dynamic spring deflection is under consideration, the helix radius and pitch angle will not be constant in time even for a circular helix spring. We therefore derive these formulae for the curvature and torsion of the general, as opposed to circular, helix.

Derivation: Let a general helix parametrized by arc length be:

$$X(s) = (r \cos \theta,\ r \sin \theta,\ h) \tag{10}$$

where helix radius, r, polar angle, θ, and local helix height, h, are functions of arc length, s. Then derivatives with respect to arc length, s, are:

$$X'(s) = \mathbf{T(s)}$$
$$= (r' \cos \theta - \theta' r \sin \theta,\ r' \sin \theta + \theta'\ r \cos \theta,\ h') \tag{11}$$

where **T(s)** is unit tangent vector of $X(s)$, since s is the arc length parameter.

$$X''(s) = \mathbf{T}'(\mathbf{s})$$
$$= (r'' \cos \theta - 2\theta' r' \sin \theta - r\,\theta'' \sin \theta - r\,\theta'^2 \cos \theta,$$
$$r'' \sin \theta + 2\theta' r' \cos \theta - \theta'^2 r \sin \theta + r\,\theta'' \cos \theta,\ h'') \tag{12}$$

From Frenet-Serret formulae (Eisenhart, 1940), the curvature is the magnitude of $\mathbf{T}'(\mathbf{s})$:

$$\mathbf{T}'(\mathbf{s}) = \kappa \mathbf{N(s)} \tag{13}$$

and since **N(s)** is a unit vector, taking inner product of $\mathbf{T}'(\mathbf{s})$, we obtain the full expression for curvature:

$$\kappa^2 = (X'', X'')$$
$$= r^2\theta'^4 + 4r'^2\theta'^2 + r^2\theta''^2 - 2r\theta'^2 r'' + 4rr'\theta'\theta'' + r''^2 + h''^2 \tag{14}$$

Note that in contrast, the common analysis of analytical geometry gives:

$$\cos^2 p = \frac{r'^2 + r^2\theta'^2}{|X'|^2}$$
$$= r'^2 + r^2\theta'^2 \tag{15}$$

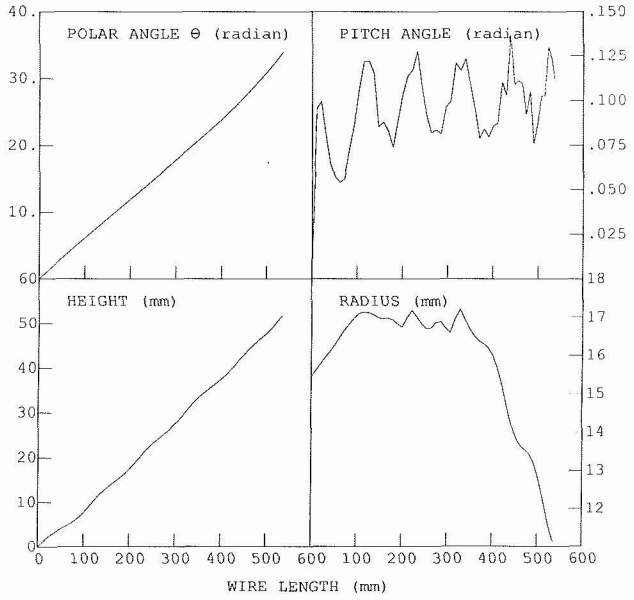

Fig. 5 Description of sample spring "P"

and then from Kelvin's curvature formula,

$$\kappa^2 = \left(\frac{\cos^2 p}{r}\right)^2$$
$$= r^2\theta'^4 + 2r'^2\theta'^2 + \frac{r'^4}{r^2} \tag{16}$$

It is seen from equation (14) that κ is a function of r'' and h'' in general, and that this is not true in Kelvin's formula equation (16). In some special cases, for example, the circular helix (equation (4)) with constant radius ($r' = 0$), linear height ($h'' = 0$), and linear polar angle ($\theta'' = 0$), the new curvature expression is identical to the old formula.

Example: In Fig. 5, measured and smoothed data for a particular helical spring is shown. The spring has constant radius, and in the middle portion the pitch angle is constant, therefore it is locally a circular helix. It is seen from the numerical results shown in Table A (Case 1) that the Kelvin curvature formula and the complete curvature formula give the same result. For the same spring, at one end (Case 2, $s = 46.35$ mm) where pitch angle is varying, the curvature calculated by the Kelvin formula has an error of four parts in one hundred thousand.

The above example shows if the spring has only a small variation in pitch angle p, but no variation in radius r, the curvatures calculated from the complete formula and from the old formula are very close. However, sometimes this difference can be considerable, as shown later in this section.

Example: One of the helical springs shown in Fig. 1 has been measured for pitch angle, radius, and height as shown in Fig. 6. The measurement of variable radius is done on a milling machine as shown in Fig. 5. Note these results have been parametrized by arc length, s. At $s = 30.05$ mm (Case 3), curvature calculated from the Kelvin formula has an error of $+0.153$ percent with respect to experimental data.

The derivation of the torsion formula for the general helix is lengthy, and an outline of this derivation is given in the Appendix. It can be seen from the derivation that the Kelvin formula of τ depends on r, h, and θ only up to first derivatives with respect to arc length. In general, however, τ will also depend on second and third derivatives of r, h, and θ. Unless all these higher order derivatives vanish, a calculation of τ from the Kelvin formula will contain errors. The magnitude of the error depends on the magnitude of higher derivatives of r, h,

Downloaded 03 May 2010 to 171.66.16.21. Redistribution subject to ASME license or copyright; see http://www.asme.org/terms/Terms_Use.cfm

Table A: Comparison of curvature and torsion using different formulae

Case	1:spr.P	2:spr.P	3:spr.F	4:spr.F
s(mm)	120.66	46.35	30.05	114.76
κ_{old}(1/mm)	0.067245	0.067378	0.061595	0.057748
κ_{new}(1/mm)	0.067245	0.067381	0.061501	0.057808
error(%)	0.000	−0.004	0.153	−0.104
τ_{old} (1/mm)	0.007253	0.006612	0.003811	0.006770
τ_{new}(1/mm)	0.007253	0.006485	0.004011	0.003667
error(%)	0.000	1.961	−4.984	84.638
ϵ(deg.)	0.000	0.479	−0.799	−1.045

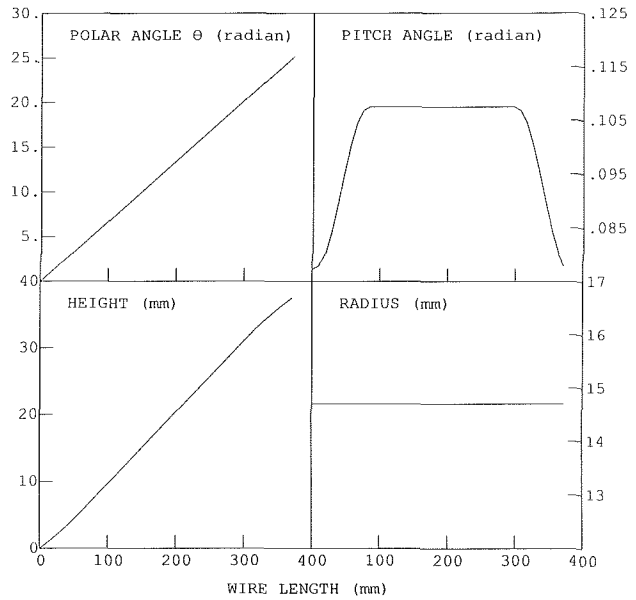

Fig. 6 Description of sample spring "*F*"

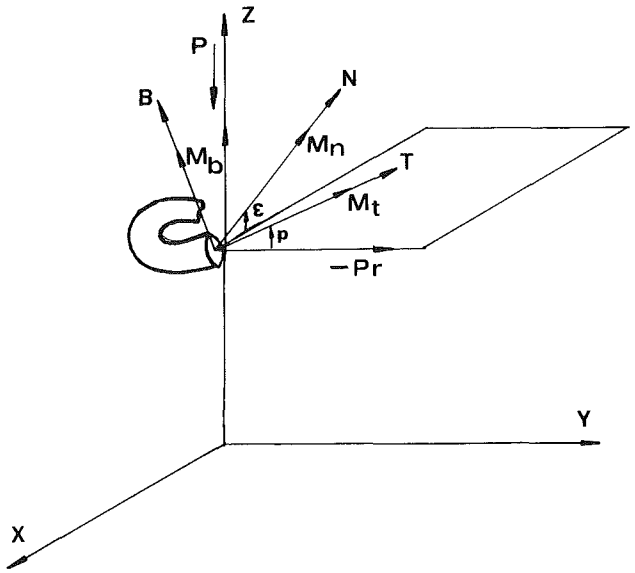

Fig. 7 Force and moment diagram for spring element

and θ of the specific helix. For more examples comparing results computed from old and new formulae, please refer to Table A. To minimize the effect of measurement error, the numerical results presented in Table A are calculated from third-order polynomial approximations of measured spring curve. The coefficients of these polynomials are obtained by least square curve fit. Note these cases are intended only to give some approximation of possible differences and they do not represent the largest possible differences. Nevertheless, in Case 4, the error in τ has calculated to be as great as +84.6 percent.

Change in the Direction of Normal Vector N

In an earlier paper (Lin and Pisano, 1987), and other work (Wahl, 1963), the normal, **N**, of the intrinsic coordinate system has always been considered parallel to X-Y plane of the global coordinate, for the purpose of calculating spring force and moment (Fig. 7). When a force, P, is applied to one end of the spring, at any point, q, a moment,

$$M_h = -\vec{r} \times \vec{P} \tag{17}$$

is produced. M_h will have to be balanced by resultant moments due to the stress in the spring material at point q. M_h can be decomposed into M_b and m_t, as shown in Fig. 7, which must be balanced by changes in curvature, κ, and torsion, τ. This kind of analysis has assumed that the normal, **N**, is parallel to the X-Y plane. It can be shown that the normal, **N**, is not parallel to the X-Y plane for the general helix.

Derivation: Let a parametrization of a general helix be:

$$X(s) = (r\cos\theta,\ r\sin\theta,\ h) \tag{18}$$

where r,θ,h are functions of arc length, s. Then,

$$\begin{aligned}\mathbf{T}'(s) &= \kappa\,\mathbf{N} \\ &= (r''\cos\theta - 2\theta' r'\sin\theta - \theta'^2 r\cos\theta, \\ &\qquad r''\sin\theta + 2r'\theta'\cos\theta - \theta'^2 r\sin\theta,\ h'') \end{aligned} \tag{19}$$

$$\begin{aligned}\mathbf{N}(s) &= \frac{\mathbf{T}'}{|\mathbf{T}'|} \\ &= \frac{\mathbf{T}'}{\sqrt{r''^2 + 4\theta'^2 r'^2 + \theta'^4 r'^2 - 2\theta'^2 r'' r' + h''^2}} \\ &= \frac{\mathbf{T}'}{\kappa} \end{aligned} \tag{20}$$

N would be parallel to the X-Y plane, if and only if $h'' = 0$, i.e., the z coordinate function, $h(s)$, of the helix were a linear function of arc length s. Otherwise **N** is not parallel to the X-Y plane.

We can conclude from the above proof, that when $h'' \neq 0$ the calculated values of M_b and M_t must be corrected by the cosine of the angle, ϵ, where ϵ is found from:

$$\epsilon = \sin^{-1}\left(\frac{h''}{\sqrt{r''^2 + 4\theta'^2 r'^2 + \theta'^4 r^2 - 2\theta'^2 r'' + h''^2}}\right) \tag{21}$$

and a new component of torque, M_n, in the direction of **N** will have to be balanced by additional stress in the spring helix. In a previous paper (Lin and Pisano, 1987), this balancing torque is called the bending moment in the T-B plane. To have a quantitative sense about the corrective angle, ϵ, consider two examples.

Example: An automotive valve spring has measured and smoothed initial pitch angle distribution data as shown in Fig. 5. Assume at 5 mm compression it has constant radius $r = 0.0147$m. Since the measurement is made on nodes evenly

Downloaded 03 May 2010 to 171.66.16.21. Redistribution subject to ASME license or copyright; see http://www.asme.org/terms/Terms_Use.cfm

distributed around a circle, the spring is conveniently represented by:

$$X(\theta) = (r\cos\theta,\ r\sin\theta,\ h(\theta))$$

However, it is more convenient in a later computation to reparametrize the spring by arc length:

$$X(s) = (r\cos\theta(s),\ r\sin\theta(s),\ h(\theta(s)))$$

with θ and s related by the mapping:

$$s(\theta) = \int_0^\theta |X'(\theta)|\,d\theta$$

$$= \int_0^\theta \sqrt{r^2 + h'^2_\theta}\,d\theta$$

At arc length equal to 46.35 mm of the spring (Case 2 in Table A),

$$\epsilon \approx 0.5°$$

Example: In Table A, Case 3, the spring has variable pitch angle and radius (shown in Fig. 6), and at arc length, s, equal to 114.76 mm, $\epsilon = -1.045$ deg.

New Formulae for Calculating Spring Forces

As a result of new formulae for calculating curvature, κ, torsion, τ, and the inclusion of a new strain energy term, a new spring force computation formula has been derived that differs from common formulae (Wahl, 1963) currently in use. Referring to Fig. 7, when a force P in the negative Z direction is applied, the internal force at any cross-section of the spring produced by strain can be decomposed into a force, F, in the positive Z direction, passing through the center of the spring wire, and into a moment, M, about Z axis, described below as:

$$F = \frac{GJ\cos p}{r}(\Delta\tau) - \frac{EI\sin p}{r}((\Delta\kappa)\cos\epsilon + (\Delta z'')\sin\epsilon) \tag{22}$$

$$M = GJ\sin p(\Delta\tau) + EI\cos p((\Delta\kappa)\cos\epsilon + (\Delta z'')\sin\epsilon) \tag{23}$$

If an accurate evaluation of the spring force is desired, the above formula is recommended. It should be noted that although the above formulae are analytical and exact, it turns out to be difficult to obtain exact values for changes in curvature and torsion, either numerically or experimentally. For the case where the spring has a constant helix radius and varying pitch angle, an experimentally-verified, simplified formula, which is repeated here for completeness, can be used to obtain very good results (Lin and Pisano, 1987):

$$\Delta p = \text{constant with respect to arc length} \tag{24}$$

where Δp is the change of pitch angle corresponding to specified spring deflection. After Δp is solved, changes in curvature and torsion are calculated from Kelvin formulae using new pitch angle distribution.

Example: If static spring force for spring "P", which is described in Table A and Fig. 5, is computed by simple formula (Shigley, 1983), maximum error between computed force and experimentally measured force is about 40 Newton (5 percent). This large error is resulted from a considerably large varying pitch angle. If approximate formula, equation 24, is applied to calculate change of curvature, $\Delta\tau$, and only first term in equation 22 is utilized to calculate the spring force, maximum error is about 9 Newton (1 percent). The third term in equation 22 has no significant contibution, because in this case $\Delta z''$ and ϵ are almost zero along the helix.

Conclusions

The more general and accurate mathematical model of a helical spring is general helix rather than circular helix. The most significant differences between the general and the circular helices are varying pitch angle and varying radius, and consequently the historically used curvature and torsion formulae have been shown to introduce errors that vary depending on application and specific configuration. A word of caution is that for realistic helical spring models, especially when spring dynamics is concerned, no helical spring is an exact circular helix. New formulae for curvature, torsion, and spring force have been derived to handle this case and are recommended where accuracy is more important than computational effort. With the availability of accurate helix models, it is now possible to take advantage of the complex shape of general helix in spring design, so as to obtain higher and variable natural frequencies and subsequently longer fatigue life.

Acknowledgment

This material is based upon work supported by the National Science Foundation under Grant Nos. MEA-8404822 and DMC-8451199 (a Presidential Young Investigator Award). Other support has been provided by the General Motors Corporation, CPC Group, under research contract No. BGMC-DD138898. The assistance of Associate Spring Company in the form of providing sample springs for this investigation is gratefully acknowledged. The first author wishes to express his appreciation to Prof. Charles Pugh, of the Department of Mathematics of UC Berkeley, for his encouragement in writing this paper. The authors also wish to acknowledge the support of the Department of Mechanical Engineering, University of California, Berkeley, in the providing of computer and laboratory resources.

References

Darboux, G., 1887, *Lecons sur la Theorie Generale des Surfaces*, Gauthier-Villars, Imprimeur-Libraire, Paris, p. 11.

Do Carmo, M. P., 1976, *Differential Geometry of Curves and Surfaces*, Prentice-Hall, Englewood Cliffs, NJ, pp. 19–22.

Costello, G. A., 1975, "Radial Expansion of Impacted Helical Springs," ASME JOURNAL OF APPLIED MECHANICS, Vol. 42, pp. 789–792.

Eisenhart, L. R., 1940, *An Introduction to Differential Geometry*, Princeton University Press, pp. 14–15.

Kato, M., 1974, "Study on Dynamic Properties of a Varying-Pitch Helical Compression Spring," *Bulletin of the JSME*, Vol. 17, No. 110, pp. 1015–1022.

Lin, Y., and Pisano, A. P., 1987, "General Dynamic Equations of Helical Springs with Static Solution and Experimental Verification," ASME JOURNAL OF APPLIED MECHANICS, Vol. 54, pp. 910–917.

Love, A. E. H., 1927, *A Treatise on the Mathematical Theory of Elasticity*, 4th Ed., Dover, New York.

Pearson, D., 1982, "The Transfer Matrix Method for the Vibration of Compressed Helical Springs," *Journal of Mechanical Engineering Science*, Vol. 24, No. 4, pp. 163–171.

Phillips, J. W., and Costello, G. A., 1972, "Large Deflections of Impacted Helical Springs," *Journal of the Acoustical Society of America*, Vol. 51, No. 3, pp. 967–973.

Pisano, A. P., and Freudenstein, F., 1983, "An Experimental and Analytical Investigation of the Dynamic Response of a High-Speed Cam Follower System, Part 2: A Combined, Lumped/Distributed Parameter Dynamic Model," ASME *Journal of Mechanisms, Transmissions and Automation in Design*, Vol. 105, pp. 699–704.

Sayre, M. F., and De Forest, A. V., 1939, "New Spring Formulas and New Materials for Precision Spring Scales," *Transactions ASME*, Vol. 58, pp. 379–387.

Shigley, J. E., and Mithcell, L. D., 1983, *Mechanical Engineering Design*, 4th Ed., McGraw-Hill, New York, p. 447.

Stoker, J. J., 1969, *Differential Geometry*, John Wiley, New York, pp. 14–21.

Stokes, V. K., 1974, "On the Dynamic Radial Expansion of Helical Springs due to Longitudinal Impact," *Journal of Sound and Vibration*, Vol. 35, pp. 77–99.

Thomson, W., and Tait, P. G., 1883, *Treatise on Natural Philosophy*, 2nd Ed., Oxford, pp. 136–144.

Vaisman, I., 1984, *A First Course In Differential Geometry*, Marcel Dekker, New York, pp. 72–73.

Velinsky, S. A., 1987, "Design and Mechanics of Multi-Lay Wire Strands," *Advances in Design Automation, Proceedings of ASME 13th Annual Design Automation Conference*, Vol. 1, pp. 221–231.

Downloaded 03 May 2010 to 171.66.16.21. Redistribution subject to ASME license or copyright; see http://www.asme.org/terms/Terms_Use.cfm

Wahl, A. M., 1963, *Mechanical Springs*, Penton Publishing Co., Cleveland, OH.

Wittrick, W. H., 1966, "On Elastic Wave Propagation in Helical Springs," *International Journal of Mechanical Science*, Vol. 8, pp. 25–47.

APPENDIX

Torsion of General Helix

Assume a general helix parametrized by arc length is:

$$X(s) = (r\cos\theta,\ r\sin\theta,\ h) \tag{A-1}$$

where r, θ, and h are functions of arc length s. From the Frenet-Serret formula of differential geometry,

$$\mathbf{N}' = -\kappa\mathbf{T} - \tau B \tag{A-2}$$

$$(\mathbf{N}',\ \mathbf{N}') = \kappa^2 + \tau^2 \tag{A-3}$$

$$\tau^2 = \kappa^2 - (\mathbf{N}',\ \mathbf{N}') \tag{A-4}$$

Since

$$\mathbf{N} = \frac{\mathbf{T}'}{\kappa} \tag{A-5}$$

$$\mathbf{N}' = \frac{\mathbf{T}''\kappa - \kappa'\mathbf{T}'}{\kappa^2} \tag{A-6}$$

where

$$\begin{aligned}\mathbf{T}' &= \mathrm{X}'' \\ &= (r''\cos\theta - 2r'\theta'\sin\theta - r\,\theta''\sin\theta - r\,\theta'^2\cos\theta,\\ &\quad r''\sin\theta + 2r'\theta'\cos\theta + r\,\theta''\cos\theta - r\,\theta'^2\sin\theta,\ h'')\end{aligned} \tag{A-7}$$

$$\begin{aligned}\mathbf{T}'' &= (r'''\cos\theta - 3r''\theta'\sin\theta - 3r'\theta''\sin\theta - 3r'\theta'^2\cos\theta\\ &\quad - r\theta'''\sin\theta - 3r\theta'\theta''\cos\theta + r\theta'^3\sin\theta,\\ &\quad r'''\sin\theta + 3r''\theta'\cos\theta + 3r'\theta''\cos\theta - 3r'\theta'^2\sin\theta\\ &\quad + \theta'''r\cos\theta - 3r\theta'\theta''\sin\theta - r\theta'^3\cos\theta,\ h''')\end{aligned} \tag{A-8}$$

$$\begin{aligned}\kappa' &= \frac{1}{2\kappa}(2h''h''' + 2r''r''' + 6r'r''\theta'^2 + 12r'^2\theta'\theta''\\ &\quad + 6rr'\theta''^2 + 2r^2\theta''\theta'''\\ &\quad + 2rr'\theta'^4 + 4r^2\theta'^3\theta'' - 2r\theta'^2r''' + 4rr'\theta'\theta''')\end{aligned} \tag{A-9}$$

Then finally,

$$\tau = \sqrt{\kappa^2 - \frac{1}{\kappa^4}(\kappa^2(\mathbf{T}'',\mathbf{T}'') + \kappa'^2(\mathbf{T}',\mathbf{T}') - 2\kappa\kappa'(\mathbf{T}',\mathbf{T}''))} \tag{A-10}$$

Downloaded 03 May 2010 to 171.66.16.21. Redistribution subject to ASME license or copyright; see http://www.asme.org/terms/Terms_Use.cfm

Theory of Elasticity of Filament Wound Anisotropic Ellipsoids With Specialization to Torsion of Orthotropic Bars

G. A. Kardomateas
General Motors Research Laboratories,
Engineering Mechanics Department,
Warren, Mich. 48090-9055
Assoc. Mem. ASME

The problem of determining the state of stress in a homogeneous ellipsoidal body (as can be produced by filament winding on a mandrel of elliptical cross-section) is formulated. The material is assumed to possess curvilinear anisotropy, referred to the coordinate system that is inherent to the geometry of the filament wound body. The differential equations that govern the stress functions are derived for the general anisotropy and loading cases. Then the results for the special case of torsion of an orthotropic body are derived.

Introduction

The theory of elasticity of an anisotropic body has been developed up to now for the cases of rectilinear (referred to a cartesian coordinate system) or cylindrical (referred to a polar coordinate system) anisotropy (Lekhnitskii, 1963). The latter one is the underlying theory for studying the mechanics of filament wound circular cylinders (see e.g., Sherrer, 1967; Pagano and Halpin, 1968).

In fact, filament winding has been employed up to now in constructing mostly fiber reinforced composite circular cylinders. This manufacturing process certainly can be applied to parts of other cross-sectional shapes. Such a case is an elliptical cross-section with potential applications in components of automotive suspension systems. Therefore, there is a need for predicting the distribution of stress that these parts experience in service. Obviously, interlaminar shear constitutes a major limitation since the shear strength is limited by the bonding between the layers. By proper design, the values of interlaminar shear can be minimized. A formulation of the mechanics of those parts can also be useful in modelling the complex filament winding process.

Consider the ellipsoid of Fig. 1, produced by filament winding on an elliptical mandrel. It is obvious that one cannot neglect the inherent geometry of the curved layers in considering the elasticity. We should choose a system of curvilinear coordinates so that the coordinate directions at each point coincide with the directions which are equivalent in the sense of the elastic properties. Such a system in this case is the ($\hat{\xi}$, $\hat{\eta}$, $\hat{z}$), where $\hat{\xi}$ is the direction normal to the layers (thicknesswise direction), $\hat{\eta}$ is the tangent to the periphery and $\hat{z}$ is along the ellipsoid axis. In this homogeneous anisotropic body all the directions $\hat{\xi}$, $\hat{\eta}$, $\hat{z}$ which are drawn through different points are equivalent with respect to the elastic properties. We shall refer to this type of curvilinear anisotropy as "elliptical anisotropy." It should be noted that since the body that is produced by filament winding on the elliptical mandrel has constant thickness, the outer bounding surface is *not* a true ellipse, as opposed to the internal one; in the limit of infinite thickness the outer contour is a circle. This is also a unique feature of the present problem shared in general by filament wound bodies.

In this work the mechanics of an elliptically anisotropic body will be developed. First, let us assume that: (1) the body possesses elliptical anisotropy of the most general kind; (2) the stresses act on the planes normal to the ellipsoid axis and do not vary along the generator; and (3) there are no body forces. After deriving the governing equations, the solution is produced for the special case of torsion of an orthotropic ellipsoid. In developing the theory, formulas from the differential geometry are used (see, for example do Carmo, 1976) to express the unit vectors, element of area, etc., in terms of the curvilinear coordinates.

Formulation

Consider an ellipse with semiaxes $c \cosh a$ and $c \sinh a$ (foci at $x = \pm c$). This is the cross-section of the mandrel. On a cartesian coordinate system, the filament wound body is defined in terms of the curvilinear coordinates ξ and η (Fig. 1),

$$x = c \cosh a \cos \eta + \xi \frac{c}{h} \sinh a \cos \eta \tag{1a}$$

$$x = c \sinh a \sin \eta + \xi \frac{c}{h} \cosh a \sin \eta \tag{1b}$$

where

Contributed by the Applied Mechanics Division for publication in the JOURNAL OF APPLIED MECHANICS.
Discussion on this paper should be addressed to the Editorial Department, ASME, United Engineering Center, 345 East 47th Street, New York, N.Y. 10017, and will be accepted until two months after final publication of the paper itself in the JOURNAL OF APPLIED MECHANICS. Manuscript received by ASME Applied Mechanics Division, July 30, 1987; final revision, April 14, 1988.

Copyright © 1988 by ASME
Downloaded 03 May 2010 to 171.66.16.21. Redistribution subject to ASME license or copyright; see http://www.asme.org/terms/Terms_Use.cfm

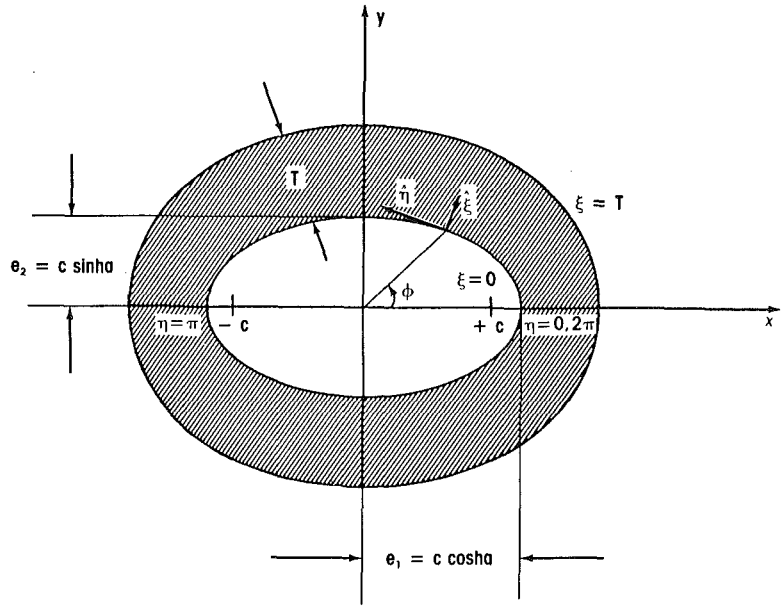

Fig. 1 Cross-section of the filament wound ellipsoid

$$h = h(\eta) = c\sqrt{\sinh^2 a + \sin^2 \eta} \tag{2}$$

Different values of ξ correspond to different layers on the elliptical mandrel. So ξ varies from 0 to T, where T is the total thickness of the body. On any of these layers ξ is constant and η varies through a range of 2π. The above equations describe the geometry in accordance with the features of the filament wound body (notice again that because of the constant thickness the outer bounding surface is not a true ellipse, as opposed to the internal one).

The components of stresses are assumed to be functions only of ξ and η. We shall deduce equations which enable us to determine the stresses and displacements in the general case under consideration.

Denote

$$q = \left[\left(\frac{\partial x}{\partial \eta}\right)^2 + \left(\frac{\partial y}{\partial \eta}\right)^2\right]^{1/2} = h + \xi \frac{c^2 \sinh 2a}{2h^2} \tag{3}$$

The equations of equilibrium of a body in which the stresses do not depend on z will have the form:

$$q\sigma_{\xi\xi,\xi} + \tau_{\xi\eta,\eta} + \frac{\partial q}{\partial \xi}(\sigma_{\xi\xi} - \sigma_{\eta\eta}) = 0 \tag{4a}$$

$$\sigma_{\eta\eta,\eta} + q\tau_{\xi\eta,\xi} + 2\frac{\partial q}{\partial \xi}\tau_{\xi\eta} = 0 \tag{4b}$$

$$(q\tau_{\xi z}),\xi + \tau_{\eta z,\eta} = 0 \tag{4c}$$

The stresses and strains will be referred to the curvilinear coordinate system $(\hat{\xi}, \hat{\eta}, \hat{z})$. In this way, the infinitesimally small elements of the body bounded by three pairs of corresponding coordinate surfaces will be identical. The stress-strain equations are given by

$$\epsilon_{\xi\xi} = a_{11}\sigma_{\xi\xi} + a_{12}\sigma_{\eta\eta} + a_{13}\sigma_{zz} + a_{14}\tau_{\eta z} + a_{15}\tau_{\xi z} + a_{16}\tau_{\xi\eta} \tag{5a}$$

$$\epsilon_{\eta\eta} = a_{12}\sigma_{\xi\xi} + a_{22}\sigma_{\eta\eta} + \ldots + a_{26}\tau_{\xi\eta} \tag{5b}$$

$$\ldots$$

$$\gamma_{\xi\eta} = a_{16}\sigma_{\xi\xi} + a_{26}\sigma_{\eta\eta} + \ldots + a_{66}\tau_{\xi\eta} \tag{5f}$$

The right sides of the last six equations (5) are functions only of ξ and η. Here a_{ij} are the elastic constants of a body with elliptical anisotropy and the strains $\epsilon_{\xi\xi}, \epsilon_{\eta\eta}, \ldots, \gamma_{\xi\eta}$ are connected with the components of displacement by the following formulas:

$$\epsilon_{\xi\xi} = u_{\xi,\xi} \tag{6a}$$

$$\epsilon_{\eta\eta} = \frac{1}{q}u_{\eta,\eta} + \frac{1}{q}\frac{\partial q}{\partial \xi}u_{\xi} \tag{6b}$$

$$\epsilon_{zz} = u_{z,z} \tag{6c}$$

$$\gamma_{\eta z} = u_{\eta,z} + \frac{1}{q}u_{z,\eta} \tag{6d}$$

$$\gamma_{\xi z} = u_{\xi,z} + u_{z,\xi} \tag{6e}$$

$$\gamma_{\xi\eta} = \frac{1}{q}u_{\xi,\eta} + u_{\eta,\xi} - \frac{1}{q}\frac{\partial q}{\partial \xi}u_{\eta} \tag{6f}$$

Let us introduce the notation

$$D = a_{13}\sigma_{\xi\xi} + a_{23}\sigma_{\eta\eta} + a_{33}\sigma_{zz} + a_{34}\tau_{\eta z} + a_{35}\tau_{\xi z} + a_{36}\tau_{\xi\eta} \tag{7}$$

Integrating the third, fourth, and fifth equations of the strain-displacement equations (6), we obtain the following:

$$u_z = zD + W_0(\xi,\eta), \tag{8a}$$

$$u_\eta = -\frac{z^2}{2}\frac{1}{q}\frac{\partial D}{\partial \eta} + z\left(a_{14}\sigma_{\xi\xi} + a_{24}\sigma_{\eta\eta} + \ldots + a_{46}\tau_{\xi\eta} - \frac{1}{q}\frac{\partial W_0}{\partial \eta}\right) + V_0(\xi,\eta), \tag{8b}$$

$$u_\xi = -\frac{z^2}{2}\frac{\partial D}{\partial \xi} + z\left(a_{15}\sigma_{\xi\xi} + a_{25}\sigma_{\eta\eta} + \ldots + a_{56}\tau_{\xi\eta} - \frac{\partial W_0}{\partial \xi}\right) + U_0(\xi,\eta). \tag{8c}$$

where U_0, V_0, W_0 are arbitrary functions of ξ and η which appear as a result of integration with respect to z. It is further required that the functions (8) satisfy the remaining three equations of the strain-displacement equations (6). By substituting the expressions (8) for u_ξ, u_η, u_z and (5) for the strains into the remaining strain-displacement equations and equating equal powers of z yields the following equations for D:

$$\frac{\partial^2 D}{\partial \xi^2} = 0, \tag{9a}$$

$$\frac{\partial^2 D}{\partial \eta^2} + q\frac{\partial q}{\partial \xi}\frac{\partial D}{\partial \xi} - \frac{1}{q}\frac{\partial q}{\partial \eta}\frac{\partial D}{\partial \eta} = 0, \tag{9b}$$

Downloaded 03 May 2010 to 171.66.16.21. Redistribution subject to ASME license or copyright; see http://www.asme.org/terms/Terms_Use.cfm

$$\frac{\partial^2 D}{\partial\xi\partial\eta}-\frac{1}{q}\frac{\partial q}{\partial\xi}\frac{\partial D}{\partial\eta}=0. \tag{9c}$$

and for U_0, V_0:

$$\frac{\partial U_0}{\partial\xi}=a_{11}\sigma_{\xi\xi}+a_{12}\sigma_{\eta\eta}+\ldots+a_{16}\tau_{\xi\eta} \tag{10a}$$

$$\frac{\partial V_0}{\partial\eta}+\frac{\partial q}{\partial\xi}U_0=q\,(a_{12}\sigma_{\xi\xi}+a_{22}\sigma_{\eta\eta}+\ldots+a_{26}\tau_{\xi\eta}) \tag{10b}$$

$$\frac{\partial U_0}{\partial\eta}+q\frac{\partial V_0}{\partial\xi}-\frac{\partial q}{\partial\xi}V_0=q\,(a_{16}\sigma_{\xi\xi}+a_{26}\sigma_{\eta\eta}+\ldots+a_{66}\tau_{\xi\eta}) \tag{10c}$$

as well as the following equations for W_0:

$$\frac{\partial}{\partial\xi}\left(a_{15}\sigma_{\xi\xi}+a_{25}\sigma_{\eta\eta}+\ldots+a_{56}\tau_{\xi\eta}-\frac{\partial W_0}{\partial\xi}\right)=0 \tag{11a}$$

$$\frac{\partial}{\partial\eta}\left(a_{14}\sigma_{\xi\xi}+a_{24}\sigma_{\eta\eta}+\ldots+a_{46}\tau_{\xi\eta}-\frac{1}{q}\frac{\partial W_0}{\partial\eta}\right)+$$
$$+\frac{\partial q}{\partial\xi}\left(a_{15}\sigma_{\xi\xi}+a_{25}\sigma_{\eta\eta}+\ldots+a_{56}\tau_{\xi\eta}-\frac{\partial W_0}{\partial\xi}\right)=0 \tag{11b}$$

$$\frac{\partial}{\partial\eta}\left(a_{15}\sigma_{\xi\xi}+a_{25}\sigma_{\eta\eta}+\ldots+a_{56}\tau_{\xi\eta}-\frac{\partial W_0}{\partial\xi}\right)$$
$$+q\frac{\partial}{\partial\xi}\left(a_{14}\sigma_{\xi\xi}+a_{24}\sigma_{\eta\eta}+\ldots+a_{46}\tau_{\xi\eta}-\frac{1}{q}\frac{\partial W_0}{\partial\eta}\right)-$$
$$-\frac{\partial q}{\partial\xi}\left(a_{14}\sigma_{\xi\xi}+a_{24}\sigma_{\eta\eta}+\ldots+a_{46}\tau_{\xi\eta}-\frac{1}{q}\frac{\partial W_0}{\partial\eta}\right)=0 \tag{11c}$$

The solution to (9) is found to be:

$$D=a_{33}\left[A\left(\cosh a+\frac{\xi}{h}\sinh a\right)\cos\eta+B\right.$$
$$\left.\times\left(\sinh a+\frac{\xi}{h}\cosh a\right)\sin\eta+C\right] \tag{12}$$

and consequently, from (8a), (6c), (5c),

$$\sigma_{zz}=A\left(\cosh a+\frac{\xi}{h}\sinh a\right)\cos\eta+B$$
$$\times\left(\sinh a+\frac{\xi}{h}\cosh a\right)\sin\eta+C-\frac{1}{a_{33}}(a_{13}\sigma_{\xi\xi}+a_{23}\sigma_{\eta\eta}$$
$$+a_{34}\tau_{\eta z}+a_{35}\tau_{\xi z}+a_{36}\tau_{\xi\eta}) \tag{13}$$

where A, B, $\mathbf{C}$, are arbitrary constants. Let us introduce the new functions U, V, W which represent the displacements accompanied by deformation. We shall also introduce the constants v_{0x}, v_{0y}, v_{0z}, ω_x, ω_y, ω_z which characterize the rigid body translation and rotation about the cartesian coordinate system:

$$U_0=U+\frac{c}{h}(v_{0x}\sinh a\cos\eta+v_{0y}\cosh a\sin\eta)$$
$$+\omega_z\frac{c^2\sin 2\eta}{2h} \tag{14a}$$

$$V_0=V+\frac{c}{h}(-v_{0x}\cosh a\sin\eta+v_{0y}\sinh a\cos\eta)$$
$$+\omega_z\left(\xi+\frac{c^2\sinh 2a}{2h}\right) \tag{14b}$$

$$W_0=W+c\omega_x\sin\eta\left(\sinh a+\frac{\xi}{h}\cosh a\right)$$
$$-c\omega_y\cos\eta\left(\cosh a+\frac{\xi}{h}\sinh a\right)+v_{0z} \tag{14c}$$

Then, from (10), (13), and (14) we obtain the equations which connect the functions U, V with the components of stresses. In terms of the reduced elastic constants β_{ij}, defined by:

$$\beta_{ij}=a_{ij}-\frac{a_{i3}a_{j3}}{a_{33}}\quad i,j=1,2,4,5,6 \tag{15}$$

these equations are:

$$\frac{\partial U}{\partial\xi}=\beta_{11}\sigma_{\xi\xi}+\beta_{12}\sigma_{\eta\eta}+\beta_{14}\tau_{\eta z}+\beta_{15}\tau_{\xi z}+\beta_{16}\tau_{\xi\eta}+$$
$$+a_{13}\left[A\left(\cosh a+\frac{\xi}{h}\sinh a\right)\cos\eta+B\right.$$
$$\left.\times\left(\sinh a+\frac{\xi}{h}\cosh a\right)\sin\eta+C\right] \tag{16a}$$

$$\frac{\partial V}{\partial\eta}+\frac{\partial q}{\partial\xi}U=q\,(\beta_{12}\sigma_{\xi\xi}+\beta_{22}\sigma_{\eta\eta}+\beta_{24}\tau_{\eta z}$$
$$+\beta_{25}\tau_{\xi z}+\beta_{26}\tau_{\xi\eta})+qa_{23}\left[A\left(\cosh a+\frac{\xi}{h}\sinh a\right)\right.$$
$$\left.\times\cos\eta+B\left(\sinh a+\frac{\xi}{h}\cosh a\right)\sin\eta+C\right] \tag{16b}$$

$$\frac{\partial U}{\partial\eta}+q\frac{\partial V}{\partial\xi}-\frac{\partial q}{\partial\xi}V=q\,(\beta_{16}\sigma_{\xi\xi}+\beta_{26}\sigma_{\eta\eta}+\beta_{46}\tau_{\eta z}$$
$$+\beta_{56}\tau_{\xi z}+\beta_{66}\tau_{\xi\eta})+qa_{36}\left[A\left(\cosh a+\frac{\xi}{h}\sinh a\right)\right.$$
$$\left.\times\cos\eta+B\left(\sinh a+\frac{\xi}{h}\cosh a\right)\sin\eta+C\right] \tag{16c}$$

Equations (11) hold if we formally substitute W for W_0 and the solution to the resulting equations is found to be:

$$a_{15}\sigma_{\xi\xi}+a_{25}\sigma_{\eta\eta}+\ldots+a_{56}\tau_{\xi\eta}-\frac{\partial W}{\partial\xi}=\bar{\theta}\frac{\partial h}{\partial\eta} \tag{17a}$$

$$a_{14}\sigma_{\xi\xi}+a_{24}\sigma_{\eta\eta}+\ldots+a_{46}\tau_{\xi\eta}-\frac{1}{q}\frac{\partial W}{\partial\eta}$$
$$=\bar{\theta}\left(\xi+h\frac{\partial q}{\partial\xi}\right) \tag{17b}$$

where $\bar{\theta}$ is a constant associated with the amount of twisting. Taking into account (13) and (15), the above equations (17) yield the expressions between W and the components of stresses:

$$\frac{\partial W}{\partial\xi}=\beta_{15}\sigma_{\xi\xi}+\beta_{25}\sigma_{\eta\eta}+\beta_{45}\tau_{\eta z}+\beta_{55}\tau_{\xi z}+\beta_{56}\tau_{\xi\eta}$$
$$+a_{35}\left[A\left(\cosh a+\frac{\xi}{h}\sinh a\right)\cos\eta+B\right.$$
$$\left.\times\left(\sinh a+\frac{\xi}{h}\cosh a\right)\sin\eta+C\right]-\bar{\theta}\frac{\partial h}{\partial\eta} \tag{18a}$$

$$\frac{1}{q}\frac{\partial W}{\partial\eta}=\beta_{14}\sigma_{\xi\xi}+\beta_{24}\sigma_{\eta\eta}+\beta_{44}\tau_{\eta z}+\beta_{45}\tau_{\xi z}+\beta_{46}\tau_{\xi\eta}$$
$$+a_{34}\left[A\left(\cosh a+\frac{\xi}{h}\sinh a\right)\cos\eta+B\right.$$
$$\left.\times\left(\sinh a+\frac{\xi}{h}\cosh a\right)\sin\eta+C\right]-\bar{\theta}\left(\xi+h\frac{\partial q}{\partial\xi}\right) \tag{18b}$$

Downloaded 03 May 2010 to 171.66.16.21. Redistribution subject to ASME license or copyright; see http://www.asme.org/terms/Terms_Use.cfm

By using (8), (14), (12), and (18) we obtain the general expressions for the displacements which correspond to stresses depending only on the two coordinates ξ and η

$$u_\xi = U(\xi,\eta) - \frac{z^2}{2}\frac{1}{h}a_{33}\,(A\,\sinh a\cos\eta + B\cosh a\sin\eta) + \\ + z\bar{\theta}\frac{\partial h}{\partial\eta} - z\frac{c}{h}(\omega_x\cosh a\sin\eta - \omega_y\sinh a\cos\eta) + \\ + \frac{c}{h}(v_{0x}\sinh a\cos\eta + v_{0y}\cosh a\sin\eta) + \frac{\partial h}{\partial\eta}\omega_z \qquad (19a)$$

$$u_\eta = V(\xi,\eta) + \frac{z^2}{2}\frac{1}{h}a_{33}\,(A\cosh a\sin\eta - B\sinh a\cos\eta) + \\ + z\bar{\theta}\left(\xi + h\frac{\partial q}{\partial\xi}\right) \\ - z\frac{c}{h}(\omega_x\sinh a\cos\eta + \omega_y\cosh a\sin\eta) \\ + \frac{c}{h}(-v_{0x}\cosh a\sin\eta + v_{0y}\sinh a\cos\eta) \\ + \left(\xi + h\frac{\partial q}{\partial\xi}\right)\omega_z \qquad (19b)$$

$$u_z = W(\xi,\eta) + za_{33}\left[A\left(\cosh a + \frac{\xi}{h}\sinh a\right)\cos\eta + B \right. \\ \left. \times\left(\sinh a + \frac{\xi}{h}\cosh a\right)\sin\eta + C\right] + \\ \xi\frac{c}{h}(\omega_x\cosh a\sin\eta - \omega_y\sinh a\cos\eta) \\ + c\,(\omega_x\sinh a\sin\eta - \omega_y\cosh a\cos\eta) + v_{0z} \qquad (19c)$$

We can satisfy the equations of equilibrium (4) by introducing the two stress functions $F(\xi,\eta)$ and $\Psi(\xi,\eta)$:

$$\sigma_{\xi\xi} = \frac{1}{q^2}F_{,\eta\eta} + \frac{1}{q}\frac{\partial q}{\partial\xi}F_{,\xi} - \frac{1}{q^3}\frac{\partial q}{\partial\eta}F_{,\eta} \qquad (20a)$$

$$\sigma_{\eta\eta} = F_{,\xi\xi} \qquad (20b)$$

$$\tau_{\xi\eta} = -\frac{1}{q}F_{,\xi\eta} + \frac{1}{q^2}\frac{\partial q}{\partial\xi}F_{,\eta} \qquad (20c)$$

$$\tau_{\xi z} = \frac{1}{q}\Psi_{,\eta},\quad \tau_{\eta z} = -\Psi_{,\xi} \qquad (20d)$$

Eliminating U, V from (16) and W from (18), gives the following system of differential equations which the stress functions F and Ψ must satisfy:

$$L_4^I F + L_3^I\Psi = \frac{1}{h}\left(\frac{3\xi}{h}\frac{\partial q}{\partial\xi}\frac{\partial h}{\partial\eta} + \frac{\partial q}{\partial\eta}\right)[(a_{13}B - a_{36}A) \\ \times\sinh a\cos\eta - (a_{13}A + a_{36}B)\cosh a\sin\eta] - \\ - \frac{3}{q}\frac{\partial q}{\partial\xi}\frac{\partial h}{\partial\eta}a_{36}\left[A\left(\cosh a + \frac{\xi}{h}\sinh a\right)\cos\eta + B \right. \\ \left. \times\left(\sinh a + \frac{\xi}{h}\cosh a\right)\sin\eta + C\right] \\ + \frac{q}{h}\frac{\partial q}{\partial\xi}\{[a_{36}B - (2a_{23} - a_{13})A]\sinh a\cos\eta - [a_{36}A \\ + (2a_{23} - a_{13})B]\cosh a\sin\eta\} \\ + \frac{q}{h}[(a_{13}B - a_{36}A)\sinh a\sin\eta + (a_{13}A + a_{36}B)\cosh a\cos\eta] \qquad (21a)$$

$$L_3^{II}F + L_2^{II}\Psi = \frac{\partial q}{\partial\xi}a_{34}\left[A\left(\cosh a + \frac{\xi}{h}\sinh a\right)\cos\eta + B \right. \\ \left. \times\left(\sinh a + \frac{\xi}{h}\cosh a\right)\sin\eta + C\right] \\ + \frac{q}{h}[(a_{35}A + a_{34}B)\cosh a\sin\eta \\ - (a_{35}B - a_{34}A)\sinh a\cos\eta] - \bar{\theta}2q \qquad (21b)$$

L_2^{II}, L_3^I, L_3^{II}, L_4^I are the differential operators of the second, third, and fourth orders which have the form:

$$L_4^I = q^2\beta_{22}\frac{\partial^4}{\partial\xi^4} + \frac{1}{q^2}\beta_{11}\frac{\partial^4}{\partial\eta^4} + q\frac{\partial q}{\partial\xi}2\beta_{22}\frac{\partial^3}{\partial\xi^3} \\ + \frac{1}{q^3}\left(q\frac{\partial q}{\partial\xi}2\beta_{16} - \frac{\partial q}{\partial\eta}6\beta_{11}\right)\frac{\partial^3}{\partial\eta^3} + \\ + \frac{1}{q}\frac{\partial q}{\partial\xi}\left[\frac{\partial h}{\partial\eta}3(\beta_{16} + \beta_{26}) - q\frac{\partial q}{\partial\xi}\beta_{11}\right]\frac{\partial^2}{\partial\xi^2} \\ - \frac{1}{q^3}\left\{\frac{\partial q}{\partial\xi}\left(\frac{\partial q}{\partial\eta} + 2\frac{\partial h}{\partial\eta}\right)6\beta_{16} \right. \\ - q\left(\frac{\partial q}{\partial\xi}\right)^2(2\beta_{12} + \beta_{66}) + \left[4\frac{\partial^2 q}{\partial\eta^2} \right. \\ \left. \left. - \frac{15}{q}\left(\frac{\partial q}{\partial\eta}\right)^2 - 2q\left(\frac{\partial q}{\partial\xi}\right)^2\right]\beta_{11}\right\}\frac{\partial^2}{\partial\eta^2} + \\ + \frac{1}{q^3}\frac{\partial q}{\partial\xi}\left\{3\frac{\partial h}{\partial\eta}\left(2\frac{\partial q}{\partial\eta} + 3\frac{\partial h}{\partial\eta}\right) \right. \\ \left. - q\left[3\frac{\partial^2 q}{\partial\eta^2} - q\left(\frac{\partial q}{\partial\xi}\right)^2\right]\right\}\beta_{11}\frac{\partial}{\partial\xi} + \\ + \frac{1}{q^4}\left\{\left[3\frac{\partial q}{\partial\xi}\left(\frac{\partial h}{\partial\eta} + \frac{\partial q}{\partial\eta}\right)\left(\frac{\partial q}{\partial\eta} + 3\frac{\partial h}{\partial\eta}\right) - \right. \right. \\ \left. - q\frac{\partial q}{\partial\xi}\left(\frac{\partial^2 q}{\partial\eta^2} + 3\frac{\partial^2 h}{\partial\eta^2} - q\left(\frac{\partial q}{\partial\xi}\right)^2\right)\right]2\beta_{16} + \\ + q\left(\frac{\partial q}{\partial\xi}\right)^2\left[q\frac{\partial q}{\partial\xi}2\beta_{26} - \left(\frac{\partial q}{\partial\eta} + 6\frac{\partial h}{\partial\eta}\right)(2\beta_{12} + \beta_{66})\right] - \\ - \left[q\frac{\partial^3 q}{\partial\eta^3} - 10\frac{\partial^2 q}{\partial\eta^2}\frac{\partial q}{\partial\eta} + \frac{15}{q}\left(\frac{\partial q}{\partial\eta}\right)^3 \right. \\ \left. \left. + q\left(\frac{\partial q}{\partial\xi}\right)^2\left(2\frac{\partial q}{\partial\eta} + 3\frac{\partial h}{\partial\eta}\right)\right]\beta_{11}\right\}\frac{\partial}{\partial\eta} - \\ - q2\beta_{26}\frac{\partial^4}{\partial\xi^3\partial\eta} + (2\beta_{12} + \beta_{66})\frac{\partial^4}{\partial\xi^2\partial\eta^2} - \frac{1}{q}2\beta_{16}\frac{\partial^4}{\partial\xi\partial\eta^3} - \\ - \frac{1}{q}\frac{\partial q}{\partial\eta}(2\beta_{12} + \beta_{66})\frac{\partial^3}{\partial\xi^2\partial\eta} + \frac{1}{q^2}\left[\frac{\partial q}{\partial\eta}6\beta_{16} \right. \\ \left. - q\frac{\partial q}{\partial\xi}(2\beta_{12} + \beta_{66})\right]\frac{\partial^3}{\partial\xi\partial\eta^2} + \\ + \frac{1}{q^2}\left\{\left[\frac{\partial^2 q}{\partial\eta^2} - \frac{3}{q}\left(\frac{\partial q}{\partial\eta}\right)^2 - q\left(\frac{\partial q}{\partial\xi}\right)^2\right]2\beta_{16} + \right. \\ \left. + \frac{\partial q}{\partial\xi}\left(\frac{\partial q}{\partial\eta} + 3\frac{\partial h}{\partial\eta}\right)(2\beta_{12} + \beta_{66}) - q\left(\frac{\partial q}{\partial\xi}\right)^2 2\beta_{26}\right.$$

Downloaded 03 May 2010 to 171.66.16.21. Redistribution subject to ASME license or copyright; see http://www.asme.org/terms/Terms_Use.cfm

$$-6\frac{\partial q}{\partial \xi}\frac{\partial h}{\partial \eta}\beta_{11}\Big\}\frac{\partial^2}{\partial \xi \partial \eta} \tag{22a}$$

$$L_3^I = -q^2\beta_{24}\frac{\partial^3}{\partial \xi^3}+\frac{1}{q}\beta_{15}\frac{\partial^3}{\partial \eta^3}+q\frac{\partial q}{\partial \xi}(\beta_{14}-2\beta_{24})\frac{\partial^2}{\partial \xi^2}$$
$$-\frac{1}{q^2}\frac{\partial q}{\partial \eta}3\beta_{15}\frac{\partial^2}{\partial \eta^2}-\frac{1}{q}\frac{\partial q}{\partial \xi}\frac{\partial h}{\partial \eta}3\beta_{46}\frac{\partial}{\partial \xi}-$$
$$-\frac{1}{q^2}\left[\frac{\partial^2 q}{\partial \eta^2}-\frac{3}{q}\left(\frac{\partial q}{\partial \eta}\right)^2\right.$$
$$\left.-q\left(\frac{\partial q}{\partial \xi}\right)^2\right]\beta_{15}\frac{\partial}{\partial \eta}+q(\beta_{25}+\beta_{46})\frac{\partial^3}{\partial \xi^2\partial \eta}-$$
$$-(\beta_{14}+\beta_{56})\frac{\partial^3}{\partial \xi \partial \eta^2}+\frac{1}{q}\left[\frac{\partial q}{\partial \eta}(\beta_{14}+\beta_{56})\right.$$
$$\left.+q\frac{\partial q}{\partial \xi}(\beta_{46}-\beta_{15})\right]\frac{\partial^2}{\partial \xi \partial \eta} \tag{22b}$$

$$L_3^{II} = -q\beta_{24}\frac{\partial^3}{\partial \xi^3}+\frac{1}{q^2}\beta_{15}\frac{\partial^3}{\partial \eta^3}-\frac{\partial q}{\partial \xi}(\beta_{14}+\beta_{24})\frac{\partial^2}{\partial \xi^2}+$$
$$+\frac{1}{q^3}\left[q\frac{\partial q}{\partial \xi}(\beta_{14}+\beta_{56})-3\frac{\partial q}{\partial \eta}\beta_{15}\right]\frac{\partial^2}{\partial \eta^2}$$
$$-\frac{1}{q^2}\frac{\partial q}{\partial \xi}\frac{\partial h}{\partial \eta}3\beta_{15}\frac{\partial}{\partial \xi}-$$
$$-\frac{1}{q^3}\left\{\frac{\partial q}{\partial \xi}\left(\frac{\partial q}{\partial \eta}+3\frac{\partial h}{\partial \eta}\right)(\beta_{14}+\beta_{56})\right.$$
$$\left.-q\left(\frac{\partial q}{\partial \xi}\right)^2\beta_{46}+\left[\frac{\partial^2 q}{\partial \eta^2}-\frac{3}{q}\left(\frac{\partial q}{\partial \eta}\right)^2\right]\beta_{15}\right\}\frac{\partial}{\partial \eta}+$$
$$+(\beta_{25}+\beta_{46})\frac{\partial^3}{\partial \xi^2\partial \eta}-\frac{1}{q}(\beta_{14}+\beta_{56})\frac{\partial^3}{\partial \xi \partial \eta^2}+$$
$$+\frac{1}{q^2}\left[\frac{\partial q}{\partial \eta}(\beta_{14}+\beta_{56})+q\frac{\partial q}{\partial \xi}(\beta_{15}-\beta_{46})\right]\frac{\partial^2}{\partial \xi \partial \eta} \tag{22c}$$

$$L_2^{II} = q\beta_{44}\frac{\partial^2}{\partial \xi^2}+\frac{1}{q}\beta_{55}\frac{\partial^2}{\partial \eta^2}+\frac{\partial q}{\partial \xi}\beta_{44}\frac{\partial}{\partial \xi}$$
$$-\frac{1}{q^2}\frac{\partial q}{\partial \eta}\beta_{55}\frac{\partial}{\partial \eta}-2\beta_{45}\frac{\partial^2}{\partial \xi \partial \eta} \tag{22d}$$

The components of stresses and displacements inside the body must be continuous and single-valued functions of the coordinates. For their determination, we must find the stress functions which satisfy equations (21) and the boundary conditions, which will next be considered.

We assume that the external tractions have components on the $\hat{\xi}$, $\hat{\eta}$ directions, denoted by Ξ_n, H_n, respectively. Then the conditions on the contour bounding the cross section (outmost and innermost layers) can be written in the following form:

$$\sigma_{\xi\xi}\cos(\hat{n},\hat{\xi})+\tau_{\xi\eta}\cos(\hat{n},\hat{\eta})=\Xi_n \tag{23a}$$
$$\tau_{\xi\eta}\cos(\hat{n},\hat{\xi})+\sigma_{\eta\eta}\cos(\hat{n},\hat{\eta})=H_n \tag{23b}$$
$$\tau_{\xi z}\cos(\hat{n},\hat{\xi})+\tau_{\eta z}\cos(\hat{n},\hat{\eta})=0 \tag{23c}$$

where $\hat{n}$ is in the direction of the exterior normal (being along the direction of $\hat{\xi}$). By integrating (23*c*) with respect to the arc length, $ds=qd\eta$, from a certain initial point ($s=0$) to the variable point s, and taking into account (20*d*), we find that the stress function Ψ is constant on the boundary:

$$\Psi = c_i \tag{24}$$

where c_i are constants corresponding to each of the boundary contours (for a simply connected region we could just set this constant equal to zero).

Now, let us consider the conditions at the ends of an ellipsoid of finite length. The conditions at the ends have the form:

$$\iint\left(\frac{\partial x}{\partial \xi}\tau_{\xi z}+\frac{1}{q}\frac{\partial x}{\partial \eta}\tau_{\eta z}\right)dS=0,\quad \iint\sigma_z y dS=M_1 \tag{25a}$$

$$\iint\left(\frac{\partial y}{\partial \xi}\tau_{\xi z}+\frac{1}{q}\frac{\partial y}{\partial \eta}\tau_{\eta z}\right)dS=0,\quad \iint\sigma_z x dS=M_2 \tag{25b}$$

$$\iint\sigma_z dS=P_z,$$
$$\iint\left[\left(\xi+h\frac{\partial q}{\partial \xi}\right)\tau_{\eta z}+\frac{\partial h}{\partial \eta}\tau_{\xi z}\right]dS=M_t \tag{25c}$$

where the integrals are taken over the entire area of the cross-section (notice that $dS=qd\xi d\eta$). Since the stresses do not depend on z, these conditions exist not only at the ends, but also in any cross-section. In the above expressions for the end loading, P_z is the resultant axial force, M_1, M_2 are the bending moments about the x, y axes, respectively, and M_t is the twisting moment.

The first equations of (25*a*) and (25*b*), which express the condition of zero resultant forces along the x and y axes, are satisfied identically. Indeed, using the equilibrium condition (4*c*),

$$\iint\left(\tau_{\xi z}\frac{\partial x}{\partial \xi}+\tau_{\eta z}\frac{1}{q}\frac{\partial x}{\partial \eta}\right)dS$$
$$=\iint\left\{\tau_{\xi z}\frac{\partial x}{\partial \xi}+\tau_{\eta z}\frac{1}{q}\frac{\partial x}{\partial \eta}+\frac{x}{q}[(q\tau_{\xi z}),\xi+\tau_{\eta z,\eta}]\right\}dS$$
$$=\iint[(xq\tau_{\xi z}),\xi+(x\tau_{\eta z})_{,\eta}]\frac{1}{q}dS$$

By transforming the double integral into a contour integral using the divergence theorem in curvilinear coordinates (contour γ), and apply (23*c*), we obtain:

$$\iint\left(\tau_{\xi z}\frac{\partial x}{\partial \xi}+\tau_{\eta z}\frac{1}{q}\frac{\partial x}{\partial \eta}\right)dS$$
$$=\int_\gamma x[\tau_{\xi z}\cos(\hat{n},\hat{\xi})+\tau_{\eta z}\cos(\hat{n},\hat{\eta})]\,ds=0$$

It can be proved in the same way that the first integral in (25*b*) is also equal to zero. Therefore, by substituting (1) and (13) in (25), we find that for a body with a bounded cross-section on the ends (and in any cross section) the following conditions must be satisfied:

$$CS-\frac{1}{a_{33}}\iint(a_{13}\sigma_{\xi\xi}+a_{23}\sigma_{\eta\eta}+a_{34}\tau_{\eta z}+a_{35}\tau_{\xi z}$$
$$+a_{36}\tau_{\xi\eta})\,qd\xi d\eta=P_z \tag{26a}$$

$$AI_1-\frac{1}{a_{33}}\iint(a_{13}\sigma_{\xi\xi}+a_{23}\sigma_{\eta\eta}+\ldots+a_{36}\tau_{\xi\eta})c$$
$$\times\left(sinh\,a\sin\eta+\frac{\xi}{h}\cosh a\sin\eta\right)qd\xi d\eta=M_1 \tag{26b}$$

$$BI_2-\frac{1}{a_{33}}\iint(a_{13}\sigma_{\xi\xi}+a_{23}\sigma_{\eta\eta}+\ldots+a_{36}\tau_{\xi\eta})c$$

Downloaded 03 May 2010 to 171.66.16.21. Redistribution subject to ASME license or copyright; see http://www.asme.org/terms/Terms_Use.cfm

$$\times\left(\cosh a\cos\eta+\frac{\xi}{h}\sinh a\cos\eta\right)qd\xi d\eta=M_2 \qquad (26c)$$

$$\iint\left[\left(\xi+h\frac{\partial q}{\partial\xi}\right)\tau_{\eta z}+\frac{\partial h}{\partial\eta}\tau_{\xi z}\right]qd\xi d\eta=M_t \qquad (26d)$$

where S is the cross-sectional area and I_1, I_2 are the principal moments of interia with respect to the x and y axes which are assumed to pass through the centroid of the section (Fig. 1).

The stress functions F and Ψ which satisfy the equations (21) and the boundary conditions on the cross-section (23) will contain the four arbitrary constants $\bar{\theta}$, A, B, C. These are in turn found from the equations (26) for the end loading.

Torsion of an Orthotropic Body

If a plane of elastic symmetry normal to the z-axis exists at each point, then the coefficients a_{14}, a_{24}, a_{34}, a_{46}, a_{15}, a_{25}, a_{35}, a_{56} in the stress-strain equations (5) are equal to zero. If there are two planes of elastic symmetry (along the normal and the tangent to the periphery of each layer), then in addition to the above, the coefficients a_{16}, a_{26}, a_{36}, a_{45}, are also equal to zero. The latter is the case of an orthotropic body with elliptical anisotropy. As a consequence, in this case:

$$\beta_{14}=\beta_{24}=\beta_{45}=\beta_{46}=\beta_{15}=\beta_{25}=\beta_{56}=0 \qquad (27)$$

The system (21) reduces to two equations: One equation involves only the function F; the other equation involves only the function Ψ.

In this case of an orthotropic body it may be more convenient to use the engineering elastic characteristics, which are denoted for the Young's moduli as E_ξ, E_η, E_z, for the Poisson's ratios as $\nu_{\xi\eta}$, $\nu_{\xi z}$, $\nu_{z\xi}$, ν_{zn}, $\nu_{\eta z}$, and for the shear moduli as $G_{\xi\eta}$, $G_{\eta z}$, $G_{\xi z}$. The reduced elastic constants are expressed as:

$$\beta_{11}=\frac{1-\nu_{\xi z}\nu_{z\xi}}{E_\xi},\ \beta_{12}=-\frac{\nu_{\xi\eta}+\nu_{\xi z}\nu_{zn}}{E_\xi},\ \beta_{22}=\frac{1-\nu_{\eta z}\nu_{zn}}{E_\eta}, \qquad (28a)$$

$$\beta_{66}=\frac{1}{G_{\xi\eta}},\ \beta_{44}=\frac{1}{G_{\eta z}},\ \beta_{55}=\frac{1}{G_{\xi z}}. \qquad (28b)$$

The other β_{ij} are either zero or do not enter into the above formulas.

Let us consider the particular problem of torsion of a filament wound orthotropic ellipsoidal bar.

The equation for the stress function Ψ becomes:

$$q\beta_{44}\Psi_{,\xi\xi}+\frac{1}{q}\beta_{55}\Psi_{,\eta\eta}+\frac{\partial q}{\partial\xi}\beta_{44}\Psi_{,\xi}-\frac{1}{q^2}\frac{\partial q}{\partial\eta}\beta_{55}\Psi_{,\eta}=-2\bar{\theta}q \qquad (29)$$

The constant $\bar{\theta}$ is the scaling factor that represents the magnitude of the twisting moment M_t, and thus can be found from the end condition (26d). To eliminate this constant from (30), set

$$\Psi(\xi,\eta)=\bar{\theta}\psi(\xi,\eta) \qquad (30)$$

Equation (29) then becomes

$$q\beta_{44}\psi_{,\xi\xi}+\frac{1}{q}\beta_{55}\psi_{,\eta\eta}+\frac{\partial q}{\partial\xi}\beta_{44}\psi_{,\xi}-\frac{1}{q^2}\frac{\partial q}{\partial\eta}\beta_{55}\psi_{,\eta}=-2q \qquad (31)$$

This equation is solved in conjunction with the boundary conditions (23c) which are equivalent to enforcing a constant value of ψ on the boundary. Notice, however, that the domain is multiply connected. So the boundary condition (24) is expressed in detail:

$$\psi=c_1 \text{ at } \xi=0,\ \psi=c_2 \text{ at } \xi=T. \qquad (32)$$

The value of ψ on the outer boundary can be chosen arbitrarily to be zero, $c_2=0$. The other constant, c_1, is yet unspecified. For its determination we use the requirement that the displacement u_z be single valued. Thus, if we make a circuit around the contour of the inner boundary, the following condition should be satisfied:

$$\int_0^{2\pi}\left(\frac{\partial u_z}{\partial\eta}\right)_{\xi=0}d\eta=0 \qquad (33)$$

By (19c) the above equation is reduced to

$$\int_0^{2\pi}\left(\frac{\partial W}{\partial\eta}\right)_{\xi=0}d\eta=0 \qquad (34)$$

Substituting (18b) for $\partial W/\partial\eta$, we obtain

$$\int_0^{2\pi}\left[h\beta_{44}\,(\tau_{\eta z})_{\xi=0}-\bar{\theta}\frac{c^2\sinh 2a}{2}\right]d\eta=0 \qquad (35)$$

By using (20) and (30) the following condition is obtained for the function ψ, that allows determining the constant $\psi\,|_{\xi=0}=c_1$:

$$\int_0^{2\pi}h\,(\psi_{,\xi})_{\xi=0}\,d\eta=-\frac{c^2\pi\sinh 2a}{\beta_{44}} \qquad (36)$$

The above equation serves as another condition on ψ which must be satisfied to ensure that the displacements are single valued. Notice also that (33) and (34) hold for general anisotropy.

Having obtained $\psi(\xi,\eta)$, the constant $\bar{\theta}$ is found from the end condition (26d). In terms of the rigidity C_R defined by

$$C_R=\iint\left[-\left(\xi+h\frac{\partial q}{\partial\xi}\right)q\psi_{,\xi}+\frac{\partial h}{\partial\eta}\psi_{,\eta}\right]d\xi d\eta \qquad (37)$$

we obtain by using (20d) and (30),

$$\bar{\theta}=M_t/C_R \qquad (38)$$

Now, let us look into the physical meaning of the constant $\bar{\theta}$. If we assume pure torsion, i.e., $F=0$, then from (26b, c) we get $A=B=0$. Then from (19a, b), it is seen that $\bar{\theta}z$ is the angle of twisting. Therefore, $\bar{\theta}$ measures the twist angle per unit length.

Finally, modelling the geometry as indicated previously, allows a direct usage of the engineering properties of the material, as these can be determined by independent tests. For example, for a unidirectional composite that is laid up at 0 deg, the η direction is the direction of the fibers, the z direction is the one at 90 deg to the fibers on the plane of the composite sheet and the ξ direction is the out-of-plane normal direction. In this manner, the elastic characteristics of the composite layers can be used directly in the above formulation.

Results and Discussion

The finite difference method was used to solve (31) and (36), together with the condition $\psi\,|_{\xi=T}=0$ (e.g., Ketter and Prawel, 1969). Two important points should be noted. First, the structure of equation (31) shows that the domain can be reduced by symmetry conditions to one quarter of the elliptical cross-section, i.e., for $0\le\eta\le\pi/2$. Then, the values of the function ψ at all other points are given for $\pi/2\le\eta\le\pi$ by $\psi(\xi,\eta)=\psi(\xi,\pi-\eta)$; for $\pi\le\eta\le 3\pi/2$ by $\psi(\xi,\eta)=\psi(\xi,\eta-\pi)$; and for $3\pi/2\le\eta\le 2\pi$ by $\psi(\xi,\eta)=\psi(\xi,2\pi-\eta)$. However, this symmetry will not exist if β_{45} is not zero, i.e., if only one plane of elastic symmetry normal to the z-axis exists, in which case, equation (31) should be modified

Downloaded 03 May 2010 to 171.66.16.21. Redistribution subject to ASME license or copyright; see http://www.asme.org/terms/Terms_Use.cfm

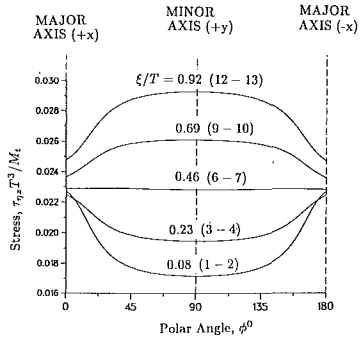

Fig. 2 Angular distribution of the shear stress $\tau_{\eta z}$ for a set of layer interfaces in a 13-ply orthotropic bar (layer numbers denoted in parentheses)

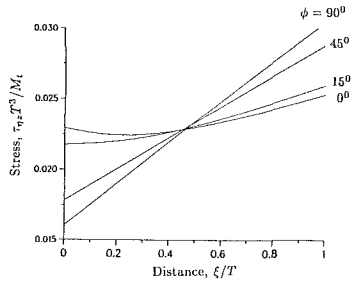

Fig. 3 Thicknesswise distribution (along ξ) of the shear stress $\tau_{\eta z}$

to include the extra term (this case arises, for example, when an orthotropic composite sheet is laid up at a different lay up angle.) In the latter case the domain can be reduced by symmetry to only one half of the cross-section, i.e., for $0 \leq \eta \leq \pi$. Then, for $\pi \leq \eta \leq 2\pi$, $\psi(\xi, \eta) = \psi(\xi, \eta - \pi)$. Second, due to local nature of the finite-difference operators, the coefficient matrix is highly banded. By storing only those terms of the coefficient matrix which fall within the bandwidth, a simple Gauss elimination scheme can be used to solve the relevant system of linear equations with maximum economy and, therefore, find the values of the unknowns ψ_{ij} at the interior points plus the unknown value c_1 on the inner boundary $\xi = 0$.

Employing the elasticity formulation and the solution technique discussed earlier, the distribution of stress was obtained for material properties typical of a glass fiber/epoxy composite (Lekhnitskii, 1963): $G_{12} = 5{,}700$ MN/m^2, $G_{23} = 5{,}000$ MN/m^2, where the direction 1 is along the fibers, 2 is the in-plane normal to the fibers and 3 the out-of-plane normal direction. If this material is laid up at 90 deg, then $1 \equiv \eta$, $2 \equiv z$, $3 \equiv \xi$. As an example case, 13 layers of 1-mm thickness each are wound on an elliptical mandrel with major semiaxis $e_1 = 35$ mm and minor one $e_2 = 20$ mm.

Figure 2 shows the angular distribution of the shearing stress $\tau_{\eta z}$ at certain distances ξ across the thickness, which correspond to layer interfaces as given in parentheses. For a distance ξ below a particular value (in this case below $\xi/T = 0.462$), this interlaminar shear has the maximum at the major axis and the minimum at the minor one. The exact opposite happens for layers that are above this threshold value. In fact, the largest interlaminar shear stress $\tau_{\eta z}$ occurs at the outermost interface (between layers 12 and 13) and at the minor axis. Furthermore, Fig. 3 shows the variation of this stress with the thicknesswise distance ξ. Near the major axis the change in $\tau_{\eta z}$ between the innermost and the outermost layers is relatively small and the curve is seen to be highly nonlinear. On the contrary, near the minor axis the variation can be characterized as linear and of relatively large magnitude. Also, the curves have a common intersection point at the threshold value of $\xi/T = 0.462$, where here is practically no angular variation.

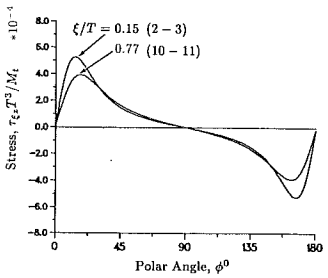

Fig. 4 Angular distribution of the shear stress $\tau_{\xi z}$ for two-layer interfaces in a 13-ply bar (layer numbers denoted in parentheses)

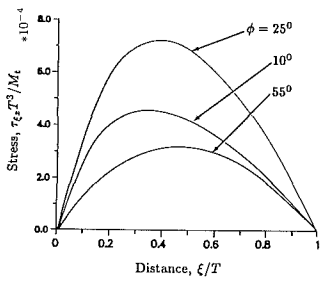

Fig. 5 Thicknesswise distribution (along ξ) of the shear stress $\tau_{\xi z}$

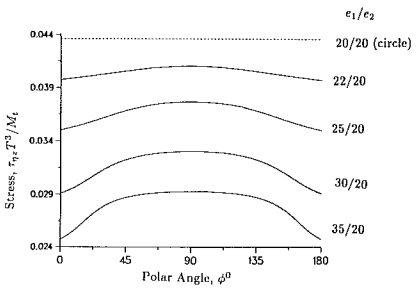

Fig. 6 Effect of a change in the major to minor axis ratio of the mandrel on the angular distribution of the shear stress $\tau_{\eta z}$ at the outermost layer interface. The dashed curve is the solution for a circular cross-section.

The distribution of the stress $\tau_{\xi z}$ with the polar angle ϕ is shown in Fig. 4 for two distinct values of ξ. It is seen that this component of stress, which is two orders of magnitude less than the stress $\tau_{\eta z}$, peaks at about $\phi = 25$ deg and it follows the same pattern for all points thicknesswise. The distribution of $\tau_{\xi z}$ across the thickness is illustrated in Fig. 5. The maximum value is shifted outwards for points closer to the minor axis, so that for $\phi = 10$ deg, the peak occurs at about $\xi/T = 0.3$, whereas for $\phi = 55$ deg, the peak is at about $\xi/T = 0.5$. Notice that $\tau_{\xi z}$ is zero at all points on both the minor and major axis, as well at all points on the inner and outer bounding surface.

Now, let us keep the minor axis of the mandrel at 20 mm while the major axis is reduced until it becomes equal to the minor one (the limit of a circular section). The effect of this variation in the major to minor axis ratio on the angular distribution of the maximum interlaminar shear stress $\tau_{\eta z}$ (between layers 12-13) is shown in Fig. 6. As the elliptical mandrel approaches a circle, the distribution becomes flatter. The solution is seen to converge to that constant value (since for a circular section there is only radial dependence) that was given for the solution of the torsion of cylindrically orthotropic rods by Lekhnitskii (1963).

Conclusion

We have presented a formulation of the theory of elasticity

Downloaded 03 May 2010 to 171.66.16.21. Redistribution subject to ASME license or copyright; see http://www.asme.org/terms/Terms_Use.cfm

of filament wound anisotropic ellipsoids. The anisotropy in this case is curvilinear, defined with respect to the directions that are equivalent in the sense of the elastic properties, and which are dictated by the regularities of the body. The differential equations for the stresses have been derived for a material possessing anisotropy of the most general kind. Furthermore, the solution for the special case of torsion of an orthotropic body was obtained and results for the angular and thicknesswise distribution of the shear stresses were presented.

References

do Carmo, M. P., 1976, *Differential Geometry of Curves and Surfaces*, Prentice-Hall, New York.

Ketter, R. L., and Prawel, Jr., S. P., 1969, *Methods of Engineering Computation*, McGraw-Hill, New York.

Lekhnitskii, S. G., 1963, *Theory of Elasticity of an Anisotropic Elastic Body*, Holden Day, (also Mir Publishers, 1981).

Pagano, N. J., and Halpin, J. C., 1968, "Tension Buckling of Anisotropic Cylinders," *Journal of Composite Materials*, Vol. 2, pp. 154–167.

Sherrer, R. E., 1967, "Filament Wound Cylinder with Axial Symmetric Loads," *Journal of Composite Materials*, Vol. 1, pp. 344–355.

Downloaded 03 May 2010 to 171.66.16.21. Redistribution subject to ASME license or copyright; see http://www.asme.org/terms/Terms_Use.cfm

J. F. Wilson
Professor.
School of Engineering.
Mem. ASME

J. M. Snyder
Lecturer.
Department of Civil Engineering.

Duke University,
Durham, NC 27706

The Elastica With End-Load Flip-Over

A high flexure manipulator arm is modeled as an elastic cantilever beam with a tip payload and an eccentric tip follower load that drives the arm. Shapes of the resulting elastic curves for finite deformations (the elastica) are calculated in terms of nondimensional system parameters. For critical combinations of these parameters, a small increment in the driving follower load causes an abrupt change in the shape of the elastica. The abrupt change in tip angle is typically of the order of π radians. These results are applicable to the design of high flexure robotic manipulators.

Introduction

A high flexure manipulator tube element is shown in Fig. 1. Typically, such an element is fabricated from a polymeric material, has a thin corrugated bellows section for part of its circumference, and a flat reinforced strip along one side. Rigid caps are provided at each end. The neutral axis of bending is located in the flat strip, eccentric from the center of pressure on the end caps. When the element is pressurized it behaves as the beam shown in Fig. 1(*b*), where the pressure load is offset by distance d_d and rotates to follow the tangent to the elastic line. Also present at the tip of the element is a payload W_d. The purpose of the present study is to present a mathematical model to predict the large static deformations of this element when it is pressurized to lift the payload W_d.

The element is modeled as an end-loaded elastic cantilever beam for which self-weight is negligible compared to the applied loads. Since the range of deformation of the beam is too large for the application of linear beam theory, the beam is analyzed using the exact curvature relations. The shape of the elastic curve of a beam derived from the exact curvatures is called the elastica.

Love (1927) summarizes the classical theory of the elastica. Schmidt and DaDeppo (1971) present a wealth of related references. Wang (1981) treats the cantilevered elastica with a concentrated tip force only. Lau (1982) considers the problem of general tip loads and Wilson (1987) presents experimental applications. We treat a more specific problem of a follower tip force and a moment which are physically related and which lead to a unique equilibrium state.

Mathematical Model

Consider the cantilever beam with end loads P_d, Q_d, and M_d as shown in Fig. 2. (The subscript d refers to a quantity with physical dimensions.) The origin of the fixed X, Y axis is at the base of the beam. The origin of the x_d, y_d axes is at the tip of the beam and the loads P_d and Q_d remain parallel to both these axes and the X, Y system. The basic assumptions of the element model are: The beam is weightless and all loads are concentrated at its tip; the beam material is linear elastic; the neutral axis of the beam is inextensible; the effects of Poisson's ratio and transverse shearing deformations on the bending deflections are negligible; unloaded, the beam is straight with length L; loaded, the curvature of the beam, $d\theta/ds_d$, is nonpositive.

Based on these assumptions, the differential equation of the elastica is

$$EI\frac{d\theta}{ds_d} = -P_d y_d - Q_d x_d - M_d \tag{1}$$

where E is the modulus of elasticity and I is the second moment of area of the beam cross-section. With the following nondimensional parameters

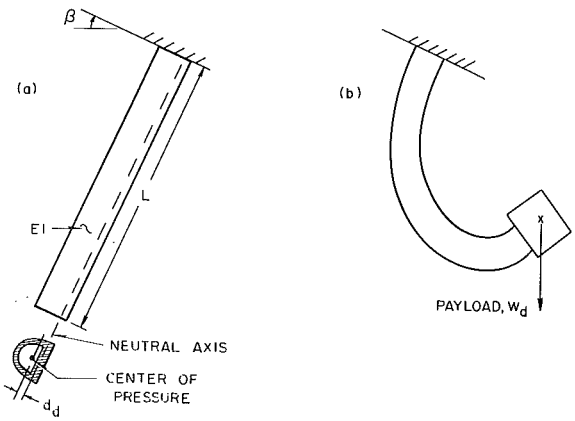

Fig. 1 (*a*) Unloaded tube element; (*b*) pressurized tube element with payload at tip

Contributed by the Applied Mechanics Division of THE AMERICAN SOCIETY OF MECHANICAL ENGINEERS, for presentation at the Joint ASCE/ASME Applied Mechanics, Biomechanics, and Fluids Engineering Conference, San Diego, CA, July 9 to 12, 1989.

Discussion on this paper should be addressed to the Editorial Department, ASME, United Engineering Center, 345 East 47th Street, New York, N.Y. 10017, and will be accepted until two months after final publication of the paper itself in the JOURNAL OF APPLIED MECHANICS. Manuscript received by ASME Applied Mechanics Division, October 26, 1987; final revision, May 26, 1988.

Paper No. 89-APM-18.

Copyright © 1988 by ASME
Downloaded 03 May 2010 to 171.66.16.21. Redistribution subject to ASME license or copyright; see http://www.asme.org/terms/Terms_Use.cfm

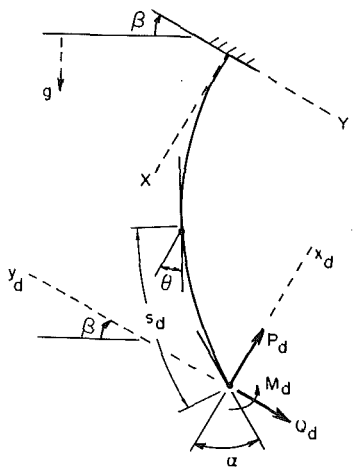

Fig. 2 Coordinate systems and general tip loads for the cantilevered beam

$$s=\frac{s_d}{L} \quad x=\frac{x_d}{L} \quad y=\frac{y_d}{L}$$

$$P=\frac{P_dL^2}{EI} \quad Q=\frac{Q_dL^2}{EI} \quad M=\frac{M_dL}{EI} \tag{2}$$

equation (1) is transformed to the following nondimensional form

$$\frac{d\theta}{ds}=-Py-Qx-M \tag{3}$$

When equation (3) is differentiated with respect to s and the following relations are used

$$dx=\cos\theta ds \qquad dy=\sin\theta ds \tag{4}$$

equation (3) becomes

$$\frac{d^2\theta}{ds^2}=-P\sin\theta-Q\cos\theta \tag{5}$$

This equation is integrated as

$$\int_{-M}^{\frac{d\theta}{ds}}\frac{d\theta}{ds}d\left(\frac{d\theta}{ds}\right)=\int_{\alpha}^{\theta}(-P\sin\theta-Q\cos\theta)d\theta \tag{6}$$

where α is the slope of the elastic curve at the tip of the beam. The result is

$$\frac{1}{2}\left(\frac{d\theta}{ds}\right)^2-\frac{1}{2}M^2=P(\cos\theta-\cos\alpha)+Q(\sin\alpha-\sin\theta) \tag{7}$$

When equation (7) is solved for $d\theta/ds$, which is nonpositive in this problem, the following equation is obtained

$$ds=\frac{-d\theta}{\sqrt{2P(\cos\theta-\cos\alpha)+2Q(\sin\alpha-\sin\theta)+M^2}} \tag{8}$$

Equation (8) is stated more concisely as

$$ds=\frac{-d\theta}{\sqrt{a+b\cos(\theta+\theta_0)}} \tag{9}$$

where

$$a=M^2-b\cos(\alpha+\theta_0)$$

$$b=2\sqrt{P^2+Q^2}$$

$$\theta_0=\arctan\left(\frac{Q}{P}\right), \text{ with } -\pi<\theta_0\le\pi \tag{10}$$

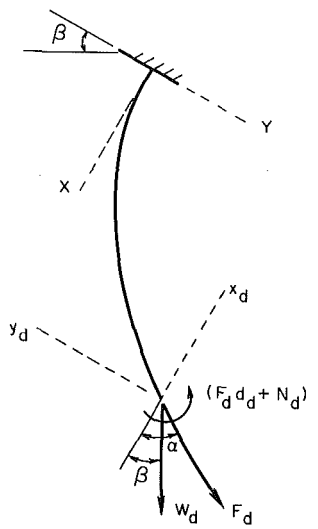

Fig. 3 Tip loads for the tube element

Equation (9) is integrated over the length of the beam to obtain

$$1-s=\int_{\theta_0}^{\theta+\theta_0}\frac{d\phi}{\sqrt{a+b\cos\phi}} \tag{11}$$

where $\phi=\theta+\theta_0$. Equation (11) is a nonexplicit, closed form solution for the rotation of the beam, θ, at the arc length coordinate s. The nondimenional coordinates at s are

$$x=\int_{\theta+\theta_0}^{\alpha+\theta_0}\frac{\cos(\phi-\theta_0)d\phi}{\sqrt{a+b\cos\phi}}$$

$$y=\int_{\theta+\theta_0}^{\alpha+\theta_0}\frac{\sin(\phi-\theta_0)d\phi}{\sqrt{a+b\cos\phi}} \tag{12}$$

Equations (11) and (12) may be expressed in terms of elliptic integrals, but this provides no advantage in obtaining numerical results for this problem. The solutions remain nonexplicit and must be solved numerically. Given the nondimensional loads P, Q, and M and the arc length coordinate s, compatible solutions $(\theta,x,y;\alpha)$ for the shape of the elastica may be calculated from equations (10)–(12). The loading is expressed next.

Loading Conditions

Define W_d and N_d as the force and moment due to the weight of the payload at the tip of the element. As shown in Figs. 2 and 3, gravity acts at the angle β to the X axis. F_d is the pressure load at the tip, acting at eccentricity d_d from the neutral axis. The direction and magnitude of W_d remains unchanged as the element rotates, while F_d rotates to match the slope at the tip of the element. N_d varies with both α and the configuration of the payload.

Define the following nondimensional loading parameters:

$$F=\frac{F_dL^2}{EI} \quad W=\frac{W_dL^2}{EI} \quad N=\frac{N_dL}{EI} \quad d=\frac{d_d}{L} \tag{13}$$

The nondimensional loads of equations (10) are

$$P=-F\cos\alpha-W\cos\beta$$

$$Q=F\sin\alpha+W\sin\beta$$

$$M=N+Fd \tag{14}$$

Downloaded 03 May 2010 to 171.66.16.21. Redistribution subject to ASME license or copyright; see http://www.asme.org/terms/Terms_Use.cfm

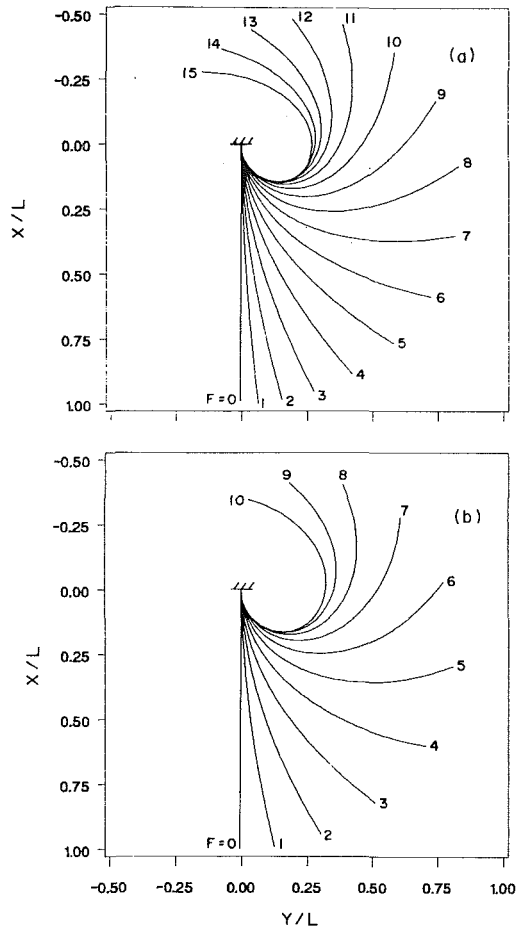

Fig. 4 Element elastica with no payload and with increasing pressure loads, where (*a*) $d = 0.1$, and (*b*) $d = 0.2$

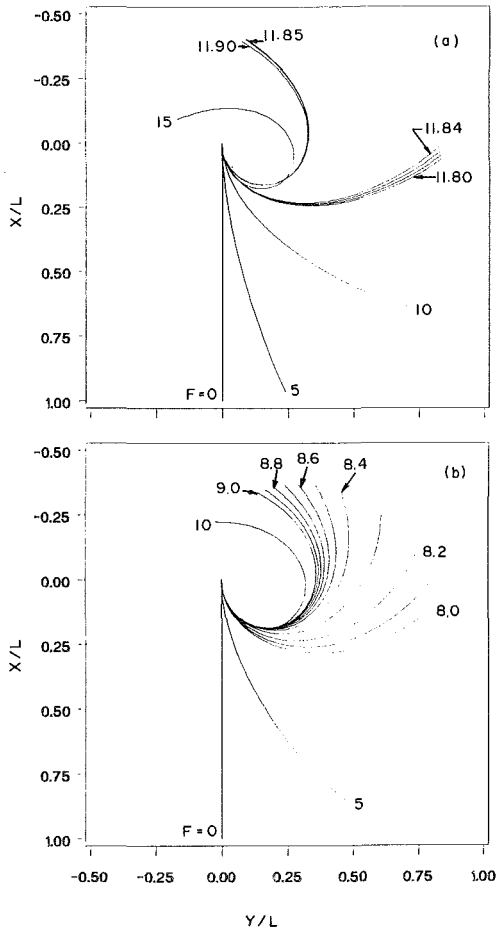

Fig. 5 Element elastica with $W = 2.5$ and increasing pressure load, where (*a*) $d = 0.1$, and (*b*) $d = 0.2$

which are used with equations (11) and (12) to calculate the elastica of the element model.

Numerical Results

Consider a vertical element ($\beta = 0$) designed to lift a point mass of weight W_d. The point mass is located at the tip of the element and on the neutral axis so that $N_d = 0$. This problem was solved numerically in nondimensional form using equations (10)-(12) and (14). Given d, F, and W, equation (11) is first solved for α ($s = 0$) using a bracketing method. After α is calculated, the equations are used in an explicit manner to determine the planar coordinates at a sufficient number of points on the neutral axis to describe its deformed shape. Numerical quadrature is used to evaluate all integrals in the equations. The computer code used for these calculations is listed by Wilson (1987).

Figures 4–7 show the calculated results for a range of nondimensional parameters representative of practical experimental elements. Each of these figures shows, for given values of d and W, the elastica of the element when subjected to different values of the nondimensional pressure load, F. For clarity, these figures employ the fixed X–Y coordinate system defined by Fig. 3, normalized by the element length L.

Figures 4(*a*) and 4(*b*) show the elastica with no dead weight load ($W = 0$). As expected, for a given level of pressure loading F the curvature and the tip rotation increase as the eccentricity d of the pressure load increases. Figures 5–7 show that shortly after the tip of the element rotates past 90 deg, a relatively small increment of pressure load causes a "flip-over," or large change in shape of the elastica. This behavior, not observed when $W = 0$ (Fig. 4), becomes more pronounced as W increases. Flip-over is of practical interest because it can cause significant problems in the control of the element position.

Figures 5(*a*) and 5(*b*), for which $W = 2.5$, present a more detailed view of the flip-over phenomenon. Figure 5(*a*), for which $d = 0.1$, shows the shape of the elastica as F varies from 0 to 15. A large change in shape occurs as F increases from 11.8 to 11.9. This figure shows the shape of the elastica as F increases from 11.8 to 11.9 in increments of 1/100. The element still changes shape in an abrupt manner as F is increased using these finer load increments, the change occurring between $F = 11.84$ and $F = 11.85$. Figure 5(*b*), for which $d = 0.2$, shows the shape of the elastica as F varies from 0 to 10. A large change in shape occurs as F increases from 8 to 9. This figure shows the shape of the element model as F increases from 8 to 9 in increments of 1/10. The element changes shape in a regular manner as F is increased using these finer load increments. The behavior illustrated by this figure represents a transition between the regular behavior exhibited in Fig. 4, for which $W = 0$, and the abrupt flip-over which occurs in Figs. 5(*a*), 6, and 7.

Table 1 presents the pressure load at the onset of flip-over, F_{cr}, the tip rotation at the onset of flip-over, α_{cr} and the change in tip rotation due to flip-over, $\Delta\alpha$, for a range of values of W and d. F_{cr} is reported to the nearest hundredth and $\Delta\alpha$ is computed by subtracting α_{cr} from the tip rotation calculated for $F_{cr} + .01$. When $W = 2.5$ and $d = 0.2$, F_{cr} is reported to an integer value and α_{cr} and $\Delta\alpha$ are not reported because the change in shape is not abrupt and, hence, these quantities cannot be precisely identified. These data show that

Downloaded 03 May 2010 to 171.66.16.21. Redistribution subject to ASME license or copyright; see http://www.asme.org/terms/Terms_Use.cfm

Table 1 Critical system parameters for flip-over (angles in radians)

	$d=0.1$			$d=0.2$		
Payload W	Pressure Load F_{cr}	Tip Rotation α_{cr}	Change in Tip Rotation $\Delta\alpha$	Pressure Load F_{cr}	Tip Rotation α_{cr}	Change in Tip Rotation $\Delta\alpha$
2.5	11.848	2.37	1.75	8	NA	NA
5.0	15.412	2.00	3.40	10.203	2.26	2.81
7.5	18.985	1.88	3.98	12.357	2.14	3.59
10.0	22.399	1.88	4.28	14.422	2.05	4.09
12.5	25.635	1.88	4.52	16.410	2.04	4.41

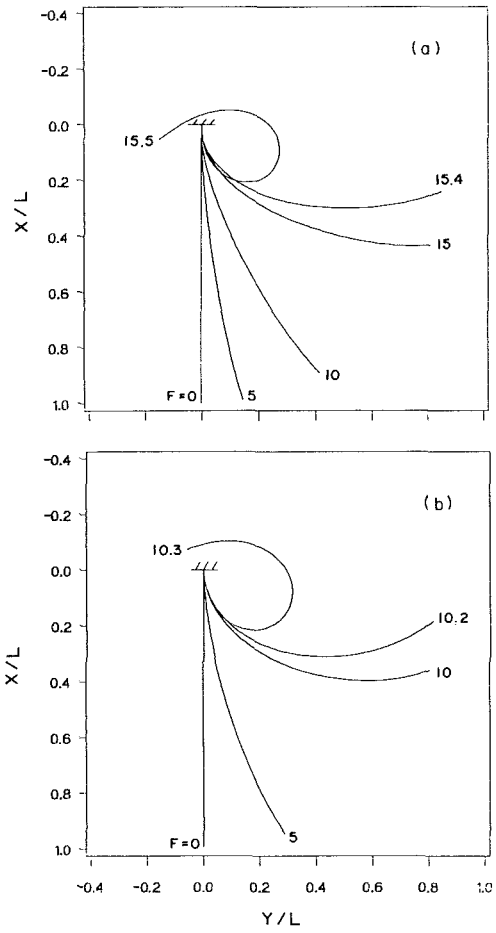

Fig. 6 Element elastica with $W=5.0$ and increasing pressure load, where (a) $d=0.1$, and (b) $d=0.2$

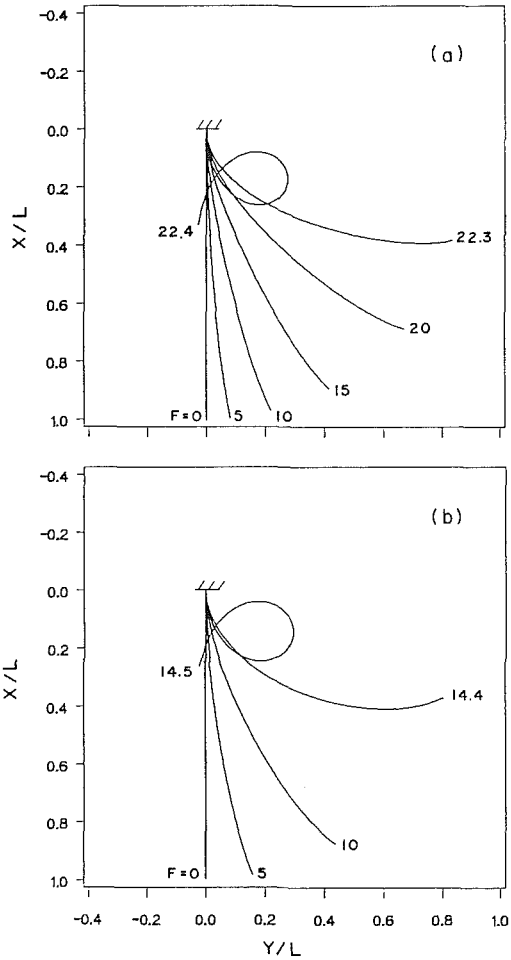

Fig. 7 Element elastica with $W=10.0$ and increasing pressure load, where (a) $d=0.1$, and (b) $d=0.2$

flip-over becomes more pronounced with increasing payload W and with decreasing eccentricity d. For a fixed d, these results show that the pressure load at the onset of flip-over increases linearly with payload.

Concluding Remarks

Flip-over is the result of interaction between the payload W and the pressure load F. The payload always acts in the same direction while the pressure load is a follower load that rotates with the tip of the elastica. Before flip-over, an initial payload tends to return the elastica to its undeformed shape. When the element is near vertical (α near 0) both F and W impose a tensile load on the element, increasing its stiffness and causing deformations to be relatively small. When the tip rotation exceeds 90 deg, the vertical component of F opposes W. This reduces the restraining effect of W on element deformation so that small changes in the pressure load lead to flip-over.

Acknowledgments

This study was sponsored by the U.S. Defense Advanced Research Projects Agency under Contract No. MDA903-84-C-0243.

References

Lau, J. H., 1982, "Large Deflections of Beams with Combined Loads," *Journal of the Engineering Mechanics Division*, ASCE, Vol. 108, No. EM1.

Love, A. E. H., 1927, *A Treatise on the Mathematical Theory of Elasticity*, 4th Ed., Dover Publications, New York.

Schmidt, R., and DaDeppo, D. A., 1971, "A Survey of Literature on Large Deflections of Nonshallow Arches. Bibliography of Finite Deflections of Straight and Curved Beams, Rings, and Shallow Arches," *The Journal of the Industrial Mathematics Society*, Vol. 21, Part 2.

Wang, C. Y., 1981, "Large Deflections of an Inclined Cantilever with an End Load," *International Journal of Non-Linear Mechanics*, Vol. 16, No. 2.

Wilson, J. F., 1987, "Compliant Robotic Structures, Part III," U.S. Department of Defense Report MDA903-84-C-0243.

Downloaded 03 May 2010 to 171.66.16.21. Redistribution subject to ASME license or copyright; see http://www.asme.org/terms/Terms_Use.cfm

Sound Radiation From Beams Under the Action of Moving Line Forces

R. F. Keltie
Assoc. Mem. ASME

H. Peng

Center for Sound and Vibration,
Mechanical and Aerospace Engineering Department,
North Carolina State University,
Raleigh, NC 27695-7910

The topic of sound radiation from beams under the action of harmonic line forces moving at subsonic speeds is studied. The nondimensional sound power is formulated through integration of the surface acoustic intensity distribution over the entire beam. Asymptotic expressions for the sound power in the low frequency region are derived depending upon the characteristics of the fluid loading and the spatial extent of the applied forces. Numerical integrations have been performed to determine the effects on the radiated sound power of the Mach number, M, the acoustic length of line force, K_0L, and the wavenumber ratio, γ. The results show that for beams under heavy fluid loading, the effect of the speed of the moving force is not pronounced, while for beams under light fluid loading, the unique coincidence radiation peak at $\gamma \sim 1$ for a stationary force ($M = \emptyset$) is split into two coincidence peaks (located in the frequency regions $\gamma < 1$ and $\gamma > 1$ respectively) due to the effects of the Doppler shift. The values of K_0L that suppress the coincidence peaks are also changed due to the motion of the line force.

Introduction

The importance of the spatial extent of stationary applied forces in structural radiation has been investigated recently by several authors (Keltie and Peng, 1985; Keltie and Peng, 1986; Junger, 1983). In this paper, the problem of sound radiation from a harmonic line force moving along an infinite beam at a constant subsonic speed V is considered. This work may be considered as an extension of the work performed by Mogilevskii (1981) who solved the same problem but for a moving point force. By integrating the surface acoustic intensity over the entire beam, the nondimensional sound power is formulated and then examined as a function of Mach number, acoustic length of the line force, and the wave number ratio.

Formulation

Assume the infinite beam occupies the plane $y = \emptyset$ and is excited by a harmonically-oscillating distributed force of length $2L$ moving at a subsonic velocity V, as shown in Fig. 1. The space $y > \emptyset$ is filled with an acoustic medium (water, air, etc.). Timoshenko beam theory is used so that the results will be valid for beams under heavy fluid loading at high frequencies or for thick beams.

The moving force distribution is defined as

$$f(x,t) = \frac{F_o}{2L}\,[H(x - Vt + L) - H(x - Vt - L)]e^{j\omega t} \tag{1}$$

where, $H(x)$ is the Heavyside step function and F_o is the total force strength per unit width. The vibration equation for the elastic beam, including rotational inertia and transverse shear effects, is given by Junger and Feit (1986) as

$$\bar{E}I\frac{\partial^4 u}{\partial x^4} + \rho_v h\frac{\partial^2 u}{\partial t^2} - \left(\rho_v I + \frac{\bar{E}I\rho_v}{\kappa^2\bar{G}}\right)\frac{\partial^4 u}{\partial x^2 \partial t^2} + \rho_v I\frac{\rho_v}{\kappa^2\bar{G}}\frac{\partial^4 u}{\partial t^4}$$
$$= \left(1 - \frac{\bar{E}I}{\kappa^2\bar{G}h}\frac{\partial^2}{\partial x^2} + \frac{\rho_v h^2}{12\kappa^2\bar{G}}\frac{\partial^2}{\partial t^2}\right)[f(x,t) - p(x,y=o,t)] \tag{2}$$

where $u(x, t)$, is the transverse displacement of the beam;

- $\bar{E} = E(1 + \eta j)$ is the complex elastic modulus;
- η is the loss factor;
- $\bar{G} = \bar{E}/(1 + \nu)$ is the complex shear modulus;
- I is the cross-sectional moment of inertia per unit width, $I = h^3/12$ where h is the height of the beam;
- ν is Poisson's ratio;
- ρ_v is the mass density of material;
- κ^2 is the cross-sectional shape factor; and
- $p(x,y=o,t)$ is the acoustic pressure acting on the beam's surface.

The dependence of κ^2 on Poisson's ratio is illustrated by noting that it ranges almost linearly from 0.76 for $\nu = 0$ to 0.91 for $\nu = 0.5$ (Mindlin, 1951).

The pressure distribution induced by the vibrating beam in the acoustic medium is denoted by $p(x, y, t)$ and satisfies the wave equation in two-dimensional space, given by:

Contributed by the Applied Mechanics Division of THE AMERICAN SOCIETY OF MECHANICAL ENGINEERS for presentation at the Joint ASCE/ASME Applied Mechanics, Biomechanics, and Fluids Engineering Conference, San Diego, CA, July 9 to 12, 1989.

Discussion on this paper should be addressed to the Editorial Department, ASME, United Engineering Center, 345 East 47th Street, New York, N.Y. 10017, and will be accepted until two months after final publication of the paper itself in the JOURNAL OF APPLIED MECHANICS. Manuscript received by ASME Applied Mechanics Division, September 4, 1987; final revision, July 28, 1988.

Paper No. 89-APM-19.

Copyright © 1988 by ASME
Downloaded 03 May 2010 to 171.66.16.21. Redistribution subject to ASME license or copyright; see http://www.asme.org/terms/Terms_Use.cfm

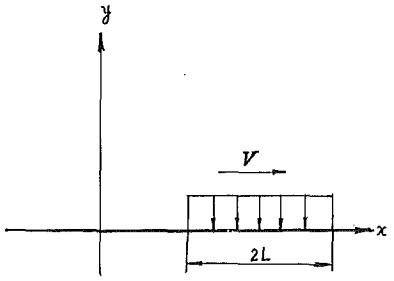

Fig. 1 The schematic representation of the problem geometry

$$\left(\frac{\partial^2}{\partial y^2}+\frac{\partial^2}{\partial x^2}-\frac{1}{C_o^2}\frac{\partial^2}{\partial t^2}\right)p(x,y,t)=0 \tag{3}$$

where C_o is the sound speed in the acoustic medium. The boundary condition at $y = 0$ is given by

$$\rho_o\frac{\partial^2 u}{\partial t^2}=-\frac{\partial p}{\partial y}\Big|_{y=0} \tag{4}$$

where ρ_o is the mass density of the acoustic medium.

By applying the spatial Fourier transformation

$$\left(FT(\ )=\int_{-\infty}^{+\infty}(\ )e^{j\xi x}dx\right)$$

where ξ is the wave number variable, the force function in the wave number domain may be written as:

$$\tilde{F}(\xi,t)=F_o\frac{\sin(\xi L)}{\xi L}e^{j(\xi V+\omega)t}=F(\xi)e^{j(\xi V+\omega)t} \tag{5}$$

This form implies that in the wave number domain, the transformed displacement $\tilde{U}(\xi, t)$ and pressure $\tilde{P}(\xi, y, t)$ both will have the common factor $e^{j(\xi V+\omega)t}$. That is,

$$\tilde{U}(\xi,t)=U(\xi)e^{j(\xi V+\omega)t} \tag{6a}$$

and

$$\tilde{P}(\xi,y,t)=P(\xi,y)e^{j(\xi V+\omega)t}. \tag{6b}$$

Upon substitution into the beam equation (2) and the acoustic equation (3), it is easily found that:

$$U(\xi)=\frac{Z_F F(\xi)}{Z_m+Z_F Z_a} \tag{7}$$

and

$$P(\xi,y=0)=\frac{j\rho_o(\omega+\xi V)^2}{K_y}U(\xi) \tag{8}$$

where,

$$Z_a=j\rho_o(\xi V+\omega)^2/K_y \tag{9a}$$

$$Z_m=\bar{E}I\xi^4-\rho_v h(\omega+\xi V)^2-\xi^2\left(\rho_v I+\frac{\bar{E}I\rho_v}{\kappa^2\bar{G}}\right)(\omega+\xi V)^2$$

$$+\rho_v I\frac{\rho_v}{\kappa^2\bar{G}}(\omega+\xi V)^4 \tag{9b}$$

$$Z_F=1+\frac{\bar{E}I}{\kappa^2\bar{G}h}\xi^2-\frac{\rho_v h^2}{12\kappa^2\bar{G}}(\omega+\xi V)^2 \tag{9c}$$

and

$$K_y=\begin{cases}-j\sqrt{\xi^2-(K_o+M\xi)^2} & \text{for } \xi^2>(K_o+M\xi)^2\\ \sqrt{(K_o+M\xi)^2-\xi^2} & \text{for } \xi^2<(K_o+M\xi)^2\end{cases} \tag{9d}$$

where M is the Mach number, V/C_o, and K_o is the acoustic wave number ω/C_o.

In order to find the total acoustic power, the surface acoustic intensity distribution may be integrated over the infinite length of the beam. Following the procedure used previously (Keltie and Peng, 1985) this integration is conveniently performed in the wave number domain. Upon substitution of the surface pressure from equation (8) and the surface velocity from time differentiation of equation (6*a*), the power radiated per unit width of the beam is given by:

$$\Pi=\frac{\rho_o}{4\pi}\,\mathrm{Re}\left\{\int_{-\infty}^{+\infty}\frac{(\xi V+\omega)^3}{K_y}|U(\xi)|^2 d\xi\right\}. \tag{10}$$

Referring to equation (9*d*), it is seen that the denominator in equation (10) is real only over a restricted interval of the integration range. Specializing to the case of subsonic motion of the traveling force, the limits within which K_y is real are given by:

$$\xi_1=\frac{-K_o}{1+M}\le\xi\le\xi_2=\frac{K_o}{1-M}. \tag{11}$$

Equation (10) for the sound power may then be rewritten as:

$$\Pi=\frac{\rho_o}{4\pi}\int_{\xi_1}^{\xi_2}\frac{(\xi V+\omega)^3}{K_y}|U(\xi)|^2 d\xi. \tag{12}$$

It is useful to nondimensionalize the sound power in equation (12), and to introduce standard parameter groupings. To this end one may define the following:

Nondimensional power per unit width W:

$$W=4\pi\omega(\rho_v h)^2\Pi/\rho_o F_o{}^2. \tag{13a}$$

Free bending wave number K_B:

$$K_B=[12\rho_v\omega^2/Eh^2]^{1/4}. \tag{13b}$$

Longitudinal wave speed C_L:

$$C_L=\sqrt{E/\rho_v}. \tag{13c}$$

Fluid loading factor α_o:

$$\alpha_o=\rho_o C_L/(\sqrt{12}\rho_v C_o). \tag{13d}$$

Wave number ratio γ:

$$\gamma=K_o/K_B. \tag{13e}$$

Then, after considerable, but straightforward, algebraic manipulation, equation (12) may be rewritten in nondimensional form given by:

$$W=\int_{\xi_1}^{\xi_2}\alpha^3\beta\left|Z_F\frac{\sin\xi K_o L}{\xi K_o L}\right|^2|D|^{-2}d\xi \tag{14}$$

where,

$$\alpha=1+M\xi$$

$$\beta=\sqrt{\alpha^2-\xi^2}$$

$$Z_F=1+\frac{2(1+\nu)\gamma^4}{\kappa^2}\left(\frac{C_o}{C_L}\right)^2\left[\xi^2-\frac{1}{(1+j\eta)}\left(\frac{C_o}{C_L}\right)^2\alpha^2\right]$$

$$D=\beta(D_1-D_2+D_3)+jD_4$$

$$D_1=\gamma^4\xi^4(1+j\eta)$$

$$D_2=\alpha^2\left[1+\left[1+\frac{2(1+\nu)}{\kappa^2}\right]\gamma^4\xi^2\left(\frac{C_o}{C_L}\right)^2\right]$$

$$D_3=\frac{2(1+\nu)}{\kappa^2(1+j\eta)}\alpha^4\gamma^4\left(\frac{C_o}{C_L}\right)^4$$

and

$$D_4=Z_F\frac{\alpha_o\alpha^2}{\gamma^2}.$$

Equation (14) is our main result. It is to be numerically investigated later for the case of a steel plate immersed in water and in air. In the following section, some asymptotic

Downloaded 03 May 2010 to 171.66.16.21. Redistribution subject to ASME license or copyright; see http://www.asme.org/terms/Terms_Use.cfm

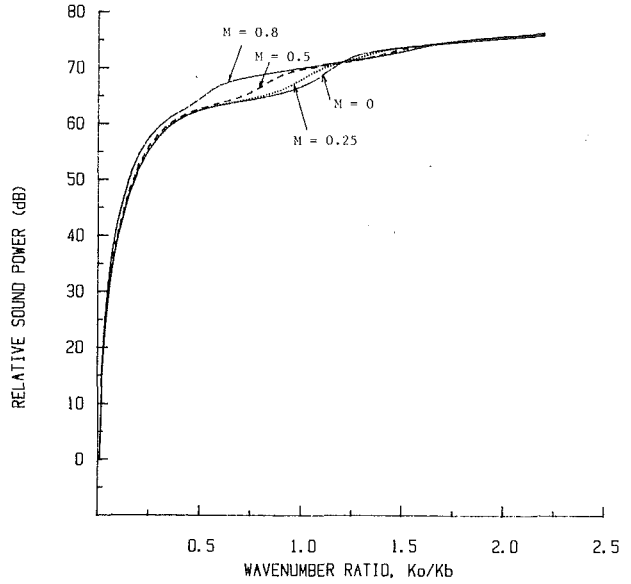

Fig. 2 Relative sound power level versus wave number ratio for a range of M values, $K_oL = 0.1$, in water

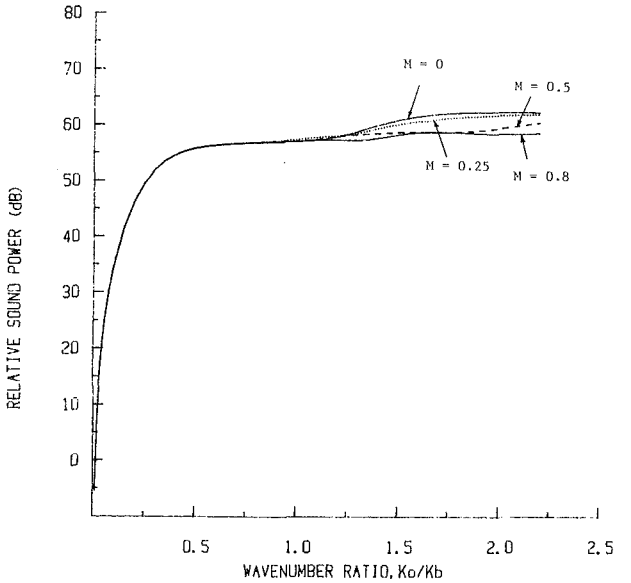

Fig. 3 Relative sound power level versus wave number ratio for a range of M values, $K_oL = 2\pi$, in water

simplifications for equation (14) in the low frequency limits are derived.

Asymptotic Solutions for $\gamma \ll 1$

Under the assumption of low frequency ($\gamma \ll 1$), the nondimensional sound power per unit width W may be approximated as

$$W \sim \int_{\xi_1}^{\xi_2} \left[\frac{\sin(\xi K_o L)}{\xi K_o L}\right] \frac{\alpha^3 \beta d\xi}{|-\beta\alpha^2 + j\alpha_0\alpha^2/\gamma^2|^2} . \tag{15}$$

(1) In the case of the beam under a light fluid loading, $\alpha_o/\gamma^2 \ll 1$, the term representing the effect of fluid loading may be omitted. Equation (15) then simplifies to:

$$W \sim \int_{\xi_1}^{\xi_2} \left[\frac{\sin(\xi K_o L)}{\xi K_o L}\right]^2 \frac{d\xi}{\alpha\beta} \tag{16}$$

(*a*) When the acoustic length of the force is small, that is, when $K_oL \ll 1$, the beam sees essentially a point force. In this case, utilizing the transformation $\xi = (M + \sin\theta)/(1 - M^2)$ and $z = \tan(\theta/2)$, one obtains:

$$W \sim \int_{\xi_1}^{\xi_2} \frac{d\xi}{\alpha\beta} = 2\tan^{-1}\left(\frac{z+M}{\sqrt{1-M^2}}\right)\Big|_{-1}^{1} = \pi \tag{17}$$

(*b*) For a force with large scale (K_oL) $\gg$ 1), using the delta function-like property of the wave number spectrum of the forces, it is found that:

$$W \sim \int_{-\infty}^{+\infty} \left[\frac{\sin(\xi K_o L)}{\xi K_o L}\right]^2 d\xi = \frac{\pi}{K_o L} . \tag{18}$$

The results obtained for cases (*a*) and (*b*), at low frequency and under light loading, show that for large and small force scales the subsonic speed of the moving force has essentially no effect at all on the radiated sound power.

(2) In the case of the beam under a heavy fluid loading, $\alpha_o/\gamma^2 \gg 1$, the loading effects will dominate in the denominator of the acoustic power equation (15). Thus, one may obtain the approximation

$$W \sim \frac{\gamma^4}{\alpha_o^2} \int_{\xi_1}^{\xi_2} \left[\frac{\sin(\xi K_o L)}{\xi K_o L}\right]^2 \cdot \frac{\beta d\xi}{\alpha} . \tag{19}$$

(*c*) For a point force ($K_oL \ll 1$), using the transformation $\xi = \sin\theta + M/1 - M^2$ and the results in equation (17), one finds

$$W \sim \frac{\gamma^4}{\alpha_o^2} \int_{\xi_1}^{\xi_2} \frac{\beta d\xi}{\alpha} = \frac{\gamma^4}{\alpha_o^2} \cdot \frac{\pi}{(1 - M^2 + \sqrt{1-M^2})} \tag{20}$$

(*d*) For a force with large scale ($K_oL \gg 1$), the corresponding result is

$$W \sim \frac{\gamma^4}{\alpha_o^2} \int_{-\infty}^{+\infty} \left[\frac{\sin(\xi K_o L)}{\xi K_o L}\right]^2 d\xi = \frac{\gamma^4 \pi}{\alpha_o^2 K_o L} . \tag{21}$$

Equations (20) and (21) show that in the case of the beam under a heavy fluid loading, the radiated sound power will increase by the factor of $2/(1 - M^2 + \sqrt{1-M^2})$ between the moving state and the stationary state for a point force; but essentially will not change for distributed forces.

One thing worth noting is that these asymptotic solutions may not be applied for $M \to 1$. Since at this time the upper limit of the power integral approaches infinity, the procedures of approximation involved are not valid.

Numerical Results and Discussion

In order to numerically evaluate the sound power integral in equation (14), several variables must be specified. The material chosen is steel with the following properties: $E = 2 \times 10^{11}$N/m^2, $\rho_v = 7800$ kg/m^3, $\nu = 0.3$, $\kappa^2 = 0.85$. The loss factor is fixed at $\eta = 0.01$. The acoustic medium is either water ($C_o = 1481$ m/s, $\rho_o = 1000$ kg/m^3) or air ($C_o = 343$ m/s, $\rho_o = 1.24$ kg/m^3). By varying the values of parameters M and K_oL, the sound power is computed and then plotted versus the wave number ratio γ (or nondimensional frequency).

The asymptotic solutions derived in the low frequency limits have been compared with the numerical results. It is concluded that for the case of air loading, equations (17) and (18) are in good agreement with the exact solutions from $\gamma = 0.05$ to $\gamma = 0.4$, with the differences being within one *dB*. For the case of water loading, equations (20) and (21) are valid for $\gamma < 0.2$ with the error less than one *dB*. These comparisons were made for the range of M less than 0.8. For higher values of M, these asymptotic solutions are not valid.

Choosing water loading and fixing M at the values of 0, 0.25, 0.50, 0.80, respectively, the nondimensional sound power is plotted in Fig. 2 for $K_oL = 0.1$ and in Fig. 3 for $K_oL = 2\pi$ in the frequency range $0.01 < \gamma < 2.2$. It is clear that the increased acoustic length K_oL reduces the sound power

Downloaded 03 May 2010 to 171.66.16.21. Redistribution subject to ASME license or copyright; see http://www.asme.org/terms/Terms_Use.cfm

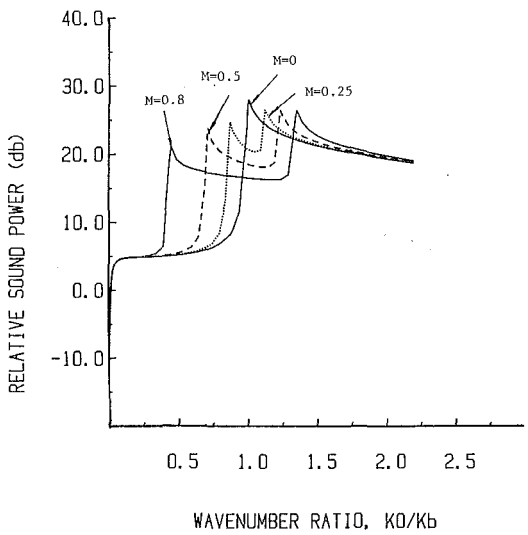

Fig. 4 Relative sound power level versus wave number ratio for a range of M values, $K_oL = 0.1$, in air

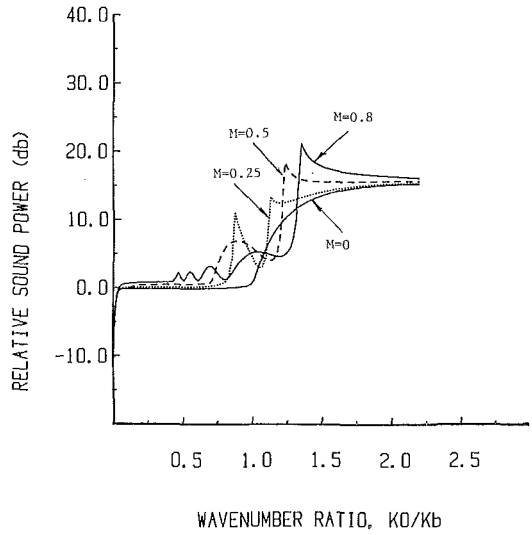

Fig. 5 Relative sound power level versus wave number ratio for a range of M values, $K_oL = \pi$, in air

level over the entire frequency range. This would be expected since the total applied force strength is kept constant. It is interesting to note that there are no pronounced peaks in the sound power curves and the effects of the Mach number in the high frequency regions are not significant. The absence of a distinct coincidence radiation peak has been noted by others (see, for example, Fig. 4 in Feit and Liu, 1985). The essential reason for the lack of a peak in the case of radiation into a dense medium like water, as compared to a light medium like air, is found in the relative proportion of structural energy converted to acoustic energy per wavelength on the structure. This proportion is considerably larger for dense media, so the radiation "drains" the energy faster from the structure than in light media. The result is larger effective damping of the structure and, hence, more rapid spatial decay of the vibration field. Conversely in air, the effective damping due to the radiation is smaller, and the velocity field persists over a greater distance, thus giving rise to the coincidence peak.

Choosing air loading and fixing M at the values of 0, 0.25, 0.50, 0.80, respectively, the sound power curves are shown in Fig. 4 for $K_oL = 0.1$ and in Fig. 5 for $K_oL = \pi$ in the same frequency range. Now, the effects of M and K_oL are very significant. In Fig. 4 for the case of essentially a point force, the strong unique coincidence radiation peak for $M = 0$ located at $\gamma = 1.0$ is split into two coincidence peaks with reduced amplitudes for all $M \neq 0$. One peak now is located in frequency range $\gamma < 1$ while the other in $\gamma > 1$. This phenomenon may be attributed to a Doppler shift and will be discussed later. In Fig. 5 the increasing acoustic length K_oL of the applied force not only reduces the sound power level in the entire frequency region but sometimes also cancels the coincidence peaks (the unique peak for $M = 0$, the peaks in $\gamma < 1$ for $M = 0.5$ and for $M = 0.8$ are suppressed) and produces relative minimum values in the sound power curves (for example, the power curve for $M = 0.8$). It is natural to ask the following questions: In the case of $M \neq 0$, where should these two new coincidence peaks be located? When and how does the acoustic length K_oL behave as to cancel these new coincidence peaks and produce relative minima in the sound power curves? A discussion of these problems will follow.

The mathematical and physical explanations of the cancellation effect introduced by K_oL for the case of $M = 0$ are given by Keltie and Peng, 1985. In the present paper, the focus is placed on the shift effects caused by the moving line forces.

Recalling equation (14), the integrand in the sound power integral can be thought of as the power wave number spectrum consisting of the product of the spatial force filter function and the lumped structure/acoustic wave number response function. In the latter, the most important factor is $|D|^2$, which is the square of the modulus of the beam admittance. For simplicity, the term D_3 is neglected and D_2 is approximated as γ^2 (since the thin plate theory will be valid for $\gamma < 2.8$ if the beam's bending wavelength is at least ten times as large as the thickness of the plate (see Mindlin, 1951). Thus,

$$D \sim \beta(\gamma^4\xi^4 - \alpha^2) + j(\eta\gamma^4\xi^4 + \alpha_o\alpha^2/\gamma^2). \tag{22}$$

For a lightly damped beam in air, the value of the reactance in D is always small in the shifted radiation circle $\xi_1 < \xi < \xi_2$ and, hence, the greatest power contribution will occur near the wave number that causes the resistance of D to approach zero. Since β is an acoustic filter function, one may look at $\gamma^4\xi^4 - \alpha^2$, or,

$$\gamma^2\xi^2 + (1 + M\xi) = 0 \tag{23a}$$

$$\gamma^2\xi^2 - (1 + M\xi) = 0. \tag{23b}$$

In equation (23a), the roots are given as $-M \pm \sqrt{M^2 - 4\gamma^2}/2\gamma^2$. If $M < 2\gamma$, these two roots are complex and represent fast-decaying, near-field wave motions, which obviously cannot make significant contributions to produce the coincidence radiation peaks. If $M > 2\gamma$, these two roots are real and represent travelling waves. It may be shown that they are located outside the radiation circle ($-1/1 + M < \xi < 1/1 - M$), and thus cannot be related to the coincidence phenomenon. Our focus is placed on equation (23b).

In equation (23b), if $M = 0$, one may get $\xi = \pm 1/\gamma = K_b/K_o$, which corresponds to the free bending wave number and represents the pronounced peak in power spectrum whenever $\gamma \geq 1$ (since $|\xi| < 1$). If $M < 1$, solving equation (23) for ξ yields:

$$\text{the positive root: } \xi_1 = \frac{M + \sqrt{M^2 + 4\gamma^2}}{2\gamma^2} \tag{24a}$$

$$\text{the negative root: } \xi_2 = \frac{M - \sqrt{M^2 + 4\gamma^2}}{2\gamma^2} \tag{24b}$$

These two equations mean that due to the Doppler shift, the wave number corresponding to the pronounced peak in the power spectrum no longer only represents the free bending wave but rather reflects the combined effects of the free bending wave, acoustic wave, and the moving speed of the applied forces.

The ranges of γ for which the peaks appear now are also

Downloaded 03 May 2010 to 171.66.16.21. Redistribution subject to ASME license or copyright; see http://www.asme.org/terms/Terms_Use.cfm

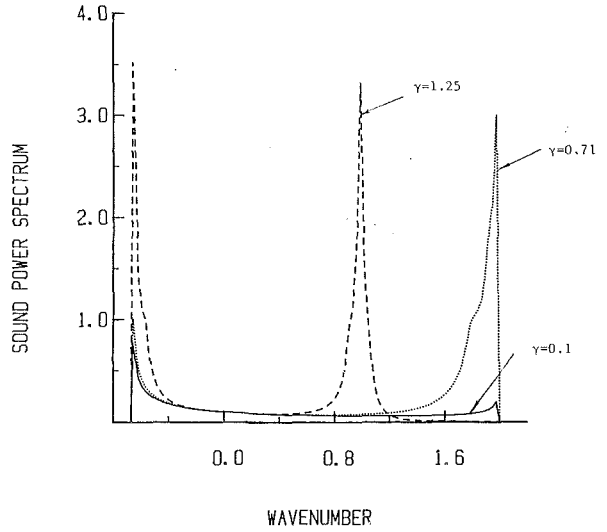

Fig. 6 Sound power spectra for a range of wave number ratio values, $K_oL = 0.1$, $M = 0.5$, in air

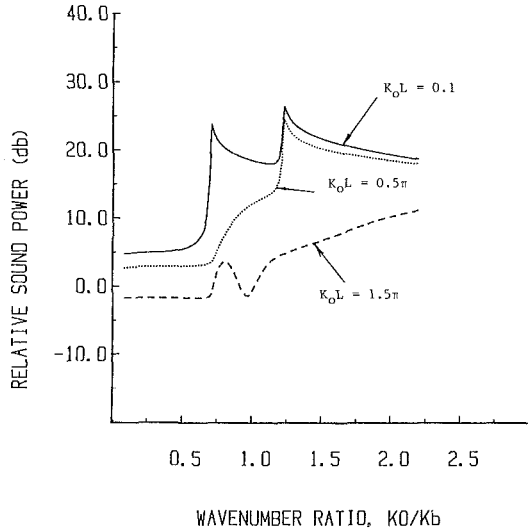

Fig. 7 Relative sound power level versus wave number ratio for a range of K_oL values, $M = 0.5$, in air

shifted. Since $-1/1+M < \xi < 1/1-M$, it may be found that,

$$\text{for the positive root to exist: } \gamma^2 \geq 1-M \tag{25a}$$

$$\text{for the negative root to exist: } \gamma^2 \geq 1+M. \tag{25b}$$

Figure 6 is the plot of the power spectrum over a range of γ for $K_oL = 0.1$, $M = 0.5$, which are in good agreement with the predictions by equation (25).

At the coincidence frequency, both β and $\gamma^4\xi^4 - \alpha^2$ should be zero, thus,

$$\text{first coincidence frequency: } \gamma_1 = \sqrt{1-M} \tag{26a}$$

$$\text{second coincidence frequency: } \gamma_2 = \sqrt{1+M} \tag{26b}$$

One should notice that: (1) Equation (26) may be rewritten as $\lambda_b = \lambda_o/\sqrt{1-M}$ and $\lambda_b = \lambda_o/\sqrt{1+M}$, which means that due to the Doppler shift, the coincidence radiation peak will occur when the free bending wavelength is larger or smaller than the acoustic wavelength. This gives a clear explanation to the phenomenon of the "split peak." (2) When $\gamma_2 = \sqrt{1+M}$, there exist two significant peaks in the power spectrum rather than just one peak for $\gamma_1 = \sqrt{1-M}$. The amplitude for the coincidence peak at $\gamma_2 = \sqrt{1+M}$, generally speaking, will be higher than that at $\gamma_1 = \sqrt{1-M}$.

Fixing M at the values of 0, 0.25, 0.50, and 0.80, the following table lists the values of wave number ratio where the shifted coincidence radiation peaks are present.

M	0	0.25	0.5	0.8
γ_1	1	0.87	0.71	0.45
γ_2		1.12	1.22	1.34

These peak values correspond to those shown in Fig. 4. Since there are strong peaks in the power spectrum, it is possible to choose the proper K_oL values to cancel these peaks, e.g., it is necessary to find such K_oL values that satisfy the relation of $\xi K_oL = n\pi$, where ξ is the root in equation (24*a*) or equation (24*b*), and n is an integer. Let $\zeta = K_oL/n\pi$, then to cancel the positive root the necessary condition is

$$\zeta\left(\frac{M+\sqrt{M^2+4\gamma^2}}{2\gamma^2}\right) = 1 \tag{27}$$

solving for γ yields

$$\gamma = \zeta\sqrt{1+M/\zeta} \qquad \text{for } \zeta \geq 1-M. \tag{28}$$

Thus, the location of the relative minima in the frequency domain are given by the following formulas:

$$\gamma_n = \zeta_n\sqrt{1+M/\zeta_n}$$
$$\zeta_n = K_oL/n\pi \quad n = 1, \ldots, N_1$$
$$N_1 = \text{INT}\{K_oL/(1-M)\pi\}. \tag{29}$$

Similarly, to cancel the negative root and to obtain the relative minimum values in the sound power curve, one may use

$$\gamma_m = \zeta_m\sqrt{1-M/\zeta_m} \quad m = 1, \ldots, N_2$$
$$\zeta_m = K_oL/m\pi$$
$$N_2 = \text{INT}\{K_oL/(1+M)\pi\}. \tag{30}$$

Example 1: Letting $M = 0.8$ and $K_oL = \pi$, using equation (29), one may find that there ought to be five relative minima in the power curve, given by $\gamma_n = 0.45, 0.51, 0.61, 0.81, 1.34$. After investigating the power curve of $M = 0.8$ in Fig. 5, it is found that the first four values of γ corresponding to the minimum values of sound power are in good agreement with the numerical predictions. From computation, the fifth minimum value should be located at $\gamma = 1.24$, which is slightly different from the predicted value. The reason for the discrepancy may be attributed to the strong effect from the negative root.

It is easy to verify that in order to suppress the coincidence radiation peak, one needs to choose the value of $K_oL/n\pi = 1-M$ to cancel the coincidence peak in the range of $\gamma < 1$ or choose the value of $K_oL/m\pi = 1+M$ to diminish the coincidence peak in $\gamma > 1$.

The condition for the same K_oL value to cancel both coincidence peaks in the $\gamma < 1$ region and in the $\gamma > 1$ region is that $1+M/1-M = n/m$ where n,m are both integers and $n > m$. For simplicity, when $m = 1$, the values of M become:

$$M = \frac{n-1}{n+1} = \frac{1}{3}, \frac{2}{4}, \frac{3}{5}, \ldots \tag{31}$$

Example 2: Let $M = 0.5$, the coincidence peaks should be located at $\gamma_1 = 0.71$ and $\gamma_2 = 1.22$. If one chooses $K_oL = 0.5$, the coincidence peak at γ_1 is suppressed, but the peak at γ_2 still survives. If the value of $K_oL = 1.5\pi$ is chosen, both coincidence peaks are cancelled since the value of M satisfies the condition in equation (31). This example is clearly shown in Fig. 7.

Downloaded 03 May 2010 to 171.66.16.21. Redistribution subject to ASME license or copyright; see http://www.asme.org/terms/Terms_Use.cfm

Summary

The effects on the sound power emitted by harmonic line forces moving on infinite elastic beams are investigated in this paper. The conclusions reached are: (1) In the low frequency range, if the acoustic length of the applied force is small, the nondimensional sound power is constant for light fluid loading, but will increase with the speed of the force for heavy fluid loading; if the acoustic length of the applied force is large, the sound power is inversely proportional to the acoustic length and totally independent of the speed. (2) Above the low frequency range and in the case of heavy fluid loading, both speed and acoustic length of the applied forces do not have significant effects on the shapes of the radiated sound power curves. The increasing acoustic length of the line forces will effectively reduce the total sound power level to some extent. (3) For light fluid loading, the unique coincidence peak typical of beams under the action of stationary forces may be split into two coincidence peaks whenever the harmonic force is moving at a subsonic speed, due to the effects of Doppler shift. These two peaks will be located at the positions of $\gamma_1 = \sqrt{1-M}$ and $\gamma_2 = \sqrt{1+M}$. The cancellation effect on the sound power owing to the finite length of the line force is also shifted spatially to the value of $K_oL/n\pi = 1-M$ and $K_oL/n\pi = 1+M$. Generally speaking, one may suppress either one of these two coincidence peaks in the sound curves by choosing proper K_oL values. However, under certian conditions, e.g., when the Mach number $M = (n-1)/(1+n)$ (n is a positive integer), one may choose one proper value of line force length to cancel both coincidence radiation peaks.

References

Feit, D., and Liu, Y. N., 1985, "The Nearfield Response of a Line Driven Fluid-Loaded Plate," *J. Acoust. Soc. Am.*, Vol. 78(2), pp. 763–767.

Junger, M. C., 1983, "Pressure Radiated by an Infinite Plate Driven by Distributed Loads," *J. Acous. Soc. Am.*, Vol. 74(2), pp. 649–653.

Junger, M. C., and Feit, D., 1986, *Sound, Structure, and Their Interaction*, 2nd Ed., MIT Press, Cambridge, MA.

Keltie, R. F., and Peng, H., 1985, "On the Acoustic Power Radiated by Line Forces on Elastic Beams," *J. Acous. Soc. Am.*, Vol. 77(6), pp. 2033–2038.

Keltie, R. F., and Peng, H., 1986a, "Acoustic Radiation for Plates Under The Action of Disc Forces," *Proceedings Inter-Noise '86*, Cambridge, MA.

Keltie, R. F., and Peng, H., 1986b, "Numerical Investigation of the Surface Acoustic Intensity Patterns on Vibrating Panels," ASME 86-WA/NCA-23.

Mindlin, R. D., 1951, "Influence of Rotatory Inertia and Shear on Flexural Motions of Isotropic, Elastic Plates," ASME JOURNAL OF APPLIED MECHANICS, pp. 31–38.

Mogilevskii, M. I., 1981, "Sound Radiation from a Plate Under the Action of Moving Harmonic Forces," *Sov. Phys. Acous.*, Vol. 27(3), pp. 250–251.

Downloaded 03 May 2010 to 171.66.16.21. Redistribution subject to ASME license or copyright; see http://www.asme.org/terms/Terms_Use.cfm

Axisymmetric Free Vibrations of a Transversely Isotropic Finite Cylindrical Rod

C. P. Lusher[1]
Post Doctoral Research Fellow.

W. N. Hardy
Professor.

Department of Physics,
University of British Columbia,
Vancouver, B.C. V6T 2A6, Canada

The frequencies of free vibration and mode shapes are calculated for axisymmetric modes of an elastic cylinder of finite length having hexagonal symmetry with the crystallographic c-axis coincident with the axis of the cylinder (a transversely isotropic finite cylindrical rod). A series solution is used which satisfies term-by-term the differential equations of linear elasticity and the boundary conditions on the shear stress; the boundary conditions on the normal stresses are satisfied by using an orthogonalization procedure. As an example, the method is applied to sapphire, with one of the six elastic constants (c_{14}) taken to be zero. The other five elastic constants are those of the hexagonal system. The calculated acoustic vibration frequencies agree to better than 1 percent with measurements made on sapphire at room temperature, for a cylinder of half-height to radius ratio ~ 1.

1 Introduction

We present here an accurate series method for calculating the frequencies of free vibration and shapes of axisymmetric modes for a transversely isotropic finite right circular cylinder with stress free boundary conditions, using the general three-dimensional equations of linear elasticity. The results of the calculation approach the exact values asymptotically as the number of terms in the series is increased. The convergence of frequencies is rapid, only a few terms being needed to give accurate results.

The problem of the free vibrations of a circular cylinder of an isotropic material was first studied in terms of the general theory of elasticity by Pochhammer in 1876 and independently by Chree in 1889. An account of this treatment is given in the books by Love (1944) and Kolsky (1953). In the latter book several references are given to numerical results which have been computed from the characteristic equation.

The Pochhammer-Chree (PC) solutions are exact for an infintely long isotropic rod which is stress free at the cylindrical surface. However these solutions cannot completely satisfy the boundary conditions for a finite rod since they do not permit stress-free ends. Various attempts have been made to obtain approximate solutions for the axisymmetric vibrations of a finite isotropic rod. The three mode theory of McNiven and Perry (1962), the finite element analysis of Gladwell and Tahbildar (1972) and the finite-difference calculation of McMahon (1970) give frequencies which agree with experimental data to within a few percent. A complete solution for the axisymmetric free vibrations of a finite length isotropic cylindrical rod was given by Hutchinson (1972). His series solution can be made as accurate as required by including enough terms in the series.

Morse (1954) has extended the PC solutions to the case of an infinitely long right circular cylinder having hexagonal symmetry (with the c-axis coincident with the cylinder axis). Morse's solution is exact for an infinitely long cylinder and can be used for obtaining approximate answers for a long finite cylinder. In this paper we extend Hutchinson's solution to the hexagonal case using the approach applied by Morse (1954) when extending the PC solutions. We thereby obtain a series solution for a finite length transversely isotropic rod which can be solved to any precision required by including enough terms. In addition, we discuss the range of half-height to radius ratios, L/a, for which Morse's simpler solution is applicable.

The motivation for developing the method came from our work on ultrastable microwave oscillators based on high Q sapphire dielectric resonators. We have developed a method for locking a free-running microwave oscillator to one of the electromagnetic resonances of a sapphire resonator (Lusher and Hardy, 1987). FM sidebands are introduced onto a reflected microwave carrier by exciting the sapphire at one of its acoustic modes of free vibration with an ultrasonic transducer. These sidebands are then used as a reference. It was necessary to calculate accurately the frequencies and displacements of the acoustic modes in sapphire in order to implement this acoustic modulation technique.

We show here, by comparing our calculation with our experimental data, that the free vibration frequencies for sapphire can be calculated to better than 1 percent using the technique described below (which is asymptotically correct for a hexagonal crystal with the c-axis coincident with the cylin-

[1]Presently at Department of Physics, Royal Holloway and Bedford New College, University of London, Egham, Surrey, TW20 0EX England.

Contributed by the Applied Mechanics Division for publication in the JOURNAL OF APPLIED MECHANICS.

Discussion on this paper should be addressed to the Editorial Department, ASME, United Engineering Center, 345 East 47th Street, New York, N.Y. 10017, and will be accepted until two months after final publication of the paper itself in the JOURNAL OF APPLIED MECHANICS. Manuscript received by ASME Applied Mechanics Division, September 14, 1987; final revision, April 11, 1988.

Copyright © 1988 by ASME
Downloaded 03 May 2010 to 171.66.16.21. Redistribution subject to ASME license or copyright; see http://www.asme.org/terms/Terms_Use.cfm

Table 1 Elastic constants of sapphire at room temperature *†

c_{11}	c_{33}	c_{44}	c_{12}	c_{13}	c_{14}
4.968	4.981	1.474	1.636	1.109	−0.235

* units of 10^{11}Nm^{-2}
† Wachtman et al. (1960)

drical axis but only approximate for sapphire, which has one additional elastic constant, c_{14}). Our method is useful for calculating the vibration frequencies for mechanical resonators of sapphire, used for gravity wave antennae and in frequency stabilization systems (Braginsky et al., 1985). It might also be of interest to those concerned with certain composite materials (Sih and Chen, 1981).

Sapphire has a trigonal crystal structure and has six independent elastic constants. In the calculation to follow we use the room temperature values of the elastic constants determined by Wachtman et al. (1960). These values are given in Table 1. The experimental errors quoted in their paper are ~0.3 percent for c_{11}, c_{33} and c_{44}, and ~1 percent for the other constants. Since the smallest elastic constant c_{14} is almost a factor of 5 smaller than the next smallest constant and a factor of over 20 smaller than c_{11}, we neglect it in our treatment. This greatly simplifies matters since the five remaining constants are those of the hexagonal system and this case can be solved with arbitrary precision for our particular geometry (equivalent to a transversely isotropic cylinder). We expect at most a few percent error in the calculated frequencies as a result of dropping c_{14}. This constant could be treated as a perturbation but since the calculation as it stands is already complex this refinement has not been attempted.

2 Equations of Motion and Boundary Conditions for the Free Vibrations of a Transversely Isotropic Finite Cylinder

We consider a finite right circular cylindrical rod of a hexagonal crystal with the crystallographic c-axis along the axis of the cylinder. The center of our cylindrical polar coordinate system (r, θ, z) is chosen to be at the center of the rod, with the cylindrical surface of the rod defined by $r=a$ and the end surfaces by the planes $z=\pm L$.

We seek axisymmetric solutions of the general three-dimensional equations of linear elasticity (displacements of the type $u_r=u_r(r, z, t)$, $u_z=u_z(r, z, t)$, $u_\theta=0$. This can be done with our geometry since the hexagonal crystal has axial symmetry and we choose the crystallographic c-axis and the cylindrical axis to be coincident.[1] In this case the elastic equations of motion for small displacements are:

$$\rho\ddot{u}_r = c_{11}\frac{\partial}{\partial r}\left[\frac{1}{r}\frac{\partial}{\partial r}(ru_r)\right] + c_{44}\frac{\partial^2 u_r}{\partial z^2} + (c_{13}+c_{44})\frac{\partial^2 u_z}{\partial r \partial z},$$

$$\rho\ddot{u}_z = c_{44}\frac{1}{r}\frac{\partial}{\partial r}\left[r\frac{\partial u_z}{\partial r}\right] + c_{33}\frac{\partial^2 u_z}{\partial z^2} + (c_{13}+c_{44})\frac{\partial}{\partial z}\left[\frac{1}{r}\frac{\partial}{\partial r}(ru_r)\right], \tag{1}$$

where the c_{ij} are the elastic constants (Nye, 1957) and ρ is the mass density of the material.

At the cylindrical surface the stress components acting radially (τ_{rr}, τ_{rz}, $\tau_{r\theta}$) must vanish, and at the end of the cylinder $\tau_{rz}=\tau_{zz}=\tau_{z\theta}=0$. Writing stresses in terms of displacements we have, for axisymmetric modes in cylindrical coordinates

$$\tau_{rr} = c_{11}\frac{\partial u_r}{\partial r} + c_{12}\frac{u_r}{r} + c_{13}\frac{\partial u_z}{\partial z},$$

$$\tau_{zz} = c_{13}\frac{1}{r}\frac{\partial}{\partial r}(ru_r) + c_{33}\frac{\partial u_z}{\partial z},$$

$$\tau_{rz} = c_{44}\left[\frac{\partial u_z}{\partial r} + \frac{\partial u_r}{\partial z}\right],$$

$$\tau_{r\theta} = \tau_{z\theta} = 0. \tag{2}$$

We notice that the boundary conditions on $\tau_{r\theta}$ and $\tau_{z\theta}$ are automatically satisfied.

Our solution was found by applying the separation of variables technique of Morse (1954), using as a guide the solution forms of Hutchinson (1972), which are appropriate for an isotropic cylinder.[2] The solution for the displacements is a sum of terms which satisfy the differential equations (1) and the boundary conditions on the shear stress ($\tau_{rz}=0$ at $r=a$ and at $z=\pm L$). The boundary conditions on the tensile stresses τ_{rr} and τ_{zz} are satisfied approximately by using an orthogonalization procedure. This leads to an eigenvalue matrix which can be solved for the free vibration frequencies. Once the eigenfrequencies have been determined, the mode shapes are then calculated. The solution can be made as near to exact as required by choosing enough terms in the sum.

3 The Stress-Free Boundary Solution

Our solution is in the form of a series

$$u_r = \Sigma A_n u_{rAn} + \Sigma B_n u_{rBn} + \Sigma C_n u_{rCn} + \Sigma D_n u_{rDn}, \tag{3}$$

with similar expressions for u_z, τ_{rr}, τ_{zz} and τ_{rz} containing the same coefficients A_n, B_n, C_n and D_n. The solutions for the displacements are as follows:

$$u_{rA} = [a_A pJ_1(pr) + b_A qJ_1(qr)]\sin(\gamma z)e^{-i\omega t},$$

$$u_{zA} = -(1/\alpha)[a_A(k^2-p^2)J_0(pr) + b_A(k^2-q^2)J_0(qr)]\cos(\gamma z)e^{-i\omega t},$$

$$u_{rB} = -(1/\delta)[a_B(l^2-d^2)\sin(dz) + b_B(l^2-e^2)\sin(ez)]J_1(\gamma r)e^{-i\omega t},$$

$$u_{zB} = [a_B d\cos(dz) + b_B e\cos(ez)]J_0(\gamma r)e^{-i\omega t},$$

$$u_{rC} = [a_C pJ_1(pr) + b_C qJ_1(qr)]\cos(\gamma z)e^{-i\omega t},$$

$$u_{zC} = (1/\alpha)[a_C(k^2-p^2)J_0(pr) + b_C(k^2-q^2)J_0(qr)]\sin(\gamma z)e^{-i\omega t},$$

$$u_{rD} = (1/\delta)[a_D(l^2-d^2)\cos(dz) + b_D(l^2-e^2)\cos(ez)]J_1(\gamma r)e^{-i\omega t},$$

$$u_{zD} = [a_D d\sin(dz) + b_D e\sin(ez)]J_0(\gamma r)e^{-i\omega t}, \tag{4}$$

where the coefficients a_A etc., are given by:

$$a_A = qJ_1(qa)[\gamma\alpha + (k^2-q^2)],$$

$$b_A = -pJ_1(pa)[\gamma\alpha + (k^2-p^2)],$$

[1] We note that for the trigonal system, with the additional elastic constant c_{14}, axisymmetric solutions do not exist. However, we take this constant to be zero in our approximate analysis of the free vibrations of a sapphire crystal.

[2] An earlier version of our paper, containing more detail on the derivation of this solution, can be obtained from the authors.

Downloaded 03 May 2010 to 171.66.16.21. Redistribution subject to ASME license or copyright; see http://www.asme.org/terms/Terms_Use.cfm

$$a_B = e\cos(eL)[\gamma\delta + (l^2 - e^2)],$$

$$b_B = -d\cos(dL)[\gamma\delta + (l^2 - d^2)],$$

$$a_C = qJ_1(qa)[\gamma\alpha + (k^2 - q^2)],$$

$$b_C = -pJ_1(pa)[\gamma\alpha + (k^2 - p^2)],$$

$$a_D = e\sin(eL)[\gamma\delta + (l^2 - e^2)],$$

$$b_D = -d\sin(dL)[\gamma\delta + (l^2 - d^2)], \tag{5}$$

and for the A series $\gamma = (2n-1)\pi/2L$ with $n = 1, 2, \ldots$, for the B and D series $\gamma a = \chi_{1n}$ with $n = 0, 1, \ldots$, and for the C series $\gamma = n\pi/L$ with $n = 0, 1, \ldots$, $J_0(\ )$ and $J_1(\ )$ are zeroth-order and first-order Bessel functions of the first kind and χ_{pm} is the mth zero of J_p i.e.,

$$J_p(\chi_{pm}) = 0, \tag{6}$$

with $\chi_{10} = 0$.

The wave numbers α, δ, k, l, d, e, p, and q are related to the frequency ω and the appropriate γ by:

$$\alpha = \gamma(c_{13} + c_{44})/c_{11},\ k^2 = (\rho\omega^2 - \gamma^2 c_{44})/c_{11},$$

$$\delta = \gamma(c_{13} + c_{44})/c_{33},\ l^2 = (\rho\omega^2 - \gamma^2 c_{44})/c_{33},$$

$$\left.\begin{matrix} d^2 \\ e^2 \end{matrix}\right\} = \frac{1}{2c_{33}c_{44}}[c_{44}(\rho\omega^2 - \gamma^2 c_{44}) + c_{33}(\rho\omega^2 - \gamma^2 c_{11}) + \gamma^2(c_{13} + c_{44})^2$$

$$\pm [(c_{44}(\rho\omega^2 - \gamma^2 c_{44}) + c_{33}(\rho\omega^2 - \gamma^2 c_{11}) + \gamma^2(c_{13} + c_{44})^2)^2$$

$$- 4c_{33}c_{44}(\rho\omega^2 - \gamma^2 c_{44})(\rho\omega^2 - \gamma^2 c_{11})]^{1/2}].$$

$$\left.\begin{matrix} p^2 \\ q^2 \end{matrix}\right\} = \frac{1}{2c_{11}c_{44}}[c_{44}(\rho\omega^2 - \gamma^2 c_{44}) + c_{11}(\rho\omega^2 - \gamma^2 c_{33}) + \gamma^2(c_{13} + c_{44})^2$$

$$\pm [(c_{44}(\rho\omega^2 - \gamma^2 c_{44}) + c_{11}(\rho\omega^2 - \gamma^2 c_{33}) + \gamma^2(c_{13} + c_{44})^2)^2$$

$$- 4c_{11}c_{44}(\rho\omega^2 - \gamma^2 c_{44})(\rho\omega^2 - \gamma^2 c_{33})]^{1/2}]. \tag{7}$$

The displacements defined by equations (4), (5), and (7) are exact solutions of equations (1). The normal stresses and shear stresses are obtained from these displacements using equations (2). The "A" series of stresses are:

$$\tau_{rrA} = [a_A\{J_0(pr)[c_{11}p^2 + c_{13}(\gamma/\alpha)(k^2 - p^2)] + p(J_1(pr)/r)(c_{12} - c_{11})\} + b_A\{J_0(qr)[c_{11}q^2 + c_{13}(\gamma/\alpha)(k^2 - q^2)] + q(J_1(qr)/r)(c_{12} - c_{11})\}] \times \sin(\gamma z)e^{-i\omega t},$$

$$\tau_{zzA} = [a_A J_0(pr)\{c_{13}p^2 + c_{33}(\gamma/\alpha)(k^2 - p^2)\} + b_A J_0(qr)\{c_{13}q^2 + c_{33}(\gamma/\alpha)(k^2 - q^2)\}]\sin(\gamma z)e^{-i\omega t},$$

$$\tau_{rzA} = (c_{44}/\alpha)\{a_A pJ_1(pr)[\gamma\alpha + (k^2 - p^2)] + b_A qJ_1(qr)[\gamma\alpha + (k^2 - q^2)]\}\cos(\gamma z)e^{-i\omega t}. \tag{8}$$

We see that given our choice for the coefficients a_A and b_A, and using the value of γ appropriate for the "A" series of functions, the shear stresses τ_{rzA} satisfy the required boundary conditions over the entire surface, however, the normal stresses do not. The same is true of the "B," "C," and "D" series of stresses. The boundary conditions on τ_{rr} and τ_{zz} are:

$$\tau_{rr}(a, z, t) = 0 \text{ and } \tau_{zz}(r, \pm L, t) = 0. \tag{9}$$

An equivalent form for the conditions on τ_{zz} is:

$$\tau_{zz}(r, +L, t) - \tau_{zz}(r, -L, t) = \tau_{zzo}(r, L, t) = 0,$$

and

$$\tau_{zz}(r, +L, t) + \tau_{zz}(r, -L, t) = \tau_{zze}(r, L, t) = 0. \tag{10}$$

The functions τ_{rr} and τ_{zz} are given by series of the form of equation (3) with the same A_n, B_n, C_n, and D_n. They are obtained by substituting equation (3) and a similar expression for u_z into equations (2). We satisfy the boundary conditions (equations (9) and (10)) approximately by making the stresses orthogonal to a complete set of functions on the boundaries:

$$\int_{-L}^{L} \tau_{rr}(a, z, t)\sin(\gamma'_m z)dz = 0, \tag{11}$$

where $\gamma'_m = (2m-1)\pi/2L$, $m = 1,2,3, \ldots$,

$$\int_{-L}^{L} \tau_{rr}(a, z, t)\cos(\gamma'_m z)dz = 0, \tag{12}$$

where $\gamma'_m = m\pi/L$, $m = 0,1,2, \ldots$,

$$\int_0^a \tau_{zzo}(r, L, t)rJ_0(\gamma'_m r)dr = 0, \tag{13}$$

where $\gamma'_m a = \chi_{1m}$, $m = 0,1,2, \ldots$, and τ_{zzo} is the axial stress containing odd functions of z (A and B series), and

$$\int_0^a \tau_{zze}(r, L, t)rJ_0(\gamma'_m r)dr = 0, \tag{14}$$

where $\gamma'_m a = \chi_{1m}$, $m = 0,1,2, \ldots$, and τ_{zze} is the axial stress containing even functions of z (C and D series).

The necessary integrals involving Bessel functions can be found in Watson (1944). Satisfying equation (11) gives

$$A_m\hat{A}_m + \sum_n B_n\hat{B}_{mn} = 0, \tag{15}$$

where

$$\hat{A}_m = L[a_A\{J_0(pa)[c_{11}p^2 + c_{13}(\gamma/\alpha)(k^2 - p^2)] + p(J_1(pa)/a)[c_{12} - c_{11}]\} + b_A\{J_0(qa)[c_{11}q^2 + c_{13}(\gamma/\alpha)(k^2 - q^2)] + q(J_1(qa)/a)[c_{12} - c_{11}]\}] \tag{16}$$

where $\gamma_m = (2m-1)/2L$, $m = 1,2, \ldots$, with subscripts m on γ, α, p, q, and k having been dropped for simplicity;

$$\hat{B}_{mn} = 2J_0(\gamma a)\sin(\gamma' L)\left[a_B[c_{13}d^2 + c_{11}(\gamma/\delta)(l^2 - d^2)]\frac{d\cos(dL)}{(d^2 - \gamma'^2)} + b_B[c_{13}e^2 + c_{11}(\gamma/\delta)(l^2 - e^2)]\frac{e\cos(eL)}{(e^2 - \gamma'^2)}\right], \tag{17}$$

where $\gamma_n = \chi_{1n}/a$, $n = 0,1,2, \ldots$, and $\gamma'_m = (2m-1)\pi/2L$, $m = 1, 2, \ldots$, with subscripts n having been omitted from γ, δ, d, e, and l, and a subscript m having been omitted from γ'. Similarly, we can satisfy equations (12) to (14) and obtain three more equations of the form of equation (15). We can combine these three and equation (15) into matrix equations:

Downloaded 03 May 2010 to 171.66.16.21. Redistribution subject to ASME license or copyright; see http://www.asme.org/terms/Terms_Use.cfm

$$\begin{bmatrix} \hat{A}_m & & \hat{B}_{mn} \\ & \cdot & \\ & \cdot & \\ \hat{A}_{mn} & & \hat{B}_m \end{bmatrix} * \begin{bmatrix} A \\ \cdot \\ \cdot \\ B \end{bmatrix} = \begin{bmatrix} 0 \\ \cdot \\ \cdot \\ \cdot \end{bmatrix}, \tag{18}$$

and

$$\begin{bmatrix} \hat{C}_m & & \hat{D}_{mn} \\ & \cdot & \\ & \cdot & \\ \hat{C}_{mn} & & \hat{D}_m \end{bmatrix} * \begin{bmatrix} C \\ \cdot \\ \cdot \\ D \end{bmatrix} = \begin{bmatrix} 0 \\ \cdot \\ \cdot \\ \cdot \end{bmatrix}. \tag{19}$$

The coefficients $\hat{B}_m$, $\hat{A}_{mn}$, $\hat{C}_m$, $\hat{D}_{mn}$, $\hat{D}_m$, and $\hat{C}_{mn}$ are given in the Appendix.

We see that our solutions separate into two uncoupled sets. The solutions containing A and B terms have axial displacements and shear stresses which are even functions of z (u_r, τ_{rr}, τ_{zz} odd). We call these even solutions (following Hutchinson (1972)). The odd solutions (containing C and D terms) have odd axial displacements and shear stresses, with u_r, τ_{rr} and τ_{zz} even functions of z.

The natural frequencies of vibration are found by searching for zeros of the determinants of the matrices in equations (18) and (19). We fix L and a, take ρ to be that of sapphire (3.986×10^3 kgm^{-3}), and choose the coefficients c_{ij} to be those of sapphire at room temperature (c_{14} is taken to be zero and the values of the other elastic constants used are those given in Table 1). The coefficients of the matrices are then just functions of ω alone as defined by equations (5), (7), (16), (17), and (A-1)-(A-6).

The search for roots is not entirely straightforward, for small ω, p^2, q^2, d^2, and e^2 can be negative. Real roots for ω can be obtained when some or all of p, q, d, and e are imaginary. All these situations must be taken into account with the restriction that $d^2>e^2$, and $p^2>q^2$. We search for roots using a simple binary chop. As pointed out by Hutchinson (1972), when using methods such as this, spurious roots will be obtained when certain coefficients in the matrices become infinite. We see from equations (17), (A-2), (A-4), and (A-6) that if $\gamma'^2=p^2$, q^2, d^2 or e^2 then one of the coefficients will approach infinity and this will produce a change of sign in the determinant on moving from $\omega<\omega_f$ to $\omega>\omega_f$ where ω_f is the frequency for which $\gamma'^2=p^2$, q^2, d^2 or e^2. We neglect these spurious roots in our program.

Once the frequencies of vibration have been calculated the displacements and stresses are obtained by calculating the coefficients A_n etc., from equations (18) and (19) and then using equation (3) and similar expressions. The coefficients a_A and b_A etc., have been chosen so as to avoid dividing by zero when calculating roots of the determinants and this choice results in equations (5) (only the ratios b_A/a_A etc., are determined by satisfying the shear stress boundary conditions). When calculating the coefficients A_n etc., we are at liberty to fix one coefficient and then calculate all the others. The set of coefficients A_n etc., determine both displacements and stresses as a function of r and z.

4 Experimental Details

Our experimental set up has been fully described elsewhere (Lusher and Hardy, 1987). The sapphire sample was used as a dielectric resonator (based on the design of Blair and Jones (1987)) in part of a high stability microwave oscillator system. The sapphire resonator, microwave cavity and piezoelectric transducer are shown in Fig. 1. The main body of the resonator was a right circular cylinder ~3 cm long and ~3 cm in diameter. The resonator had posts 0.625 cm in diameter extending from the center of each end which served as supports. The entire resonator (which was supplied by Union Carbide) was cut from a single crystal of sapphire with the c-axis coincident with the axis of the cylinder to within 0.5°. A 0.635 cm diameter rod of sapphire was bonded onto one of the posts as an extension. In order to reduce the acoustic mismatch at the joint, both surfaces were polished almost to an optical finish using diamond paste before bonding with clear epoxy. Vacuum grease was used for bonding the transducer to the copper base and to the sapphire. A small ring of indium was placed on the top post which helped to keep the resonator in place. The cavity was evacuated through the tube that contained the microwave coupling probe.

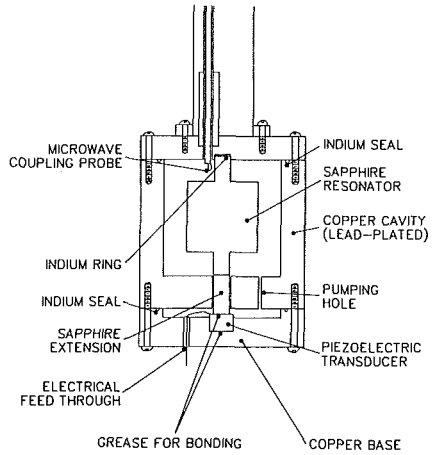

Fig. 1 The sapphire resonator and ultrasonic transducer

Using this set up, FM sidebands could be introduced onto a reflected microwave carrier by exciting the sapphire at one of its modes of free vibration with the transducer, the microwave resonance frequencies being determined by the size of the sapphire. The acoustic resonance frequency was determined by monitoring the microwave signal. Also, the frequencies of the acoustic modes themselves were measured independently by monitoring the impedance of the transducer as a function of frequency. Information on the shapes of the acoustic modes was obtained by placing a rubber band around the body of the sapphire (with the resonator outside the cavity) and observing the dependence of the quality factor of the acoustic mode in question on the position of the band.

5 Results

All data presented in this section were produced using the values of the elastic constants given in Table 1. The success of this series solution to the differential equations can be seen by examining the convergence of frequencies as the number of terms N in the series is increased (the size of the matrices in equations (18) and (19) is $2N\times2N$). In Tables 2 and 3 we show the convergence of the first six frequencies for the even and odd modes. We take the half-height to radius ratio to be that which corresponds to our sapphire sample ($(L/a)=0.9936447$). We show in the tables a dimensionless frequency parameter

$$\omega a/v_{sz} \tag{20}$$

where v_{sz}, defined by

$$v_{sz}^2=[c_{33}-2c_{13}^2/(c_{11}+c_{12})]/\rho,$$

is the velocity of compressional waves in the long wavelength limit for an infinite hexagonal cylinder with the crystallographic c-axis aligned with the axis of the cylinder.

It can be seen that using five terms in each series is good enough to obtain reasonable convergence of the first six frequencies both for even and odd modes. We have calculated the

Downloaded 03 May 2010 to 171.66.16.21. Redistribution subject to ASME license or copyright; see http://www.asme.org/terms/Terms_Use.cfm

Table 2 Convergence of frequencies for the first six even modes

	Frequency parameter $\omega a/v_{sz}$*					
Terms	1	2	3	4	5	6
1	1.9237139	2.6821147	-	-	-	-
2	1.6997204	2.2325966	2.8432621	3.2783463	3.8339737	3.9783367
3	1.6881193	2.2220091	2.7913188	3.2762638	3.6504470	3.7819453
4	1.6837723	2.2176996	2.7811003	3.2761413	3.6364357	3.7764747
5	1.6816995	2.2155973	2.7769697	3.2761045	3.6289928	3.7747865
6	1.6805579	2.2144314	2.7748323	3.2760864	3.6246500	3.7739079

* $L/a = 0.9936447$.

Table 3 Convergence of frequencies for the first six odd modes

	Frequency parameter $\omega a/v_{sz}$*					
Terms	1	2	3	4	5	6
1	1.5454311	-	-	-	-	-
2	1.5279595	1.8988680	2.1830747	2.9031258	3.5761529	-
3	1.5254496	1.8678706	2.1829276	2.8333277	3.3845967	4.0430474
4	1.5245812	1.8579358	2.1829037	2.8301353	3.3525182	4.0047427
5	1.5241871	1.8535909	2.1828982	2.8294003	3.3377440	3.9982258
6	1.5239768	1.8513169	2.1828965	2.8290756	3.3296621	3.9961662
7	1.5238519	1.8499805	2.1828958	2.8288898	3.3247813	3.9952974

* $L/a = 0.9936447$.

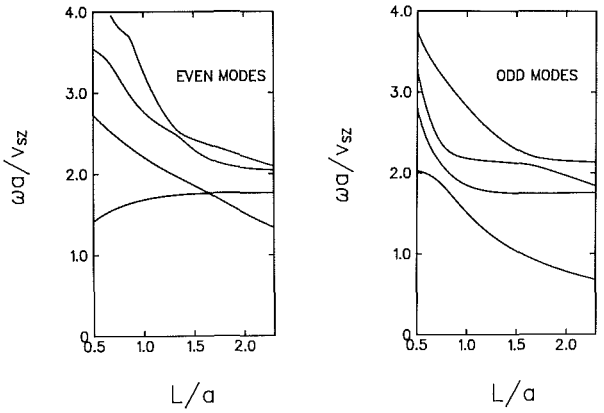

Fig. 2 Frequency parameter versus half-height to radius ratio for the first four even and first four odd solutions of the free vibration equations for axisymmetric modes, using the values of the elastic constants given in Table 1

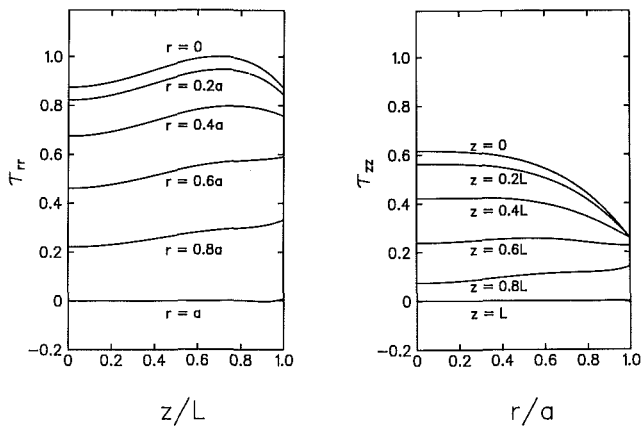

Fig. 3 Normal stresses of the third odd mode

frequencies of the first four even modes and the first four odd modes as a function of L/a. The results are shown in Fig. 2. We used five terms in each series.

The extent to which the boundary conditions on the normal stresses are satisfied can be seen for the third odd mode in Figs. 3 and 4. The stresses are normalized so as to make the maximum normal stress unity. Figure 4 shows the normal stresses at the boundaries from Fig. 3 multiplied by a factor of one hundred. Seven terms in the series were used. We use a value for L/a of 0.9936447. It can be seen that the boundary conditions are well satisfied for this mode, the largest error being at the corner ($r=a$, $z=L$). The mode shapes of the first four even modes are shown in Fig. 5 and those of the first four odd modes are shown in Fig. 6. Six terms were used to calculate the even mode displacements and seven terms for the odd modes. This was enough for convergence. These modes are all axisymmetric, the displacements being independent of the azimuthal angle.

5.1 Comparison With Morse's Solution. We have compared our calculation with the generalized PC equations of Morse (1954), who obtained a dispersion equation which relates the frequency to the ratio of the circumference to the wavelength for travelling wave solutions for an infinite circular rod of a transversely isotropic material. This solution is exact for an infinite circular rod since it satisfies the zero stress condition on the circumferential boundary. For a finite rod this solution does not permit stress-free ends. By superimposing two travelling wave solutions, one can satisfy end boundary conditions for a finite rod of zero axial stress and radial displacement (we compared our solution with this case) or zero radial stress and axial displacement. Solutions in which

Downloaded 03 May 2010 to 171.66.16.21. Redistribution subject to ASME license or copyright; see http://www.asme.org/terms/Terms_Use.cfm

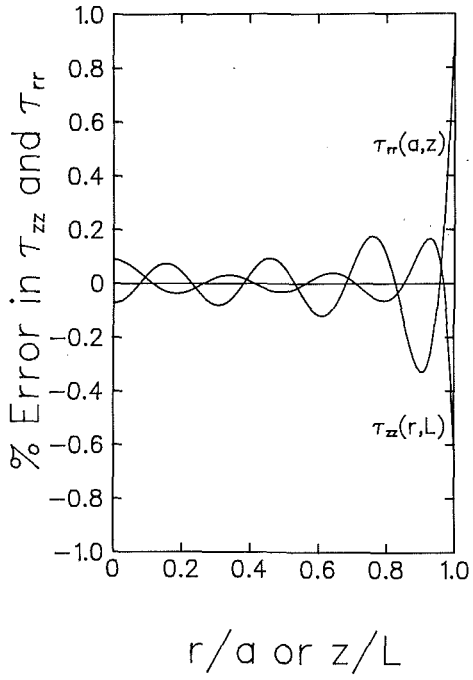

Fig. 4 Error in satisfying the normal stress boundary conditions for the third odd mode

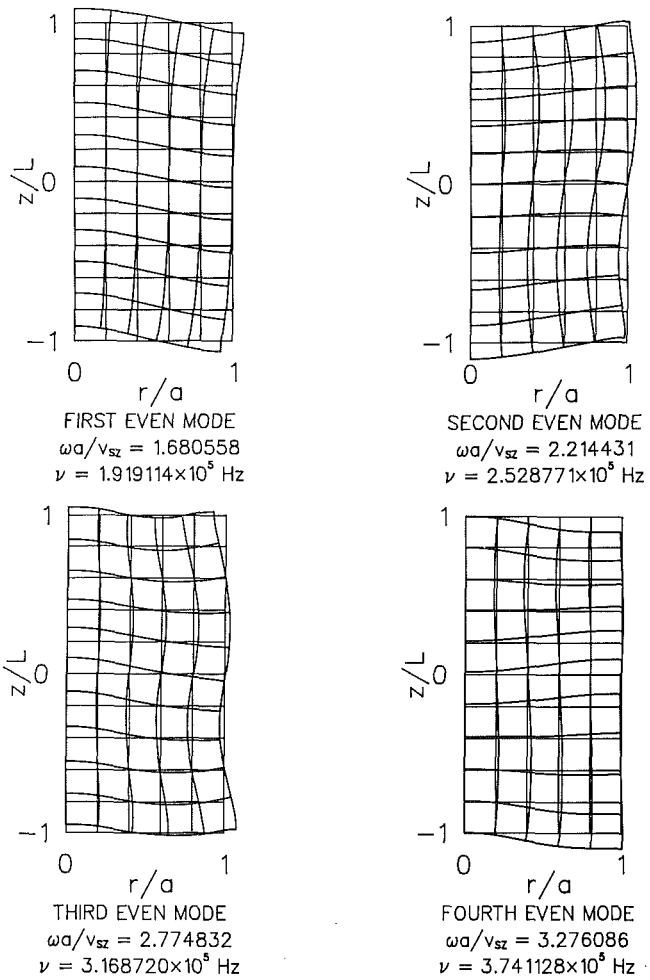

Fig. 5 Mode shapes and frequencies of the first four even modes for a half-height to radius ratio *L/a* of 0.9936447

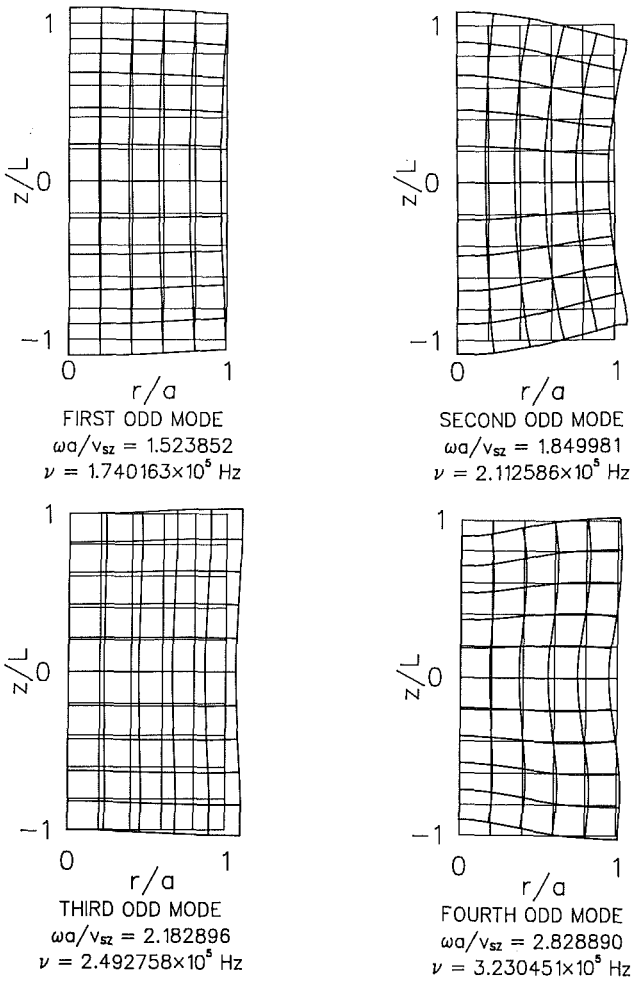

Fig. 6 Mode shapes and frequencies of the first four odd modes for a half-height to radius ratio *L/a* of 0.9936447

both radial and axial displacements are finite at the free planar surfaces are not permitted with this approach.

Hutchinson (1972) gives a detailed comparison between the PC solutions and his accurate series solution for an isotropic rod. Our results were similar to his. Certainly for $L/a \geq 1$ the generalized PC equations give excellent results for the frequency of the first odd mode (using the same values for the elastic constants as in the main calculation we obtained a value of the frequency which agreed with our "seven term" result to within bettter than 0.02 percent for $L/a = 0.9936447$). However, when seeking frequencies of higher vibrational modes, Morse's infinite rod solution cannot be used and our more complicated solution must be employed, especially if an accurate determination of the mode shapes is also required.

5.2 Comparison With Experiment. Using the method described above, the frequencies and mode of shapes of a transversely isotropic finite right circular cylinder can be calculated to any precision required, and agreement with experimental data should be excellent for that system. We were interested in applying the method to sapphire, which has one additional elastic constant. Moreover, our sapphire sample was not a perfect right circular cylinder, having supporting posts extending from the center of each plane face (see Fig. 1).

The frequencies ν quoted in Figs. 5 and 6 are those we would expect from our sample of radius 1.4986×10^{-2}m, taking a value of 3.986×10^3 kgm^{-3} for ρ. Many acoustic modes were observed by monitoring the impedance of the transducer (~ 50 modes between 150 kHz and 450 kHz). Without detailed

Downloaded 03 May 2010 to 171.66.16.21. Redistribution subject to ASME license or copyright; see http://www.asme.org/terms/Terms_Use.cfm

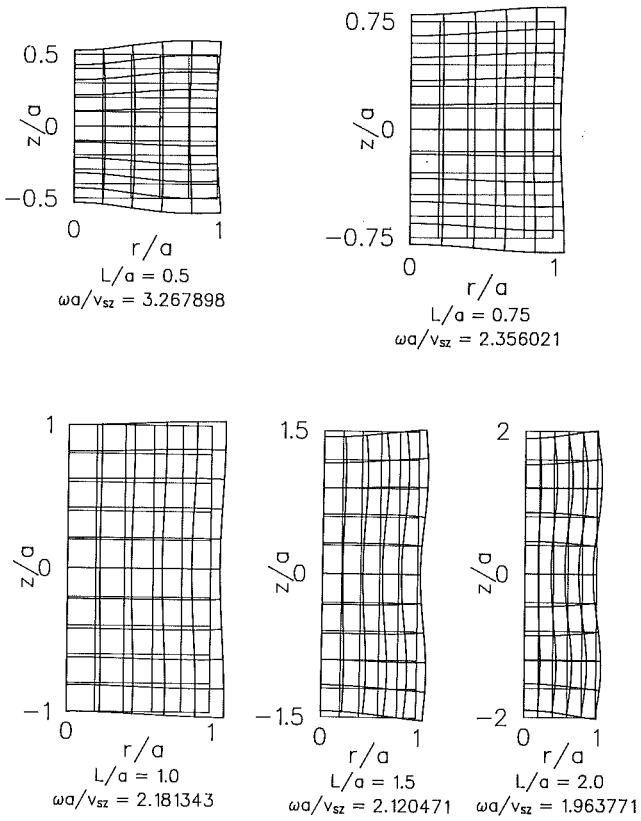

Fig. 7 Mode shapes and frequenices of the third odd mode for various *L/a* ratios

knowledge of the shapes of the acoustic modes excited, it was not easy to assign the modes with confidence. However, for reasons discussed below, we were able to identify unequivocally the third odd mode and its frequency was in very good agreement with the calculated value. Also, because of the shape of this mode, we expect the perturbing effects of the supporting posts to be small.

For the other modes, the situation is less straightforward. However, some insight can be gained by comparing our results with the experimental data of McMahon (1964) for aluminum and steel cylinders. McMahon observed that for a value of $L/a \sim 1$ the first axisymmetric mode is not the lowest acoustic mode, and there is a mode with two azimuthal nodes very close in frequency to that of the first odd mode. The lowest acoustic modes we observed had frequencies of 163.3 kHz and 163.4 kHz, and were not axisymmetric. The calculated frequency of the lowest axisymmetric mode (the first odd mode) is 174.0163 kHz. We observed modes at 175.1 kHz and 175.2 kHz. By symmetry one would not expect to observe a doublet, however, the close proximity of a mode with one or more azimuthal nodes (similar to the case of aluminum) would explain this result.

The third odd mode, with a calculated frequency of 249.2758 kHz, looks particularly suitable for use in the acoustic modulation technique. The body length and radius shrink and grow together, resulting in a larger volume change. This should produce a larger effect on the microwave resonance frequencies than for example the first odd mode, where there may be compensating effects due to the radius shrinking while the length grows. Only one of the many acoustic modes of the sapphire that were excited with the transducer produced observable FM sidebands on the microwave carrier. The frequency of this mode was 249.88 kHz at room temperature. The dissipation introduced when probing the shape of the mode using a rubber band was consistent with the shape of the third odd mode given in Fig. 6. It seems clear that this was the third odd mode being excited.

An interesting feature of the shape of the third odd mode is that the axial displacement of the plane faces near $r=0$ is very close to zero. This is advantageous if one wishes to use this mode in an acoustic modulation experiment since it means that the mode is only weakly coupled to the outside world (at least for our experimental set up), and therefore insensitive to any unwanted vibrations in the system. In order to see if this lack of motion on the plane faces near $r=0$ was accidental, resulting from our particular choice of L/a, we calculated the mode shapes for the third odd mode for various L/a ratios. The results are shown in Fig. 7. It is clearly seen from this figure that the weak coupling is a result of the particular value of L/a chosen. From an experimental point of view, it should therefore be possible to "fine tune" the coupling by varying L/a.

The excellent agreement between the calculated frequency of the third odd mode and the measured frequency may be due in part to the fact that this mode has very little displacement where the supporting posts are formed on the resonator, thus reducing the perturbing effects of these posts.

6 Conclusions

We have given a series solution for the frequencies and mode shapes of axisymmetric free vibrations of a finite length, right circular cylinder of a hexagonal crystal with the crystallographic *c*-axis oriented along the axis of the cylinder (a transversely isotropic cylinder). This is the simplest extension to the problem of the finite isotropic cylinder. The series solution satisfies the elastic equations of motion exactly and the zero stress boundary conditions can be satisfied to any required precision by including enough terms in the series. The frequencies converge rapidly to the exact results, only a few terms being needed to give accurate values.

This solution can give answers as near to exact as required for the transversely isotropic cylinder. However, it is complicated and unable to handle other geometries. Nevertheless, it can be used to test the range of validity of approximate theories which are either simpler or have the capability of handling other geometries. As an example, Morse's simpler infinite rod solution was found to give excellent results for the lowest axisymmetric mode of a finite cylinder with $L/a \geq 1$ but was not as good for higher modes.

Our solution was used to calculate free vibration frequencies for a sapphire crystal. The results were in good agreement with our experimental data on sapphire (within ~ 1 percent) for a cylinder with a half-height to radius ratio of ~ 1, even though one of the elastic constants of sapphire was neglected in order to make the calculation manageable. Furthermore, our sample was not a perfect right circular cylinder, having 0.635 cm diameter supporting rods coming from both plane faces.

Acknowledgments

We would like to thank M. W. Reynolds and M. Holzer for guidance on certain aspects of the numerical calculation. This work was supported by the National Research Council of Canada.

References

Blair, D. G., and Jones, S. K., 1987, "A High-Q Sapphire Loaded Superconducting Cavity Resonator," *Journal of Physics D: Applied Physics*, Vol. 20, pp. 1559–1566.

Braginsky, V. B., Mitrofanov, V. P., and Panov, V. I., 1985, *Systems with Small Dissipation*, University of Chicago Press, Chicago.

Gladwell, G. M. L., and Tahbildar, U. C., 1972, "Finite Element Analysis of the Axisymmetric Vibrations of Cylinders," *Journal of Sound and Vibration*, Vol. 22, pp. 143–157.

Downloaded 03 May 2010 to 171.66.16.21. Redistribution subject to ASME license or copyright; see http://www.asme.org/terms/Terms_Use.cfm

Hutchinson, J. R., 1972, "Axisymmetric Vibrations of a Free Finite-Length Rod," *Journal of the Acoustical Society of America*, Vol. 51, pp. 233–240.

Kolsky, H., 1953, *Stress Waves in Solids*, Clarendon, Oxford.

Love, A. E. H., 1944, *A Treatise on the Mathematical Theory of Elasticity*, 4th ed., Dover, New York.

Lusher, C. P., and Hardy, W. N., 1987, "Frequency Stabilization of a Sapphire Resonator Oscillator Using an Acoustic Modulation Technique," *Japanese Journal of Applied Physics*, Vol. 26, Supplement 26-3, pp. 1701–1702.

McMahon, G. W., 1964, "Experimental Study of the Vibrations of Solid, Isotropic, Elastic Cylinders," *Journal of the Acoustical Society of America*, Vol. 36, pp. 85–92.

McMahon, G. W., 1970, "Finite-Difference Analysis of the Vibrations of Solid Cylinders," *Journal of the Acoustical Society of America*, Vol. 48, pp. 307–312.

McNiven, H. D., and Perry, D. C., 1962, "Axially Symmetric Waves in Finite, Elastic Rods," *Journal of the Acoustical Society of America*, Vol. 34, pp. 433–437.

Morse, R. W., 1954, "Compressional Waves along an Anisotropic Circular Cylinder Having Hexagonal Symmetry," *Journal of the Acoustical Society of America*, Vol. 26, pp. 1018–1021.

Nye, J. F., 1957, *Physical Properties of Crystals,* Oxford University Press, London.

Sih, G. C., and Chen, E. P., 1981, *Cracks in Composite Materials*, Martinus Nijhoff, The Netherlands.

Wachtman, Jr., J. B., Tefft, W. E., Lam, Jr., D. G., and Stinchfield, R. P., 1960, "Elastic Constants of Synthetic Single Crystal Corundum at Room Temperature," *Journal of Research of the National Bureau of Standards-A. Physics and Chemistry*, Vol. 64A, pp. 213–228.

Watson, G. N., 1944, *A Treatise on the Theory of Bessel Functions*, 2nd ed., Cambridge University Press, Cambridge.

APPENDIX

The coefficients of the matrices in equations (18) and (19) are as follows:

$$\hat{B}_m = -\frac{a^2}{2} J_0{}^2(\gamma a)\{a_B \sin(dL)[c_{33}d^2 + c_{13}(\gamma/\delta)(l^2 - d^2)] + b_B \sin(eL)[c_{33}e^2 + c_{13}(\gamma/\delta)(l^2 - e^2)]\}, \quad (A\text{-}1)$$

$$\hat{A}_{mn} = aJ_0(\gamma' a)\sin(\gamma L)\left[a_A[c_{13}p^2 + c_{33}(\gamma/\alpha)(k^2 - p^2)]\frac{pJ_1(pa)}{(p^2 - \gamma'^2)} + b_A[c_{13}q^2 + c_{33}(\gamma/\alpha)(k^2 - q^2)]\frac{qJ_1(qa)}{(q^2 - \gamma'^2)}\right], \quad (A\text{-}2)$$

$$\hat{C}_m = K_m L[a_C\{J_0(pa)[c_{11}p^2 + c_{13}(\gamma/\alpha)(k^2 - p^2)] + p(J_1(pa)/a)[c_{12} - c_{11}]\} + b_C\{J_0(qa)[c_{11}q^2 + c_{13}(\gamma/\alpha)(k^2 - q^2)] + q(J_1(qa)/a)[c_{12} - c_{11}]\}], \quad (A\text{-}3)$$

where

$$K_m = \begin{cases} 2 & m = 0 \\ 1 & \text{otherwise,} \end{cases}$$

$$\hat{D}_{mn} = 2J_0(\gamma a)\cos(\gamma' L)\left[a_D[c_{13}d^2 + c_{11}(\gamma/\delta)(l^2 - d^2)]\frac{d\sin(dL)}{(d^2 - \gamma'^2)} + b_D[c_{13}e^2 + c_{11}(\gamma/\delta)(l^2 - e^2)]\frac{e\sin(eL)}{(e^2 - \gamma'^2)}\right], \quad (A\text{-}4)$$

$$\hat{D}_m = \frac{a^2}{2} J_0{}^2(\gamma a)\{a_D \cos(dL)[c_{33}d^2 + c_{13}(\gamma/\delta)(l^2 - d^2)] + b_D \cos(eL)[c_{33}e^2 + c_{13}(\gamma/\delta)(l^2 - e^2)]\}, \quad (A\text{-}5)$$

$$\hat{C}_{mn} = aJ_0(\gamma' a)\cos(\gamma L)\left[a_C[c_{13}p^2 + c_{33}(\gamma/\alpha)(k^2 - p^2)]\frac{pJ_1(pa)}{(p^2 - \gamma'^2)} + b_C[c_{13}q^2 + c_{33}(\gamma/\alpha)(k^2 - q^2)]\frac{qJ_1(qa)}{(q^2 - \gamma'^2)}\right]. \quad (A\text{-}6)$$

Wave numbers γ, α, p, q, and k have subscripts m in equations (*A*-3) and subscripts n in (*A*-2) and (*A*-6). γ, δ, d, e, and l have subscripts m in equations (*A*-1) and (*A*-5), and subscripts n in (*A*-4). γ' has subscripts m in equations (*A*-2), (*A*-4) and (*A*-6). For each matrix element γ and γ' are defined and α, δ, d, e, p, q, k, and l at a particular frequency ω are given by equations (7), using the appropriate γ. γ and γ' are defined as follows:

$\gamma_m = \chi_{1m}/a$	in equations (*A*-1) and (*A*-5),
$\gamma'_m = \chi_{1m}/a, \gamma_n = (2n-1)\pi/2L$	in equation (*A*-2),
$\gamma_m = m\pi/L$	in equation (*A*-3),
$\gamma'_m = m\pi/L$, $\gamma_n = \chi_{1n}/a$	in equation (*A*-4),
$\gamma'_m = \chi_{1m}/a$, $\gamma_n = n\pi/2L$	in equation (*A*-6).

In equations (*A*-1) to (*A*-6) n, $m = 0, 1, \ldots$, with the exception that in equation (*A*-2) $n = 1, 2, \ldots$, and χ_{pm} is defined by equation (6).

Downloaded 03 May 2010 to 171.66.16.21. Redistribution subject to ASME license or copyright; see http://www.asme.org/terms/Terms_Use.cfm

Ultrasonic Wave Reflection From Liquid-Coupled Orthotropic Plates With Application to Fibrous Composites

Adnan H. Nayfeh
Department of Aerospace Engineering and Engineering Mechanics, University of Cincinnati, Cincinnati, Ohio 45221
Mem. ASME

D. E. Chimenti
Materials Laboratory, Wright-Patterson Air Force Base, Dayton, Ohio 45433

We present a unified analytical treatment supported by extensive experimental data of the interaction of ultrasonic waves with arbitrarily-oriented orthotropic elastic plates. The plates are assumed to be immersed in a fluid and subjected to incident acoustic beams at arbitrary polar and azimuthal angles. Reflection and transmission coefficients are derived from which all propagation characteristics are identified. Highly complex reflection behavior, expressed as phase velocity-frequency dispersion, is observed. Extensive experimental data has been collected in ultrasonic reflection measurements on a plate of T300/Ciba-Geigy 914 composite, selected as a model system to test the theory. Comparisons between theory and experiment show good agreement at several azimuthal angles between 0 deg and 90 deg.

Introduction

In recent years considerable efforts have been expended upon the modeling, testing, and analysis of fibrous composites. This is due in part to their popularity in applications requiring high stiffness-to-weight ratios and also to their intrinsic interest as challenging mechanical systems. However, the morphology of fiber-reinforced composites, as compared with that of homogeneous isotropic media, can seriously complicate their mechanical response. For example, these materials differ from isotropic homogeneous materials in that they are anisotropic and dispersive. However, the degrees of anisotropy and dispersivity depend upon the specific material under consideration and also upon the specific application.

Since most fibrous structural components are subjected to cyclic or impulsive loads which can lead to degradation in load-carrying capability, initial inspection and continued monitoring of these materials for detection and sizing of strength-degrading flaws is necessary in order to insure structural reliability. Ultrasonic nondestructive evaluation is one useful means to provide information related to structural integrity of composites. To assist in the exploitation of this technique for inspecting composites, a full understanding of the propagation of elastic waves in fibrous composites is highly desirable.

Contributed by the Applied Mechanics Division for presentation at the Winter Annual Meeting, Chicago, IL, November 28 to December 2, 1988, of THE AMERICAN SOCIETY OF MECHANICAL ENGINEERS.

Discussion on this paper should be addressed to the Editorial Department, ASME, United Engineering Center, 345 East 47th Street, New York, N.Y. 10017, and will be accepted until two months after final publication of the paper itself in the JOURNAL OF APPLIED MECHANICS. Manuscript received by ASME Applied Mechanics Division, August 21, 1987; final revision, April 12, 1988.

Paper No. 88-WA/APM-55.

Compared with the voluminous literature on the propagation of elastic waves in isotropic media, a limited amount of work exists on anisotropic materials. This is particularly true for the classes of guided waves such as surface, Love, Lamb, and Stoneley waves. Investigation of the propagation of bulk waves in anisotropic materials is relatively well established (see, for example, Musgrave, 1970; Synge, 1957; Fedorov, 1968). Comparatively speaking, few quantitative results have been reported on solutions of guided waves in anisotropic media.

Several authors (Merkulov and Yakovlev, 1962; Merkulov, 1963; Musgrave, 1960; Gates, 1965; Joel, 1961; Henneke, 1972; Lim and Musgrave, 1970; Johnson, 1970; Chadwick and Currie, 1974; Rokhlin et al., 1986) have discussed the reflection and refraction problems from interfaces of anisotropic media in varying degrees of detail. Stoneley (1955) studied Rayleigh surface wave propagation on an anisotropic half-space having cubic crystal symmetry. Since then several other authors (Buchwald, 1961; Buchwald and Davis, 1961; Buchwald and Davis, 1963; Gazis et al., 1960; Rollings et al., 1968; Lim and Farnell, 1969) have considered and reported on similar problems. Theoretical analyses have been undertaken for free Lamb waves in plates of orthotropic (Markus et al., 1985; Nikiforenko et al., 1972), transversely isotropic (Abubakar, 1962; Kosevich and Syrkin, 1985; Baylis and Green, 1986), and cubic (Merkulov and Tursonov, 1969; Solie and Auld, 1973) materials. Some limited approximate theoretical and experimental results for wave propagation in thin (small values of fd where f is the frequency and d is the plate thickness) orthotropic plates with arbitrary orientations have been presented (Moon, 1972; Rose et al., 1987; Thompson et al., 1987).

Because fiber-reinforced composites are often employed in

Copyright © 1988 by ASME
Downloaded 03 May 2010 to 171.66.16.21. Redistribution subject to ASME license or copyright; see http://www.asme.org/terms/Terms_Use.cfm

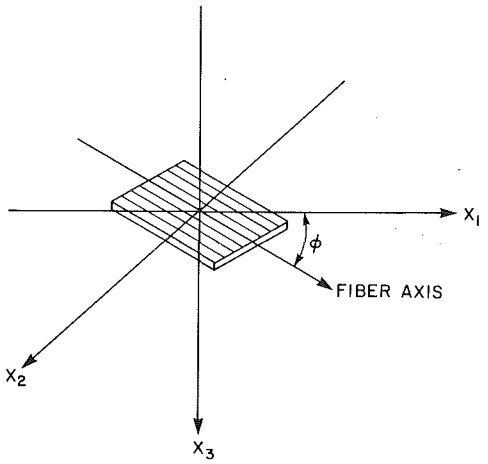

Fig. 1 Coordinate system for leaky plate wave problem. Incident beam strikes plate at angle θ, and ϕ is angle between fiber axis and plane of incidence.

plate-like structures and ultrasonic testing is conveniently performed in immersion, we recently investigated both theoretically and experimentally the behavior of guided elastic waves in liquid-coupled plates of unidirectional fibrous composites (Chimenti and Nayfeh, 1985; Nayfeh and Chimenti, 1988). For consistency we refer, in our work, to the liquid-coupled modes as plate modes. Hereafter, we refer to liquid or fluid coupling synonymously. These excitations may be contrasted with Lamb modes for a plate in vacuum, like those studied in Brekhovskikh (1960) and Viktorov (1967). In Chimenti and Nayfeh (1985) and Nayfeh and Chimenti (1988) results were presented for cases where the plate wave vector is along the direction of symmetry, i.e., the fiber axis.

As compared with isotropic cases, solutions to the anisotropic problem are much more difficult to obtain. This is because of the added algebraic complications in handling of the pertinent equations. Based on the widely used slowness waves surface techniques (Musgrave, 1970; Synge, 1957; Fedorov, 1968) several differences between the wave propagation characteristics of isotropic and anisotropic media can be identified. In the isotropic case, the slowness surface consists of two concentric spherical sheets, the inner one represents longitudinal wave and the outer represents two coincident shear waves. For the anisotropic case, however, there are three general surfaces, one for a quasi-longitudinal and two for quasi-shear waves. This means that incident and reflected waves in anisotropic media can no longer be thought of as purely longitudinal or shear with appropriate directionally independent wave speeds. This also implies that the direction of energy flow (i.e., group velocity) does not, in general, coincide with the normal to the wave front (Federov, 1968). The uncoupling of the longitudinal and shear potentials in the isotropic case simplifies the algebraic treatment of their wave propagation characteristics compared to the corresponding anisotropic case. Generally speaking, in the case of anisotropic media equations describing the motions of the three waves are coupled, and in order to identify them one needs to solve a sixth order polynomial characteristic equation. For special material symmetry directions the equation of one of the shear waves uncouples, leading to fourth order polynomial equations which are relatively easier to handle. Taken together, these complications perhaps explain why many of the available treatments of wave propagation in anisotropic media emphasize wave motions along material symmetry directions.

In this paper we develop the analysis for, and present extensive experimental results on, the propagation of guided waves in a liquid-coupled, arbitrarily in-plane oriented orthotropic plate. The wave is allowed to be incident at an arbitrary direction on the plate (i.e., incident and azimuthal angles). The solutions obtained will thus include, as special cases, those of transversely isotropic (an example of which is unidirectionally reinforced composite), cubic, and isotropic media. The reflection and the transmission coefficients are derived, and algebraic expressions for the characteristic symmetric and antisymmetric plate modes are obtained. Detailed comparisons are presented between the experimental data and the theory for a graphite-epoxy fibrous composite plate.

A key condition which is found to facilitate our subsequent analysis is the fact that the wave vectors of the incident and refracted waves must all lie in the same plane. This result is a consequence of satisfying continuity conditions at the liquid-solid interface (see Henneke (1972) for justification). We will therefore conduct our analysis in a coordinate system formed by incident and interfacial planes rather than by material symmetry axes. This leads to a simplification in our algebraic analysis and computations.

Theoretical Background

Consider an infinite orthotropic plate having the thickness d and immersed in fluid such that its symmetry axes are oriented originally along the cartesian coordinate system $x_i' = (x_1', x_2', x_3')$. The plane $x_1' - x_2'$ is chosen to coincide with the upper surface of the plate, and the x_3' coordinate is normal to it, as illustrated in Fig. 1. With respect to this primed coordinate system, the elastic field equations of the plate are given by the momentum equations

$$\frac{\partial \sigma_{ij}'}{\partial x_j'} = \rho' \frac{\partial^2 u_i'}{\partial t^2} \tag{1}$$

and, from the general constitutive relations for anisotropic media,

$$\sigma_{ij}' = c_{ijkl}' e_{kl}' \tag{2}$$

by the specialized expanded matrix form to orthotropic media

$$\begin{bmatrix} \sigma_{11}' \\ \sigma_{22}' \\ \sigma_{33}' \\ \sigma_{23}' \\ \sigma_{13}' \\ \sigma_{12}' \end{bmatrix} = \begin{bmatrix} C_{11}' & C_{12}' & C_{13}' & 0 & 0 & 0 \\ C_{12}' & C_{22}' & C_{23}' & 0 & 0 & 0 \\ C_{13}' & C_{23}' & C_{33}' & 0 & 0 & 0 \\ 0 & 0 & 0 & C_{44}' & 0 & 0 \\ 0 & 0 & 0 & 0 & C_{55}' & 0 \\ 0 & 0 & 0 & 0 & 0 & C_{66}' \end{bmatrix} \begin{bmatrix} e_{11}' \\ e_{22}' \\ e_{33}' \\ \gamma_{2}' \\ \gamma_{13}' \\ \gamma_{12}' \end{bmatrix} \tag{3}$$

where we used the contracting subscript notations $1 \to 11$, $2 \to 22$, $3 \to 33$, $4 \to 23$, $5 \to 13$, and $6 \to 12$ to relate $\mathbf{c}_{ijkl}'$ *to* C_{pq}' ($i, j, k, l = 1, 2, 3$ and $p, q = 1, 2 \ldots . 6$). Thus, C_{55}' stands for c_{1313}, for example. Here σ_{ij}', e_{ij}' and u_i' are the components of stress, strain, and displacement, respectively, and ρ' is the material density. In equation (3), $\gamma_{ij}' = 2e_{ij}'$ (with $i \neq j$) defines the engineering shear strain components.

Since $\mathbf{c}_{ijkl}'$ is a fourth order tensor, then for any orthogonal transformation of the primed to the nonprimed coordinates, i.e., x_i' to x_i, it transforms according to

$$\mathbf{c}_{mnop} = \beta_{mi}\, \beta_{nj}\, \beta_{ok}\, \beta_{pl}\, \mathbf{c}_{ijkl}' \tag{4}$$

where β_{ij} is the cosine of the angle between x_i' and x_j, respectively. For a rotation of angle ϕ in the $x_1' - x_2'$ plane, the transformation tensor β_{ij} reduces to

$$\begin{bmatrix} \cos\phi & \sin\phi & 0 \\ -\sin\phi & \cos\phi & 0 \\ 0 & 0 & 1 \end{bmatrix} \tag{5}$$

Downloaded 03 May 2010 to 171.66.16.21. Redistribution subject to ASME license or copyright; see http://www.asme.org/terms/Terms_Use.cfm

which, if applied to equation (2) through the relation of equation (3), yields well known relations (see Love (1927))

$$\begin{bmatrix} \sigma_{11} \\ \sigma_{22} \\ \sigma_{33} \\ \sigma_{23} \\ \sigma_{13} \\ \sigma_{12} \end{bmatrix} = \begin{bmatrix} C_{11} & C_{12} & C_{13} & 0 & 0 & C_{16} \\ C_{12} & C_{22} & C_{23} & 0 & 0 & C_{26} \\ C_{13} & C_{23} & C_{33} & 0 & 0 & C_{36} \\ 0 & 0 & 0 & C_{44} & C_{45} & 0 \\ 0 & 0 & 0 & C_{45} & C_{55} & 0 \\ C_{16} & C_{26} & C_{36} & 0 & 0 & C_{66} \end{bmatrix} \begin{bmatrix} e_{11} \\ e_{22} \\ e_{33} \\ \gamma_{23} \\ \gamma_{13} \\ \gamma_{12} \end{bmatrix} \tag{6}$$

where the transformation relations between the C_{pq} and C'_{pq} can be extracted from Love (1927), for example. Notice that, no matter what rotational angle ϕ is used, the zero entries in equation (6) will remain zero. In fact, the matrix of equation (6), although particularized to orthotropic media, resembles that of monoclinic media (i.e., media which has only $x_3 = 0$ as a plane of symmetry). In terms of the rotated coordinate system x_k, we write the momentum equations as

$$\frac{\partial \sigma_{ij}}{\partial x_j} = \rho \frac{\partial^2 u_i}{\partial t^2}. \tag{7}$$

Analysis

Substituting from equation (6) into equation (7) results in a system of three coupled equations for the displacements u_1, u_2, and u_3. If we now identify the plane of incidence to be the $x_1 - x_3$, as in Fig. 1, a formal solution for the displacements u_i can be written as

$$(u_1, u_2, u_3) = (1, V, W) U e^{i\xi(x_1 + \alpha x_3 - ct)}, \tag{8}$$

where ξ is the wave number, c is the phase velocity ($= \omega/\xi$), ω is the circular frequency, α is still an unknown parameter, and V, W are ratios of the displacement amplitudes of u_2 and u_3 to u_1, respectively. Combinations of equations (8), (7), and (6) yield the matrix relation

$$\begin{bmatrix} C_{11} - \rho c^2 + C_{55}\alpha^2 & C_{16} + C_{45}\alpha^2 & (C_{13} + C_{55})\alpha \\ C_{16} + C_{45}\alpha^2 & C_{66} - \rho c^2 + C_{44}\alpha^2 & (C_{36} + C_{45})\alpha \\ (C_{13} + C_{55})\alpha & (C_{36} + C_{45})\alpha & C_{55} - \rho c^2 + C_{33}\alpha^2 \end{bmatrix} \begin{bmatrix} 1 \\ V \\ W \end{bmatrix} = \begin{bmatrix} 0 \\ 0 \\ 0 \end{bmatrix} \tag{9}$$

Nontrivial solutions for V and W demand the vanishing of the determinant in equation (9) and yield an algebraic equation relating α to c. This equation is reduced (see Appendix and Rokhlin et al. (1986) for an alternative procedure) to a sixth-degree polynomial equation in α, namely

$$\alpha^6 + A_1\alpha^4 + A_2\alpha^2 + A_3 = 0 \tag{10}$$

Equation (10) admits six solutions for α which, because of the absence of odd-power terms in equation (10), are related as follows

$$\alpha_2 = -\alpha_1, \ \alpha_4 = -\alpha_3, \ \alpha_6 = -\alpha_5 \tag{11}$$

Using superposition, together with equation (9), we can relate the displacement ratios V_q and W_q for each α_q as

$$V_q = \frac{F_{23}(F_{11} + C_{55}\alpha_q^2) - (F_{12} + C_{45}\alpha_q^2)F_{13}}{F_{13}(F_{22} + C_{44}\alpha_q^2) - (F_{12} + C_{45}\alpha_q^2)F_{23}} \tag{12}$$

$$W_q = \alpha_q \frac{F_{23}(F_{11} + C_{55}\alpha_q^2) - (F_{12} + C_{45}\alpha_q^2)F_{13}}{(F_{12} + C_{45}\alpha_q^2)(F_{33} + C_{33}\alpha_q^2) - F_{13}F_{23}\alpha_q^2}, \quad q = 1, 2 \ldots 6 \tag{13}$$

where F_{st}, $s, t = 1, 2, 3$ are defined in the Appendix. Combining equations (12) and (13) with the stress-strain relations, equation (6), we rewrite the formal solutions for the displacements and stresses as

$$(u_1, u_2, u_3) = \sum_{q=1}^{6} (1, V_q, W_q) U_q e^{i\xi(x_1 + \alpha_q x_3 - ct)} \tag{14}$$

$$(\sigma_{33}, \sigma_{13}, \sigma_{23}) = \sum_{q=1}^{6} i\xi (D_{1q}, D_{2q}, D_{3q}) U_q e^{i\xi(x_1 + \alpha_q x_3 - ct)} \tag{15}$$

where

$$D_{1q} = [C_{13} + C_{36}V_q + C_{33}\alpha_q W_q] \tag{16a}$$

$$D_{2q} = [C_{55}(\alpha_q + W_q) + C_{45}\alpha_q V_q] \tag{16b}$$

and

$$D_{3q} = [C_{45}(\alpha_q + W_q) + C_{44}\alpha_q V_q], \ q = 1, 2, \ldots, 6 \tag{16c}$$

With reference to equation (11) and by inspection of equations (12)–(16c), one deduces the relations

$$V_2 = V_1, \ V_4 = V_3, \ V_6 = V_5 \tag{17a}$$

$$W_2 = -W_1, \ W_4 = -W_3, \ W_6 = -W_5 \tag{17b}$$

$$D_{12} = D_{11}, \ D_{14} = D_{13}, \ D_{16} = D_{15} \tag{18a}$$

$$D_{22} = -D_{21}, \ D_{24} = -D_{23}, \ D_{26} = -D_{25} \tag{18b}$$

$$D_{32} = -D_{31}, \ D_{34} = -D_{33}, \ D_{36} = -D_{35} \tag{18c}$$

Derivation of the Reflection and Transmission Coefficients

To determine the reflection and transmission coefficients for plane waves incident from the fluid onto the plate surface at an angle θ we need to obtain general solutions for the upper and lower fluids similar to those of equations (14) and (15). Recognizing that the fluid does not support shear deformation, its field equations reduce to

$$\frac{\partial \sigma_{ij}^{(f)}}{\partial x_j} = \rho_f \frac{\partial u_i^{(f)}}{\partial t^2} \tag{19}$$

$$\sigma_{ij}^{(f)} = \lambda_f \frac{\partial u_k^{(f)}}{\partial x_k} \delta_{ij}, i, j = 1, 2, 3, \tag{20}$$

where both equations hold only for $i = j$; ρ_f and λ_f are the fluid density and Lamé constant. If the wave is assumed to be incident and, hence, reflected in the upper fluid and transmitted into the lower fluid, then using similar analysis to that of the plate yields, for the upper fluid,

$$(u_1, u_2, u_3, \sigma_{33})^{(u)} = \sum_{k=1}^{2} (1, 0, W_k^{(u)}, i\xi\rho_f c^2) U_k^{(u)} e^{i\xi[x_1 + (-1)^{k+1}\alpha_f x_3 - ct]} \tag{21}$$

and for the lower fluid

$$(u_1, u_2, u_3, \sigma_{33})^{(l)} = (1, 0, \alpha_f, i\xi\rho_f c^2) U^{(l)} e^{i\xi[x + \alpha_f (x_3 - d) - ct]}, \tag{22}$$

where

$$W_1^{(u)} = \alpha_f, \ W_2^{(u)} = -\alpha_f \tag{23a}$$

$$\alpha_f = \left[\frac{c^2}{c_f^2} - 1\right]^{1/2}, \ c_f = \left[\frac{\lambda_f}{\rho_f}\right]^{1/2} \tag{23b}$$

Notice the vanishing of shear component u_2 in both the upper and lower fluids.

By invoking the continuity of the normal displacements and stresses at $x_3 = 0$ and $x_3 = d$ and setting the solid shear stresses

Downloaded 03 May 2010 to 171.66.16.21. Redistribution subject to ASME license or copyright; see http://www.asme.org/terms/Terms_Use.cfm

σ_{13} and σ_{23} equal to zero at $x_3 = 0$ and $x_3 = d$ we obtain, for a given incident amplitude $U_1^{(u)}$, a system of eight linear simultaneous equations for the amplitudes $U_2^{(u)}$, $U^{(l)}$, U_1, U_2, U_3, U_4, U_5, and U_6 is obtained. Solving these equations with the help of the relations (17) and (18) and applying rather lengthy algebraic reductions and manipulations, we derive the following expressions for the reflection and the transmission coefficients

$$R = \frac{U_2^{(u)}}{U_1^{(u)}} = \frac{AS - Y^2}{(S+iY)(A-iY)} \tag{24}$$

$$T = \frac{U^{(l)}}{U_1^{(u)}} = \frac{iY(S+A)}{(S+iY)(A-iY)} \tag{25}$$

where

$$S = D_{11}G_1\cot(\gamma\alpha_1) - D_{13}G_3\cot(\gamma\alpha_3) + D_{15}G_5\cot(\gamma\alpha_5) \tag{26a}$$

$$A = D_{11}G_1\tan(\gamma\alpha_1) - D_{13}G_3\tan(\gamma\alpha_3) + D_{15}G_5\tan(\gamma\alpha_5) \tag{26b}$$

$$Y = \frac{\rho_f c^2}{\alpha_f}(W_1G_1 - W_3G_3 + W_5G_5) \tag{26c}$$

with

$$G_1 = D_{23}D_{35} - D_{33}D_{25} \tag{27a}$$

$$G_3 = D_{21}D_{35} - D_{31}D_{25} \tag{27b}$$

$$G_5 = D_{21}D_{33} - D_{31}D_{23} \tag{27c}$$

$$\gamma = \xi d/2 = \omega d/2c. \tag{27d}$$

Except for the more complicated definitions of the functions S, A, and Y, the expressions R and T resemble those reported in our earlier paper (Nayfeh and Chimenti, 1988), and our notation was chosen for consistency with this previous calculation.

The expressions of equations (24) and (25) for the reflection and the transmission coefficients contain, as a by-product, the characteristic equation for the propagation of modified (leaky) guided waves in the plate. We refer to such waves as plate waves (Nayfeh and Chimenti, 1988) rather than Lamb waves, whose properties were derived originally by Lamb (1917) for isotropic solids in the absence of the fluid. Setting either denominator equal to zero, namely

$$(S+iY)(A-iY) = 0 \tag{28}$$

defines the characteristic equations for such waves, where the vanishing of the first term corresponds to symmetric and the second to antisymmetric mode propagation. In the absence of the fluid, i.e., for ρ_f (or Y) $= 0$, equations (28) reduce to $SA = 0$ which is the characteristic equation for Lamb-like waves in the orthotropic plate.

For the special cases of propagation along axes of symmetry (in the present example $\phi = 0$ deg or 90 deg), the off-diagonal tensor components C_{16}, C_{26}, C_{36}, and C_{45} vanish in equation (6). The implication is that the displacements u_2, out of the $x_1 - x_3$ plane, go to zero, thereby confining all particle motion to the plane of incidence. This result is equivalent to the decoupling of the wave equations for vertical and horizontal shear motions in the plate, noted by us and other authors in treating anisotropic plates (Markus et al., 1985; Nayfeh and Chimenti, 1988). In addition, the secular equation (10) for the x_3-component of the wave vector factors and reduces to the lower dimensional result presented in our earlier analysis (Chimenti and Nayfeh, 1985; Nayfeh and Chimenti, 1988). In fact, for symmetry axis propagation we recover entirely our previous results for the reflection coefficient from the fluid-coupled composite plate.

Experimental Technique

Extensive experiments have been undertaken to test the validity of the theoretical results derived above. These measurements consist principally of ultrasonic reflection studies on a uniaxial graphite-epoxy composite plate. The geometry of the experiment is shown schematically in Fig. 2. Here, a wideband finite-beam transducer transmits ultrasound through the liquid-coupling medium, which in all cases consists of room temperature distilled water, to the plate completely immersed in the liquid. At those incident angles and frequencies where reflection minima occur (also corresponding generally to plate wave mode conversion), there will often be a characteristic displacement and distortion of the reflected field of the incident beam. This behavior is illustrated schematically in Fig. 2 with the shaded regions of the beam carrying most of the reflected energy away from the plate, accompanied by an exponentially decreasing trailing field to the right of the figure. The normal specular reflection is indicated in dashed lines. The transmitted field below the plate has been omitted for clarity.

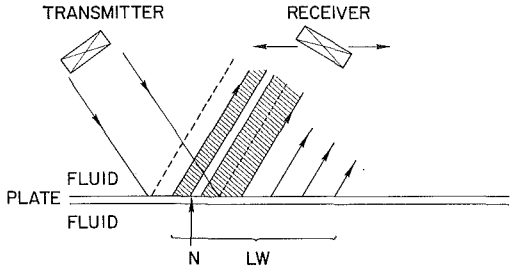

Fig. 2 Experimental geometry of ultrasonic reflection measurements in fibrous composite plates. Transmitter is fixed with respect to the sample, while receiver is scanned parallel to interface. Dashed lines show specular reflection. When plate wave is excited, reflected energy is redistributed as indicated. Null zone is denoted by *N*, and *LW* stands for leaky wave field. A similar radiation pattern exists below the plate.

Novel ultrasonic instrumentation is used to monitor the amplitude of the reflected field. The approach is to establish an incident angle with high resolution (0.001 deg), servo-driven optical rotators and position the nominally identical receiver along the x_1-axis to achieve the largest peak-to-valley ratio in the reflected field. Then, with the plate in the far field of both transducers, the frequency of a tone-burst excitation is stepped at 0.02 MHz intervals under computer control to acquire the data. Digitized at 13-bit resolution, the received signal is automatically stored in a computer file to await further processing. As in our earlier investigations, we have removed the transducer response from the signal before extracting the reflection minima. Additional details of the electronic instrumentation and data acquisition procedure can be found in our previous work (Chimenti and Nayfeh, 1985).

In these experiments we have studied a 0.92-mm plate of Ciba-Geigy 914 epoxy resin reinforced with Thornel T300 high modulus graphite fibers (composite elastic constants are collected in Table I).

Table I

Graphite-epoxy

$C'_{11} = 115.6$ GPa $C'_{22} = 11.5$ GPa

$C'_{33} = 15.95$ GPa $\rho = 1.6$ gm/cm^3

$C'_{13} = 3.72$ GPa $C'_{23} = 4.33$ GPa $C'_{44} = 5.81$ GPa $C'_{55} = 7.46$ GPa

Water

$$c_f = 1.48 \text{ Km/sec } \rho_f = 1 \text{ gm/cm}^3$$

The fiber volume fraction in this sample is 0.65 with a fiber diameter of about 5 μm. Therefore, all velocity dispersive effects can be attributed to the finite plate thickness and not to the fiber dimension, since frequencies employed in these experiments are typically between 1 and 12 MHz. The composite plate sample has been fabricated in a uniaxial lay-up with planar surfaces parallel to within 0.01 mm in the central region where measurements are performed. Rotation of the sample

Downloaded 03 May 2010 to 171.66.16.21. Redistribution subject to ASME license or copyright; see http://www.asme.org/terms/Terms_Use.cfm

about the x_3 axis is accomplished by a calibrated platform which permits an angular resolution in ϕ of 1 deg. Owing to the complexity of the reflection data for a general azimuthal angle ϕ, no attempt is made to interpret the data until all experimental results have been collected and analyzed.

Results and Discussion

In comparisons between the results of many measurements at several azimuthal angles and the model calculation, we have concentrated our attention, as in previous investigations (Chimenti and Nayfeh, 1985; Nayfeh and Chimenti, 1988), on the reflection coefficient. Since the basis of the experimental data is an amplitude signal in the reflected field of the incident beam, we calculate the plane-wave reflection coefficient for the plate and investigate it for the same type of behavior as we observe in the measurements. In addition to direct comparisons of amplitude spectra, we have also expressed our results as dispersion-like curves, where the results correspond to functions conditioned by the reflection coefficient. The theoretical dispersion curves are based on the occurrence of total transmission for given Fd and incident angle. Numerically, the curves are generated by searching equation (24) for the minima in the magnitude of the reflection coefficient which are accompanied by a rapid reversal in its phase. Both of these aspects of our studies are presented below.

A finite ultrasonic beam is composed of a range of plane wave components which define its angular spread,

$$\beta(x) = \int \hat{\beta}(\xi) \exp(-2\pi i \xi x) d\xi \qquad (29)$$

where $\beta(x)$ is the one-dimensional real space incident beam profile, x is a coordinate perpendicular to the beam direction, and the caret denotes Fourier transform. When such a finite beam interacts with a plate, each Fourier component of the incident field will contribute to the reflected field, weighted by the appropriate value of the reflection coefficient for that ξ. The resulting expression for the reflected field is given by

$$A(Fd, x_i) = \int \hat{\beta}(\xi) R(\xi, Fd) \exp[-2\pi i \xi (x_1 - \alpha_f x_3)] d\xi \qquad (30)$$

where $R(\xi, Fd)$ is the reflection coefficient from equation (24) for the composite plate. The expression of equation (30) evaluated over frequency is an approximation to the experimental spectrum of the plate, if the beam profile $\beta(x)$ is chosen to represent the incident beam. We have performed such calculations for a variety of our experimental conditions. Some typical comparisons are contained in Figs. 3(*a*)–(*d*).

Figure 3(*a*) shows the measured and predicted spectra from 1 to 8 MHz for an incident angle $\theta = 12$ deg and azimuthal angle $\phi = 30$ deg. The two curves have been vertically scaled, but in no other way adjusted. The solid curve is the expression of equation (30), and the dashed curve is the experimental data deconvolved to remove transducer response. Positions of the deep minima in the two curves are nearly coincident, as we have observed for propagation in the fiber direction (Nayfeh and Chimenti, 1988). We conjecture that the additional shallower sharp dips, some of which do not appear in the data, arise from the coupling between vertical and horizontal shear displacements, referred to in the Theory section, which occurs for propagation in a general azimuthal direction. At $\theta = 28$ deg and $\phi = 15$ deg in Fig. 3(*b*), similar results are found, where the general trend of the data is well reproduced by the model calculation. In particular, the two shallower minima between 2 and 4 MHz are given fairly accurately by the prediction. This structure disappears for $\phi = 0$ deg, leaving only the deep minima at 1.9, 4.3 MHz, and beyond. Holding the incident angle constant and incrementing ϕ to 30 deg, the structure of the curve has evolved in Fig. 3(*c*) with the two minima near 3 MHz approaching each other more closely and deepening considerably. These features are also seen in the model calculations. In the final frame, Fig. 3(*d*), results are given for $\theta = 24$ deg and $\phi = 90$ deg. This case corresponds to symmetry axis propagation and, therefore, the complex structure of the previous examples is largely absent. The positions of the minima are well modeled by the theory, whereas the minor differences in the line shape details may be attributed to transducer wavefront distortion, sound absorption, or nonideal mechanical behavior of the composite, none of which is considered in the model.

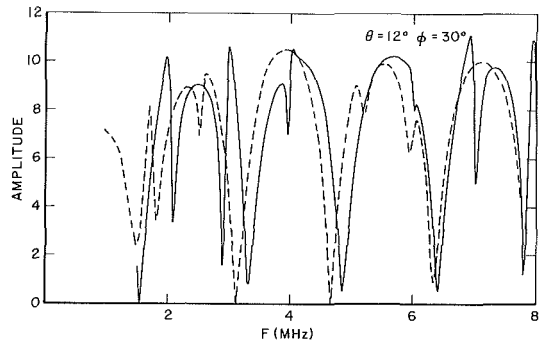

Fig. 3(*a*) Reflection (plate-wave) spectrum for $\theta = 12°$ and $\phi = 30°$. Theory is solid curve and experiment is dashed curve. Data have been deconvolved to remove transducer response.

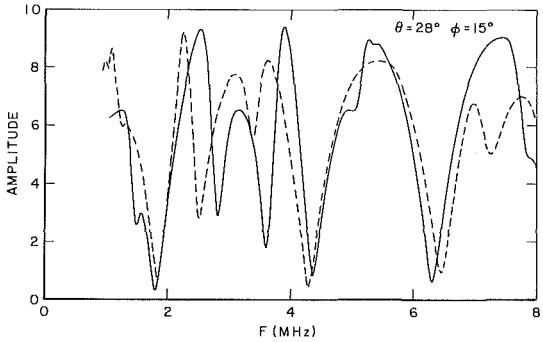

Fig. 3(*b*) Reflection spectrum for $\theta = 28°$ and $\phi = 15°$

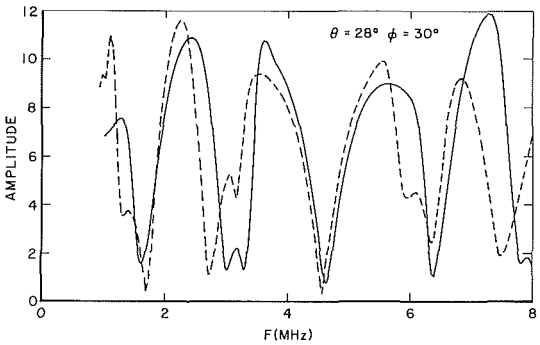

Fig. 3(*c*) Reflection spectrum for $\theta = 28°$ and $\phi = 30°$

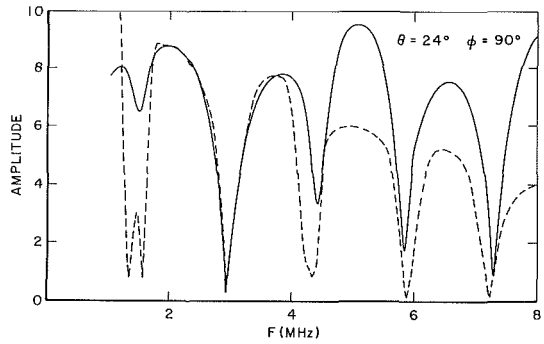

Fig. 3(*d*) Reflection spectrum for $\theta = 24°$ and $\phi = 90°$

Downloaded 03 May 2010 to 171.66.16.21. Redistribution subject to ASME license or copyright; see http://www.asme.org/terms/Terms_Use.cfm

Taking the results of many dozens of experimental spectra such as those shown in Fig. 3 and recording the minima as a function of the incident angle (expressed through Snell's law as a phase velocity), yields a dispersion-like plot of the ultrasonic reflection behavior. In previous work (Nayfeh and Chimenti, 1988; Chimenti and Nayfeh, 1986) we demonstrated that the hypothesis of Cremer (1942) concerning the coincidence of reflection minima with the excitation of Lamb wave modes is not well satisfied in all regions of plate wave dispersion in graphite-epoxy composites. Therefore, although we present these data in the manner of a velocity dispersion curve, it must be stressed that it is the reflection properties which are being reported.

Figure 4(*a*) shows data acquired in the current study at an azimuthal angle $\phi = 0$ deg plotted together with the results of the analytical prediction derived by examining the behavior of the reflection coefficient, equation (24). To obtain the theoretical curves rapid phase variations in the reflection coefficient, generally indicative of total transmission, have been recorded as a function of Fd for many values of phase velocity. These calculations are presented as solid curves. In Fig. 4(*a*) the data, plotted as open circles, are in good agreement with the prediction of our new, more general model. All features of the data from $\theta = 12$ deg to $\theta = 40$ deg are well explained in the model. Propagation in the other material symmetry direction $\phi = 90$ deg is shown in Fig. 4(*b*). Here the results reflect the substantial effective softening of the composite as the fiber axis is rotated out of the plane of incidence. Therefore, we observe a marked reduction in the phase velocities at which certain features occur. The vertical intercept of the curve, which is similar to the S_0 mode, is seen to be near $c_p = 2.2$ km/sec. Likewise, the point of diminishing slope of some of the higher order curves is much lower here than for $\phi = 0$ deg in Fig. 4(*a*). In fact, the phase velocity axis intercept is not even visible in Fig. 4(*a*) because it occurs above $c_p = 9.8$ km/sec.

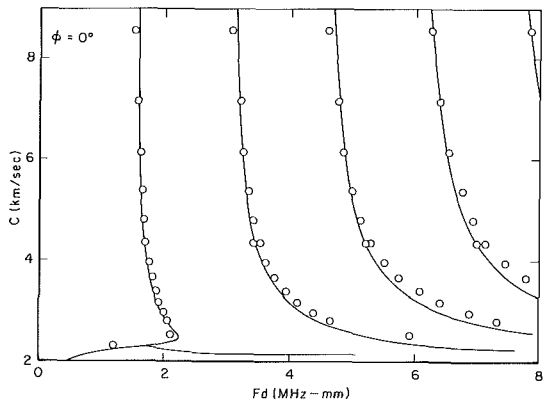

Fig. 4(*a*) Reflection results expressed as phase velocity dispersion curves for $\phi = 0°$. Data are plotted as discrete circles; theory presented by solid curves are small filled circles.

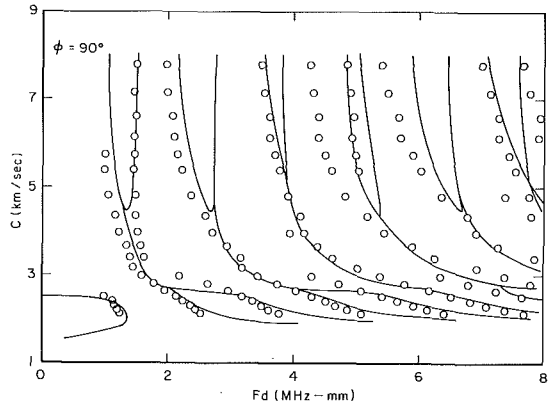

Fig. 4(*b*) Dispersion plot for $\phi = 90°$. Data are circles; solid curves are theoretical.

For a transversely isotropic material, setting $\phi = 90$ deg implies that elastic behavior in the plane of the incidence ($x_2' - x_3'$ plane) will be isotropic. An important experimental finding of the present study is the suggestion that transverse isotropy is not an appropriate symmetry class for the eight-ply Thornel/Ciba-Geigy composite sample we studied. Our result on the inequality of C_{22}' and C_{33}' stands in contrast to previous investigations, both mechanical (Knight, 1982) and ultrasonic (Prosser, 1987), on thick-section T300-5208 unidirectional composite. In these earlier studies the ratio C_{22}'/C_{33}' was measured to be within 2 percent of unity. Because of the method of fabrication of these materials in which compressive stresses are exerted on the surfaces of the curing composite, fibers might tend to be distributed nonuniformly in the plate. That is, the number of fibers per unit length in the x_3' direction could be higher than the same quantity in the x_2' direction (refer to equations (1)–(3)). Our experimental data for $\phi = 90$ deg are consistent with the above interpretation and draw us to the conclusion that orthotropy is the correct symmetry class for thin sections of this material. Since the elastic constant denoted C_{22}' in equation (3) is difficult to measure independently, we have inferred this quantity from our reflection data and the model calculation. The results of this evaluation yield a ratio of C_{22}' to C_{33}' of 0.72. Once this adjustment in C_{22}' is made, all subsequent comparisons at intermediate values of ϕ are carried out using this same constant. Here we note that C_{22}' does not influence the propagation behavior along $\phi = 0$ deg, and hence this issue was not encountered in our previous work (Nayfeh and Chimenti, 1988). A set of slowness curves with the elastic constants of Table I for orthotropic graphite epoxy at $\phi = 90$ deg is shown in Fig. 5. This representation illustrates the degree of anisotropy in the $x_2' - x_3'$ plane. It may be noted that while the quasi-longitudinal and slow quasi-transverse wavespeeds vary with propagation direction in this plane, the fast transverse velocity surface is still isotropic. Of course, if the composite were transversely isotropic, all three slowness curves would be circles with the two transverse waves coincident.

If we now depart from the principal axis directions, the reflection behavior becomes substantially more complicated, as can be seen in Fig. 6(*a*) for $\phi = 30$ deg. The simple structure

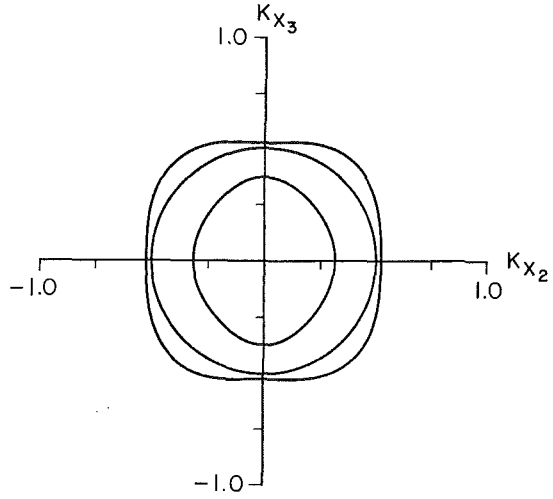

Fig. 5 Slowness curves with the elastic constants of Table I for $\phi = 90°$. Anisotropy in this plane is due to orthotropic nature of plate studied. Fast quasi-transverse wave is still seen to be isotropic.

Downloaded 03 May 2010 to 171.66.16.21. Redistribution subject to ASME license or copyright; see http://www.asme.org/terms/Terms_Use.cfm

of Fig. 4(*a*) is replaced by curves which split apart, rejoin, and cross over each other. Throughout the range of the measurements, relatively good agreement with the theory is apparent. Although interpretation of these results is delicate, we may note a few arguably consistent trends. As the fiber direction is rotated out of the plane of incidence, the effective material constants begin to soften, causing the phase velocity intercept of the S_0-like curve to decrease, as in Fig. 4(*b*). In Fig. 6(*a*) that velocity is about 8.5 km/sec, whereas the value is 9.8 km/sec for propagation along the fibers. Moreover, an additional set of curves seems to have nucleated, in agreement with our calculations and data starting as low as $\phi = 15$ deg. These general features will be seen to persist in the results for higher values of ϕ as well.

Comparison of measurement and theory for $\phi = 45$ deg is contained in Fig. 6(*b*). As expected, the intercept velocity has decreased to about 7 km/sec, and behavior of even higher complexity has appeared above this value. The series continues with $\phi = 60$ deg in Fig. 6(*c*), where the overall pattern established earlier is evident here also. Finally, in Fig. 6(*d*) for $\phi = 75$ deg we have the last of the comparisons. The intercept velocity here is near 3.4 km/sec, nearly a factor of three below its $\phi = 0$ deg value. These curves contain an extremely rich variety of reflection phenomena, considering the relatively simple form of the $\phi = 0$ deg curves in Fig. 4(*a*). As we have stated earlier, it is our conjecture that these additional features arise from the coupling of the vertically and horizontally polarized waves, which are independent for propagation along principal axes. We note in closing this section that in all these comparisons, but especially Figs. 6(*c*) and 6(*d*), agreement between measurements and theory is not simply a matter of general trends. Good detailed agreement is seen over most of these plots, in spite of the complex behavior observed for a general azimuthal angle. This observation lends confidence in the validity of the theoretical approach.

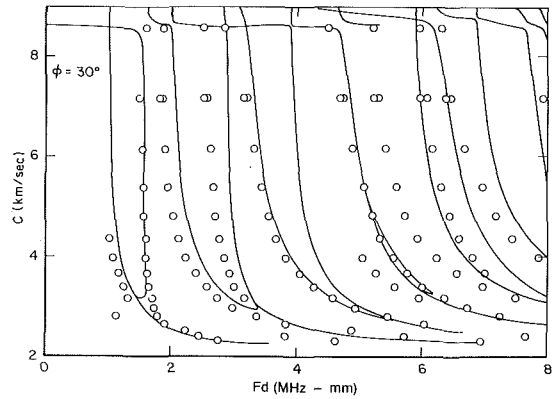

Fig. 6(*a*) Dispersion plot for $\phi = 30°$

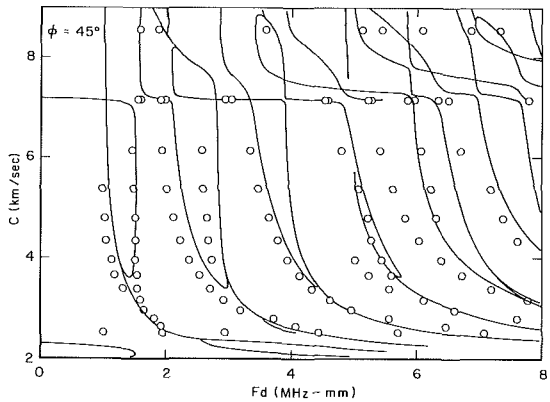

Fig. 6(*b*) Dispersion plot for $\phi = 45°$

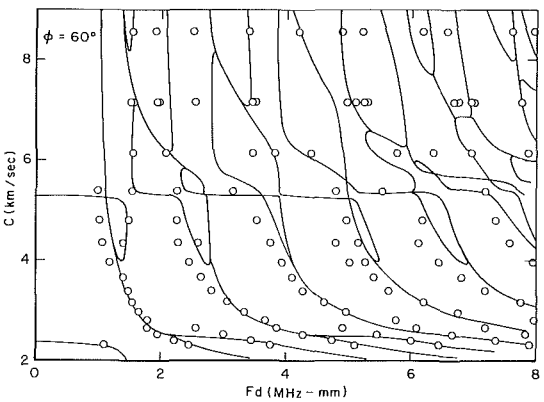

Fig. 6(*c*) Dispersion plot for $\phi = 60°$

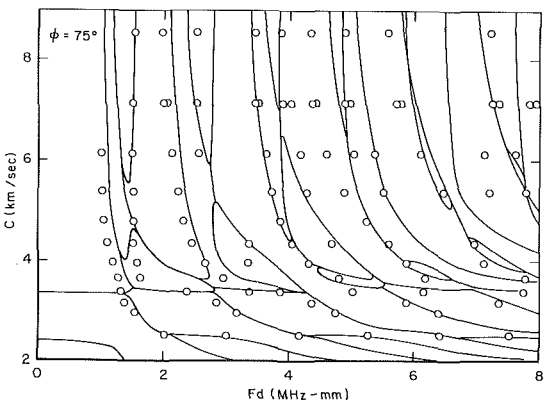

Fig. 6(*d*) Dispersion plot for $\phi = 75°$

Summary and Conclusions

In this paper we have reported theoretical and experimental studies of the interaction of ultrasonic waves with generally oriented orthotropic elastic plates immersed in liquid. The theoretical analysis is based on an exact two-dimensional wave-mechanics calculation of the amplitude of the reflected and transmitted partial waves. The plane of incidence of the acoustic wave makes an arbitrary angle with respect to material symmetry axes, resulting in coupling of the equations describing the motion of the vertically and horizontally polarized waves in the plates. Highly complex reflection behavior, expressed in velocity dispersion, is observed in the model prediction. Comparisons have been made to extensive experimental data collected in ultrasonic reflection measurements on a plate of T300/Ciba-Geigy 914 composite, selected as a model system to test the theory. Good agreement is seen in curves at several azimuthal angles between 0 deg and 90 deg, despite the complicated behavior of the propagation. It has been found experimentally that transverse isotropy is not an appropriate symmetry class for a thin section T300/914 composite plate and that orthotropic symmetry is consistent with all experimental data presented here.

Acknowledgment

This work is supported by AFOSR. The authors are pleased to acknowledge the competent computer programming assistance of T. W. Taylor and C. J. Fieldler.

References

Abubakar, I., 1962, "Free Vibrations of a Transversely Isotropic Plate," *Quarterly Journal of Mechanics and Applied Mathematics*, Vol. 15, pp. 129–136.

Baylis, E. .R., and Green, W. A., 1986, "Flexural Waves in Fiber Reinforced

Downloaded 03 May 2010 to 171.66.16.21. Redistribution subject to ASME license or copyright; see http://www.asme.org/terms/Terms_Use.cfm

Laminated Plates," *Journal of Sound and Vibration*, Vol. 110, pp. 1-26.

Brekhovskikh, L. M., 1960, *Waves in Layered Media*, Academic Press, New York.

Buchwald, V. T., 1961, "Rayleigh Waves in Anisotropic Media," *Quarterly Journal of Mechanics and Applied Mathematics*, Vol. 14, pp. 461-469.

Buchwald, V. T., and Davis, A., 1961, "Surface Waves in Anisotropic Elastic Media," *Nature* (London), Vol. 191, pp. 899-900.

Buchwald, V. T., and Davis, A., 1963, "Surface Waves in Elastic Media with Cubic Symmetry," *Quarterly Journal of Mechanics and Applied Mathematics*, Vol. 16, pp. 283-294.

Chadwick, P., and Currie, P. K., 1974, "Stoneley Waves at an Interface between Elastic Crystals," *Quarterly Journal of Mechanics and Applied Mathematics*, Vol. 27, pp. 497-503.

Chimenti, D. E., and Nayfeh, A. H., 1985, "Leaky Lamb Waves in Fibrous Composite Laminates," *Journal of Applied Physics*, Vol. 33, p. 4531-4538.

Chimenti, D. E., and Nayfeh, A. H., 1986, "Anomalous Ultrasonic Dispersion in Fluid-Coupled, Fibrous Composite Plates," *Applied Physics Letters*, Vol. 49, p. 492-493.

Cremer, L., 1942, "Theory of Sound Damming by Thin Walls," *Akust. Z.*, Vol. 7, pp. 81-104.

Fedorov, F. I., 1968, *Theory of Elastic Waves in Crystals*, Plenum, New York.

Gates, E., 1965, "Propagation and Oblique Reflection of Slant-Mode Hypersonic Waves in Quartz," *Applied Physics Letters*, Vol. 7, pp. 187-189.

Gazis, D. C., Herman, R., and Wallis, R. F., 1960, "Surface Elastic Waves in Cubic Crystals," *Physical Review*, Vol. 119, pp. 533-544.

Henneke, II, E. G., 1972, "Reflection-Refraction of a Stress Wave at a Plane Bounary between Anisotropic Media," *Journal of the Acoustical Society of America*, Vol. 51, pp. 210-217.

Joel, N., 1961, "Reflection and Polarization of Elastic Waves in a LiF Crystal: Mode Conversion from Longitudinal to Transverse," *Proc. Physics Society, Section A*, Vol. 78, pp. 38-45.

Johnson, W. W., 1970, "The Propagation of Stoneley and Rayleigh Waves in Anisotropic Elastic Media," *Bulletin of the Seismological Society of America*, Vol. 60, pp. 1105-1121.

Knight, M., 1982, "Three-Dimensional Elastic Moduli of Graphite/Epoxy Composites," *Journal of Composite Materials*, Vol. 16, pp. 153-159.

Kosevich, Yu. A., and Syrkin, E. S., 1985, "Elastic Waves in Plates of Highly Anisotropic Crystals," *Soviet Physics Acoustics*, Vol. 31, pp. 365-367.

Lamb, H., 1917, "Waves in an Elastic Plate," *Proc. Royal Society* (*London*), *Ser. A*, Vol. 93, pp. 114-128.

Lim, T. C., and Musgrave, M. J. P., 1970, "Stoneley Waves in Anisotropic Media," *Nature*, Vol. 225, p. 372.

Lim, T. C., and Farnell, G. W., 1969, "Character of Pseudo Surface Waves on Anisotropic Crystals," *Journal of the Acoustical Society of America*, Vol. 45, pp. 845-851.

Love, A. E. H., 1927, *A Treatise on the Mathematical Theory of Elasticity*, 4th ed., Dover, New York.

Markus, S. A., Kaplan, M. D., and Veremeenko, S. V., 1985, "Propagation of Normal Waves in Orthotropic Plates," *Soviet Journal of Nondestructive Testing*, Vol. 21, p. 739.

Merkulov, L. G., 1963, "Ultrasonic Waves in Crystals," *Applied Material Res.*, Vol. 2, pp. 231-240.

Merkulov, L. G., and Yakovlev, L. A., 1962, "Propagaton and Reflection of Ultrasonic Beams in Crystals," *Soviet Physics Acoustics*, Vol. 8, pp. 72-77.

Merkulov, L. G., and Tursonov, D. A., 1969, "Normal Mode Phase Velocities in a Plate of a Cubic Crystal," *Soviet Physics Acoustics*, Vol. 15, pp. 115-117.

Moon, F. C., 1972, "Wave Surfaces Due to Impact on Anisotropic Plates," *Journal of Composite Materials*, Vol. 6, pp. 62-79.

Musgrave, M. J. P., 1970, *Crystal Acoustics*, Holden Day, San Francisco.

Musgrave, M. J. P., 1960, "Reflection and Refraction of Plane Elastic Waves at a Plane Boundary of Aelotropic Media," *Geophysics*, Vol. 3, pp. 406-418.

Nayfeh, A. H., and Chimenti, D. E., 1988, "Propagation of Guided Waves in Fluid-Coupled Plates of Fiber-Reinforced Composites," *Journal of the Acoustical Society of America*, Vol. 83, p. 1736.

Nikiforenko, Zh. G., Bobrov, V. T., and Averbukh, I. I., 1972, "Propagation of Lamb Waves in Anisotropic Sheets," *Soviet Journal of Nondestructive Testing*, Vol. 8, p. 543.

Prosser, W., 1987, M. S. Thesis, Johns Hopkins University.

Rokhlin, S. I., Bolland, T. K., and Adler, L., 1986, "Reflection and Refraction of Elastic Waves on a Plane Interface between Two Generally Anisotropic Media," *Journal of the Acoustical Society of America*, Vol. 79, pp. 906-918.

Rollins, F. R., Lim, T. C., and Farnell, G. W., 1968, "Ultrasonic Reflectivity and Surface Wave Phenomena on Surfaces of Copper Crystals," *Applied Physics Letters*, Vol. 12, pp. 236-238.

Rose, W. R., Rokhlin, S. I., and Adler, L., 1987, "Evaluation of Anisotropic Properties of Graphite-epoxy Composites Using Lamb Waves," *Review of Progress in Quantitative Nondestructive Evaluation*, Vol. 6, D. O. Thompson and D. E. Chimenti, eds., Plenum, New York, pp. 1111-1118.

Solie, L. P., and Auld, B. A., 1973, "Elastic Waves in Free Anisotropic Plates," *Journal of the Acoustical Society of America*, Vol. 54, pp. 50-65.

Stoneley, R., 1955, "The Propagaton of Surface Elastic Waves in a Cubic Crystal," *Proc. Royal Society of Acoustics*, Vol. 232, pp. 447-458.

Synge, J. L., 1957, "Elastic Waves in Anisotropic Media," *Journal of Mathematical Physics*, Vol. 25, pp. 323-334.

Thompson, R. B., Lee, S. C., and Smith, J. F., 1987, "Relative Anisotropes of Plane Waves and Guided Modes in Thin Orthorhombic Plates: Implication for Texture Characterization," *Ultrasonics*, Vol. 25, pp. 133-137.

Viktorov, I. A., 1967, *Rayleigh and Lamb Waves*, Plenum, New York.

APPENDIX

Expanding the determinant relation (9) and collecting powers of α we have

$$\alpha^6 + A_1\alpha^4 + A_2\alpha^2 + A_3 = 0$$

where:

$$A_1 = (P_1F_{11} + P_2C_{55} - P_4F_{12} - P_5C_{45} + P_7F_{13})/\Delta$$

$$A_2 = (P_2F_{11} + P_3C_{55} - P_5F_{12} - P_6C_{45} + P_8F_{13})/\Delta$$

$$A_3 = (P_3F_{11} - P_6F_{12})/\Delta$$

$$\Delta = P_1C_{55} - P_4C_{45}$$

$$P_1 = C_{44}C_{33};\ P_3 = F_{22}F_{33}$$

$$P_2 = F_{22}C_{33} + F_{33}C_{44} - F_{23}{}^2$$

$$P_4 = C_{33}C_{45},\ P_6 = F_{12}F_{33}$$

$$P_5 = C_{33}F_{12} + F_{33}C_{45} - F_{13}F_{23}$$

$$P_7 = F_{23}C_{45} - F_{13}C_{44};\ P_8 = F_{12}F_{23} - F_{13}F_{22}$$

$$F_{11} = C_{11} - \rho c^2$$

$$F_{12} = C_{16}$$

$$F_{13} = C_{13} + C_{55}$$

$$F_{22} = C_{66} - \rho c^2$$

$$F_{23} = C_{36} + C_{45}$$

$$F_{33} = C_{55} - \rho c^2$$

Downloaded 03 May 2010 to 171.66.16.21. Redistribution subject to ASME license or copyright; see http://www.asme.org/terms/Terms_Use.cfm

R. Paskaramoorthy

Department of Civil Engineering,
University of Manitoba,
Winnipeg, Canada R3T 2N2

S. K. Datta

Department of Mechanical Engineering and
CIRES,
University of Colorado,
Boulder, CO 80309-0427
Fellow, ASME

A. H. Shah

Department of Civil Engineering,
University of Manitoba,
Winnipeg, Canada R3T 2N2

Effect of Interface Layers on Scattering of Elastic Waves

Scattering of elastic waves by spheroidal elastic inclusions has been studied in this paper. Particular attention has been focused on the effect of interface layers between the inclusions and the matrix on the scattering cross-sections. It has been assumed that properties of each layer is constant through its thickness. For spheroidal inclusion this problem cannot be solved by exact means. We have used a hybrid finite element and wave function expansion technique to analyze the problem. It is shown that solutions thus obtained for spherical inclusions and cavities agree well with analytical solutions. For spheroidal inclusions we show that when the interface layer properties are intermediate between those of the particles and the matrix the scattering cross-section increases. These results can be useful in characterizing interface layer properties.

Introduction

The scattering of elastic waves by obstacles in an infinite elastic medium has been a topic of interest to many researchers mainly because of its practical importance in dynamic soil-structure interaction, nondestructive evaluation, etc. When the solid inclusion is three-dimensional, analytical solutions are available only for simple shapes such as sphere (Pao and Mow, 1973). For most of the complicated geometries encountered in practice, closed-form solutions are not feasible and, therefore, it is necessary to resort to numerical methods. A numerical technique worthy of mention is the T-matrix approach (Varatharajulu and Pao, 1976; Waterman, 1976; Varadan and Varadan, 1979; Tsao et al., 1982) which is based on the integral equation formulation. Application of this method to spheroidal inclusions and voids is reported by Varadan and Varadan (1979) and Tsao et al. (1982). In all these works it is assumed that the material properties jump from those of the inclusions to those of the matrix across the interface.

Recently, a numerical technique combining an analytical procedure with the finite element method has been proposed to study the diffraction of elastic waves in two dimensions by cracks and cavities located in infinite or semi-infinite media (Shah et al., 1982; Datta et al., 1982; Datta and Shah, 1982; Abduljabbar et al., 1983; Shah et al., 1983; Shah et al., 1985; Shah et al., 1987).

This paper is the natural extension of these works to a three-dimensional problem. In this study, the scattering of elastic waves by an axisymmetric scatterer embedded in isotropic elastic medium is considered. Though the scatterer may be a general axisymmetric solid or cavity, we consider either a prolate spheroid or an oblate spheroid for the purpose of illustration. The geometry is depicted in Fig. 1 where z-axis is the symmetry axis; $2a$ and $2b$ are diameters of the inclusion along the x and z axes, respectively. The spheroid, which is prolate for $b/a > 1$ and oblate for $b/a < 1$, is excited by time harmonic plane P or SV waves that are incident obliquely to the axis of symmetry. Without loss of generality, the plane of propagation may be taken as the xz-plane.

The strategy to solve the problem is to draw a ficticious spherical boundary B enclosing the scatterer. The region interior to this boundary which consists of the scatterer and a finite region of the host medium is modeled through an assemblage of finite elements. The solution in the exterior region is represented by spherical wave functions. Continuity

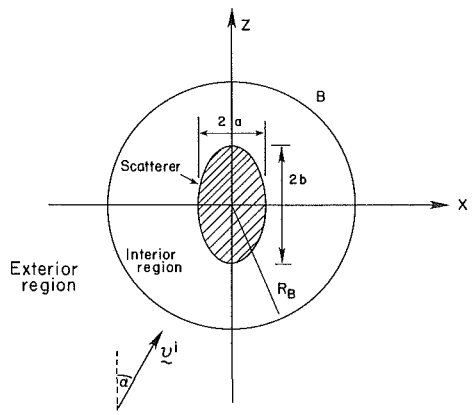

Fig. 1 Geometry of the spheroidal inclusion showing the enclosing circle of radius R_B

Contributed by the Applied Mechanics Division of THE AMERICAN SOCIETY OF MECHANICAL ENGINEERS for presentation at the Joint ASCE/ASME Applied Mechanics, Biomechanics, and Fluids Engineering Conference, La Jolla, CA, July 9–12, 1989.

Discussion on this paper should be addressed to the Editorial Department, ASME, United Engineering Center, 345 East 47th Street, New York, N.Y. 10017, and will be accepted until two months after final publication of the paper itself in the JOURNAL OF APPLIED MECHANICS. Manuscript received by ASME Applied Mechanics Division, May 27, 1987; final revision, May 20, 1988.

Paper No. 89-APM-10.

Copyright © 1988 by ASME

Downloaded 03 May 2010 to 171.66.16.21. Redistribution subject to ASME license or copyright; see http://www.asme.org/terms/Terms_Use.cfm

of displacements and tractions between the interior and exterior regions are imposed on the boundary B. The model then yields the displacements for nodes lying on the boundary, which in turn yields both the displacements of the interior nodes and the unknown coefficients associated with the spherical wave functions. Mention is made of a similar study by Goestschel et al. (1982) in which finite elements and spherical wave functions were used in a similar manner. They imposed traction continuity along the boundary first-and-then displacement continuity on the basis of least-square error minimization. They presented results only for the axisymmetric problem of plane P waves propagating along the z-axis. This is the simplest case of the more general problem studied in this paper. It should be noted that in this study traction and displacement continuity has been enforced along the boundary B at the nodes on B. The results obtained are in good agreement with the analytical solutions.

Finite Element Formulation of the Interior Region

The finite element formulation of the interior region is that of an axisymmetric structure subjected to arbitrary loading. This is done by an established procedure (Cook, 1981; Zienkiewicz, 1977) in finite element analysis and only details relevant to the problem at hand will be presented here.

To analyze problems with axisymmetric geometries, the force and displacement components are expressed in Fourier series in the azimuthal direction. For example, the expressions for displacement components in cylindrical coordinate system (Fig. 2(a)) are

$$U_r = \sum_{m=0}^{\alpha} \{\bar{U}_{rm}(r,z)\cos m\phi + \bar{\bar{U}}_{rm}(r,z)\sin m\phi\} \tag{1a}$$

$$U_z = \sum_{m=0}^{\alpha} \{\bar{U}_{zm}(r,z)\cos m\phi + \bar{\bar{U}}_{zm}(r,z)\sin m\phi\} \tag{1b}$$

$$U_\phi = \sum_{m=0}^{\alpha} \{-\bar{U}_{\phi m}(r,z)\sin m\phi + \bar{\bar{U}}_{\phi m}(r,z)\cos m\phi\} \tag{1c}$$

where the single overbar denotes the amplitudes of the displacement components symetric about the $\phi = 0$ axis and the double overbars denote the antisymmetric parts. m represents the azimuthal harmonic number. The negative sign before $\bar{U}_{\phi m}$ yields identical stiffness matrix for both symmetric and antisymmetric components. The steady-state time variation e^{-iwt}, which is assumed throughout the paper, will be suppressed for notational convenience.

The excitation is due to the incident P or SV waves which propagate in the xz-plane making an angle α with the z-axis as shown in Fig. 1. Owing to the nature of the excitation of these waves, we need to consider only the symmetric component of the displacements. Also, there is no coupling between any two harmonics because of the linearity of the problem. We can, therefore, consider each harmonic as a separate problem and superimpose the results. The amplitude of displacements within an element "e" for harmonic m is interpolated from the nodal amplitude as

$$\{\bar{\mathbf{U}}_m^e\} = [N^e(r,z)]\{\bar{\mathbf{q}}_m^e\} \tag{2}$$

where $[N^e(r,z)]$ contains the interpolation functions (Cook, 1981; Zienkiewicz, 1977), $\{\bar{\mathbf{q}}_m^e\}$ is the vector of nodal amplitudes for element e. The governing equations of motions are obtained by minimizing the functional

$$F = \frac{1}{2}\int_v (\boldsymbol{\sigma}\cdot\boldsymbol{\epsilon}^* - \rho w^2 \mathbf{u}\cdot\mathbf{u}^*) r dr d\phi dz - \frac{1}{2}\int_B (\mathbf{P}_B\cdot\mathbf{U}_B^* + \mathbf{P}_B^*\cdot\mathbf{U}_B) ds \tag{3}$$

where (*) indicates complex conjugate and σ and ϵ are the stress and strain vectors, respectively; $\mathbf{P}_B$ and $\mathbf{U}_B$ are, respectively, the traction and displacement vectors on the boundary B.

The strains and stresses are derived for the displacement field given by equation (2) and substituted in equation (3) which, upon minimization, yields

$$[\mathbf{S}_m(w)]\{\bar{\mathbf{q}}_m(w)\} = \{\bar{\mathbf{P}}_m(w)\} \tag{4}$$

where $[\mathbf{S}_m(w)]$ is the modified system stiffness matrix defined by

$$[\mathbf{S}_m(w)] = [\mathbf{K}] - w^2[\mathbf{M}] \tag{5}$$

in which $[\mathbf{K}]$ and $[\mathbf{M}]$ are, respectively, the global stiffness and mass matrices of the interior region, $\{\bar{\mathbf{q}}_m\}$ is the vector of nodal amplitudes, and $\{\bar{\mathbf{P}}_m\}$ is the vector of amplitudes of nodal loads which have nonzero components corresponding to the interface degrees-of-freedom only. The subscript represents the harmonic number which is dropped in the sequel with the understanding that the problem is solved for each harmonic and the results are superposed later.

If the vector $\{\bar{\mathbf{q}}\}$ of nodal displacements is separated into two parts: $\{\bar{\mathbf{q}}_B\}$ corresponding to nodal displacements at the boundary B and $\{\bar{\mathbf{q}}_I\}$ corresponding to nodal displacements elsewhere in the interior region, equation (4) can be written as

$$\begin{bmatrix} \mathbf{S}_{II} & \mathbf{S}_{IB} \\ \mathbf{S}_{BI} & \mathbf{S}_{BB} \end{bmatrix} \begin{Bmatrix} \bar{\mathbf{q}}_I \\ \bar{\mathbf{q}}_B \end{Bmatrix} = \begin{Bmatrix} \mathbf{o} \\ \bar{\mathbf{P}}_B \end{Bmatrix} \tag{6}$$

in which $\{\bar{\mathbf{P}}_B\}$ represents amplitude of interaction forces between the interior and exterior regions and is given by

$$\{\bar{\mathbf{P}}_B\} = \{\bar{\mathbf{P}}_B^{(i)}\} + \{\bar{\mathbf{P}}_B^{(s)}\} \tag{7}$$

where $\{\bar{\mathbf{P}}_B^{(i)}\}$ and $\{\bar{\mathbf{P}}_B^{(s)}\}$ are vector amplitudes of interaction forces due to the incident and scattered waves, respectively.

Similarly, the vector $\{\bar{\mathbf{q}}_B\}$ of nodal amplitudes of displacements can be written as

$$\{\bar{\mathbf{q}}_B\} = \{\bar{\mathbf{q}}_B^{(i)}\} + \{\bar{\mathbf{q}}_B^{(s)}\} \tag{8}$$

where the superscripts (i) and (s) stand for incident and scattered fields, respectively.

It will be shown later that the vectors $\{\bar{\mathbf{P}}_B^s\}$ and $\{\bar{\mathbf{q}}_B^s\}$ are related through

$$\{\bar{\mathbf{P}}_B^{(s)}\} = [\mathbf{S}_f]\{\bar{\mathbf{q}}_B^{(s)}\} \tag{9}$$

where the impedance matrix $[\mathbf{S}_f]$ is complex-valued and depends on the frequency and the radius of the boundary B.

Substituting equations (7), (8), and (9) into (6), we get

$$\begin{bmatrix} \mathbf{S}_{II} & \mathbf{S}_{IB} \\ \mathbf{S}_{BI} & \mathbf{S}_{BB} - \mathbf{S}_f \end{bmatrix} \begin{Bmatrix} \bar{\mathbf{q}}_I \\ \bar{\mathbf{q}}_B \end{Bmatrix} = \begin{Bmatrix} \mathbf{o} \\ \bar{\mathbf{P}}_B^{(i)} - \mathbf{S}_f\{\bar{\mathbf{q}}_B^{(i)}\} \end{Bmatrix} \tag{10}$$

The equation (10) can now be solved for the unknown vectors $\{\bar{\mathbf{q}}_I\}$ and $\{\bar{\mathbf{q}}_B\}$ through conventional methods. Note that the solution process should be in complex mode since the impedance matrix $\mathbf{S}_f$ has complex valued coefficients. Moreover, the number of nodes N_B on the boundary B is significantly smaller than the number of nodes elsewhere in the interior region. Hence, a substantial reduction in computer time and storage can be achieved by assigning complex storage only to the submatrix $\mathbf{S}_{BB} - \mathbf{S}_f$ and condensing $\{\bar{\mathbf{q}}_I\}$ out from equation (10) resulting in

$$[\mathbf{S}_{BB} - \mathbf{S}_{BI}\mathbf{S}_{II}^{-1}\mathbf{S}_{IB} - \mathbf{S}_f]\{\bar{\mathbf{q}}_B\} = \{\bar{\mathbf{P}}_B^{(i)}\} - \mathbf{S}_f\{\bar{\mathbf{q}}_B^{(i)}\} \tag{11}$$

which is solved for $\{\bar{\mathbf{q}}_B\}$ in complex mode. Note that all the operations involved in obtaining $\mathbf{S}_{BB} - \mathbf{S}_{BI}\mathbf{S}_{II}^{-1}\mathbf{S}_{IB}$ can be carried out in real mode and the rest in complex mode.

The vector $\{\bar{\mathbf{q}}_I\}$ can be obtained from

$$\{\bar{\mathbf{q}}_I\} = -[\mathbf{S}_{II}]^{-1}[\mathbf{S}_{IB}]\{\bar{\mathbf{q}}_B\} \tag{12}$$

Downloaded 03 May 2010 to 171.66.16.21. Redistribution subject to ASME license or copyright; see http://www.asme.org/terms/Terms_Use.cfm

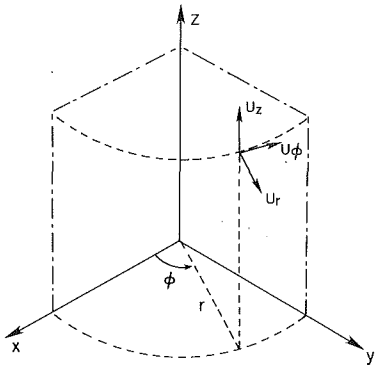

(a) Cylindrical Coordinate System

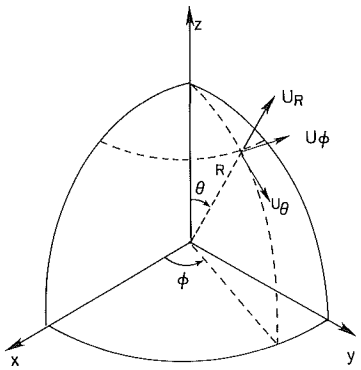

(b) Spherical Coordinate System

Fig. 2 Cylindrical and spherical polar coordinates system

Spherical Wave Functions for the Exterior Region

The total displacement **u** at any point is due to both incident and scattered fields and satisfies the equation of motion

$$(\lambda+2\mu)\nabla(\nabla\cdot\mathbf{u})-\mu\nabla\times\nabla\times\mathbf{u}=-\rho w^2\mathbf{u} \tag{13}$$

where it has been assumed that the motion is simple harmonic in time with circular frequency w, λ and μ are Lamé constants and ρ the density of the host medium.

The displacement field due to incident waves satisfying equation (13), and propagating and polarized in the xz-plane can be written, in cylindrical coordinates systems, as

$$\mathbf{u}^{(i)}=\nabla\phi^{(i)}+\frac{1}{k_2}\nabla\times\nabla\times(\mathbf{e}_z\chi^{(i)}) \tag{14}$$

where $\phi^{(i)}$ and $\chi^{(i)}$ are the P and SV wave potentials, repectively.

Similarly, the scattered displacement field can be written, in spherical coordinate system (refer to Fig. 2(b)), as

$$\mathbf{u}^{(s)}=\nabla\phi^{(s)}+\nabla\times(\mathbf{e}_R R\psi^{(s)})+\frac{1}{k_2}\nabla\times\nabla\times(\mathbf{e}_R R\chi^{(s)}) \tag{15}$$

where $\phi^{(s)}$, $\psi^{(s)}$, and $\chi^{(s)}$ represent the P, SH, and SV wave potentials, respectively; $\mathbf{e}_R$ and $\mathbf{e}_z$ are unit vectors along the R and z directions, respectively.

For the problem at hand, the potentials associated with the scattered field can be expressed in spherical wave functions as (Stratton, 1941)

$$\phi^{(s)}=\sum_{m=0}^{\alpha}\sum_{n=m}^{\alpha}a_{1nm}h_n(k_1R)P_n^m(\cos\Theta)\cos m\phi \tag{16a}$$

$$\chi^{(s)}=\sum_{m=0}^{\alpha}\sum_{n=m}^{\alpha}a_{2nm}h_n(k_2R)P_n^m(\cos\Theta)\cos m\phi \tag{16b}$$

$$\psi^{(s)}=\sum_{m=0}^{\alpha}\sum_{n=m}^{\alpha}b_{3nm}h_n(k_2R)P_n^m(\cos\Theta)\sin m\phi \tag{16c}$$

in which h_n is the spherical Hankel function of the first kind, P_n^m the associated Legendre functions, k_1 and k_2 are P and SV wave numbers defined by

$$k_1=w\sqrt{\frac{\rho}{\lambda+2\mu}}=w/c_1 \tag{17a}$$

$$k_2=w\sqrt{\frac{\rho}{\mu}}=w/c_2 \tag{17b}$$

a_{1nm}, a_{2nm}, and b_{3nm} are constants.

Substituting equations (16a–c) in equation (15), we get

$$u_R^{(s)}=\sum_{m=0}^{\alpha}\bar{u}_{Rm}^{(s)}\cos m\phi \tag{18a}$$

$$u_\Theta^{(s)}=\sum_{m=0}^{\alpha}\bar{u}_{\Theta m}^{(s)}\cos m\phi \tag{18b}$$

$$u_\phi^{(s)}=-\sum_{m=0}^{\alpha}\bar{u}_{\phi m}^{(s)}\sin m\phi \tag{18c}$$

where the amplitudes $\bar{u}_R^{(s)}$, $\bar{u}_\Theta^{(s)}$, and $\bar{u}_\phi^{(s)}$ are expressed as

$$\bar{u}_{Rm}^{(s)}=\sum_{n=m}^{\alpha}(a_{1nm}g_{R1}^n+a_{2nm}g_{R2}^n)P_n^m \tag{19a}$$

$$\bar{u}_{\Theta m}^{(s)}=\sum_{n=m}^{\alpha}\left\{(a_{1nm}g_{\Theta1}^n+a_{2nm}g_{\Theta2}^n)\frac{dP_n^m}{d\Theta}+b_{3nm}g_{\Theta3}^n\frac{P_n^m}{\sin\Theta}\right\} \tag{19b}$$

$$\bar{u}_{\phi m}^{(s)}=\sum_{n=m}^{\alpha}\left\{(a_{1nm}g_{\phi1}^n+a_{2nm}g_{\phi2}^n)\frac{P_n^m}{\sin\phi}+b_{3nm}g_{\phi3}^n\frac{dP_n^m}{d\Theta}\right\} \tag{19c}$$

For the sake of conserving space, expressions for g_{R1}^n, g_{R2}^n, $g_{\Theta1}^n$, $g_{\Theta2}^n$, $g_{\Theta3}^n$, $g_{\phi1}^n$, $g_{\phi2}^n$ and $g_{\phi3}^n$ are not presented here.

Evaluating the equations (19a–c) at each of the nodes lying on the boundary B, the vector $\{\bar{\mathbf{q}}_B^{(s)}\}$ of nodal amplitudes due to scattered field can be written as

$$\{\bar{\mathbf{q}}_B^{(s)}\}_{\text{sph}}=[\mathbf{G}]\{\mathbf{a}\} \tag{20}$$

where $\{\bar{\mathbf{q}}_B^{(s)}\}_{\text{sph}}$ contains the amplitudes of the displacement components in spherical coordinates system, evaluated at the nodes on the boundary B, $\{\mathbf{a}\}$ contains the unknown coefficients a_{1nm}, a_{2nm}, and b_{3nm} ($n=m$, $m+1$, ...).

In writing equation (20), the summation of the series in equation (19) is taken up to some value of n (depending on the azimuthal wave number m and the number of nodes N_B on the boundary B) so that **[G]** is a square matrix. For instance, when $m=2$, all three displacement components at $\theta=0$ and $\theta=\pi$ vanish identically. In assembling the matrix **[G]**, the above vanishing displacement components are not included in the vector $\{\bar{\mathbf{q}}_B^{(s)}\}_{\text{sph}}$ and the summation of the series in equation (19) is taken for $n=m$, $m+1$, . . . , $m+N_B-3$.

In general, only the nonvanishing displacement components are included in the vector $\{\bar{\mathbf{q}}_B^{(s)}\}$ which ensures that the matrix **[G]** is nonsingular.

The stress for the displacement field given by equations (18a–c) can be expressed as

Downloaded 03 May 2010 to 171.66.16.21. Redistribution subject to ASME license or copyright; see http://www.asme.org/terms/Terms_Use.cfm

$$\sigma_{RR}^{(s)} = \sum_{m=0}^{\alpha} \bar{\sigma}_{RRm}^{(s)} \cos m\phi \tag{21a}$$

$$\sigma_{R\theta}^{(s)} = \sum_{m=0}^{\alpha} \bar{\sigma}_{R\theta m}^{(s)} \cos m\phi \tag{21b}$$

$$\sigma_{R\phi}^{(s)} = \sum_{m=0}^{\alpha} -\bar{\sigma}_{R\theta m}^{(s)} \sin m\phi \tag{21c}$$

where the amplitudes $\bar{\sigma}_{RRm}^{(s)}$, $\bar{\sigma}_{R\theta m}^{(s)}$, and $\bar{\sigma}_{R\phi m}^{(s)}$, are given by

$$\bar{\sigma}_{RRm}^{(s)} = \sum_{n=m}^{\alpha} (a_{1nm} f_{R1}^{n} + a_{2nm} f_{R2}^{n}) P_n^m \tag{22a}$$

$$\bar{\sigma}_{R\theta m}^{(s)} = \sum_{n=m}^{\alpha} \left\{ (a_{1nm} f_{\theta 1}^{n} + a_{2nm} f_{\theta 2}^{n}) \frac{dP_n^m}{d\theta} + b_{3nm} f_{\theta 3}^{n} \frac{P_n^m}{\sin\theta} \right\} \tag{22b}$$

$$\bar{\sigma}_{R\phi m}^{(s)} = \sum_{n=m}^{\alpha} \left\{ (a_{1nm} f_{\phi}^{n} + a_{2nm} f_{\phi 2}{}^{n}) \frac{P_n^m}{\sin\theta} + b_{3nm} f_{\phi 3}^{n} \frac{dP_n^m}{d\theta} \right\} \tag{22c}$$

Expressions for $f_{R1}^{n}, f_{R2}^{n}, f_{\theta 1}{}^{n}, f_{\theta 2}{}^{n}, f_{\theta 3}{}^{n}, f_{\phi 1}{}^{n}, f_{\phi 2}{}^{n}$ and $f_{\phi 3}{}^{n}$ are not reproduced here.

Evaluating the stresses at the nodes lying on the boundary B, and multiplying them by the corrsponding area, we get the interaction force vector $\{\bar{\mathbf{P}}_B^{(s)}\}$ which can be written as

$$\{\bar{P}_B{}^{(s)}\}_{\text{sph}} = [\mathbf{F}]\{\mathbf{a}\} \tag{23}$$

It should be noted that the number of n's considered in writing equation (23) is same as that for equation (20). The matrix [F] is, therefore, square and nonsingular.

In view of equation (20), equation (23) can be written as

$$\{\bar{\mathbf{P}}_B^{(s)}\}_{\text{sph}} = [\mathbf{F}][\mathbf{G}]^{-1}\{\bar{\mathbf{q}}_B^{(s)}\}_{\text{sph}} \tag{24}$$

The vectors $\{\bar{\mathbf{P}}_B^{(s)}\}$ and $\{\bar{\mathbf{q}}_B^{(s)}\}$ in equation (24) are in spherical coordinate system. They can be transformed into cylindrical coordinate system as

$$\{\bar{\mathbf{P}}_B^{(s)}\}_{\text{cyl}} = [\mathbf{T}]^T[\mathbf{F}][\mathbf{G}]^{-1}[\mathbf{T}]\{\bar{\mathbf{q}}_B^{(s)}\}_{\text{cyl}} \tag{25a}$$

in which [T] is the transformation matrix. From equation (9), it can be observed that the matrix $[\mathbf{S}_f]$ can be expressed as

$$[\mathbf{S}_f] = [\mathbf{T}]^T[\mathbf{F}][\mathbf{G}]^{-1}[\mathbf{T}] \tag{25b}$$

Incident Wave Field

So far, we have presented a general theory in which a quantity of interest is calculated for each harmonic m and superposed. However, when the angle of incidence α is zero, we need to consider only one harmonic number in equation (16), namely $m=0$ for incidence P wave and $m=1$ for incident SV wave. The degenerate and the general cases of incidence are discussed below.

Zero Angle of Incidence.

(*a*) P *wave*: The case of P wave traveling along the z-axis represents a purely axisymmetric problem in which both geometry and loads are axisymmetric. We, then, need to consider only one harmonic number, namely $m=0$, in equation (16). The displacement in the azimuthal direction is zero due to the symmetry of the problem.

The incident wave potentials in equation (14) are given by

$$\phi^i = \frac{1}{ik_1} e^{ik_1 z}, \quad \Psi^i = 0 \tag{26}$$

The vectors $\{\mathbf{P}_B^{(i)}\}$ and $\{\bar{\mathbf{q}}_B^{(i)}\}$ can be constructed by evaluating the stress and displacements at each nodes lying on the boundary B. Now from symmetry the condition on $r=0$ is

$$\bar{u}_r(r,z)\Big|_{r=0} = 0 \tag{27a}$$

or, in spherical coordinates

$$\bar{u}_\theta(R, \theta) = 0 \text{ at } \theta = 0 \text{ and } \theta = \pi \tag{27b}$$

This condition is imposed on the finite element algorithm for nodes lying on the z-axis.

(*b*) SV *wave*: The case of SV wave traveling along the z-axis is completely defined by one harmonic number, namely $m=1$. For this case, the incident displacement field is given as

$$u^i = \hat{e}_x e^{ik_2 z} \tag{28}$$

The conditions at r = 0 are

$$\bar{u}_z(r, z) = 0 \tag{29a}$$

$$\bar{u}_r(r, z) = \bar{u}_\theta(r, z) \tag{29b}$$

or, in spherical coordinates

$$\bar{u}_R(R, \theta) = 0 \text{ at } \theta = 0 \text{ and } \pi \tag{30a}$$

$$\bar{u}_\theta(R, \theta) = \pm \bar{u}_\phi(R, \theta) \text{ at } \theta = 0 \text{ and } \pi \tag{30b}$$

The (+) sign is taken for $\theta=0$ and the (−) sign for $\theta=\pi$. The condition given by equation (29*a*) is easy to impose on a finite element algorithm, but not the one given by equation (29*b*). For this, an orthogonal transformation given by

$$\begin{bmatrix} \bar{v}_r \\ \bar{v}_\theta \end{bmatrix} = \begin{bmatrix} 1/\sqrt{2} & 1/\sqrt{2} \\ -1/\sqrt{2} & 1/\sqrt{2} \end{bmatrix} \begin{bmatrix} \bar{u}_r \\ \bar{u}_\theta \end{bmatrix} \tag{31}$$

is applied for those nodes lying on the z-axis, resulting in two new fictitious displacement components $\bar{v}_r$ and $\bar{v}_\theta$. The equivalent form of equation (29*b*) is

$$\bar{v}_\theta(r, z) = 0 \text{ at } r = 0 \tag{32}$$

which can be imposed without much difficulty.

Oblique Angle of Incidence. For plane P and SV waves that are incident obliquely to the axis of symmetry, it is necessary to consider all the harmonics $m=0, 1, 2, \ldots$. The incident field is then expanded as Fourier-Bessel series as shown below.

For a P wave having an angle of incidence α, the incident wave potentials are

$$\phi^{(i)} = \frac{i}{ik_1} e^{ik_1(z\cos\alpha + x\sin\alpha)}, \quad \chi^{(i)} = 0 \tag{33}$$

or, in series form

$$\phi^{(i)} = \frac{1}{ik_1} e^{ik_1 z\cos\alpha} \sum_{m=0}^{\alpha} \epsilon_m i^m J_m(k_1 r\sin\alpha)\cos m\phi \tag{34}$$

where

$$\epsilon_m = \begin{cases} 1, & m=0 \\ 2, & m\neq 0 \end{cases} \tag{35}$$

and J_m is the Bessel function of the first kind and order m. For an SV wave incident obliquely to the symmetry axis, the wave potentials are

$$\chi^{(i)} = -\frac{1}{k_2\sin\alpha} e^{ik_2(z\cos\alpha + x\sin\alpha)}, \quad \phi^{(i)} = 0 \tag{36}$$

or, in series form

$$\chi^{(i)} = -\frac{1}{k_2\sin\alpha} e^{ik_2 z\cos\alpha} \sum_{m=0}^{\alpha} \epsilon_m i^m J_m(k_2 r\sin\alpha)\cos m\phi \tag{37}$$

The conditions for $m=0$ and $m=1$ are the same as given by equations (27) and (29), respectively, and for $m \geq 2$,

Downloaded 03 May 2010 to 171.66.16.21. Redistribution subject to ASME license or copyright; see http://www.asme.org/terms/Terms_Use.cfm

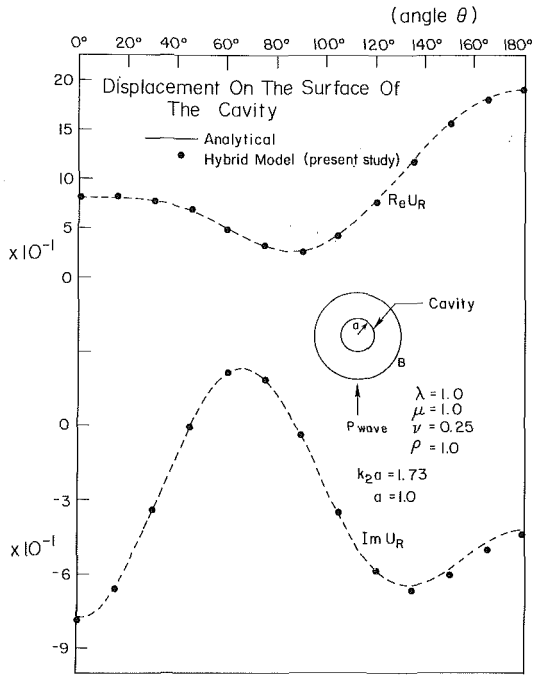

Fig. 3 Radial displacement of the surface of the spherical cavity due to incident P wave

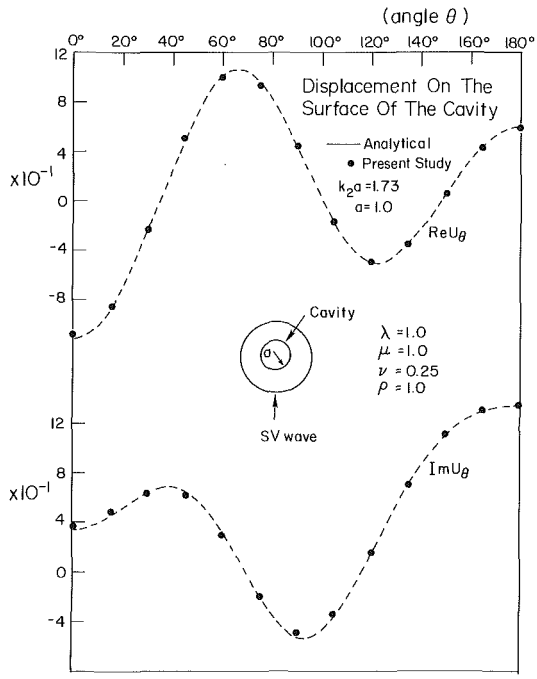

Fig. 4 Tangential displacement of the surface of the spherical cavity due to incident SV wave

$$\bar{u}_r(r, z) = \bar{u}_z(r, z) = \bar{u}_\theta(r, z) = 0 \text{ at } r = 0 \tag{38}$$

or, in spherical coordinates system

$$\bar{u}_R(R, \theta) = \bar{u}_\theta(R, \theta) = \bar{u}_\phi(R, \theta) = 0 \text{ at } \theta = 0 \text{ and } \theta = \pi \tag{39}$$

These conditions are easy to impose on a finite element algorithm. Note that the conditions given by equations (27*b*), (30*a*), (30*b*), and (39) are satisfied identically by the displacement field given in equations (19*a*–*c*).

Numerical Results and Discussion

In scattering problems, a quantity of general interest is the scattering cross-section. Expressions for scattering cross-section are given in Appendix A. In this paper, we present results for scattering cross-sections for various frequencies. The elastic inclusions considered are: (*i*) spherical solid, (*ii*) prolate spheroid, and (*iii*) oblate spheroid.

The first case, namely the spherical solid inclusion, also serves as a test case for the proposed method due to the availability of analytical solutions. However, it does not provide a rigorous test for the proposed method as the scattering cross-section for a given frequency represents the integrated characteristics of the scattered field over the surface of a large sphere. A better test for the validity of the proposed method would be the comparison of the displacements at a number of points with the analytical solutions.

Two sets of computer programs were developed in this study; the first set to implement the proposed method and the second to obtain analytical solutions for simple test problems.

In order that the finite elements transmit waves effectively, the dimensions of the finite elements should be kept within a certain limit of the minimum wave length of the type of waves being considered. Lysmer and Kuhlemeyer (1969) reported that, in order to obtain accurate results using four noded elements, the maximum dimension of the elements should be less than 1/12 of the shear wave length. In this study, four noded elements with 2×2 Gauss quadrature are used to model the interior region, and the element size is kept within 1/8 of the minimum wave length.

In order to test the validity of the model, the scattering of incident plane P and SV waves by a spherical cavity is considered. The incident waves are propagating along the z-axis. The displacements along the circumference of the cavity are computed for discrete values of the dimensionless frequency k_2a (0.1–3.4), "a" being the radius of the cavity. The results are found to be in close agreement with the analytical solution. As an illustration, the comparison of a displacement component for the dimensionless frequency $k_2a = 1.732$ is shown in Figs. 3 and 4. It should be noted here that even though the element size employed is larger than the one suggested by Lysmer and Kuhlemeyer the error is within acceptable limits.

Another problem solved using the proposed method is the scattering by a spherical solid inclusion, which may be surrounded by interface layers (Fig. 5). In this and other subsequent problems, the inclusion is SiC and the host medium is Aluminum. The material properties are given in Appendix B. The incident waves considered are P or SV wave, the angle of incidence being zero. In Tables 1–3 real and imaginary parts of $4\pi/k_1^2\ A_p(0)$ and $4\pi/k_2^2\ A_s(0)$ obtained from this study are shown along with the analytical solutions. It is seen that there is good agreement between them. Some discrepancies in solutions for low frequencies arise because the wave function expansions for the exterior region are undefined at zero frequency. Also, for high frequencies, a finer finite element model has to be used.

It has been mentioned earlier that the scattering problem is completely defined by a single harmonic number m when the angle of incidence is zero, but a number of harmonics has to be considered for oblique incidence and the final results are obtained through superposition. It appears that superposition may accumulate more error. To test the superposition, the scattering problem of solid spherical inclusion for different angles of incidence was considered. It was found that the results for angles of incidence of 45 deg and 90 deg agreed well with the analytical solution, which is the same as for the zero angle of incidence because of symmetry.

Downloaded 03 May 2010 to 171.66.16.21. Redistribution subject to ASME license or copyright; see http://www.asme.org/terms/Terms_Use.cfm

A more complicated case occurs when the scatterer is a spheroid which may be surrounded by layers (Fig. 6). The matieral properties are given in Appendix B. In the xz-plane, the cross-section of a spheroid is an ellipse, the geometry of which is completely defined by the lengths of the diameters along the x and z axes. For prolate spheriodal inclusion, the diameters along the z-axis are $4a$ for the core solid, $4.2a$ for the first layer and $4.4a$ for the second layer. The corresponding values along the x-axis are $2a$, $2.2a$, and $2.4a$. In the case of oblate spheroidal inclusion, the diameters along the z-axis are $2b$ for the core solid, $2.2b$ for the first layer and $2.4b$ for the second layer, and the corresponding values along the x-axis are $4b$, $4.2b$, and $4.4b$. The problem is easily solved by the proposed method due to the great flexibility of the finite element technique. It should be mentioned here that there are no

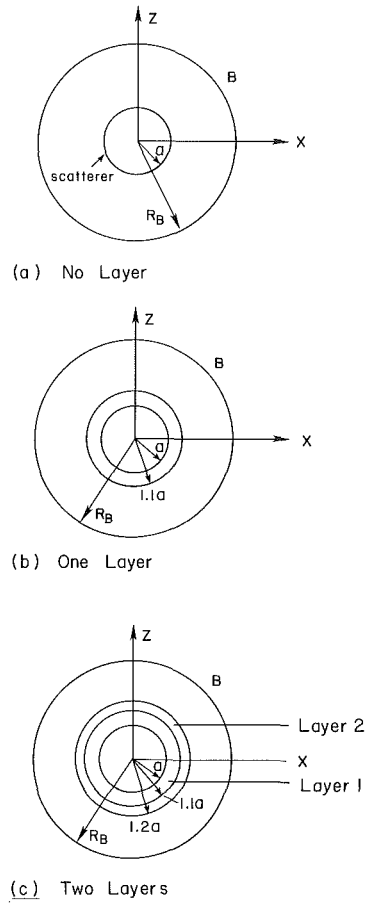

Fig. 5 Spherical inclusion with interface layers

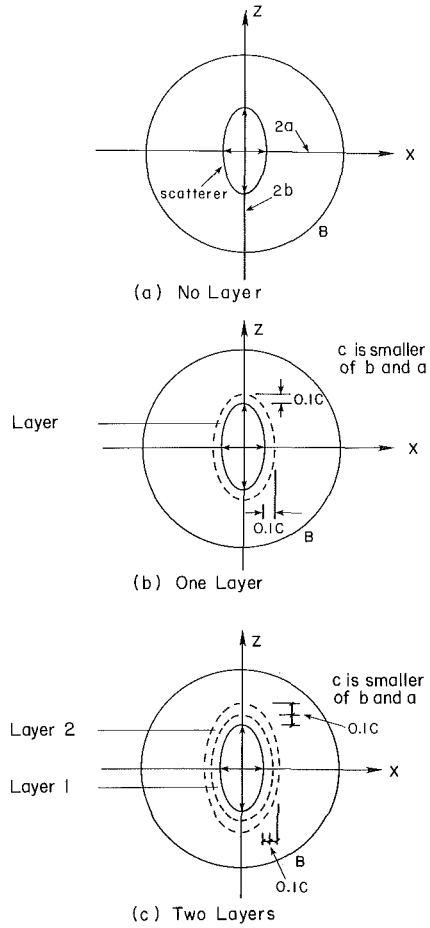

Fig. 6 Spheroidal inclusion with interface layers

Table 1 Comparison of analytical and numerical results for real and imaginary parts of $4\pi/K_1^2\ A_p(O)$ and $4\pi/K_2^2\ A_s(O)$ for scattering by spherical SiC particles in Al matrix

P-wave, $\alpha=O^0$, $\frac{4\pi}{K_1^2}\ A_p(O)$

K_2a	K_1a	Analytical		Hybrid Model	
	$=0.4916\ K_2a$	Re	Im	Re	Im
0.1	0.0491	-0.1869	0.2671×10^{-4}	-0.1878	0.2109×10^{-4}
0.5	0.2458	-0.8951	0.0143	-0.9050	0.0114
1.0	0.4916	-1.653	0.1585	-1.6653	0.1440
1.5	0.7373	-2.293	0.5296	-2.2865	0.4885
2.0	0.9831	-2.853	1.110	-2.7950	1.0637

SV-wave, $\alpha=O^0$, $\frac{4\pi}{K_2^2}\ A_s(O)$

0.1	0.0431	-0.5899	0.1452×10^{-3}	-0.6101	0.1324×10^{-3}
0.5	0.2458	-2.789	0.7366×10^{-1}	-2.8475	0.7098×10^{-1}
1.0	0.4916	-5.053	0.7031	-5.1378	0.6837
1.5	0.7373	-6.937	1.960	-6.9702	1.9272
2.0	0.9831	-8.336	3.566	-8.2169	3.5430

Table 2 Comparison of analytical and numerical results for $4\pi/K_1^2\ A_p(O)$ and $4\pi/K_2^2\ A_s(O)$ for scattering by a SiC particle with one interface layer in Al matrix

P-wave, $\alpha=O^0$, $\frac{4\pi}{K_1^2}\ A_p(O)$

K_2a	K_1a	Analytical		Hybrid Model	
	$=0.4916\ K_2a$	Re	Im	Re	Im
0.1	0.0491	-0.2373	0.4232×10^{-4}	-0.2397	0.3549×10^{-4}
0.5	0.2458	-1.134	0.2212×10^{-1}	-1.149	0.1865×10^{-1}
1.0	0.4916	-2.074	0.2339	-2.092	0..2175
1.5	0.7373	-2.864	0.7504	-2.862	0.7095
2.0	0.9831	-3.544	1.557	-3.486	1.5044

SV-wave, $\alpha=O^0$, $\frac{4\pi}{K_2^2}\ A_s(O)$

0.1	0.0491	-0.7551	0.2322×10^{-3}	-0.7782	0.2192×10^{-3}
0.5	0.2458	-3.544	0.1140	-3.608	0.1110
1.0	0.4916	-6.373	1.022	-6.460	1.002
1.5	0.7373	-8.661	2.728	-8.681	2.692
2.0	0.9831	-10.21	4.842	-10.05	4.802

Downloaded 03 May 2010 to 171.66.16.21. Redistribution subject to ASME license or copyright; see http://www.asme.org/terms/Terms_Use.cfm

Table 3 Comparison of analytical and numerical results for $4\pi/K_1^2\ A_p(O)$ and $4\pi/K_2^2\ A_s(O)$ for scattering by an SiC particle with two interface layers in Al matrix

P-wave, $\alpha=0^0$, $\frac{4\pi}{K_1^2} A_p(O)$

K_2a	K_1a	Analytical		Hybrid Model	
	$=0.4916\,K_2a$	Re	Im	Re	Im
0.1	0.0491	-0.2883	0.6212×10^{-4}	-0.2924	0.5423×10^{-4}
0.5	0.2458	-1.371	0.3172×10^{-1}	-1.394	0.2778×10^{-1}
1.0	0.4916	-2.434	0.3223	-2.521	0.3053
1.5	0.7373	-3.432	1.007	-3.4394	0.966
2.0	0.9831	-4.230	2.062	-4.1804	2.010

SV-wave, $\alpha=0^0$, $\frac{4\pi}{K_2^2} A_s(O)$

0.1	0.0491	-0.9238	0.3428×10^{-3}	-0.9494	0.3252×10^{-3}
0.5	0.2458	-4.307	0.1632	-4.382	0.1602
1.0	0.4916	-7.700	1.384	-7.801	1.365
1.5	0.7373	-10.37	3.567	-10.39	3.535
2.0	0.9831	-12.02	6.205	-11.86	6.161

analytical solutions available for this problem. Results for prolate and oblate spheroidal inclusions are presented in Fig. 7 for various angles of incidence of P wave. It is seen that the scattering cross-section increases with the addition of layers. This is to be expected since the addition of layers of properties stiffer than the matrix increases the effective cross-section of the inclusion. This increase will of course depend on the material properties of the layers chosen. Present limited numerical results do not lead in an obvious manner to an estimation of the effective cross-section. Further work is needed to gain more insight.

It is seen from Fig. 7 that for incident P waves scattering cross-section of prolate spheroidal inclusions decreases with increasing angle of incidence. For oblate spheroidal inclusions, on the other hand, it increases with increasing angle of incidence. This is an interesting result and quite different from the result for the SV wave as shown in Fig. 8. There it is found that the maximum cross-section for a prolate spheroid occurs at increasing angles of incidence as frequency increases. For oblate spheroids, on the other hand, it occurs at decreasing angles of incidence.

For both P and SV waves it is found that the scattering cross-sections of oblate spheroids are larger than those of prolate spheroids, and both of these are larger than those of inscribed spheres. This behavior can be used to ultrasonically characterize different inclusion shapes.

Conclusions

A hybrid finite element and wave function expansion technique is used here to study scattering of P and SV waves by prolate and oblate spheroids with and without interface layers between the inclusions and the matrix. It is found that the scattering cross-sections increase with increasing thickness of interface layer when the mechanical properties of the layers are intermediate between those of the inclusions and the matrix. Although this behavior is to be expected, the actual increase depends on the material properties and the thickness of the interphase zone. The problems considered here arise when there is an interaction zone between the reinforcing particles and the matrix and when the particles are coated.

Interphase or interface zones in these problems play an important role in determining the mechanical behavior of composite materials. The present study shows that changes in the scattering cross-sections may be used to parametrically

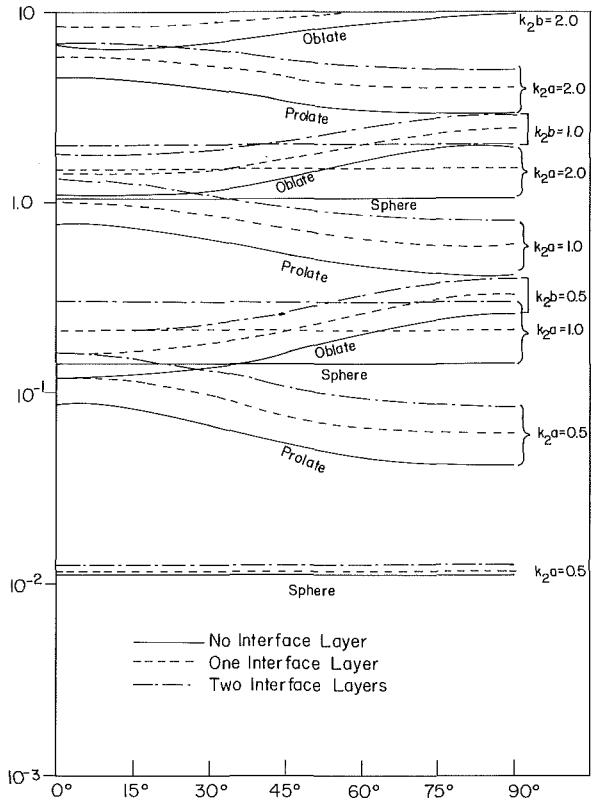

Fig. 7 Scattering cross-section of spheroidal inclusion for incident P waves

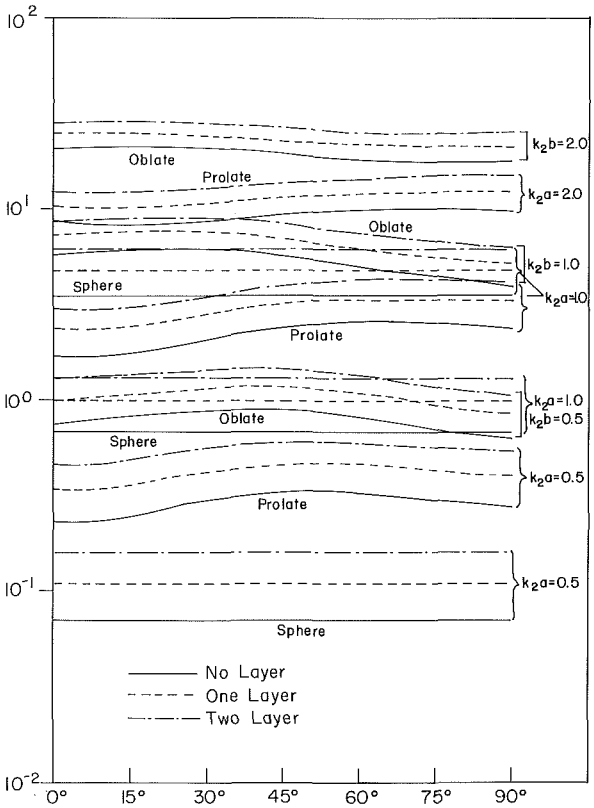

Fig. 8 Scattering cross-section of spheroidal inclusion for incident SV waves

characterize the interphase properties and thickness. However, to do so would require further investigation. In a recent paper (Datta et al., 1988) we have presented results of a

Downloaded 03 May 2010 to 171.66.16.21. Redistribution subject to ASME license or copyright; see http://www.asme.org/terms/Terms_Use.cfm

parametric study in which a simplified model of the interface layer was used. It was assumed to be very thin across which stresses were allowed to suffer jumps. This simplified model indicates that the inertial effect of the layer plays the dominant role in determining the scattering cross-section. Further studies are needed in order to fully understand the complicated effect of the interfacial layer.

Acknowledgment

The work reported here was supported in part by a grant (N00014-86-K-0280) from the Office of Naval Research (Program Officer: Dr. Y. Rajapakse). Support was also received from the Natural Science and Engineering Research Council of Canada (Grant #A-7988). The second author gratefully acknowledges the support received from the University of Colorado, Boulder, in the form of a Faculty Fellowship award for the 1986-87 academic year. He also was a Fulbright Research Scholar during part of this period at the Technical University of Vienna, where he had many helpful discussions with his generous host, Prof. F. Ziegler.

References

Abduljabbar, Z., Datta, S. K., and Shah, A. H., 1983, "Diffraction of Horizontally Polarized Shear Waves by Normal Edge Cracks in a Plate," *Journal of Applied Physics*, Vol. 54, pp. 461–472.

Cook, R. D., 1981, *Concepts and Applications of Finite Element Analysis*, John Wiley, New York.

Datta, S. K., and Shah, A. H., 1982, "Scattering of SH-waves by Embedded Cavities," *Wave Motion*, Vol. 4, pp. 265–283.

Datta, S. K., Shah, A. H., and Fortunko, C. M., 1982, "Diffraction of Medium and Long Wavelength SH-waves by Edge Cracks," *Journal of Applied Physics*, Vol. 53, pp. 2895–2903.

Datta, S. K., Olsson, P., and Boström, A., 1988, "Elastodynamic Scattering from Inclusions with Thin Interface Layers," presented at the Applied Mechanics and Engineering Science Meeting, June 20–22, Univ. of California, Berkeley in *Wave Propagation in Structural Composites*, eds. A. K. Mal, and T. C. T. Ting, ASME, New York, pp. 109–116.

Goetschel, D. B., and Dong, S. B., and Muki, R., 1982, "A Global Local Finite Element Analysis of Axisymmetric Scattering of Elastic Waves," ASME JOURNAL OF APPLIED MECHANICS, Vol. 49, pp. 816–820.

Lysmer, J., and Kuhlemeyer, R. L., 1969, "Finite Dynamic Model for Infinite Media," *Journal of Engineering Mechanics*, ASCE, Vol. 95, pp. 859–877.

Pao, Y. H., and Mow, C. C., 1973, *Diffraction of Elastic Waves and Dynamic Stress Concentrations*, Crane and Russak, New York.

Shah, A. H., Chin, Y. F., and Datta, S. K., 1987, "Elastic Wave Scattering by Surface-breaking Planar and Non-planar Cracks," ASME JOURNAL OF APPLIED MECHANICS, Vol. 54, pp. 761–767.

Shah, A. H., Wong, K. C., and Datta, S. K., 1982, "Diffraction of Plane SH-waves in a Half Space," *Earthquake Engineering and Structural Dynamics*, Vol. 10, pp. 519–528.

Shah, A. H., Wong, K. C., and Datta, S. K., 1983, "Single and Multiple Scattering of Elastic Waves in Two Dimensions," *Journal of the Acoustical Society of America*, Vol. 74, pp. 1033–1044.

Shah, A. H., Wong, K. C., and Datta, S. K., 1985, "Surface Displacements Due to Elastic Wave Scattering by Buried Planar and Non-planar Cracks," *Wave Motion*, Vol. 7, pp. 319–333.

Tsao, S. J., Varadan, V. V., and Varadan, V. K., 1982, "Comparison of Matrix Methods for Elastic Wave Scattering Problems," *Review of Progress in Quantitative Nondestructive Evaluation*, D. O. Thompson and D. E. Chimenti, eds., Plenum Press, New York, pp. 441–458.

Varadan, V. V., and Varadan, V. K., 1979. "Scattering Matrix for Elastic Waves III. Applications to Spheroids," *Journal of the Acoustical Society of America*, Vol. 65, pp. 896–905.

Varatharajulu, V., and Pao, Y. H., 1976, "Scattering Matrix for Elastic Waves I. Theory," *Journal of the Acoustical Society of America*, Vol. 60, pp. 556–566.

Waterman, P. C., 1976, "Matrix Theory for Elastic Wave Scattering," *Journal of the Acoustical Society of America*, Vol. 60, pp. 567–580.

Zienkiewicz, O. C., 1977, *Finite Element Method*, McGraw-Hill, London.

APPENDIX A

The expressions for scattering cross-section for the various incident fields are given below.

(*A*) P wave, angle of incidence $\alpha = 0$

$$\Sigma_p = \frac{4\pi}{k_1} Im \sum_{n=0}^{\alpha} (-i)^n a_{1mn} P_n^m(\cos\theta) \,|\theta = 0,\ m = 0.$$

$$= Im\left(\frac{4\pi}{k_1^2} A_p^{(0)}\right)$$

(*B*) SV wave, angle of incidence $\alpha = 0$

$$\Sigma_s = \frac{4\pi}{k_2^2} Im \sum_{n=0}^{\alpha} (-i)^n \left[a_{2mn} \frac{dP_n^m}{d\theta} - imb_{3mn} \frac{P_n^m}{\sin\theta}\right]\theta = 0,\ m = 1.$$

$$= Im\left(\frac{4\pi}{k_2^2} A_s^{(0)}\right)$$

(*C*) P wave, angle of incidence $\alpha \neq 0$.

$$\Sigma_p = 4\frac{\pi}{k_1} Im\left\{\sum_{m=0}^{\alpha}\sum_{n=m}^{\alpha} (-i)^n a_{1mn} P_n^m(\cos\theta)\right\}\theta = \alpha$$

$$= Im\left(\frac{4\pi}{k_1^2} A_p(\alpha)\right)$$

(*D*) SV wave, angle of incidence $\alpha \neq 0$.

$$\Sigma_s = \frac{4\pi}{k_2^2} Im\left\{\sum_{m=0}^{\alpha}\sum_{n=m}^{\alpha} (-i)^n \left[a_{2mn} \frac{dP_n^m}{d\theta} - ib_{3mn} m \frac{P_n^m}{\sin\theta}\right]\right\}\theta = \alpha$$

$$= Im\left(\frac{4\pi}{k_2^2} A_s(\alpha)\right)$$

APPENDIX B

Material Properties

In this study we considered a SiC inclusion in Al matrix.

SiC: $(\lambda + 2\mu,\ \mu) = (4.742, 1.881) \times 10^{11} N/\text{m}^2,\ \rho = 3.181\ \text{gm/cm}^3$

Al: $(\lambda + 2\mu,\ \mu) = (1.105, 0.267) \times 10^{11} N/\text{m}^2,\ \rho = 2.706\ \text{gm/cm}^3$

The layers smooth out the abrupt transition of material properties between the inclusion and the host medium. The material properties of the layers given below are calculated at the midpoint of each layer assuming a linear variation from the boundary of the inclusion to the matrix medium.

Case 1: One layer (Fig. 5(*b*), 6(*b*))

Layer: $(\lambda + 2\mu,\ \mu) = (2.9235, 1.074) \times 10^{11} N/M^2,\ \rho = 2.9435\ \text{gm/cm}^3$

Case 2: Two layers (Fig. 5(*c*), 6(*c*))

Layer 1: $(\lambda + 2\mu,\ \mu) = (3.833, 1.478) \times 10^{11} N/M^2,\ \rho = 3.062\ \text{gm/cm}^3$

Layer 2: $(\lambda + 2\mu,\ \mu) = (2.014, 0.671) \times 10^{11} N/M^2,\ \rho = 2.825\ \text{gm/cm}^3$

Downloaded 03 May 2010 to 171.66.16.21. Redistribution subject to ASME license or copyright; see http://www.asme.org/terms/Terms_Use.cfm

The Normal Impact of a Rod-Mass System on a Viscoelastic Layered Half Space

H. A. Downey, Jr.
IBM Corporation,
Charlotte, NC 28257
Assoc. Mem. ASME

D. B. Bogy
University of California,
Berkeley, CA 94720
Mem. ASME

A rod with a lumped mass attached to its trailing end travels axially with a uniform velocity and strikes an elastic half space that is covered with an adhering viscoelastic layer. The problem is reduced to integral equations for the average contact stress and the displacement of the rod tip into the contact surface. The kernels of these integral equations are composed of temporal Green's functions for the rod and the layered half space, which represent the response of each to an impulsive uniform normal traction. The Green's function for the rod is obtained in closed form, while that for the layered half space is obtained through a numerical Laplace transform inversion. The integral equations are solved numerically with a second-order stable scheme. Solutions are computed for a wide variety of materials and configurations, providing the stress and displacement history, as well as the stress-displacement response. The results show the effects of changes in rod material and length, lumped mass, layer material, substrate material, and viscoelastic material parameters.

1 Introduction

In wire-matrix printing, a thin wire is accelerated by an electromagnet and then strikes an inked ribbon and paper, causing ink to transfer from the ribbon to the paper and form a dot. The two basic physical quantities that govern printing speed and quality are contact force and contact time. Contact force must be adequate to assure proper transfer of ink to the paper. Contact time, while not a significant factor in print quality, physically limits printing speed. Consequently, in order to increase printer speed, a better understanding of the parameters that govern these two quantities, such as wire length and material, impact velocity, and platen properties, is needed so that contact time can be reduced while maintaining sufficient print force.

Wire-matrix printing is reduced here to an idealized model. The impact of a single straight wire in a stationary printhead is considered. It is assumed that when the print wire strikes the paper, it has a uniform velocity and is free of the driving mechanism. A one-dimensional rod model with a lumped mass on its trailing end represents the print wire, a linear viscoelastic layer represents the ribbon and paper, and an elastic half space represents the platen. The analysis shown here can be extended to the two-layer case, but the consideration of the ribbon and paper layers as a single layer is a reasonable simplifying assumption, since the paper and ribbon properties are similar when compared to the platen. In addition, the problem is solved for an elastic layer, since this solution is required as a preliminary for the viscoelastic layer problem.

This paper is a continuation of the work published previously by Downey and Bogy (1987a), (1987b), in which the problems of a rod striking a homogeneous elastic or viscoelastic half space were solved. These papers will be relied upon here for much of the formulation and other details, and they will be referred to as Paper I, and Paper II, respectively.

2 Formulation

Figure 1 shows the geometry and coordinate system for the problem to be solved. The coordinate system is cylindrical polar, (r, θ, z). The origin is at the surface of the layer, and z is directed into the half space. The layer has thickness h, Young's modulus E, Poisson's ratio ν and density ρ; α and τ_σ are the viscoelastic parameters. The elastic substrate, which is bonded to the layer at $z=h$, has properties E_s, ν_s, and ρ_s. The rod has length L, and has a lumped mass M at $z=-L$. Its radius is a, and it has initial velocity V_o, modulus E_o and density ρ_o.

2.1 Solution Method. The layer is a linearly viscoelastic solid. As in Paper II, identical time-dependent viscoelastic behavior in bulk and shear is assumed, and the viscoelastic model is the three-parameter standard linear solid. The viscoelastic constitutive relations are introduced into the Laplace transformed elastic solution through the corresponding principle, (Christensen (1971)). After the elastic solution is obtained in the Laplace domain, the material constants are replaced by the complex-valued viscoelastic moduli

Contributed by the Applied Mechanics Division for publication in the JOURNAL OF APPLIED MECHANICS.
Discussion on this paper should be addressed to the Editorial Department, ASME, United Engineering Center, 345 East 47th Street, New York, N.Y. 10017, and will be accepted until two months after final publication of the paper itself in the JOURNAL OF APPLIED MECHANICS. Manuscript received by ASME Applied Mechanics Division, November 6, 1987; final revision, April 12, 1988.

Copyright © 1988 by ASME
Downloaded 03 May 2010 to 171.66.16.21. Redistribution subject to ASME license or copyright; see http://www.asme.org/terms/Terms_Use.cfm

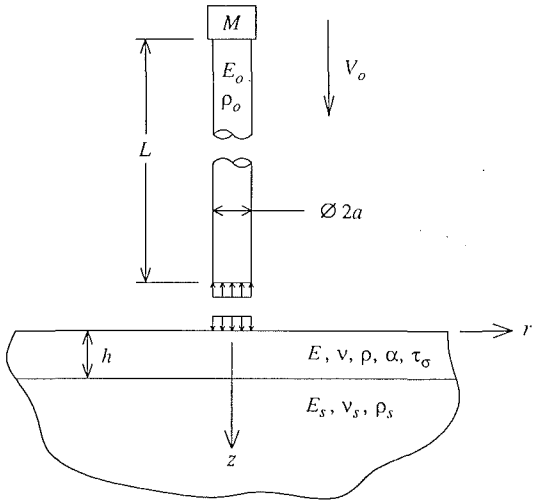

Fig. 1 Geometry and coordinate system

that are functions of s, the transform variable. Thus, the elastic shear modulus μ and bulk modulus k are replaced by

$$\bar{\mu}(s) \equiv \tilde{\mu} \frac{(s+\alpha/\tau_\sigma)}{(s+1/\tau_\sigma)}, \quad \bar{k}(s) \equiv \tilde{k} \frac{(s+\alpha/\tau_\sigma)}{(s+1/\tau_\sigma)}, \tag{1}$$

the complex shear and bulk moduli, where τ_σ is the stress relaxation time, and α is the ratio of stress to strain relaxation time. The constants $\tilde{\mu}$ and $\tilde{k}$ are called the instantaneous shear and bulk moduli. Similar substitutions are made if other elastic constants are used, and any quantities in the elastic solution that depend on the moduli, such as the two elastic wave speeds, also become complex in the viscoelastic formulation. The problem is then reduced to the inversion of Laplace transforms.

All the quantities in the solution are nondimensional, as in Papers I and II. The most important ones (indicated by asterisks) are

$$u_i^* = u_i/a, \ \tau_{ij}^* = \tau_{ij}/2\tilde{\mu}, \ r^* = r/a, \ z^* = z/a,$$
$$t^* = \tilde{c}_1 t/a, \ w^* = w/a, \ \sigma_z^* = -c_o \sigma_z / E_o V_o. \tag{2}$$

where u_i are the displacement components, τ_{ij} are the stress components, and $\tilde{c}_1 = \sqrt{(\tilde{\lambda}+2\tilde{\mu})/\rho}$. Also, w is the rod axial displacement, $c_o \equiv \sqrt{E_o/\rho_o}$ is the rod wave speed, and σ_z is the axial stress in the rod.

In the substrate the nondimensionalization is the same as in the layer, and the substrate quantities will be indicated by a super- or subscripted s. Throughout the following, all asterisks will be dropped, and all quantities except V_o are dimensionless unless otherwise specified.

The elastic solution will be formulated first, but the distinction between ($\tilde{\mu}$ and $\tilde{c}_1$) and (μ and c_1) is preserved, to allow the introduction of viscoelasticity later. The displacement vector is represented in terms of the potentials Φ and Ψ. The displacement-potential relations, the potential wave equations, and the stress-potential relations for the layer are given in Paper II, equations (5)–(8) where the entire half space is viscoelastic. These also hold here for the substrate with u_r, u_z, Φ, Ψ, τ_{zz}, τ_{rz}, λ, μ, κ, and c_1 replaced by u_r^s, u_z^s, Φ_s, Ψ_s, τ_{zz}^s, τ_{rz}^s, λ_s, μ_s, κ_s and c_{1s}, where

$$\kappa_s^2 = \tilde{c}_1^2/c_{2s}^2, \ c_{1s}^2 = (\lambda_s + 2\mu_s)/\rho_s, \ c_{2s}^2 = \mu_s/\rho_s. \tag{3}$$

The equation of motion and constitutive relation for the rod are also given in Paper II, equations (9) and (10).

2.2 Boundary Conditions. At the layer-substrate interface, perfect adherence is assumed. This implies continuous displacement in the radial and normal directions, and continuous shear and normal stresses. This is a major simplifying assumption for this interface that needs to be verified. It is a reasonable assumption in the immediate region of the contact, where the interface will be under compression from the impact. Thus, the boundary conditions at the interface are

$$\tau_{zz}(r,h,t) = \tau_{zz}^s(r,h,t), \ \tau_{rz}(r,h,t) = \tau_{rz}^s(r,h,t), \tag{4}$$
$$u_z(r,h,t) = u_z^s(r,h,t), \ u_r(r,h,t) = u_r^s(r,h,t). \tag{5}$$

The assumptions for the boundary conditions at the interface of the rod and the layer surface are the same as those in Papers I and II. The traction on the surface is assumed to be uniform and equal and opposite to the traction on the rod. The rod-tip displacement is assumed to be the average displacement of the surface of the layer in the contact region. These are given in equations (11)–(13) of Paper II.

At the rod's trailing end, the boundary condition for the lumped mass is equation (14) of Paper II. The initial conditions, with everything at rest except for the rod, are given by equations (15) of Paper II. The substrate is also initially at rest.

3 Derivation of the Integral Equations

Since the important quantities for printing are contact force and contact time, the problem is solved for the time-dependent interface stress and displacement of the rod tip. Integral equations can be derived for these expressions. The derivation of the integral equations in this paper utilizes a Green's function approach that provides more insight than the derivation in Paper I. It also yields two different integral representations for the displacement in terms of the contact stress.

Before this can be accomplished, however, temporal Green's functions for the rod and layered half space must be obtained. The Green's function needed for the layered half space is the average displacement response of a circular region subjected to a uniform stress impulse over that region. That boundary condition is

$$\tau_{zz}(r,0,t) = \begin{cases} -\delta(t) & 0 \le r \le 1 \\ 0 & r \ge 1. \end{cases} \tag{6}$$

The Green's function, $F(t)$, which is the average displacement of that region is defined by

$$F(t) \equiv \underset{0 \le r \le 1}{\text{avg}} \, u_z(r,0,t) = \frac{1}{\pi} \int_0^1 u_z \Big|_{z=0} 2\pi r \, dr. \tag{7}$$

Similarly, for the rod, the necessary Green's function is the displacement response of the rod tip to an impulsive stress on that end. The boundary condition on the rod is an impulse, but a constant multiplier is needed to make it consistent with the normal stress boundary condition of the coupled problem,

$$\sigma_z(0,t) = -\frac{E_1 \tilde{c}_1}{V_o} \delta(t). \tag{8}$$

The Green's function, $G(t)$, the rod tip displacement, is defined as

$$G(t) \equiv w(0,t) \equiv w_o(t). \tag{9}$$

The next step in deriving the integral equations is to use the two Green's functions to express the displacement response of both the rod (with an initial velocity) and the layered half space to an arbitrary stress history. There is a possibility for confusion because the nondimensionalization of the stress in the rod and in the layer are different and opposite in sign. The boundary condition (equation (11) of Paper II) for the normal stress in the contact region provides the proper conversion between the two.

Since $G(t)$ is the rod tip response to a stress $-E_1\tilde{c}_1/V_o \ \delta(t)$, then the rod tip response to the arbitrary stress $\sigma_o(t)$ will be

Downloaded 03 May 2010 to 171.66.16.21. Redistribution subject to ASME license or copyright; see http://www.asme.org/terms/Terms_Use.cfm

$$w_o(t) = -\frac{V_o}{E_1\tilde{c}_1}\int_0^t G(t-\tau)\sigma_o(\tau)d\tau + \frac{V_o}{\tilde{c}_1}t. \tag{10}$$

where the extra term comes from the initial rod velocity.

In the layered half space, since $F(t)$ is the response to a stress $-\delta(t)$, then for the same arbitrary stress, $\sigma_o(t)$ (which is in rod stress units), the average displacement in the region is,

$$\underset{0\le r\le 1}{\text{avg}}\, u_z(r,0,t) = \frac{V_o}{E_1\tilde{c}_1}\int_0^t F(t-\tau)\sigma_o(\tau)d\tau. \tag{11}$$

where the sign change and the multiplication of the integral by $V_o/E_1\tilde{c}_1$ comes from the different nondimensionalization.

3.1 Stress Integral Equation. The integral equation is now derived using the displacement boundary condition (equation (13) of Paper II), coupling the rod tip displacement to the layer surface. Thus, the two displacement integrals (10) and (11) are set equal, yielding the stress integral equation, a Volterra integral equation of the first kind,

$$\int_0^t [F(t-\tau)+G(t-\tau)]\sigma_o(\tau)d\tau = E_1 t. \tag{12}$$

The solution of this equation will yield the contact stress history for the rod striking the layered half space, provided one knows the two Green's functions $F(t)$ and $G(t)$.

3.2 Displacement Integral Equation. The displacement history can be found by using either of the displacement integrals (10) and (11), once the stress is known. Alternatively, the unknown displacement can be represented as an integral equation. First, take the Laplace transform of the two displacement integrals, (10) and (11), to get

$$\bar{w}_o(s) = \frac{V_o}{E_1\tilde{c}_1}\bar{F}(s)\bar{\sigma}_o(s), \tag{13}$$

and

$$\bar{w}_o(s) = -\frac{V_o}{E_1\tilde{c}_1}\bar{G}(s)\bar{\sigma}_o(s) + \frac{V_o}{\tilde{c}_1 s^2}. \tag{14}$$

Solve both equations for $\bar{\sigma}_o(s)$, and equate the results to get

$$[\bar{G}(s)+\bar{F}(s)]\bar{w}_o(s) = \frac{V_o}{\tilde{c}_1 s^2}\bar{F}(s). \tag{15}$$

Now, apply the convolution theorem of Laplace transforms to get the displacement integral equation,

$$\int_0^t [F(t-\tau)+G(t-\tau)]w_o(\tau)d\tau = \frac{V_o}{\tilde{c}_1}\int_0^t F(t-\tau)\tau d\tau. \tag{16}$$

3.3 Derivation of the Green's Function in the Laplace Domain for the Layered Half Space.

3.3.1 Layered Elastic Half Space Green's Function. To find the Green's function for the elastic half space with an elastic layer, dual transforms are used. The Hankel transform (in r) of order ν is indicated by a superposed caret, with a superscript indicating the order, and the Laplace transform (in t) is indicated by an overbar. The transforms are applied to the wave equations for both the layer and the substrate, and the resulting differential equations in z yield the following formal solutions:

In the layer,

$$\hat{\bar{\Phi}}^0 = \frac{a(\xi,s)}{\xi}e^{-\gamma z} + \frac{b(\xi,s)}{\xi}e^{\gamma z},\ \gamma=(\xi^2+\kappa_1^2 s^2)^{1/2}, \tag{17}$$

$$\hat{\bar{\Psi}}^1 = \frac{c(\xi,s)}{\xi}e^{-\delta z} + \frac{d(\xi,s)}{\xi}e^{\delta z},\ \delta=(\xi^2+\kappa^2 s^2)^{1/2}. \tag{18}$$

In the substrate, after the coefficients of the terms which are unbounded for large z are set equal to zero,

$$\hat{\bar{\Phi}}_s^0 = \frac{f(\xi,s)}{\xi}e^{-\alpha z},\ \alpha=(\xi^2+\kappa_{1s}^2 s^2)^{1/2}, \tag{19}$$

$$\hat{\bar{\Psi}}_s^1 = \frac{g(\xi,s)}{\xi}e^{-\beta z},\ \beta=(\xi^2+\kappa_s^2 s^2)^{1/2}, \tag{20}$$

where $\kappa_1^2=c_1^2/\tilde{c}_1^2$, $\kappa_{1s}^2=c_{1s}^2/\tilde{c}_1^2$, and the branches of the radicals α, β, γ, and δ are chosen to assure outgoing waves.

The six unknown functions are determined from the six boundary conditions. The displacement-potential equations and the stress-potential equations for the layer are first transformed to yield,

$$\hat{\bar{u}}_r^1 = -\xi\hat{\bar{\Phi}}^0 - \frac{d\bar{\Psi}^1}{dz}, \tag{21}$$

$$\hat{\bar{u}}_z^0 = \frac{d\hat{\bar{\Phi}}^0}{dz} + \xi\bar{\Psi}^1, \tag{22}$$

$$\hat{\bar{\tau}}_{rz}^1 = \frac{\mu}{\tilde{\mu}}\left[-\xi\frac{d\hat{\bar{\Phi}}^0}{dz} - (\xi^2+\kappa^2 s^2/2)\hat{\bar{\Psi}}^1\right], \tag{23}$$

$$\hat{\bar{\tau}}_{zz}^0 = \frac{\mu}{\tilde{\mu}}\left[(\xi^2+\kappa^2 s^2/2)\hat{\bar{\Phi}}^0 + \xi\frac{d\hat{\bar{\Psi}}^1}{dz}\right]. \tag{24}$$

In the substrate, the equations are the same except for a subscripted s on the displacement and stress components, the potentials, and μ and κ.

The layer-substrate boundary conditions (4) and (5) are unchanged after transformation, but the surface boundary conditions become:

$$[\hat{\bar{\tau}}_{rz}^1]_{z=0} = 0, \tag{25}$$

$$[\hat{\bar{\tau}}_{zz}^0]_{z=0} = -\frac{J_1(\xi)}{\xi}. \tag{26}$$

To solve for the six unknowns, a useful method is described by Brekhovskikh (1980), which casts the equations for the quantities $\{\hat{\bar{u}}_r^1, \hat{\bar{u}}_z^0, \hat{\bar{\tau}}_{rz}^1, \hat{\bar{\tau}}_{zz}^0\}$, called **f**, as transfer matrices that express their values at the top of the layer in terms of their values at the bottom of the layer. Substituting the potential solutions (17) and (18) into the four displacement and stress equations (21)–(24), the equations for the layer in matrix form become,

$$\begin{bmatrix} \hat{\bar{u}}_r^1 \\ \hat{\bar{u}}_z^0 \\ \hat{\bar{\tau}}_{rz}^1 \\ \hat{\bar{\tau}}_{zz}^0 \end{bmatrix} = \begin{bmatrix} -e^{-\gamma z} & -e^{\gamma z} & \frac{\delta}{\xi}e^{-\delta z} & -\frac{\delta}{\xi}e^{\delta z} \\ -\frac{\gamma}{\xi}e^{-\gamma z} & \frac{\gamma}{\xi}e^{\gamma z} & e^{-\delta z} & e^{\delta z} \\ \frac{\mu\gamma}{\tilde{\mu}}e^{-\gamma z} & -\frac{\mu\gamma}{\tilde{\mu}}e^{\gamma z} & -\frac{\mu\Delta}{\tilde{\mu}\xi}e^{-\delta z} & -\frac{\mu\Delta}{\tilde{\mu}\xi}e^{\delta z} \\ \frac{\mu\Delta}{\tilde{\mu}\xi}e^{-\gamma z} & \frac{\mu\Delta}{\tilde{\mu}\xi}e^{\gamma z} & -\frac{\mu\delta}{\tilde{\mu}}e^{-\delta z} & \frac{\mu\delta}{\tilde{\mu}}e^{\delta z} \end{bmatrix} \begin{bmatrix} a(\xi,s) \\ b(\xi,s) \\ c(\xi,s) \\ d(\xi,s) \end{bmatrix}, \tag{27}$$

where $\Delta=(\xi^2+\kappa^2 s^2/2)$. This can be written in matrix notation,

Downloaded 03 May 2010 to 171.66.16.21. Redistribution subject to ASME license or copyright; see http://www.asme.org/terms/Terms_Use.cfm

$$\mathbf{f}(z) = \mathbf{C}(z)\mathbf{a}. \tag{28}$$

This holds throughout the layer, including both $z=0$ and $z=h$, so $\mathbf{f}(0)$ can be expressed in terms of $\mathbf{f}(h)$, eliminating the unknowns $\mathbf{a}$:

$$\mathbf{f}(0) = \mathbf{C}(0)\mathbf{C}^{-1}(h)\mathbf{f}(h). \tag{29}$$

In the substrate, the equivalent of equation (27) is

$$\begin{bmatrix} \hat{u}_r^1 \\ \hat{u}_z^0 \\ \hat{\tau}_{rz}^1 \\ \hat{\tau}_{zz}^0 \end{bmatrix}_s = \begin{bmatrix} -e^{-\alpha z} & \frac{\beta}{\xi} e^{-\beta z} \\ -\frac{\alpha}{\xi} e^{-\alpha z} & e^{-\beta z} \\ \frac{\mu_s \alpha}{\tilde{\mu}} e^{-\alpha z} & -\frac{\mu_s \Delta_s}{\tilde{\mu}\xi} e^{-\beta z} \\ \frac{\mu_s \Delta_s}{\tilde{\mu}\xi} e^{-\alpha z} & -\frac{\mu_s \beta}{\tilde{\mu}} e^{-\beta z} \end{bmatrix} \begin{bmatrix} f(\xi,s) \\ g(\xi,s) \end{bmatrix}, \tag{30}$$

(30)

where $\Delta_s = (\xi^2 + \kappa_s^2 s^2/2)$. In matrix notation this is

$$\mathbf{f}_s(z) = \mathbf{C}_s(z)\mathbf{a}_s. \tag{31}$$

At the layer-substrate interface, $\mathbf{f}(h) = \mathbf{f}_s(h)$, in accordance with the boundary conditions. Thus, the quantities $\mathbf{f}$ at the surface are,

$$\mathbf{f}(0) = \mathbf{C}(0)\mathbf{C}^{-1}(h)\mathbf{C}_s(h)\mathbf{a}_s. \tag{32}$$

All that remains are the two surface boundary conditions, from which $f(\xi,s)$ and $g(\xi,s)$ are determined. If the indicated multiplications of the $\mathbf{C}$ matrices in equation (32) are carried out, and the product matrix is denoted as $\mathbf{H}$, the resulting equation has the form:

$$\begin{bmatrix} \hat{u}_r^1 \\ \hat{u}_z^0 \\ \hat{\tau}_{rz}^1 \\ \hat{\tau}_{zz}^0 \end{bmatrix}_{z=0} = \begin{bmatrix} h_{11} & h_{12} \\ h_{21} & h_{22} \\ h_{31} & h_{32} \\ h_{14} & h_{42} \end{bmatrix} \begin{bmatrix} f(\xi,s) \\ g(\xi,s) \end{bmatrix}. \tag{33}$$

The boundary conditions (25) and (26) are applied to find

$$f(\xi,s) = \frac{J_1(\xi)h_{32}}{\xi(h_{31}h_{42} - h_{32}h_{41})}, \tag{34}$$

$$g(\xi,s) = -\frac{J_1(\xi)h_{31}}{\xi(h_{31}h_{42} - h_{32}h_{41})}. \tag{35}$$

The Green's function is the average normal surface displacement in the contact region. The transformed normal surface displacement is $\hat{u}_z^0$, which can be found by substituting $f(\xi,s)$ and $g(\xi,s)$ from above into equation (33) to get

$$\hat{u}_z^0 = \frac{J_1(\xi)(h_{21}h_{32} - h_{22}h_{31})}{\xi(h_{31}h_{42} - h_{32}h_{41})} \equiv \frac{1}{\xi} J_1(\xi)h(\xi,s). \tag{36}$$

Using the inverse Hankel transform, and averaging over the contact region, we obtain the Laplace transformed Green's function,

$$\bar{F}(s) = 2\int_0^\infty h(\xi,s)\frac{J_1^2(\xi)}{\xi}\,d\xi. \tag{37}$$

The algebraic manipulations to calculate $h(\xi,s)$ were performed with the symbolic computer algebra system REDUCE, Hearn (1983). The results, after more manipulations to simplify the form, are,

$$h(\xi,s) = \frac{\tilde{\mu}}{\mu}\frac{N}{D}, \tag{38}$$

where

$$\begin{aligned} N = {} & \gamma(\xi^2-\Delta)\{\delta\gamma[\alpha\beta\xi^2(\mu_o-1)^2 - (\mu_o\xi^2-\Delta_s)^2](e^{-2h(\delta+\gamma)} \\ & - e^{-2h\delta} + e^{-2h\gamma} - 1) + [\xi^2(\mu_o\Delta-\Delta_s)^2 \\ & - \alpha\beta(\xi^2-\mu_o\Delta)^2](e^{-2h(\delta+\gamma)} + e^{-2h\delta} - e^{-2h\gamma} - 1) \\ & + \beta\gamma\mu_o(\xi^2-\Delta)(\xi^2-\Delta_s)(e^{-2h(\delta+\gamma)} - e^{-2h\delta} - e^{-2h\gamma} + 1) \\ & + \alpha\delta\mu_o(\xi^2-\Delta)(\xi^2-\Delta_s)(e^{-2h(\delta+\gamma)} + e^{-2h\delta} + e^{-2h\gamma} + 1)\}, \end{aligned} \tag{39}$$

and

$$\begin{aligned} D = {} & \{8\delta\gamma\xi^2\Delta[\alpha\beta(\mu_o-1)(\mu_o\Delta-\xi^2) \\ & + (\Delta_s - \mu_o\xi^2)(\mu_o\Delta - \Delta_s)]e^{-h(\delta+\gamma)} \\ & + [\mu_o\delta(\xi^2-\Delta)(\xi^2-\Delta_s)(\beta\gamma^2\xi^2 - \alpha\Delta^2)](e^{-2h(\delta+\gamma)} - e^{-2h\delta} \\ & + e^{-2h\gamma} - 1) + [\mu_o\gamma(\xi^2-\Delta)(\xi^2-\Delta_s)(\alpha\delta^2\xi^2 \\ & - \beta\Delta^2)](e^{-2h(\delta+\gamma)} + e^{-2h\delta} - e^{-2h\gamma} - 1) + [\alpha\beta\delta^2\xi^4(\mu_o-1)^2 \\ & - \gamma^2\delta^2\xi^2(\mu_o\xi^2-\Delta_s)^2 + \alpha\beta\Delta^2(\xi^2-\mu_o\Delta)^2 - \xi^2\Delta^2(\mu_o\Delta \\ & - \Delta_s)^2](e^{-2h(\delta+\gamma)} - e^{-2h\delta} - e^{-2h\gamma} + 1) \\ & - \delta\gamma[\alpha\beta\xi^2\Delta^2(\mu_o-1)^2 - \Delta^2(\mu_o\xi^2-\Delta_s)^2 \\ & + \alpha\beta\xi^2(\xi^2-\mu_o\Delta)^2 - \xi^4(\mu_o\Delta-\Delta_s)^2](e^{-2h(\delta+\gamma)} + e^{-2h\delta} \\ & + e^{-2h\gamma} + 1)\}, \end{aligned} \tag{40}$$

where $\mu_o = \mu/\mu_s$.

The Laplace transfer of the Green's function given by equations (37)–(40) remains to be inverted.

3.3.2 Viscoelastic Layered Half Space Green's Function. To derive the Laplace transformed Green's function for the case of a viscoelastic layer, the appropriate substitutions for the complex moduli need to be made in the layer, as discussed previously. The material constants are replaced with their counterparts that are now functions of s, given by equation (22) of Paper II. These complex "constants" are substituted into δ, γ, and Δ, defined in equations (17), (18), and (27) respectively, so that they become

$$\gamma(\xi,s) = \left(\xi^2 + s^2\frac{(s+1/\tau_\sigma)}{(s+\alpha/\tau_\sigma)}\right)^{1/2}, \tag{41}$$

$$\delta(\xi,s) = \left(\xi^2 + s^2\tilde{\kappa}^2\frac{(s+1/\tau_\sigma)}{(s+\alpha/\tau_\sigma)}\right)^{1/2}, \tag{42}$$

$$\Delta = \left(\xi^2 + \frac{\tilde{\kappa}^2 s^2}{2}\frac{(s+1/\tau_\sigma)}{(s+\alpha/\tau_\sigma)}\right). \tag{43}$$

The Green's function is given by equations (37)–(40), but the new definitions for δ, γ, Δ, and μ given above are used.

3.4 Green's Function for the Rod. The other necessary Green's function, $G(t)$, is for the rod. The rod is initially at rest for the Green's function since the rod velocity for the impact problem was taken into account separately when deriving the displacement integral, equation (10). The closed form result for this Green's function in the time domain is given by equation (41) of Paper I.

4 Numerical Inversion of the Layered Half Space Green's Function

The next step in the solution is the inversion of the Laplace transformed Green's function for the layered half space. This is done numerically. A good source of information on numerical methods for Laplace transform inversion is the review article by Davies and Martin (1979), that classifies the available methods, and tests 14 of them on 16 different functions. The method used in Paper II for the viscoelastic half space, by Papoulis (1956), was not adequate for the layered half space. Thus, a method was used which represents the inverse as a finite Fourier transform, Crump (1976). Accurate

Downloaded 03 May 2010 to 171.66.16.21. Redistribution subject to ASME license or copyright; see http://www.asme.org/terms/Terms_Use.cfm

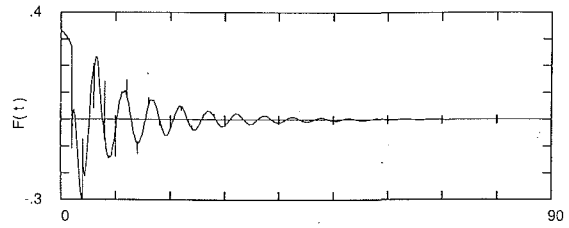

Fig. 2 Layered half space Green's function for nylon on aluminum; $h = 1$, $\nu = .4$, $\nu_S = .33$

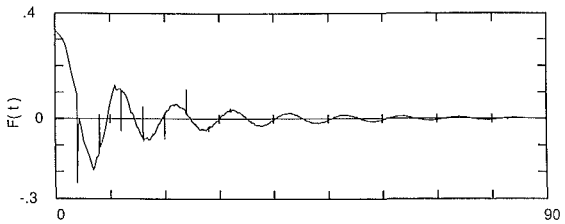

Fig. 3 Layered half space Green's function for nylon on aluminum; $h = 2$, $\nu = .4$, $\nu_S = .33$

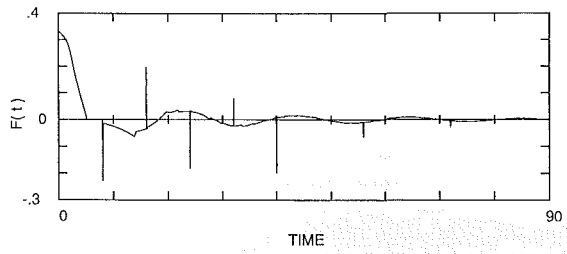

Fig. 4 Layered half space Green's function for nylon on aluminum; $h = 4$, $\nu = .4$, $\nu_S = .33$

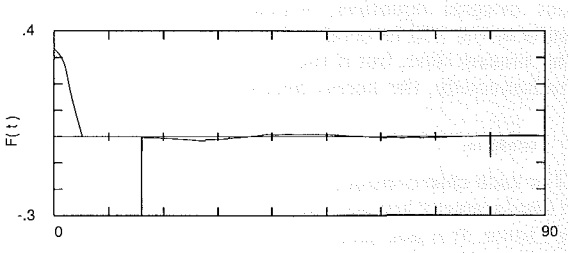

Fig. 5 Layered half space Green's function for nylon on aluminum; $h = 8$, $\nu = .4$, $h = .33$

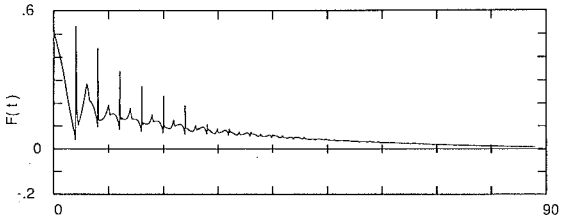

Fig. 6 Layered half space Green's function for aluminum on nylon; $h = 2$, $\nu = .33$, $\nu_S = .40$

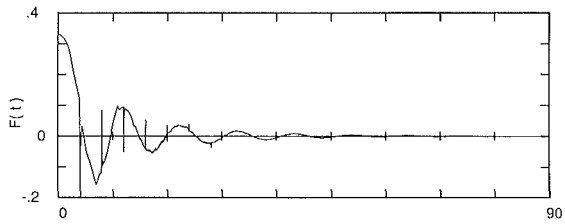

Fig. 7 Green's function for a viscoelastic layer on an elastic half space. Layer thickness is $h = 2$, nylon on aluminum; $\alpha = .75$, $\tau_\sigma = 5$

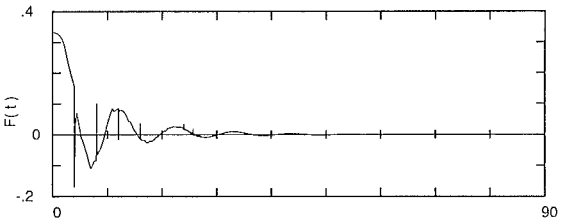

Fig. 8 Green's function for a viscoelastic layer on an elastic half space. Layer thickness is $h = 2$, nylon on aluminum; $\alpha = .50$, $\tau_\sigma = 5$

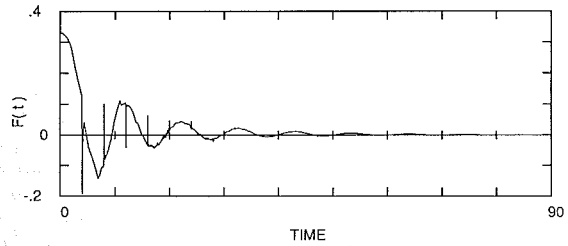

Fig. 9 Green's function for a viscoelastic layer on an elastic half space. Layer thickness is $h = 2$, nylon on aluminum; $\alpha = .50$, $\tau_\sigma = 10$

results can be obtained with this method, but the discontinuities in the Green's function from the longitudinal wave front reflections from the layer-substrate interface must be handled analytically. Downey (1987) discusses these details for the Green's function inversion, and also shows results for three other inversion schemes.

4.1 Results for the Green's Function. The Green's function is calculated for several different cases. The cases are chosen to show the range of results, but are not intended to be a complete parameter study.

The first set of results are for the elastic layered half space. The family of cases in Figs. 2–5 are for a nylon layer on an aluminum substrate, with the layer thickness ranging from $h = 1$ to $h = 8$.

It is important to remember that these Green's functions are solutions to a physical problem, the displacement response of the surface to an impulse load. The first important characteristic is the initial response. In all cases this response is identical to that for an elastic half space of the layer material (see Paper I for the analytical result). Figures 4 and 5 show this best; there is an initial jump with magnitude $2/\tilde{\kappa}^2$, and then it declines to zero at the time corresponding to the Rayleigh wave traveling across the circular region of the applied impulse (at $t = 4.25$ for $\nu = 0.33$). After this time, in the case of a half space, the response remains at zero. With the layer overlying a half space of a different material, reflections from the interface arrive at multiples of $t = 2h$ for the longitudinal wave. The magnitude and sign of this reflection are governed by the normal incidence reflection coefficient.

Using Fig. 4 for an example, the response initially looks identical to a half space, and is zero after $t = 4.25$, but at $t = 8$ the first reflection from the interface arrives, showing a sign change due to the faster substrate. This reflection is a discontinuous jump, just as the response at $t = 0$ is a positive jump. Subsequent reflections of the initial jump alternate in sign, with the magnitudes declining by the reflection coefficient each time. The response then appears as a decaying sine wave whose period is on the order of two reflections.

The next case, Fig. 6, shows the response for a hard layer on a soft substrate. The most significant change for the hard-on-soft case, compared with the soft-on-hard case is that the reflected wave has no sign change, and the response does not oscillate about zero. The decay times are similar, and the wave front arrivals are still seen as spikes.

The last set of Green's functions are for the viscoelastic

Downloaded 03 May 2010 to 171.66.16.21. Redistribution subject to ASME license or copyright; see http://www.asme.org/terms/Terms_Use.cfm

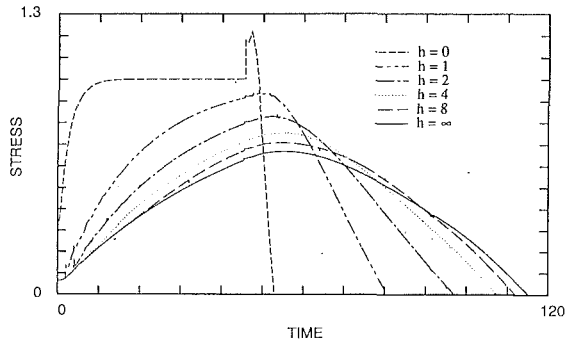

Fig. 10 Interface stress response of a rod striking a layered half space that is nylon on aluminum, and the layer thickness varies from 0 to ∞. The steel rod has length 50, a lumped mass of of 5, and an initial velocity of 100 in/s. The time scales are normalized to the nylon case.

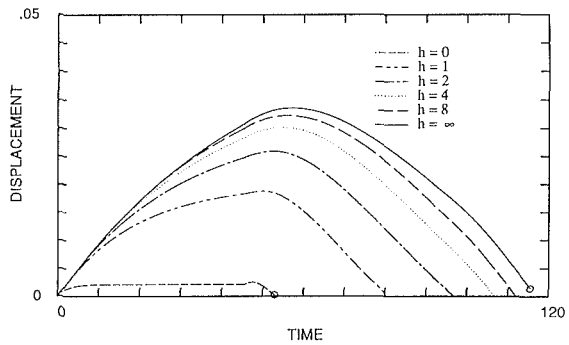

Fig. 11 Displacement response of a rod striking a layered half space that is nylon on aluminum, and the layer thickness varies from 0 to ∞. The steel rod has length 50, a lumped mass of 5, and an initial velocity of 100 in/s. The time scales are normalized to the nylon case.

layer. All have the same layer thickness, $h=2$. Results for nine cases of the two time-dependent viscoelastic parameters, α and τ_σ, were computed, but only three representative cases are shown in Figs. 7, 8, and 9. Comparing these to the corresponding elastic layer case, Fig. 3, they appear similar, but differ in several ways. The viscoelasticity produces an upward shift in the response, which is most noticable for small α. In addition, when $\alpha=0.25$, and after the oscillations die out, the response is still positive and declines smoothly to zero. Another difference is that the oscillations are damped out sooner than in the elastic case, and when τ_σ is small the response is damped out most quickly.

5 Numerical Solution of the Integral Equations

The Volterra integral equations for the contact stress and displacement are solved numerically. Baker (1977) discusses many of the available methods. The trapezoid method was used in Papers I and II for the cases of the elastic and viscoelastic half spaces. But, since that method is only weakly stable, it does not work for the layered half space because of the multiple discontinuities in the kernel.

Thus, the midpoint method is used, which is a second-order strongly stable method. In addition, a modification of the method was necessary to make it less sensitive to the wavefront discontinuities and errors in the kernel. This is a three-point smoothing of the layered half space portion of the kernal. Instead of using the Green's function values $F((2n+1)h)$, an average was used,

$$F_A((2n+1)h) \equiv \frac{1}{3}\left[F(2nh)+F((2n+1)h)+F((2n+2)h)\right]. \tag{44}$$

The disadvantage is that the layered half space Green's function must be calculated and stored for twice as many points.

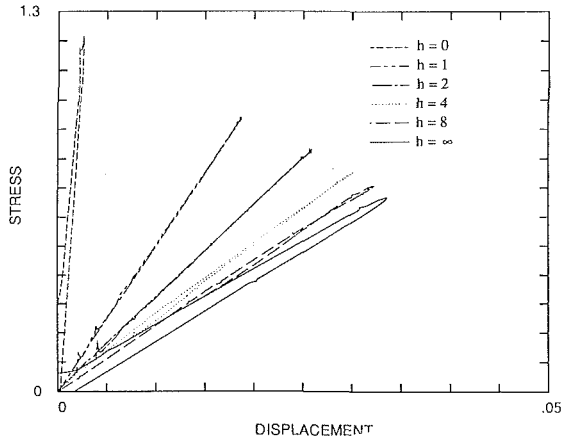

Fig. 12 Stress-displacement response of a rod striking a layered half space that is nylon on aluminum, and the layer thickness varies from 0 to ∞. The data are from Figs. 10 and 11.

The stability analysis is unaffected, since this is independent of the kernel. Consistency is also unaffected, since as h goes to zero, F_A goes to F.

In the derivation of the stress integral equation, two different integrals which use the known stress history, equations (10) and (11), were derived for the displacement. Either of these can be used to calculate the displacement of the rod tip after the stress integral equation is solved. A problem is that the displacement values are computed on even intervals of t, while the stress-time results from the integral equation solution are for odd intervals of t. This makes it difficult to plot stress versus displacement. It is simpler to solve the displacement integral equation, which provides the displacement results at the odd intervals of t. There is a small difference in computation time, but if the two integral equations are solved simultaneously, the kernel needs to be calculated only once.

6 Results

For each case considered, the contact stress history, the rod tip displacement history, and the stress-displacement response are shown. It is not necessary to show results for different impact velocities of the rod. Both the actual (dimensional) stress and displacement are proportional to the initial rod velocity. The velocity is in the nondimensionalization of the stress, and appears on the right-hand side of the displacement integral equation, scaling the displacement. For the cases shown, a fixed real velocity was used, so that initial energy of the rod was unchanged.

The first set of results for the impact on a layered half space, Figs. 10–12, demonstrate the effect of the thickness of the layer on the response. These cases have a nylon layer on an aluminum substrate, and the layer thickness varies from zero (aluminum half space) to infinity (nylon half space). The time scale for the aluminum half space case has been normalized to that of nylon, to allow comparison.

The stress and displacement response for the impact on the layer lie within the extremes for the half space results ($h=0$ and $h=\infty$), as one might expect. The stress has an initial jump of $E_1/(E_1+2/\bar{\kappa}^2)$, and the initial displacement is zero. The contact time is primarily governed by the length of the rod, the first reflection from the rod end arrives at about $t=45$, which is seen most clearly in the stress response. The stress jumps at that point because of the lumped mass on the rod's trailing end. For thicker layers, a second rod reflection occurs before bounce off. The small jumps at smaller multiples of time are due to reflections from the substrate, and they occur every $t=2h$.

Downloaded 03 May 2010 to 171.66.16.21. Redistribution subject to ASME license or copyright; see http://www.asme.org/terms/Terms_Use.cfm

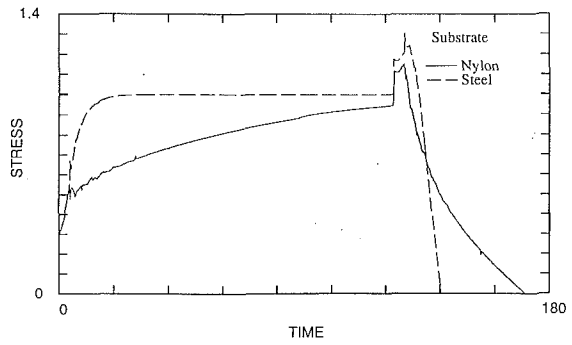

Fig. 13 Interface stress response of a rod striking a layered half space showing the effect of softer and harder substrate materials. The layer is aluminum with thickness 2, the steel rod has length 50, a lumped mass of 5, and an initial velocity of 100 in/s.

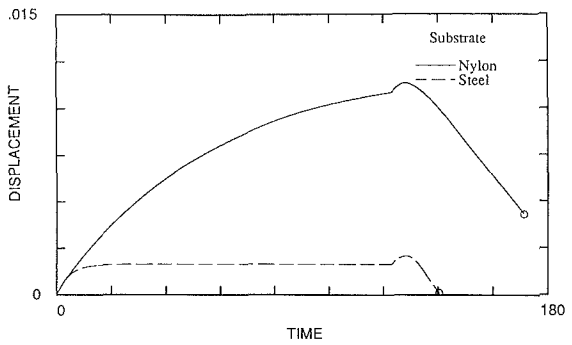

Fig. 14 Displacement response of a rod striking a layered half space showing the effect of softer and harder substrate materials. The layer is aluminum with thickness 2, the steel rod has length 50, a lumped mass of 5, and an initial velocity of 100 in/s.

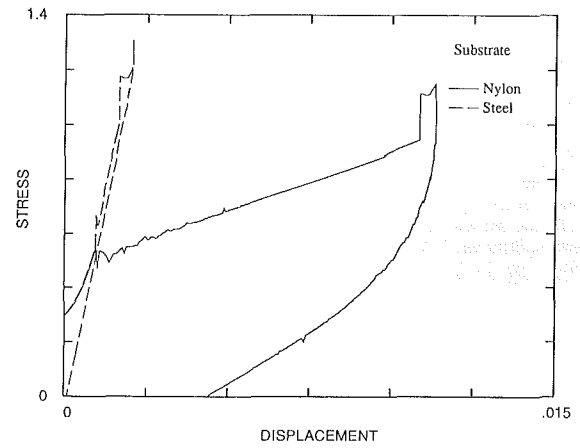

Fig. 15 Stress-displacement response of a rod striking a layered half space with softer and harder substrate materials. The data are from Figs. 13 and 14.

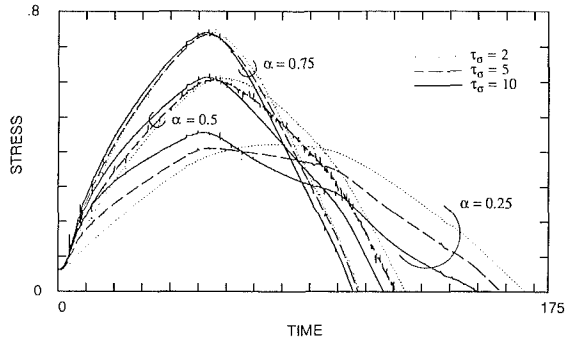

Fig. 16 Interface stress response of a rod striking a viscoelastic layered half space that is nylon on aluminum, for nine combinations of the viscoelastic parameters. The layer thickness is 2, the steel rod has length 50, a lumped mass of 5, and an initial velocity of 100 in/s.

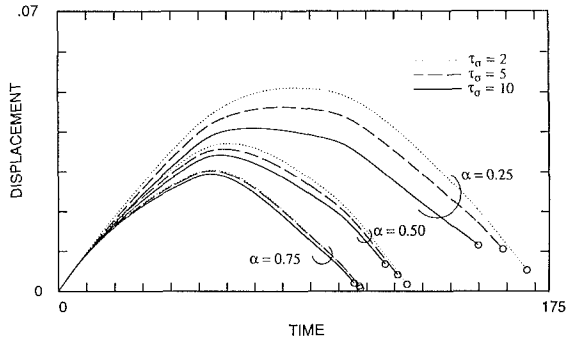

Fig. 17 Displacement response of a rod striking a viscoelastic layered half space that is nylon on aluminum, for nine combinations of the viscoelastic parameters. The layer thickness is 2, the steel rod has length 50, a lumped mass of 5, and an initial velocity of 100 in/s.

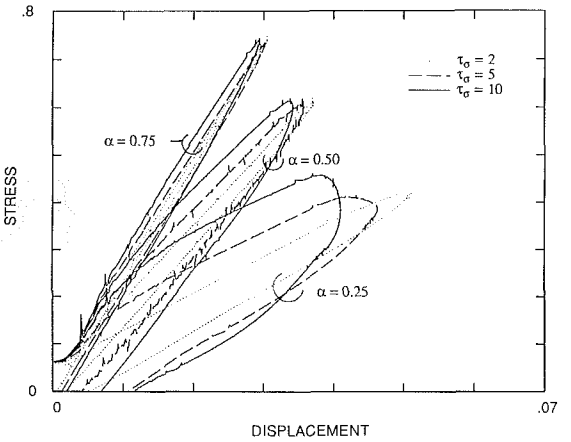

Fig. 18 Stress-displacement response of a rod striking a viscoelastic layered half space that is nylon on aluminum, for nine combinations of the viscoelastic parameters. The data are from Figs. 16 and 17.

As the layer thickness is decreased, the effective stiffness of the system increases. One can also see that the layer must be fairly thin before the result is significantly different from that for a half space of the layer material. For example, when the layer thickness is one, the response is about halfway between that for the nylon and aluminum half spaces. In addition, the layer reduces the hysteresis in the stress-displacement response (Fig. 12). Since the substrate is much stiffer than the layer, most of the wave energy is reflected back from the interface with a sign change. In the half space case, wave energy is not returned to the contact region, so more energy is lost to the rod in the impact.

When the substrate is softer than the layer, there is no sign change for the reflected waves, and energy loss is increased. Figures 13–15 show the responses for an aluminum layer over nylon, and for an aluminum layer over steel. When the first layer reflection arrives, the stress jumps downward for the case with a softer substrate. The stress-displacement result shows a large amount of hysteresis, thus the wave energy is being transmitted away from the contact region very efficiently. The hard layer on a soft substrate acts like a plate and the wave energy is propagated in bending modes of the plate.

The last set of results are for the viscoelastic layer overlying an elastic half space. Figures 16–18 are for a layer with the

Downloaded 03 May 2010 to 171.66.16.21. Redistribution subject to ASME license or copyright; see http://www.asme.org/terms/Terms_Use.cfm

modulus of nylon, thickness 2, on an aluminum substrate. There are nine combinations of the viscoelastic parameters α, and τ_σ.

The results fall naturally into three groups, identified by the value of α. The first group, for $\alpha = .75$, are closest to the elastic case; for these, τ_σ has a small effect. As α gets smaller, changes in τ_σ have a much greater effect. In all the cases, increasing τ_σ has the effect of decreasing the contact time and maximum indentation, and increasing the peak stress and hysteresis. As α decreases, the peak stress decreases, and the contact time, maximum indentation, and hysteresis all increase. The contact time goes from less than three rod reflections, to less than four, to less than five rod reflections as α goes from .75 to .5 to .25.

The parameter α has the largest effect on the maximum displacement. This is attributable to the other definition of α, the ratio of the "infinity" or long-time modulus to the instantaneous modulus. Thus smaller α means a smaller infinity modulus, since the instantaneous modulus is held constant.

The stress-displacement response, Fig. 18, exhibits the greatest difference from what was seen for the elastic layer. The amount of energy lost in the impact becomes quite large, especially for the combination of a small α and a large τ_σ. For this case, the energy lost is greater than half the energy required to reach maximum indentation.

7 Discussion and Conclusions

The results most similar to printing occur with a viscoelastic layer. Viscoelasticity increases the contact time and indentation, and decreases stress. It also increases the energy loss to the rod in the impact. This dissipation is similar in magnitude to that of actual printing, but during the loading portion of the stress-displacement curve, the viscoelastic results show a softening effect, while experimental results show stiffening as indentation increases, see Naemura and Kobayashi (1979), and Wang and Hall (1983). The unloading portion of the cycle is closer to the experimental results.

A consequence of the linearity of the problem formulation is that the stress and indentation are both directly proportional to the actual (dimensional) impact velocity of the rod. The initial rod velocity also has no effect on the contact time. This is not the case for the experimentally based model of Wang and Hall (1983), where contact time is approximately inversely proportional to the square root of the rod velocity. Thus the fact that this model is linear may be the main source of discrepancy between this solution and experiments, rather than some of the other simplifying assumptions, such as in the boundary conditions.

The effect of the layer depends on its stiffness relative to the substrate. The soft layer on hard substrate cases provide results similar to those for an elastic half space (Paper I), but there is less hysteresis, and there are small discontinuities from the substrate reflections. The hard layer on soft substrate case provides very different results. The dissipation is similar to that of the viscoelastic half space. There may be an application for this, whereby purely elastic layered materials effectively cause damping.

Acknowledgment

H. A. Downey would like to thank IBM for its support under the IBM Resident Study Program during the course of this research at U.C. Berkeley.

References

Baker, C. T. H., 1977, *The Numerical Treatment of Integral Equations*, Oxford University Press, Oxford, pp. 896–914.

Brekhovskikh, L. M., 1980, *Waves in Layered Media*, Academic Press, New York, pp. 53–57.

Christensen, R. M., 1971, *Theory of Viscoelasticity*, Academic Press, New York, pp. 41–43.

Crump, K. S., 1976, "Numerical Inversion of Laplace Transforms Using a Fourier Series Approximation," *Journal ACM*, Vol. 23, No. 1, pp. 89–96.

Davies, B., and Martin, B., 1979, "Numerical Inversion of the Laplace Transform: A Survey and Comparison of Methods," *J. Comp. Phys.*, Vol. 33, pp. 1–32.

Downey, H. A., 1987, "The Normal Impact of a Rod-Mass System on a Viscoelastic Layered Half Space; A Model for Wire-Matrix Printing," Ph.D. Dissertation, University of California, Berkeley.

Downey, H. A., and Bogy, D. B., 1987a, "The Normal Impact on an Elastic Half Space of an Elastic Rod-Mass System," ASME JOURNAL OF APPLIED MECHANICS, Vol. 54, No. 2, pp. 359–366, (Paper I).

Downey, H. A., and Bogy, D. B., 1987b, "The Normal Impact of an Elastic Rod-Mass System on a Viscoelastic Half Space," ASME JOURNAL OF APPLIED MECHANICS, Vol. 54, No. 2, pp. 367–372, (Paper II).

Hearn, A. C., ed., 1983, *REDUCE User's Manual*, The Rand Corporation, Santa Monica, CA, Ver. 3.0.

Naemura, A., and Kobayashi, M., 1979, "Impact Printing Fundamental Properties," *Review of the Electrical Communication Laboratories, Tokyo*, Vol. 27, No. 9–10, pp. 864–875.

Papoulis, A., 1956, "A New Method of Inversion of the Laplace Transform," *Quart. Appl. Math.*, Vol. 14, pp. 405–414.

Wang, H. C., and Hall, S. A., 1983, "Paper-Function Model for Wire-Matrix Printing," *Proceedings of the Society for Information Display*, Vol. 24, No. 1, pp. 13–15.

Downloaded 03 May 2010 to 171.66.16.21. Redistribution subject to ASME license or copyright; see http://www.asme.org/terms/Terms_Use.cfm

Low Velocity Impact of an Elastic Plate Resting on Sand

H. L. Chen

W. Lin

L. M. Keer
Fellow ASME.

S. P. Shah

Northwestern University
Evanston, IL 60208

This article describes the measurement and analysis of plate and soil response under low velocity impact. A free-drop impact system was developed to generate the dynamic loading on the plate free surface. The radial strain of the target plate, the longitudinal wave speed and the acceleration of the sand were measured. The measured wave speed data were then used to evaluate the elastic constants of the sand. An analysis based on linear elastodynamics was developed for transient waves on a thin plate resting on an elastic half space. The contact stresses and the normal displacements of the plate were taken as unknown functions. The contact between the plate and the half space were assumed frictionless. The experimental results of the radial strain at the bottom of the target plate and the acceleration of the sand beneath the center of the target plate were compared with the analytical solution. The arrival time, the duration, and the magnitude have good correlation between the analysis and experiment. The overall results appear good and provide an understanding of the transmission of impact load through the plate, the interaction between the plate and the sand, and the propagation of the load into the sand.

Introduction

An impulsive loading can be produced by impact where the duration of the impulse is on the order of microseconds. The particular problem of a circular aluminum plate impacted at its center by a steel ball was considered in this study. The contact duration as well as the radius of the contact area were measured and compared with an estimation based upon a Hertzian contact assumption. An excellent review of the works related to experimental studies of wave propagation due to low velocity impact was given by Al-Mousawi (1986). A detailed study of low velocity impact of circular plates was conducted by Greszczuk (1982).

In this paper, an analysis based on linear elastodynamics for the transient waves on an elastic plate which rests on an elastic half space (sand) was developed to understand the applied loading, the interfacial conditions between plate and sand, the validity of the assumed constitutive law for sand and the free field response. Two difficulties addressed in this study were the measurement of the response of the soil, and in adopting an appropriate constitutive law for the soil. The contact stresses and the normal displacements of the plate were taken as unknown functions. The contact between the plate and the half space was assumed frictionless. The measured responses of the radial strains of the target plate, the longitudinal wave speeds, and the accelerations of sand are compared with analytical results to provide a better understanding of how the dynamic load is transmitted through a plate into the soil and how well the elastic half space assumption can be used to model the sand. A review of the analytical approaches used in this study are described as follows.

By assuming the distribution of the contact pressure between the foundation and the soil, Reissner and Sagoci (1944), Quinlan (1954), Sung (1954), Arnold et al. (1955), and Bycroft (1956) considered the dynamic response of a rigid disc placed on an elastic half space based on Lamb's (1904) solution for the elastic half space. Collins (1962), Robertson (1966), Karasudhi et al. (1968), Luco and Westmann (1972), and Veletsos and Verbic (1974) studied the vertical, tangential, and rocking oscillations of a rigid strip on an elastic or viscoelastic half space by solving the actual mixed boundary value problem, either through application of integral transforms or by reduction of the governing equations to an integral equation (essentially a boundary element formulation). A detailed review of pertinent research on the dynamic response of rigid footings can be found in Richard et al. (1970) and Luco et al. (1971, 1987).

The assumption of a rigid foundation may be inappropriate for studying the dynamic interaction between the soil and a structure which has large planar dimensions compared with the incident wave length. The response of an infinite and a semi-infinite flexural plate in smooth contact with an elastic half space subjected to harmonic plane waves was solved by Achenbach et al. (1966), and Freund and Achenbach (1968). In 1973, Oien expanded the motion of the plate in a series of vibrational modes and obtained the response of the plate on the elastic half space using the Bubnov-Galerkin method. In 1978, Lin presented an integral equation approach for the case of a flexible circular plate having a rigid perimeter. Recently, a similar approach was adopted by Iguchi and Luco (1982) to

Contributed by the Applied Mechanics Division of THE AMERICAN SOCIETY OF MECHANICAL ENGINEERS for presentation at the Joint ASCE/ASME Applied Mechanics, Biomechanics, and Fluids Engineering Conference, San Diego, CA, July 9 to 12, 1989.

Discussion on this paper should be addressed to the Editorial Department, ASME, United Engineering Center, 345 East 47th Street, New York, N.Y. 10017, and will be accepted until two months after final publication of the paper itself in the JOURNAL OF APPLIED MECHANICS. Manuscript received by ASME Applied Mechanics Division, December 30, 1987; final revision, April 12, 1988.

Paper No. 89-APM-13.

Copyright © 1988 by ASME

Downloaded 03 May 2010 to 171.66.16.21. Redistribution subject to ASME license or copyright; see http://www.asme.org/terms/Terms_Use.cfm

Table 1 Contact duration and radius of contact area

Velocity of Impactor (m/sec)	Target Plate (Thickness(cm) × Diameter(cm))	Contact Duration T_o(msec)) Measured/Calculated	Contact Radius a(cm) Measured/Calculated
2.95	Steel(2.54 × 15.24)	0.169/0.135	0.160/0.180
2.95	Aluminum(1.27 × 15.24)	0.238/0.174	0.175/0.204
5.06	Steel(2.54 × 15.24)	0.132/0.121	0.263/0.222
5.06	Aluminum(2.54 × 20.32)	0.180/0.156	0.275/0.253

1 Impactor: 4.76 cm diameter steel ball (E52100)
2 Calculated by Hertzian Contact Law

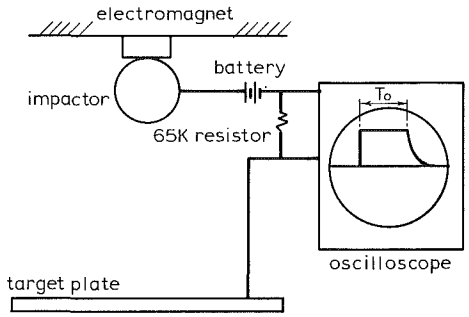

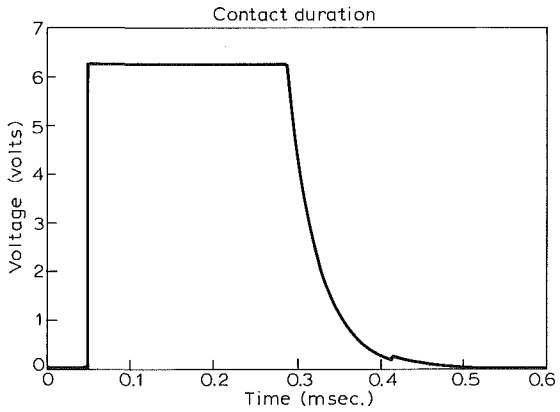

Fig. 1 Test set-up for measuring contact duration

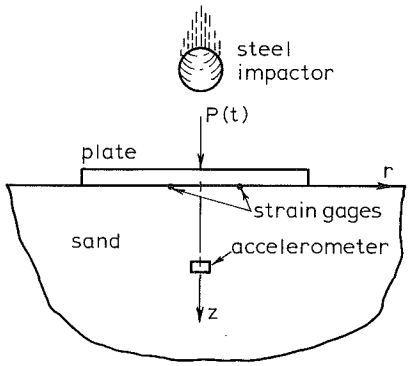

Fig. 2 Test configuration for measuring strain and acceleration

solve the dynamic response of a massless flexible circular plate with a rigid core supported on a layered viscoelastic half space subjected to harmonic vertical and rocking excitation. Krenk and Schmidt (1981) used a polynomial expansion of the contact stress and the normal displacement of the plate to obtain the response of an oscillating elastic circular plate on an elastic half space. Whittaker and Christiano (1982), who studied the dynamic behavior of rectangular plates on an elastic half space, combined the discretized Lamb's solutions with the plate treated by finite element method.

The dynamic response of an elastic plate resting on sand is a practical topic for investigation that covers a wide range of applications. First, the plate can be viewed as a footing of a structure, which has significance for foundation-vibration studies. Secondly, the finite plate response due to an impact force is a fundamental problem in structural design. Morever, investigating the impact force itself is also important and interesting since an accurate knowledge of the live load on the impacted structure enables a better design and prediction of the damage to the structure. Finally, it is important to understand fully the impact loading transmission through the soil.

Test Set-Up

For the impact test, the duration and the contact area can be predicted from a theoretical approach based on the assumptions of Hertzian contact. The impactor is a steel ball and the target is either a steel or an aluminum plate placed over Ottawa 20–30 standard sand. The test data were recorded by a Nicolet 4094 Digital oscilloscope with XF-44 Dual Disk Recorder.

The test set-up to measure the contact duration is shown in Fig. 1. By using a large resistor to increase the voltage jump, the contact duration was measured from the time of first contact with the target plate until contact was lost. The contact duration, T_o, is also shown in Fig. 1. The experimentally measured contact areas are taken as the plastic deformed region of the plate surface. The measured values of contact duration and radius of contact area are given in Table 1.

In order to understand the loading function, two strain gages were placed at the bottom of the target plate. One was placed 1.27 cm from the center of the plate and the other 1.91 cm from the center (Fig. 2). A Wheatstone Bridge Circuit was used for each strain measurement. Since the total experimental duration was within a few milliseconds, temperature compensation was not applied. The length of the strain gage was 0.8 mm.

The test set-up to determine the wave speed of the sand is shown in Fig. 3. Three piezoelectric accelerometers (Glennite Model A30T) were buried in the sand. The tank was partially filled with sand which was compacted at approximately every 5 cm. The compaction was done by 25 uniform strokes with a 24.5N hammer and 30 cm free drop. After the compaction, the total density was calculated by the measured weight and volume. The accelerometers were carefully placed and leveled in order to get excitations only in the vertical direction. The surface of the sand was covered with the target plate which was leveled. The water content of the sand was 0.05 percent. The sand was fairly condensed with a void ratio of 0.492. The accelerations were recorded after each impact by using a sampling rate of 1 μsec per point. Three to five tests were conducted for each test configuration to verify the reproducibility of the data.

The way to locate the axis of impact loading is described next. The sand bed was at a depth of about 7 cm and well compacted. An accelerometer was placed at the center of the sand bed. A plumb bob was used to aim the accelerometer; the plumbline was marked as a ruler. To ensure that the accelerometer is horizontal, a bull's-eye level was placed on its

Downloaded 03 May 2010 to 171.66.16.21. Redistribution subject to ASME license or copyright; see http://www.asme.org/terms/Terms_Use.cfm

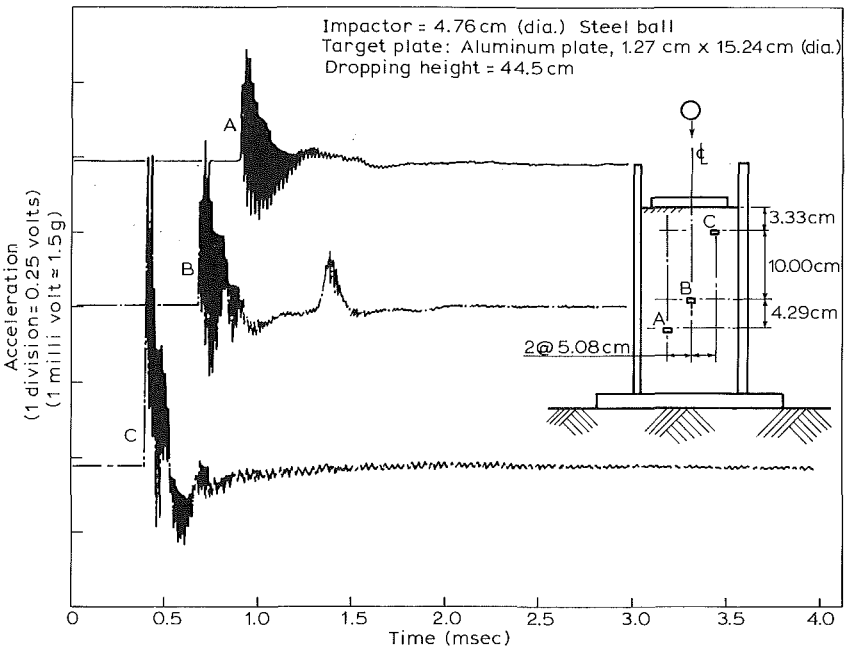

Fig. 3 Typical time history of acceleration in sand

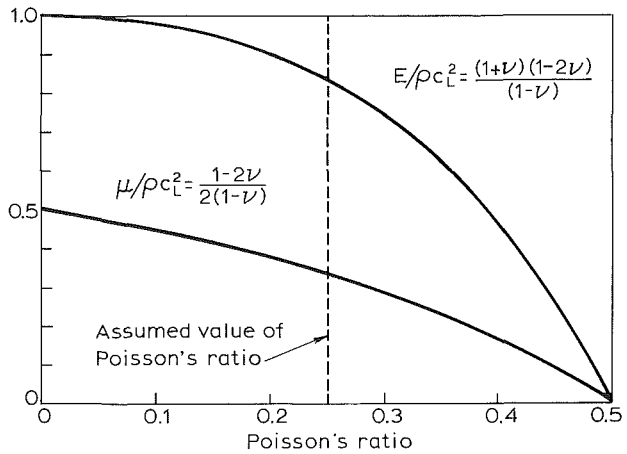

Fig. 4 Influence of Poisson's ratio

surface. Then, the plumb bob was pulled up by the plumb line through the pulley which was assumed fixed. After the accelerometer was covered by sand and the sand was compacted, an aluminum plate was used to cover the sand. The center of the plate was located by the plumb bob and this was taken as the dropping point. The plate was leveled and the dropping axis was the same as the plumb line axis.

It should be noted that after each test, the position of the accelerometer was measured again when the sand was ladled out. The accelerometer settled about 3.2 mm for each 7 cm of buried depth and caused about 5 percent error for determining the wave speed of the sand.

Analysis

To analyze the results obtained from the experimental setup as shown in Fig. 2, three modeling tasks were performed: An estimate was made of the impact loading, the interfacial conditions between the target plate and sand was determined, and the properties of the sand were evaluated. Among these three, accurate modeling of the properties of the sand is perhaps the most difficult, even in the "dry" condition.

(*a*) Modeling of the Sand. A large, short duration load applied to sand may cause it to crush, deform, slide, and change its void ratio. Such complex behavior is far beyond the capability that elasticity and viscoplastic modeling can accurately handle. Even if the properties of sand are assumed fixed within the framework of elasticity and plasticity, the sand's nonlinearity must be taken into account, since the secant modulus of sand depends highly on the stress level, loading rate, and loading history (see Kiger et al., 1984). As a consequence, when an impact which may cause a highly nonuniform stress distribution is applied, the secant shear and Young's moduli will also be highly nonuniform. Thus, an effective and efficient calculation may prove difficult to obtain. Furthermore, it is noted that unloading must be taken into account when the peak has passed.

Sand can not support tensile loads. In order to avoid the consequences of this property and strengthen the analysis, the experimental program has been designed to subject the sand only to compressive loads. By putting a plate on the surface of the sand to provide sufficient compression, the separation between the sand particles can be prevented. Thus it is assumed that no tensile force exists in the sand during the loading process.

To obtain an analytical result as a first-order approximation, sand was modeled as an elastic, isotropic, and homogeneous medium. The related elastic properties can be determined from the observed wave speed. This idea was suggested in a study by Lambe and Whitman (1969) where they evaluated the secant modulus of Ottawa sand by using the wave speed under different initial stress levels. The same concept is used here to estimate the elastic constants under the current loading rate in an average sense. Figure 3 is the recorded response of the accelerometer at various depths. From this figure, the longitudinal wave speed, C_L, can be evaluated by dividing the distance between two accelerometers by the difference of the arrival times. The shear wave speed can not be obtained since the shear wave front has not separated from the longitudinal wave in the time frame of measurements. Thus, a value for Poisson's ratio had to be assumed to evaluate the Young's modulus E and shear modulus μ. In Fig. 4, the influence of Poisson's ratio, ν, on the moduli are plotted. A summary of sand properties are given in Table 2.

(*b*) Impact Analysis. As shown in Fig. 2, the impact force to be transmitted to sand is provided from the dropped ball. The considerations on this impact force are threefold.

Downloaded 03 May 2010 to 171.66.16.21. Redistribution subject to ASME license or copyright; see http://www.asme.org/terms/Terms_Use.cfm

Table 2 Material properties

	ν	ρ (kg/m^3)	C_L (m/sec)	C_T (m/sec)	E (MPa)
Aluminum	1/3	2821 (2700)[1]	6054 (6300)[1]	3027 (3100)[1]	68928 (69192)
Ottawa[2] 20-30 Sand	1/4 (assumed)	1776 (1762)[3]	241 (256)[3]	139 (158)[4]	86 (110)

1 Achenbach, 1980
2 Void Ratio $e=0.492$
3 Lambe and Whitman, 1969
4 Richart et al., 1970

First, to study the wave phenomenon in soil-structure interaction, the impact duration, T_o, multiplied by the longitudinal wave speed of sand, should be of the same order of magnitude as the depth of the buried structure or instrument. Second, to simplify the calculation, the contact area should be small enough that the impact loading can be represented as a point load, i.e.,

$$P(r,t)=p(t)\delta(r)/2\pi r \tag{1}$$

where $\delta(r)$ is the delta function.
Finally, the point force, $p(t)$ should be able to be assumed or verified reasonably well.

From the Hertzian contact assumptions, the impact duration is given as (Timoshenko and Goodier, 1951, p. 421)

$$T_o=2.94\,(5M_b/4n)^{2/5}/(2gH)^{1/5} \tag{2}$$

where M_b is the mass of the ball; H is the dropping height, g is the value of acceleration of gravity;

$$n=\frac{4/3R_b^{1/2}}{(1-\nu_b^2)/E_b+(1-\nu_p^2)/E_p} \tag{3}$$

R_b is the radius of the ball; and E_b, ν_b, and E_p and ν_p are the Young's modulus and Poisson's ratio of the ball and the target plate, respectively. The maximum contact radius is

$$a=R_b^{1/2}(5gHM_b/2n)^{1/5} \tag{4}$$

In Table 1, the measured contact radius and contact duration are compared to those evaluated and are seen to be reasonably close to the theoretical predictions. The measured contact duration is expected to be longer than the Hertzian contact duration due to the boundary effect (Greszczuk, 1982). Since the contact radius a is much smaller than the buried depth of the accelerometer, the acceleration in the sand may be evaluated by assuming it arises from a point force on the plate. However, a is not small compared to h, the thickness of the plate, and r, the distance between the strain gage and the center of the plate. Thus, some inaccuracy is introduced when the strain is evaluated by using the point force assumption. As can be seen from Table 1, the contact duration is of the right order of magnitude for investigating the wave phenomenum in this study.

(c) Analysis of System. The target plate was relatively thick to prevent its separation from the foundation and to prevent permanent deformation in the plate except at the contact point. However, a layer model is unsuitable to analyze the target plate because the contact duration, T_o, is too long compared to the time for a longitudinal wave to travel from the top to the bottom of the plate. Thus, a thin plate model was used to simulate the response of the target plate. The governing equation is

$$D\nabla^4 w+\rho h\partial^2 w/\partial t^2=p(t)\delta(r)/2\pi r-q(r,t) \tag{4a}$$

$$D=E_p h^3/12(1-\nu_p^2) \tag{4b}$$

where D, w, and ρ are the rigidity, deflection, and density of the plate, respectively; ∇^4 is a biharmonic operator, $p(t)$ is the impact force, and $q(r, t)$ is the interfacial normal traction. The transformed solution of equation (4) has the following form:

$$\bar{w}^0=(\bar{p}/2\pi-\bar{q}^0)/D(\xi^4-\lambda^4)+B_1+B_2 \tag{5}$$

Here, a superscript bar denotes a Fourier transform and superscript zero denotes a Hankel transform, i.e.,

$$\bar{w}=\int_{-\infty}^{\infty} we^{i\omega t}dt,\quad \bar{w}^0=\int_0^{\infty}\bar{w}J_o(\xi r)rdr \tag{6),(7}$$

and

$$\lambda^4=\rho\omega^2 h/D \tag{8}$$

The terms B_1 and B_2, can be determined from the boundary conditions of the target plate, i.e., vanishing shear force and bending moment at $r=R$.

$$\frac{\partial}{\partial r}\left(\frac{\partial^2\bar{w}}{\partial r^2}+\frac{1}{r}\frac{\partial\bar{w}}{\partial r}\right)\Big|_{r=R}=0 \tag{9}$$

$$\left(\frac{\partial^2\bar{w}}{\partial r^2}+\nu_p\frac{1}{r}\frac{\partial\bar{w}}{\partial r}\right)\Big|_{r=R}=0 \tag{10}$$

Next, the transfer of load into the sand is considered. Two extra interfacial conditions were assumed. First, no separation was assumed between the plate and sand, leading to continuous normal traction and displacement across the interface. Next, the friction force between the plate and sand was assumed negligible when compared to the interfacial normal traction. This condition could be modified, for example, by assuming that the interfacial shear force is proportional to the interfacial normal force.

The response in the elastic half space due to a normal traction applied on the surfaces is Lamb's problem. The transformed normal displacement in sand due to q is

$$\bar{w}^0=\bar{q}^0(\alpha/\mu\Omega)[(2\xi^2-k_T^2)e^{-\alpha z}-2\xi^2 e^{-\beta z}] \tag{11}$$

where,

$$\alpha=(\xi^2-k_L{}^2)^{1/2} \tag{11a}$$

$$\beta=(\xi^2-k_T{}^2)^{1/2} \tag{11b}$$

$$\Omega=(2\xi^2-k_T{}^2)^2-4\xi^2\alpha\beta \tag{11c}$$

$$k_L=\omega/C_L \tag{11d}$$

$$K_T=\omega/C_T \tag{11f}$$

C_L and C_T are the longitudinal and shear wave speeds in the sand.

The interfacial traction $\bar{q}^0$ can be obtained by eliminating $\bar{w}^o$ in equation (5) and equation (11). The result is

$$\bar{q}^0=\frac{\mu\Omega}{\mu\Omega-k_T^2\alpha D(\xi^4-\lambda^4)}\left[\frac{\bar{P}}{2\pi}+(B_1+B_2)D(\xi^4-\lambda^4)\right] \tag{12}$$

It should be noted that B_1 and B_2 contain the integral form of $\bar{q}$. Hence a numerical method must be used to solve for $\bar{q}^o$.

Downloaded 03 May 2010 to 171.66.16.21. Redistribution subject to ASME license or copyright; see http://www.asme.org/terms/Terms_Use.cfm

However, as a first order approximation, R was assumed so large (infinite plate) that B_1 and B_2 approach 0. If R is considered as moderately large, $\bar{q}^o$ may be obtained by the method of substitution. Whether R can be considered large enough depends also on the range of the loading frequency. After $\bar{q}^o$ is obtained, $\bar{w}^0$ is evaluated via equation (11) and $\bar{q}$ is obtained by evaluating the Hankel integral. The numerical value of acceleration of sand in the frequency domain is $-\omega^2\bar{w}$. Also, the strain along the bottom of the plate can be evaluated by the following formula:

$$\bar{\epsilon}_r = -\frac{h}{2}\frac{\partial^2 \bar{w}}{\partial r^2} \tag{13}$$

Numerical and Experimental Results

(a) Radial Strain on the Plate. The first part of the numerical results is the computation of the Green's function of strain along the bottom of the plate. Mathematically, the strain caused by the impact force is written as:

$$\bar{\epsilon}_r(r, \omega) = G(r, \omega) * \bar{p}(\omega) \tag{14}$$

where G is the Green's function. In Fig. 5, the spectrum of $|G(r,\omega)|$ is plotted at various locations along the bottom of an aluminum plate with $h = 1.27$ cm and $R = \infty$. The strain at $r = 0$ is not plotted because the deflection due to a point load contains a $r^2\log(r)$ term, thus, the strain at $r = 0$ has a logarithmic singularity. Strain gages were put at $r = 1.27$ cm and 1.91 cm such that the following conditions were met: $a \cong 0.2$ cm $< h = 1.27$ cm $\leq r \ll R = 7.62$ cm. The influence of the size of strain gages and the deviation of impact point in the experiment are not important because they are smaller than the maximum contact radius. For the static case of an infinite plate rested on an elastic half space, there is an integral form available for the deflection curve from Timoshenko and Woinowsky-Krieger (1959).

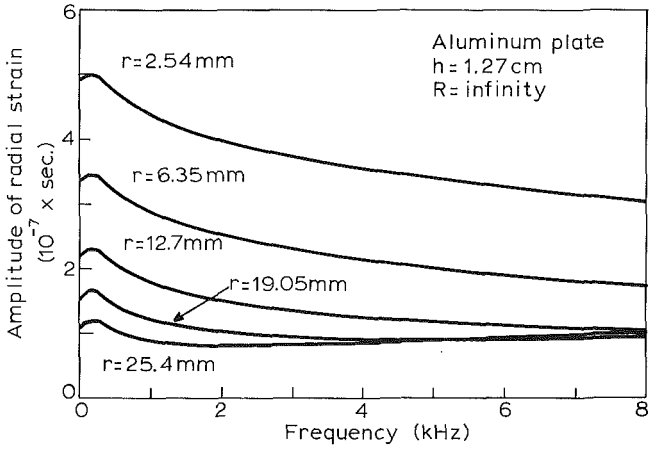

Fig. 5 Spectrum of radial strain due to a point force

$$w(r) = \frac{Pl_0^2}{2\pi D}\int_0^\infty \frac{J_0(\zeta r/l_0)}{1+\zeta^3}d\zeta, \tag{15}$$

where,

$$l_0^3 = \frac{2D(1-\nu^2)}{E}$$

After differentiating the Bessel function twice with respect to r, the strain can be evaluated; this evaluation provides a check of the numerical results at $\omega = 0$. Also, it is noted that the ratio of the amplitude of the strain at $r = 76.2$ mm (calculated but not shown in Fig. 5) to the strain at $r = 12.7$ mm is only 0.11 at $\omega = 0$, which implies that the infinite plate assumption is valid for the static case. Next, the curves in Fig. 5 are ascending as the frequency slightly increases because there is a pole along the positive real axis at a frequency of 350 Hz. Finally, it is observed that the boundary effect becomes larger as the frequency becomes higher. At frequency equal to 4 kHz, the ratio of amplitude of the strain at $r = 76.2$ mm to the strain at $r = 12.7$ mm is 0.75.

Since $G(r,\omega)$ is based on several assumptions such as point impact, an infinite plate, and a frictionless interfacial condition along with uncertainties in soil properties, to invert $p(t)$ from the strain gage measurement is not reliable. Consequently, $p(t)$ is estimated in the following way. First, assume

$$p(t) = Af(t) \tag{16a}$$

where $f(t)$ is a monopeak, nonzero smooth shape function in the interval $0 < t < T_0$. Then, the amplitude, A, is determined from a momentum balance, i.e.,

$$A = M_b(2gH)^{1/2} \Big/ \int_0^{T_0} f(t)dt \tag{16b}$$

In Fig. 6, three $f(t)$ curves are plotted. The curve No. 1 is the Hanning function. The curve No. 2 is recommended by

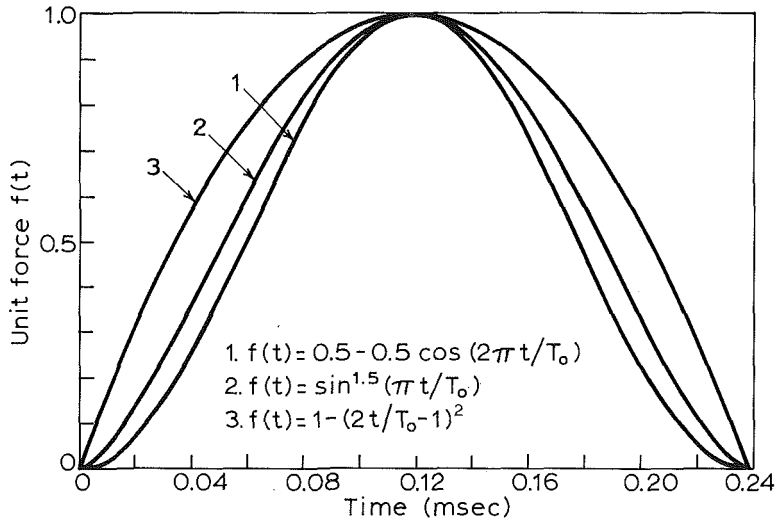

Fig. 6 Loading shape function

Downloaded 03 May 2010 to 171.66.16.21. Redistribution subject to ASME license or copyright; see http://www.asme.org/terms/Terms_Use.cfm

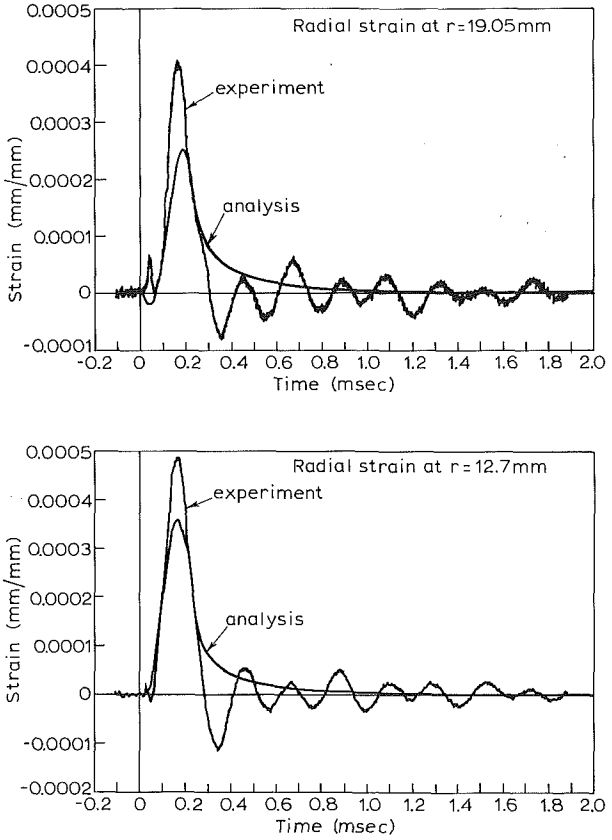

Fig. 7 Comparison of simulated strains with experimental results

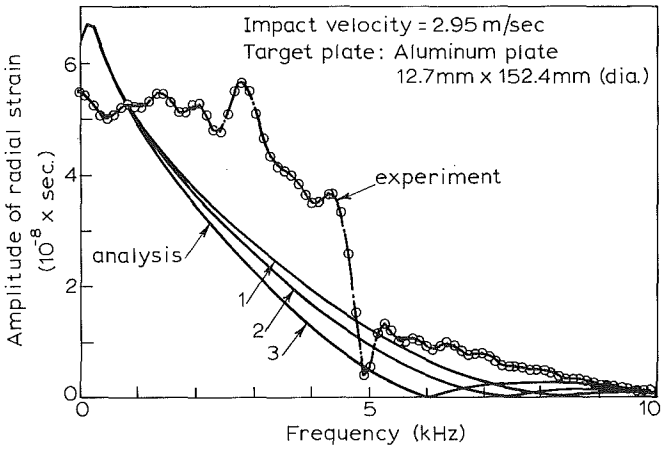

Fig. 8 Spectrum of strain at $r = 1.27$ cm

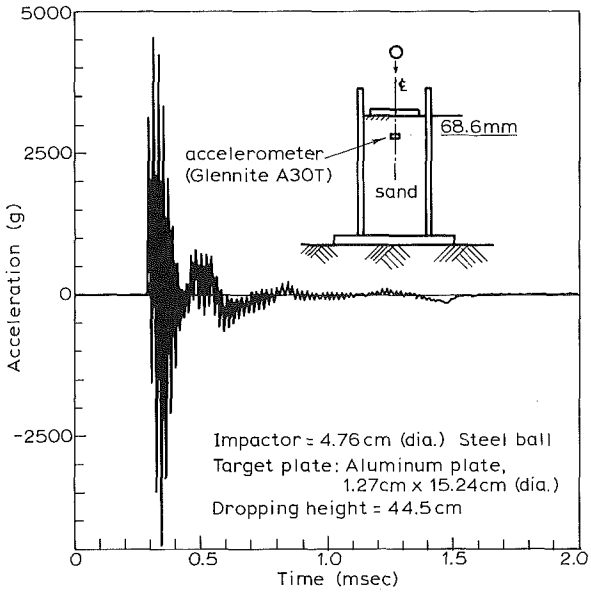

Fig. 9 Measured acceleration history

Gresczuk (1982) to approximate the Hertzian contact force. The curve No. 3 is the parabolic function. It is noted that the first two curves are very close.

Next, the impact of a steel ball dropped from $H = 44.5$ cm, hitting an aluminum plate $h = 1.27$ cm and $R = 7.62$ cm, is considered. The impact duration is 0.238 msec and the amplitude is evaluated via equation (16*b*). From $p(t)$, the Fourier transform $\ddot{p}(\omega)$ is evaluated and multiplied with the Green's function. Thus, the numerical result for the strain in the frequency domain is obtained. After applying the inverse Fast Fourier Transform, the time domain response is obtained. In Fig. 7, the measured strain histories at $r = 1.27$ cm and $r = 1.91$ cm are plotted and compared with the simulated strains assuming $f(t)$ is the Hanning function. The general agreement is satisfactory. The oscillations in the experimental results are due to the finite plate vibration.

To obtain the spectrum of measured strain, FFT was applied to the experimental results. At $\omega = 0$, there is good agreement between experimental results and numerical results (Fig. 8). As was mentioned previously, the infinite plate assumption is valid in static cases. It should be noted that all three numerical curves corresponding with three $f(t)$ from Fig. 6, have the same value at $\omega = 0$ because they have to satisfy momentum balance. However, there are large differences between the numerical results and experimental results between about 2 to 5 kHz range. The reason is that the numerical results are evaluated using an infinite plate assumption while the experimental results are for a finite plate. If the finite plate vibration is considered, the natural frequency of the plate is of the form

$$\omega = \eta^2 \left(\frac{D}{\rho_p h R^4} \right)^{1/2} \tag{17}$$

where η^2 is a constant which depends only on the boundary conditions at $r = R$. For a completely free circular plate, the first root $\eta^2 = 9.084$ (Leissa, 1961) with corresponding frequency of 4.78 kHz is the same as the frequency of the oscillation which was observed after the loading (Fig. 7). To determine $f(t)$ more accurately, a finite plate analysis must be performed.

(*b*) Acceleration in the Sand. The next set of results describe the acceleration in the sand. The impactor is a 4.76 cm diameter steel ball and is dropped from $H = 44.5$ cm. The target plate is an aluminum plate with $h = 1.27$ cm and $R = 7.62$ cm. Only the Hanning function is considered for the loading shape function. The testing geometry was similar as shown in Fig. 3. The accelerometers A and C were removed and reburied B at depth $d = 6.86$ cm. Figure 9 is the record of acceleration. The corresponding spectrum is plotted in Fig. 10.

The Glennite Model A30T piezoelectric accelerometer is a general-purpose accelerometer for shock acceleration measurement from a fraction of 10 g to 10,000 g. It was calibrated with a response of 1.46 g/mv. The size of the accelerometer is 1.8 cm × 2.5 cm × 2.5 cm and its natural frequency is 50 kHz. The basic difficulty in choosing the accelerometer for this experiment is that the size of the accelerometer must be very small; otherwise, a large scale test must be performed. However, due to its availability and con-

Downloaded 03 May 2010 to 171.66.16.21. Redistribution subject to ASME license or copyright; see http://www.asme.org/terms/Terms_Use.cfm

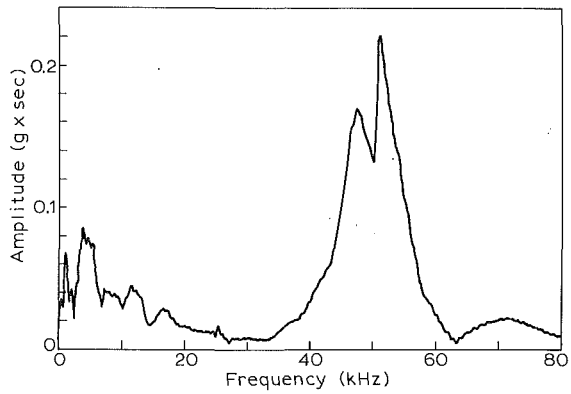

Fig. 10 Complete spectrum of measured acceleration

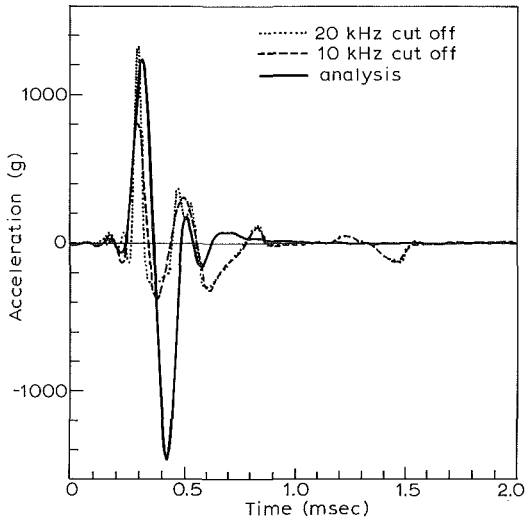

Fig. 11 Simulated acceleration and measured acceleration

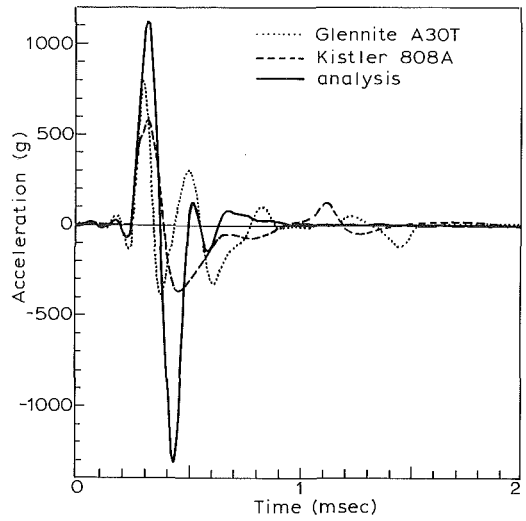

Fig. 12 Acceleration measured from different accelerometers

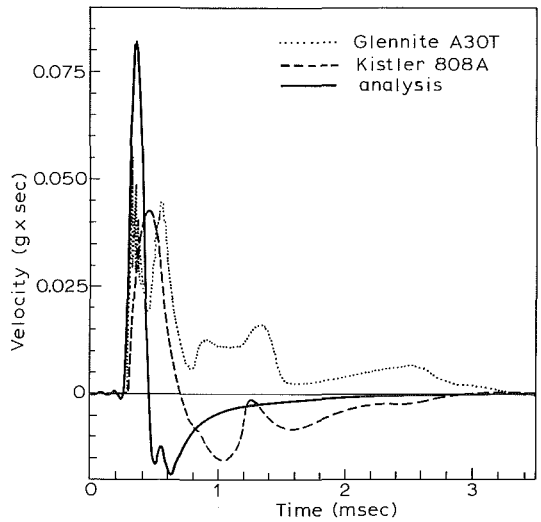

Fig. 13 Simulated velocity history and integrated velocity history

venience, the Glennite A30T was used in measuring the wave speed of the sand. It is noted that the arrival time was distinct (Fig. 3) and the response of accelerometer was within the right order of magnitude. In Fig. 11, the simulated acceleration and the measured acceleration are plotted. For the dotted line, the frequency above 20 kHz has been filtered out; for the dashed line, the frequency above 10 kHz has been filtered. It is noted that the peak positive acceleration is quite sensitive to the cutoff frequency and the experimental result is comparable to its numerical simulation.

It was noted from the strain measurement (Fig. 8) that the frequency range of the impact loading was within 10 kHz. Therefore, the 50 kHz noise in the acceleration measurements (shown in Fig. 10) implied some problems with accelerometer. In Fig. 12, the simulated acceleration history and the measured acceleration history obtained by a different accelerometer are plotted. A smaller accelerometer was used. The Kistler model 808A Quartz accelerometer with a size of 1.27 cm (hex.) $\times$ 2.29 cm is a general purpose piezoelectric accelerometer for vibration, shock and acceleration measurements with a full scale range from 1 g to 10,000 g. By using this accelerometer, the measured acceleration in frequency domain shows almost no amplitude after 10 kHz. This coincided with the strain measurements.

There are three points to be noted in Fig. 12. First, the arrival time of the simulated acceleration is quite satisfactory, which provides an indirect check of the simulated acceleration spectrum. Second, the acceleration is very small after 1.6 msec for all 3 curves. This coincides with the duration measured by the strain gages. Finally, the numerical peak negative acceleration is quite close to the peak positive acceleration, while the measured peak negative acceleration is significantly less than the peak positive acceleration. Since negative acceleration means the velocity is decreasing as are the stresses, the negative acceleration period is an unloading period. Thus, the significant reduction in measured peak negative acceleration implies that the stress-strain relationship in the unloading phase may be quite different from the loading phase. Therefore, the current linear elastic assumption may be violated. This last point can be clarified after the finite plate analysis is performed.

In Fig. 13, the velocity histories, which are obtained from the integration of simulated and measured accelerations without filtering out any frequency component, are plotted. As a check, all three velocity curves become 0 at around 3 msec. In Fig. 14, the spectrums of simulated acceleration and measured accelerations are plotted. The agreement is good at frequencies up to 1.5 kHz. It may be possible to have better correlation between the experimental and numerical results by introducing attenuation into the analysis. The wave speed in sand is 240 m/s and as the frequency increases to 10 kHz, the wave length in sand can be as short as 2.4 cm. Since the accelerometer is apparently too large, a better calculation may be done by considering a scattering problem.

The current analytical approach can provide a reliable strain

Downloaded 03 May 2010 to 171.66.16.21. Redistribution subject to ASME license or copyright; see http://www.asme.org/terms/Terms_Use.cfm

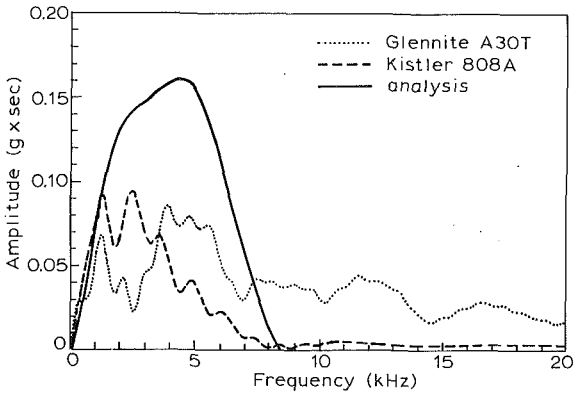

Fig. 14 Simulated spectrum and experimental spectrum

history and acceleration history within the same order of magnitude in comparison with the experimental results. The major errors arise from the infinite plate assumption and the dimensions of instruments used to measure acceleration in the sand.

Summary

In this paper, the basic approach was expressed. The main objective is to understand the physical phenomena. The *arrival time*, *duration*, and *magnitude* have good correlation between the analysis and experiment. The overall results are reasonably good and provide an understanding of the transmission of impact load through the plate, the interaction between the plate and the sand, and the propagation of the load into the sand.

The following conclusions can be made at this point:

1 Using the current approach, numerical results are comparable to experimental results. The accuracy is within the same order of magnitude.
2 To get a better estimate of the impact loading, it is necessary to consider finite plate effects.
3 The accelerometer size effect is not negligible in current testing scales.
4 The errors from the assumptions of interfacial conditions and point impact are much smaller than the errors from (2) and (3). The effect of an assumed Poisson's ratio on soil response needs further investigation.
5 Attenuation may be introduced to compensate for the energy consumed on sliding (internal friction between soil particles).

Acknowledgment

The authors are grateful for support from the Air Force Office of Scientific Research. They are pleased to acknowledge the Program Manager, Directorate of Aerospace Sciences, Major Steven C. Boyce and former Program Manager Dr. Spencer T. Wu.

References

Achenbach, J. D., 1980, *Wave Propagation in Elastic Solids*, North-Holland Publishing Co., Amsterdam.

Achenbach, J. D., Keshava, S. P., and Herrmann, G., 1966, "Waves in a Smoothly Joined Plate and Half Space," *Journal of the Engineering Mechanics Division, Proceedings*, ASCE, Vol. 92, No. EM2, pp. 113–129.

Al-Mousawi, M. M., 1986, "On Experimental Studies of Longitudinal and Flexural Wave Propagations: An Annotated Bibliography," *Applied Mechanics Reviews*, ASME, Vol. 39, No. 6, pp. 853–865.

Arnold, R. N., Bycroft, G. N., and Warburton, G. B., 1955, "Forced Vibrations of a Body on an Infinite Elastic Solid," ASME JOURNAL OF APPLIED MECHANICS, Vol. 22, pp. 391–400.

Bycroft, G. N., 1956, "Forced Vibrations of a Rigid Circular Plate on a Semi-Infinite Elastic Space and on an Elastic Stratum," *Phil. Transactions Royal Society London*, Vol. A248, pp. 327–368.

Collins, W. D., 1962, "The Forced Torsional Oscillations of an Elastic Half-Space and an Elastic Stratum," *Proceedings of London Mathematical Society*, Vol. 12, pp. 226–244.

Freund, L. B., and Achenbach, J. D., 1968, "Waves in a Semi-Infinite Plate in Smooth Contact With a Harmonically Disturbed Half Space," *International Journal of Solids and Structures*, Vol. 4, pp. 605–621.

Greszczuk, L. B., 1982, "Damage in Composite Materials Due to Low Velocity Impact," *Impact Dynamics*, J. A. Zukas et al., eds., John Wiley, New York.

Iguchi, M., and Luco, J. E., 1982, "Vibration of Flexible Plate on Viscoelastic Medium," *Journal of the Engineering Mechanics Division, Proceedings*, ASCE, Vol. 108, No. EM6, pp. 1103–1120.

Karasudhi, P., Keer, L. M., and Lee, S. L., 1968, "Vibratory Motion of a Body on an Elastic Half-Plane," ASME JOURNAL OF APPLIED MECHANICS, Vol. 35, pp. 697–705.

Kiger, S. A., Getchell, J. V., Slawson, T. R., and Hyde, D. W., 1980–1984, "Vulnerability of Shallow-Buried Flat Roof Structures," US Army Engineer Waterways Experiment Station, Technical Report SL-80-7, six parts.

Krenk, S., and Schmidt, H., 1981, "Vibration of an Elastic Circular Plate on an Elastic Half Space—A Direct Approach," ASME JOURNAL OF APPLIED MECHANICS, Vol. 48, pp. 161–168.

Lamb, H., 1904, "On the Propagation of Tremors over the Surface of an Elastic Solid," *Philosophy Transactions Royal Society London, Ser. A*, Vol. 203, pp. 1–42.

Lambe, T. W., and Whitman, R. V., 1969, *Soil Mechanics*, John Wiley, New York.

Leissa, A. W., 1969, "Vibration of Plates," NASA Report No. SP-160.

Lin, Y. J., 1978, "Dynamic Response of Circular Plates Resting on Viscoelastic Half-Space," ASME JOURNAL OF APPLIED MECHANICS, Vol. 45, pp. 379–384.

Luco, J. E., and Mita, A., 1987, "Response of a Circular Foundation on a Uniform Half-Space to Elastic Waves," *Earthquake Engineering and Structural Dynamics*, Vol. 15, pp. 105–118.

Luco, J. E., and Westmann, R. A., Oct. 1971, "Dynamic Response of a Circular Footings," *Journal of the Engineering Mechanics Division, Proceedings*, ASCE, No. EM5, pp. 1381–1395.

Luco, J. E., and Westmann, R. A., 1972, "Dynamic Response of a Rigid Footing Bonded to an Elastic Half-Space," ASME JOURNAL OF APPLIED MECHANICS, Vol. 39, pp. 527–534.

Oien, M. A., 1973, "Steady Motion of a Plate on an Elastic Half-Space," ASME JOURNAL OF APPLIED MECHANICS, Vol. 40, Series E, No. 2, pp. 478–484.

Quinlan, P. M., 1954, "The Elastic Theory of Soil Dynamics," *Symposium on Dynamic Testing of Soils*, ASTM, STP No. 156, pp. 3–34.

Reissner, E., and Sagoci, H. F., 1944, "Forced Torsional Oscillations of an Elastic Half-Space," *Journal of Applied Mechanics*, Vol. 15, pp. 652–662.

Richard, Jr., F. E., Hall, Jr., J. R., and Woods, R. D., 1970, *Vibrations of Soils and Foundations*, Prentice-Hall, Englewood Cliffs, N.J.

Robertson, I. A., 1966, "Forced Vertical Vibration of a Rigid Circular Disc on a Semi-Infinite Elastic Solid," *Proceedings of Cambridge Philosophy Society*, Vol. 62, pp. 547–553.

Sung, T. Y., 1954, "Vibrations in Semi-Infinite Solids Due to Periodic Surface Loadings," *Symposium on Dynamic Testing of Soils*, ASTM, STP No. 156, pp. 35–64.

Timoshenko, S., and Goodier, J. N., 1970, *Theory of Elasticity*, 3rd Ed., McGraw-Hill, New York.

Timoshenko, S., and Woinowsky-Krieger, S., 1959, *Theory of Plates and Shells*, McGraw-Hill, New York.

Veletsos, A. S., and Verbic, B., 1974, "Basic Response Functions for Elastic Foundations," *Journal of the Engineering Mechanics Division, Proceedings*, ASCE, Vol. 100, No. EM2, pp. 189–202.

Whittaker, W. L., and Christiano, P., 1982, "Dynamic Response of Flexible Plates on Elastic Half-Space," *Journal of the Engineering Mechanics Division*, ASCE, Vol. 108, pp. 133–154.

Downloaded 03 May 2010 to 171.66.16.21. Redistribution subject to ASME license or copyright; see http://www.asme.org/terms/Terms_Use.cfm

D. J. Inman[1]
Center for Control Sciences,
Division of Applied Mathematics,
Brown University,
Providence, RI 01912
Mem. ASME

A Sufficient Condition for the Stability of Conservative Gyroscopic Systems

A sufficient condition for the stability of conservative gyroscopic systems with negative definite stiffness is presented. The conditions for stability are stated in terms of the definiteness of certain combinations of the coefficient matrices of the equations of motion. These conditions yield design constraints in terms of the physical parameters of the system. An example is given to illustrate the correctness of the result, as well as to provide a comparison with the results of other researchers.

Dedicated to the memory of Prof. H. H. E. Leipholz

Introduction

Several results have been published discussing the stability of gyroscopic systems. One interesting phenomena is that unstable conservative systems can be made stable by introducing stabilizing gyroscopic forces. The work presented here examines such systems. Several results for conservative gyroscopic systems already exist (see, for instance, Huseyin, 1978).

The stability result presented here is similar to those of Hagedorn (1975), Teschner (1977), and Huseyin, Hagedorn, and Teschner (1983). The condition derived here assumes that the stiffness matrix of the system is negative definite and that a certain related matrix is bounded away from zero. The result yields a new sufficient condition for stabilizing a system with gyroscopic forces.

The systems of interest here are conservative gyroscopic systems of the type successfully described by a set of ordinary differential equations satisfying the vector equation

$$M\ddot{\mathbf{x}}(t) + \tilde{G}\dot{\mathbf{x}}(t) + \tilde{K}\mathbf{x}(t) = \mathbf{0}. \tag{1}$$

Here $\mathbf{x}(t)$ is an n-dimensional vector representing the displacements of the n lumped masses of the system, and its time derivatives $\dot{\mathbf{x}}(t)$ and $\ddot{\mathbf{x}}(t)$ represent the velocity and acceleration, respectively. The $n \times n$ mass matrix M is assumed to be real valued, symmetric, and positive definite. The skew symmetric real valued matrix $\tilde{G}$ represents the gyroscopic forces in the system and the $n \times n$ real valued symmetric matrix $\tilde{K}$ represents the position dependent forces in the system. The special case of interest here is when the matrix $\tilde{K}$ is restricted to be negative definite and $\tilde{G}$ is nonsingular. An example of such a system is a simple model of a disc mounted on a weightless uniformly rotating shaft.

The system described by equation (1) with $\tilde{K}$ negative definite and $\tilde{G}$ set to zero is unstable. If $\tilde{G}$ is non zero, i.e., if gyroscopic forces are introduced, then the system described by equation (1) may be stable or unstable. The following result indicates how to choose the physical parameters contained in the matrices M, $\tilde{G}$, and $\tilde{K}$ so that the system of equation (1) is stable.

Background Results

In this section several results are stated and/or derived which are required to present and prove the stability result of interest. First, a formal definition of stability is presented. This is followed by a derivation of an alternative symmetric form of equation (1) and a discussion of the properties of the matrix coefficients that result from this form.

The system defined by equation (1) is linear and, hence, its equilibrium position can be taken to be the origin. Likewise, the stability properties are global and the stability of all motions, i.e., of each response, will have the same stability property. In this context, the stability of the response also describes the stability of the system, or of the system's equilibrium (see, for instance, Willems, 1970).

According to Lyapunov (with zero taken as the equilibrium position) the system described by equation (1) is stable if it is possible to find a positive number $\delta(\alpha)$, for any sufficiently small positive number α, such that

$$\|\mathbf{x}(t)\| + \|\dot{\mathbf{x}}(t)\| = (\mathbf{x}^T\mathbf{x})^{1/2} + (\dot{\mathbf{x}}^T\dot{\mathbf{x}})^{1/2} < \alpha \tag{2}$$

for all $t > 0$, if $\|\mathbf{x}(0)\| + \|\dot{\mathbf{x}}(0)\| < \delta(\alpha)$. Here $\mathbf{x}(0)$ and $\dot{\mathbf{x}}(0)$ denote the initial position and velocity, respectively, and the superscript T denotes the transpose of the vector $\mathbf{x}$. This simply states that the motion for all time is bounded as long as the initial conditions are bounded.

It is well known that the system of equation (1) is stable if the eigenvalues associated with (1) are purely imaginary (see,

[1] On leave from the Department of Mechanical and Aerospace Engineering, State University of New York, Buffalo, N.Y.

Contributed by the Applied Mechanics Division for presentation at the Winter Annual Meeting Chicago, IL, November 28 to December 2, 1988 of THE AMERICAN SOCIETY OF MECHANICAL ENGINEERS.

Discussion on this paper should be addressed to the Editorial Department, ASME, United Engineering Center, 345 East 47th Street, New York, N.Y. 10017, and will be accepted until two months after final publication of the paper itself in the JOURNAL OF APPLIED MECHANICS. Manuscript received by ASME Applied Mechanics Division, April 12, 1988; final revision, June 29, 1988.

Paper No. 88-WA/APM-76.

Copyright © 1988 by ASME
Downloaded 03 May 2010 to 171.66.16.21. Redistribution subject to ASME license or copyright; see http://www.asme.org/terms/Terms_Use.cfm

for instance, Huseyin, 1978). To that end, assume the solution of equation (1) is of the form

$$\mathbf{x}(t) = \mathbf{y}e^{i\omega t} \tag{3}$$

where $\mathbf{y}$ is a vector of constants and $i = \sqrt{-1}$. Substitution of expression (3) into equation (1) yields

$$(-\omega^2 M + i\omega\tilde{G} + \tilde{K})\mathbf{y} = \mathbf{0}. \tag{4}$$

Since M is positive definite, it has a positive definite square root, denoted $M^{1/2}$, such that $M^{1/2}M^{1/2} = I$, the $n \times n$ identity (see, for instance, Ortega, 1988). Furthermore, since $M^{1/2}$ is positive definite and therefore nonsingular, it has an inverse, denoted $M^{-1/2}$, such that the following holds:

$$M^{-1/2}M^{1/2} = M^{1/2}M^{-1/2} = I.$$

Next let $\mathbf{y} = M^{-1/2}\mathbf{q}$ in equation (4) and premultiply this expression by $M^{-1/2}$. This results in

$$(-\omega^2 I + i\omega G + K)\mathbf{q} = \mathbf{0} \tag{5}$$

where $G = M^{-1/2}\tilde{G}M^{-1/2}$ is still skew symmetric and $K = M^{-1/2}\tilde{K}M^{-1/2}$ is symmetric and negative definite as long as $\tilde{K}$ is. This system will be stable if each ω satisfying equation (5) can be shown to be a real number, since for real values of ω

$$\|\mathbf{x}(t)\| + \|\dot{\mathbf{x}}(t)\| \leq \|\mathbf{q}\|\,|e^{i\omega t}| < \alpha \tag{6}$$

for all $t > 0$, for any bounded initial conditions.

In general, the vector $\mathbf{q}$ in equation (5) will be complex valued of the form

$$\mathbf{q} = \mathbf{u} + i\mathbf{v} \tag{7}$$

where $\mathbf{u}$ and $\mathbf{v}$ are real valued constant n-dimensional vectors. Substitution of (7) into equation (5), and writing down separate equations for the real part and for the imaginary part results in two equations which can be written in the form

$$(\omega^2 I + \omega B + C)\mathbf{z} = \mathbf{0} \tag{8}$$

where I is the $2n \times 2n$ identity matrix, $\mathbf{z}$ is the $2n \times 1$ vector $[\mathbf{u}^T\mathbf{v}^T]^T$, $\mathbf{0}$ is the $2n \times 1$ vector of zeros, B is defined to be the $2n \times 2n$ matrix

$$B = \begin{bmatrix} 0 & G \\ -G & 0 \end{bmatrix} \tag{9}$$

and C is defined to be the $2n \times 2n$ matrix

$$C = \begin{bmatrix} -K & 0 \\ 0 & -K \end{bmatrix}. \tag{10}$$

Note that $B = B^T$ is symmetric and $C = C^T$ is symmetric and positive definite as long as K is negative definite. The eigenvalue problem associated with the $2n$-dimensional symmetric system of equation (8) is equivalent to the n-dimensional conservative gyroscopic problem of equation (5) in the sense that the $2n$ values of ω satisfying equation (8), are the n values of ω satisfying equation (5) repeated twice. This is discussed by Lancaster (1966). Thus if it can be shown that the values of ω satisfying (8) are real, the values of ω satisfying equation (5) will be real as well and the solution of equation (2) will be stable. This transformation to a symmetric problem was first pointed out by Duffin (1960) and has several useful properties.

The coefficient matrix B in equation (9) is symmetric and has eigenvalues associated with the eigenvalues of the matrix G. Note that if λ is an eigenvalue of B then

$$B\mathbf{x} = \lambda\mathbf{x} \tag{11}$$

or

$$\begin{bmatrix} 0 & G \\ -G & 0 \end{bmatrix}\begin{bmatrix} \mathbf{u} \\ \mathbf{v} \end{bmatrix} = \begin{bmatrix} \lambda\mathbf{u} \\ \lambda\mathbf{v} \end{bmatrix}. \tag{12}$$

This last expression implies the two equalities

$$G\mathbf{v} = \lambda\mathbf{u} \tag{13}$$

and

$$-G\mathbf{u} = \lambda\mathbf{v}. \tag{14}$$

Multiplying (14) by G and substitution of (13) yields

$$-G^2\mathbf{u} = \lambda^2\mathbf{u}. \tag{15}$$

Thus the eigenvalues of B are the square roots of the eigenvalues of $-G^2$, i.e.,

$$\lambda_i(B) = \pm\sqrt{\lambda_i(-G^2)} \tag{16}$$

where $\lambda_i(A)$ denotes the eigenvalues of the matrix A. Since $-G^2$ is positive definite and since B is symmetric, (16) also illustrates that B is indefinite. Note that (16) also implies that

$$\lambda_{\max}(-G^2) = \lambda^2_{\max}(B) \tag{17}$$

i.e., that the largest eigenvalue of the matrix $(-G^2)$ is the square of the largest eigenvalue of the matrix B.

The above properties of the matrices B, C, and the symmetric form of the system given in equation (8) can now be used to provide a sufficient condition for the stability of nonconservative gyroscopic systems with negative definite stiffness.

Main Result

This section proves the following sufficient condition for the stability of a conservative gyroscopic system with negative definite stiffness. If the matrix K is negative definite, the conservative gyroscopic system of equation (1) is stable if the matrix $(4K - G^2 - \epsilon I)$ is positive definite where $2\epsilon = \lambda_{\max}(-G^2)$.

To see that this is true, multiply equation (8) by $\mathbf{z}^*$, the complex conjugate transpose of the vector $\mathbf{z}$ to obtain the scalar equation

$$\omega^2 + b\omega + c = 0. \tag{18}$$

Here the scalar $b = \mathbf{z}^*B\mathbf{z}$, the scalar $c = \mathbf{z}^*C\mathbf{z}$ and it is assumed that $\mathbf{z}^*\mathbf{z} = 1$ for convenience of presentation. The values of ω are those determined by solving the simple quadratic equation (18) which yields

$$2\omega = -b \pm \sqrt{b^2 - 4c} \tag{19}$$

for all complex vectors $\mathbf{z}$ satisfying equation (8).

If the discriminate defined by $d = b^2 - 4c$ is always positive for any vector $\mathbf{z}$ satisfying equation (8), then each ω is real and nonzero as desired. Note that the scalar c cannot be zero since the matrix C is nonsingular (i.e., C is positive definite).

By hypothesis the matrix $4K - G^2 - \epsilon I$ is positive definite so that

$$\mathbf{x}^*(4K - G^2 - \epsilon I)\mathbf{x} > 0 \tag{20}$$

for all nonzero $n \times 1$ vectors $\mathbf{x}$. Here, recall that if A is symmetric and positive definite then $\mathbf{x}^TA\mathbf{x} > 0$ for all real vectors $\mathbf{x}$ and $\mathbf{y}^*A\mathbf{y} > 0$ for all complex vectors $\mathbf{y}$. Inequality (20) also implies that for all complex $2n \times 1$ vectors $\mathbf{z}$

$$\mathbf{z}^*(B^2 - 4C)\mathbf{z} > 2\epsilon. \tag{21}$$

To see that inequality (21) follows from (20) let $\mathbf{z}^* = [\mathbf{r}^*\ \mathbf{s}^*]$ and consider the partitioned form of $B^2 - 4C$. Then

$$\mathbf{z}^*(B^2 - 4C)\mathbf{z} = \mathbf{r}^*(4K - G^2)\mathbf{r} + \mathbf{s}^*(4K - G^2)\mathbf{s}$$
$$\geq \epsilon + \epsilon = 2\epsilon = \lambda_{\max}(-G^2) \tag{22}$$

for all complex vectors $\mathbf{z}$, $\mathbf{r}$, and $\mathbf{s}$.

The last part of the derivation is to show that inequality (22) forces the discriminate, $(d = b^2 - 4c)$ in equation (19) to be positive for all complex vectors $\mathbf{z}$. To see that this follows recall that

Downloaded 03 May 2010 to 171.66.16.21. Redistribution subject to ASME license or copyright; see http://www.asme.org/terms/Terms_Use.cfm

$$d = (\mathbf{x}^* B\mathbf{x})^2 - 4\mathbf{x}^* C\mathbf{x} \tag{23}$$

for all complex vectors $\mathbf{x}$. However from a rearrangement of inequality (21) the last term in equation (23) can be estimated by

$$-4\mathbf{x}^* C\mathbf{x} > \lambda_{\max}(-G^2) - \mathbf{x}^* B^2 \mathbf{x}. \tag{24}$$

Combining equation (23) and inequality (24) yields

$$d > (\mathbf{x}^* B\mathbf{x})^2 - \mathbf{x}^* B^2\mathbf{x} + \lambda_{\max}(-G^2). \tag{25}$$

However, from the special form of the matrix, equation (17) yields that $\lambda_{\max}(-G^2) = \lambda^2_{\max}(B)$. From the variational characterization of the eigenvalues of a symmetric matrix

$$\lambda^2_{\max}(B) \geq \mathbf{x}^* B^2 \mathbf{x}. \tag{26}$$

Inequality (25) now becomes

$$d > (\mathbf{x}^* B\mathbf{x})^2 - \mathbf{x}^* B^2\mathbf{x} + \mathbf{x}^* B^2\mathbf{x} = (\mathbf{x}^* B\mathbf{x})^2 > 0 \tag{27}$$

for all complex vectors $\mathbf{x}$ since B^2 is positive definite and thus nonsingular. Thus, under the hypothesis that the matrix $(4K - G^2 - \epsilon I)$ is positive definite, where $2\epsilon = \lambda_{\max}(-G^2)$, the values of ω satisfying (5) for nonzero $\mathbf{q}$ are all real and the system of equation (1) is stable.

Previous Results

Hagedorn (1975) stated a sufficient condition for the system of equation (1) to be unstable and so doing motivated several attempts to prove a corresponding stability result. Hagedorn's result states that if the matrix $4K - G^2$ is negative definite, then the system of equation (1) is unstable. Teschner (1977) was able to show for a two-degree-of-freedom system that stability results for K negative definite and $4K - G^2$ positive definite. Inman and Saggio (1985) extended this $n = 2$ result and showed that stability results for K negative definite if the trace of the matrix $4K - G^2$ and determinant of the matrix K are both positive and applied these conditions to the design of a dynamically tuned inertial grade gyroscope. These results produce a larger range of parameter values to choose from for stable operation than previously indicated in the literature.

Recently Huseyin, Hagedorn and Teschner (1983) succeeded in establishing a stability result for n-degree-of-freedom systems based on the matrix $4K - G^2$. The two part Huseyin-Hagedorn-Teschner theorem states that

(*i*) If $4K - G^2$ is positive definite and if $GK - KG$ is positive definite then the system of equation (1) is stable
and
(*ii*) If $GK = KG$, then the system of equation (1) is stable if and only if $4K - G^2$ is positive definite.

The first part of the theorem assumes only that K is nonsingular and makes no assumption about the definiteness of K. The second part of the theorem is a necessary and sufficient condition for that subclass of systems which can be decoupled. The following example serves as a comparison of the various stability and instability criteria for a simple system, as well as to illustrate the correctness and usefulness of the stability results based on the definiteness of the matrix $4K - G^2$.

Example

A standard example used in illustrating stability results for conservative gyroscopic systems is that of a simplified model of a mass mounted on a non circular weightless rotating shaft subject to a constant axial compression force. Such a system is gyroscopic when treated in a rotating reference frame. Huseyin (1976) gives the equation of motion as

$$\begin{bmatrix} 1 & 0 \\ 0 & 1 \end{bmatrix} \ddot{\mathbf{x}} + 2\xi \begin{bmatrix} 0 & -1 \\ 1 & 0 \end{bmatrix} \dot{\mathbf{x}} + \begin{bmatrix} k_1 - \xi^2 - \eta & 0 \\ 0 & k_2 - \xi^2 - \eta \end{bmatrix} \mathbf{x} = \mathbf{0} \tag{28}$$

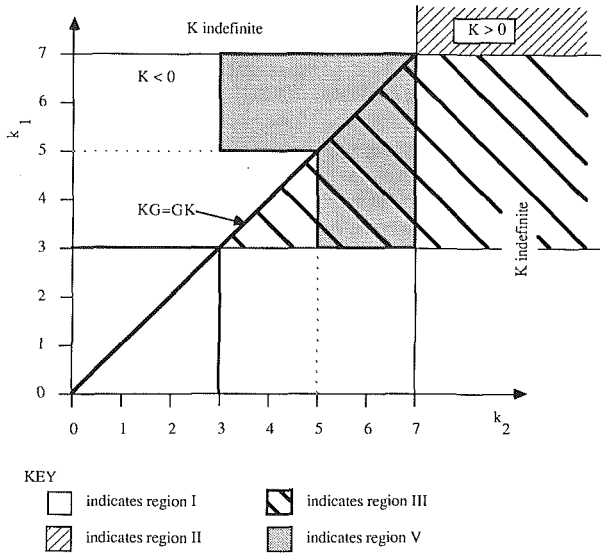

Fig. 1 Parameter regions corresponding to the known stability for a two-degree-of-freedom system. The stability result derived here is shown as region V.

where $\mathbf{x}$ represents the displacement, ξ is the shaft angular velocity, η is the axial compression force and k_1 and k_2 are elastic rigidities in the two principle directions.

Each of the stability criteria discussed in the previous section, as well as the condition presented here, are next applied to the system of equation (28) and compared. It is interesting to fix the values of ξ^2 and η, say, at $\xi^2 = 4$ and $\eta = 3$, and examine regions of stability on a plot of k_1 versus k_2. This is done in Fig. 1 which could also be thought of as a design chart (see Inman, 1989, for instance). Figure 1 also provides a visual comparison of the various stability results.

The matrix $4K - G^2$ for this system becomes the diagonal matrix $4K - G^2 = \text{diag}\ (k_1 - 3,\ k_2 - 3)$, and the matrix K becomes the diagonal matrix $K = \text{diag}\ (k_1 - 7,\ k_2 - 7)$. The eigenvalues of G result in $\lambda_{\max}(-G^2) = 16$, so that $\epsilon = 8$. Thus, the matrix $4K - G^2 - \epsilon I$ becomes the diagonal matrix $4K - G^2 - \epsilon I = \text{diag}\ (4k_1 - 20,\ 4k_2 - 20)$. These matrices are all diagonal so that checking their definiteness is just a matter of requiring each of the diagonal elements to have the appropriate sign. The matrix $GK - KG$ becomes $GK - KG = (k_1 - k_2)I$, where I is the 2×2 identity matrix. The various stability theorems yield various inequalities in the two parameters k_1 and k_2. These are sketched in Fig. 1. Each theorem corresponds to a different region in the figure. Each region is defined by inequalities in k_1 and k_2 as indicated in the following:

I Hagedorn's Instability Theorem. The system is unstable if $4K - G^2$ is negative (i.e., if $k_1 < 3$ and $k_2 < 3$, which is the lightly shaded box in the lower left corner of the figure).

II Energy Stability Theorem. The system is stable if K is positive definite (i.e., $k_1 > 7$ and $k_2 > 7$, this corresponds to the hatched area in the upper right corner of the figure).

III Huseyin-Hagedorn-Teschner Theorem I. The system is stable if $4K - G^2$ and $GK - KG$ are both positive definite (i.e., if $k_1 > 3$, $k_2 > 3$, and $k_2 > k_1$, represented by the thick slanting lines in the figure).

IV Huseyin-Hagedorn-Teschner Theorem 2. If $GK = KG$ (i.e., if $k_1 = k_2$) the system is stable if $4K - G^2$ is positive definite (i.e., if $k_1 > 3$ and $k_2 > 3$) and unstable if $4K - G^2$ is negative definite (i.e., $k_1 < 3$ and $k_2 < 3$). This result is represented by the dark 45 deg line passing through the origin in the figure.

Downloaded 03 May 2010 to 171.66.16.21. Redistribution subject to ASME license or copyright; see http://www.asme.org/terms/Terms_Use.cfm

V Proposed Theorem. The system is stable if $4K-G^2-\epsilon I$ is positive definite and K is negative definite (i.e., if $5<k_1<7$ and $5<k_2<7$, represented by the darkened "dog leg" area in the figure).

In Fig. 1, definiteness of a matrix is denoted by inequality signs in the obvious fashion (e.g., $K>0$ denotes that the matrix K is positive definite). The numbered regions in the key correspond to the above numbering of the various theories.

Note that there are several regions in this plot, i.e., several combinations of k_1 and k_2, that are not accounted for in the above stated results. Because this example is a simple two-degree-of-freedom system, the trace condition of Inman and Saggio (1985) can also be applied to obtain more regions of stable operation. The two-degree-of-freedom theories are sketched in Inman (1989) which yields stable operations for k_1 and $k_2>6$, with $k_1<7$ and $k_2<7$. This in not plotted here because the purpose of the example is to visualize the differences between the various results available for n-degree-of-freedom systems. However, Fig. 1 indicates that more results for multiple degree-of-freedom systems are needed to yield a complete range of parameters for stable operation.

Summary

In the present paper a sufficient condition for the stability of a linear conservative gyroscopic system with an arbitrary, but finite number of degrees-of-freedom and negative definite stiffness has been established. The condition presented here is stated in such a way as to render it useful as a design criteria by directly relating the system's stability to values of the system's parameters. The results are compared to previous work on the same class of system and the differences between the various theories are illustrated with a simple example.

A comparison of the various stability conditions for conservative gyroscopic systems for a simple two-degree-of-freedom system seems to indicate that further theorems might be developed. For instance, Fig. 1 suggests the conjecture that the Huseyin-Hagedorn-Teschner theorem might also hold for cases with $GK-KG$ being negative definite. Another conjective might be based on the estimate of the value of ϵ in equation (21). The value of ϵ was chosen for the convenience of proof. It may be that some smaller values of the parameter ϵ would work. However, counter examples exist for the limit of $\epsilon=0$. The question of choosing the smallest possible ϵ is open.

It is also important to note that the stability results presented here are false if positive definite damping is also present in the system. The paper by Zajac (1964) clearly points this out.

Acknowledgments

The author gratefully acknowledges the support of the National Aeronautics and Space Administration (grant number NAG-1785), the Air Force Office of Scientific Research (contract numbers AFOSR 85 0220, F49620-88-C-0018 and F49620-86-C-0111), and the National Science Foundation (grant number MSM 8351807). The reviewer's comments and suggestions are also gratefully acknowledged.

References

Duffin, R. J., 1960, "The Rayleigh-Ritz Method for Dissipative or Gyroscopic Systems," *Quarterly of Applied Math.*, Vol. 18, pp. 2115–221.

Hagedorn, P., 1975, "Uber Die Instabilitat Konservativer Systeme Mit Gyroskopischen Kraften," Arch. Rat. Mech. Anal., Vol. 58, pp. 1–9.

Huseyin, K., 1976, "Standard Forms of the Eigenvalue Problems Associated with Gyroscopic Systems," *Journal of Sound and Vibration*, Vol. 45, No. 1, pp. 29–37.

Huseyin, K., 1978, *Vibrations and Stability of Miltiple Parameter Systems*, Noordholl International Publishing.

Huseyin, K., Hagedorn, P., and Teschner, W., 1983, "On the Stability of Linear Conservative Gyroscopic Systems," *Journal of Applied Mathematics and Physics*, Vol. 34, No. 6, pp. 807–815.

Inman, D. J., 1989, *Vibration with Control Measurement and Stability*, Prentice-Hall.

Inman, D. J., and Saggio, III, F., 1985, "Stability Analysis of a Gyroscopic System by Matrix Methods," *AIAA Journal of Guidance, Control and Dynamics*, Vol. 8, No. 1, pp. 150–152.

Lancaster, P., 1966, *Lambda Matrices and Vibrating Systems*, Pergamon Press, pp. 135–136.

Ortega, J. A., 1988, *Matrix Theory, a Second Course*, Plenum Press, New York.

Teschner, W., 1977, "On the Stability of Gyroscopic Systems," Doctoral Thesis, Darmstadt Technische Hochschule, p. 41, (in German).

Willems, J. L., 1976, *Stability Theory of Dynamical Systems*, John Wiley & Sons, Inc., New York, p. 11.

Zajac, E. E., 1964, "The Kelvin-Tait-Chetaev Theorem and Extensions," *Journal of the Astronautical Sciences*, Vol. 11, No. 2, pp. 46–49.

Downloaded 03 May 2010 to 171.66.16.21. Redistribution subject to ASME license or copyright; see http://www.asme.org/terms/Terms_Use.cfm

Coordinate Reduction in the Dynamics of Constrained Multibody Systems—A New Approach

S. K. Ider
Mem. ASME

F. M. L. Amirouche
Assistant Professor,
Mem. ASME

Department of Mechanical Engineering,
University of Illinois at Chicago,
Chicago, Ill. 60680

In this paper a new theorem for the generation of a basis for the null space of a rectangular matrix, with m *linearly independent rows and* n (n>m) *columns is presented. The method is based on Gaussian row operations to transform the constraint Jacobian matrix to an uptriangular matrix. The Gram-Schmidt process is then utilized to identify basis vectors orthogonal to the uptriangular matrix. A complement orthogonal array which forms the basis for the null space for which the algebraic constraint equations are satisfied is then formulated. An illustration of the theorem application to constrained dynamical systems for both Lagrange and Kane's equations is given. A numerical computer algorithm based on Kane's equations with embedded constraints is also presented. The method proposed is well conditioned and computationally efficient and inexpensive.*

1 Introduction

Recently there has been an increasing interest in the efficient development of governing dynamic equations of constrained mechanical systems. The dealing with constrained multibody systems has been somehow limited. While large amount of research and publications have been attributed to the development of the equations of motion, the handling of the constraint equations have been accomplished with less computational efficiency.

Introduction of the constraints as kinematical equations at an early stage of the analysis unnecessarily complicate the development of the equations of motion. In order to improve computing efficiency it is desirable to find algorithms which automatically reduce the governing equations, and either form the equations in terms of independent coordinates or reduce the governing equations by eliminating the associated generalized constraint forces.

These automated approaches are based on utilizing complement arrays obtained through algorithmic transformations to reduce and express the governing equations of motion in terms of the independent coordinates. In numerical solutions of such problems, the updated transformations are computed automatically when the constraints are violated to ensure the natural dynamics of the system.

Methods leading to such an approach include the zero eigenvalue theorem, the singular value decomposition method, the generalized coordinate-partitioning methods, the Pseudo-uptriangular decomposition method, and other matrix procedures.

In the zero eigenvalue method Kamman and Huston (1984) used a theorem introduced by Walton and Steeves (1969), to generate an orthogonal complement $\mathbf{T}$ of the $m \times n$ constraint Jacobian matrix $\mathbf{B}$ for a dynamical system of n generalized coordinates and m constraints. The eigenvectors of $\mathbf{B}^T\mathbf{B}$ corresponding to the zero eigenvalues form the transformation matrix $\mathbf{T}$, which is then used to reduce the governing equations of motion as obtained from Kane's equations (Kane and Levinson, 1985). A similar approach presented by Singh and Likins (1985) uses the singular value decomposition to extract the orthogonal complement matrix. Solving for the eigenvalue problem in both cases results in computational time deficiency, especially if the structure size becomes more pronounced.

In the procedure developed by Uicker (1969), the dependent variables are evaluated from the algebraic constraint equations by an iterative numerical scheme and then the independent coordinates are integrated using these initial values. This method is based on prior proper selection of the independent coordinates and the iterative procedure is computationally expensive.

Wehage and Haug (1982) developed a generalized coordinate partitioning algorithm to identify independent generalized coordinates by using LU factorization of the constraint matrix. The selection of the independent and dependent coordinates is usually not automatic, and a repeated LU decomposition could lead to singularities.

A recent method introduced by Amirouche and Jia uses a pseudo-uptriangular decomposition of the constraint matrix

Contributed by the Applied Mechanics Division of THE AMERICAN SOCIETY OF MECHANICAL ENGINEERS for presentation at the Joint ASCE/ASME Applied Mechanics, Biomechanics, and Fluids Engineering Conference, San Diego, CA, July 9-12, 1989.

Discussion on this paper should be addressed to the Editorial Department, ASME, United Engineering Center, 345 East 47th Street, New York, N.Y. 10017, and will be accepted until two months after final publication of the paper itself in the JOURNAL OF APPLIED MECHANICS. Manuscript received by ASME Applied Mechanics Division, October 15, 1987; final revision, April 28, 1988.

Paper No. 89-APM-15.

Copyright © 1988 by ASME
Downloaded 03 May 2010 to 171.66.16.21. Redistribution subject to ASME license or copyright; see http://www.asme.org/terms/Terms_Use.cfm

based on successive multiplications of Householder transformations to compute an orthogonal complement matrix, which is then utilized to obtain the equations of motion by eliminating the unknown generalized constraint forces from Kane's equations. This method is computationally more efficient than the previous methods since it is achieved by successive multiplications of m Householder transformation matrices, and does not require computations of eigenvectors or matrix inverses.

In the course of revising the proofs we came across a similar approach called the QR decomposition introduced by Kim and Vanderploeg (1986). In the QR decomposition the orthogonal complement matrix was obtained by partitioning the orthogonal matrix Q. In the PUTD the transformation matrix (equivalent to Q) need not to be orthogonal, hence a QR decomposition is not necessary.

In this paper a new method based on equivalence transformation of the constraint matrix to an uptriangular form is introduced for the generation of the orthogonal complement matrix. This method presents an alternative to the previously developed methods. The transformation matrix is generated by simple Gauss elimination row operations and is believed to be computationally more efficient. A numerical algorithm for the dynamic analysis of constrained multibody systems utilizing Kane's equations together with the method proposed in this paper is given. The method is applicable for both holonomic and nonholonomic systems.

This paper is divided into five sections. The first section gives an introduction to the background and motivation described previously. The second section describes the general form of the constraint equations considered. In the third section, the generation of the transformation matrix by equivalence transformation to triangular form is developed. The fourth section presents the formulation of the equations of motion and algorithm for the dynamic analysis of constrained multibody systems. In the fifth section an example is presented. Conclusions form the last section.

2 Constraint Equations

Let $q_1, \ldots, q_n$ be a set of generalized coordinates chosen for convenience to specify the configuration of a mechanical system. Assume that these coordinates are not independent but are subject to m independent constraint equations of the form

$$B_{il}\dot{q}_l = g_i \qquad i=1, \ldots, m \qquad l=, \ldots, n \tag{1}$$

where B_{il} and g_i are, in general, functions of $q_1, \ldots q_n$ and time t. In the notation used in this paper the summation sign is omitted. So a repeated index in a term implies summation over the range of that index, unless otherwise stated. Equations (1) are known as nonholonomic constraints if they are nonintegrable. Consider holonomic constraints which can be expressed as

$$\phi_i(q_1, \ldots, q_n, t)=0 \qquad i=, \ldots, k \tag{2}$$

Differentiation of equations (2) leads to the same form given in equation (1). Hence, equation (1) represents a set of m holonomic and nonholonomic constraint equations.

Selection of n-m independent generalized coordinates by solving the constraint equations for the other m coordinates is not suitable for relatively large systems and for computer automation.

A convenient way of formulating the equations of motion of a complex dynamical system with constraints is by introducing generalized constraint forces in Lagrange equations via Lagrange multipliers. Alternatively, making use of Kane's equations eliminate the need for computing the kinetic and potential energies of the system, and even the undetermined multipliers if they are not needed in the analysis.

In this paper an automated procedure will be developed for the computation of a transformation matrix **C** which is orthogonal to the constraint matrix **B**. This leads to a transformation between the n generalized coordinate derivatives and n-m independent coordinate derivatives where the latter are abstract in character and do not lend themselves to physical interpretations. The method eliminates the need of computing the superfluous independent coordinates and their derivatives. Moreover, the introduction of the undetermined multipliers in Kane's equations make the analysis more complete, should a need for computing the constraint forces arises (Amirouche and Ider, 1988).

3 Generation of a Basis for the Null Space

In this section we shall formulate a basis for the null space of **B**, i.e., a basis for the set of solution vectors of the homogeneous system,

$$B_{il}\, y_l = 0 \qquad i=1, \ldots, m; \qquad l=1, \ldots, n \tag{3}$$

The matrix **C** composed of these basis vectors as columns is then an orthogonal complement of **B**.

Consider the transpose of the constraint matrix, $B_{ij}^{\mathrm{T}} = B_{ji}$, $i=1, \ldots, n$; $j=1, \ldots, m$; $n > m$. Let the m constraint equations be linearly independent, so that rank of **B** is m.

The analysis involves formulating an uptriangular matrix **U** which is equivalent to $\mathbf{B}^{\mathrm{T}}$, by utilizing elementary row operations, i.e.,

$$\mathbf{P}\mathbf{B}^{\mathrm{T}} = \mathbf{U} \tag{4}$$

where **P** is a $n \times n$ nonsingular matrix, and

$$\mathbf{U} = \begin{bmatrix} **\ldots\ldots\ldots * \\ 0*\ldots\ldots\ldots * \\ 0\ldots\ldots\ldots 0* \\ 0\ldots\ldots\ldots 0 \\ 0\ldots\ldots\ldots 0 \end{bmatrix} \tag{5}$$

and then finding n-m orthonormal vectors, in the n-dimensional space R^n, which are orthogonal to the columns of **U**.

From the definition of **B** and given **P** to be a nonsingular matrix by equations (4), the columns of **U** are linearly independent, with nonzero diagonal elements.

A sequence of elementary row operations can be accomplished on a matrix **A** by premultiplying **A** by a nonsingular elementary matrix which is obtained by performing the same sequence of elementary row operations on the nth order identity matrix, **I**.

In the Gauss-elimination method, for reducing a matrix **A** to uptriangular form, the matrix is premultiplied by a sequence of elementary matrices $\mathbf{M}_k$, $k=1, \ldots, m$ each involving a sequence of elementary row operations chosen to introduce a column with zeros below the diagonal. At the kth step, let $\mathbf{a}^k$ denote the kth column of the matrix. Then, $\mathbf{M}_k$ is given as

$$\mathbf{M}_k = \mathbf{I} - \alpha\, \mathbf{e}_k{}^{\mathrm{T}} \tag{6}$$

where $\mathbf{e}_k$ denotes the kth column of **I**,

$$\alpha = [0, \ldots, 0, \alpha_{k+1}, \ldots, \alpha_n]^{\mathrm{T}} \tag{7}$$

and

$$\alpha_i = \frac{a_i^k}{a_k^k}, \qquad i=k+1, \ldots, n \tag{8}$$

Partial pivoting is necessary since a_k^k may be zero at any step. This involves, at each step, interchanging rows k and ρ_k, $\rho_k \geq k$, so that $a_{\rho k}^k \neq 0$. Since the rank of $\mathbf{B}^{\mathrm{T}}$ is m, m of the n rows must be linearly independent. So row pivoting ensures the completion of the process for the m columns without encountering a zero pivot.

The matrix can be considered to have a rank of less than m, if a sufficiently small pivot is obtained in a step, since round-

Downloaded 03 May 2010 to 171.66.16.21. Redistribution subject to ASME license or copyright; see http://www.asme.org/terms/Terms_Use.cfm

ing errors make the probability of encountering an exactly zero pivot remote.

An algorithm is defined to be stable if the solution computed by the algorithm corresponds to the exact solution of the system with "small" perturbations of the system parameters. The growth of the elements during elmination is a measure of the estimated perturbations. Since the elements of the reduced matrices usually remain of the same order of magnitude, Gauss elimination with partial pivoting is considered to be a stable algorithm (Golub and Van Loan, 1983).

Denoting the elementary matrix involving row interchange at the kth step by $\mathbf{Q}_k$, the transformation $\mathbf{B}^{\mathbf{T}}$ to the uptriangular matrix $\mathbf{U}$ can be expressed as

$$\mathbf{M}_m\mathbf{Q}_m\mathbf{M}_{m-1}\mathbf{Q}_{m-1}\ \ldots\ \mathbf{M}_1\mathbf{Q}_1\mathbf{B}^{\mathbf{T}}=\mathbf{U} \tag{9}$$

Hence, the matrix $\mathbf{P}$ in equation (4) is

$$\mathbf{P}=\mathbf{M}_m\mathbf{Q}_m\mathbf{M}_{m-1}\ \ldots\ \mathbf{M}_1\mathbf{Q}_1 \tag{10}$$

Formation of the matrices $\mathbf{Q}_k$ and $\mathbf{M}_k$, $k=1, \ldots, m$ and computation of the products of these matrices involve unnecessary computations. Instead, at each step the corresponding row operations are performed on rows $k+1, \ldots, n$. And the same sequence of row operations which reduce $\mathbf{B}^{\mathbf{T}}$ to $\mathbf{U}$ is performed on $\mathbf{I}$ in the same order to obtain the equivalence transformation matrix.

Let $\mathbf{I}_1$ and $\mathbf{I}_2$ denote matrices composed of, respectively, the first m columns, and the last n-m columns of the nth order identity matrix. The columns of $\mathbf{I}_1$ form an orthonormal basis of the vector space composed of the linear combinations of the columns of $\mathbf{U}$. This can be seen by inspection or by application of the Gram-Schmidt orthogonalization process to the columns of $\mathbf{U}$ in the same order.

Therefore, since $\mathbf{I}_2$ is orthogonal to $\mathbf{I}_1$, and since the columns of $\mathbf{U}$ are linear combinations of the columns of $\mathbf{I}_1$, $\mathbf{I}_2$ is also orthogonal to $\mathbf{U}$. Then, using equation (4) we obtain

$$\mathbf{I}_2^{\mathrm{T}}\,\mathbf{P}\mathbf{B}^{T}=0 \tag{11}$$

or

$$\mathbf{B}\ \mathbf{P}^{\mathrm{T}}\mathbf{I}_2=0 \tag{12}$$

Since $\mathbf{P}$ is nonsingular, the columns of $\mathbf{P}^{\mathrm{T}}\mathbf{I}_2$ are linearly independent. Therefore in R^n, the n-m columns of $\mathbf{P}^{\mathrm{T}}\mathbf{I}_2$ form a basis of the set of solution vectors of equation (3). A linear combination of these columns is also a solution. Therefore, in general

$$\mathbf{B}\ \mathbf{P}^{\mathrm{T}}\mathbf{I}_2\ \mathbf{p}=0 \tag{13}$$

where $\mathbf{p}$ is an arbitrary column vector of order n-m. Hence, the proof of the following theorem has been completed.

Theorem. Consider a set of m-independent linear homogeneous equations in n unknowns $y_1, \ldots, y_n$, where $n>m$,

$$\mathbf{B}\ \mathbf{y}=0 \tag{14}$$

there exists a matrix $\mathbf{C}\triangleq\mathbf{P}^{\mathbf{T}}\,\mathbf{I}_2$ with n-m linearly independent columns, where $\mathbf{I}_2$ is a matrix whose columns are the last n-m columns of the nth order identity matrix $\mathbf{I}$, and $\mathbf{P}$ is obtained by applying on $\mathbf{I}$ the same sequence of Gauss-elimination row operations which transform $\mathbf{B}^{\mathbf{T}}$ to an uptriangular matrix, such that

$$\mathbf{BC}=0 \tag{15}$$

and

$$\mathbf{y}=\mathbf{Cp} \tag{16}$$

is the general solution, where $\mathbf{p}$ is an arbitrary column vector of order n-m.

The algorithm for the computation of $\mathbf{C}$ is given next.

Algorithm. 1 Initialization

$k=1$

$A_{ij}=B_{ji}\quad i=1, \ldots, n;\ j=1, \ldots, m$

$P_{ij}=\delta_{ij}\quad i, j=1, \ldots, n$

2 Pivoting

Find $\rho_k \geq k$ such that $|A_{\rho_k,k}|=\max\{|A_{ik}|: i\geq k\}$

If $A_{\rho_k,\,k}=0$, (rank $<m$), stop.

$A_{kj}\leftrightarrow A_{\rho_k j}\quad j=k, \ldots, m$

$P_{kj}\leftrightarrow P_{\rho_k j}\quad j=1, \ldots, n$

3 Elimination of $\mathbf{A}$ and formation of $\mathbf{P}$

$$\mu_{ik}=A_{ik}/A_{kk}\quad i=k+1, \ldots, n$$

$$A_{ij}=A_{ij}-\mu_{ik}A_{kj}\quad i=k+1, \ldots, n;\ j=k+1, \ldots, m$$

$$P_{ij}=P_{ij}-\mu_{ik}P_{kj}\quad i=k+1, \ldots, n;\ j=1, \ldots, n$$

4 $k=k+1$

If $k\leq m$, go to step 2.

5 Formation of $\mathbf{C}$

$$C_{ij}=P_{m+j,\,i}\quad i=1, \ldots, n;\ j=1, \ldots, n-m$$

4 Equations of Motion for Constrained Mechanical Systems

4.1 Kane's Equations with the Undetermined Multipliers. Kane's equations with the undetermined multipliers are given as

$$F_l+F_l^*+F_l^c=0\quad l=1, \ldots, n \tag{17}$$

where

$$F_l^c=\lambda_i\ B_{li}^T\quad i=1, \ldots, m \tag{18}$$

Further details on the generalized constraint forces F_l^c could be found in Amirouche and Ider (1988).

The generalized external and inertia forces F_l and F_l^* can be obtained without formulating the kinetic and potential energies of the system, as follows (Kane and Levinson, 1985; Huston and Passarello, 1980).

Consider a mechanical system with N bodies. Let y_l denote the generalized speeds of the system, selected for convenience as independent linear combinations of $\dot{q}_p$, $p=1, \ldots, n$. The angular velocities $\underset{\sim}{\omega}_k$ and the mass center translational velocities $\underset{\sim}{v}_k$ of the bodies can be expressed as

$$\underset{\sim}{\omega}_k=\omega_{klr}y_l\underset{\sim}{n}_r\qquad k=1, \ldots, N;\ l=1, \ldots, n;\ r=1,2,3 \tag{19}$$

$$\underset{\sim}{v}_k=v_{klr}y_l\underset{\sim}{n}_r \tag{20}$$

where $\underset{\sim}{n}_r$ are orthogonal unit vectors fixed in stationary reference frame. ω_{klr} and v_{klr} are functions of q_l and are denoted as partial angular velocity and partial velocity arrays, respectively. ω_{klr} and v_{klr} are formulated by multibody system kinematics and can be easily coded for generation in computer (Huston and Passerello, 1980; Amirouche, 1986). Let the externally applied force field on body k be represented by a force $\underset{\sim}{F}_k$ passing through the mass center and by a moment $\underset{\sim}{M}_k$. Similarly, the inertia force field is denoted by $\underset{\sim}{F}_k^*$ and $\underset{\sim}{M}_k^*$.

The generalized external forces are then obtained as

$$F_l=\frac{\partial \underset{\sim}{v}_k}{\partial y_l}\cdot\underset{\sim}{F}_k+\frac{\partial \underset{\sim}{\omega}_k}{\partial y_l}\cdot\underset{\sim}{M}_k \tag{21}$$

or

$$F_l=v_{klr}F_{kr}+\omega_{klr}M_{kr}\quad k,=1, \ldots, N;\quad l=1, \ldots, n;\ r=1,2,3 \tag{22}$$

Similarly, the generalized inertia forces are

$$F_l^*=v_{klr}F_{kr}^*+\omega_{klr}M_{kr}^* \tag{23}$$

$\underset{\sim}{F}_k^*$ and $\underset{\sim}{M}_k^*$ may be expressed as

$$\underset{\sim}{F}_k^*=-m_k\ \underset{\sim}{a}_k\ \text{(no sum on } k) \tag{24}$$

and

Downloaded 03 May 2010 to 171.66.16.21. Redistribution subject to ASME license or copyright; see http://www.asme.org/terms/Terms_Use.cfm

$$\underline{M}_k^* = -\underline{I}_k \cdot \underline{\alpha}_k - \underline{\omega}_k \times (\underline{I}_k \cdot \underline{\omega}_k) \text{ (no sum on } k) \quad (25)$$

where m_k and $\underline{I}_k$ are the mass and the inertia dyadic of body k, and $\underline{a}_k$ and $\underline{\alpha}_k$ are obtained, respectively, from equations (20) and (19) as

$$\underline{a}_k = (v_{klr}\dot{y}_l + \dot{v}_{klr}y_l)\underline{n}_r \quad k=1, \ldots, N; \quad r=1,2,3 \quad l=1, \ldots, n \quad (26)$$

and

$$\underline{\alpha}_k = (\omega_{klr}\dot{y}_l + \dot{\omega}_{klr}y_l)\underline{n}_r \quad (27)$$

Substitution of equations (24)–(27) into equation (23) yields

$$F_l^* = (b_{lp}y_p + c_{lp}y_p + d_{lps}y_s y_p) \quad s, l, p = 1, \ldots, n \quad (28)$$

where

$$b_{lp} = -I_{krs}\ \omega_{klr}\omega_{kps} + m_k\ v_{klr}v_{kpr}$$
$$k=1, \ldots, N; \ r, s = 1,2,3; \quad l, p = 1, \ldots, n \quad (29)$$

$$c_{lp} = m_k v_{klr}\dot{v}_{kpr} + I_{krs}\omega_{klr}\dot{\omega}_{kps} \quad (30)$$

and

$$d_{lps} = e_{hrv}I_{krq}\omega_{kph}\omega_{ksq}\omega_{klv} \quad (31)$$

$$k=1, \ldots, N; \ l, p, s = 1, \ldots, n; \ h, r, v, q = 1,2,3$$

In equation (31) e_{hrv} is the standard permutation symbol.

4.2 Coordinate Reduction and Numerical Solution. When equation (17) is premultiplied by $\mathbf{C}^T$, the undetermined multipliers are eliminated, as indicated by equation (15), yielding the following n-m equations

$$C_{pl}F_l + C_{pl}F_l^* = 0 \quad p=1, \ldots, n\text{-}m; \ l=1, \ldots, n \quad (32)$$

or

$$K_p + K_p^* = 0 \quad p=1, \ldots, n\text{-}m \quad (33)$$

where

$$K_p = C_{pl}F_l, \quad K_p^* = C_{pl}\ F_l^* \quad (34)$$

The governing dynamical equations of motion of a mechanical system with n generalized coordinates, subject to holonomic and nonholonomic constraints are given by the n-m equations (41) and m equations (1).

When the constraint equations (1) are differentiated one obtains

$$B_{il}\dot{y}_l = -\dot{B}_{il}y_l + \dot{g}_i \quad i=1, \ldots, m; \ l=1, \ldots, n \quad (35)$$

Combining equations (33) and (35) and making use of equations (28) and (34) we obtain

$$\dot{y}_p = H_{lp}^{-1}R_l \quad p, l = 1, \ldots, n \quad (36)$$

where

$$\mathbf{H} = \left[\frac{C_{pl}\ b_{lq}}{B_{iq}}\right] \quad p=1, \ldots, n\text{-}m; \quad q,1=1, \ldots, n; \ i=1, \ldots, m \quad (37)$$

and

$$\mathbf{R} = \left[\frac{C_{pl}\ F_l - C_{pl}c_{lq}\ y_q - C_{pl}\ d_{lqs}y_s y_q}{-\dot{B}_{il}y_l + \dot{g}_i}\right]$$
$$p=1, \ldots, n\text{-}m; \quad q, l=1, \ldots, n; \quad l=1, \ldots, m \quad (38)$$

The n equations (36) together with the relations between y_l and $\dot{q}_l$ constitute a set of first order differential equations which can be numerically integrated e.g., with variable step predictor-corrector algorithm, to yield the time history of the unknowns y_l and q_l.

It may be desired to determine the individual restraint forces imposed by the constraints. It can be shown that the multipliers λ_i, $i=1, \ldots, m$, each corresponding to one constraint equation are the restraining constraint forces and moments developed by the constraints (Amirouche and Ider, 1988). They represent the external forces and moments in the unconstrained system that would yield the same motion of the constrained system. Once F_l and F_l^* are computed, F_l^c can be obtained from equation (17). Then equation (18) can be utilized for determining the individual restraint forces λ_i. Premultiplying equation (18) by $\mathbf{B}$ we have, in matrix notation

$$\lambda = \mathbf{E}^{-1}\mathbf{B}\ \mathbf{F}^c \quad (39)$$

where

$$\mathbf{E} = \mathbf{B}\mathbf{B}^T \quad (40)$$

To avoid calculations involving matrix inversion, one can make use of the equivalence transformation matrix P which is already available. Premultiplying equation (18) by $\mathbf{I}_1^T\mathbf{P}$ yields a triangular system which can be solved for λ_i, $i=1, \ldots, m$ by back substitution.

In the numerical procedure, the evaluation of the constraint matrix $\mathbf{B}$ and the transformation matrix $\mathbf{C}$, as well as the matrices $\mathbf{b}$, $\mathbf{c}$, and $\mathbf{d}$ at each step, involves large amount of computations. It is observed that for multibody systems with closed loops and with some bodies under prescribed motion, these matrices may be kept constant throughout an integration interval.

Therefore, the interval size needs to be tested against constraint violations. This is achieved by numerically comparing the left- and right-hand sides of equation (1) as evaluated at the end of the interval.

The numerical algorithm for the dynamic analysis of multibody systems subject to holonomic and nonholonomic constraints follows.

Algorithm. Let L denote the integration time interval size.

(*1*) Read the topological and geometrical data describing the multibody structure, initial values for y_l and q_l which are consistent with the constraint equations, and initial value for L. Initially time $t=0$.

(*2*) Calculate ω_{klr}, v_{klr}, B_{il} and their derivatives. If $t=0$, go to step 4.

(*3*) Check for constraint violations by calculating $e=\max|B_{il}y_l - g_i|$. Depending on the magnitude of error e, decrease or increase L.

(*4*) Compute the matrix $\mathbf{C}$ by the method of equivalence transformation to triangular form using the algorithm given in Section 3.

(*5*) Calculate F_l and the matrices $\mathbf{b}$, $\mathbf{c}$, and $\mathbf{d}$ by equations (22), (29), (30), and (31).

(*6*) Using equations (37) and (38) calculate $\mathbf{H}^{-1}$, and form $\mathbf{H}^{-1}\mathbf{R}$ as functions of y_l and t.

(*7*) Integrate equations (36) from t to $t+L$.

(*8*) If required for output, calculate the mass center velocities and accelerations by equations (20), (26), the angular velocities and accelerations by equations (19) and (27), and the constraint forces by equation (39).

(*9*) If the simulation has reached to final time, stop. Otherwise, set $t = t+L$ and go to step 2.

A computer program for general spatial multibody structures has been developed utilizing the above algorithm.

The program automatically reduces the number of generalized coordinates to the allowed motions at the joints in the tree structure, hence eliminating the need to describe these restrictions as separate constraint equations. Further efficiencies are achieved by operating only with the nonzero columns of the partial velocity arrays as identified from the topology.

Closed loops, prescribed angular motions of the bodies, and prescribed translational motions of points in the system are in-

Downloaded 03 May 2010 to 171.66.16.21. Redistribution subject to ASME license or copyright; see http://www.asme.org/terms/Terms_Use.cfm

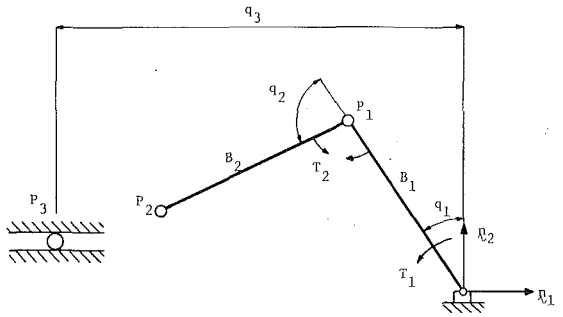

Fig. 1 Unconstrained system

cluded into the analysis by the methods presented in this paper.

5 Numerical Example

To illustrate the foregoing procedures, consider the unconstrained system shown in Fig. 1 as given by Wampler et al. (1985). The system consists of two subsystems, the first of which consists of two rigid massless links B_1 and B_2, each of length L, and two particles P_1 and P_2, each of mass m, assembled as shown. Motors at the joints exert a torque T_1 on B_1 and a torque T_2 between B_1 and B_2. The second subsystem is composed solely of a particle P_3 of mass M which slides in a frictionless track. The system represents a simplified model of a two-link robot manipulator where P_3 is the load that the robot will grasp and move.

The configuration of the system can be described by three generalized coordinates: the two angles q_1 and q_2, and the position of P_3, q_3. The generalized speeds y_l, $l = 1,2,3$ are defined as

$$y_1 = \dot{q}_1,\ y_2 = \dot{q}_2,\ y_3 = \dot{q}_3 \tag{41}$$

By equating the sum of the generalized active and inertia forces, the equations of motion are obtained as

$$\begin{aligned} T_1 + mgL(2s_1 + s_{12}) - mL^2\ \{(3+2c_2)\ \dot{y}_1 + (1+c_2)\ \dot{y}_2 + s_2\ [y_1^2 \\ - (y_1+y_2)^2]\} = 0 \\ T_2 + mgL\ s_{12} - mL^2\ [(1+c_2)\ \dot{y}_1 + \dot{y}_2 + s_2 y_1^2] = 0 \\ M\dot{y}_3 = 0 \end{aligned} \tag{42}$$

where g is the acceleration of gravity,

$$s_i = \sin q_i\ (i=1,2),\ c_i = \cos q_i\ (i=1,2),$$
$$s_{12} = \sin\ (q_1+q_2),\ \text{and}\ c_{12} = \cos\ (q_1+q_2)$$

Consider next the system given by Fig. 2, where P_2 is now constrained to be coincident with P_3. The two constraint equations are obtained by equating the velocities of P_2 and P_3, which yields

$$B_{il} y_l = 0 \quad i=1,2; \quad l=1,2,3 \tag{43}$$

where

$$\mathbf{B} = \begin{bmatrix} s_1 + s_{12} & s_{12} & 0 \\ L\ (c_1 + c_{12}) & Lc_{12} & -1 \end{bmatrix} \tag{44}$$

The constraint matrix $\mathbf{B}$ and, hence, the orthogonal complement matrix $\mathbf{C}$ vary during the motion depending on the values of q_1 and q_2. Let us assume that $L = 0.5$ m and initially $q_1 = 75°$ and $q_2 = 15°$.

Then $\mathbf{B}$ becomes

$$\mathbf{B} = \begin{bmatrix} 1.9659 & 1.0 & 0.0 \\ 0.1294 & 0.0 & -1.0 \end{bmatrix} \tag{45}$$

The equivalence transformation matrix $\mathbf{P}$ is calculated by the algorithm given in Section 3, yielding

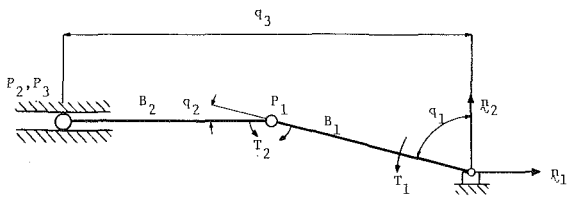

Fig. 2 Constrained system

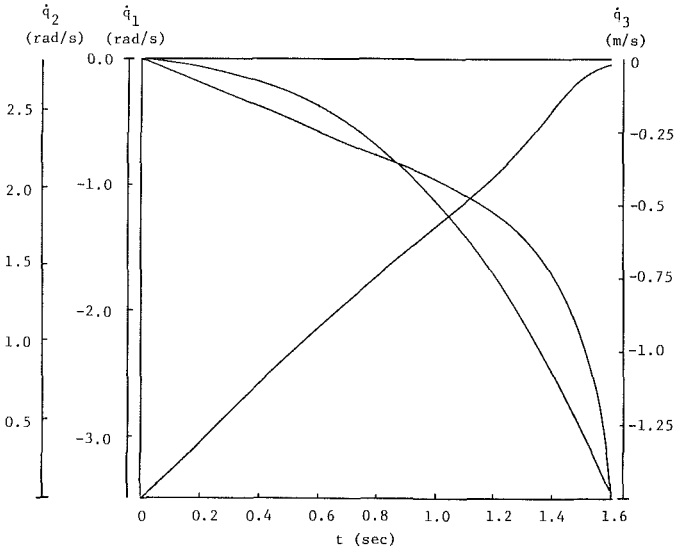

Fig. 3 Simulation of the constrained system

$$\mathbf{P} = \begin{bmatrix} 1.0 & 0.0 & 0.0 \\ -0.5087 & 1.0 & 0.0 \\ 7.7310 & -15.1976 & 1.0 \end{bmatrix} \tag{46}$$

And $\mathbf{C} = \mathbf{P}^T\mathbf{I}_2$ is obtained as

$$\mathbf{C} = \begin{bmatrix} 7.7310 \\ -15.1976 \\ 1.0 \end{bmatrix} \tag{47}$$

At this stage, the method developed in this paper will be compared to the previous methods, especially with the methodologies employed in the zero eigenvalue theorem and the pseudo-uptriangular decomposition method. In general each method extracts a different basis for the null space of $\mathbf{B}$. Therefore, the columns of an orthogonal complement matrix obtained by one method can be expressed as linear combinations of the columns of that generated by another method.

In the zero eigenvalue method (Kamman and Huston, 1984), it can be shown that

$$\mathbf{y} = \hat{\mathbf{T}}\ \mathbf{p} \tag{48}$$

where $\hat{\mathbf{T}}$ is a $nx(n\text{-}m)$ matrix whose columns are the eigenvectors corresponding to the zero eigenvalues of $\mathbf{S} = \mathbf{B}^T\mathbf{B}$, and $\mathbf{p}$ is a $n\text{-}m$ vector of new independent generalized coordinates.

For the constraint matrix given in equation (44), $\hat{\mathbf{T}}$ is calculated as

$$\hat{\mathbf{T}} = \begin{bmatrix} 1.0 \\ -1.9659 \\ 0.1294 \end{bmatrix} \tag{49}$$

In pseudo-uptriangular decomposition method (Amirouche et al., 1988), successive Householder transformations are applied to $\mathbf{B}^T$, to obtain an uptriangular matrix. Then, the orthogonal complement of $\mathbf{B}$ is obtained as

$$\mathbf{B}\ \mathbf{H}^T\mathbf{D}_2 = 0 \tag{50}$$

where $\mathbf{H}$ is formed by successive multiplications of

Downloaded 03 May 2010 to 171.66.16.21. Redistribution subject to ASME license or copyright; see http://www.asme.org/terms/Terms_Use.cfm

Householder transformations, $\mathbf{H} = \mathbf{H}_1\mathbf{H}_2 \ldots \mathbf{H}_m$, and $\mathbf{D}_2$ is a matrix composed of the last n-m columns of $\mathbf{I}$.

Application of the pseudo-uptriangular method to the constraint matrix given in equation (44) yields

$$\mathbf{H}^T\mathbf{D}_2 = \begin{bmatrix} -0.4526 \\ 0.8898 \\ -0.0586 \end{bmatrix} \tag{51}$$

In this example, the orthogonal complement matrix consists of only one column. It is seen that $\mathbf{C}$, $\hat{\mathbf{T}}$, and $\mathbf{H}^T\mathbf{D}_2$ given by equations (47), (49), and (51) are constant multiples of each other.

The simulation of the constrained system (Fig. 2) is performed by the algorithm given in Section 4. The system is assumed to be initially at rest. The numerical data used are; $m = 10$ kg, $M = 10$ kg, T_1, $= -50$ N-m, $T_2 = 0$, the weights are in the $-\underline{n}_2$ direction, $L = 0.5$ m, and the initial position for q_1 and q_2 are 75° and 15° respectively. $\dot{q}_1$, $\dot{q}_2$ and $\dot{q}_3$ are plotted in Fig. 3, for a period of 1.5 secs.

6 Conclusion

A new method to automatically reduce the equations of motion when subjected to constraints is presented. The method is based on simple row operations for transforming the constraint Jacobian matrix into an equivalent uptriangular matrix. The method is computationally inexpensive since it does not require solution for an eigenvalue problem, matrix inversion, or an LU decomposition. The procedures and method outlined in this paper will add a new dimension to the analysis of complex constrained mechanical systems and especially in the area of robotics, space structures, and biosystems. This alternative approach to previously popular methods such as the singular value decomposition, the zero eigenvalue theorem, and others, is also tailored for generic computer programs that uses Kane's equations.

References

Amirouche, F. M. L., Jia, T., and Ider, S. K., 1988, "Recursive Householder Transformation for Complex Dynamical Systems with Constraints," ASME JOURNAL OF APPLIED MECHANICS, in press.

Amirouche, F. M. L., and Ider, S. K., 1988, "Determination of Constraint Forces in Multibody System Dynamics Using Kane's Equations," *Journal of Theoretical and Applied Mechanics*, Vol. 7, No. 1, pp. 3–20.

Amirouche, F. M. L., 1986, "Dynamic Analysis of 'Tree-Like' Structures Undergoing Large Motions – A Finite Segment Approach, *Journal of Engineering Analysis – Computational Mechanics Publication*, Vol. 3, No. 2, pp. 111–117.

Golub, G. H., and Van Loan, C. F., 1983, *Matrix Computations*, The Johns Hopkins University Press, Baltimore, MD.

Hemami, H., and Weimer, F. C., 1981, "Modelling of Nonholonomic Dynamic Systems with Applications," ASME JOURNAL OF APPLIED MECHANICS, Vol. 48, p. 177.

Huston, R. L., and Passarello, C. E., 1980, "Multibody Structural Dynamics Including Translation Between the Bodies," *Computers and Structures*, Vol. 12, pp. 713–720.

Kamman, J. W., and Huston, R. L., 1984, "Dynamics of Constrained Multibody Systems," ASME JOURNAL OF APPLIED MECHANICS, Vol. 51, pp. 899–903.

Kane, T. R., and Levinson, D. A., 1985, *Dynamics: Theory and Applications*, McGraw-Hill, New York.

Kim, S. S., and Vanderploeg, M. J., 1986, "QR Decomposition for State Space Representation of Constrained Mechanical Dynamic Systems," ASME *Journal of Mechanisms, Transmissions, and Automation in Design*, Vol. 108, pp. 183–188.

Singh, R. P., and Likins, P. W., 1985, "Singular Value Decomposition for Constrained Dynamical Systems," ASME JOURNAL OF APPLIED MECHANICS, Vol. 52, pp. 943–948.

Uicker, Jr., J. J., 1969, "Dynamic Behavior of Spatial Linkages, Part 1 – Exact Equations of Motion," ASME *Journal of Engineering for Industry*, February, pp. 251–258.

Walton, W. C., and Steeves, E. C., 1969, "A New Matrix Theorem and its Application for Establishing Independent Coordinates for Complex Dynamical Systems with Constraints", NASA Technical Report TR R-326.

Wampler, C., Buffington, K., and Sui-hui, J., 1985, "Formulation of Equations of Motion for Systems Subject to Constraints," ASME JOURNAL OF APPLIED MECHANICS, Vol. 52, pp. 465–470.

Wehage, R. A., and Haug, E. J., 1982, "Generalized Coordinate Partitioning for Dimension Reduction in Analysis of Constrained Dynamic Systems," ASME *Journal of Mechanical Design*, Vol. 104, No. 1, pp. 247–255.

Downloaded 03 May 2010 to 171.66.16.21. Redistribution subject to ASME license or copyright; see http://www.asme.org/terms/Terms_Use.cfm

M. Grigoriu
Department of Structural Engineering,
Cornell University,
Ithaca, N.Y.

S. T. Ariaratnam
Solid Mechanics Division,
Faculty of Engineering,
University of Waterloo,
Waterloo, Ontario, Canada

Response of Linear Systems to Polynomials of Gaussian Processes

Moments and mean crossing rates are determined for the response of linear systems subject to polynomial forms in Gauss-Markov processes. Differential equations describing the evolution in time of response moments are developed by the use of Itô's calculus. Estimators are obtained for mean crossing rates based on higher order moments and approximations of the distribution of the response. The method is applied to the analysis of a simple oscillator subject to the square of an Ornstein-Uhlenbeck process.

Introduction

An important class of non-Gaussian processes, referred to as translation processes, consists of memoryless nonlinear transformations of stationary Gaussian processes (Grigoriu, 1984). Polynomials of Gaussian processes have been applied, e.g., to model wind and wave forces acting on structural systems (Grigoriu, 1986; Grigoriu and Ariaratnam, 1987; Soize, 1978; Winterstein, 1987). The response to these forces usually follows non-Gaussian distributions even for linear structures. Gaussian responses may result under very restrictive conditions that do not usually prevail in practice (Kotulski and Sobczyk, 1981; Rosenblatt, 1981).

The methods for analyzing the response of linear systems to polynomials of stationary Gaussian processes include algorithms for calculating high-order moments of the response based on the Kolmogorov equation associated with the system state vector or multiple convolution integrals (Karlin and Taylor, 1981; Kotulski and Sobczyk, 1981; Soize, 1978) and methods for finding the characteristic function of the response (Grigoriu, 1986). Special techniques have also been developed to determine higher order moments of the response of linear systems subject to delta-correlated processes (Lutes, 1985).

This paper develops an alternative method for analyzing the response of linear systems to polynomial forms of stationary Gaussian processes with time-dependent coefficients. It is shown that moments of any order of the transient response can be obtained from a closed system of linear differential equations. Moments of the stationary response are the solution of a closed system of algebraic equations. The Itô differentiation rule is used to develop moment equations. The paper also develops estimates for the mean upcrossing rate of the response based on response moments and approximations of the probablistic characteristics of the response. Theoretical developments are applied to determine moments and estimate mean crossing rates for the stationary response of a simple oscillator subject to the square of an Ornstein-Uhlenbeck process. Results are used to evaluate various estimators of the mean crossing rate including the one assuming that the response is a Gaussian process.

Statement of Problem

A three-phase method is developed for calculating moments and mean crossing rates for the response of linear systems subject to polynomial forms of stationary Gaussian processes with time-dependent coefficients. In the first phase, the equations of motion are combined with the differential equations characterizing the excitation so that the augmented states in these equations represent a diffusion process satisfying a nonlinear system of differential equations driven by Gaussian white noise. In the second phase, the Itô differentiation rule is applied to develop moment equations for the response. It is shown that the moment equations form a closed hierarchy so that the moments of the response can be calculated exactly. In the third phase, various estimates are developed for mean crossing rates based on (*i*) truncated series expansions of the probability density function of the response and its derivative and (*ii*) approximate representations of the response by memoryless transformations of Gaussian processes.

Consider a simple oscillator with damping ratio ζ and natural frequency ω_o subject to a stationary non-Gaussian excitation $Z(t)$. The displacement $X(t)$ of the oscillator satisfies the differential equation

$$\ddot{X}(t)+\beta\dot{X}(t)+kX(t)=Z(t) \tag{1}$$

in which $\beta=2\zeta\omega_o$ and $k=\omega_o^2$. Assume that the excitation has the form

$$Z(t)=\sum_{l=0}^{L} a_l(t)\,Y(t)^l \tag{2}$$

in which $a_l(t)$ are time-dependent coefficients and $Y(t)$ is a stationary Gaussian process that can be represented as a component of a Gauss-Markov vector process. For example, $Y(t)$ can be the Ornstein – Uhlenbeck process satisfying the differential equation

$$dY(t)=-\alpha Y(t)dt+\sigma_Y\sqrt{2\alpha}dB(t) \tag{3}$$

Contributed by the Applied Mechanics Division for publication in the JOURNAL OF APPLIED MECHANICS.

Discussion on this paper should be addressed to the Editorial Department, ASME, United Engineering Center, 345 East 47th Street, New York, N.Y. 10017, and will be accepted until two months after final publication of the paper itself in the JOURNAL OF APPLIED MECHANICS. Manuscript received by ASME Applied Mechanics Division, October 29, 1987; final revision, April 11, 1988.

Copyright © 1988 by ASME
Downloaded 03 May 2010 to 171.66.16.21. Redistribution subject to ASME license or copyright; see http://www.asme.org/terms/Terms_Use.cfm

in which $1/\alpha$ is the relaxation time, σ_Y denotes the stationary standard deviation of $Y(t)$, and $B(t)$ is the standard Brownian motion process with independent increments $dB(t)$ having mean zero and variance dt.

From equations (1)-(3) the augmented states of the oscillator and excitation satisfy the Itô differential equation

$$d\begin{bmatrix} X_1(t) \\ X_2(t) \\ X_3(t) \end{bmatrix} = \begin{bmatrix} 0 & 1 & 0 \\ -k & -\beta & \sum_{l=0}^{L} a_l(t)\, X_3(t)^{l-1} \\ 0 & 0 & -\alpha \end{bmatrix} \begin{bmatrix} X_1(t) \\ X_2(t) \\ X_3(t) \end{bmatrix} dt + \begin{bmatrix} 0 \\ 0 \\ \sigma_Y\sqrt{2\alpha} \end{bmatrix} dB(t) \tag{4}$$

in which $X_1(t) = X(t)$, $X_2(t) = \dot{X}(t)$, $X_3(t) = Y(t)$. The evolution of system and excitation states can be represented by Itô equations of the form

$$d\mathbf{X}(t) = \mathbf{g}(\mathbf{X}(t), t)dt + \mathbf{h}d\mathbf{B}(t) \tag{5}$$

even when the structure has two or more degrees of freedom and $Z(t)$ is a vector process depending on components of a multivariate Gauss-Markov process.

The response vector $\{X_1(t), X_2(t)\}$, in equation (4) cannot usually be characterized fully so that the reliability analysis of the oscillator in equation (1) must generally be based on a partial characterization of the response. This paper develops equations for response moments and estimates of the mean crossing rate of the response from moments of $\mathbf{X}(t)$. Mean crossing rates can be used to estimate the lifetime of dynamic systems that may fail at the first excursion of response above a critical level or as the result of a process of damage accumulation caused by alternating stresses (Grigoriu, 1986; Lutes, 1985; Soong, 1973; Winterstein, 1987).

Moment Equations

Consider a general Itô equation of the form

$$d\mathbf{X}(t) = \mathbf{g}(\mathbf{X}(t), t)dt + \mathbf{h}(\mathbf{X}(t), t)d\mathbf{B}(t) \tag{6}$$

in which $E[dB_i(t)dB_j(t)] = b_{ij}dt$ where E signifies the expectation operator. Let $\xi(\mathbf{X}(t), t)$ be a scalar function of the n-dimensional state vector $\mathbf{X}(t)$ and time t. According to Itô's differentiation rule (Ariaratnam and Loh, 1968; Karlin and Taylor, 1981),

$$\frac{dE[\xi]}{dt} = E\left[\frac{\partial \xi}{\partial t}\right] + \sum_{i=1}^{n} E\left[\frac{\partial \xi}{\partial X_i} g_i\right] + \frac{1}{2}\sum_{i,j=1}^{n} E\left[(\mathbf{hbh}^T)_{ij}\frac{\partial^2 \xi}{\partial X_i \partial X_j}\right] \tag{7}$$

in which T denotes matrix transposition, $(\mathbf{d})_{ij}$ = the (i, j)th component of matrix $\mathbf{d}$, and $\mathbf{b} = \{b_{ij}\}$. Note that $E[\partial\xi/\partial t] = 0$ when ξ does not depend explicitly on time and $dE[\xi]/dt = 0$ if $\mathbf{X}(t)$ is a stationary process. From equation 7, the moments $m(p, q, r) = E[X_1^p X_2^q X_3^r]$ of the state vector $\mathbf{X}(t) = \{X_1(t), X_2(t), X_3(t)\}$ in equation (4) satisfy the ordinary linear differential equation

$$\dot{m}(p,q,r) = pm(p-1, q+1, r) - qkm(p+1, q-1, r) - (q\beta + r\alpha)m(p,q,r) + q\sum_l a_l m(p, q-1, r+l) + r(r-1)\alpha\sigma_Y^2 m(p,q,r-2) \tag{8}$$

Note that the moments in this equation vanish when any of the powers of the components of $\mathbf{X}(t)$ take on negative values. The solution of equation (8) depends on the initial state of the system $\mathbf{X}(0)$. For example, all moments of the response are zero at $t=0$ if $\mathbf{X}(0)=0$. As previously mentioned, $\dot{m}(p,q,r)=0$ when $\mathbf{X}(t)$ is stationary so that the moments of the response satisfy linear algebraic equations.

Suppose that moments $m(p, q, 0) = E[X_1^p X_2^q]$ for a given value of $s = p+q$ are required. From equation (8), these moments satisfy the system of linear differential equations

$$\frac{d}{dt}\begin{bmatrix} m(s, 0, r) \\ m(s-1, 1, r) \\ \vdots \\ m(1, s-1, r) \\ m(0, s, r) \end{bmatrix} = \mathbf{c}\begin{bmatrix} m(s, 0, r) \\ m(s-1, 1, r) \\ \vdots \\ m(1, s-1, r) \\ m(0, s, r) \end{bmatrix} + \begin{bmatrix} r(r-1)\alpha\sigma_Y^2 m(s, 0, r-2) \\ \sum_l a_l(t)m(s-1, 0, r+l) + r(r-1)\alpha\sigma_Y^2 m(s-1, 1, r-2) \\ \vdots \\ (s-1)\sum_l a_l(t)m(1, s-2, r+l) + r(r-1)\alpha\sigma_Y^2 m(1, s-1, r-2) \\ s\sum_l a_l(t)m(0, s-1, r+l) + r(r-1)\alpha\sigma_Y^2 m(0, s, r-2) \end{bmatrix} \tag{9}$$

$(r = 0, 1, 2, \ldots)$

in which $\mathbf{c}$ is a time-variant matrix that follows from equation (8). It depends on characteristics of the system and the excitation.

The moments of order s of $X_1(t)$ and $X_2(t)$ can be obtained from equation (9) applied for $p+q = 1, 2, \ldots, s$. The algorithm is based on the observations that (i) $m(p, q, r)$ depends on moments $m(p', q', r')$ with $p'+q' < p+q$ and (ii) $m(p, q, r)$ with $p+q=1$ can be calculated recursively for increasing values of r because $m(0, 0, r) = E[X_3(t)^r]$ is known and equal to

$$m(0, 0, r) = \begin{cases} 0 & , r = \text{odd} \\ \dfrac{r!\sigma_Y^r}{2^{r/2}\left(\frac{r}{2}\right)!} & , r = \text{even} \end{cases} \tag{10}$$

Note that the determination of the moments of order s of $X_1(t)$ and $X_2(t)$ requires the calculation of moments $m(p, q, r)$ for $p+q=1$; $r=1, 2, \ldots (s-1)L$; $p+q=2$, $r=1, 2, \ldots (s-2)L$; $\ldots$; $p+q=s-2$; $r=1, 2, \ldots L$; and $p+q=s-1$; $r=1, 2, \ldots L$.

Downloaded 03 May 2010 to 171.66.16.21. Redistribution subject to ASME license or copyright; see http://www.asme.org/terms/Terms_Use.cfm

Mean Crossing Rates

The distribution $P(\sup X(t) \le x, 0 \le t \le \tau)$ of the maximum of a differentiable response process $X(t)$ in a period τ can be approximated by $\exp\{-\int_0^\tau \nu(x)dt\}$ for relatively large values of x, in which (Cramer and Leadbetter, 1967; Karlin and Taylor, 1981; Lin, 1976; Soong, 1973)

$$\nu(x) = \int_0^\infty \dot{x} f(x,\dot{x}) d\dot{x} \tag{11}$$

is the mean rate at which $X(t)$ crosses x with positive slope (upcrosses) and $f(x, \dot{x})$ is the joint density of $X(t)$ and $\dot{X}(t)$ at time t. Mean crossing rates have also been used to estimate fatigue lifetime (Lin, 1976).

Two estimators are developed for ν. They involve (*i*) an approximate representation of $f(x, \dot{x})$ based on generalized Hermite polynomials, and (*ii*) approximate transformations of $X(t)$ into a Gaussian process with zero mean and unit variance. Both estimators are determined using moments $m(p, q, 0)$ calculated in the previous section.

Approximations of $f(x, \dot{x})$. It can be shown that the joint distribution of the bivariate random vector $\{X(t), \dot{X}(t)\}$ can be expressed in the form (Stratonovich, 1963; Tikhonov and Tolkachev, 1965)

$$f(x,\dot{x}) = \left\{1 + \sum_{s=3}^{\infty} \frac{1}{s!} \sum_{\substack{p+q=s \\ p,q\ge 0}} \frac{1}{\sigma^p \dot{\sigma}^q} \times b_{(p,q)} H_{(p,q)}\left(\frac{x-m}{\sigma}, \frac{\dot{x}-\dot{m}}{\dot{\sigma}}\right)\right\} f^o(x,\dot{x}) \tag{12}$$

where $b_{(p,q)}$ = the quasi-moments of the vector $\{X(t), \ldots, X(t), \dot{X}(t), \ldots, \dot{X}(t)\}$, in which $X(t)$ is repeated p times and $\dot{X}(t)q$ times, $\{m, \dot{m}\}$ and $\{\sigma, \dot{\sigma}\}$ denote the means and standard deviations of $\{X(t), \dot{X}(t)\}$, $H_{(p,q)}(\xi, \zeta) = \exp(q(\xi,\zeta))(-\partial/\partial\xi)^{(p)}(-\partial/\partial\zeta)^{(q)}\exp(-q(\xi,\zeta)) =$ the generalized Hermite polynomials, $q(\xi, \zeta) = 1(2(1-\xi^2))(\xi^2 - 2\rho\xi\zeta + \zeta^2)$, ρ = the correlation coefficient between $X(t)$, $\dot{X}(t)$, and $f^o(x, \dot{x})$ = the joint density of the vector $\{X(t), \dot{X}(t)\}$ assumed to Gaussian. From equations (11) and (12),

$$\nu(x) = \nu_G(x)(1 + h(x)) \tag{13}$$

in which

$$\nu_G(x) = \int_o^\infty \dot{x} f^o(x,\dot{x}) d\dot{x} \tag{14}$$

denotes the mean crossing rate of a Gaussian process with the same mean and covariance functions as $X(t)$, and

$$h(x) = \frac{1}{\nu_G(x)} \sum_{s=3}^{\infty} \frac{1}{s!} \sum_{\substack{p+q=s \\ p,q\ge 0}} \frac{1}{\sigma^p \dot{\sigma}^q} \times b_{(p,q)} \int_o^\infty \dot{x} H_{(p,q)}\left(\frac{x-m}{\sigma}, \frac{\dot{x}-\dot{m}}{\dot{\sigma}}\right) f^o(x,\dot{x}) d\dot{x} \tag{15}$$

The function $h(x)$ is a correction factor that accounts for differences between the Gaussian distribution and the distribution of $X(t)$.

If $X(t)$ is a stationary process,

$$f^o(x,\dot{x}) = \frac{1}{2\pi\sigma\dot{\sigma}} \exp\left\{-\frac{1}{2}\left[\left(\frac{x-m}{\sigma}\right)^2 + \left(\frac{\dot{x}}{\dot{\sigma}}\right)^2\right]\right\}. \tag{16}$$

$$\nu_G(x) = \frac{1}{2\pi}\frac{\dot{\sigma}}{\sigma} \exp\left[-\frac{1}{2}\left(\frac{x-m}{\sigma}\right)^2\right], \tag{17}$$

and

$$h(x) = \sum_{s=3}^{\infty} \frac{1}{s!} \sum_{\substack{p+q=s \\ p,q\ge o}} \frac{b_{(p,q)}}{\sigma^p \dot{\sigma}^q} H_p\left(\frac{x-m}{\sigma}\right) h_q \tag{18}$$

in which $H_p(\xi) = e^{\xi^2/2}(-\partial/\partial\xi)^p e^{-\xi^2/2}$ = the Hermite polynomials of order p and $h_q = \int_o^\infty \xi H_q g(\xi) e^{-\xi^2/2} d\xi$. From the definition of the Hermite polynomials, $H_o(\xi) = 1$, $H_1(\xi) = \xi$, $H_2(\xi) = \xi^2 - 1$, $H_3(\xi) = \xi^3 - 3\xi$, and $H_4(\xi) = \xi^4 - 6\xi^2 + 3$, so that the coefficients h_q take on the values 1, $\sqrt{\pi/2}$, 1, 0, and -1 for $q = 0, 1, 2, 3$, and 4.

The mean crossing rate ν can be approximated from equation (13) in which the correction factors $h(x)$ in equations (15) and (18) are determined approximately from truncations of the series in these equations. For example, the stationary mean crossing rate $\nu(x)$ can be approximated by

$$\tilde{\nu}_S(x) = \nu_G(x)\left[1 + \sum_{s=3}^{S} \frac{1}{s!} \sum_{\substack{p+q=s \\ p,q\ge o}} \frac{b_{(p,q)}}{\sigma^p \dot{\sigma}^q} H_p\left(\frac{x-m}{\sigma}\right) h_q\right] \tag{19}$$

if one considers quasi-moments $b_{(p,q)}$ of order $s = p + q \le S$. These quasi-moments are simply related to moments $m(p, q, 0)$ with $p + q = s$ (Stratonovich, 1963; Tikhonov and Tolkachev, 1965).

Approximate Transformations of $X(t)$. Consider a non-Gaussian process $X(t)$ with first order distribution F and let

$$X_T(t) = F^{-1}(\Phi(U(t))) = g(U(t)) \tag{20}$$

in which Φ is the standard Gaussian distribution and $U(t)$ a Gaussian process with zero mean and unit variance. Recent studies (Grigoriu, 1984) have shown that $X(t)$ and $X_T(t)$ have nearly equal mean crossing rate if $X(t)$ is stationary and the covariance function of the stationary process $U(t)$ is so chosen that the covariance function of $X(t)$ and $X_T(t)$ coincide in a small vicinity of the origin. Since the mapping g is a monotonically increasing function, the stationary mean crossing rate of $X_T(t)$ has the expression

$$\nu_T(x) = \nu_U(g^{-1}(x)) = \frac{\sigma_{\dot{u}}}{2\pi} \exp\left\{-\frac{1}{2}[g^{-1}(x)]^2\right\} \tag{21}$$

where ν_U denotes the mean crossing rate of $U(t)$ and σ_U the standard deviation of $\dot{U}(t)$. The approximation ν_T of ν can be extended directly to nonstationary processes because the expression for the mean crossing rate depends only on instantaneous probabilistic characteristics of $\dot{X}(t)$ and $X(t)$.

The mapping g in equation (20) is unknown when the distribution F is not available. However, it can be approximated from moments of $X(t)$. Two approximations are considered in this section. They are based, respectively, on an optimal estimator of F and a Hermite polynomial approximation of g.

Optimal Estimator of F. Consider a set of distribution F_i with the same mean and variance as F and the class of estimators

$$\hat{F}(x) = \sum_{i=1}^{I} p_i F_i(x); \quad \sum_{i=1} p_i = 1; \; p_i \ge 0 \tag{22}$$

of F. The optimal estimator $\hat{F}_{\text{opt}}$ in this class corresponds to values of p_i minimizing an objective function (Grigoriu and Lind, 1980)

$$\epsilon_N = \sum_{n=3}^{N} (\gamma_n - \hat{\gamma}_n)^2 \tag{23}$$

in which $\gamma_n = 1/\sigma_n \int (x-m)^n dF(x)$ and $\hat{\gamma}_n = 1/\sigma\pi_n \int (x-m)^n d\hat{F}(x)$ denote dimensionless moments of order n of F and $\hat{F}$, respectively. To obtain satisfactory estimators of F the moments of order $n \ge 3$ of the distributions F_i in equation (22) have to bound the corresponding moments of F.

From equation (20), $X(t)$ is approximated by

$$\hat{X}_T(t) = \hat{F}_{\text{opt}}^{-1}(\Phi(U(t))) = \hat{g}(U(t)) \tag{24}$$

Downloaded 03 May 2010 to 171.66.16.21. Redistribution subject to ASME license or copyright; see http://www.asme.org/terms/Terms_Use.cfm

Table 1 Mean upcrossing rates of X(t)

$\frac{x-m}{\sigma}$	$\nu_G(x)$	$\tilde{\nu}_S(x)$ [Eq. 19]		$\hat{\nu}_T(x)$	$\nu_H(x)$	$\nu(x)$
	[Eq. 17]	$S=3$	$S=4$	[Eq. 25]	[Eq. 26]	[Simulation]
2	1.34×10^{-2}	3.38×10^{-2}	7.88×10^{-3}	1.33×10^{-2}	1.70×10^{-2}	7.45×10^{-3}
3	1.10×10^{-3}	1.10×10^{-2}	2.82×10^{-2}	4.47×10^{-3}	9.60×10^{-3}	4.47×10^{-3}
4	3.32×10^{-5}	8.49×10^{-4}	3.50×10^{-3}	1.36×10^{-3}	5.61×10^{-3}	1.74×10^{-3}
5	3.69×10^{-7}	1.91×10^{-5}	1.04×10^{-4}	4.35×10^{-4}	3.37×10^{-3}	9.94×10^{-4}

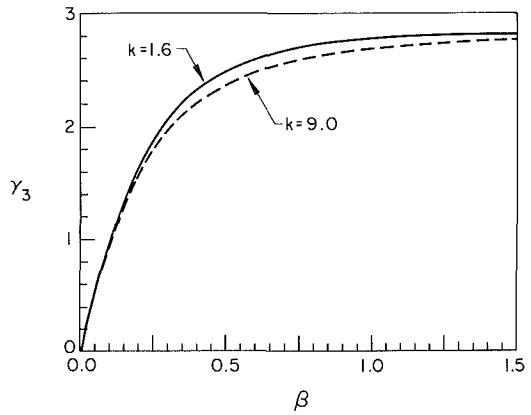

Fig. 1 Coefficient of skewness, γ_3

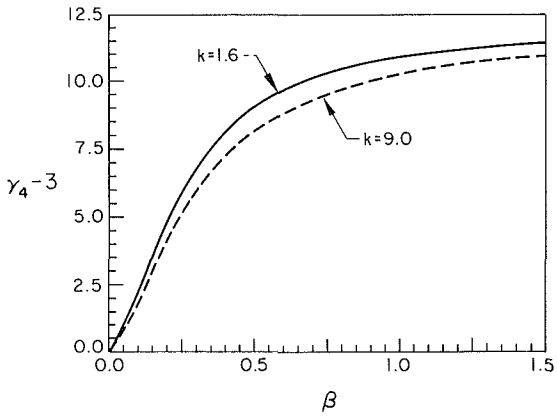

Fig. 2 Coefficient of excess, γ_4-3

so that the mean crossing rate of the response can be estimated from

$$\hat{\nu}_T(x)=\nu_U(\hat{g}^{-1}(x)) \tag{25}$$

Hermite Polynomial Approximation. The mapping g in equation (20) can also be approximated by a sum of Hermite polynomials, g_H, from the condition that $g_H(U(t))$ and $X(t)$ have similar moments (Winterstein, 1987). From equation 21, the mean crossing rate $\nu(x)$ can be estimated by

$$\nu_H(x)=\frac{\sigma_{\dot{U}}}{2\pi}\exp\left\{-\frac{1}{2}[g_H^{-1}(x)]^2\right\} \tag{26}$$

It can be shown that (Winterstein, 1987)

$$g_H^{-1}(x)=\zeta_1\left(\frac{x-m}{\sigma}\right)\left[\left(1+\xi_2\left(\frac{x-m}{\sigma}\right)\right)^{1/3}+\left(1-\xi_2\left(\frac{x-m}{\sigma}\right)\right)^{1/3}\right]-\lambda \tag{27}$$

in which

$$\zeta_1(z)=[1.5\delta(1+z)-\lambda^3]^{1/3} \tag{28}$$

$$\zeta_2(z)=\left\{1+\left[\frac{\delta-1-\lambda^2}{\zeta_1(z)^2}\right]^3\right\}^{1/2}$$

$$\lambda=\frac{\tilde{j}_3}{3\tilde{j}_4},\quad \delta=\frac{1}{3\tilde{j}_4}$$

$$\tilde{j}_4=\frac{\sqrt{1+1.5(\gamma_4-3)}-1}{18}$$

$$\tilde{j}_4=\frac{\gamma_3/6}{1+6\tilde{j}_4}$$

Applications

Consider the stationary response of the oscillator in equation (1) and assume that the excitation $Z(t)$ is the square of the Ornstein-Uhlenbeck process in equation (3) (i.e., $a_l(t)=0$ for $l\neq2$ and $a_2(t)=1$ in equation (2) with $\alpha=0.12$ and $\sigma_Y=1.0$. Equation 8 becomes in this case (Grigoriu and Ariaratnam, 1987)

$$-pm(p-1,q+1,r)+qkm(p+1,q-1,q-1,r)+(q\beta+r\alpha)m(p,q,r)=$$
$$=qm(p,q-1,r+2)+r(r-1)\alpha\sigma_Y^2m(p,q,r-2) \tag{29}$$

The moments of the state vector $X(t)$ can be determined exactly from linear algebraic equations for any $s=p+q$ and r following the algorithm in equation (9). The appendix gives closed-form expressions for several moments of $\mathbf{X}(t)$. These expressions have been used to determine moments $m(p,q,r)$ of order $s=p+q\leq4$.

Figures 1 and 2 show the variations of the coefficient of skewness, γ_3, and the coefficient of excess, γ_4-3, of the response $X_1(t)=X(t)$ with the damping parameter β for various values of the stiffness k. The skewness and the excess coefficients are increasing functions of β and vanish when $\beta=0$. The result for $\beta=0$ is consistent with a theorem by Rosenblatt giving the necessary conditions for the response of a linear system to be Gaussian (Kotulski and Sobczyk, 1981; Rosenblatt, 1961). Note also that the response is not Gaussian when $\beta\neq0$.

Table 1 gives values of $\nu(x)$ obtained by simulation, estimates of $\nu(x)$ in equations (19), (25), and (26), and mean crossing rates $\nu_G(x)$ in equation 17 for $k=1.6$ and $\beta=0.75$. The values of the corresponding moments used in this analysis are $m(1,0,0)=0.62500$, $m(2,0,0)=1.288535$; $\gamma_3=2.688366$; $\gamma_4=14.273323$; $m(0,1,0)=0$; and $m(0,2,0)=0.348280$. From equation 19, $\nu(x)$ can be approximated

$$\hat{\nu}_3(x)=\nu_G(x)\left[1-1.033279\,\frac{x-m}{\sigma}+0.448061\left(\frac{x-m}{\sigma}\right)^3\right] \tag{30}$$

or

Downloaded 03 May 2010 to 171.66.16.21. Redistribution subject to ASME license or copyright; see http://www.asme.org/terms/Terms_Use.cfm

$$\tilde{\nu}_4(x) = \nu_G(x)\left[1.93929 - 1.033279\,\frac{x-m}{\sigma} - 2.596212\left(\frac{x-m}{\sigma}\right)^2 + 0.448061\left(\frac{x-m}{\sigma}\right)^3 - 0.469722\left(\frac{x-m}{\sigma}\right)^4\right] \quad (31)$$

when the estimators of $f(x, \dot{x})$ are based on quasi-moments with $s = p + q \leq 3$ or 4. The class of estimators in equation (22) consists of linear combinations $p_1 F_{EX1}(x) + p_2 F_{EX2}(x)$ of extreme type 1 and extreme type 2 distributions. The third and fourth dimensionless moments of these distributions are 1.1395 and 5.4000 for F_{EX1} and 2.8056 and 24.6780 for F_{EX2} with shape parameter 6.0. Note that these moments bound the moments γ_3 and γ_4 of $X(t)$. The optimal estimator $\hat{F}_{opt}$ defining the mapping $\hat{g}$ in equation (25) is

$$\hat{F}_{opt}(x) = 0.536551 \exp\{-\exp[-1.353499(x - 0.198538)]\} + 0.463449 \exp\left\{-\left(\frac{0.553747}{x}\right)^{6.0}\right\} \quad (32)$$

The mapping g_H in equations (26) and (27) is defined by the functions ζ_1 and ζ_2 in equation (28) with the coefficients λ, δ, $\tilde{j}_3$, and $\tilde{j}_4$ taking the values 0.400411, 1.856421, 0.215690, and 0.179557.

From Table 1, it is evident that the Gaussian assumption is not satisfactory. It is conservative for moderate thresholds and underestimates significantly the mean upcrossing rate for relatively large values of x. The estimates of ν in equation (19) based on Hermite polynomial representations of $f(x, \dot{x})$ improve when additional moments are considered in the analysis. Nevertheless, these estimates may exhibit fluctuations that cannot be eliminated. They are less satisfactory than estimates of ν in equations (25) and (26) based on approximate transformations of $X(t)$ into a Gaussian process.

Conclusions

Equations have been developed for calculating moments of the response of linear systems to polynomial forms of Gaussian processes. It has been shown that moments of any order of both nonstationary and stationary responses can be obtained from closed sets of linear differential and algebraic equations when the input is a component of a Gauss-Markov vector process. The Itô differentiation rule has been used to derive equations for response moments. Several estimators are based on approximations of (*i*) the distribution of the response and (*ii*) transformations of the response into a Gaussian process. Moments of the response have been used in the analysis.

The proposed method has been applied to the study of the stationary response of a simple oscilator subject to the square of an Ornstein-Uhlenbeck process. This example shows that the distribution of the response departs significantly from the Gaussian distribution when damping is not small. Unsatisfactory estimators may result for mean crossing rates if based on the Gaussian assumption or on Hermite polynomial approximations of the distribution of the response. On the other hand, mean crossing rates can be estimated satisfactorily if the response is represented by a transformed Gaussian process.

The approach used in the paper can be extended to more general linear systems subject to functions of Gaussian processeses that can be approximated by polynomials. The excitation may consist of polynomials in components of Gaussian-Markov vector processes.

References

Ariaratnam, S. T., and Loh, N. K., 1968, "Optimal Control and Filtering of Linear Stochastic Systems," *International Journal of Control*, Vol. 7, No. 5, pp. 433–445.

Cramer, H., and Leadbetter, M. R., 1967, *Stationary and Related Stochastic Processes*, Wiley, New York.

Grigoriu, M., and Lind, N. C., 1980, "Optimal Estimation of Convolution Integrals," *Journal of the Engineering Mechanics Division*, ASCE, Vol. 106, No. EM6, pp. 1349–1364.

Grigoriu, M., 1984, "Crossing of Non-Gaussian Translation Processes," *Journal of Engineering Mechanics*, ASCE, Vol. 110, No. 4, pp. 610–620.

Grigoriu, M., 1986, "Response of Linear Systems to Quadratic Gaussian Excitations," *Journal of Engineering Mechanics*, ASCE, Vol. 112, No. 6, pp. 523–535.

Grigoriu, M., and Ariaratnam, S. T., 1987, "Stationary Response of Linear Systems to Non-Gaussian Excitations," *Reliability and Risk Analysis in Civil Engineering 2*, edited by N. C. Lind, Institute for Risk Research, University of Waterloo, pp. 718–724.

Karlin, S., and Taylor, H. M., 1981, *A Second Course in Stochastic Processes*, Academic Press, New York.

Kotulski, Z., and Sobczyk, K., 1981, "Linear Systems and Normality," *Journal of Statistical Physics*, Vol. 24, No. 2, pp. 359–373.

Lin, Y. K., 1976, *Probablistic Theory of Structural Dynamics*, Robert E. Krieger Publishing Company, Melbourne, Florida.

Lutes, L. D., 1985, "State Space Analysis of Stochastic Response Cumulants," *Report No. 34*, Department of Civing Engineering, Rice University, Houston, Texas.

Rosenblatt, M., 1961, "Some Comments on Narrow Band-Pass Filters," *Quarterly Applied Mathematics*, Vol. XVIII, No. 4, pp. 387–393.

Soize, C., 1978, "Gust Loading Factors with Nonlinear Pressure Terms," *Journal of the Structural Division*, ASCE, Vol. 104, No. ST6, Proc. Paper 13844, pp. 991–1007.

Soong, T. T., 1973, *Random Differential Equations in Science and Engineering*, Academic Press, New York.

Stratonovich, R. L., 1963, *Topics in the Theory of Random Noise*, Vol. 1, Gordon and Breach Science Publishers, New York.

Tikhonov, V. I., and Tolkachev, A. A., 1965, "The Effect of Non-Normal Fluctuations on Linear Systems," *Non-Linear Transformation of Stochastic Processes*, edited by P. I. Kuznetsov, R. L. Stratonovich, and V. I. Tikhonov, Pergamon Press, New York.

Winterstein, S. R., 1987, "The Use of Higher Moments in Reliability Estimation," *Reliability and Risk Analysis in Civil Engineering 2*, edited by N. C. Lind, Institute for Risk Research, University of Waterloo.

APPENDIX

Following are expressions for some stationary moments $m(p, q, r)$ of $\mathbf{X}(t)$ in equation (4) with $a_l(t) = 0$ for $l \neq 2$ and $a_2(t) = 1$. The moments are obtained by solving equation (9) for the case $\sigma_Y = 1$.

$$m(1, 0, 0) = E[X(t)] = 1/k$$

$$m(0, 1, 0) = E[\dot{X}(t)] = 0.$$

$$m(2, 0, 0) = E[X^2(t)] = (4k\alpha + 3k\beta + 4\alpha^2\beta + 2\alpha\beta^2)/ \times [(k + 2\alpha\beta + 4\alpha^2)k^2\beta]$$

$$m(0, 2, 0) = E[X^2(t)] = 4\alpha/[(k + 2\alpha\beta + 4\alpha^2)\beta]$$

$$m(3, 0, 0) = E[X^3(t)] = [126k\alpha^3\beta^3 + 64k\alpha^4\beta^2 + 217k^2\alpha^2\beta^2 + 84k\alpha^2\beta^4 + 141k^2\alpha\beta^3 + 24k^3\alpha^2 + 122k^2\alpha^3\beta + 66k^3\alpha\beta + 24k^2\alpha^4 + 4\alpha^2\beta^6 + 20\alpha^3\beta^5 + 18k\alpha\beta^5 + 32\alpha^4\beta^4 + 15k^3\beta^2 + 30k^2\beta^4 + 8k\alpha^5\beta + 16\alpha^5\beta^3]/[(k + 2\alpha\beta + 4\alpha^2) \times (k + \alpha\beta + \alpha^2)(k + 2\beta^2)(2\alpha + \beta)k^3\beta]$$

$$m(4, 0, 0) = E[X^4(t)] = [4544480k^4\alpha^4\beta^5 + 4791264k^3\alpha^5\beta^6 + 4455008k^3\alpha^6\beta^5 + 4493376k^4\alpha^5\beta^4$$

Downloaded 03 May 2010 to 171.66.16.21. Redistribution subject to ASME license or copyright; see http://www.asme.org/terms/Terms_Use.cfm

$$+ 2542144k^3\alpha^7\beta^4 + 1750110k^5\alpha^3\beta^4$$
$$+ 2649744k^4\alpha^3\beta^6 + 3173032k^3\alpha^4\beta^7$$
$$+ 929985k^5\alpha^2\beta^5 + 334632k^6\alpha^3\beta^2$$
$$+ 1800928k^5\alpha^4\beta^3 + 1031456k^5\alpha^5\beta^2$$
$$+ 2556736k^4\alpha^6\beta^3 + 299724k^6\alpha^2\beta^3$$
$$+ 814080k^4\alpha^7\beta^2 + 1259052k^3\alpha^3\beta^8$$
$$+ 553112k^2\alpha^4\beta^9 + 1342416k^2\alpha^5\beta^8$$
$$+ 1948576k^2\alpha^6\beta^7 + 878388k^4\alpha^2\beta^7$$
$$+ 1736384k^2\alpha^7\beta^6 + 128610k^6\alpha\beta^4 + 246195k^5\alpha\beta^6$$
$$+ 860672k^3\alpha^8\beta^3 + 939520k^2\alpha^8\beta^5 + 133056k^6\alpha^4\beta$$
$$+ 268032k^5\alpha^6\beta + 125952k^4\alpha^8\beta + 158208k^3\alpha^9\beta^2$$
$$+ 292352k^2\alpha^9\beta^4 + 10368k^7\alpha^2\beta + 20520k^7\alpha\beta^2$$
$$+ 3780k^7\alpha^3 + 17955k^6\beta^5 + 126496k\alpha^5\beta^{10}$$
$$+ 303760k\alpha^6\beta^9 + 431456k\alpha^7\beta^8 + 368512k\alpha^8\beta^7$$
$$+ 184064k\alpha^9\beta^6 + 45056k^2\alpha^{10}\beta^3 + 49408k\alpha^{10}\beta^5$$
$$+ 12288k^3\alpha^{10}\beta + 2048k^2\alpha^{11}\beta^2 + 5632k\alpha^{11}\beta^4$$
$$+ 1248960k^2\alpha^3\beta^{10} + 28704k\alpha^4\beta^{11}$$
$$+ 274680k^3\alpha^2\beta^9 + 154800k^4\alpha\beta^8$$
$$+ 26460k^5\beta^7 + 3456k^7\alpha^3 + 18816k^6\alpha^5$$
$$+ 21504k^5\alpha^7 + 6144k^4\alpha^9 + 3072\alpha^5\beta^{12}$$
$$+ 13728\alpha^6\beta^{11} + 33216\alpha^7\beta^{10} + 46848\alpha^8\beta^9$$
$$+ 38400\alpha^9\beta^8 + 16896\alpha^{10}\beta^7 + 3072\alpha^{11}\beta^6$$
$$+ 2736k\alpha^3\beta^{12} + 288\alpha^4\beta^{13} + 11880k^2\alpha^2\beta^{11}$$
$$+ 25380k^3\alpha\beta^{10} + 11340k^4\beta^9]/[(k + 2\alpha\beta + 4\alpha^2)^2$$
$$\times (9k + 6\alpha\beta + 4\alpha^2)(k + \alpha\beta + \alpha^2)(k + 6\alpha\beta$$
$$+ 4\alpha^2 + 2\beta^2)(k + 2\beta^2)(4k + 3\beta^2)(2\alpha + \beta)k^4\beta^2]$$

Downloaded 03 May 2010 to 171.66.16.21. Redistribution subject to ASME license or copyright; see http://www.asme.org/terms/Terms_Use.cfm

Some Observations on the Random Response of an Elasto-Plastic System

L. G. Paparizos[1]
Research Fellow.

W. D. Iwan
Fellow ASME

Division of Engineering and Applied Science,
California Institute of Technology,
Pasadena, Calif. 91125

The nature of the response of strongly yielding systems subjected to random excitation, is examined. Special attention is given to the drift response, defined as the sum of yield increments associated with inelastic response. Based on the properties of discrete Markov process models of the yield increment process, it is suggested that for many cases of practical interest, the drift can be considered as a Brownian motion. The approximate Gaussian distribution and the linearly divergent mean square value of the process, as well as an expression for the probability distribution of the peak drift response, are obtained. The validation of these properties is accomplished by means of a Monte Carlo simulation study.

Introduction

The hysteretic response behavior of structural systems subjected to strong stochastic excitation is of great research interest, due to practical applications in the fields of earthquake, ocean, and aeronautical engineering. Two basic methods have typically been employed in the analysis of the such systems; the now classical equivalent linearization approach exemplified by the work of Caughey (1960) and the yield increment approach exemplified by the work of Karnopp and Scharton (1966).

As applied by Caughey, the method of equivalent linearization is based on the assumption of narrowbanded response. However, Iwan and Lutes (1968) and the authors (Iwan and Paparizos, 1987) have shown that in the case of an elasto-plastic or nearly elasto-plastic system, the narrowbandness assumption is not applicable and equivalent linearization generally provides inaccurate response statistics. Thus, the applicability of this and similar techniques is restricted to the case of hysteretic systems which exhibit significant residual stiffness. This is a consequence of the fact that such techniques do not provide information regarding the nature of the drift or yield increment response behavior.

In order to overcome this shortcoming, Karnopp and Scharton formulated the problem in terms of the yield increment associated with inelastic response. Their analysis was limited to the calculation of yield increment statistics for an elasto-plastic system, and no results were obtained concerning the drift response statistics. It should be pointed out, however, that the yield increment formulation is physically motivated and provides the basis for the understanding of the random response of general discrete or continuum systems that exhibit an incremental constitutive relation.

The analysis presented in this paper is motivated by applications in earthquake engineering. Of primary concern in earthquake-resistant design is the ability of structures to survive large seismic excitations. The reliability of such structures is often discussed in terms of the peak inelastic response, which can be calculated analytically from the first excursion probability of the desired threshold level. In the past, consideration has been given primarily to the calculation of second-order response statistics of inelastic systems, while the first passage problem has been solved by application of general semiempirical approximate solution schemes. The main objective of the present analysis is to provide general results regarding the features of the random response of elasto-plastic systems subjected to strong stochastic excitation. Because of its significance for practical applications, consideration is also given to the derivation of an analytical solution of the first passage probability of an elasto-plastic system. The present investigation does not aim at the development of a numerical algorithm for the calculation of the drift response statistics. This issue is examined elsewhere by the authors (Paparizos, 1986; Paparizos and Iwan, 1988).

Formulation

For an elasto-plastic system subjected to a zero mean stationary Gaussian stochastic base excitation, $a(t)$, the equation of motion for the relative response, x, may be expressed as

$$\ddot{x} + 2\zeta\omega_0\dot{x} + \omega_0^2 y = -a(t) \tag{1}$$

with

$$\dot{y} = \dot{x}g(y) \tag{2}$$

where the internal variable, y, represents the elastic compo-

[1] Presently with the Department of Mechanical Engineering, Carnegie Mellon University.

Contributed by the Applied Mechanics Division for presentation at the Winter Annual Meeting, Chicago, IL, November 28 to December 2, 1988, of THE AMERICAN SOCIETY OF MECHANICAL ENGINEERS.

Discussion on this paper should be addressed to the Editorial Department, ASME, United Engineering Center, 345 East 47th Street, New York, N.Y. 10017, and will be accepted until two months after final publication of the paper itself in the JOURNAL OF APPLIED MECHANICS. Manuscript received by ASME Applied Mechanics Division, July 31, 1987; final revision, April 22, 1988.

Paper No. 88-WA/APM-64.

Copyright © 1988 by ASME
Downloaded 03 May 2010 to 171.66.16.21. Redistribution subject to ASME license or copyright; see http://www.asme.org/terms/Terms_Use.cfm

nent of the response, and ζ accounts for any additional viscous damping. $g(y)$ is given by

$$g(y) = \begin{cases} 0 & \text{if } |y| = x_y \text{ and } y\dot{x} > 0; \\ 1 & \text{otherwise} \end{cases} \tag{3}$$

where x_y denotes the yield displacement.

Of particular interest in the analysis of strongly yielding systems is the plastic drift, z, defined as the inelastic component of the displacement response, which herein becomes

$$z = x - y. \tag{4}$$

The nature of the drift response depends strongly on the low frequency content of the excitation. Hence, careful consideration must be given to the modeling of the excitation acceleration process. Based on results obtained by Kameda (1977), Boore (1983), and Iwan and Paparizos (1987), a stationary excitation model which is appropriate for earthquake excitation studies may be obtained by filtering a zero mean white noise signal through a second-order linear filter with zero low frequency content. The process, $a(t)$ is therefore represented as

$$-a(t) = 2\zeta_g \omega_g \dot{x}_g(t) \tag{5a}$$

$$\ddot{x}_g(t) + 2\zeta_g \omega_g \dot{x}_g(t) + \omega_g^2 x_g(t) = w(t), \tag{5b}$$

where $w(t)$ is a zero-mean Gaussian white noise process with spectral density $S_0/2\pi$. For the excitation model given by the equation (5), the power spectral density function will behave as ω^2 for $\omega \to 0$. The proposed model represents a significant improvement over commonly used excitation models, such as white noise and the Kanai-Tajimi filter for problems where drift is important. The model parameters also have a useful physical interpretation with ω_g corresponding to the predominant frequency of the excitation process, ζ_g being a measure of the bandwidth of the process and S_0 specifying the strength of the excitation.

It can be also shown (Paparizos, 1986) that equations (1)–(5) can be normalized with respect to the natural frequency, ω_0, and the yield displacement, x_y. For this reason, in the analysis that follows consideration is given to the normalized case, corresponding to $\omega_0 = 1$ and $x_y = 1$. The derived results, though, are presented in terms of the corresponding normalized parameter values.

Yield Increment Process Formulation

A time history sample of the drift, $z(t)$ is illustrated in Fig. 1. It can be seen that the response exhibits three distinct types of behavior. These are: purely elastic response (state S_3), yielding in the positive sense (state S_1), and yielding in the negative sense (state S_2).

Consider a time T, for which $n(T)$ yield increments have occurred between $t = 0$ and $t = T$. Then for larger T,

$$z(T) \approx \sum_{i=1}^{n(T)} d_i \tag{6}$$

where d_i is defined as the yield increment associated with the ith yield occurrence, and is given by

$$d_i = z(t_e^{(i)}) - z(t_b^{(i)}). \tag{7}$$

In equation (7), $t_b^{(i)}$ and $t_e^{(i)}$ denote the beginning and the ending time of the ith yield increment, and therefore represent the transition times between the response states S_1, S_2, and S_3. They are solutions of the first passage problems associated with the crossings by the process $\{y(t), z(t)\}$ of the barrier levels.

For the case of an elasto-plastic system subjected to a zero-mean stationary excitation, it is implied that the yield increment process is a zero process. Even if the correlation between the excitation and the elastic component of the response is significant and strongly dependent upon the excitation strength and frequency content, it can be assumed that after the first yield occurrence the yield increment process achieves approximate stationarity. From equation (6), using the previous assumptions, an expression for the mean square value of the drift may be obtained as

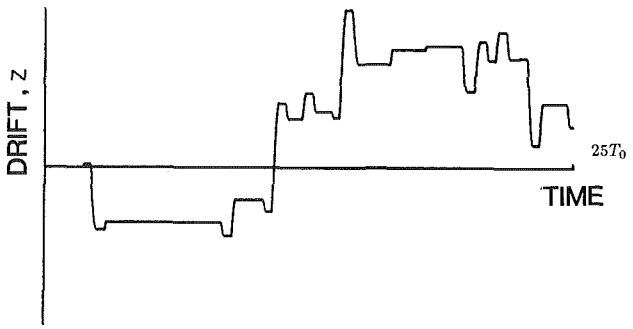

Fig. 1 Time history of drift response

$$E[z^2(T)] \approx E[n(T)Q_0 + 2(n(T)-1)Q_1 + 2(n(T)-2)Q_2 + \ldots 2Q_{(n(T)-1)}] \tag{8}$$

where Q_j is the autocorrelation of the process d_i.

Because an exact solution for the first passage times, $t_b^{(i)}$ and $t_e^{(i)}$, cannot be obtained, the autocorrelation, Q_j, cannot be evaluated analytically. However, based on the observed linear divergence of the mean square value of the drift, it can be assumed that the form of equation (8) is

$$E[z^2(T)] \approx E_0 + AQ_0 E[n(T)] = E_0 + \nu_y T A Q_0, \tag{9}$$

where ν_y is the expected value for the rate of yield occurrences. The coefficient A gives a measure of the correlation of the yield increments. For this reason, A is herein referred to as the correlation factor. For the case of mutually independent yield increments, the coefficient A is equal to one.

Numerical simulation results suggest that the linear divergent behavior of the mean square value of the drift is approximately valid for $t > T_{ex}$, where T_{ex} is the expected time of the first yield occurrence. Thus, for $t > T_{ex}$, the mean square drift response is expressible as

$$\sigma_z^2(t) = E[z^2(t)] \approx \epsilon_0' Q_0 + \nu_y A Q_0 (t - T_{ex}) \tag{10}$$

where ϵ_0' is herein defined as the offset coefficient.

First-Order Probability Density for Yield Increment Process

At time $t_b^{(i)}$, the response leaves the elastic state S_3 with a crossing velocity $\dot{z}(t_b^{(i)})$ and yielding will occur until the velocity $\dot{z}(t)$ becomes zero. Without loss of generality, we consider herein only the case of yielding in the positive direction, corresponding to positive values of yield increment, d_y, upcrossing velocity, v_y, and yield duration, t_y.

Based on previous observations (Paparizos, 1986) it is considered that stationarity of v_y, t_y and d_y is approximately achieved after the first yield occurrence. From continuity, it is implied that the stationary probability density function, $p_{v_y}(v_y)$, of the process v_y, is related to the stationary probability density $p^s_{\dot{x}y}(\dot{x}, y)$ of the response variables $(\dot{x}, y)$ corresponding to the elastic state S_3. Using the definition of the conditional probability for a discrete process, Karnopp and Scharton (1966) obtained an expression for $p_{v_y}(v_y)$, given by

$$p_{v_y}(v_y) = \lim_{\epsilon \to 0} \frac{p^s_{\dot{x}y}(v_y, 1-\epsilon)}{\int_0^\infty p^s_{\dot{x}y}(\dot{x}, 1-\epsilon)\, d\dot{x}} \quad \text{for } v_y \geq 0. \tag{11}$$

Downloaded 03 May 2010 to 171.66.16.21. Redistribution subject to ASME license or copyright; see http://www.asme.org/terms/Terms_Use.cfm

Equation (11) has been used by numerous investigators in the calculation of yield increment statistics. However, a more careful look at the relationship between $p_{v_y}(v_y)$ and $p^s_{\dot{x}y}(\dot{x}, y)$ reveals that equation (11) is actually in error (Kac and Slepian, 1959; Paparizos, 1986). The correct form of the equation is

$$p_{v_y}(v_y) = \lim_{\epsilon \to 0} \frac{v_y p^s_{\dot{x}y}(v_y, 1-\epsilon)}{\int_0^\infty \dot{x} p^s_{\dot{x}y}(\dot{x}, 1-\epsilon) d\dot{x}} \text{ for } v_y \geq 0. \quad (12)$$

Let's consider that the time $t=0$ represents the beginning of a yield increment in the positive direction, with an initial velocity, $v_\eta(0) = v_y$. Then the equation of motion for the velocity $v_\eta(t) = \dot{z}(t)$ is given by

$$\dot{v}_\eta + 2\zeta v_\eta + 1 = -a(t) \text{ for } t \in (0, t_y), \quad (13)$$

where t_y is the first passage time of the barrier level $v_\eta(t_y) = 0$. The yield increment d_y can be expressed in terms of $v_\eta(t)$ as

$$d_y = \int_0^{t_y} v_\eta(t) dt. \quad (14)$$

The stationary probability densities for t_y and d_y are obtained as solutions of stochastic differential equations. Because of the complexity of these problems, no exact solution has been obtained analytically. Instead, the following approximate solution is employed.

Consider the excitation $-a(t)$ to be composed of a deterministic mean value $m_0(t)$ and the random process $\eta(t)$, such that

$$-a(t) = m_0(t) + \eta(t). \quad (15)$$

Assume that for small yield durations $\eta(t)$ is much less than $m_0(t)$, and that $m_0(t)$ remains essentially constant during the yield occurrence. Then, for $\zeta \ll 1$, the stochastic differential equation for $v_\eta(t)$ reduces to the deterministic equation

$$\dot{v}_\eta + 1 \approx m_0, \quad (16)$$

with $v_\eta(0) = v_y$. The assumption regarding the constant value of the mean value for the excitation is justified in the case of small duration yield occurrences and for the excitation model described by a single peak spectral density function and zero low frequency content. Indeed, in this case the excitation exhibits oscillations at the characteristic frequency ω_g and strong autocorrelation for small time differences.

From equation (16), it is implied that

$$v_\eta(t) \approx v_y - (1-m_0)t \text{ for } t \in (0, t_y) \quad (17)$$

and

$$t_y \approx \frac{v_y}{(1-m_0)}. \quad (18)$$

Then, from equation (14) it is implied that

$$d_y \approx \frac{v_y^2}{2(1-m_0)}. \quad (19)$$

The mean and mean square values for the yield duration and drift increment are then calculated as

$$E[t_y] = \frac{1}{(1-m_0)} E[v_y], \quad (20)$$

$$E[d_y] = \frac{1}{2(1-m_0)} E[v_y^2]. \quad (21)$$

The approximate transformations given by the equations (12), (18)–(21) enable the expression of the first order yield increment statistics in terms of the stationary probability density function $p^s_{\dot{x}y}$. It can be actually shown that accurate estimates for $p^s_{\dot{x}y}$ can be obtained using equivalent linearization (Paparizos, 1986). Furthermore, numerical simulation results suggest that for the excitation model given by the equation (5), $p^s_{\dot{x}y}$ is approximately Gaussian distributed. Under these conditions,

$$p^s_{\dot{x}y}(v_y, 1) = Ce^{-\frac{v_y^2}{2B^2}}. \quad (22)$$

where C is a constant dependent-upon system and excitation parameter.

From equations (12) and (18)–(21), it is implied that the random variables v_y and t_y are approximately Rayleigh distributed, while an approximate exponential distribution is obtained for the yield increment process. Furthermore, the first order yield increment statistics are given by

$$E[v_y] = \sqrt{\frac{\pi}{2}} B; \quad E[v_y^2] = 2B^2; \quad E[t_y] = \frac{1}{(1-m_0)} \sqrt{\frac{\pi}{2}} B$$

$$E[d_y] = \frac{1}{(1-m_0)} B^2; \quad E[d_y^2] = \frac{2}{(1-m_0)^2} B^4. \quad (23)$$

Two-State Markov Process Model for Drift

Consider the two-state process, $S^{(i)}$, defined as the inelastic state in which the ith yielding occurs. Then, the yield increment, d_i, is described by the magnitude, $d_y^{(i)}$, and the direction of yield occurrence determined by the process $S^{(i)}$. For the models introduced in this section, it is assumed that $d_y^{(i)}$ and $S^{(i)}$ are independent processes. It is also assumed that the magnitude of the yield increments are mutually independent processes, while $S^{(i)}$ is a two-state Markov process, with transition probabilities, P^+ and P^-, defined as

$$P^+ = P(S_1 | S_1) = P(S_2 | S_2) \quad (24a)$$

$$P^- = P(S_1 | S_2) = P(S_2 | S_1) = 1 - P^+. \quad (24b)$$

Equation (24) implies that the transition probability for the stationary process, $(d_y^{(i)}, S^{(i)})$, is given by

$$p_{Sd_y}(d_y^{(i+j)}; S^{(i+j)} | d_y^{(i)}; S^{(i)} = p_{d_y}(d_y^{(i+j)}) P(S^{(i+j)} | S^{(i)}). \quad (25)$$

For the simplified yield increment model, the mean square value of the yield increment, Q_0, and the transition probabilities, P^+ and P^-, are equal to the corresponding values of the actual yield increment process. In order to account for the possible correlation between the magnitude of yield increments, two extreme cases are considered, as follows. For the determinsitic steady-state response of an elasto-plastic system, the magnitude of yield increments is constant. Based on this observation, a Type I process is defined as a process with constant magnitude yield increments. The other extreme case corresponds to uncorrelated $d_y^{(i)}$. As previously stated, in this case the first-order probability density of d_y is approximately exponentially distributed. Based on this observation, a Type II process is defined as a process with mutually independent and exponentially distributed magnitude of the yield increments.

First-Order Probability Density of Drift Response

The drift, $z^{(n)}$, is defined as the sum of yield increments, or

$$z^{(n)} = \sum_{i=1}^{n} d_i. \quad (26)$$

This implies that for zero mean yield increments, the drift is a zero mean process, with covariance, $\sigma_z^{(n)^2}$, given by

$$\sigma_z^{(n)^2} = E[z^{(n)^2}] = nQ_0 + 2(n-1)Q_1 + \ldots + 2Q_{n-1}, \quad (27)$$

where Q_j are the autocorrelation functions of the yield incre-

Downloaded 03 May 2010 to 171.66.16.21. Redistribution subject to ASME license or copyright; see http://www.asme.org/terms/Terms_Use.cfm

ment process. For the yield increment models with transition probability given by equation (25), it follows that

$$Q_j = E[\mathrm{sgn}(d_{i+j}d_i)]\begin{cases} E[d_y^2], & \text{if } j=0; \\ E^2[d_y], & \text{if } j \geq 1. \end{cases} \tag{28}$$

But $\mathrm{sgn}(d_{i+1}d_i)$ depends on the transition probability of the two-state Markov process $S^{(i)}$. Following standard procedure for the treatment of Markov chains (see, for example, Feller, 1971), it can be shown that as $n \to \infty$

$$E[z^{(n)^2}] = n\left[E[d_y^2] + \frac{2E^2[d_y]\beta_0}{1-\beta_0}\right] - \frac{2\beta_0 E^2[d_y]}{(1-\beta_0)^2} . \tag{29a}$$

where

$$\beta_0 = 1 - 2P^- . \tag{29b}$$

By considering the equivalent discrete model for the drift process, equations (10) and (29) provide approximate expressions for the correlation factor A and offset coefficient ϵ_0'. For the Type I process, $E^2[d_y] = E[d_y^2]$, which yields

$$A = \frac{P^+}{P^-} \tag{30a}$$

$$\epsilon_0' = \frac{(4P^- - 2P^{-2} - 1)}{2P^{-2}} . \tag{30b}$$

In the case of the Type II process, $2E^2[d_y] = E[d_y^2]$, which implies that

$$A = \frac{1}{2P^-} \tag{31a}$$

$$\epsilon_0' = \frac{4P^- - 1}{4P^{-2}} . \tag{31b}$$

For both processes I and II, it can also be shown that as $n \to \infty$, the drift, $z^{(n)}$, defined by equation (26), becomes a Gaussian distributed process. It should also be pointed out that the starting times of each yield occurrence are also random variables, which implies that a faster convergence towards a Gaussian distribution is noticed for the continuous drift process.

First Passage Probability

It can be shown (Paparizos, 1986) that for both Type I and Type II processes, as $n \to \infty$, the survival probability for the type D barrier at $|z| = b$ is only a function of the ratio between b and $\sigma_z^{(n)}$, and does not depend on n. Hence,

$$W_b^{(n)} = \mathrm{Prob}(|z^{(i)}| < b \ \ \forall i = 1, \ldots, n) \approx p_0\left(\frac{b}{\sigma_z^{(n)}}\right). \tag{32}$$

In equation (32), $p_0(\gamma)$ represents the survival probability of Brownian motion for a type D barrier at $|z| = \gamma t$, and is given by (Simon, 1979)

$$p_0(\gamma) = \frac{4}{\pi}\sum_{k=0}^{\infty}\frac{(-1)^k}{(2k+1)}\, e^{-\frac{(2k+1)^2\pi^2}{8\gamma^2}} . \tag{33}$$

For computational purposes, the series expansion expression for $p_0(\gamma)$, given by equation (33), can be efficiently applied for low barrier levels, or for small γ. For high barrier levels, a similar expression for $p_0(\gamma)$ with γ large can be obtained asymptotically as

$$p_0(\gamma) \approx 1 - \frac{2}{\gamma}\, e^{-\frac{\gamma^2}{2}}\left[1 - \frac{1}{\gamma^2}\right]. \tag{34}$$

Monte Carlo Simulation

Based on the properties of the discrete model, it is suggested that for large duration of stationary excitation, the drift response converges towards Brownian motion. This implies that certain drift statistics should be invariant with respect to system and excitation parameters. It remains to be shown whether such large durations correspond to problems of practical significance. Because no analytical tools are available to examine this issue, the results of Monte Carlo simulation study of the elasto-plastic system subjected to stationary stochastic excitation are presented herein.

The following properties are verified on a sample set of 54 simulation cases:

Property 1. The approximate stationarity of the response variables $\dot{x}$, y, $d_y^{(i)}$, $t_y^{(i)}$, P^+, ν_y, for times $t > T_{ex}$.

Property 2. The approximate Rayleigh distribution of the probability density function of the upcrossing velocity, υ_y and yield duration, t_y, as well as exponential distribution for the yield increment process, d_y.

Property 3. The Brownian motion nature of the drift for long duration of stationary excitation, implies: (1) linear divergent mean square drift; (2) zero-mean Guassian distribution of the drift response; and (3) distribution for the normalized peak drift response independent of t, and given by $p_0(z_{\max}(t)/\sigma_z(t))$.

The system and excitation parameters used in this analysis are selected to represent cases of practical interest. The ratio between the characteristic frequency of the excitation and the natural frequency of the system is taken as $\omega_g/\omega_0 = 0.3$, 0.5, 0.7, 1.0, 1.5, 3.0, and 5.0, while the values $\zeta_g = 0.25$ and 0.50 are selected for the bandwidth of the excitation, to represent both narrow- and broad-banded excitation, respectively. The results presented in this analysis mostly correspond to peak ductility ratios between one and ten, which is considered the range of practical interest for most structural applications. Because the objective of this study is to examine whether the Brownian motion model can be applied for excitation durations of practical interest, the duration of the simulated records is chosen as $25T_0$, were T_0 is the natural period of the system.

Yield Increment Statistics. For each set of system and excitation parameters, 250 simulated records of the response variables (x, $\dot{x}$, z, y) are obtained by numerical integration of the equations of motion (1) and (2). Since the system responds linearly in each of the three states, S_1, S_2, S_3, the equation of motion is solved exactly for each case, while the transition times $t_b^{(i)}$, $t_e^{(i)}$ are numerically calculated. From the simulated records, second-order statistics of the response variables (x, $\dot{x}$, z, y), the expected time of the first yield occurence T_{ex}^{sim} and stationary transition probabilities P^+ and P^-, are calculated. For all 54 cases studied in this analysis, a linear divergence of the mean square value of the drift and stationarity in mean square value for the response variables ($\dot{x}$, y) is approximately achieved for times $t > T_{ex}^{\mathrm{sim}}$. Following the stationarity assumption, it is also assumed that for $t > T_{ex}^{\mathrm{sim}}$, the ($\dot{x}$, y) process is ergodic. This enables the creation of large samples for the yield increment and velocity response.

A comparison of the analytical and simulation results for the probability density functions of the yield duration and yield increment processes is illustrated in Fig. 2, for parameter values $S_0/(\omega_0^3 x_y^2) = 0.40$, $\omega_g/\omega_0 = 0.70$ and bandwidth of the excitation, $\zeta_g = 0.50$. Similar results were obtained for most of the cases examined, which implies that the assumption of the Rayleigh and exponential distribution for the random variables, t_y and d_y, is very good agreement with the simulation results.

Correlation Factor and First-Order Drift Statistics. Numerical simulation estimates for the correlation factor, A, and offfset coefficient, ϵ_0', can be obtained from equation (10) and a least square fit of the corresponding numerical simula-

Downloaded 03 May 2010 to 171.66.16.21. Redistribution subject to ASME license or copyright; see http://www.asme.org/terms/Terms_Use.cfm

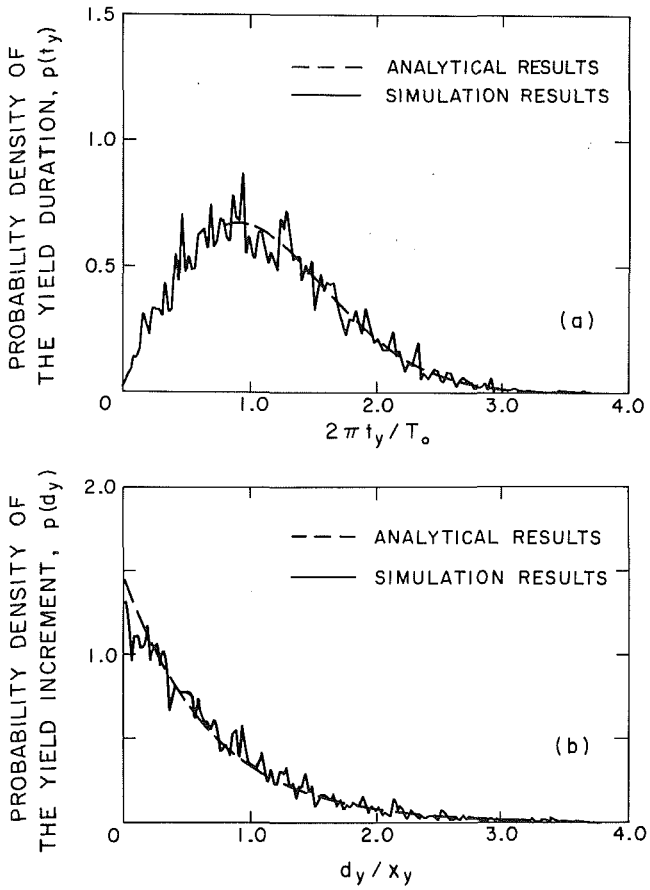

Fig. 2 *Probability density function of the (a) yield duration, t_y (b) yield increment, d_y,* **for parameter values $S_0/(\omega_0^3 x_y^2) = 0.40$, $\omega_g/\omega_0 = 0.70$ and bandwidth of excitation, $\zeta_g = 0.50$**

tion results for $\sigma_z^2(t)$. A comparison between the simulated results for $\sigma_z^2(t)$ and the corresponding least square linear fit, is illustrated in Fig 3, for the case $S_0/(\omega_0^3 x_y^2) = 0.40$, $\omega_g/\omega_0 = 1.0$ and $\zeta_g = 0.50$. Similar variations of the residual have been observed for all cases examined.

In Fig. 4, a comparison is shown between the values of A and P^+/P^- obtained from Monte Carlo simulation and the analytical results predicted by the discrete Markow process models. From the results presented, it can be seen that equation (30*a*) corresponding to the Type I process, is in better overall agreement with the simulation data. This suggests that for the actual process, the magnitude of the yield increments are not mutually independent. Nevertheless, for $\omega_g/\omega_0 > 1$ the simulated results show an increasing divergence from the Type I process, while approaching the analytical results predicted by the Type II process. Due to the actual complexity of the yield increment process, these results cannot be proofed analytically. It should be pointed out, however, that the transition probabilities P^+ and P^- provide a measure of the narrowbandness of the response. For small values of P^+/P^-, the response is narrowbanded and a yield increment in one direction will most probably be followed by yielding in the opposite direction. By contrast, for larger values of P^+/P^-, the response becomes broadbanded and the sequence of yield increments approaches a random walk type of behavior. The assumption of independent yield increments magnitude is valid in such a case, and the Type II model is justified, as illustrated in Fig. 4.

In Fig. 5, the values for the offset coefficient, ϵ_0' obtained from numerical simulation studies are compared to the expression for ϵ_0' obtained from the discrete Markov process model (equations (30*b*) and (31*b*)). It can be seen that although

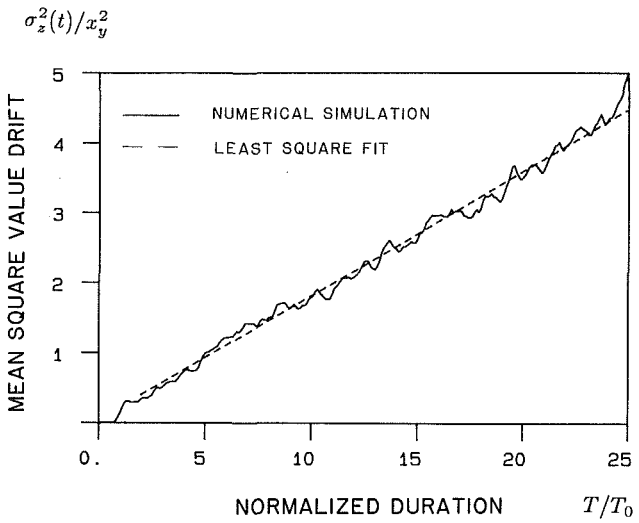

Fig. 3 Comparison between the simulated results for $\sigma_z^2(t)$ and the corresponding least square value fit, for parameter values $S_0/(\omega_0^3 x_y^2) = 0.40$, $\omega_g/\omega_0 = 1.0$ and bandwidth of excitation, $\zeta_g = 0.50$. The figure illustrates typical variations of residual that have been obtained in the present simulation study.

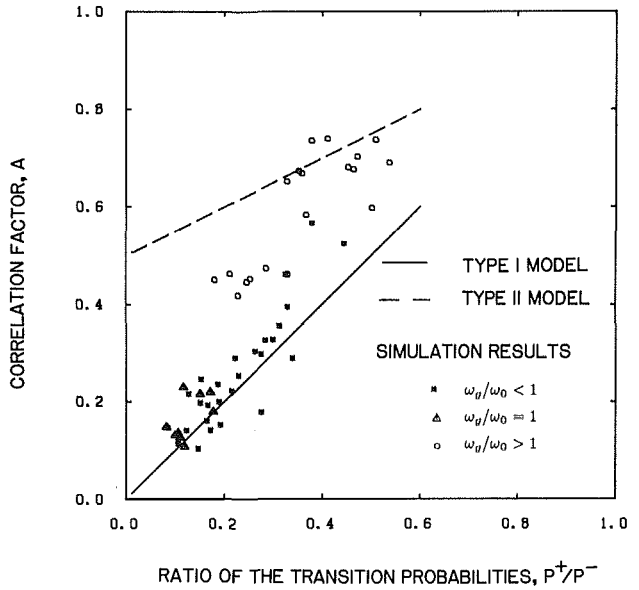

Fig. 4 Correlation factor, A, versus the ratio of transition probabilities, p^+/p^-. Comparison between analytical and numerical simulation results.

neither model is in close agreement with simulation data, an approximate value of $\epsilon_0' \approx 0.5$ gives good conservative estimates for the offset of the mean square value of the drift.

In Fig. 6, the probability distribution of the drift response at time $t = 20T_0$ is illustrated for the values of model parameters $S = 0.40$, $\omega_0/\omega_g = 1$, $\zeta = 0.01$ and $\zeta_g = 0.50$. The simulated data are obtained from a set of 2500 samples. It can be seen that the drift response indeed becomes Gaussian distributed. For structural systems, $20T_0$ would correspond to a duration of the excitation in the range of (4–60) sec.

First Passage Results. For a Brownian motion, the survival probability for of a type D barrier level at $|z| = \gamma\sigma_z(t)$ is given by equation (33). It can also be shown that the probability distribution of the peak drift response, $z_{\max}(t)$, is given by

$$\text{Prob}\left(\left|\frac{z_{\max}(t)}{\sigma_z(t)}\right| < \gamma\right) = p_0(\gamma). \qquad (35a)$$

Downloaded 03 May 2010 to 171.66.16.21. Redistribution subject to ASME license or copyright; see http://www.asme.org/terms/Terms_Use.cfm

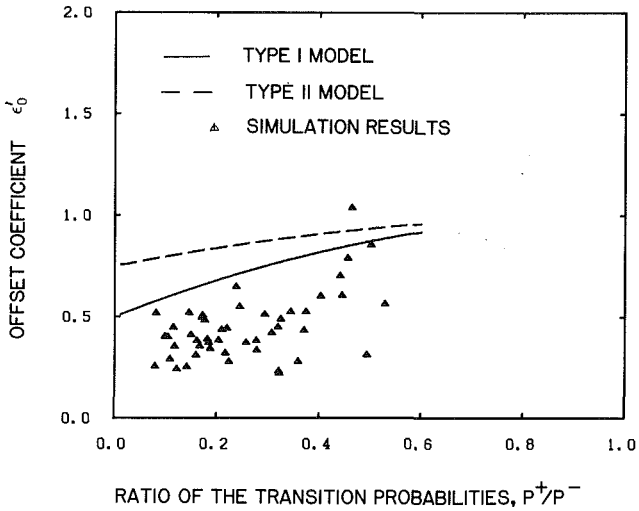

Fig. 5 Offset coefficient, ϵ_0', versus the ratio of transition probabilities, p^+/p^-. Comparison between analytical and numerical simulation results.

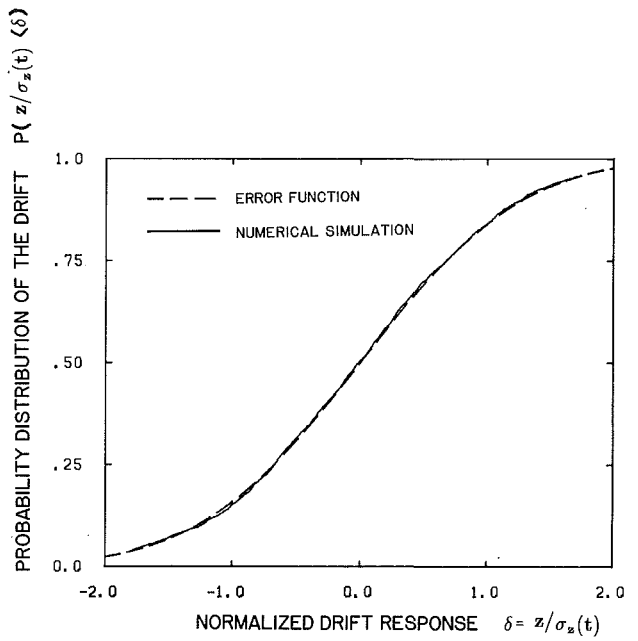

Fig. 6 Probability distribution of the drift response at time $t = 20T_0$ and for $S_0/(\omega_0^3 x_y^2) = 0.40$, $\omega_g/\omega_0 = 1.0$ and $\zeta_g = 0.50$. Numerical simulation data obtained from 2500 samples of drift response.

where

$$z_{\max}(t) = \max_{s\in(0,t)} |z(s)|. \tag{35b}$$

In Fig. 7, the simulated probability distributions for the normalized peak drift response at $t = 15T_0$ and $252T_0$ are compared with the corresponding analytical curve $p_0(\gamma)$, for the parameters values $S_0/(\omega_0^3 x_y^2) = 0.40$, $\zeta_g = 0.50$, $\zeta = 0.01$ and $\omega_0/\omega_g = 1.0$, and for 2500 simulated records. It can be seen that the analytical results are in excellent agreement with the simulation results for this case. A statistical examination of the first passage probability performed over the 54 cases considered in this analysis, is illustrated in Figs. 8 and 9.

In Figs. 8(*a*) and 8(*b*), the analytical prediction for the first passage probability distribution, $p_0(\gamma)$, is compared to the corresponding simulation results, $\mu_\gamma^{p_0} \pm \sigma_\gamma^{p_0}$, for cases corresponding to $\omega_g/\omega_0 \le 1$ and for durations $t = 25T_0$ and $t = 15T_0$, respectively. In this study, $\mu_\gamma^{p_0}$ and $\sigma_\gamma^{p_0}$ represent the

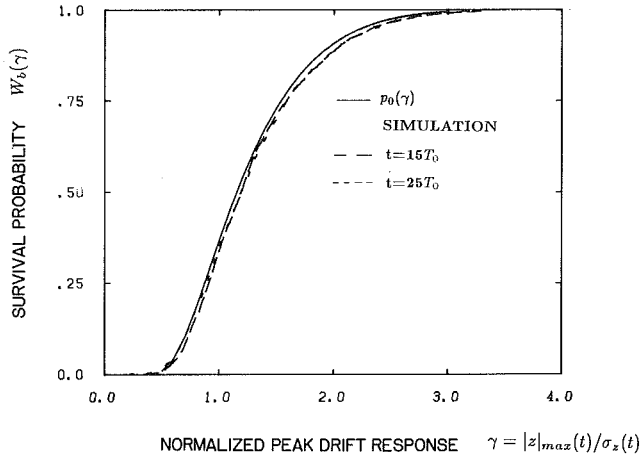

Fig. 7 Survival probability for the drift response at times $t = 15T_0$ and $t = 25T_0$, for $S_0/(\omega_0^3 x_y^2) = 0.40$, $\omega_g/\omega_0 = 1.0$ and $\zeta_g = 0.50$. Numerical simulation data obtained from 2500 samples of drift response. The results suggest the Brownian motion nature of the drift of an elasto-plastic system.

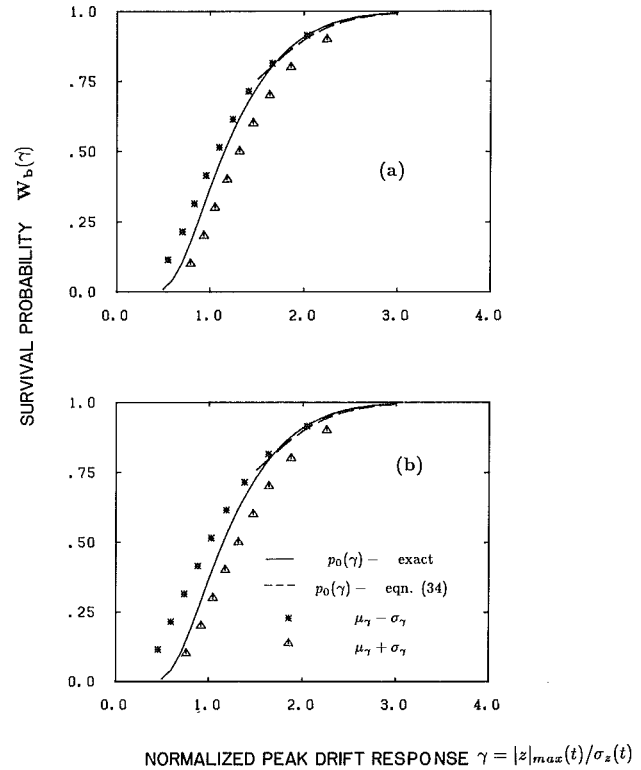

Fig. 8 Statistical examination of the survival probability for the drift response, for cases corresponding to $\omega_g/\omega_0 \le 1$. Comparison with the corresponding results for a Brownian motion at times; (*a*) $t = 25T_0$ and (*b*) $t = 15T_0$.

mean and RMS value of the parameter γ, obtained for fixed survival probability, p_0. It can be noticed that the simulation results, calculated from a set of 36 samples, are in excellent agreement with the analytical prediction. Similar conclusions can be drawn for cases corresponding to $\omega_g/\omega_0 \ge 1.$, as illustrated in Fig. 9. In this case the simulation results were calculated from a set of 27 samples. In Figs. 8 and 9, the results are also compared to the approximate expression for $p_0(\gamma)$, given by the equation (34). From this comparison, it can be concluded that the approximate expression (34), can be used for large values of the normalized peak response, or for $\gamma > 1.5$.

Downloaded 03 May 2010 to 171.66.16.21. Redistribution subject to ASME license or copyright; see http://www.asme.org/terms/Terms_Use.cfm

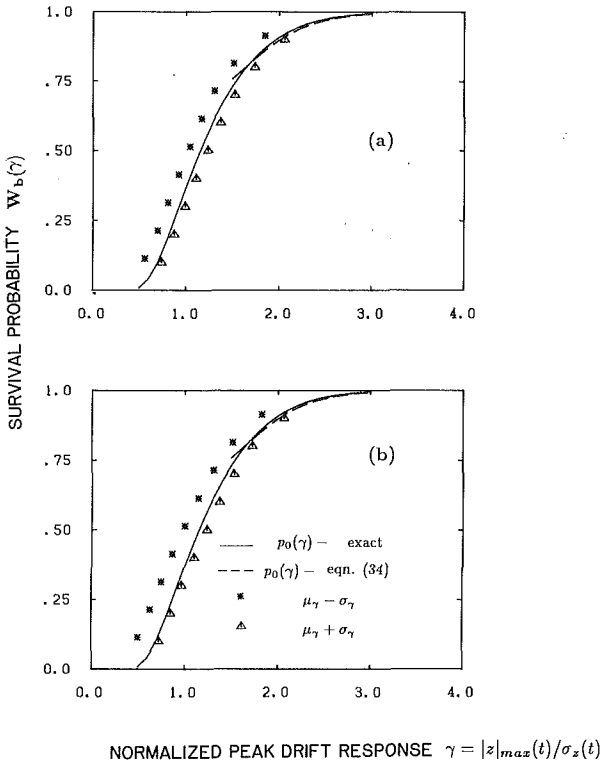

Fig. 9 Statistical examination of the survival probability for the drift response, for cases corresponding to $\omega_g/\omega_0 \geq 1$. Comparison with the corresponding results for a Brownian motion at times; (a) $t = 25T_0$ and (b) $t = 15T_0$.

Conclusions

The objective of the analysis presented in this paper is to determine the features of the response of strongly yielding structural systems subjected to random excitation. Although the presented analysis is motivated by applications in earthquake engineering, the obtained results can be extended to more general stationary excitation models. Because of the drift dependence on the low frequency content of the excitation, consideration is also given to the modeling of the ground motion acceleration spectrum.

The analysis is based on the properties of discrete Markov process models of the yield increment process, while the yield increment statistics are expressed in terms of the probability density of the velocity and elastic component of the displacement response. Using this approach, an approximate exponential and Rayleigh distribution for the yield increment and yield duration, respectively, are established. It is suggested that, for duration of stationary excitation of practical significance, the drift exhibits a Brownian motion type of behavior. Such behavior is observed for durations of at least $15T_0$, which for most structural systems corresponds to duration in the range of 3–45 sec. The implications of this observation are significant for the analysis of the random response of elasto-plastic systems. For the case of a stationary excitation, the drift response is a zero-mean Gaussian distributed random process, with transient mean square value given by the equation (10). Based on this result an analytical solution is obtained for the first passage probability of an elasto-plastic system, given by equation (33). This solution, and the asymptotic expression (34), may be applied in the reliability analysis of strongly yielding systems.

Although herein obtained for the random response of an elasto-plastic system, it is believed that the analytical results presented offer the basis for a better understanding of response behavior of general hysteretic systems.

Acknowledgments

This investigation was sponsored in part by a grant from the National Science Foundation. Any opinions, findings, conclusions, or recommendations are those of the authors and do not necessarily reflect the views of the National Science Foundation.

References

Boore, D. M., 1983, "Stochastic Simulation of High-Frequency Ground Motions Based on Seismological Models of the Radiated Spectra," *Bulletin of the Seismological Society of America*, Vol. 76, No. 6, pp. 1865–1894.

Caughey, T. K., 1960, "Random Excitation of a System With Bilinear Hysteresis," ASME JOURNAL OF APPLIED MECHANICS, Vol. 27, pp. 649–652.

Ditlevsen, O., 1986, "Elasto-Plastic Oscillator with Gaussian Excitation," *Journal of Engineering Mechanics*, ASCE, Vol. 112, No. 4, pp. 386–406.

Feller, W., 1971, *An Introduction to Probability Theory and its Applications*, John Wiley, New York.

Iwan, W. D., 1966, "A Distributed-Element Model for Hysteresis and Its Steady-State Dynamic Response," ASME JOURNAL OF APPLIED MECHANICS, Vol. 33, No. 4, pp. 893–900.

Iwan, W. D., and Lutes, L. D., 1968, "Response of the Bilinear Hysteretic System to Stationary Random Excitation," *The Journal of the Acoustical Society of America*, Vol. 43, No. 3, pp. 545–552.

Iwan, W. D., and Paparizos, L. G., 1987, "The Stochastic Response of Strongly Yielding Systems," *Probabilistic Engineering Mechanics*, (in press).

Kac and Slepian, 1959, "Large Excursions in Gaussian Processes," *Annals of Mathematics Statistics*, Vol. 30, pp. 1215–1228.

Kameda, H., 1977, "Stochastic Process Models of Strong Earthquake Motions for Inelastic Structural Response," *Proceedings of the U.S.-Southeast Asia Symposium on Engineering for Natural Hazards Protection*, Manila.

Karnopp, D., and Scharton, T. D., 1966, "Plastic Deformation in Random Vibration," *The Journal of the Acoustical Society of America*, Vol. 39, No. 6, pp. 1154–1161.

Paparizos, L. G., 1986, "Some Observations on the Random Response of Hysteretic Systems," EERL 86-02 Earthquake Engineering Research Laboratory, California Institute of Technology.

Paparizos, L. G., and Iwan, W. D., 1988, "Response Statistics for the Elasto-Plastic System, (in preparation).

Shinozuka, M., 1972, "Monte Carlo Solution of Structural Dynamics," *Computers and Structures*, Vol. 2, pp. 854–874.

Simon, B., 1979, *Functional Integration and Quantum Physics*, Academic Press.

Slepian, D., 1962, "On the Zeros of Gaussian Noise," *Time Series Analysis*, M. Rosenblatt, ed., John Wiley, New York.

Tajimi, H., 1960, "A Statistical Method of Determining the Maximum Response of a Building Structure During an Earthquake," *Proceedings of the Second World Conference on Earthquake Engineering*, Tokyo and Kyoto, Japan, Vol. II, pp. 781–797.

Downloaded 03 May 2010 to 171.66.16.21. Redistribution subject to ASME license or copyright; see http://www.asme.org/terms/Terms_Use.cfm

Equivalent Stochastic Systems

Y. K. Lin
Charles E. Schmidt
Professor and Director.

G. Q. Cai
Research Assistant.

Center for Applied Stochastics Research,
Florida Atlantic University,
Boca Raton, FL 33431

Equivalent stochastic systems are defined as randomly excited dynamical systems whose response vectors in the state space share the same probability distribution. In this paper, the random excitations are restricted to Gaussian white noises; thus, the system responses are Markov vectors, and their probability densities are governed by the associated Fokker-Planck equations. When the associated Fokker-Planck equations are identical, the equivalent stochastic systems must share both the stationary probability distribution and the transient nonstationary probability distribution under identical initial conditions. Such systems are said to be stochastically equivalent in the strict (or strong) sense. A wider class, referred to as the class of equivalent stochastic systems in the wide (or weak) sense, also includes those sharing only the stationary probability distribution but having different Fokker-Planck equations. Given a stochastic system with a known probability distribution, procedures are developed to identify and construct equivalent stochastic systems, both in the strict and in the wide sense.

Introduction

Consider two dynamical systems governed, respectively, by the following equations of motion

$$\dot{X}_j = h_j(\mathbf{X},t) + f_{jk}(\mathbf{X},t)\xi_k(t); \quad j=1,2,\ldots,n; \quad k=1,2,\ldots,m \tag{1}$$

and

$$\dot{Y}_l = H_l(\mathbf{Y},t) + F_{lr}(\mathbf{Y},t)\eta_r(t); \quad l=1,2,\ldots,n; \quad r=1,2,\ldots,s \tag{2}$$

where X_j are components of $\mathbf{X}$, Y_l are components of $\mathbf{Y}$, an overdot denotes the time differentiation, $\xi_k(t)$ and $\eta_r(t)$ are random excitations, a repeated subscript in a product implies a summation, and where $h_j(\ )$, $f_{jk}(\ )$, $H_l(\ )$, and $F_{lr}(\ )$ represent deterministic functional forms. In some cases, it is possible to determine the probability distributions for the system responses $\mathbf{X}(t)$ and $\mathbf{Y}(t)$. The two dynamical systems are said to be stochastically equivalent, if the two system responses $\mathbf{X}(t)$ and $\mathbf{Y}(t)$ share the same probability distribution.

Under certain conditions, $\mathbf{X}(t)$ and $\mathbf{Y}(t)$ tend to statistically stationary vector processes as t increases. This can occur if $h_j(\ )$, $f_{jk}(\ )$, $H_l(\ )$, and $F_{lr}(\ )$ are not explicit functions of t, if the excitations $\xi_k(t)$ and $\eta_r(t)$ are stationary random processes, and if energy can be dissipated from each of the two systems to balance the energy inputs from the excitations. Then it is possible that $\mathbf{X}(t)$ and $\mathbf{Y}(t)$ share only the same stationary probability distribution, but have different transient nonstationary distributions under identical initial conditions. In such a case, the two systems (1) and (2) are said to be stochastically equivalent in the wide (or weak) sense. On the other hand, if $\mathbf{X}(t)$ and $\mathbf{Y}(t)$ share also the transient nonstationary distribution, then systems (1) and (2) are said to be stochastically equivalent in the strict (or strong) sense. It is of interest to note that (to be explained later), first-order systems, namely each system governed by a single first-order differential equation, can be stochastically equivalent in the wide sense, not in the strict sense.

The assertion that different dynamical systems can share the same probabilistic solution, either in the wide sense or in the strict sense, may sound strange to readers accustomed to deterministic analyses. However, this is possible in the case of stochastic systems, since the assertion merely means that the probabilistic distribution of all sample solutions is the same for either system, while individual sample solutions may be all different. In fact, they are generally different even for one stochastic system.

The form of the ordinary differential equation (1) or (2) suggests that the system considered is spatially discrete. However, spatially continuous systems represented by partial differential equations, can usually be discretized using, for example, the standard Galerkin or finite element procedure. Thus, for practical purposes, such a discretized version is quite general. The functions h_j, f_{jk}, H_l, and F_{lr} can be nonlinear. Each random excitation, such as each $\xi_k(t)$ in equation (1), can be either a multiplicative excitation or an additive excitation depending on whether its accompanying factor $f_{jk}(\ )$ is or is not an explicit function of the system response $\mathbf{X}$. The multiplicative and additive random excitations are known also as the parametric and external random excitations, respectively.

In the present paper, we shall be concerned only with exact solutions and with systems which are generally nonlinear. In order to obtain specific results, we shall assume that all the random excitations are Gaussian white noises; therefore, $\mathbf{X}(t)$ in equation (1) and $\mathbf{Y}(t)$ in equation (2) are n-dimensional Markov vectors. In such a case, the probability density of the

Contributed by the Applied Mechanics Division for presentation at the Winter Annual Meeting, Chicago, IL, November 28 to December 2, 1988, of THE AMERICAN SOCIETY OF MECHANICAL ENGINEERS.

Discussion on this paper should be addressed to the Editorial Department, ASME, United Engineering Center, 345 East 47th Street, New York, N.Y. 10017, and will be accepted until two months after final publication of the paper itself in the JOURNAL OF APPLIED MECHANICS. Manuscript received by ASME Applied Mechanics Division, September 24, 1987; final revision, February 25, 1988.

Paper No. 88-WA/APM-77.

Copyright © 1988 by ASME
Downloaded 03 May 2010 to 171.66.16.21. Redistribution subject to ASME license or copyright; see http://www.asme.org/terms/Terms_Use.cfm

system response is governed by a corresponding Fokker-Planck equation (e.g., Bharucha-Reid, 1960), which can be derived from the equations of motion. We note in passing that all the stochastic equations of motion in this paper are to be interpreted in the sense of Stratonovich (1963), unless stated otherwise.

We became aware of the existence of equivalent stochastic systems when seeking systematic procedures to solve the Fokker-Planck equations associated with various nonlinear systems (Yong and Lin, 1987; Lin and Cai, 1987; Lin, Yong, and Cai, 1987). We examined in Yong and Lin (1987), the following nonlinear system

$$\ddot{X}+(\alpha+\beta X^2)\dot{X}+\omega_0^2[1+\xi_1(t)]X=\xi_2(t); \quad \alpha,\beta>0 \tag{3}$$

under a multiplicative random excitation $\xi_1(t)$ and an additive random excitation $\xi_2(t)$ which were assumed to be independent. We found that, in the state of statistical stationarity, the joint probability density of $X(t)$ and $\dot{X}(t)$ would assume the form of

$$p_s(x_1,x_2)=C\exp\left[-\frac{\beta}{2\pi K_{11}}(x_2^2+\omega_0^2x_1^2)\right] \tag{4}$$

provided $\beta/\alpha = \omega_0^4 K_{11}/K_{22}$. In equation (4), K_{11} and K_{22} are the spectral densities of $\xi_1(t)$ and $\xi_2(t)$, respectively, and x_1 and x_2 are the state variables (namely, possible values) for $X(t)$ and $\dot{X}(t)$, respectively.[1] Equation (4) implies that $X(t)$ and $\dot{X}(t)$ are independent and jointly Gaussian distributed. This is the same joint probability for the stationary-state response of the following linear system

$$\ddot{X}+\beta\dot{X}+\omega_0^2X=\xi_1(t); \quad \beta>0 \tag{5}$$

under only an additive random excitation $\xi_1(t)$. Thus, (3) and (5) are weakly equivalent stochastic systems.

Another pair of weakly equivalent stochastic systems can be constructed by adding a nonlinear spring term to both equations (3) and (5); namely,

$$\ddot{X}+(\alpha+\beta X^2)\dot{X}+\omega_0^2[1+\xi_1(t)]X+f(X)=\xi_2(t); \quad \alpha,\beta>0 \tag{6}$$

and

$$\ddot{X}+\beta\dot{X}+\omega_0^2X+f(X)=\xi_1(t); \quad \beta>0. \tag{7}$$

It has been shown (Lin and Cai, 1987) that the two stochastic systems (6) and (7) share a stationary probability distribution

$$p_s(x_1,x_2)=C\exp\left\{-\frac{\beta}{2\pi K_{11}}\left[x_2^2+\omega_0^2x_1^2+\int_0^{x_1}f(u)\,du\right]\right\} \tag{8}$$

under the same condition $\beta/\alpha = \omega_0^4 K_{11}/K_{22}$.

It appears that the restriction $\beta/\alpha = \omega_0^4 K_{11}/K_{22}$ imposed on the spectral levels of the random excitations when both multiplicative and additive random excitations are present, as in the case of (3) or (6), provides the necessary statistical balance, so that the same statistical solution can be obtained as the ones due to external excitation alone.

In the above examples, two equivalent stochastic systems, (3) and (5) or (6) and (7), are associated with different Fokker-Planck equations. These examples have shown that while sharing a common Fokker-Planck equation is a sufficient condition, it is not a necessary condition for weakly equivalent stochastic systems. It will be shown in this paper that within a class of stochastic systems for which exact probabilistic solutions are presently obtainable, subclasses of equivalent stochastic systems can be identified and constructed quite simply.

Since two systems cannot be stochastically equivalent in the strong sense unless they are of a second or higher order, and since only some stationary solutions are presently known if such systems are also nonlinear, the following discussion will focus on weakly equivalent stochastic systems. The qualification phrase "weakly" or "in the wide sense" will be omitted for convenience. The limited case of strong equivalence will be considered later in the paper.

[1] The convention of using a lowercase symbol to represent the state variable of a random quantity will also be adopted hereafter.

The Case of Vanishing Probability Flow

The probability density q of a Markov vector $\mathbf{X} = \{X_1, X_2, \ldots, X_n\}$ is governed by an associated Fokker-Planck equation which has the general form of

$$\frac{\partial q}{\partial t}+\frac{\partial}{\partial x_i}G_i=0; \quad i=1, 2, \ldots, n \tag{9}$$

where

$$G_i=A_iq-\frac{1}{2}\frac{\partial}{\partial x_j}(B_{ij}q); \quad i,j=1, 2, \ldots, n \tag{10}$$

is the probability flow in the ith direction, and where A_i are called the drift coefficients and B_{ij} called the diffusion coefficients. Equation (9) is a statement of the conservation of total probability. We shall assume that a stationary probability distribution exists which requires among other things that A_i and B_{ij} are at most functions of the state variables x's. This stationary probability density, to be denoted by p_s, must be the limit of q as t approaches infinity, and it is governed by the reduced Fokker-Planck equation

$$\frac{\partial}{\partial x_i}G_i=0; \quad i=1, 2, \ldots, n \tag{11}$$

where the probability flow G_i is now

$$G_i=A_ip_s-\frac{1}{2}\frac{\partial}{\partial x_j}(B_{ij}p_s). \tag{12}$$

Equation (9) is solved with appropriate initial and boundary conditions, and equation (11) solved with only boundary conditions. In most practical applications, the boundary conditions are natural; namely, $G_i = 0$ at the boundaries. We shall be concerned only with natural boundary conditions.

The special case of stationary potential considered by Stratonovich (1963b) is one in which G_i vanishes not only at the boundaries but also everywhere. Without loss of generality, let

$$p_s=C\exp(-\phi) \tag{13}$$

which guarantees a non-negative solution for a non-negative normalization constant C. By substituting (13) into the following equation

$$G_i=A_ip_s-\frac{1}{2}\frac{\partial}{\partial x_j}(B_{ij}p_s)=0 \tag{14}$$

we obtain

$$A_i=\frac{1}{2}\left[\frac{\partial B_{ij}}{\partial x_j}-B_{ij}\frac{\partial\phi}{\partial x_j}\right]. \tag{15}$$

Usually in a stochastic dynamics problem, the drift and diffusion coefficients are obtained from the equations of motion, and the objective is to find the stationary probability potential ϕ. Since there are a total of n equations in (15), it is not always possible to find a consistent ϕ satisfying all these equations. If such a consistent solution is indeed obtainable, then the problem is said to belong to the class of stationary potential. However, in the context of the present paper, we assume *a priori* that a potential function ϕ is known. Then (15) can be used to construct equivalent stochastic systems within the class of stationary potential.

It is easy to visualize that, at the stationary state, the probability flow of a one-dimensional (scalar) stochastic process, Markovian or otherwise, must vanish everywhere if it vanishes at the boundaries. Consider a Markov process which

Downloaded 03 May 2010 to 171.66.16.21. Redistribution subject to ASME license or copyright; see http://www.asme.org/terms/Terms_Use.cfm

represents the response of the following first-order linear system

$$\dot{X} = -\beta X + \xi(t), \quad \beta > 0 \tag{16}$$

where $\xi(t)$ is a Gaussian white noise with a spectral density K. It can be shown that the drift and diffusion coefficients in the corresponding Fokker-Planck equation are $A = -\beta x$ and $B = 2\pi K$, and that the stationary probability density for the system response $X(t)$ is

$$p_s(x) = C \exp\left(-\frac{\beta}{2\pi K} x^2\right). \tag{17}$$

An equivalent stochastic system, with the same stationary probability density but a different diffusion coefficient $B = 2\pi K x^2$ must have a drift coefficient

$$A = 2\pi K x - \beta x^3 \tag{18}$$

according to equation (15). These drift and diffusion coefficients can be obtained from a stochastic system

$$\dot{X} = \pi K X - \beta X^3 + X\xi(t). \tag{19}$$

Therefore, (16) and (19) are stochastically equivalent. Note that the well-known correction of Wong and Zakai (1965) must be taken into account in obtaining the drift coefficient for the stochastic system (19). This correction is required whenever a multiplicative random excitation is present at the $(n-1)$th derivative term in an nth-order differential equation. Again, the Fokker-Planck equations associated with the two stochastic systems, (16) and (19), are different, although they have the same stationary solution, equation (17).

Circulatory Probability Flow

Unfortunately, equation (15) is not very useful when applying to higher order stochastic systems since circulatory probability flow can exist and usually exists in a multi-dimensional space. To provide for additional flexibility, we split each of the drift coefficients and the diffusion coefficients into two parts:

$$A_i = A_i^{(1)} + A_i^{(2)} \tag{20}$$

$$B_{ij} = B_{ij}^{(i)} + B_{ji}^{(j)}. \tag{21}$$

Equation (21) retains the symmetry condition for the diffusion coefficients; namely, $B_{ij} = B_{ji}$. Substituting (20) and (21) into (11), we obtain

$$\frac{\partial}{\partial x_i}\left[A_i^{(1)} p_s - \frac{\partial}{\partial x_j} B_{ij}^{(i)} p_s\right] + \frac{\partial}{\partial x_i}\left[A_i^{(2)} p_s\right] = 0. \tag{22}$$

We choose that $A_i^{(1)}$ be associated with the vanishing probability flow, and $A_i^{(2)}$ be associated with the circulatory probability flow. Then, for a p_s expressed in the form of (13), we find that

$$\frac{\partial}{\partial x_i} A_i^{(2)} = A_i^{(2)} \frac{\partial \phi}{\partial x_i} \tag{23}$$

$$A_i^{(1)} = \frac{\partial}{\partial x_j} B_{ij}^{(i)} - B_{ij}^{(i)} \frac{\partial \phi}{\partial x_j}. \tag{24}$$

Equation (24) is equivalent to equation (15) in the absence of circulatory flow. The factor 1/2 on the right-hand side of (15) could have been removed also by splitting B_{ij} in the manner of (21). There are a total of $n+1$ equations in the set of (23) and (24). If our objective is to obtain an exact solution for a given stochastic system, which is the case in Yong and Lin (1987), Lin and Cai (1987), and Lin, Yong, and Cai (1987), then these equations may be viewed as equations for ϕ. A problem is solvable if a consistent ϕ function can be obtained from these equations by properly splitting the drift and diffusion coefficients A_i and B_{ij}. Such a solvable problem is said to belong to the class of generalized stationary potential (Lin and Cai, 1987).

Instead, our present objective is to identify a group of dynamical systems which are stochastically equivalent to a given stochastic system with a known solution. From this viewpoint, the ϕ function is known. We shall attempt to find possible A_i and B_{ij} coefficients such that equations (23) and (24) can all be satisfied.

In order to satisfy (23), we let

$$A_i^{(2)} = \frac{\partial}{\partial x_j} \delta_{ij}^{(1)} - \delta_{ij}^{(1)} \frac{\partial \phi}{\partial x_j} \tag{25}$$

where δ_{ij} is anti-symmetric; namely, $\delta_{ji}^{(1)} = -\delta_{ij}^{(1)}$. It can easily be verified by substitution that (25) satisfies (23). Adding (24) and (25),

$$A_i = \frac{\partial}{\partial x_j}\left(B_{ij}^{(i)} + \delta_{ij}^{(1)}\right) - \left(B_{ij}^{(i)} + \delta_{ij}^{(1)}\right) \frac{\partial \phi}{\partial x_j}. \tag{26}$$

Now, since B_{ij} is symmetric, it is always possible to write

$$B_{ij}^{(i)} = \frac{1}{2} B_{ij} + \delta_{ij}^{(2)} \tag{27}$$

where $\delta_{ij}^{(2)}$ are also anti-symmetric. Then equation (26) becomes

$$A_i = \frac{\partial}{\partial x_j}\left(\frac{1}{2} B_{ij} + \delta_{ij}\right) - \left(\frac{1}{2} B_{ij} + \delta_{ij}\right) \frac{\partial \phi}{\partial x_j} \tag{28}$$

where

$$\delta_{ij} = \delta_{ij}^{(1)} + \delta_{ij}^{(2)} \tag{29}$$

is again anti-symmetric. The set of n equations in (28), which replaces the set of $n+1$ equations in (23) and (24), is simpler since the process of splitting A_i and B_{ij} are now replaced by a single process of selecting δ_{ij}. With the knowledge of the solution of one stochastic system, namely, the knowledge of ϕ, we can construct a large number of equivalent stochastic systems by selecting physically meaningful combinations of B_{ij} and δ_{ij} matrices. It is of interest to note that San Miguel and Chaturvedi 1980,[2] have considered previously a more restrictive type of stochastically equivalent systems which share the same *reduced* Fokker-Planck equation by varying only the δ_{ij} matrix, while keeping the B_{ij} matrix fixed. Such systems are still stochastically equivalent only in the weak sense because they satisfy (28) which has been obtained from the reduced Fokker-Planck equation (11).

We digress to remark that as seen from (25), the case of $\delta_{ij} = 0$ implies $A_i(^2) = 0$, namely, the absence of the circulatory probability flow. It follows from (28) that the reduced Fokker-Planck equations must be different for two stochastically equivalent systems. Thus, the full Fokker-Planck equations must be also different, and the two systems can at most be stochastically equivalent in the wide sense. In particular, two first-order stochastic systems can, at most, be equivalent in the wide sense.

The constitutive relation (28) for equivalent stochastic systems is given in terms of drift and diffusion coefficients of the associated Fokker-Planck equations. For practical applications, it is more convenient to operate directly on the equations of motion. Consider a stochastic system governed by equation (1) in the sense of Stratonovich, where h_j and f_{jk} are functions of $\mathbf{X}$, and where the excitation Gaussian white noises are generally correlated with correlation functions

$$E[\xi_k(t)\xi_s(t+\tau)] = 2\pi K_{ks}\delta(\tau). \tag{30}$$

The drift and diffusion coefficients of the associated Fokker-Planck equation are (Wong and Zakai, 1965)

$$A_i = h_i(\mathbf{x}) + \pi K_{ls} f_{rs}(\mathbf{x}) \frac{\partial}{\partial x_r} f_{il}(\mathbf{x}) \tag{31}$$

$$B_{ij} = 2\pi K_{ls} f_{il}(\mathbf{x}) f_{js}(\mathbf{x}) \tag{32}$$

[2] We are indebted to Prof. L. Arnold for this information.

Downloaded 03 May 2010 to 171.66.16.21. Redistribution subject to ASME license or copyright; see http://www.asme.org/terms/Terms_Use.cfm

where $\mathbf{x}$ is the state vector of $\mathbf{X}$. Equations (28), (31), and (32) imply that for a stochastic system having a stationary probability density of the form of (13), the h and f functions in (1) must be related as

$$h_i(\mathbf{X}) = \pi K_{ls} f_{js}(\mathbf{X}) \frac{\partial}{\partial X_j} f_{il}(\mathbf{X}) - \pi K_{ls} f_{il}(\mathbf{X}) f_{js}(\mathbf{X}) \frac{\partial \phi}{\partial X_j} + \frac{\partial}{\partial X_j} \delta_{ij}(\mathbf{X}) - \delta_{ij}(\mathbf{X}) \frac{\partial \phi}{\partial X_j} \tag{33}$$

where δ_{ij} are anti-symmetric. We obtain the wide-sense equivalent stochastic systems by varying both the f_{ij} and δ_{ij} functions.

Oscillatory Stochastic Systems

Dynamical systems encountered in structural and mechanical engineering applications are often oscillatory which are described by a set of second-order equations as follows

$$\ddot{Z}_i + \psi_i(\mathbf{Z}, \dot{\mathbf{Z}}) = \theta_{ij}(\mathbf{Z}, \dot{\mathbf{Z}}) \xi_j(t); \quad i = 1, 2, \ldots, n; \quad j = 1, 2, \ldots, m. \tag{34}$$

Letting $X_{2i-1} = Z_i$ and $X_{2i} = \dot{Z}_i$, the system of second-order equations are replaced by the first-order ones,

$$\dot{X}_{2i-1} = X_{2i} \tag{35a}$$

$$\dot{X}_{2i} = -\psi_i(\mathbf{X}) + \theta_{ij}(\mathbf{X}) \xi_j(t). \tag{35b}$$

Applying (33) to the present case, we obtain

$$X_{2i} = \frac{\partial}{\partial X_r} \delta_{2i-1,r} - \delta_{2i-1,r} \frac{\partial}{\partial X_r} \phi; \quad i = 1, 2, \ldots, n; \quad r = 1, 2, \ldots, 2n \text{ and } r \neq 2i-1 \tag{36}$$

$$\psi_i = -\pi K_{ls} \theta_{qs} \frac{\partial}{\partial X_{2q}} \theta_{il} + \pi K_{ls} \theta_{il} \theta_{qs} \frac{\partial}{\partial X_{2q}} \phi - \frac{\partial}{\partial X_r} \delta_{2i,r} + \delta_{2i,r} \frac{\partial}{\partial X_r} \phi;$$

$$i = 1, 2, \ldots, n; \quad q = 1, 2, \ldots, n; \quad l = 1, 2, \ldots, m; \quad s = 1, 2, \ldots, m; \quad r = 1, 2, \ldots, 2n \text{ and } r \neq 2i. \tag{37}$$

Condition imposed in (36) for possible δ functions is quite restrictive. For example, the choice of $\delta_{pr} = 0$, which implies a vanishing probability flow, is not possible because it requires that all $X_{2i} = 0$, thus contradicting the very existence of the relation (35b).

Additional insight can be gained by examining in detail a single degree-of-freedom system

$$\ddot{Z} + \psi(Z, \dot{Z}) = \theta_j(Z, Z) \xi_j(t) \tag{38}$$

or

$$\dot{X}_1 = X_2 \tag{39a}$$

$$\dot{X}_2 = -\psi(X_1, X_2) + \theta_j(X_1, X_2) \xi_j(t). \tag{39b}$$

The conditions for equivalent stochastic systems are

$$X_2 = \frac{\partial}{\partial X_2} \delta - \delta \frac{\partial \phi}{\partial X_2} \tag{40}$$

$$\psi = -\pi K_{ls} \theta_s \frac{\partial}{\partial X_2} \theta_l + \pi K_{ls} \theta_l \theta_s \frac{\partial \phi}{\partial X_2} + \frac{\partial \delta}{\partial X_1} - \delta \frac{\partial \phi}{\partial X_1} \tag{41}$$

where $\delta = \delta_{12} = -\delta_{21}$. The most general δ function which satisfies (40) is given by

$$\delta = [D(X_1) + \int X_2 \exp(-\phi) dX_2] \exp(\phi) \tag{42}$$

where $D(X_1)$ is an arbitrary function of X_1. Substituting (42) into (41)

$$\psi = -\pi K_{ls} \theta_s \frac{\partial}{\partial X_2} \theta_l + \pi K_{ls} \theta_l \theta_s \frac{\partial \phi}{\partial X_2} - \exp(\phi) \int X_2 \frac{\partial \phi}{\partial X_1} \exp(-\phi) dX_2 + D'(X_1) \exp(\phi). \tag{43}$$

Equation (43) can be used to construct second-order equivalent stochastic systems sharing a same stationary probability density of the form of equation (13).

Of special interest is a potential function (Caughey and Ma, 1983; Lin, Yong, and Cai, 1987)

$$\phi = -ln\lambda_Y + \phi_0(\lambda) \tag{44}$$

where λ is an arbitrary function of $X = X_1$ and $Y = \frac{1}{2}X_2^2$, and λ_Y denotes the partial derivative of λ with respect to Y. Of course, the ϕ function must satisfy the general condition that the probability density expressed as in equation (13) is normal. Substitution of (44) into (43) yields

$$\psi = -\pi K_{ls} \theta_s \frac{\partial}{\partial X_2} \theta_l + \pi X_2 K_{ls} \theta_l \theta_s \left[\lambda_Y \frac{d}{d\lambda} \phi_0(\lambda) - \lambda_{YY}/\lambda_Y \right] + \lambda_X/\lambda_Y + \lambda_Y^{-1} D'(X_1) \exp[\phi_0(\lambda)]. \tag{45}$$

They further specialize to the case

$$\lambda = \frac{1}{2} X_2^2 + \int_0^{X_1} g(u) du = Y + \int_0^X g(u) du \tag{46}$$

and $D'(X_1) = 0$

$$\psi = -\pi K_{ls} \theta_s \frac{\partial}{\partial X_2} \theta_l + \pi X_2 K_{ls} \theta_l \theta_s \frac{d}{d\lambda} \phi_0(\lambda) + g(X_1). \tag{47}$$

Among the numerous stochastic systems sharing the same stationary probability density

$$p_s(x_1, x_2) = C \exp\left\{ -\frac{\beta}{\pi K_{11}} \left[x_2^2 + 2 \int_0^{x_1} g(u) du \right] \right\} \tag{48}$$

we cite the following examples

$$\ddot{Z} + 2\beta \dot{Z} + g(Z) = \xi_1(t)$$

$$\ddot{Z} + 2\beta Z^2 \dot{Z} + g(Z) = Z \xi_1(t)$$

$$\ddot{Z} - \pi K_{11} \dot{Z} + 2\beta \dot{Z}^3 + g(Z) = \dot{Z} \xi_1(t)$$

$$\ddot{Z} + 2\beta \dot{Z} [1 + (K_{22}/K_{11}) Z^2] + g(Z) = \xi_1(t) + Z \xi_2(t)$$

$$\ddot{Z} + (2\beta - \pi K_{33}) \dot{Z} + 2\beta \dot{Z} [(K_{22}/K_{11}) Z^2 + (K_{33}/K_{11}) \dot{Z}^2] + g(Z) = \xi_1(t) + Z \xi_2(t) + \dot{Z} \xi_3(t)$$

where $\xi_1(t)$, $\xi_2(t)$, and $\xi_3(t)$ are assumed independent, having spectral densities K_{11}, K_{22}, and K_{33}, respectively.

Equivalent Stochastic Systems in the Strict Sense

Strictly equivalent stochastic systems share an identical probability distriction in both stationary and nonstationay states. To investigate the existence and the forms of such systems, we begin with the full Fokker-Planck equation (9). This equation remains unchanged by adding anti-symmetric elements to the diffusion terms; namely,

$$\frac{\partial q}{\partial t} + \frac{\partial}{\partial x_i} \left\{ A_i q - \frac{1}{2} \frac{\partial}{\partial x_j} [(B_{ij} + \delta_{ij}) q] \right\} = 0. \tag{49}$$

The anti-symmetric terms δ_{ij} cancel, upon differentiations with respect to x_j and x_i. However, the diffusion matrix B_{ij} must remain symmetric. This means that strictly equivalent stochastic systems must have the same B_{ij} matrix, and that given a set of A_i and B_{ij} of a system, the others can be constructed by requiring

$$A_i^* q = A_i q - \frac{1}{2} \frac{\partial}{\partial x_j} (\delta_{ij} q). \tag{50}$$

The nonstationary probability density q in (50) is time dependent, which can be cast in the form of

Downloaded 03 May 2010 to 171.66.16.21. Redistribution subject to ASME license or copyright; see http://www.asme.org/terms/Terms_Use.cfm

$$q(\mathbf{x},t) = C(t)\exp[-\phi(\mathbf{x},t)]. \tag{51}$$

Substitution of (51) into (50) results in

$$A_i^* = A_i - \frac{1}{2}\left(\frac{\partial}{\partial x_j}\,\delta_{ij} - \delta_{ij}\,\frac{\partial\phi}{\partial x_j}\right). \tag{52}$$

With the understanding that the diffusion matrix must remain unchanged, (52) specifies a set of additional conditions for stochastically equivalent systems in the strict sense.

For example, consider again the single degree-of-freedom system governed by equation (38), or by equations (39*a*,*b*). Denote its strictly equivalent systems by

$$\ddot{Z} + \psi^*(Z,\dot{Z}) = \theta_j^*(Z,\dot{Z})\xi_j^*(t). \tag{53}$$

The condition for an identical diffusion matrix requires

$$K_{ls}^*\theta_l^*\theta_s^* = K_{ls}\theta_l\theta_s \tag{54}$$

which, for practical purposes, may be replaced by the more restrictive $K_{ls}^* = K_{ls}$ and $\theta_l^* = \theta_l$. Then condition (52) leads to

$$\frac{\partial}{\partial X_2}\,\delta - \delta\,\frac{\partial\phi}{\partial X_2} = 0 \tag{55}$$

$$\psi^* = \psi - \frac{\partial}{\partial X_1}\,\delta + \delta\,\frac{\partial\phi}{\partial X_1}\,. \tag{56}$$

Equation (55) is satisfied by

$$\delta = F(X_1,t)\exp(\phi) \tag{57}$$

where F is an arbitrary function of X_1 and t. Consequently,

$$\psi^* = \psi + f(X_1,t)\exp(\phi) \tag{58}$$

where f is also arbitrary in X_1 and t. Slightly more complicated ψ^* function is obtained if the less restrictive condition (54) is imposed.

It should be noted that exact nonstationary probabilistic solutions are largely unknown for the second and higher order systems, except for the simple case of a linear system under purely additive Gaussian excitations. Thus, results for strictly equivalent stochastic systems given here are more of a theoretical interest at the present time.

Concluding Remarks

Initially a by-product of earlier efforts to obtain exact solutions for nonlinear systems under both additive and multiplicative random excitations (Yong and Lin, 1987; Lin and Cai, 1987; Lin, Yong, and Cai, 1987), the concept of equivalent stochastic systems is further developed and presented here as a separate paper, because the concept itself has important practical implications. The knowledge of the existence and of the forms of equivalent stochastic systems is useful in system identification using random inputs and outputs. Such an identification technique is now considered less problematic if the inputs are purely additive. If the possibility of multiplicative excitations exists, additional measurements may be required to properly identify the system. Another important application is in the development of approximation schemes for systems for which exact solutions are presently not obtainable. Within a class of solvable equivalent stochastic systems, the one closest to the original system may be selected on the basis of a suitable statistical criterion. Such an approximation scheme will be the subject of a forthcoming paper.

Acknowledgment

The research reported in this paper was supported by the National Science Foundation under Grant ECE-8607183. Opinions, findings, and conclusions expressed are those of the writers and do not necessarily reflect the views of NSF. The Pao Zao-long and Pao Yo-kong Scholarship received by G. Q. Cai while pursuing his research at the Florida Atlantic University is also gratefully acknowledged.

References

Bharucha-Reid, A. T., 1960, *Elements of the Theory of Markov Processes and Their Applications*, McGraw-Hill, New York.

Caughey, T. K., and Ma, F., 1983, "The Exact Steady-State Solution of a Class of Nonlinear Stochastic Systems," *Int. J. Non-Linear Mechanics*, Vol. 17, pp. 137–142.

Lin, Y. K., and Cai, G. Q., 1988, "Exact Stationary-Response Solution for Second-Order Nonlinear Systems under Parametric and External White-Noise Excitations, Part II," ASME JOURNAL OF APPLIED MECHANICS, Vol. 55, pp. 702–705.

Lin, Y. K., Yong, Y., and Cai, G. Q., 1987, "Exact Solutions for Nonlinear Systems under Parametric and External White-Noise Excitations," *Proc. US-Austria Joint Seminar on Stochastic Structural Mechanics*, Y. K. Lin and G. I. Schuëller, eds., Springer-Verlag.

San Miguel, M., and Chaturvedi, S., 1980, "Limit Cycles and Detailed Balance in Fokker-Planck Equations," *Zeitschrift fur Physik*, Vol. B40, pp. 167–174.

Stratonovich, R. L., 1963a, "A New Representation for Stochastic Integrals and Equations," translation by N. H. Choksy, *J. SIAM Control*, Vol. 4, No. 2, 1966, pp. 362–371.

Stratonovich, R. L., 1963b, *Topics in Theory of Random Noise*, Vol. 1, Gordon and Breach, New York.

Wong, E., and Zakai, M., 1965, "On the Relation Between Ordinary and Stochastic Equations," *Int. J. Eng. Sci.*, Vol. 3, No. 2, pp. 213–229.

Yong, Y., and Lin, Y. K., 1987, "Exact Stationary-Response Solution for Second Order Nonlinear Systems under Parametric and External White-Noise Excitations," ASME JOURNAL OF APPLIED MECHANICS, Vol. 54, pp. 414–418.

Downloaded 03 May 2010 to 171.66.16.21. Redistribution subject to ASME license or copyright; see http://www.asme.org/terms/Terms_Use.cfm

Hopf Bifurcation in the Presence of Both Parametric and External Stochastic Excitations

N. Sri Namachchivaya
Department of Aeronautical and Astronautical Engineering, University of Illinois at Urbana-Champaign, Urbana, Ill. 61801

In this paper the effect of small parametric and external stochastic perturbations on a two-dimensional system exhibiting Hopf bifurcation is discussed in detail. It is shown that even small fluctuations in parameters can have an important effect when the system is in the neighborhood of bifurcation points. The Markov diffusion approximation is used to obtain analytical results relating to the statistical properties of the stochastic response. Both moment and sample stability conditions along with the stationary moments are obtained. For the nonlinear system, stationary and transient probability densities are found along with their stationary moments. It was found that in nonlinear systems, a shift of the bifurcation point takes place due to the presence of parametric noise.

1 Introduction

The numerous studies made in recent years of bifurcation behavior of nonlinear dynamical systems have almost invariably assumed that these systems operate in an environment which is constant in time. Even though the phenomena of bifurcation of autonomous nonlinear dynamical systems is well understood, the study of the parametrically perturbed bifurcations has not received much attention. The effect of periodic perturbations upon a bifurcating system have been studied by Rosenblat and Cohen (1980, 1981), Kath (1971), Bajaj (1986), and Sri Namachchivaya and Ariaratnam (1987), using various techniques. The assumption that the system parameters and operating environment are constant or periodic in time is, indeed, a simplification of reality in many engineering systems. In addition to deterministic fluctuattions, which are not considered in this paper, there can be stochastic environmental and parametric fluctuations due to several factors; for example, forces generated by jet and rocket engines in modern high-powered flight vehicles and missile structures, excitations due to earthquakes, ocean waves and wind gusts, etc. In this paper, it is shown that even small fluctuations in parameters can have an important effect when the system is on the point of changing from one equilibrium state to another, in other words, in the neighborhood of bifurcation points. Furthermore, it is shown that, from the phenomenological point of view, the parametric and external stochastic fluctuations have different features. In the first case, the thresholds depend on the strength of excitation term and eventually new instabilities appear which are completely noise-induced while, in the second case, the stability thresholds are not modified by the noise term.

In the past two decades the study of nonlinear stochastic dynamical systems has received a lot of attention. Most of these studies deal with nonlinear systems which are externally excited. Furthermore, the analysis is usually carried out by the use of either a Markov diffusion approximation in the case of wide-band excitation or a method of equivalent linearization (see, e.g., Lin, (1967)). However, the procedure for the analysis of parametrically perturbed nonlinear stochastic systems is somewhat different. A specific nonlinear system was investigated by Ariaratnam (1980) to illustrate the phenomenon of stochastic bifurcation and the possibility of errors in the use of the Gaussian closure technique for the approximate analysis. Recently, Lin and co-workers (1983, 1984) have considered cumulant-neglect closure for nonlinear systems under both parametric and external excitations, and have shown improvements in the results for stationary mean square amplitude as compared to those obtained using Gaussian closure. In this paper, the approach of Ariaratnam (1980) and Ariaratnam and Tam (1979) is followed to understand the bifurcation phenomenon of two-dimensional nonlinear dynamical systems which, in the absence of the stochastic parametric and external excitations, undergo a Hopf bifurcation.

2 Statement of the Problem

Since, in Hopf bifurcation problems the bifurcation behavior is restricted to the two-dimensional center manifold, no essential generality would be lost by restricting ourselves to a two-dimensional system. However, even a two-dimensional system with general structure leads to some tedious algebraic computations. To circumvent the cumbersome algebra we

Contributed by the Applied Mechanics Division for presentation at the Winter Annual Meeting, Chicago, IL, November 28 to December 2, 1988, of THE AMERICAN SOCIETY OF MECHANICAL ENGINEERS.

Discussion on this paper should be addressed to the Editorial Department, ASME, United Engineering Center, 345 East 47th Street, New York, N.Y. 10017, and will be accepted until two months after final publication of the paper itself in the JOURNAL OF APPLIED MECHANICS. Manuscript received by ASME Applied Mechanics Division, September 9, 1986; final revision, April 23, 1988.

Paper No. 88-WA/APM-63.

Copyright © 1988 by ASME
Downloaded 03 May 2010 to 171.66.16.21. Redistribution subject to ASME license or copyright; see http://www.asme.org/terms/Terms_Use.cfm

shall analyze in this paper one specific pair of equations, which reveals all the principal phenomena contained in the general problem. We thus consider a nonautonomous system of differential equations

$$x' = \mu x + \omega_0 y - x^3 + \alpha_0 G(t)x + \beta_0 H(t),$$
$$y' = -\omega_0 x + \mu y - x^2 y, \tag{1}$$

where μ, ω_0, α_0, and β_0 are real quantities, $\omega_0 > 0$. In equation (1), $G(t)$ and $H(t)$ are stationary stochastic processes with zero mean representing the parametric and the external excitations, respectively. In the absence of the stochastic excitations characterized by $G(t)$ and $H(t)$, i.e., when $\alpha_0 = \beta_0 = 0$, the system (1) has the solution $x=y=0$ which loses stability as μ increases through zero and the system undergoes a Hopf bifurcation at $\mu=0$. The bifurcating solution exists for $\mu>0$ (supercritical) and, therefore, from Hopf bifurcation theory, it is orbitally asymptotically stable. We are interested in predicting the probabilistic description of the response process along with the conditions for sample (or almost sure asymptotic) stability and moment stability of the trivial and the bifurcating solutions, when $\alpha_0 \neq 0$, and $\beta_0 \neq 0$.

3 Transformation to Standard Form

Rescaling the variables x, y using the transformation $x=\epsilon^{1/2}u$ $y=\epsilon^{1/2}v$ and assuming that the constants α_0 and β_0 are of the order $\epsilon^{1/2}$ and ϵ, respectively, a set of weakly nonlinear equations in terms of the new variable u, v can be determined as

$$u' = \mu u + \omega_0 v - \epsilon u^3 + \epsilon^{1/2}(G(t)x + H(t)),$$
$$v' = -\omega_0 u + \mu v - \epsilon u^2 v. \tag{2}$$

Finally, to obtain a set of equations in "standard form," equation (2) is transformed from u, v to new variables a, ϕ by means of the transformation

$$u = a\sin\Phi, \quad v = a\cos\Phi, \quad \Phi = \omega_0 t + \phi,$$

where the quantities a, ϕ are regarded, respectively, as the amplitude and phase of the motion. This procedure yields a set of equations in the form

$$a' = \mu a - \epsilon\frac{a^3}{2}[1-\cos 2\Phi] + \epsilon^{1/2}\left\{\frac{a}{2}[1-\cos 2\Phi]G(t) + H(t)\sin\Phi\right\} \tag{3}$$

$$\phi' = \epsilon^{1/2}\left\{\frac{1}{2}[\sin 2\Phi]G(t) + \frac{1}{a}H(t)\cos\Phi\right\}.$$

Equations (3), which are in the standard form, are exactly equivalent to the original equations of motion given by equations (2).

4 Approximation to Markov Process

An exact solution of equation (3) for arbitrary random process $G(t)$ and $H(t)$ is not available. However, if the intensities as well as the correlation times of the processes are sufficiently small, then using the limit theorem of Stratonovich (1963) and Khas'miniskii (1966), the solution process $\{a(t), \phi(t)\}$ may be approximated in the weak sense by a diffusive Markov vector process. It is then possible to solve for the response amplitudes. This method of approximation is known as stochastic averaging. Thus, applying the stochastic averaging procedure to equations (3) yields a set of Itô equations

$$da = \left\{\left(\alpha + \frac{\gamma}{2}\right)a + \frac{\beta}{2a} - \frac{a^3}{2}\right\}dt + [\gamma a^2 + \beta]^{1/2}dW_a,$$
$$d\phi = \{-\eta\}dt + \left[\delta + \frac{\beta}{d^2}\right]dW_\phi, \tag{4}$$

where $W_a(t)$ and $W_\phi(t)$ are independent Wiener processes of unit intensity, and

$$\alpha = \mu + \frac{1}{8}S_G(2\omega_0), \quad \gamma = \frac{1}{8}\{2S_G(0) + S_G(2\omega_0)\},$$

$$\beta = \frac{1}{2}S_H(\omega_0), \quad \eta = \frac{1}{8}\Psi_G(2\omega_0),$$

$$S_G(\omega) = 2\int_0^\infty E[G(t)\cdot G(t+\tau)]\cos(\omega\tau)d\tau,$$

$$\Psi_G(\omega) = 2\int_0^\infty E[G(t)\cdot G(t+\tau)]\sin(\omega\tau)d\tau.$$

Here $E[\cdot]$ denotes the expected value of the quantity within the brackets. It is evident from equations (4) that the amplitude equation is decoupled from that of the phase. Hence, the averaged amplitude $a(t)$ by itself constitutes a Markov diffusion process. In order to investigate the stability of the system, the norm of the response is defined by $[u^2 + v^2]^{1/2} = a(t)$. Therefore, the Itô equation governing the norm of the response can be written concisely as

$$da = \left\{\left[\alpha + \frac{\gamma}{2} - Ra^2\right]a + \frac{\beta}{2a}\right\}dt + [\gamma a^2 + \beta]^{1/2}dW_a, \tag{5}$$

where $R = 1/2$. In the sequel, equation (5) will be examined to determine the response process of the nonlinear stochastic dynamical system (1). The results obtained in this work can be broadly divided into two categories, namely (*i*) stability of linear system ($R=0$), and (*ii*) bifurcation behavior of a nonlinear system.

5 Linear System

In this section the linear Itô equation corresponding to (5) i.e., when R is identically zero, is considered to examine the transition and stationary probability density of the amplitude process and the stability of the trivial solution. There are several definitions of stochastic stability in the literature but most investigations have been concerned with only two types; namely, stability in the moments and almost sure or sampled stability. These two concepts of stochastic stability for the trivial solution are presented.

When β is identically zero, i.e., $H(t) \equiv 0$, the transition probability density, can be obtained as

$$p_a(a,t|a_0,0) = \frac{1}{a(2\pi\gamma t)^{1/2}}\exp\left\{-\frac{1}{2\gamma t}\left[\ln\left(\frac{a}{a_0}\right) - \alpha t\right]^2\right\}, \tag{6}$$

where α and γ are as defined previously. The stationary probability density $p_{st}(a)$, if it exists, can be found using the stationary Fokker-Planck equation. Instead of solving the Fokker-Planck equation, we examine the transition probability distribution function with the help of equation (6). The probability of the event $a(t) > \xi$, where ξ is an arbitrary amplitude level, is given by

$$P\{a(t) > \xi\} = \int_\xi^\infty p_a(a,t)da = \frac{1}{2}\left\{1 - erf\left[\frac{\ln(\xi/a_0)}{(2\gamma t)^{1/2}} - \alpha\left(\frac{t}{2\gamma}\right)^{1/2}\right]\right\}. \tag{7}$$

It is evident that as $t\to\infty$ the steady-state distribution function $P\{a>\xi\}$ approaches 0 if $\alpha<0$ and 1 if $\alpha > 0$. Therefore, a stationary region of parametric oscillations is impossible in a linear system, since the oscillations would either increase without limit or die down to zero. In any real systems the amplitude cannot become arbitrarily large. Thus, the corresponding nonlinear system must be examined in order to calculate the stationary amplitude distribution and densities.

Downloaded 03 May 2010 to 171.66.16.21. Redistribution subject to ASME license or copyright; see http://www.asme.org/terms/Terms_Use.cfm

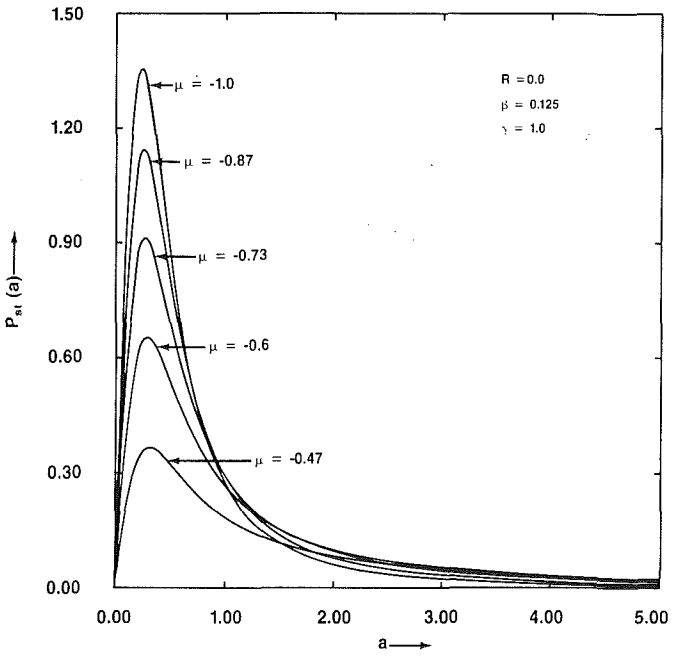

Fig. 1 Stationary p.d.f., $p_{st}(a)$ for the linear system with $a_0 \neq 0$, $\beta_0 \neq 0$

Although the closed-form solution of the transition probability density, when $\beta \neq 0$, is not found, the stationary probability $p_{st}(a)$ is found to be

$$p_{st}(a) = -\frac{2\alpha}{\beta^{\bar{v}}}\, a(\gamma a^2+\beta)^{\bar{v}-1}, \tag{8}$$

provided $\bar{v} = \alpha/\gamma < 0$, i.e., $\mu < -\frac{1}{8} S_G(2\omega_0)$. The stationary distribution function for different values of the bifurcation parameter is shown in Fig. 1. Using the stationary density, the steady-state values of various response statistics can be found

$$M_n^s = n\bar{v}\left(\frac{\beta}{\gamma}\right)^{n/2} \frac{\Gamma(n/2)\Gamma(1-(\bar{v}+n/2))}{(2\bar{v}+n)\Gamma(1-\bar{v})}. \tag{9}$$

provided $n > -2$ and $2\bar{v} + n > 0$. It is evident for n even, equation (9) reduces to

$$M_n^S = \frac{(-1)^{n/2}(n/2)!}{(\bar{v}+1)(\bar{v}+2)\ldots(\bar{v}+n/2)}\left(\frac{\beta}{\gamma}\right)^{n/2}, \ (n \text{ even}). \tag{10}$$

5.1 Moment Stability. The norm of the response, given by $a(t)$, is considered in order to establish the condition for stability in the moments. If $E[a^n(t)]$ tends to a finite value as $t \to \infty$, the system will be stable in the nth moment. The equation governing the powers of $a(t)$, $a^n(t)$, can be deduced from equation (5) with R set to zero.

$$da^n = \left[n\left(\alpha+\frac{n}{2}\gamma\right)a^n + \frac{1}{2}n^2\beta a^{n-2}\right]dt + n(\gamma a^2+\beta)^{1/2}a^{n-1}dW_a. \tag{11}$$

Now, taking the expectations of both sides of equation (11) and defining $M_n(t) = E[a^n(t)]$, the differential equation governing the nth moment is obtained as

$$\frac{dM_n}{dt} = n\left(\alpha+\frac{n}{2}\gamma\right)M_n(t) + \frac{1}{2}n^2\beta M_{n-1}(t). \tag{12}$$

It is evident that, when $\beta = 0$, the moment of order n of $a(t)$ can be evaluated as

$$\bar{M}_n(t) = a_0^n \exp\left\{\left[\mu + \frac{1}{16}\left((n+2)S_G(2\omega_0)+2nS_G(0)\right)\right]nt\right\} \tag{13}$$

and the condition for stability in the nth norm is

$$16\mu + 2nS_G(0) + (n+2)S_G(2\omega_0) < 0. \tag{14}$$

When $\beta \neq 0$, the stationary value of $M_1(t)$ exists and can be found from equation (10) as

$$M_1^S = \frac{\pi^{1/2}\bar{v}\,\Gamma(1/2-\bar{v})}{(2\bar{v}+1)\Gamma(1-\bar{v})}\left(\frac{\beta}{\gamma}\right)^{1/2}, \tag{15}$$

provided $\bar{v} + 1/2 < 0$. Since $M_1(t)$ is bounded, it can be shown from equation (12) that $M_n(t)$ will be bounded if $(\alpha + (n/2)\gamma) < 0$, which is identical to condition (14). Thus, the external excitation $H(t)$ does not influence the moment stability condition for the linear system. Furthermore, when $(\alpha + n/2\gamma) < 0$, the steady-state values of the moment, M_n^S, are obtained as

$$M_n^S = \frac{n!!}{(-2)^{(n-1)/2}(\bar{v}+3/2)(\bar{v}+5/2)\ldots(\bar{v}+n/2)} \times \left(\frac{\beta}{\gamma}\right)^{(n-1)/2} M_1^S, \ (n \text{ odd}). \tag{16}$$

5.2 Sample Stability. The stability with probability one of the homogeneous system, i.e., with the external excitation $H(t) \equiv 0$, is considered. The solution of the linear Itô equation can be written as

$$a(t) = a_0 \exp\{\alpha t + \gamma^{1/2} W(t)\}, \tag{17}$$

with the initial condition $a(0) = a_0$. Since it is known that the Wiener process $W(t) \sim (t \log\log t)^{1/2}$ as $t \to \infty$ with probability one (w.p.1), it is deduced from equation (17) that $a(t) \to 0$ as $t \to \infty$ w.p.1 provided $\alpha < 0$, i.e.,

$$\mu + \frac{1}{8}S_G(2\omega_0) < 0. \tag{18}$$

Now, we employ a result of Kozin and Sugimoto (1977) pertaining to the fractional moments to verify the above result for asymptotic sample stability. According to this, a necessary and sufficient condition for the sample stability of a linear homogeneous stochastic system is that

$$\lim_{n \downarrow 0} \frac{1}{n} \log[E\{\|a(t)\|^n / \|a(0)\|^n\}] < 0.$$

Substituting the value of $\bar{M}_n(t)$ from equation (13) in the above inequality yields

$$\lim_{n \downarrow 0} \frac{1}{n}\left\{\left[\mu + \frac{1}{16}\left(2nS_G(0) + (n+2)S_G(2\omega_0)\right)\right]nt\right\} < 0,$$

which simplifies in the limit to

$$\mu + \frac{1}{8}S_G(2\omega_0) < 0.$$

It is evident that the above stability criterion is identical to that obtained in equation (18) by the use of the Stratonovich equation (17). Since equation (4) coverges to a Markov diffusion process only in the weak sense, we can only conclude that violation of the above condition will imply that the original system is unstable w.p.1 (Khas'miniskii, 1966). Hence,

$$\mu + \frac{1}{8}S_G(2\omega_0) \geq 0.$$

as only an instability condition.

6 Nonlinear System

In order to evaluate the response process of the nonlinear stochastic dynamic system (1), the Itô equation (5) including the nonlinear effects must be examined. Thus, retaining the nonlinear term Ra^3, the transition probability density $p_a(a,t|a_0,t_0)$, $t > t_0$ of the response process is governed by the Fokker-Plank equation.

Downloaded 03 May 2010 to 171.66.16.21. Redistribution subject to ASME license or copyright; see http://www.asme.org/terms/Terms_Use.cfm

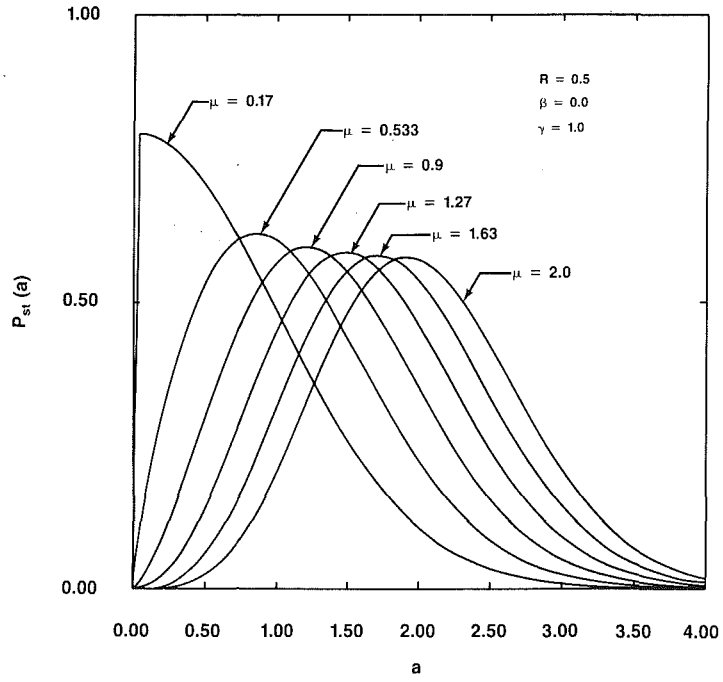

Fig. 2 Stationary p.d.f., $p_{st}(a)$ for the nonlinear system with $a_0 \neq 0$, $\beta_0 \neq 0$

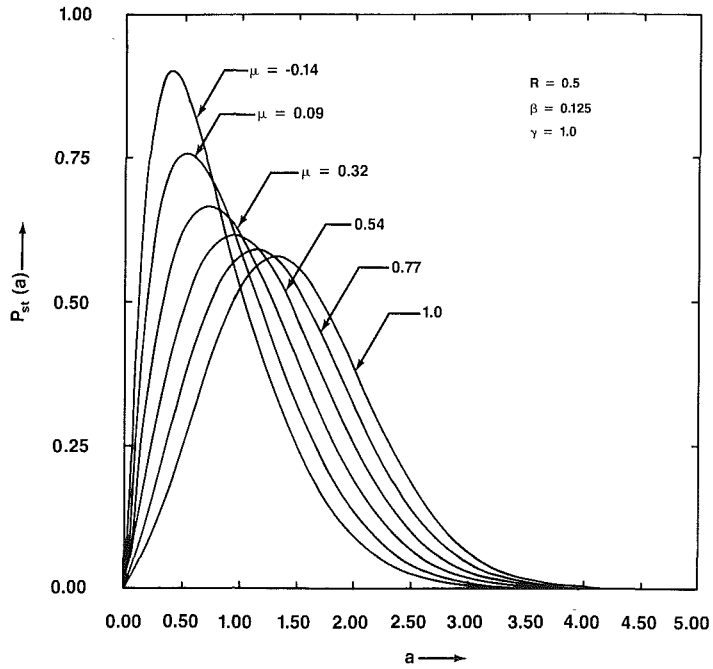

Fig. 3 Stationary p.d.f., $\bar{p}_{st}(a)$ for the nonlinear system with $a_0 \neq 0$, $\beta_0 = 0$

$$\frac{\partial p}{\partial t} = -\frac{\partial}{\partial a}\left[\left\{\left(\alpha+\frac{\gamma}{2}\right)a+\frac{\beta}{2a}-Ra^3\right\}p\right] + \frac{1}{2}\frac{\partial^2}{\partial a^2}[(\gamma a^2+\beta)p], \tag{19}$$

with initial condition

$$p(a,t|a_0,t_0)\to\delta(a-a_0) \text{ as } t\to t_0.$$

6.1 Stationary Solution. The steady-state solution $p_{st}(a)$ corresponding to $(\partial p/\partial t) = 0$ can be determined after performing a straightforward integration on equation (19), as

$$p_{st}(a) = \frac{2\zeta^{v}\exp(-\zeta)}{\Gamma(v,\zeta)}\,(\gamma/\beta)a[(\gamma/\beta)a^2+1]^{v-1} \times \exp[-Ra^2/\gamma], \tag{20}$$

where $v = \alpha/\gamma + \zeta$ and $\zeta = R\beta/\gamma^2$. When the external excitation, $H(t)$, is identically zero, i.e., $\beta = 0$, the stationary probability density can be obtained as

$$\bar{p}_{st}(a) = 2\left(\frac{R}{\gamma}\right)^{\bar{v}}\frac{a^{2\bar{v}-1}}{\Gamma(\bar{v})}\exp[-Ra^2/\gamma], \tag{21}$$

provided $\bar{v} = \alpha/\gamma > 0$. The stationary density functions (20) and (21) are plotted for different values of μ in Figs. 2 and 3.

Downloaded 03 May 2010 to 171.66.16.21. Redistribution subject to ASME license or copyright; see http://www.asme.org/terms/Terms_Use.cfm

6.2 Transient Solution. In order to solve for the transient probability density the time-dependent Fokker-Plank equation is examined. The closed-form solution of equation (19) can be obtained only for the case $\beta = 0$, i.e., when the external forcing function is zero. Applying the transformation $x = \gamma/Ra^2$, $\gamma = 2\gamma t$, and using Itô's lemma, the nonlinear Itô equation (5) with β identically zero gets modified to

$$dx = [1 - (\alpha/\gamma - 1)x]d\tau - \sqrt{2}xdW_\tau. \tag{22}$$

The corresponding Fokker-Planck equation can be written as

$$\frac{\partial \bar{p}}{\partial \tau} = -\frac{\partial}{\partial x}[1 - (\alpha/\gamma - 1)x]\bar{p} + \frac{\partial^2}{\partial x^2}[x^2]\bar{p}, \tag{23}$$

with initial condition

$$\bar{p}(x,\tau|x_0,\tau_0) \to \delta(x - x_0) \quad \text{as} \quad \tau \to \tau_0,$$

whose stationary solution is

$$\bar{p}_{st}(x) = \bar{N}\frac{\exp(-1/x)}{2x^{(\alpha/\gamma+1)}}.$$

Now, using the method of separation of variables,

$$\bar{p}(x,\tau) = \Psi(x)\exp(-\lambda\tau), \tag{24}$$

the following differential equation for $\Psi(x)$ is obtained:

$$\frac{d^2}{dx^2}[x^2]\Psi(x) - \frac{d}{dx}[1 - (\alpha/\gamma - 1)x]\Psi(x) = -\lambda\Psi(x). \tag{25}$$

By setting

$$\Psi(x) = \bar{p}_{st}(x)\phi(x),$$

the eigenvalue problem for the Fokker-Planck equation is transformed into a Sturm-Liouville problem

$$[x^{1-\alpha/\gamma}\exp(-1/x)\phi'(x)]' + \lambda x^{-(\alpha/\gamma+1)}\exp(-1/x)\phi(x) = 0, \tag{26}$$
$$x^{1-\alpha/\gamma}\exp(-1/x)\phi'(x)\big|_{x=0,\infty} = 0,$$

where $'$ denotes differentiation with respect to the new variable x.

From the classical Sturm-Liouville theory, it is known that the spectrum of equation (26) consists of a continuous range of eigenvalues in addition to the usual discrete eigenvalues when one or both of the boundaries of the problem are infinite. Solving the above equation, it is found that the spectrum consists of $N+1$ discrete eigenvalues satisfying

$$\lambda_n = n(\alpha/\gamma - n) > 0, \quad n = 0, 1, \ldots, N \tag{27a}$$

and a continuous range of eigenvalues

$$\lambda > \frac{\alpha^2}{4\gamma^2}. \tag{27b}$$

Accordingly, the transition probability density function can be written as

$$\bar{p}(x,\tau) = x^{-(\alpha/\gamma+1)}\exp(-1/x)\left\{\sum_{n=0}^{N} A_n e^{-\lambda_n\tau}\phi_n(x_0)\phi_n(x) + \frac{1}{2\pi}\int_0^\infty e^{-\lambda\tau}A(\lambda)\phi_\lambda(x_0)\phi_\lambda(x)d\lambda\right\}. \tag{28}$$

The eigenfunctions $\phi_n(x)$ and $\phi_\lambda(x)$ satisfy the usual orthonomality conditions (with weight $\bar{p}_{st}(x)$). In equation (28), $\phi_n(x)$ are orthogonal polynomials of degree n given by

$$\phi_n(x) = (-1)^n x^{\alpha/\gamma H}\exp(1/x) \times \frac{d^n}{dx^n}(x^{2n-\alpha/\gamma-1}\exp(-1/x)) \tag{29a}$$

and the eigenfunctions for the continuous spectrum are (e.g., Erdelyi, 1953; Wong, 1971)

$$\phi_\lambda(x) = {}_2F_0\left(-\frac{\alpha}{2\gamma} - i\lambda, \; -\frac{\alpha}{2\gamma} + i\lambda, \; -x\right), \tag{29b}$$

where ${}_2F_0$ is the generalized hypergeometric series. The normalization factors A_n and $A(\lambda)$ for the discrete and the continous ranges of eigenvalues are given as

$$A_n = \frac{(\alpha/\gamma - 2n)}{\Gamma(\alpha/\gamma + 1 - n)}\frac{1}{n!},$$

$$A(\lambda) = \frac{\Gamma(\alpha/2\gamma + i\lambda)\Gamma(-\alpha/2\gamma - i\lambda)}{\Gamma(i\lambda)\Gamma(-i\lambda)},$$

respectively. Now, taking into account the rescaling of time $\tau = 2\gamma t$ and the transformation of state variable $x = \gamma/Ra^2$, the probability density function in the original variables can be obtained as

$$\bar{p}(a,t) = 2\left(\frac{R}{\gamma}\right)^{\alpha/\gamma} a^{(2\alpha/\gamma-1)}\left\{\sum_{n=0}^{N}\frac{(\alpha/\gamma - 2n)}{\Gamma(\alpha/\gamma + 1 - n)}\frac{1}{n!} \times \exp[-2n\gamma(\alpha/\gamma - n)t]\cdot\phi_n\left(\frac{\gamma}{Ra_0^2}\right)\phi_n\left(\frac{\gamma}{Ra^2}\right) + \frac{1}{2\pi}\int_{\alpha^2/4\gamma^2}^{\infty}\frac{\Gamma(\alpha/2\gamma + i\lambda)\Gamma(-\alpha/2\gamma - i\lambda)}{\Gamma(i\lambda)\Gamma(-i\lambda)} \cdot\exp[-2\gamma\lambda t]\phi_\lambda\left(\frac{\gamma}{Ra_0^2}\right)\phi_\lambda\left(\frac{\gamma}{Ra_0^2}\right)d\lambda\right\}, \tag{30}$$

where $\lambda > (\alpha/2\gamma)^2$. It is evident from the above expression, that in the limit when $t \to \infty$, the only term that survives is that corresponding to $n = 0$ and the integral vanishes; hence, $\bar{p}(a, \infty) = \bar{p}_{st}(a)$ given by equation (21). It is worth pointing out that the Fokker-Plank equation (19), with $\beta = 0$, can also be solved by transforming the eigenvalue problem into the form of Whittaker's equation with appropriate boundary conditions, and this method was used by Schenzle and Brand (1978) to solve the Verhulst equations.

6.3 Extrema and Stationary Moments. The extrema of the distribution function, $p_{st}(a)$, are of importance for three main reasons, namely (*i*) the number and location of the extrema are the most distinguishing features of $p_{st}(a)$ and contain essential information on the stationary behavior of the nonlinear system, (*ii*) the extrema are, so to speak, the continuation of the deterministic steady-states and furthermore, as $\epsilon \to 0$ the extrema tend to the steady-states of the deterministic system, and (*iii*) if a_t is ergodic, we can interpret the distribution function $p_{st}(a)$ as a meansure for that part of the time an arbitrary sample path spends in an infinitesimal vicinity of a. This motivates the usual identification of the extrema: the maxima, where the process spends relatively much time, as the stable steady-states and the minima, which the process leaves rather quickly as unstable ones. Thus, the most probable amplitudes are now found from the conditions

$$\frac{dp_{st}}{da}\bigg|_{a=\bar{a}} = 0, \quad \frac{d^2p_{st}}{da^2}\bigg|_{a=\bar{a}} < 0.$$

Applying the first condition to equation (20), two values for a are obtained:

$$\text{(I)}\ a^2 + \beta/\gamma = 0, \quad \text{(II)}\ a^4 + \frac{[\gamma - 2\alpha]a^2}{2R} = \beta/2R.$$

It is evident that for $\beta \neq 0$, $a^2 + \beta/\gamma = 0$ gives only imaginary solution, and the second condition yields

$$\frac{d^2p_{st}}{da^2}\bigg|_{a=\bar{a}} = -\frac{2N}{a}\{\beta + 2Ra^4\}(\gamma a^2 + \beta)^{\nu-2}\exp\left[-\frac{Ra^2}{\gamma}\right] < 0.$$

Hence, the most probable value of the amplitude process is given by

$$a^2 = \frac{\lambda}{2} + \left\{\left(\frac{\lambda}{2}\right)^2 + \beta\right\}^{1/2}, \tag{31}$$

where

Downloaded 03 May 2010 to 171.66.16.21. Redistribution subject to ASME license or copyright; see http://www.asme.org/terms/Terms_Use.cfm

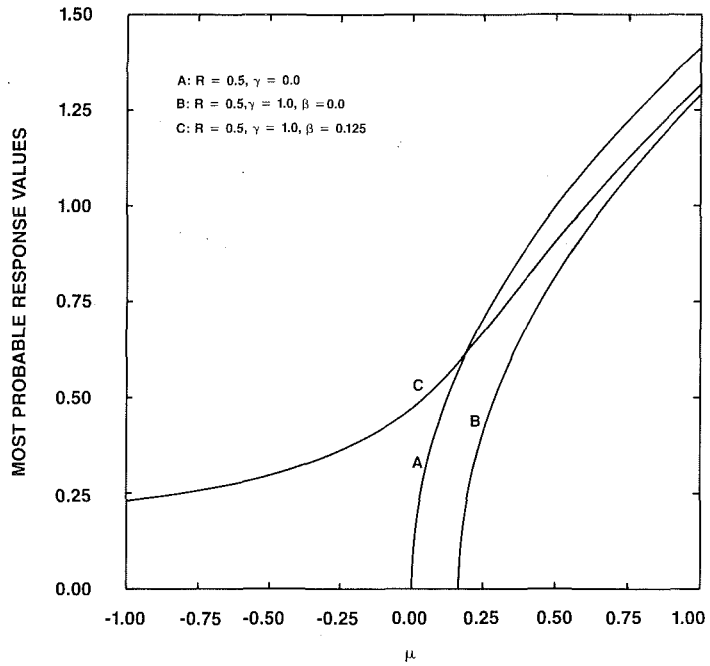

Fig. 4 Most probable values as a function of the bifurcation parameter μ for three cases; (A) ordinary, (B) parametrically perturbed, and (C) externally and parametrically perturbed, Hopf bifurcations

$$\lambda = 2\mu + \frac{1}{8}\{S_G(2\omega_0) - 2S_G(0)\}, \quad \beta = \frac{1}{2} S_H(\omega_0)$$

and, in the absence of external excitation, i.e., $\beta = 0$, the above expression reduces to

$$a = \sqrt{\lambda}, \quad \lambda > 0. \tag{32}$$

It may be noted that in the absence of stochastic excitation, i.e., when $G(t) = H(t) = 0$, the amplitude parameter relationship given by equation (32) reduces to that of Hopf bifurcation (see, e.g., Chow and Mallet-Paret, 1976). Furthermore, if the excitation has a broad-band spectrum with a constant spectral density S_0 over a wide band of frequencies, i.e., $S_G(\omega) = S_0$, then the most probable value of the response process can be expressed in terms of S_0 as

$$a^2 = \left(\mu - \frac{1}{16} S_0\right) + \left|\mu - \frac{1}{16} S_0\right| \left[1 + \beta\left(\mu - \frac{1}{16} S_0\right)^{-2}\right]^{1/2} \tag{33a}$$

and

$$a = \sqrt{2}\sqrt{\mu - S_0/16}, \quad \mu > S_0/16 \tag{33b}$$

for forced and unforced ($H(t) = 0$) parametrically excited system, respectively. A sketch of the above results is shown in Fig. 4.

Stationary moments of the reponse process of the nonlinear system can be evaluated from the stationary probability density function (20). The nth stationary moment is thus given as

$$M_n^S = \frac{\exp[-\zeta]}{\Gamma(v,\zeta)} \times \left\{\left(\frac{\gamma}{R}\right)^{n/2} \Gamma(v + n/2) M(1 - v, 1 - (v + n/2), \zeta) + \zeta^v \left(\frac{\beta}{\gamma}\right)^{n/2} \frac{\Gamma(n/2+1)\Gamma(-(n/2+v))}{\Gamma(1-v)} \times M(n/2+1, 1+(v+n/2), \zeta)\right\}, \tag{34}$$

provided $n > -2$ and $v = (\alpha/\gamma) + \zeta$. In the above expression, $M(a, b, z)$ is the Kummer function. When the external excitation is identically zero, the nth stationary moment can be obtained from equation (21) as

$$\bar{M}_n^s = \left(\frac{\gamma}{R}\right)^{n/2} \frac{\Gamma(\bar{v} + n/2)}{\Gamma(\bar{v})} \tag{35}$$

provided $\bar{v} + n/2 > 0$. It is evident that the above result can be obtained from equation (34) by letting $\beta \to 0$. The stationary moments are plotted in Fig. 5.

6.4 Transient Moments. The moment equations for the norm of the response for the nonlinear system can be deduced from equation (5), with β identically zero, by the use of Itô's lemma:

$$\frac{d\bar{M}_n}{dt} = n\left(\alpha + \frac{n}{2}\right)\bar{M}_n - nR\bar{M}_{n+2}, \quad n = 1, 2, \ldots \tag{36}$$

Setting $\bar{\mathbf{M}} = \{\bar{M}_1, \bar{M}_2, \ldots \bar{M}_n, \ldots\}$, the above equation can be written as

$$\frac{d\bar{\mathbf{M}}}{dt} = \mathbf{A}\bar{\mathbf{M}} \text{ with initial condition } \bar{\mathbf{M}}\Big|_{t=0} = \bar{\mathbf{M}}_0 = \begin{Bmatrix} \bar{M}_0^1 \\ \cdot \\ \cdot \\ \bar{M}_0^n \\ \cdot \\ \cdot \end{Bmatrix} \tag{37}$$

where $\mathbf{A}$ is an upper triangular matrix whose eigenvalues are diagonal elements given by

$$\lambda_r = \Gamma\left(\alpha + \frac{r}{2}\gamma\right), \quad r = 1, 2, \ldots,$$

$$\text{and } \bar{M}_0^n = \int_0^\infty a^n \delta(a - a_0) da = a_0^n. \tag{38}$$

Equation (37) constitutes an infinite hierarchy of linear moment equations and has direct and adjoint eigenvalue problems

Downloaded 03 May 2010 to 171.66.16.21. Redistribution subject to ASME license or copyright; see http://www.asme.org/terms/Terms_Use.cfm

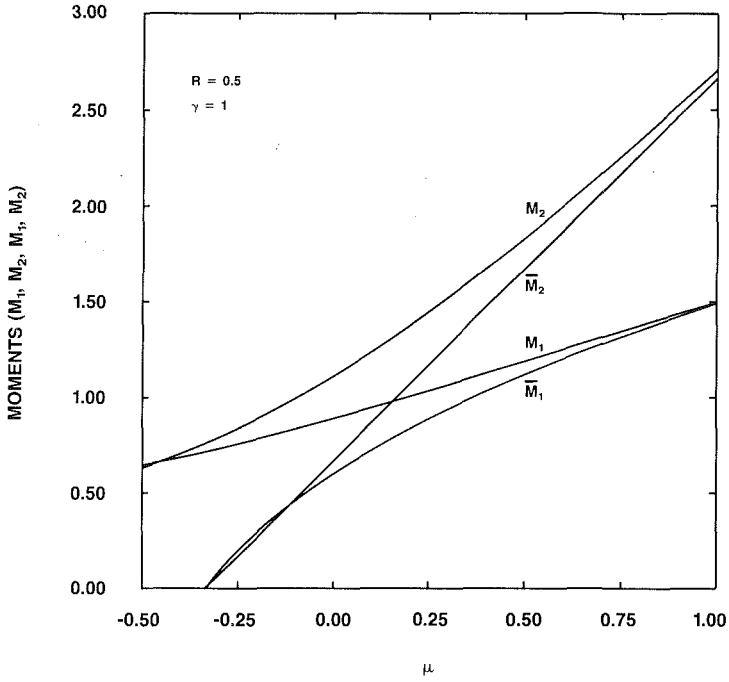

Fig. 5 Stationary moments M (forced) and $\bar{M}$ (unforced) parametrically perturbed nonlinear dynamical system

$$(\lambda_n-\lambda_r)\phi_n^r=nR\phi_n^r,$$
$$(\lambda_{n+2}-\lambda_r)\Psi_{n+2}^r=nR\Psi_n^r, \tag{39}$$

respectively, where ϕ_n^r and Ψ_n^r are the nth component of the eigenvectors corresponding to the rth eigenvalue of the respective problems. Bypassing some of the algebraic details, the direct and the adjoint eigenvectors can be evaluated as

$$\phi_{r-2k}^r=\left(-\frac{R}{\gamma}\right)^k\frac{\Gamma(r/2)\Gamma(r+\alpha/\gamma-k)}{k!\Gamma(r+\alpha/\gamma)\Gamma(r/2-k)}, \tag{40}$$

$$\phi_j^r=0 \quad \text{for } j\neq r-2k, \quad k=0, 1, \ldots, \text{ and } r-2k>0$$

and

$$\Psi_{r+2k}^r=\left(\frac{R}{\gamma}\right)^k\frac{\Gamma(r/2+k)\Gamma(r+\alpha/\gamma+1)}{k!\Gamma(r+\alpha/\gamma+1+k)\Gamma(r/2)}, \tag{41}$$

$$\Psi_j^r=0 \quad \text{for } j\neq r+2k, \quad k=0, 1, \ldots$$

Furthermore, the eigenvectors satisfy the usual orthogonality conditions and in the expressions (40) and (41), ϕ_r^r and Ψ_r^r are taken to be 1 without loss of generality. Now consider the transformation

$$\bar{\mathbf{M}}=\Phi\mathbf{X} \quad \text{where} \quad \Phi=[\underline{\phi}^1, \underline{\phi}^2, \ldots, \underline{\phi}^n \ldots],$$

which simplifies the linear equation (37) to a diagonal form. Substituting the above transformation in (37), and premultiplying by the transposed adjoint eigenvector Ψ^T, yields

$$\frac{dX}{dt}=\text{diag}[\lambda]\mathbf{X}, \text{ with initial condition } \mathbf{X}_0=\Psi^T\mathbf{M}_0, \tag{42}$$

whose solution can be written as

$$X_n=X_0^n\exp(\lambda_n t)$$

where

$$X_0^r=a_0^r M\left(r/2,\ r+\alpha/\gamma+1,\ \frac{Ra_0^2}{\gamma}\right)$$

and $M(a, b, z)$ is the Kummer function (see, for e.g., Erdelyi, 1953). Now transforming back to the original variables the expression for the nth moment can be obtained as

$$M_n=a_0^n\left\{\sum_{j=0}^{\infty}\exp\left[(n+2j)\left\{\alpha+\frac{(n+2j)}{2}\gamma\right\}\right]t^j\left[-\frac{Ra_0^2}{\gamma}\right]^j\frac{1}{j!}\right.$$
$$\cdot\frac{\Gamma\left(\frac{n}{2}+j\right)\Gamma(n+\alpha/\gamma+j)}{\Gamma\left(\frac{n}{2}\right)\Gamma(n+\alpha/\gamma+2j)}$$
$$\left.\times M\left(\frac{n}{2}+j,\ n+\frac{a}{\gamma}+1+2j,\ \frac{Ra_0^2}{\gamma}\right)\right\}, \tag{43}$$

provided $n+\alpha/\gamma+j$ is not equal to a negative integer. Using the integral form of the Kummer function and the identities given in A-1 and A-2 (see Appendix) the above equation for moments can be written concisely as

$$\bar{M}_n=\frac{a_0^n}{(\pi)^{1/2}}\frac{\Gamma(n+\alpha/\gamma+1)}{\Gamma(n/2)\Gamma(n/2+\alpha/\gamma+1)}\exp[n\alpha t]$$
$$\int_{-\infty}^{\infty}\int_0^1\exp[-x^2+(n\sqrt{2\gamma t'})x]\cdot\exp[Ra_0^2y/\gamma]$$
$$\cdot y\cdot(1-y)^{n/2+\alpha/\gamma}\cdot{}_2F_2(n+\alpha/\gamma, n/2+\alpha/2\gamma+1;$$
$$n/2+\alpha/\gamma+1, n/2+\alpha/2\gamma; Z)\,dy\,dx$$

where

$$Z=\exp[2(\alpha t+\sqrt{2\gamma}tx)]\cdot y\cdot(1-y)\,(-Ra_0^2/\delta)$$

and ${}_2F_2$ $(a,b;c,d;Z)$ is the generalized hypergeometric function.

In order to understand the behavior of the solutions of equation (36) corresponding to $n=2$, consider a simple closure scheme for the amplitude, a. It is well known that applying the Gaussian closer to x and y is equivalent to approximating the amplitude a by a Rayleigh distributed process. Thus, the fourth moment on the r.h.s. of equation (36) for $n=2$ can be approximated, and the resulting nonlinear equation for $\bar{M}_2$ is

Downloaded 03 May 2010 to 171.66.16.21. Redistribution subject to ASME license or copyright; see http://www.asme.org/terms/Terms_Use.cfm

$$\frac{d\bar{M}_2}{dt} = 2(\alpha/\gamma)\bar{M}_2 - 4R\bar{M}_2^2, \tag{44}$$

whose solution can be written explicitly as

$$\bar{M}_2(t) = \frac{\bar{M}_2(0)(\alpha+\gamma)/2R}{[\bar{M}_2(0) + (1+\bar{M}_2(0))e^{-2(\alpha\times\gamma)t}]} \tag{45}$$

It is evident that as $t\to\infty$, $\bar{M}_2(t)\to 0$ if $(\alpha+\gamma) < 0$ and $\bar{M}_2(t) \to (\alpha+\gamma)/2R$ if $(\alpha+\gamma) > 0$ which are the two stationary solutions of (44). Furthermore, the bifurcating solution is stable for $(\alpha+\gamma) > 0$.

7 Conclusion

The effect of small parametric and external stochastic perturbations on the bifurcation behavior of a two-dimensional nonlinear differential equation has been considered. It was shown that even small fluctuations in parameters could have an important effect when the system is in the neighborhood of a bifurcation point. The equation of motion was first transformed into first-order equations in the amplitude and phase variables. These equations, under suitable conditions, converge to a Markov vector which satisfies Itô's equations. For the linear problem, the criteria for mean square stability and almost sure stability were obtained. In addition, the stationary moments for the nonlinear system were found along with the stationary distribution functions. However, the transient probability density function was obtained explicitly for the case where the external excitation was identically zero. This indeed facilitates the explicit calculation of various statistical properties of the transient response. In particular, these results can be used to evaluate the two-time correlation function, and the spectral density.

Furthermore, the maxima and minima of the stationary distribution, which are identified with stable and unstable steady-states, respectively, were evaluated. It was found that in two-dimensional nonlinear dynamical systems which ordinarily exhibit Hopf bifurcation, the addition of small stochastic parametric excitation gives rise to a shift of the bifurcation point. However, the addition of external excitation modifies the bifurcation behavior.

References

Ariaratnam, S. T., 1980, "Bifurcations in Nonlinear Stochastic Systems," *New Approaches to Nonlinear Problems in Dynamics*, P. J. Holmes, ed., SIAM Publications, Philadelphia, PA, pp. 470-474.

Ariaratnam, S. T., and Tam, D. S. F., 1979, "Random Vibration and Stability of Linear Parametrically Excited Oscillator," *Z. Angew. Math. Mech. (ZAMM)*, Vol. 59, pp. 79-84.

Bajaj, A. K., 1986, "Resonant Parametric Perturbations of the Hopf Bifurcation," *SIAM Journal of Applied Mathematics*, Vol. 115, pp. 214-224.

Chow, S. N., and Mallet-Parnet, J., 1976, "Integral Averaging and Hopf Bifurcations," *Journal of Differential Equations*, Vol. 26, pp. 112-159.

Erdelyi, A., 1953, *Higher Transcendental Functions*, Vol. 1, McGraw-Hill, New York.

Kath, W. L., 1981, "Resonance in Periodically Perturbed Hopf Bifurcation," *Studies in Applied Mathematics*, Vol. 65, pp. 95-112.

Khas'minskii, R. Z., 1966, "A Limit Theorem for the Solutions of Differential Equations with Random Right-hand Sides," *Theory of Probability and its Applications*, Vol. 11, pp. 340-406.

Kozin, F., and Sugimoto, S., 1977, "Relations between Sample and Moment Stability for Linear Stochastic Differential Equations," *Proc. Conf. on Stochastic Differential Equations and Applications*, J. David Mason, ed., Academic Press, New York, pp. 1-18.

Lin, Y. K., 1967, *Probabilistic Theory of Structural Dynamics*, McGraw-Hill, New York.

Lin, Y. K., and Wu, W. F., 1983, "Applications of Cumulant Closure to Random Vibration Problems," ASME *Random Vibrations*, AMD, Vol. 65, pp. 113-125.

Rosenblat, S., and Cohen, D. S., 1980, "Periodically Perturbed Bifurcation, I, Simple Bifurcation," *Studies in Applied Mathematics*, Vol. 63, pp. 1-23.

Rosenblat, S., and Cohen, D. S., 1981, "Periodically Perturbed Bifurcation, II, Hopf Bifurcation," *Studies in Applied Mathematics*, Vol. 64, pp. 143-175.

Schenzle, A., and Brand, H., 1978, "Multiplicative Stochastic Processes in Statistical Physics," *Physics Letters*, Vol. 68, pp. 313-315.

Sri Namachchivaya, N., and Ariaratnam, S. T., 1987, "Periodically Perturbed Hopf Bifurcations," *SIAM Journal of Applied Mathematics*, Vol. 47, pp. 15-39.

Stratonovich, R. C., 1963, *Topics in the Theory of Random Noise*, Vol. 1, Gordon and Breach, New York.

Wong, E., 1971, *Stochastic Processes in Information and Dynamical Systems*, McGraw-Hill, New York.

Wu, W. F., and Lin, Y. K., 1984, "Cumulant-neglect Closure for Nonlinear Oscillators Under Random Parametric and External Excitations," *International Journal of Nonlinear Mechanics*, Vol. 19, pp. 349-362.

APPENDIX

In order to express equation (43) in a compact form, we consider the integral form of the Kummer function

$$\frac{\Gamma(b-a)}{\Gamma(b)} M(a,b,z) = \int_0^1 e^{zt} t^{a-1}(1-t)^{b-a-1} dt$$

and the following identity

$$\int_{-\infty}^{\infty} \exp[-ax^2 + bx]dx = \frac{\sqrt{\pi}}{a} e^{b^2/ra} a > 0.$$

Thus, we can write

$$\frac{\Gamma\left(\frac{n}{2}+j\right)\Gamma(n+\alpha/\gamma+j)}{\Gamma\left(\frac{n}{2}\right)\Gamma(n+\alpha/\gamma+2j)} M\left(\frac{n}{2}+j,\ n+\frac{\alpha}{\gamma}+1+2j,\ \frac{Ra_0^2}{\gamma}\right)$$

$$= \frac{\Gamma(n+\alpha/\gamma+1)}{\Gamma\left(\frac{n}{2}\right)\Gamma\left(\frac{n}{2}+\alpha/\gamma+1\right)}$$

$$\times \left[\frac{(n+\alpha/\gamma)_j \left(\frac{n}{2}+\gamma/2\gamma+1\right)_j}{\left(\frac{n}{2}+\alpha/2\gamma\right)_j \left(\frac{n}{2}+\alpha/\gamma+1\right)_j}\right]$$

$$\int_0^1 \exp\left[\frac{Ra_0^2}{\gamma} y\right] \cdot y^{n/2+j-1} \cdot (1-y)^{n/2+\alpha/\gamma+j} dy$$

and

$$\exp\left[(n+2j)\left\{\alpha + \frac{(n+2j)}{2} j\right\}\right] t$$

$$= \frac{1}{(\pi)^{1/2}} \exp[(n+2j)\alpha t] \int_{-\infty}^{\infty} \exp\{-x^2 + [(x+2j)\sqrt{2\gamma t}]x\} dx,$$

where $(a)_j = a(a+1)\ldots(a+n-1)$. The expressions ($A$-1) and ($A$-2) are used in equation (43) to obtain a concise integral for the nth moment of the response.

Downloaded 03 May 2010 to 171.66.16.21. Redistribution subject to ASME license or copyright; see http://www.asme.org/terms/Terms_Use.cfm

Optimal Control of Nonlinear Structures

J. N. Yang
Professor.

F. X. Long
Visiting Scholar.

D. Wong
Graduate Student.

Department of Civil, Mechanical, and Environmental Engineering,
The George Washington University,
Washington, DC 20052

Three optimal control algorithms are proposed for reducing oscillations of flexible nonlinear structures subjected to general stochastic dynamic loads, such as earthquakes, waves, winds, etc. The optimal control forces are determined analytically by minimizing a time-dependent quadratic performance index, and nonlinear equations of motion are solved using the Wilson-θ numerical procedures. The optimal control algorithms developed for applications to nonlinear structures are referred to as the instantaneous optimal control algorithms, including the instantaneous optimal open-loop control algorithm, instantaneous optimal closed-loop control algorithm, and instantaneous optimal closed-open-loop control algorithm. These optimal algorithms are computationally efficient and suitable for on-line implementation of active control systems to realistic nonlinear structures. Numerical examples are worked out to demonstrate the applications of these optimal control algorithms to nonlinear structures. In particular, control of structures undergoing inelastic deformations under strong earthquake excitations are illustrated. The advantage of using combined passive/active control systems is also demonstrated.

I Introduction

To improve the reliability and safety of tall buildings under strong earthquakes the use of protective systems, such as passive or active control devices, has received considerable attention (e.g., Abdel-Rohman and Nayfeh, 1987; Kelly, 1981; Leipholz, 1980, 1985; Reinhorn and Manolis, 1985; Soong et al., 1985; Yang and Soong, 1988; Yao and Soong, 1984). These control systems have been shown theoretically and, in some cases, experimentally to be effective in safeguarding structural integrity. Numerous studies have been conducted for applications of passive control systems, such as lead-core rubber base isolators, tuned mass dampers, etc., and in some cases these passive control systems have been installed in representative buildings. While passive control systems are effective in some circumstances, they also suffer from a number of limitations, in particular the transient nature of strong earthquakes. As a result, active control systems, such as active mass dampers, active tendon systems, gas pulse generators, etc., whose performance depends on the supply of external energy, have been investigated intensively in the last decade mostly in the theoretical aspects. It is only until recently that experimental studies of active control systems for building structures have been conducted realistically (Soong et al., 1985, and Lin et al., 1987). Likewise, the study of possible use of combined passive/active control systems is currently being initiated.

In reality, many tall buildings undergo large deformation or yielding when subjected to strong earthquake ground motions, and, hence, exhibit nonlinear or inelastic behavior. Structures are in the critical stage when their deformations enter into the inelastic range. It is at this critical stage that the protective system is needed most. Consequently, active control systems must be able to operate in the nonlinear range of motion for tall buildings. Further, for the combined use of passive/active control systems passive devices, such as rubber base isolators, exhibit large deformation and inelastic behavior, leading to nonlinear equations of motion for the entire structural system. Hence, the active control system should be capable of dealing with nonlinear structures.

Traditionally, active control has been applied to linear structures, and control theories for nonlinear systems are very limited. In an attempt to control nonlinear structures, active pulse control has been investigated recently by Masri et al. (1981a, 1981b), and Reihorn et al. (1987). In using active pulse control, several variables should be determined from the control algorithm, including the time at which pulses should be applied, the magnitude of each pulse, shape and duration, etc. In general, the pulse shape and duration are given because of limitations of control devices. Pulses usually are triggered when the response reaches certain levels. The determination of pulse magnitude is important in order to achieve given control efficiency. When the pulse magnitude is too small, the effectiveness of active control will be insignificant. However, if the pulse magnitude is too large, the structure (or system) may become unstable or the structural response may be worse than that without control. In the work of Masri et al. (1981a), the pulse magnitude is chosen to be proportional to some power of the response velocity, whereas the proportional constant is selected empirically. Given a selected proportional constant, the stability condition for the structure is examined. This type of control is nonoptimal.

Contributed by the Applied Mechanics Division for presentation at the Winter Annual Meeting, Chicago, IL, November 28 to December 2, 1988, of THE AMERICAN SOCIETY OF MECHANICAL ENGINEERS.

Discussion on this paper should be addressed to the Editorial Department, ASME, United Engineering Center, 345 East 47th Street, New York, N.Y. 10017, and will be accepted until two months after final publication of the paper itself in the JOURNAL OF APPLIED MECHANICS. Manuscript received by ASME Applied Mechanics Division, March 25, 1988; final revision, June 10, 1988.

Paper No. 88-WA/APM-75.

Copyright © 1988 by ASME
Downloaded 03 May 2010 to 171.66.16.21. Redistribution subject to ASME license or copyright; see http://www.asme.org/terms/Terms_Use.cfm

Later, Masri et al. (1981b) assumed that the structural motion consists of stochastic components superimposed on top of a deterministic component. The pulse magnitudes are determined to minimize the deterministic component of the system response over a relatively short time segment after pulses are triggered. The optimal control algorithm is developed utilizing the model analysis of the structure and, hence, it is applicable to linear structures. However, such a control algorithm can be used for control of nonlinear structures provided that reasonable equivalent linear properties can be used to represent nonlinear structures satisfactorily. In the work of Reinhorn et al. (1987), the response of a SDOF nonlinear structure at every time instant t is monitored, and the response at the next time interval $t+\Delta t$ is estimated. If the estimated response at $t+\Delta t$ exceeds a specified level, a pulse is triggered. Then, the magnitude of the pulse is estimated such that the response at $t+\Delta t$ is brought back to the specified level. The estimation of the pulse magnitude can be made using the initial conditions at time t and the specified response at $t+\Delta t$. Such a control algorithm again is nonoptimal, and it is, in effect, an approximate bounded state control algorithm.

In this paper we proposed three optimal control algorithms applicable to flexible nonlinear structures, including inelastic structures, subjected to general dynamic loads, deterministic or stochastic. These include the instantaneous optimal closed-loop control algorithm, instantaneous optimal open-loop control algorithm and instantaneous optimal closed-open-loop control algorithm. These optimal control algorithms are simple and reliable for on-line control operations and they are effective in mitigating structural oscillation.

Unlike pulse control, control forces considered herein are continuous in time and active control can be implemented by electrohydraulic servomechanisms along with tendons or mass dampers, referred to as active tendon control system and active mass damper, respectively. Particular emphasis is placed on the mitigation of the inelastic response of flexible tall buildings subjected to strong earthquakes. Numerical examples are worked out to demonstrate the applications of these optimal control algorithms to nonlinear structures. The advantage of using combined passive/active control systems is also illustrated.

II Formulation

For simplicity, consider a one-dimensional nonlinear building structure implemented by an active tendon control system as shown in Fig. 1. The structure is idealized by an n-degree-of-freedom system and subjected to a one-dimensional earthquake ground acceleration $\ddot{X}_0(t)$. The matrix equation of motion can be expressed as

$$\mathbf{M}\,\ddot{\mathbf{Y}}(t)+\mathbf{F}_D(t)+\mathbf{F}_s(t)=-\mathbf{M}\,\mathbf{v}\ddot{X}_0(t)+\mathbf{H}\,\mathbf{U}(t) \tag{1}$$

in which $\mathbf{Y}(t)$ is an n vector denoting the displacements of the structure relative to the moving base, $\mathbf{v}$ is a unit vector of order n, i.e., $\mathbf{v}=[1, 1, 1, \ldots, 1]'$, $\mathbf{U}(t)$ is a r-dimensional control vector, and $\mathbf{H}$ is a $(n \times r)$ matrix denoting the location of r controllers. A super dot $(\cdot)$ represents differentiation with respect to time, and a letter printed in boldface type denotes a vector or matrix. In equation (1), $\mathbf{M}$ is a $(n \times n)$ constant mass matrix, $\mathbf{F}_D(t)$ is an n vector denoting the damping force, and $\mathbf{F}_s(t)$ is an n vector denoting the stiffness restoring force. Both $\mathbf{F}_D(t)$ and $\mathbf{F}_s(t)$ are general nonlinear functions of $\dot{\mathbf{Y}}(t)$ and $\mathbf{Y}(t)$, respectively, i.e., $\mathbf{F}_D(t)=\mathbf{F}_D[\dot{Y}(t)]$ and $\mathbf{F}_s(t)=\mathbf{F}_s[\mathbf{Y}(t)]$.

For convenience of step-by-step numerical integration with a step size Δt, the nonlinear terms in equation (1) are approximated by

$$\left.\begin{aligned}\mathbf{F}_D(t)&=\mathbf{F}_D(t-\Delta t)+\mathbf{C}^*(t-\Delta t)[\dot{\mathbf{Y}}(t)-\dot{\mathbf{Y}}(t-\Delta t)]\\ \mathbf{F}_s(t)&=\mathbf{F}_s(t-\Delta t)+\mathbf{K}^*(t-\Delta t)[\mathbf{Y}(t)-\mathbf{Y}(t-\Delta t)]\end{aligned}\right\} \tag{2}$$

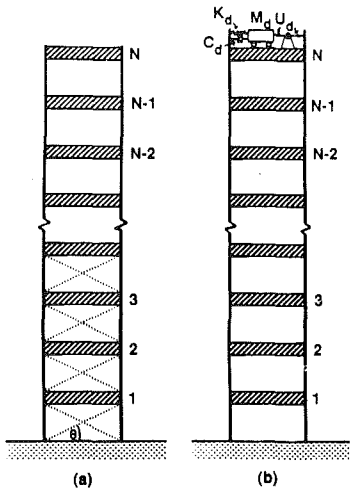

Fig. 1 Structural model of a multistory building with active control system; (a) active tendon control system; (b) active mass damper

in which $\mathbf{C}^*(t-\Delta t)$ and $\mathbf{K}^*(t-\Delta t)$ are $(n \times n)$ matrices evaluated at $t-\Delta t$. The $i-j$th elements of $\mathbf{C}^*(t-\Delta t)$ and $\mathbf{K}^*(t-\Delta t)$ matrices, denoted by $C^*_{ij}(t-\Delta t)$ and $K^*_{ij}(t-\Delta t)$, respectively, are the influence coefficients given by (Clough et al., 1975; Wilson et al., 1973)

$$\left.\begin{aligned}C^*_{ij}(t-\Delta t)&=\partial F_{Di}(t-\Delta t)/\partial \dot{y}_j(t-\Delta t)\\ K^*_{ij}(t-\Delta t)&=\partial F_{si}(t-\Delta t)/\partial y_j(t-\Delta t)\end{aligned}\right\} \tag{3}$$

in which $F_{Di}(t-\Delta t)$ and $F_{si}(t-\Delta t)$ are the ith elements of vectors $\mathbf{F}_D(t-\Delta t)$ and $\mathbf{F}_s(t-\Delta t)$, respectively, whereas $\dot{y}_j(t-\Delta t)$ and $y_j(t-\Delta t)$ are the jth element of the response vectors $\dot{\mathbf{Y}}(t-\Delta t)$ and $\mathbf{Y}(t-\Delta t)$, respectively. The influence coefficients, $C^*_{ij}(t-\Delta t)$ and $K^*_{ij}(t-\Delta t)$, represent the tangent damping and tangent stiffness at $t-\Delta t$ (Clough et al., 1975).

Thus, the matrix equation of motion, equation (1), can be expressed conveniently as

$$\begin{aligned}\mathbf{M}\,\ddot{\mathbf{Y}}(t)+\mathbf{F}_D(t-\Delta t)+\mathbf{C}^*(t-\Delta t)[\dot{\mathbf{Y}}(t)\\ -\dot{\mathbf{Y}}(t-\Delta t)]+\mathbf{F}_s(t-\Delta t)+\mathbf{K}^*(t-\Delta t)[\mathbf{Y}(t)\\ -\mathbf{Y}(t-\Delta t)]=-\mathbf{M}\,\mathbf{v}\,\ddot{X}_0(t)+\mathbf{H}\,\mathbf{U}(t).\end{aligned} \tag{4}$$

The solution of nonlinear equations, equation (4), can be obtained using the Wilson-θ numerical integration procedure. Then the $2n$ state vector $\mathbf{Z}(t)$ defined by

$$\mathbf{Z}(t)=\begin{bmatrix}\mathbf{Y}(t)\\ \cdots\cdots\\ \dot{\mathbf{Y}}(t)\end{bmatrix} \tag{5}$$

can be expressed in terms of the response state vector $\mathbf{Z}(t-\Delta t)$, nonlinear damping vector $\mathbf{F}_D(t-\Delta t)$, nonlinear stiffness vector $\mathbf{F}_s(t-\Delta t)$, earthquake base excitation $\ddot{X}_0(t-\Delta t)$, and the control vector $\mathbf{U}(t-\Delta t)$, all at time $t-\Delta t$, as well as the control vector $\mathbf{U}(t)$ and the earthquake base excitation $\ddot{X}_0(t)$ at time t as follows (see Yang et al. (1988) for detail derivations):

$$\mathbf{Z}(t)=\mathbf{D}^*(t-\Delta t)+\mathbf{A}_1\ddot{X}_0(t)+\mathbf{A}_2\mathbf{U}(t) \tag{6}$$

in which

$$\begin{aligned}\mathbf{D}^*(t-\Delta t)=\mathbf{A}_3\mathbf{Z}(t-\Delta t)+\mathbf{A}_4[\mathbf{F}_D(t-\Delta t)+\mathbf{F}_s(t-\Delta t)]\\ +\mathbf{A}_5\ddot{X}_0(t-\Delta t)+\mathbf{A}_6\mathbf{U}(t-\Delta t).\end{aligned} \tag{7}$$

In equations (6) and (7), $\mathbf{A}_j$ for $j=1,2, \ldots, 6$ are vectors or matrices given in the following.

Downloaded 03 May 2010 to 171.66.16.21. Redistribution subject to ASME license or copyright; see http://www.asme.org/terms/Terms_Use.cfm

$$\mathbf{A}_1=\theta^{-2}\left[\begin{array}{c}\mathbf{T}_1\\ \hline \frac{3}{\Delta t}\mathbf{T}_1\end{array}\right];\quad \mathbf{A}_2=\theta^{-2}\left[\begin{array}{c}\mathbf{T}_2\\ \hline \frac{3}{\Delta t}\mathbf{T}_2\end{array}\right]$$

$$\mathbf{A}_3=\left[\begin{array}{c|c}\mathbf{I}_1 & \theta^{-2}\mathbf{E}\,\mathbf{T}_3\\ \hline \mathbf{0} & \mathbf{I}_1+\theta^{-2}\mathbf{E}\,\mathbf{T}_4\end{array}\right];\quad \mathbf{A}_4=\theta^{-2}\left[\begin{array}{c}\mathbf{E}\,\mathbf{T}_5\\ \hline \mathbf{E}\,\mathbf{T}_6\end{array}\right] \tag{8}$$

$$\mathbf{A}_5=-\theta^{-2}\left[\begin{array}{c}\mathbf{E}\,\mathbf{T}_7\\ \hline \mathbf{E}\,\mathbf{T}_8\end{array}\right]\mathbf{M}\,\mathbf{v};\quad \mathbf{A}_6=\theta^{-2}\left[\begin{array}{c}\mathbf{E}\,\mathbf{T}_7\\ \hline \mathbf{E}\,\mathbf{T}_8\end{array}\right]\mathbf{H}$$

in which $\mathbf{I}_1$ is an $(n\times n)$ identity matrix, θ is chosen to be greater than 1.37, and

$$\begin{aligned}\mathbf{T}_1 &= -\mathbf{E}\,\mathbf{M}\,\mathbf{v},\ \mathbf{T}_2=\mathbf{E}\,\mathbf{H},\ \mathbf{T}_3=(6/\Delta t)\mathbf{M}+3\theta\mathbf{C}^*\\ &\quad +\Delta t(\theta^2-1)\mathbf{K}^*\\ \mathbf{T}_4 &= -3\,\mathbf{K}^*,\ \mathbf{T}_5=-(3\mathbf{I}_1+\mathbf{S}_1),\ \mathbf{T}_6=-(6/\Delta t)\mathbf{I}_1-\mathbf{S}_2\\ \mathbf{T}_7 &= 2\,\mathbf{I}_1+\mathbf{S}_1,\ \mathbf{T}_8=(3/\Delta t)\mathbf{I}_1+\mathbf{S}_2\\ \mathbf{E} &= \left[\frac{6}{(\theta\Delta t)^2}\mathbf{M}+\frac{3}{\theta\Delta t}\mathbf{C}^*+\mathbf{K}^*\right]^{-1}\\ \mathbf{S}_1 &= [\Delta t(1.5\theta-1)\mathbf{C}^*+0.5(\Delta t)^2(\theta^2-\theta)\mathbf{K}^*]\mathbf{M}^{-1}\\ \mathbf{S}_2 &= [3(\theta-1)\mathbf{C}^*+\Delta t\theta(\theta-1.5)\mathbf{K}^*]\mathbf{M}^{-1}\end{aligned} \tag{9}$$

In equation (9), the argument $t-\Delta t$ for influence coefficient matrices $\mathbf{C}^*$ and $\mathbf{K}^*$ has been omitted for simplicity. For a particular case in which damping is linear viscous damping, i.e.,

$$\mathbf{F}_D(t-\Delta t)=\mathbf{C}\,\dot{\mathbf{Y}}(t-\Delta t) \tag{10}$$

where $\mathbf{C}$ is a $(n\times n)$ constant matrix, equation (7) becomes

$$\begin{aligned}\mathbf{D}^*(t-\Delta t)&=\mathbf{A}_7\mathbf{Z}(t-\Delta t)+\mathbf{A}_4\mathbf{F}_s(t-\Delta t)\\ &\quad +\mathbf{A}_5\ddot{X}_0(t-\Delta t)+\mathbf{A}_6\mathbf{U}(t-\Delta t)\end{aligned} \tag{11}$$

in which

$$\mathbf{A}_7=\left[\begin{array}{c|c}\mathbf{I}_1 & \theta^{-2}\mathbf{E}\,\mathbf{T}_9\\ \hline \mathbf{0} & \mathbf{I}_1+\theta^{-2}\mathbf{E}\,\mathbf{T}_{10}\end{array}\right] \tag{12}$$

$$\begin{aligned}\mathbf{T}_9&=(6/\Delta t)\mathbf{M}+[3(\theta-1)\mathbf{I}_1-\mathbf{S}_1]\mathbf{C}+\Delta t(\theta^2-1)\mathbf{K}^*(t-\Delta t)\\ \mathbf{T}_{10}&=-[(6/\Delta t)\mathbf{I}_1+\mathbf{S}_2]\mathbf{C}-3\mathbf{K}^*(t-\Delta t).\end{aligned} \tag{13}$$

It follows from equations (8)–(13) that $\mathbf{A}_j$ for $j=1,2,\ldots,7$ are functions of influence coefficient matrices $\mathbf{C}^*(t-\Delta t)$ and $\mathbf{K}^*(t-\Delta t)$ at time $t-\Delta t$. Hence, they are evaluated at $t-\Delta t$, i.e., $\mathbf{A}_1=\mathbf{A}_1(t-\Delta t)$, $\mathbf{A}_2=\mathbf{A}_2(t-\Delta t)$, $\mathbf{A}_3=\mathbf{A}_3(t-\Delta t)$, $\mathbf{A}_4=\mathbf{A}_4(t-\Delta t)$, $\mathbf{A}_5=\mathbf{A}_5(t-\Delta t)$, $\mathbf{A}_6=\mathbf{A}_6(t-\Delta t)$, $\mathbf{A}_7=\mathbf{A}_7(t-\Delta t)$. Again, for simplicity of notation, the argument $t-\Delta t$ for these vectors and matrices have been omitted.

2.1 Optimal Control Algorithms for Nonlinear Structures. Unlike linear systems, control theories for nonlinear structures, including inelastic structures, are not well developed. For linear systems, the quadratic performance index

$$J=\int_0^{t_f}[Z'(t)\mathbf{Q}\,\mathbf{Z}(t)+\mathbf{U}'(t)\mathbf{R}\,\mathbf{U}(t)]dt \tag{14}$$

has been used to arrive at various classical optimal control theories. In equation (14), a prime denotes the transpose of a vector or matrix, t_f is the terminal time at which the state vector, $\mathbf{Z}(t)$, will die down, and $\mathbf{Q}$ and $\mathbf{R}$ are weighting matrices denoting the relative importance between the response state vector $\mathbf{Z}(t)$ and the control vector $\mathbf{U}(t)$. Unfortunately, even for linear structures subjected to earthquake excitation, these classical optimal control theories are not applicable as pointed out by Yang et al. (1985, 1987b). The reason is that these classical control theories require the prior knowledge of earthquake ground motion. Since earthquake ground acceleration is a random process, it is not known *a priori*.

While the earthquake ground motion is not known *a priori*, the base excitation of the building can be measured on-line real-time by installing sensors on the basement floor. In other words, at any particular time t, the base excitation record is available up to that time instant t. Such an important information has been utilized recently by Yang et al. (1985, 1987b) to develop three new optimal control algorithms, referred to as instantaneous optimal control algorithms.

A time-dependent quadratic objective function $J(t)$ was proposed to establish three instantaneous optimal control algorithms for linear structures as follows (Yang et al., 1985, 1987b),

$$J(t)=\mathbf{Z}'(t)\mathbf{Q}\,\mathbf{Z}(t)+\mathbf{U}'(t)\mathbf{R}\,\mathbf{U}(t). \tag{15}$$

The implication of minimizing the objective function (equation (15)), is that the performance index $J(t)$ is minimized at every time instant t for all $0\le t\le t_f$. Hence, the optimal control algorithms thus obtained are referred to as instantaneous optimal control algorithms (Yang et al., 1985, 1987b). Further, these three instantaneous optimal control algorithms have also been verified experimentally using a scale building model excited by simulated earthquakes on a shaking table (Lin et al., 1987).

For nonlinear structures, we propose the same time dependent objective function given in equation (15). Thus, we shall determine the optimal control vector $\mathbf{U}(t)$ by minimizing the objective function $J(t)$ given by equation (15) subjected to the constraint of the solution of nonlinear equations of motion given by equation (6) as follows. The Hamiltonian H is obtained by introducing a $2n$-dimensional Lagrangian multiplier vector $\lambda(t)$ (or co-state vector) to the objective function,

$$\begin{aligned}H=\mathbf{Z}'(t)\mathbf{Q}\,\mathbf{Z}(t)+\mathbf{U}'(t)\mathbf{R}\,\mathbf{U}(t)+\lambda'(t)\{\mathbf{Z}(t)-\mathbf{D}^*(t-\Delta t)\\ -\mathbf{A}_1\ddot{X}_0(t)-\mathbf{A}_2\mathbf{U}(t)\}\end{aligned} \tag{16}$$

in which $\mathbf{D}^*(t-\Delta t)$ is given by equation (7).

The necessary conditions for minimizing the performance index $J(t)$ subjected to the constraint given by equation (6) are as follows

$$\frac{\partial H}{\partial \mathbf{Z}}=0,\ \frac{\partial H}{\partial \mathbf{U}}=0,\ \frac{\partial H}{\partial \lambda}=0. \tag{17}$$

Substitution of equation (16) into equation (17) leads to the following three matrix equations

$$2\,\mathbf{Q}\,\mathbf{Z}(t)+\lambda(t)=0 \tag{18}$$

$$2\,\mathbf{R}\,\mathbf{U}(t)-\mathbf{A}_2'\lambda(t)=0 \tag{19}$$

$$\mathbf{Z}(t)=\mathbf{D}^*(t-\Delta t)+\mathbf{A}_1\ddot{X}_0(t)+\mathbf{A}_2\mathbf{U}(t). \tag{20}$$

Thus, the optimal control vector $\mathbf{U}(t)$, the co-state vector $\lambda(t)$, and the reponse state vector $\mathbf{Z}(t)$ can be obtained from equations (18)–(20).

2.2 Instantaneous Optimal Open-Loop Control. Note that the control vector $\mathbf{U}(t)$ is linearly proportional to the co-state vector $\lambda(t)$ at every time instant t as shown in equation (19). Assuming that the control vector $\mathbf{U}(t)$, or the co-state vector $\lambda(t)$, is regulated by the measured earthquake ground motion without a feedback state vector $\mathbf{Z}(t)$, the optimal control vector $\mathbf{U}(t)$ can be obtained from equations (18)–(20) as follows: (*i*) $\mathbf{Z}(t)$ is eliminated by substituting equation (20) into equation (18), and (*ii*) the resulting $\lambda(t)$ obtained from equation (18) is substituted into equation (19); with the result

$$\mathbf{U}(t)=\mathbf{L}\,\mathbf{G}(t) \tag{21}$$

Downloaded 03 May 2010 to 171.66.16.21. Redistribution subject to ASME license or copyright; see http://www.asme.org/terms/Terms_Use.cfm

in which

$$\left.\begin{aligned}\mathbf{L} &= -[\mathbf{R}+\mathbf{A}_2'\mathbf{Q}\,\mathbf{A}_2]^{-1}\mathbf{A}_2'\,\mathbf{Q}\\ \mathbf{G}(t) &= \mathbf{D}^*(t-\Delta t)+\mathbf{A}_1\ddot{X}_0(t)\end{aligned}\right\}. \tag{22}$$

As observed from equations (21)-(22), the control vector at time t is regulated by the measured earthquake ground accelerations $\ddot{X}_0(t)$ and $\ddot{X}_0\ (t-\Delta t)$ at time t and $t-\Delta t$, respectively, as well as the computed quantity $\mathbf{D}^*\ (t-\Delta t)$ at time $t-\Delta t$, equation (7). The control vector $\mathbf{U}(t)$ is not regulated by the state vector $\mathbf{Z}(t)$ and the optimal control algorithm thus obtained is referred to as the instantaneous optimal open-loop control algorithm.

The response state vector $\mathbf{Z}(t)$ under instantaneous optimal open-loop control is obtained by substituting equation (21) into equation (20),

$$\mathbf{Z}(t)=[\mathbf{I}-\mathbf{A}_2(\mathbf{R}+\mathbf{A}_2'\mathbf{Q}\,\mathbf{A}_2)^{-1}\mathbf{A}_2'\mathbf{Q}]\mathbf{G}(t) \tag{23}$$

in which $\mathbf{I}$ is a $(2n\times 2n)$ identity matrix.

2.3 Instantaneous Optimal Closed-Loop Control. For closed-loop control, the control vector $\mathbf{U}(t)$, or the co-state vector $\lambda(t)$, is regulated by the feedback state vector $\mathbf{Z}(t)$, i.e.,

$$\lambda(t)=\Lambda\,\mathbf{Z}(t) \tag{24}$$

Substitution of equation (24) into equation (18) leads to the following expression,

$$(2\mathbf{Q}+\Lambda)\mathbf{Z}(t)=0. \tag{25}$$

For $\mathbf{Z}(t)\neq 0$, the unknown matrix Λ is obtained as

$$\Lambda=-2\mathbf{Q}. \tag{26}$$

Thus, the optimal control vector $\mathbf{U}(t)$ follows from equations (19) and (26) as

$$\mathbf{U}(t)=-\mathbf{R}^{-1}\mathbf{A}_2'\mathbf{Q}\,\mathbf{Z}(t) \tag{27}$$

and the response state vector is obtained by substituting equation (27) into equation (20)

$$\mathbf{Z}(t)=[\mathbf{I}+\mathbf{A}_2\mathbf{R}^{-1}\mathbf{A}_2'\mathbf{Q}]^{-1}\mathbf{G}(t) \tag{28}$$

in which $\mathbf{G}(t)$ is given by equation (22). The control algorithm derived above is referred to as the instantaneous optimal closed-loop control algorithm.

It is important to notice that for the instantaneous optimal closed-loop control algorithm, the measurement of earthquake base acceleration $\ddot{X}_0(t)$ is not necessary. In other words, the control vector $\mathbf{U}(t)$ is regulated only by the measured state vector $\mathbf{Z}(t)$.

2.4 Instantaneous Opitmal Closed-Open-Loop Control. Let the control vector $\mathbf{U}(t)$, or the co-state vector $\lambda(t)$, be regulated by both the feedback response state vector $\mathbf{Z}(t)$ and the measured base excitation $\ddot{X}_0(t)$, i.e.,

$$\lambda(t)=\tilde{\Lambda}\,\mathbf{Z}(t)+\tilde{\mathbf{q}}(t) \tag{29}$$

in which $\tilde{\Lambda}$ and $\tilde{\mathbf{q}}$ are unknown matrix and vector, respectively, to be determined from equations (18)-(20) as follows. Substituting equation (29) into equation (19) yields the expression for $\mathbf{U}(t)$. Then, the resulting $\mathbf{U}(t)$ is substituted into equation (20) leading to the following expression for $\mathbf{Z}(t)$

$$\mathbf{Z}(t)=\mathbf{D}^*(t-\Delta t)+\mathbf{A}_1\ddot{X}_0(t)+\frac{1}{2}\mathbf{A}_2\mathbf{R}^{-1}\mathbf{A}_2'[\tilde{\Lambda}\,\mathbf{Z}(t)+\tilde{\mathbf{q}}(t)]. \tag{30}$$

The term $2\mathbf{Q}\,\mathbf{Z}(t)$ in equation (18) is expressed as $\mathbf{Q}[\mathbf{Z}(t)+\mathbf{Z}(t)]$, and the first term of $\mathbf{Z}(t)$ is replaced by equation (30), whereas equation (29) is used for $\lambda(t)$ in equation (18); with the result,

$$\left\{\mathbf{Q}+\left[\frac{1}{2}\mathbf{Q}\,\mathbf{A}_2\mathbf{R}^{-1}\mathbf{A}_2'+\mathbf{I}\right]\tilde{\Lambda}\right\}\mathbf{Z}(t)+\left[\frac{1}{2}\mathbf{Q}\,\mathbf{A}_2\mathbf{R}^{-1}\mathbf{A}_2'+\mathbf{I}\right]\tilde{\mathbf{q}}(t)+\mathbf{Q}\,\mathbf{G}(t)=0. \tag{31}$$

For $\mathbf{Z}(t)\neq 0$ and $\tilde{\mathbf{q}}(t)\neq 0$, one obtains the solutions for unknown matrix $\tilde{\Lambda}$ and unknown vector $\tilde{\mathbf{q}}(t)$,

$$\tilde{\Lambda}=-\left[\frac{1}{2}\mathbf{Q}\,\mathbf{A}_2\mathbf{R}^{-1}\mathbf{A}_2'+\mathbf{I}\right]^{-1}\mathbf{Q} \tag{32}$$

$$\tilde{\mathbf{q}}(t)=\tilde{\Lambda}\,\mathbf{G}(t). \tag{33}$$

Thus, the optimal control vector $\mathbf{U}(t)$ and the response state vector $\mathbf{Z}(t)$ are determined from equations (19) and (20) as follows

$$\mathbf{U}(t)=\frac{1}{2}\mathbf{R}^{-1}\mathbf{A}_2'\tilde{\Lambda}[\mathbf{Z}(t)+\mathbf{G}(t)] \tag{34}$$

$$\mathbf{Z}(t)=\left[\mathbf{I}-\frac{1}{2}\mathbf{A}_2\mathbf{R}^{-1}\mathbf{A}_2'\tilde{\Lambda}\right]^{-1}\left[\mathbf{I}+\frac{1}{2}\mathbf{A}_2\mathbf{R}^{-1}\mathbf{A}_2'\tilde{\Lambda}\right]\mathbf{G}(t). \tag{35}$$

The optimal algorithm presented above is referred to as the instantaneous optimal closed-open-loop control algorithm.

III Numerical Examples

To illustrate the effectiveness of the instantaneous optimal control algorithms developed in this paper for control of nonlinear structures, three examples are presented in the following. The structure is assumed to exhibit nonlinear material behavior with bilinear elastic-plastic characteristics. For simplicity, damping is assumed to be linear viscous damping. It should be mentioned that the three instantaneous optimal control algorithms result in identical structural response quantities as well as identical control force under ideal control environment. Ideal control environment refers to that without a system time delay, system uncertainty, estimation errors, etc., during the control process. This has been expected because the three instantaneous optimal control algorithms minimize the same time-dependent objective function $J(t)$. Hence, in what follows, the instantaneous optimal closed-loop control algorithm will be used for simplicity.

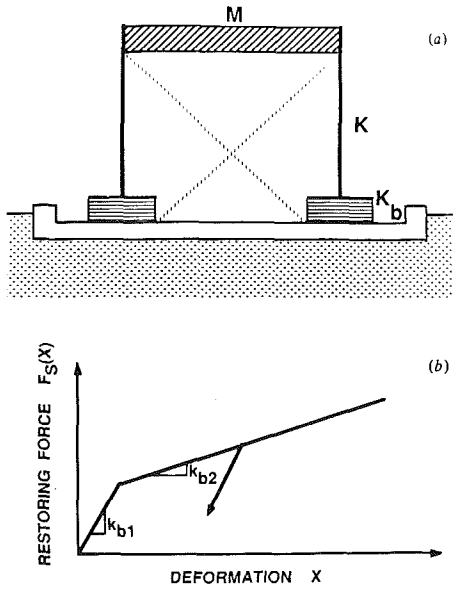

Fig. 2 Structural model and characteristics of restoring force; (a) SDOF model with base isolators and active tendon system; (b) bilinear elastic-plastic restoring force

Downloaded 03 May 2010 to 171.66.16.21. Redistribution subject to ASME license or copyright; see http://www.asme.org/terms/Terms_Use.cfm

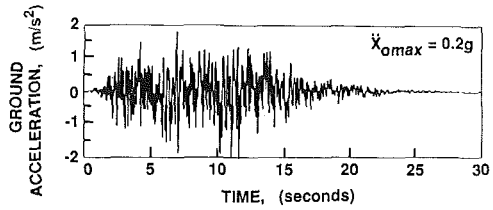

Fig. 3 A simulated earthquake ground acceleration

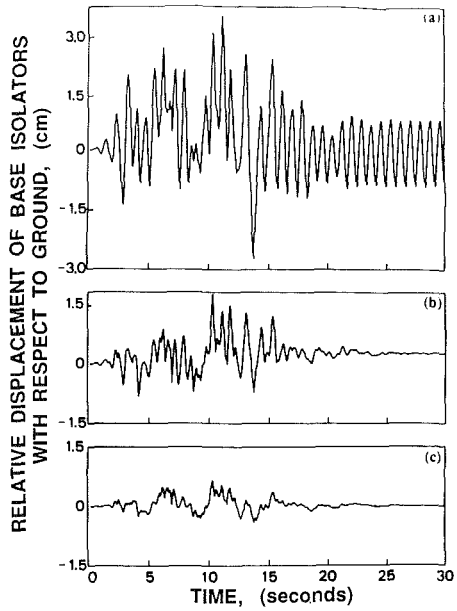

Fig. 4 Relative displacement of base isolators with respect to ground; (*a*) without control; (*b*) $Q_0/R_0 = 2 \times 10^7$; (*c*) $Q_0/R_0 = 9 \times 10^7$

Example 1: Building Isolated by Rubber Bearings. A five story building resting on lead-core rubber bearings considered by Megget (1978) has been modeled by Reinhorn et al. (1987) mathematically as a SDOF system in approximation as shown in Fig. 2(*a*). This representation seems to be reasonable since the effect of rubber bearings is to introduce a "soft story" with inelastic characteristics whereas, in comparison, the superstructure behaves like a rigid body. As a result, we shall consider herein a representative SDOF structure resting on rubber bearings shown in Fig. 2(*a*). Active tendon control is introduced to limit the relative displacement of the rubber bearings to avoid instability failure as well as the relative displacement of the superstructure. The instantaneous optimal closed-loop control algorithm is most suitable for such applications. The superstructure is assumed to be linear elastic, whereas the rubber bearings exhibit bilinear elastic-plastic behavior as shown in Fig. 2(*b*). The structural properties are given in the following: (1) m = mass of superstructure = 153.06 tons (2) k = translational stiffness of superstructure = 6.71×10^4 kN/m and, hence, the natural frequency is 3.33 Hz, (3) C = damping coefficient of superstructure = 0, (4) k_1 = elastic stiffness of base isolators = 10,000 kN/m, (5) k_2 = post-elastic stiffness of base isolators = 2,500 kN/m (6) y_a = yielding deformation of base isolators = 10.1 mm, and (7) y_b = failure deformation of base isolators = 150 mm. The angle of inclination of tendons is 25 deg. A simulated earthquake ground acceleration shown in Fig. 3 is considered as the input excitation, where the maximum ground acceleration is 0.2g (2.05 m/s^2). The integration time step Δt is 0.015 seconds.

Without control, the relative displacement of rubber isolators with respect to the ground and the hysteresis loop of elastic-plastic shear force in rubber isolators are shown in

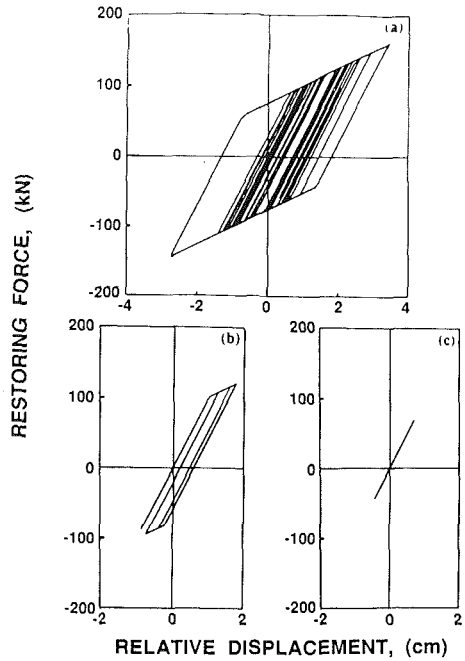

Fig. 5 Hysteresis loop of inelastic shear force in rubber isolators; (*a*) without control; (*b*) $Q_0/R_0 = 2 \times 10^7$; (*c*) $Q_0/R_0 = 9 \times 10^7$

Figs. 4(*a*) and 5(*a*). With the active tendon control system, the structural response and active control force depend on the weighting matrices **Q** and **R**. In the present example, **Q** is a (2×2) matrix, whereas **R** is a (1×1) matrix. For simplicity, **Q** matrix is chosen to be diagonal, i.e., $Q_{12} = Q_{21} = 0$, and the diagonal elements are identical, i.e., $Q_{11} = Q_{22} = Q_0$. The only element of **R** matrix is denoted by R_0. The controlled response quantities for two different Q_0/R_0 ratios are presented in Figs. 4(*b*), 4(*c*), 5(*b*), and 5(*c*) for comparison.

To illustrate the control efficiency the maximum relative displacement of the superstructure, maximum relative displacement of rubber isolators and maximum required active control force in 30 seconds of the earthquake episode are depicted in Fig. 6 as functions of Q_0/R_0 ratio. It is observed from Figs. 4–6 that the active tendon control system is capable of drastically reducing not only the superstructural response but also the deformation of base isolators. Likewise, both the deformations of the structure and rubber base isolators are mitigated consistently as the ratio Q_0/R_0 increases. The ability to safeguard severe damage for passive control devices against earthquakes by means of active control is quite obvious. The basic idea presented herein for the use of combined passive/active control systems is explained in the following. The base isolation system (passive) is used to absorb large deformation and dissipate input energies such that smaller excitations are transmitted to the superstructure. However, base isolators must be protected against severe damage or instability failure. This is achieved by use of active control devices along with the optimal control algorithms developed herein. The advantage of the combined passive/active control system is clearly demonstrated.

Example 2: Eight Story Building With Active Mass Damper. An eight story building in which every story unit is identically constructed is considered for illustrative purposes. The stiffness of each story unit is assumed to be bilinear elastic-plastic with elastic stiffness $k_{i1} = k_1 = 3.404 \times 10^5$ kN/m, and post-elastic stiffness $k_{i2} = k_2 = 10$ percent $k_1 = 3.404 \times 10^4$ kN/m ($i = 1,2, \ldots, 8$). The yielding level is identical for each story unit at a lateral deformation of 2.4 cm. The floor mass is $m = 345.6$ tons and the internal damping coefficient C for each story unit is $C = 734.3$ kN.s/m which

Downloaded 03 May 2010 to 171.66.16.21. Redistribution subject to ASME license or copyright; see http://www.asme.org/terms/Terms_Use.cfm

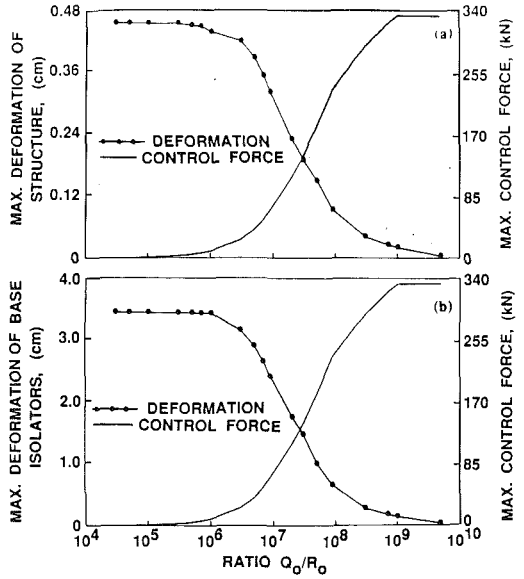

Fig. 6 Maximum response quantities and control force as functions of Q_0/R_0 ratio; (*a*) maximum relative displacement of superstructure and maximum control force; (*b*) maximum relative displacement of rubber base isolators and maximum control force

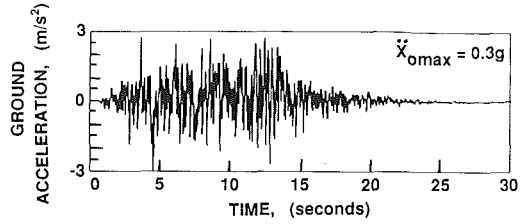

Fig. 7 A simulated earthquake ground acceleration

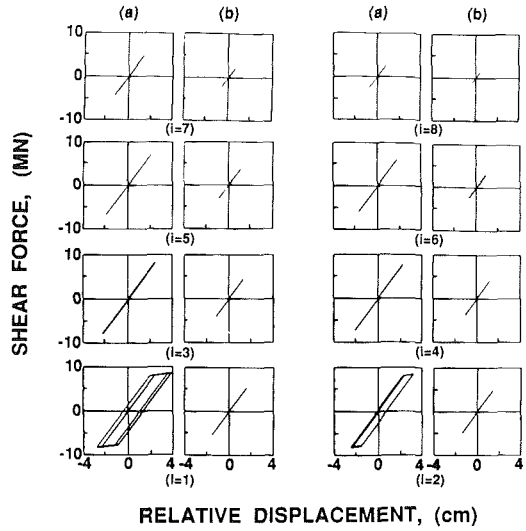

Fig. 8 Hysteresis loops for shear force in each story unit (0.3 g earthquake); (*a*) without control; (*b*) with active mass damper

corresponds to a 0.5 percent damping ratio for the first vibrational mode of the entire building. The external damping is assumed to be zero. The computed natural frequencies are 5.79, 17.18, 27.98, 37.82, 46.38, 53.36, 58.53, and 61.69 rad/s. The simulated earthquake shown in Fig. 7 with a maximum ground acceleration $\ddot{X}_{0max} = 0.3$ g is considered as the input excitation. Without any control system, hysteresis loops for the shear force in each story unit are displayed in Fig. 8(*a*), in which "*i*" signifies the *i*th story unit. As observed from Fig. 8(*a*), yielding occurs in the lower three story units.

An active mass damper is installed on the top floor of the building as shown in Fig. 1(*b*). The properties of the mass damper are: m_d = mass of the damper = 36.3 tons; C_d = damping of the damper = 31.0 kN.s/m; K_d = stiffness of the damper = 1173.0 kN/m. Note that the damper mass m_d is 10.5 percent of the generalized mass associated with the first vibrational mode, the frequency of the damper is 98 percent of the first natural frequency of the building, and the damping ratio of the damper is approximately 7.5 percent. Without the active control force, the mass damper is passive. It has been shown that the passive mass damper is not effective (Yang et al., 1988). The integration time step Δt is 0.015 seconds.

With an active mass damper, the structural response depends on the weighting matrices **R** and **Q**. In this example, the weighting matrix **R** consists of only one element denoted by R_0, whereas the dimension of the **Q** matrix is (18×18). R_0 is chosen to be 10^{-5}. The (18×18) **Q** matrix is partitioned more efficiently as follows (Yang et al., 1987a and 1987b),

$$\mathbf{Q} = \alpha \begin{bmatrix} \mathbf{0} & \mathbf{0} \\ \mathbf{Q}_{21} & \mathbf{Q}_{22} \end{bmatrix} \tag{36}$$

in which $\mathbf{Q}_{21}$ and $\mathbf{Q}_{22}$ are (2×9) matrices. The following values are assigned to elements of these two matrices for illustrative purposes:

A value of 5.12 is chosen for α, such that the top floor relative displacement with respect to the ground is reduced approximately by 47.1 percent and all the response quantities are well within the elastic limit. Time histories of all response quantities, the required active control force from the controller, and the relative displacement of the mass damper with respect to the top floor have been computed. Because of space limitation they are not presented (Yang et al., 1988). Only the hysteresis loops for the shear force in each story unit are depicted in Fig. 8(*b*) for comparison. Within 30 seconds of the earthquake episode, the maximum deformation of each story unit (or the relative displacement between adjacent floors), x_i(i = 1,2, . . . , 8), and the maximum shear force, S_i, in each story unit are presented in Table 1 for comparison. The maximum control force is 820.7 kN and the maximum relative displacement of the mass damper with respect to the top floor is 1.64 m. It is observed from Fig. 8 and Table 1 that with an active mass damper the response of the entire building is well within the elastic range.

In the example above, yielding in the lower three story units is moderate without control. Let us consider the case in which a large scale yielding occurs and the structure would have failed without control. Suppose the earthquake time history shown in Fig. 7 is scaled up uniformly so that the maximum ground acceleration is $\ddot{X}_{0max} = 0.55$ g. Such a severe earth-

$$\mathbf{Q}_{21} = \begin{bmatrix} -33.5 & -67. & -100.5 & -134. & -167.5 & -201. & -234.5 & -268. & -375.6 \\ -33.5 & -67. & -100.5 & -134. & -167.5 & -201. & -234.5 & -268. & 32.2 \end{bmatrix}$$

$$\mathbf{Q}_{22} = \begin{bmatrix} 67.5 & 135.0 & 202.5 & 270.0 & 338.5 & 405.0 & 472.5 & 540.0 & 32.2 \\ 5.8 & 11.6 & 17.6 & 23.2 & 29.0 & 34.7 & 40.5 & 46.3 & 5.7 \end{bmatrix}$$

Downloaded 03 May 2010 to 171.66.16.21. Redistribution subject to ASME license or copyright; see http://www.asme.org/terms/Terms_Use.cfm

Table 1 Maximum response quantities (0.3 g earthquake): x_i = maximum interstory deformation of ith story unit; S_i = maximum shear force in ith story unit; U_{max} = 820.7 kN = maximum control force for mass damper, U_i = maximum control force from ith controller

Floor	Without Control		Active Mass Damper		Active Tendons $\alpha = 2500$		
No. (i)	x_i (cm)	S_i (kN)	x_i (cm)	S_i (kN)	x_i (cm)	S_i (kN)	U_i (kN)
1	3.89	8677	1.62	5529	1.78	6051	1725
2	3.22	8447	1.48	5042	1.51	5134	1722
3	2.49	8200	1.32	4497	1.26	4298	1677
4	2.30	7812	1.27	4310	1.33	4537	1126
5	2.11	7184	1.14	3877	1.45	4938	0
6	1.84	6274	0.93	3169	1.25	4269	0
7	1.45	4951	0.68	2327	1.03	3499	0
8	0.80	2722	0.60	2043	0.56	1900	0

Table 2 Maximum response quantities (0.55 g earthquake): x_i = maximum interstory deformation of ith story unit; S_i = maximum shear force in ith story unit; U_{max} = 1505 kN = maximum control force for mass damper, U_i = maximum control force from ith controller

Floor	Without Control		Active Mass Damper		Active Tendons $\alpha = 2500$		
No. (i)	x_i (cm)	S_i (kN)	x_i (cm)	S_i (kN)	x_i (cm)	S_i (kN)	U_i (kN)
1	5.32	9164	4.25	8800	3.68	8604	3129
2	3.90	8681	2.66	8257	2.51	8206	3123
3	4.03	8725	2.41	8174	2.23	7593	3043
4	3.48	8536	2.32	7896	2.31	7876	2043
5	3.06	8395	2.09	7106	2.94	8352	0
6	2.93	8350	1.71	5808	2.31	7873	0
7	2.19	7456	1.22	4135	1.90	6452	0
8	1.24	4206	0.94	3193	1.03	3504	0

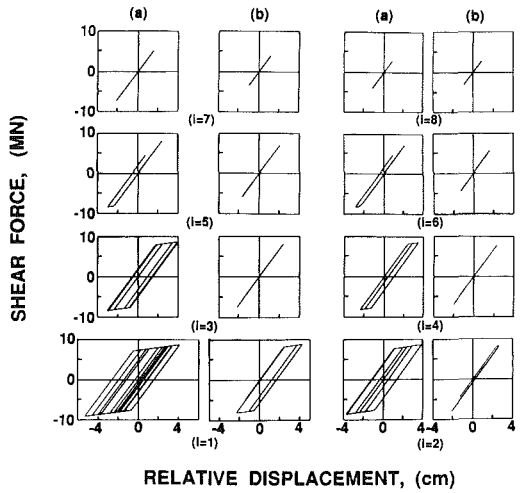

Fig. 9 Hysteresis loops for shear force in each story unit (0.55 g earthquake); (*a*) without control; (*b*) with active mass damper

quake is considered as the input excitation. The hysteresis loops for the shear force in each story unit for the building with and without active mass damper are shown in Fig. 9. Within 30 seconds of the earthquake episode, the maximum interstory relative displacement, $x_i (i = 1, 2, \ldots, 8)$, and the maximum interstory shear force are summarized in Table 2 for comparison. The maximum active control force is 1505 kN and the maximum relative displacement of the mass damper with respect to the top floor is 2.79 m. The following observations are made from Fig. 9 and Table 2: (*i*) The building may have failed without an active control system and structural failure can be prevented using an active mass damper, and (*ii*) a large scale yielding and severe inelastic damage can be reduced significantly using an active mass damper. Further numerical results indicate that the response of the entire building can be brought back to the elastic range with an increase of the control force.

Example 3: Eight Story Building With Active Tendon Control System. The same eight story building subjected to the same earthquake ground acceleration input illustrated in Example 2 is considered herein. Instead of installing an active mass damper on the top floor, four active tendon controllers are installed in the lowest story units and the angle of inclination of tendons with respect to the floor is 25 deg as shown in Fig. 1(*a*). In the present example, the dimension of the weighting matrices $\mathbf{Q}$ and $\mathbf{R}$ are (16 × 16) and (4 × 4), respectively. The weighting matrix $\mathbf{R}$ is chosen to be a diagonal matrix with elements $R_{ii} = 10^{-4}$ $(i = 1,2,3,4)$. The (16 × 16) weighting matrix $\mathbf{Q}$ is again partitioned as shown in equation (36), in which $\mathbf{Q}_{21}$ and $\mathbf{Q}_{22}$ are (8 × 8) matrices and α is a constant. Note that $\mathbf{Q}_{11}$ and $\mathbf{Q}_{12}$ do not contribute to the active control forces and, hence, they are chosen to be zero (Yang et al., 1987a and 1987b). The choice of $\mathbf{Q}_{21}$ and $\mathbf{Q}_{22}$ requires some considerations. For simplicity, $\mathbf{Q}_{21}$ and $\mathbf{Q}_{22}$ are chosen to be equal, i.e., $\mathbf{Q}_{21} = \mathbf{Q}_{22} = \mathbf{Q}^*$. The elements of $\mathbf{Q}^*$, denoted by $Q^*(i,j)$, are given in the following; $Q^*(i,j,) = i$ for $i \leq 4$ and $Q^*(i,j) = 0$ for $i > 4$. For a 47 percent reduction of the building response, a value of 2500 is used for α. Under the earthquake with a maximum ground acceleration of 0.3 g, Fig. 7, time histories of the response quantities with active tendon control have been computed. Within 30 seconds of the earthquake episode, the maximum response quantities and maximum control forces are summarized in Table 1. It is observed from Table 1 that all the response quantities of the structure are well within the elastic range when the active tendon control system is used.

To examine the effectiveness of active tendon control for a large scale yielding in the structure, the earthquake with a

Downloaded 03 May 2010 to 171.66.16.21. Redistribution subject to ASME license or copyright; see http://www.asme.org/terms/Terms_Use.cfm

maximum ground acceleration of 0.55 g is considered as the input excitation. The results are shown in Table 2. It is observed from Table 2 that the active tendon control system is effective in alleviating severe inelastic damages although the required active control forces are quite large.

IV Conclusions and Discussions

Three instantaneous optimal algorithms have been developed for active control of nonlinear structures subjected to general dynamic loads. These include the instantaneous optimal closed-loop control algorithm, instantaneous optimal open-loop control algorithm, and instantaneous optimal closed-open-loop control algorithm. Under ideal control environments, these three optimal algorithms yield identical results. Emphasis is placed on applications of active control to inelastic tall buildings subjected to strong earthquake ground motions.

Instantaneous optimal control algorithms are derived by minimizing a time-dependent quadratic performance index, whereas nonlinear equations of motion are solved using the Wilson-θ numerical method. These optimal control algorithms are shown to be computational efficient and suitable for on-line implementation of control systems to nonlinear tall buildings under earthquake excitations. While control of inelastic structures has been demonstrated exclusively, these optimal algorithms are equally applicable to structures with other types of nonlinearity, such as the geometric nonlinearity. Likewise, they are applicable to linear structures as a special case.

The following conclusions are obtained from numerical results: (1) Significant yielding of building structures, which generally results in a severe damage, can be mitigated or even eliminated through active control systems using the proposed optimal control algorithms. It is possible and may be practical to keep the structural response well within the elastic limits. (2) The proposed instantaneous optimal control algorithms are reliable and they are capable of consistently mitigating structural response quantities as regulated by the weighting matrices. (3) The combined use of passive/active control systems can be very beneficial. Since base isolators usually exhibit nonlinear behavior, the optimal algorithms developed herein for controlling nonlinear structural systems are quite significant.

For the instantaneous optimal algorithms proposed herein, the quadratic objective function $J(t)$, equation (15), is minimized independently in each small time interval Δt. Hence, these algorithms are not optimal in the global sense as defined by equation (14). As discussed previously, it is very difficult, if not impossible, to achieve global optimal control, because the earthquake excitation history is not known *a priori*. This is a subject of future research. In fact, most dynamic loads of natural hazards, such as earthquakes, strong wind turbulences, high waves, storms, etc., are stochastic processes and their future sample functions are not known *a priori*.

A quadratic function of $\mathbf{U}(t)$ and $\mathbf{Z}(t)$ is used as the performance index for simplicity. In fact, other functional forms of the performance index may result in a better control strategy, for instance, the minimization of vibrational energy with some constraints on available power from controllers. However, more definitive conclusions can be obtained only after a careful experimental demonstrations using available or soon to be available control devices, such as the large-scale electrohydraulic servomechanisms.

Frequently, after yielding occurs resulting from excessive deformation, structural properties may change and degrade thus deviating significantly from the original estimated values. In this connection, the adaptive control algorithm should be developed in conjunction with the instantaneous optimal control algorithms proposed herein. This is a subject of future research. Further, based on the present optimal control algorithms, the control efficiency is regulated at every time instant by the weighting matrices $\mathbf{Q}$ and $\mathbf{R}$. In order to guarantee that the structural response be always within specified limits, weighting matrices should be time-dependent and they should be adaptive to the feedback response at every time instant t. This subject of research is currently being undertaken. Finally, experimental programs will be undertaken in the near future to verify the applicability of these proposed instantaneous optimal control algorithms.

Acknowledgment

This research is supported by National Science Foundation Grant No. NSF-ECE-85-21496 and National Center For Earthquake Engineering Research Grant No. NCEER-87-2004.

References

Abdel-Rohman, M., and Nayfeh, A. H., 1987, "Active Control of Nonlinear Oscillations in Bridges," *Journal of Engineering Mechanics*, ASCE, Vol. 113, No. 3, pp. 335–334.

Clough, R. W., and Penzies, J., 1975, *Dynamics of Structures*, McGraw-Hill Book Co., New York, Chapters 8 and 15.

Kelly, J. M., 1981, "Aseismic Base Isolator: Its History and Prospects," Proceedings, World Congress on Joints and Bearing, American Concrete Institute Publication SP-70, Detroit, MI.

Leipholz, H. H. E., ed., 1980, *Structural Control*, North-Holland Publishing Co., Proc. of First International Symposium on Structural Control, University of Waterloo, Waterloo, Canada.

Leipholz, H. H. E., ed., 1985, *Structural Control*, Martinus Nijhoff Publishing Co., Amsterdam, Proc. of Second International Symposium on Structural Control, University of Waterloo, Waterloo, Canada.

Lin, R. C., Soong, T. T., and Reinhorn, A. M., 1987, "Experimental Evaluation of Instantaneous Optimal Algorithms for Structural Control," National Center For Earthquake Engineering Research, Technical Report NCEER-TR-87-0002.

Masri, S. F., Bekey, G. A., and Caughey, T. K., 1981a, "On-Line Control of Nonlinear Flexible Structures," ASME JOURNAL OF APPLIED MECHANICS, Vol. 49, No. 4, pp. 871–884.

Masri, S. F., Bekey, G. A., and Caughey, T. K., 1981b, "Optimal Pulse Control of Flexible Structures," ASME JOURNAL OF APPLIED MECHANICS, Vol. 48, pp. 619–626.

Megget, L. M., 1978, "Analysis and Design of a Base-Isolated Reinforced Concrete Frame Building," *Bulletin of New Zealand Society for Earthquake Engineering*, Vol. 11, No. 4, pp. 245–254.

Reinhorn, A. M., and Manolis, G. D., 1985, "Current State of Knowledge on Structure Control," *The Shock and Vibration Digest*, Vol. 17, No. 10, pp. 35–41.

Reinhorn, A. M., Manolis, G. D., and Wen, C. Y., 1987, "Active Control of Inelastic Structures," *Journal of Engineering Mechanics*, ASCE, Vol. 113, No. 3, pp. 315–332.

Soong, T. T., Reinhorn, A. M., and Yang, J. N., 1985, "A Standardized Model for Structural Control Experiments and Some Experimental Results," *Structural Control*, Second International Symposium on Structural Control, Univ. of Waterloo, Ontario, Canada, H. H. E. Leipholz, ed., Martinus Nijhoff Publishing Co., Amsterdam, pp. 669–693.

Wilson, E. L., Fahoomand, I., and Bathe, K. J. 1973, "Nonlinear Dynamic Analysis of Complex Structures," *Journal of Earthquake Engineering and Structural Dynamics*, Vol. 1, pp. 241–252.

Yang, J. N., Akbarpour, A., and Ghaemmaghami, P., 1985, "Optimal Control Algorithms For Earthquake Excited Building Structures," *Structural Control*, Proc. 2nd International Symposium on Structural Control, H. H. E. Leipholz, ed., Martinus Nijhoff, Amsterdam, pp. 748–761.

Yang, J. N., Akbarpour, A., and Ghaemmaghami, P., 1987a, "Instantaneous Optimal Control Laws For Tall Buildings Under Seismic Excitations," National Center For Earthquake Engineering Research, Technical Report NCEER-TR-87-0007.

Yang, J. N., Akbarpour, A., and Ghaemmaghami, P., 1987b, "New Optimal Control Algorithms For Structural Control," *Journal of Engineering Mechanics*, ASCE, Vol. 113, No. 9, pp. 1369–1386.

Yang, J. N., Long, F. X., and Wong, D., 1988, "Optimal Control of Nonlinear Flexible Structures," National Center For Earthquake Engineering, Technical Report NCEER-TR-88-0002.

Yang, J. N., and Soong, T. T., 1988, "Recent Advancement in Active Control of Civil Engineering Structures," paper to appear in *Journal of Engineering Probabilistic Mechanics*.

Yao, J. T. P., and Soong, T. T., 1984, "Importance of Experimental Studies in Structural Control," ASCE, Reprint 84-010, Atlanta Convention.

Downloaded 03 May 2010 to 171.66.16.21. Redistribution subject to ASME license or copyright; see http://www.asme.org/terms/Terms_Use.cfm

Trade-Offs Between Identification and Control in Dynamic Systems

Firdaus E. Udwadia
Professor of Civil Engineering, Decision Systems, and Mechanical Engineering.

Henryk Flashner
Assistant Professor of Mechanical Engineering.

University of Southern California, Los Angeles, Calif. 90089-1453

A quantitative study of the trade-offs between the tasks of control law design and plant identification for linear dynamic systems is presented. The problem is formulated in the context of optimal control and optimal identification through the intermediary concept of an optimal input. The duality between identification and control is quantified by optimal inputs, which have a specified amount of energy, and which minimizes the objective function. The optimization problem together with the energy constraint is formulated by using an augmented state vector. This results in a nonlinear two-point boundary value problem and eliminates the need for using a trial and error approach to satisfy the energy constraint. An example of a single-degree-of-freedom oscillator is used to illustrate the basic concepts underlying the proposed approach. Significant trade-offs between identification and control tasks are observed, the trade-offs becoming increasingly important for increasing levels of input energy.

Introduction

The control of large flexible structures is an area that has attracted considerable interest in recent years from both the professional and the research community (Meirovitch (1985); Rodriguez (1985); Aubrun (1980); Benhabib et al. (1981); Meirovitch (1982)). This interest is primarily motivated by the need to precisely control flexible structures in various developing fields of modern technology. In the area of earthquake engineering, the reduction of structural response may be necessary to reduce internal stresses caused by dynamic loads thereby reducing the damage potential and increasing the useful life of structures (Martin and Soong (1976)). In space applications, the availability of the Space Shuttle to transport large payloads into orbit at reasonable costs presents an opportunity for large systems to perform new missions in space. However, because of launch weight and volume constraints, these structures are generally very flexible and pose new challenges in all aspects of control such as attitude control and maneuvering, precision pointing, vibration attenuation, and structural and shape control (AIAA (1978)).

A necessary prelude to the effective control of a structure is a knowledge of its characteristics and properties. In other words, one needs to have information about the structural system so that adequate control algorithms can be devised. This has led to a considerable interest in the identification of structures subjected to dynamic loads (Udwadia (1985); Graupe (1972); Mehra and Lainiotis (1976); Tung (1981); Dale and Cohen (1971)). For structural systems that are described by parametric models, this involves knowledge of the nature of the governing differential equations and knowledge of the values of the parameters that are involved or, at least, knowledge of the bounds within which the parameters lie. Clearly, the better the system is identified (the smaller the bounding intervals within which the parameters are known to lie), the more finely tuned the controller can be made, so that for a given amount of available control energy, the control would be more efficient. The less knowledge we have about the structural system the more robust the controller needs to be and, in general, the less efficient the control for a given amount of available control energy. Thus, heuristically speaking, there exists a duality between the concepts of identification and control, because (1) robust controllers may require reduced efforts at identification (for purposes of control), and (2) increased efforts at identification may require less robust and more efficient controllers. However, the tradeoffs between identification and control, from a practical standpoint, are still usually difficult to assess quantitatively. Little work has been reported to date in this area of quantitative cost-benefit analysis between these two dual concepts. A simulation study comparing adaptive control and identification algorithms is given in Benhabib and Tung (1980), though, here again, no quantitative results were presented.

In this paper we formulate the trade-off problem between identification and control, and study in a *quantitative* manner their duality through the use of the intermediary concept of an optimal input. Thus, the paper attempts to answer the following question: Given that the optimal input time function is to have a certain prescribed energy, how does it change in character and in its effectiveness as one changes the objective criterion from one that emphasizes control to one that emphasizes identification? While the analytical work presented here has been motivated by our need to control flexible structural systems the methodology developed and the results obtained are applicable to all systems governed by ordinary dif-

Contributed by the Applied Mechanics Division for publication in the JOURNAL OF APPLIED MECHANICS.

Discussion on this paper should be addressed to the Editorial Department, ASME, United Engineering Center, 345 East 47th Street, New York, N.Y. 10017, and will be accepted until two months after final publication of the paper itself in the JOURNAL OF APPLIED MECHANICS. Manuscript received by ASME Applied Mechanics Division, June 8, 1987; final revision, February 29, 1988.

Copyright © 1988 by ASME
Downloaded 03 May 2010 to 171.66.16.21. Redistribution subject to ASME license or copyright; see http://www.asme.org/terms/Terms_Use.cfm

ferential equations; thus it applies to the general multivariable and multiparameter systems commonly encountered in chemical, civil, electrical, and mechanical engineering. Some simple numerical examples are provided to indicate the quantitative nature of the results and provide a feel for them. We believe that these examples capture the important aspects of the problem without unnecessary complication of the concept. The results in these examples show that significant trade-offs exist between identification and control and that for the same amount of energy in the input signal, the emphasis on control could lead to very high covariances of the parameter estimates. Similarly, inputs that are optimal for identification could yield responses whose mean squared values may be several times those obtained for inputs that yield optimal control.

Problem Formulation

Consider a dynamic system modelled by the first order set of differential equations

$$\dot{\mathbf{x}}(t) = \mathbf{F}_1\mathbf{x} + \mathbf{G}_1\mathbf{f} \qquad \mathbf{x}(0) = \mathbf{x}_0 \tag{1}$$

$$\mathbf{z}(t) = H_1\ \mathbf{x}(t) + v(t) \tag{2}$$

where $\mathbf{x}$ is an $x \times 1$ state vector, $\mathbf{f}$ is an $m \times 1$ control vector, $\mathbf{z}$ is an $r \times 1$ measurement vector and the $n \times 1$ initial condition vector, $\mathbf{x}_0$, is given. We shall assume that the measurement noise is representable as a zero mean Gaussian White Noise process so that

$$E[v(t)] = 0, \text{ and,} \tag{3}$$

$$E[v(t)v(\tau)] = R_1\delta(t-\tau). \tag{4}$$

Let the vector of unknown parameters in the system modelled by equations (1) and (2) be given by the $p \times 1$ vector $\boldsymbol{\Theta}$. Let us assume that the identification is carried out with an efficient unbiased estimator so that the covariance of the estimate of $\boldsymbol{\Theta}$ namely $\hat{\boldsymbol{\Theta}}$ is provided by the inverse of the Fisher Information Matrix [13]. Hence,

$$\text{Cov}[\hat{\boldsymbol{\Theta}}] = \mathbf{M}^{-1}. \tag{5}$$

The matrices $\mathbf{F}_1$ and $\mathbf{G}_1$ are taken to be functions of, in general, the parameter vector $\boldsymbol{\Theta}$. The optimal input for identification of the parameter vector $\boldsymbol{\Theta}$ is then sought such that a suitable norm related to the matrix $\mathbf{M}$ is maximized or minimized. Different measures of performance related to $\mathbf{M}$ have been used in the literature Mehra (1974):

(1) *A*-Optimality, where $\text{Tr}(\mathbf{M}^{-1})$ is minimized;
(2) *D*-Optimality, where the determinant of $\mathbf{M}^{-1}$ is minimized; and,
(3) *E*-Optimality, where the maximum eigenvalue of $\mathbf{M}^{-1}$ is minimized.

In this paper, for expository purposes, we shall use the criterion for obtaining the optimal inputs for identification as the maximization of the Trace $\{\mathbf{W}^{1/2}\mathbf{M}\ \mathbf{W}^{1/2}\}$ where $\mathbf{W}$ is a suitable positive definite weighting matrix. Thus, the criterion for obtaining the optimal input for paramter identification is taken to be

$$J_I = \int_0^T \text{Trace}\ \{\Psi_p^T H_1^T R_1^{-1} H_1 \Psi_p\}\ dt \tag{6}$$

where

$$\Psi_p = \mathbf{X}_p\ \mathbf{W}^{1/2}, \tag{7}$$

and the matrix $\mathbf{X}_p$ is given by,

$$[\mathbf{X}_p]_{i,j} = \frac{\partial \mathbf{x}_i}{\partial \boldsymbol{\Theta}_j} \tag{8}$$

In addition to the objective function generated by our need for identification, the objective function required to be maximized for control is,

$$J_C = -\int_0^T \{\mathbf{x}^T\mathbf{Q}_1\mathbf{x}\}\ dt. \tag{9}$$

Here $\mathbf{Q}_1$ is a symmetric positive definite, $n \times n$ weighting matrix. This then yields the composite objective function which is required to be maximized as [13]

$$J = -(\alpha/2)\int_0^T \{\mathbf{x}^T\mathbf{Q}_1\mathbf{x}\}\ dt + (\beta/2)$$

$$\int_0^T \text{Trace}\ \{\Psi_p^T\mathbf{H}_1^T\mathbf{R}_1^{-1}\mathbf{H}_1\Psi_p\}dt \tag{10}$$

where α and β are positive scalars. Clearly, when $\alpha >> \beta$, finding $\mathbf{f}(t)$ to maximize J is tantamount to finding the optimal control for the system (1)–(2), while when $\beta >> \alpha$, the $\mathbf{f}(t)$ that maximizes J is simply the optimal input for identification of the $p \times 1$ parameter vector $\boldsymbol{\Theta}$. In particular, when $\alpha = 0$, and $\beta = 1$, the optimal input for "best" identification is obtained; when $\alpha = 1$, and $\beta = 0$, the optimal input for "best" control is obtained. Denoting the $n \times 1$ vector

$$\mathbf{x}_{\Theta_i} = \frac{\partial \mathbf{x}}{\partial \boldsymbol{\Theta}_i} \tag{11}$$

and assuming that the matrix $\mathbf{W}$ is diagonal, so that,

$$\mathbf{W} = \text{Diag}(w_1, w_2, \ldots, w_p) \tag{12}$$

we can generate an augmented $n(p+1)$ vector,

$$y(t) = \begin{bmatrix} \mathbf{x}(t) \\ w_1^{1/2}\ \partial\mathbf{x}(t)/\partial/\boldsymbol{\Theta}_1 \\ w_2^{1/2}\ \partial\mathbf{x}(t)/\partial\boldsymbol{\Theta}_2 \\ \cdot\ \ \cdot \\ w_p^{1/2}\ \partial\mathbf{x}(t)/\boldsymbol{\Theta}_p \end{bmatrix}, \text{ with, } y(0) = \begin{bmatrix} x_0 \\ 0 \\ 0 \\ \cdot \\ 0 \end{bmatrix} \tag{13}$$

which is then governed by the differential equation

$$\dot{y} = \mathbf{F}y + \mathbf{G}\mathbf{f},\ y^T(0) = \{\mathbf{x}_0^T,\ 0\} \tag{14}$$

where $\mathbf{F}$ is the $n(p+1) \times n(p+1)$ matrix given by

$$\mathbf{F} = \begin{bmatrix} \mathbf{F}_1 & 0 & 0 & 0 & 0 \\ w_1^{1/2}\ \mathbf{F}_{\Theta_1} & \mathbf{F}_1 & 0 & 0 & 0 \\ w_2^{1/2}\ \mathbf{F}_{\Theta_2} & 0 & \mathbf{F}_1 & 0 & 0 \\ \cdot & \cdot & \cdot & \cdot & \cdot \\ w_p^{1/2}\ \mathbf{F}_{\Theta_p} & 0 & 0 & 0 & \mathbf{F}_1 \end{bmatrix}, \tag{15}$$

and,

$$\mathbf{G} = \begin{bmatrix} \mathbf{G}_1 \\ w_1^{1/2}\ \mathbf{G}_{\Theta_1} \\ w_2^{1/2}\ \mathbf{G}_{\Theta_2} \\ \cdot \\ w_p^{1/2}\ \mathbf{G}_{\Theta_p} \end{bmatrix}, \tag{16}$$

with

$$\mathbf{F}_{\Theta_i} = \frac{\partial \mathbf{F}_1}{\partial \boldsymbol{\Theta}_i},\ \mathbf{G}_{\Theta_i} = \frac{\partial \mathbf{G}_1}{\partial \boldsymbol{\Theta}_i},\ i = 1,2, \ldots, p. \tag{17}$$

We note in passing that the stability of the equation set (14) is controlled by the stability of the equation set (1) since the eigenvalues of the matrix $\mathbf{F}$ are identical to those of the matrix $\mathbf{F}_1$, as seen in equation (15), except for the increased multiplicities. The objective function (10) can now be rewritten, after some algebra, as

Downloaded 03 May 2010 to 171.66.16.21. Redistribution subject to ASME license or copyright; see http://www.asme.org/terms/Terms_Use.cfm

$$J = -(\alpha/2)\int_0^T y^T\mathbf{Q}y^T dt + (\beta/2)\int_0^T y^T\mathbf{H}^T\mathbf{R}^{-1}\mathbf{H}y dt \quad (18)$$

where, the matrices $\mathbf{Q}$, $\mathbf{H}$, and $\mathbf{R}^{-1}$ are the block diagonal matrices given by

$$\begin{aligned}\mathbf{Q} &= \text{Diag}\{\mathbf{Q}_1,0,0,\ldots,0,0\},\\ \mathbf{H} &= \text{Diag}\{0,\mathbf{H}_1,\mathbf{H}_1,\mathbf{H}_1,\ldots,\mathbf{H}_1\}, \text{ and,}\\ \mathbf{R}^{-1} &= \text{Diag}\{\mathbf{R}_1^{-1},\mathbf{R}_1^{-1},\mathbf{R}_1^{-1},\ldots,\mathbf{R}_1^{-1}\}\end{aligned} \quad (19)$$

Thus, the objective function needs to be maximized under the constraint equations (14) and the energy constraint

$$\int_0^T \mathbf{f}^T\mathbf{f}\, dt = E, \quad (20)$$

where the parameter E is given *a priori*.

The assumption of finite energy constraint, given in equation (20), for the control signal is a crucial step in the analysis that puts the trade-off study between identification and control in a meaningful context. From an analytical point of view, however, the constraint in equation (20) converts the standard linear two point boundary value problem to a nonlinear two point boundary value problem, thus making the numerical solution of the optimization problem much more involved.

Determination of Optimal Inputs for Simultaneous Control and Identification

Having formulated the problem for constrained maximization, we next use the standard Lagrange multiplier method to obtain the function $\mathbf{f}(t)$ which maximizes the objective (18) subject to (14) and (20). Using the Lagrange multipliers $\lambda(t)$ and $\eta(t)$ we therefore obtain the augmented objective function to be

$$\bar{J} = -\frac{\alpha}{2}\int_0^T \{y^T\mathbf{Q}_y\}\, dt + \frac{\beta}{2}\int_0^T \{y^T\mathbf{H}^T\mathbf{R}^{-1}\mathbf{H}y\}\, dt$$

$$+\int_0^T \lambda^T(t)\,\{\mathbf{F}y + \mathbf{G}\mathbf{f} - \dot{y}\}\, dt + \int_0^T \frac{\eta(t)}{2}(\mathbf{f}^T\mathbf{f} - \dot{y}_{N+1})\, dt \quad (21)$$

Here we augmented the state vector by the variable

$$y_{N+1}(t) = \int_0^t \mathbf{f}^T(\tau)\mathbf{f}(\tau)d\tau$$

where $N = n(p+1)$ and we use the additional Lagrange multiplier $\eta(t)$. By doing this we can satisfy the equality constraint (20) without having to resort to the usual trial and error procedure.

Taking the first variation, we obtain the following set of equations for the variables $y(t)$, $\lambda(t)$ and $\eta(t)$ (see Appendix):

$$\begin{aligned}&\dot{y}(t) - \mathbf{F}y = \frac{1}{\eta}V\lambda(t),\ y(0) = y_0\\ &\dot{\lambda}(t) + \mathbf{F}^T\lambda(t) = -\alpha\{\mathbf{Q}\}y + \beta\{\mathbf{H}^T\mathbf{R}^{-1}\mathbf{H}\}y,\ \lambda(T) = 0, \quad (22a)\\ &\dot{y}_{N+1} = \mathbf{f}^T\mathbf{f} = \frac{1}{\eta^2}\lambda^T(t)V\lambda(t),\ y_{N+1}(0) = 0,\ y_{N+1}(T) = E\\ &\dot{\eta}(t) = 0\end{aligned}$$

where $V = (\mathbf{G}\mathbf{G}^T)$. We note that the equation set (22*a*) constitutes a nonlinear two point boundary value problem containing $2[np+n+1]$ first-order differential equations. The optimal input vector, $\mathbf{f}(t)$, is obtained through the solution of this two point boundary value problem using the relation:

$$\mathbf{f}(t) = -\frac{1}{\eta}\mathbf{G}^T\lambda(t) \quad (23a)$$

It is interesting to note that had we used the objective function

$$J_C' = \left[\int_0^T \mathbf{x}^T\mathbf{Q}_1\mathbf{x}\, dt\right]^{-1} \quad (24)$$

instead of J_C in equation (9) we would obtain,

$$J' = \frac{\alpha}{2}J_C' + \frac{\beta'}{2}J_I \quad (25)$$

where J_I is given in equation (6), and the relative weighting of the contributions of the control and the identification objectives are denoted by α and β'. Following the same procedure as before and using the augmented vector $\mathbf{y}$, maximization of this objective function, J', along with the constraints (14) and (20) would then yield the following set of equations:

$$\begin{aligned}&\dot{\mathbf{y}}(t) - \mathbf{F}\mathbf{y}(t) = \frac{1}{\tilde{\eta}}V\tilde{\lambda}(t),\ \mathbf{y}(0) = \mathbf{y}_0,\\ &\dot{\tilde{\lambda}}(t) + \mathbf{F}^T\tilde{\lambda}(t) = -\alpha\{\mathbf{Q}\}\mathbf{y} + (\beta'\Delta)\{\mathbf{H}^T\mathbf{R}^{-1}\mathbf{H}\}\mathbf{y},\ \tilde{\lambda}(T) = 0, \quad (22b)\\ &\dot{\mathbf{y}}_{N+1} = \frac{1}{\tilde{\eta}^2}\tilde{\lambda}^T(t)V\tilde{\lambda}(t),\ \mathbf{y}_{N+1}(0) = 0,\ \mathbf{y}_{N+1}(T) = E\\ &\dot{\tilde{\eta}}(t) = 0\end{aligned}$$

where, Δ is the positive quantity defined by

$$\Delta = \left[\int_0^T \mathbf{y}^T\mathbf{Q}\mathbf{y}\, dt\right]^2 = \left[\int_0^T \mathbf{x}^T\mathbf{Q}_1\mathbf{x}\, dt\right]^2 \quad (26)$$

The optimal input is obtained from the relation

$$\mathbf{f}(t) = -\frac{1}{\tilde{\eta}}\mathbf{G}^T\tilde{\lambda}(t). \quad (23b)$$

Comparing equations (22*a*) and (22*b*), we observe that the only difference that arises in the use of the objective function (25) instead of (18) is the effective change in weighting parameter β. Setting $\beta'\Delta = \tilde{\beta}$ the equation set (22*b*) becomes identical with the set (22*a*). The Lagrange multipliers $\lambda(t)$ of (22*a*) and λ of (22*b*) are related by $\tilde{\lambda} = \lambda\Delta$; similarly, $\tilde{\eta} = \eta\Delta$. It should be noted that the two equations become identical only when the function $\mathbf{y}(t)$ in (26) corresponds to the response for the optimal input $\mathbf{f}(t)$, i.e., the solution $\mathbf{y}$, of the set (22*a*). With this rescaling of the parameter β', the optimal input $\mathbf{f}(t)$ is identical for the two objective functions J and J' of (10) and (24). Having thus shown the quasi-equivalence of the two objective functions (10) and (25) through this rescaling, in this sequel we shall illustrate our results by using the objective function in the form of equation (10) which leads to the boundary value problem described in equation (22*a*).

This two-point boundary value problem can be numerically solved in various ways. An extensive literature on numerical techniques for solving such problems is available (Roberts and Shipman (1972)). Among the methods most commonly used are multiple shooting techniques [15] with Newton-Raphson iterations, and the Kalaba Method (Kagiwada and Kalaba (1968)) where the two point boundary value problem is converted to an equivalent Cauchy initial value problem. In this sequel, the equation set (22) is solved using the multiple shooting technique with the Newton iteration method.

Illustrative Examples

To exemplify the *concepts* developed, let us consider a system modelled by a single-degree-of-freedom oscillator described by the differential equations

Downloaded 03 May 2010 to 171.66.16.21. Redistribution subject to ASME license or copyright; see http://www.asme.org/terms/Terms_Use.cfm

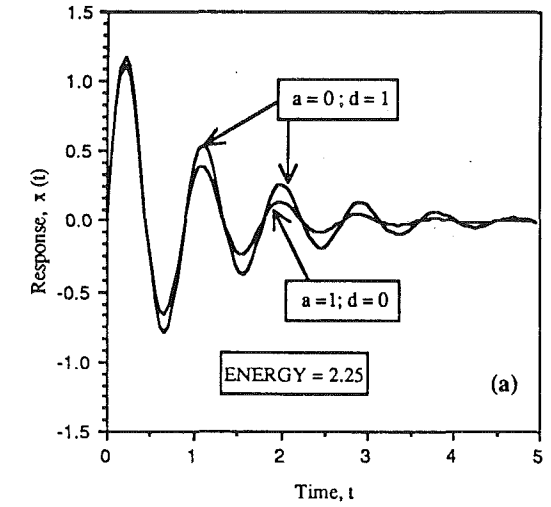

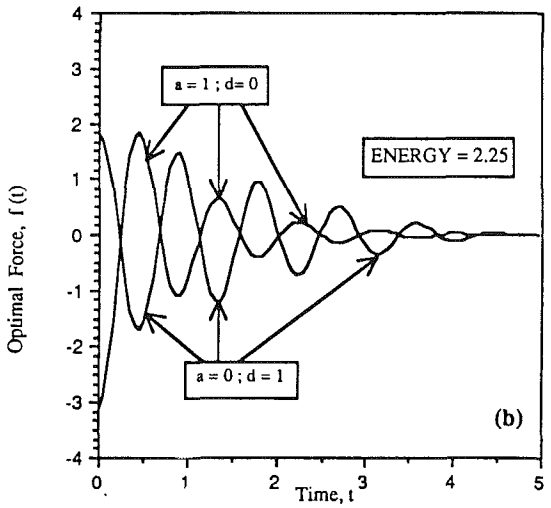

Fig. 1 (*a*) Comparison of responses for optimal identification ($a=0$, $d=1$) and minimum response ($a=1$, $d=0$) for $E=2.25$; (*b*) comparison of optimal forces for optimal identification ($a=0$, $d=1$) and minimum response ($a=1$, $d=0$) for $E=2.25$.

$$\frac{d}{dt}\begin{bmatrix}\mathbf{x}_1\\ \mathbf{x}_2\end{bmatrix}=\begin{bmatrix}0 & 1\\ -k & -c\end{bmatrix}\begin{bmatrix}\mathbf{x}_1\\ \mathbf{x}_2\end{bmatrix}+\begin{bmatrix}0\\ 1\end{bmatrix}$$

$$\mathbf{f}(t);\ \mathbf{x}_1(0)=a_0,\ \mathbf{x}_2(0)=b_0 \tag{27}$$

where $\mathbf{f}(t)$ is the optimal input to be applied. Denoting $\mathbf{x}=[\mathbf{x}_1\ \mathbf{x}_2]^T$, $\mathbf{x}_k=\partial\mathbf{x}/\partial k$, and $\mathbf{x}_c=\partial\mathbf{x}/\partial c$, the objective function is taken to be

$$J(T)=-a\,J_f(T)+b\,J_k(T)+d\,J_c(T) \tag{28}$$

where,

$$J_f(T)=\int_0^T \mathbf{x}_1^2\,dt, \tag{29a}$$

$$J_k(T)=\int_0^T \mathbf{x}_k^2\,dt, \tag{29b}$$

and,

$$J_c(T)=\int_0^T \mathbf{x}_c^2\,dt. \tag{29c}$$

The weighting factors a, b, and d are taken to be non-negative. This may be thought of as being produced by choosing $\alpha=a$, $\beta=1$, $\mathbf{W}=\text{Diag}\,(b, d)$, $\mathbf{Q}_1=\text{Diag}\,(1, 0)$ and $\mathbf{H}_1=[1\ 0]$ and the scalar $\mathbf{R}_1=\sigma^2=1$ in our general formulation of equations (10)–(18). The six component vector $\mathbf{y}$ is then given by

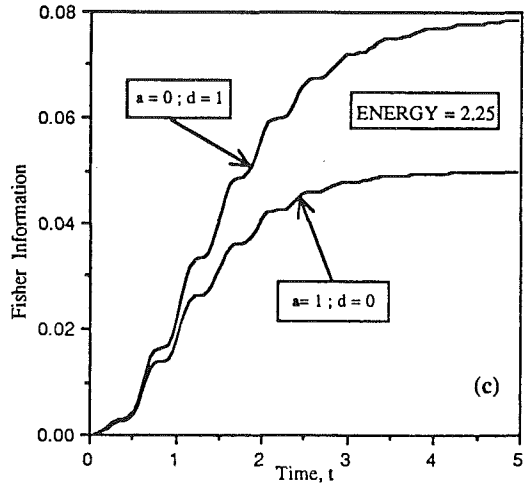

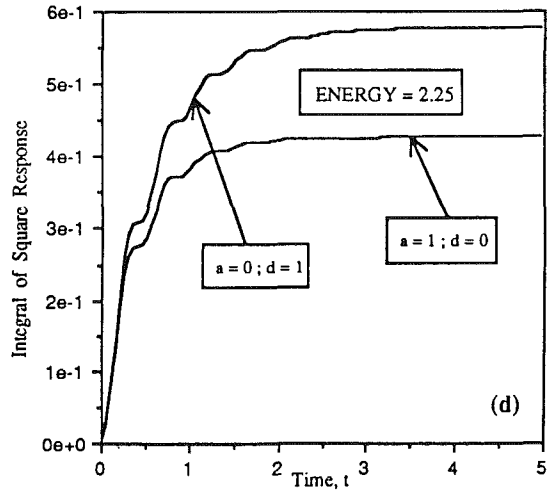

Fig. 1 (*c*) (Comparison of Fisher information matrix $J_c^{(T)}$ for optimal identification ($a=0$, $d=1$) and minimum response ($a=1$, $d=0$) for $E=2.25$; (*d*) Comparison of integral of square response for optimal identification ($a=0$, $d=1$) and minimum response ($a=1$, $d=0$) for $E=2.25$; (*d*) Comparison of integral of square response for optimal identification ($a=0$, $d=1$) and minimum response ($a=1$, $d=0$) for $E=2.25$.

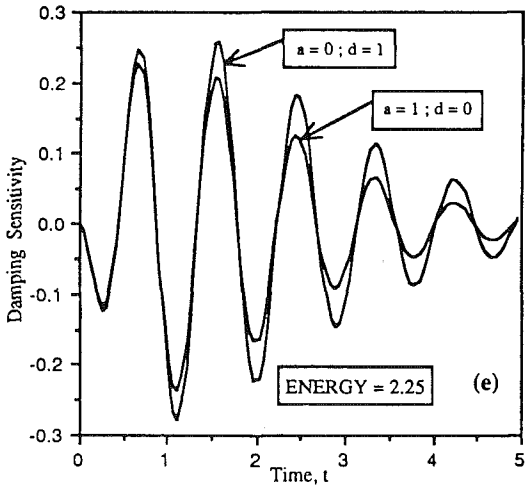

Fig. 1 (*e*) Comparison of damping sensitivity for optimal identification ($a=0$, $d=1$) and minimum response ($a=1$, $d=0$) for $E=2.25$

$$y=\begin{bmatrix}\mathbf{x}\\ b^{1/2}\mathbf{x}_k,\\ d^{1/2}\mathbf{x}_c\end{bmatrix}, \tag{30}$$

and the matrix $\mathbf{F}$ becomes

Downloaded 03 May 2010 to 171.66.16.21. Redistribution subject to ASME license or copyright; see http://www.asme.org/terms/Terms_Use.cfm

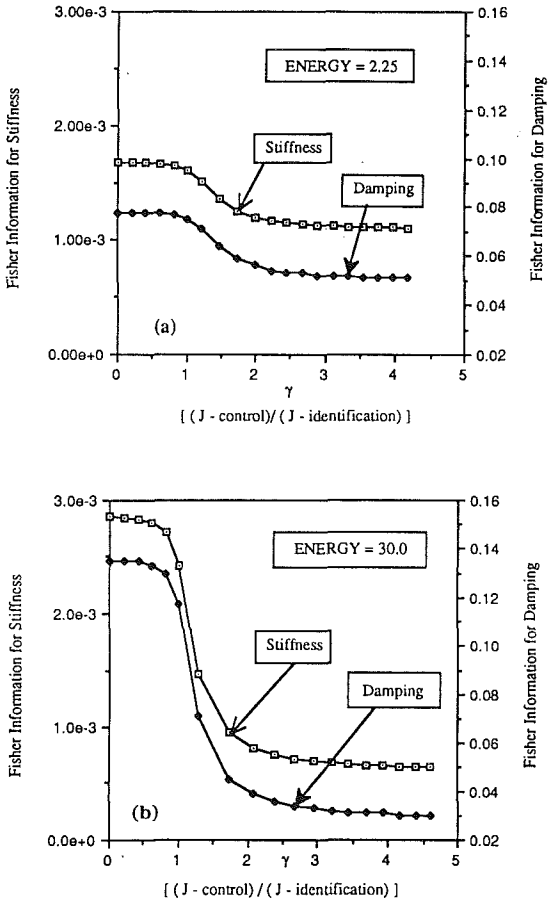

Fig. 2 *(a)* **Fisher information matrices $J_c(T)$ and $J_k(T)$ as function of γ for $E = 2.25$; *(b)* Fisher information matrices $J_c(T)$ and $J_k(T)$ as function of γ for $E = 30.00$.**

$$\mathbf{F} = \begin{bmatrix} 0 & 1 & 0 & 0 & 0 & 0 \\ -k & -c & 0 & 0 & 0 & 0 \\ 0 & 0 & 0 & 1 & 0 & 0 \\ -b^{1/2} & 0 & -k & -c & 0 & 0 \\ 0 & 0 & 0 & 0 & 0 & 1 \\ 0 & -d^{1/2} & 0 & 0 & -k & -c \end{bmatrix}. \tag{31}$$

Since the vector $\mathbf{G} = [0\ 1\ 0\ 0\ 0\ 0]$, the vector $\{\mathbf{V}\lambda/\eta\}$ has only one nonzero component, namely, $\lambda_2(t)/\eta$, where $\lambda_2(t)$ is the second element of the vector $\lambda(t)$. Figure 1 shows some of the numerical results for the following parameters values (which we shall assume are taken in consistent units):

$$b = 0,\ T = 5,\ E = 2.25;\ \text{and,} \tag{32a}$$

$$k = 50,\ c = 2,\ \mathbf{x}_1(0) = 0,\ \mathbf{x}_2(0) = 10. \tag{32b}$$

These parameters thus look at a single-degree-of-freedom oscillator whose spring constant is 50 units, and whose viscous damping is 2 units. This yields a system which has an undamped natural frequency of vibration of about 7 radians/sec and a percentage of critical damping of about 15 percent. It is subjected to an initial velocity of 10 units. The aim is to study the trade-off between (1) identifying (in equation (27)) the damping parameter, c, in the best possible way, and (2) controlling the system so that its mean square response over the time period T is a minimum, given that an input (forcing function) of 5 units duration with an energy of up to 2.25 units is to be used. The two point boundary value problem posed in equation set (22*a*) is numerically solved using the standard multiple shooting technique (Roberts and Shipman (1972)). The local error tolerance during integration of the differential equations and the permitted error in the satisfaction of the boundary conditions are each set to 10^{-4}. The responses of the system together with the optimal inputs as obtained from equation (23*a*) are shown for the two extreme cases: (1) $a = 0$, $d = 1$, corresponding to the optimal input required for identification of the damping parameter c, and (2) $a = 1$, $d = 0$, corresponding to the optimal input required for minimizing the response. As seen from Fig. 1(*b*), the optimal inputs required for "best" identification and for "best" control (the term "best" is used in terms of the cost function (28) utilized) are widely different from each other. In fact they are seen to be, for the entire duration over which they last, almost exactly out of phase. Differences in the response of the system to combined influence of the initial velocity and the forcing functions obtained for the two cases are shown in Fig. 1(*a*). Figure 1(*c*) shows the Fisher Information Matrices for damping, which in this case are scalars, namely $J_c(t)$, for the abovementioned two extreme cases, as a function of time, t. The difference between these at $T = 5$ is about 55 percent. Alternatively put, the input forcing function, which controls the system response maximally, causes a response which is only about 55 percent as informative about the system parameter c as that caused by a forcing function that is designed to maximally provide information about the parameter c. The manner in which the integral of the response quantity squared, $J_f(t)$, changes with time for the two cases mentioned above is shown in Fig. 1(*d*). As seen at $T = 5$, the optimal control input is about 35 percent more effective in reducing the mean square response than the input which optimally determines the parameter c. Figure 1(*e*) provides the sensitivity of the response to the damping parameter (at $c = 2$) as a function of time.

Figure 2(*a*) shows the manner in which the Fisher Information matrices $J_c(T)$ and $J_k(T)$ change for various values of the ratio, $\gamma = [\{a\ J_f(T)\}/\{d\ J_c(T)\}]$ when the Fisher values are normalized to unity. It is to be noted that the optimal input when $a = 0$ corresponds to that required for "best" estimation of the parameter c in equation (27). Figure 2(*b*) shows the effect of changing the available control energy, E, from a value of 2.25 to 30 keeping all other parameters the same. From a loss of information in the parameter c of 55 percent in the case of $E = 2.25$, the loss in information when $E = 30$ jumps to about 450 percent. Similarly, the extent to which the system's performance can be controlled deteriorates by about a factor of 3 if one aims purely at identification instead of control. The parameter η which is calculated for each objective function ratio, γ, is shown in Fig. 3. As mentioned in the formulation, this quantity is simultaneously solved for, in the set (22*a*), thereby eliminating the need to find its value by trial and error. Had this not been done, a very high computational expense would have been incurred to ensure that the energy constraint is satisfied. Noting that the inverse of $J_c(T)$, for an efficient unbiased estimator, is the covariance of the estimate of the parameter c, Figs. 4(*a*) and 4(*b*) provide the trade-off between control and identification. As seen in Fig. 4(*a*), in going from $\gamma = 0$ to $\gamma = 4$, $J_f(T)$, the mean square response, *falls off* by about 35 percent, similarly, the covariance of the estimate of c *increases* by about 55 percent as γ varies over the same interval. For larger values of the input energy, Fig. 4(*b*) shows that significant reductions in J_f and significant increases in the covariance of the parameter estimates can occur.

Conclusions and Discussion

In this paper we have presented an approach to quantifying the trade-off between the tasks of control law development and plant identification. To the best of our knowledge this trade-off has never been analyzed quantiatively before. The problem is formulated in the context of optimal control and optimal identification through the intermediary concept of an optimal input. A suitable objective function is chosen so that

Downloaded 03 May 2010 to 171.66.16.21. Redistribution subject to ASME license or copyright; see http://www.asme.org/terms/Terms_Use.cfm

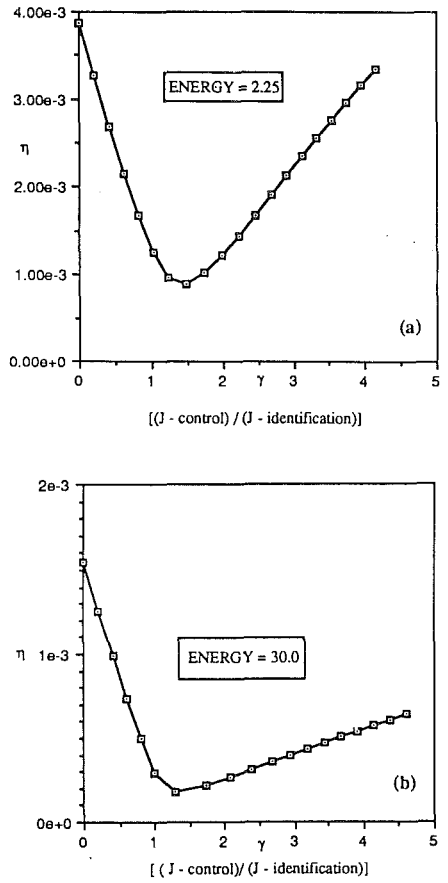

Fig. 3 *(a)* **The parameter η as function of γ for E = 2.25; (*b*) the parameter η as function of γ for E = 30.00.**

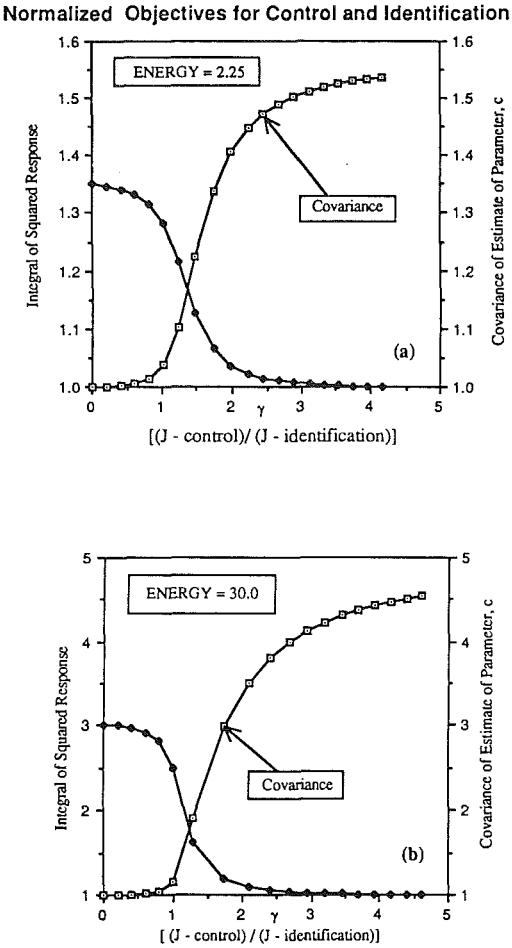

Fig. 4 *(a)* **Integral of squared response as function of γ for E = 2.25; (*b*) Integral of squared response as function of γ for E = 30.00.**

the emphasis from control to identification can be changed in a continuous manner. It is shown that the duality between identification and control can be quantified by determining optimal inputs, which have a specified amount of energy, and which minimize the objective function. Augmenting the state by an additional variable allows simultaneous solution of the optimization problem together with the energy constraint. Using variational calculus this leads to a two point boundary value problem that is nonlinear due to the introduction of the energy constraint. The boundary value problem is solved numerically using the multiple shooting technique and Newton-Raphson iterations.

A numerical example, which deals with control and identification of the parameters of a single-degree-of-freedom oscillator, is used to illustrate the concepts involved. It is shown that improved control leads to serious deterioration in the covariance of the parameter estimation and vice versa. In general, as the energy of the input increases the trade-offs between identification and control are shown to become more and more intense.

The above example shows the potential of the approach introduced in this paper. The numerical computations can be easily generalized to vibratory systems with many degrees-of-freedom, making the method presented here useful in various fields, like control and identification of large flexible structures. A study of the trade-off between identification and control for systems that follow a prescribed input is currently underway.

References

AIAA/AAS, 1978, "Conference on Large Space Platforms; Future Needs and Capabilities," Los Angeles.

Aubrun, J. N., 1980, "Theory of the Control of Structures by Low Authority Controllers," *Journal of Guidance and Control*, Vol. 3, pp. 444–451.

Benhabib, R. J., Iwens, R. P., and Jackson, R. L., 1981, "Stability of Large Space Structure Control Systems Using Positivity Concepts," *Journal of Guidance and Control*, Vol. 4, pp. 487–494.

Benhabib, R. J., and Tung, F. C., 1980, "Large Space Structure Control: System Identification Versus Direct Adaptive Control," *Proceedings of the Joint Automatic Control Conference*, San Francisco, California.

Dale, O. B., and Cohen, R., 1971, "Multiparameter Identification in Linear Continuous Vibratory Systems" ASME *Journal of Dynamic Systems, Measurement and Control*, Vol. 93, pp. 45–52.

Graupe, D., 1972, *Identification of Systems*, Van Nostrand Reinhold, New York.

Kagiwada, H., and Kalaba, R., 1968, "Derivation and Validation of an Initial Valve Method for Certain Nonlinear Two Point Boundary-Value Problems," *Journal of Optimization Theory and Applications*, Vol. 2, pp. 378–385.

Martin, C., and Soong, T. T., 1976, "Modal Control of Multistory Structures," *Journal of Engineering Mechanics Division*, ASCE, Vol. 102, No. EM4, pp. 613–623.

Mehra, R. K., 1974, Optimal Inputs for Linear System Identification, *IEEE Transactions on Automatic Control*, Vol. 19, No. 3, pp. 192–200.

Mehra, R. K., and Lainiotis, D. E., 1976, *System Identification-Advances and Case Studies*, Academic Press.

Meirovitch, L., ed., 1985, *Proceedings of the Fifth VPI/AIAA Symposium on Dynamics and Control of Large Flexible Spacecraft*, VPI&SU, Blacksburg, Virginia.

Meirovitch, L., and Baruh, H., 1982, "Control of Self-Adjoint Distributed Control Systems," *Journal of Guidance and Control*, Vol. 5, pp. 60–66.

Roberts, S. M., and Shipman, J. S., 1972, *Two-Point Boundary Value Problems: Shooting Methods*, Elsevier, New York.

Rodriguez, G., ed., 1985, *Proceedings of the Workshop on Identification and Control of Flexible Space Structures*, Vol. 1 and 2, JPL Publication 85-29.

Tung, F. C., 1981, "Application of System Identification Technique to Modelling of Large Space Structures" *Proceedings of AIAA Guidance and Control Conference*, Albuquerque, NM.

Udwadia, F. E., 1985, "Some Uniqueness Results Related to Soil and Structural Identification," *SIAM Journal of Applied Mathematics*, Vol. 45, No. 4, pp 674–685.

Downloaded 03 May 2010 to 171.66.16.21. Redistribution subject to ASME license or copyright; see http://www.asme.org/terms/Terms_Use.cfm

APPENDIX

Taking the first variation of equation (21) we obtain

$$\delta\bar{J} = -\alpha\int_0^T \{\delta\mathbf{y}^T\mathbf{Q}\mathbf{y}\}\,dt + \beta\int_0^T \{\delta\mathbf{y}^T\mathbf{H}^T\mathbf{R}^{-1}\mathbf{H}\mathbf{y}\}\,dt$$

$$-\lambda^T(t)\delta\mathbf{y}\,\Big|_0^T + \int_0^T \{\dot{\lambda}^T + \lambda^T\mathbf{F}\}\delta\mathbf{y}\,dt + \int_0^T \lambda^T\mathbf{G}\delta\mathbf{f}\,dt$$

$$+\int_0^T \eta(t)\delta\mathbf{f}^T\mathbf{f}\,dt - \frac{\eta(t)}{2}\,\delta\mathbf{y}_{N+1}\,\Big|_0^T + \int_0^T \frac{\eta}{2}\,\delta\mathbf{y}_{N+1}\,dt. \qquad (A.1)$$

Collecting terms in $\delta\mathbf{y}$, $\delta\mathbf{f}$, and $\delta\mathbf{y}_{N+1}$, we get the relations:

$$\dot{\lambda}(t) + \mathbf{F}^T\lambda(t) = -\alpha\{\mathbf{Q}\}\mathbf{y} + \beta\{\mathbf{H}^T\mathbf{R}^{-1}\mathbf{H}\}\mathbf{y}, \qquad (A.2)$$

$$\mathbf{f}(t) = -\frac{\mathbf{G}^T\lambda(t)}{\eta(t)} \qquad (A.3)$$

$$\dot{\mathbf{y}}_{N+1}(t) = \mathbf{f}^T\mathbf{f} = \frac{\lambda^T(t)\mathbf{G}\mathbf{G}^T\lambda(t)}{\eta(t)^2} \qquad (A.4)$$

$$\dot{\eta} = 0 \qquad (A.5)$$

along with the boundary conditions

$$\mathbf{y}_{N+1}(0) = 0;\ \mathbf{y}_{N+1}(T) = E;\ \lambda(T) = 0 \qquad (A.6)$$

hence, the result given by equation (22*a*).

Downloaded 03 May 2010 to 171.66.16.21. Redistribution subject to ASME license or copyright; see http://www.asme.org/terms/Terms_Use.cfm

On the Dynamics of Large Systems With Localized Nonlinearities

P. Hagedorn
Institut für Mechanik, TH Darmstadt,
6100 Darmstadt,
Federal Republic of Germany

W. Schramm
Robert Bosch GmbH,
7000 Stuttgart 30,
Federal Republic of Germany

In this paper, a certain class of dynamical systems is discussed, which can be decomposed into a large linear subsystem and one or more nonlinear subsystems. For this class of nonlinear systems the dynamic behavior is represented in the time domain by means of an integral equation. A simple numerical procedure for the solution of this integral equation is given. It is also shown how the decomposition of the system can be used in measuring the frequency response of the large linear subsystem, without actually separating it from the nonlinear subsystems. An elastostatic analogy is used to illustrate the ideas and a numerical example is given for a dynamic system.

1 Introduction

Numerical simulations of the dynamics of large mechanical and electromechanical systems are becoming more and more common in the area of aerospace structures and in other fields. In many of these systems the nonlinearities are concentrated in a few elements only, the larger part of the system being linear. This class of systems forms the subject of the present paper.

While powerful tools such as Fourier and Laplace transforms and the representation in the frequency domain are available for the analysis and simulation of the dynamics of *linear* systems, this is not the case for *nonlinear* systems. The transfer properties of *nonlinear* systems are normally described in the time domain through nonlinear differential equations, Volterra series, or other means.

In the simulation of the systems composed of a large linear subsystem and several small nonlinear elements, the linear subsystem is represented by its impulse response matrix, while the nonlinear subsystems are described by nonlinear functional relations. An *exact* description of the dynamics of the composed system is then given by a *nonlinear integral equation*. This representation does not involve the approximations made e.g., in the use of "nonlinear transfer functions," but takes into account fully all the system's nonlinearities. For a number of important technical applications the nonlinear integral equation can be numerically solved in a simple manner, and this approach is, for example, being used successfully in vehicle dynamics.

In certain problems the large linear subsystem is not known in detail, but its impulse response matrix can be measured. It is particularly in these cases, where the system of differential equations representing the large linear subsystem is not known, that the description by means of the nonlinear integral equation can be useful. In what follows, it is also shown how the decomposition into linear and nonlinear subsystems can be used in the identification and in the experimental determination of the transfer properties.

2 Simulation of Large Systems With Localized Nonlinearities

We consider a system according to Fig. 1 composed of a large linear subsystem with input

$$\mathbf{x}(t) = (x_1(t), x_2(t), \ldots, x_n(t))^T \tag{1}$$

and output

$$\mathbf{y}(t) = (y_1(t), y_2(t), \ldots, y_m(t))^T \tag{2}$$

containing also several nonlinear elements. The dynamic behavior of the linear part can be described by its $m \times n$ transfer matrix $\mathbf{G}(\omega)$, for which the relation

$$\mathbf{Y}(\omega) = \mathbf{G}(\omega)\mathbf{X}(\omega) \tag{3}$$

holds between the Fourier transforms $\mathbf{X}(\omega)$ and $\mathbf{Y}(\omega)$ of the input vector $\mathbf{x}(t)$ and the output vector $\mathbf{y}(t)$, ω being the frequency parameter.

The relation (3) can also be written in the time domain as

$$\mathbf{y}(t) = \int_0^t \mathbf{H}(\tau)\mathbf{x}(t-\tau)d\tau, \tag{4}$$

the $m \times n$ matrix $\mathbf{H}(t)$ being the inverse Fourier transform of $\mathbf{G}(\omega)$. The physical significance of $\mathbf{H}(t)$ is that of an impulse response matrix, i.e., the element $h_{ij}(t)$ is the response of the output $y_i(t)$ to an input of the type $x_j(t) = \delta(t)$. The lower boundary of the interval of integration in (4) is zero and the upper is t, since we are only concerned with *causal* systems (see Papoulis, 1985). For these systems we suppose $\mathbf{H}(t) = 0$, $\mathbf{x}(t) = 0$ for $t \leq 0$. For practical purposes the upper boundary in this integral can be substituted by a finite "decay time," depending on the damping in the system.

Contributed by the Applied Mechanics Division for publication in the JOURNAL OF APPLIED MECHANICS.
Discussion on this paper should be addressed to the Editorial Department, ASME, United Engineering Center, 345 East 47th Street, New York, N.Y. 10017, and will be accepted until two months after final publication of the paper itself in the JOURNAL OF APPLIED MECHANICS. Manuscript received by ASME Applied Mechanics Division, August 31, 1987; final revision, February 25, 1988.

Copyright © 1988 by ASME
Downloaded 03 May 2010 to 171.66.16.21. Redistribution subject to ASME license or copyright; see http://www.asme.org/terms/Terms_Use.cfm

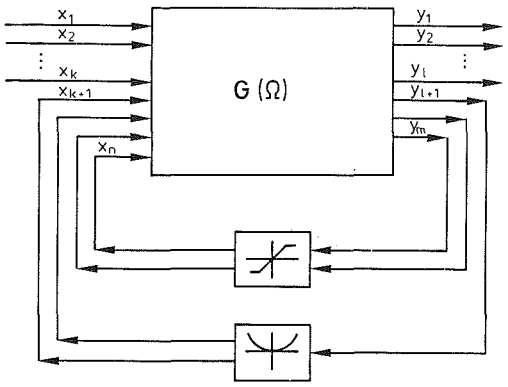

Fig. 1 Complex system with linear and nonlinear subsystems

In addition to the large linear subsystem, the system of Fig. 1 contains also nonlinear elements or subsystems, through which some of the outputs, say, $y_{l+1}, y_{l+2}, \ldots, y_m$ are fed back to some of the inputs, for example, $x_{k+1}, x_{k+2}, \ldots, x_n$. Only the inputs $x_1, x_2, \ldots, x_k$ are then accessible and only these variables are inputs for the *complex system* (i.e., the composed system). They may, for example, be control variables accessible to a human operator. The input-output relations between the $x_1, x_2, \ldots, x_k$ and the $y_1, y_2, \ldots, y_l$ in the complex system of Fig. 1 are sought, that is, the outputs $y_1(t), y_2(t), \ldots, y_l(t)$ are to be obtained via numerical simulations from given inputs $x_1(t), x_2(t), \ldots, x_k(t)$. This can, of course, be done in the time domain by solving numerically the system of nonlinear differential equations describing the dynamics of the complex system. In what follows we wish to solve this problem using directly the transfer properties of the linear subsystem.

Suppose for a moment that the nonlinearities are such that the $y_{l+1}, y_{l+2}, \ldots, y_m$ are simply functions of the values of the input variables $x_{k+1}, x_{k+2}, \ldots, x_n$ taken at the same time, as would be the case for example for nonlinear springs with displacements and forces as inputs and outputs. Since the $x_1, x_2, \ldots, x_k$ are given as time functions and the $x_{k+1}, x_{k+2}, \ldots, x_n$ as functions of some of the $y_1, y_2, \ldots, y_m$, we can write

$$\mathbf{x}(t) = \mathbf{x}[\mathbf{y}(t), t]. \tag{5}$$

This notation does not reflect the fact that $\mathbf{x}$ does not depend on $y_1, y_2, \ldots, y_l$ but has the advantage of being very simple. With (5) in (4) we now obtain the vector integral equation

$$\mathbf{y}(t) = \int_0^t \mathbf{H}(\tau)\mathbf{x}[\mathbf{y}(t-\tau),\ t-\tau]d\tau, \tag{6}$$

in which the time function $\mathbf{y}(t)$ is the unknown, while $\mathbf{x}(\mathbf{y}, t)$ is given. This integral equation has to be solved numerically for $\mathbf{y}(t)$ in order to obtain the system response.

Equation (6) can be solved numerically for $\mathbf{y}(t)$ using any integration scheme. Since we assume the right-hand side to be a Riemann integral, its value does not depend on the value of the integrand at a single point of the integration interval. This means that, in particular, the value of the integral does not depend on the value of $\mathbf{y}(\bullet)$ at time t and (6) can be evaluated if $\mathbf{y}(\bullet)$ is known for times smaller than t.

The simplest approximation for the integral (6) is obtained using

$$\mathbf{y}(t) = \int_0^t \mathbf{H}(\tau)\mathbf{x}[\mathbf{y}(t-\tau),\ t-\tau]d\tau =$$

$$= \lim_{m\to\infty}\left\{\frac{t}{m}\sum_{k=0}^{m}\mathbf{H}\left(k\frac{t}{m}\right)\mathbf{x}\left[\mathbf{y}\left(t-k\frac{t}{m}\right),\ t-k\frac{t}{m}\right]\right\}. \tag{7}$$

The sum on the right-hand side of (7) only contains the values of $\mathbf{y}(\bullet)$ at times up to $t-t/m$. In carrying out the calculations on a computer the functions are defined at discrete times Δt, $2\Delta t$, $3\Delta t$, . . . , only and this holds, in particular, for the function $\mathbf{H}(\bullet)$, obtained from measurements. The passage to the limit $m\to\infty$ is not performed and instead of t/m a small but finite step size Δt is used.

This gives

$$y(n\Delta t) = \Delta t \sum_{k=1}^{n}\mathbf{H}(k\Delta t)\mathbf{x}[\mathbf{y}(n\Delta t - k\Delta t),\ n\Delta t - k\Delta t] + 0(\Delta t). \tag{8a}$$

The right-hand side of (8*a*) only involves the values of the function $\mathbf{y}(\bullet)$ at times $t=0$, Δt, $2\Delta t$, . . . , $(n-1)\Delta t$, i.e., at times smaller than $n\Delta t$. This formula can therefore be used to compute the function $\mathbf{y}(t)$ from $\mathbf{H}(\bullet)$ and $\mathbf{x}[\mathbf{y}(\bullet), \bullet]$.

Formula (8*a*) can be simplified in still another way. Mechanical systems are often damped so that the impulse response matrix $\mathbf{H}(t)$ vanishes numerically for $t \geq \bar{n}\Delta t$, with some $\bar{n} \in \mathbf{N}$ sufficiently large. In this case, (8*a*) can be substituted by

$$y(n\Delta t) = \Delta t \sum_{k=1}^{\min(n,\bar{n})}\mathbf{H}(k\Delta t)\mathbf{x}[\mathbf{y}(n\Delta t - k\Delta t),\ n\Delta t - k\Delta t]. \tag{8b}$$

Of course, any of the known integration schemes can, in principle, be used to compute the integral (6). There is a vast literature on the numerical stability, convergence, and consistence of these algorithms, which will not be discussed here (see, for example, Törnig, (1979)). It should, however, be noted that the nonlinearities may contain backlash, piecewise constant springs and even more severe discontinuities. The function $\mathbf{x}[\mathbf{y}, t]$ may therefore be discontinuous in $\mathbf{y}$ and therefore $\mathbf{x}[\mathbf{y}(t), t]$ will then also be discontinuous in t. In this case, the integrand in (6) will, in general, be a piecewise continuous function of t, with the location of the discontinuities on the t-axis unknown beforehand. The integral of a piecewise continuous function is, of course, better approximated by the sum (8*a*) than by a higher order integration formula. While the discontinuities can be accurately modelled by (8*a*), they are smoothened by higher order integration formulas. Of course one could use the higher order integration schemes for the time intervals in which the integrand is continuous. The discontinuities would then have to be detected by additional computations, and additional efforts must be undertaken in order to reproduce them correctly. Due to this fact the integration via the simple formula (8*a*) will probably be the simplest solution for many practical problems.

If the nonlinear elements are such that the $x_{k+1}, x_{k+2}, \ldots, x_n$ are functions not only of the values of $y_{l+1}, y_{l+2}, \ldots, y_m$, but, for example, also of their derivatives, then (5) has to be substituted by

$$\mathbf{x}(t) = \mathbf{x}[\mathbf{y}(t), \dot{\mathbf{y}}(t), t]. \tag{9}$$

Similarly, higher order derivatives could also be included in (9). The problem can, however, always be recast into the form (6), by introducing additional variables.

The integral equation (6) is a simple representation of the dynamics of the complex system of Fig. 1 in terms of the matrix $\mathbf{H}(t)$ of the linear subsystem and of the behavior of the nonlinear elements given by functional relations of type (5). It has been used successfully for numerical simulations in several cases by the authors. Examples will be given in Section 4.

3 Measurement of the Transfer Function of the Linear Subsystem

The simulation of the dynamical behavior of the complex system shown in Fig. 1 requires the knowledge of the matrix

Downloaded 03 May 2010 to 171.66.16.21. Redistribution subject to ASME license or copyright; see http://www.asme.org/terms/Terms_Use.cfm

$\mathbf{H}(t)$ (or $\mathbf{G}(\omega)$) and of the relations (5). The transfer matrix $\mathbf{G}(\omega)$ can e.g., be calculated from a mathematical model of the system. In large technical systems these calculations often have to be complemented by identification of some of the parameters from measurements carried out in the physical system. In these cases one may as well measure the transfer matrix $\mathbf{G}(\omega)$ directly, using this measured matrix function (or its inverse transform $\mathbf{H}(t)$) for the simulation of the complex systems.

Powerful system analyzers are available for measuring the input-output relations of linear systems, and often the experiments are done by exciting the system with broad-band signals (e.g., band limited white noise) and measuring the response. The matrix $\mathbf{G}(\omega)$ is then obtained from

$$\mathbf{G}(\omega) = \mathbf{S}_{xy}(\omega)\mathbf{S}_{xx}^{-1}(\omega) \tag{10}$$

where $\mathbf{S}_{xy}(\omega)$ is the cross-power spectrum matrix of $\mathbf{x}(t)$ and $\mathbf{y}(t)$ and $\mathbf{S}_{xx}(\omega)$ the auto-power spectrum matrix; the necessary computations are automatically carried out in the signal analyzer. Of course it has to be assured that the matrix $\mathbf{S}_{xx}(\omega)$ be nonsingular in the frequency range under consideration.

In the complex system under consideration (Fig. 1) not all the input variables $x_1, x_2, \ldots, x_n$ are externally accessible, but only the first k ones $k<n$). Nevertheless the complete matrix $\mathbf{G}(\omega)$ or $\mathbf{H}(t)$, describing the input-output relations between $x_1, x_2, \ldots, x_n$ and $y_1, y_2, \ldots, y_m$, is needed for a description of the complex system in the form (6). It can be obtained by choosing appropriate time signals for the accessible inputs $x_1, x_2, \ldots, x_k$ and forming the matrix $\mathbf{S}_{xx}(\omega)$ using the complete input process $x_1(t), x_2(t), \ldots, x_k(t)$, $x_{k+1}(t), \ldots, x_n(t)$, with the last $n-k$ input components obtained from measurements. The matrix $\mathbf{S}_{xx}(\omega)$ will be nonsingular if only the nonlinear elements are *completely nonlinear*. To show this, let

$$\bar{\mathbf{x}} := (x_1, x_2, \ldots, x_k)^T, \tag{11}$$

$$\tilde{\mathbf{x}} := (x_{k+1}, x_{k+2}, \ldots, x_n)^T, \tag{12}$$

$$\bar{\mathbf{y}} := (y_1, y_2, \ldots, y_l)^T, \tag{13}$$

$$\tilde{\mathbf{y}} := (y_{l+1}, y_{l+2}, \ldots, y_m)^T, \tag{14}$$

then, by partitioning the matrix $\mathbf{G}(\omega)$ in (3) one has

$$\tilde{\mathbf{Y}}(\omega) = \mathbf{G}_{11}(\omega)\ \bar{\mathbf{X}}(\omega) + \mathbf{G}_{12}(\omega)\ \tilde{\mathbf{X}}(\omega), \tag{15}$$

$$\tilde{\mathbf{Y}}(\omega) = \mathbf{G}_{21}(\omega)\ \bar{\mathbf{X}}(\omega) + \mathbf{G}_{22}(\omega)\ \tilde{\mathbf{X}}(\omega). \tag{16}$$

If the "nonlinear elements" in Fig. 1 were, in fact, linear, a relation of the type

$$\tilde{\mathbf{X}}(\omega) = \mathbf{K}(\omega)\tilde{\mathbf{Y}}(\omega) \tag{17}$$

would hold, with $\mathbf{K}(\omega)$ as the transfer matrix of the corresponding linear subsystem. In this case, substituting (16) in (17) gives

$$(\mathbf{I} - \mathbf{K}\ \mathbf{G}_{22})\tilde{X} = \mathbf{K}\ \mathbf{G}_{21}\bar{X} \tag{18}$$

and

$$\tilde{X}(\omega) = Q(\omega)\bar{X}(\omega) \tag{19}$$

with

$$\mathbf{Q} := (\mathbf{I} - \mathbf{K}\ \mathbf{G}_{22})^{-1}\mathbf{K}\ \mathbf{G}_{21}, \tag{20}$$

$\mathbf{I}$ being the identity matrix. Equation (19) implies

$$\mathbf{S}_{\tilde{x}\tilde{x}} = \mathbf{Q}\ \mathbf{S}_{\bar{x}\bar{x}}, \tag{21}$$

$$\mathbf{S}_{\tilde{x}\bar{x}} = \mathbf{Q}^*\ \mathbf{S}_{\bar{x}\bar{x}} \tag{22}$$

and

$$\mathbf{S}_{\tilde{x}\tilde{x}} = \mathbf{Q}\ \mathbf{Q}^*\ \mathbf{S}_{\bar{x}\bar{x}}, \tag{23}$$

so that $\mathbf{S}_{xx}$ is given by

$$\mathbf{S}_{xx} = \begin{bmatrix} \mathbf{I} & \mathbf{Q} \\ \mathbf{Q}^*\ \mathbf{Q}\ \mathbf{Q}^* & \end{bmatrix} \mathbf{S}_{\bar{x}\bar{x}} \tag{24}$$

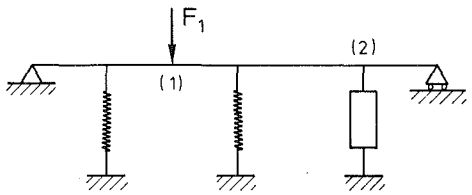

Fig. 2 An elastostatic analogy

and clearly the determinant of $\mathbf{S}_{xx}$ vanishes whatever power spectrum $\mathbf{S}_{\bar{x}\bar{x}}$ is chosen for the accessible input variables.

In the above considerations the nonlinear subsystems were substituted by a completely linear system, represented by the transfer matrix $\mathbf{K}(\omega)$ in (17). In the case of nonlinear system, if the complete system contains at least one "linear channel," i.e., if a relation of the type

$$\mathbf{a}^T(\omega)\bar{\mathbf{X}}(\omega) = \mathbf{b}^T(\omega)\tilde{\mathbf{X}}(\omega) \tag{25}$$

holds for some vector-valued functions $\mathbf{a}(\omega)$, $\mathbf{b}(\omega)$ then again $\mathbf{S}_{xx}$ is always singular (see Papoulis, (1985)). The relation (25) implies that the nonlinear subsystem contains a linear channel, i.e., that an equation such as

$$\mathbf{c}^T(\omega)\tilde{\mathbf{Y}}(\omega) = \mathbf{d}^T(\omega)\tilde{\mathbf{X}}(\omega) \tag{26}$$

holds between the imputs $\tilde{\mathbf{y}}(t)$ and the outputs $\tilde{\mathbf{x}}(t)$ of the nonlinear subsystem.

On the other hand, if the nonlinear subsystems are *completely nonlinear*, in the sense that no relation of the type (26) holds, then $\mathbf{S}_{xx}$ will, in general, be nonsingular, as long as the matrix $\mathbf{S}_{\tilde{x}\tilde{x}}$ formed with the accessible inputs $\tilde{\mathbf{x}}(t)$ is nonsingular.

Therefore, the complete matrix $\mathbf{G}(\omega)$ can be obtained for a complex system of the type of Fig. 1, where only part of the input variables, namely $x_1, x_2, \ldots, x_k$ can be changed at will, but still all the input variables can be *measured*. For example, in the case of a complex machine containing as only nonlinear elements several nonlinear dampers, one has to measure the damper inputs and outputs $(\tilde{\mathbf{y}}(t), \tilde{\mathbf{x}}(t))$ as well as all the other outputs and excite the accessible inputs $(\bar{\mathbf{x}}(t))$. From these measurements all the information necessary to simulate the dynamic behavior of the complex machine is obtained, and the simulation can then also be done for the machine with nonlinear dampers *different* from the ones with which the tests were carried out. The only additional information needed is the functional representation of the nonlinear dynamics of the different dampers.

4 Examples

4.1 An Elastostatic Analogy for the Measurement Problem. The measurement procedure can be illustrated by means of a simple elastostatic analogy. Consider the lineary elastic beam of Fig. 2, supported at its ends by means of two linear springs and at a third intermediate point L_2 by a *nonlinear* spring. The nonlinear elastostatic behavior of the complete system subjected to a force F_1 at the location L_1 is to be described for different nonlinear supports in L_2. This clearly is a system of the type shown in Fig. 1, where, of course, static variables now replace the time functions. The linear subsystem is shown in Fig. 3(*a*) and only the force F_1 can be changed at will during the measurements of the linear subsystem; the nonlinear characteristics of the spring is not given in these experiments (Fig. 3(*b*)), but y_1, y_2, F_1, F_2 can be measured. Using the influence coefficients α_{ij} $(i, j = 1, 2)$ one has

$$y_1 = \alpha_{11}F_1 + \alpha_{12}F_2, \tag{27}$$

$$y_2 = \alpha_{21}F_1 + \alpha_{22}F_2. \tag{28}$$

Downloaded 03 May 2010 to 171.66.16.21. Redistribution subject to ASME license or copyright; see http://www.asme.org/terms/Terms_Use.cfm

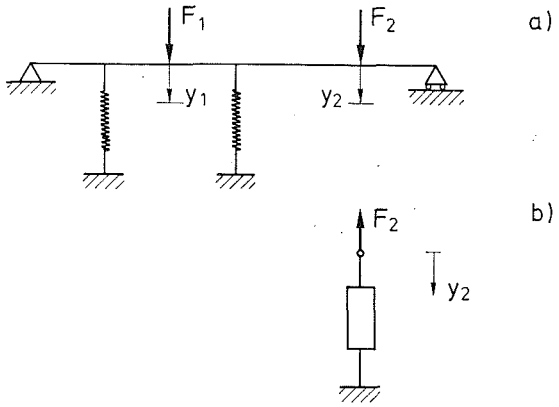

Fig. 3 Determination of the influence coefficients: (a) linear subsystem; (b) nonlinear subsystem

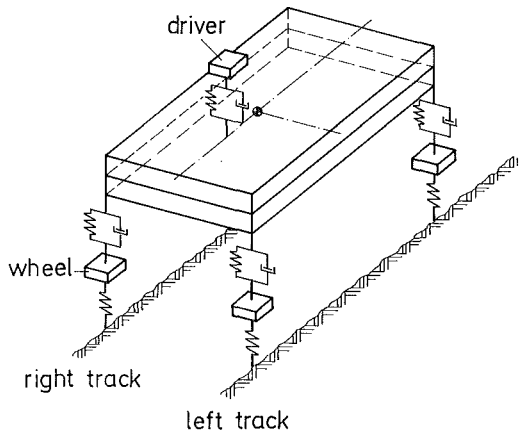

Fig. 4 Simple model for the dynamics of a car

We restrict our attention to the measurement of α_{11}, α_{12}, which appear in (27) only.

If tests are carried out with one value of F_1 only, the unknowns α_{11}, α_{12} obviously cannot be determined from the single equation (27). If, however, the experiment is repeated k times with different values F_{1s}, $s=1, 2, \ldots, k$ of the force F_1, one obtains the k equations

$$y_{1s}=\alpha_{11}F_{1s}+\alpha_{12}F_{2s},\ s=1, 2, \ldots, k, \tag{29}$$

provided there are no measurement errors. Multiplying (29) by F_{1s} and F_{2s} respectively, and adding the equations, results in

$$(\Sigma F_{1s}^2)\alpha_{11}+(\Sigma F_{1s}F_{2s})\alpha_{12}=\Sigma F_{1s}y_{1s}, \tag{30}$$

$$(\Sigma F_{1s}F_{2s})\alpha_{11}+(\Sigma F_{2s}^2)\alpha_{12}=\Sigma F_{2s}y_{2s}, \tag{31}$$

and this system of two equations in the two variables α_{11}, α_{12} has a unique solution provided the determinant

$$\Delta(k):=(\Sigma F_{1s}^2)(\Sigma F_{2s}^2)-(\Sigma F_{1s}F_{2s})^2 \tag{32}$$

does not vanish. Obviously, one has $\Delta(1)=0$. For $k>1$ we define the vectors

$$\mathbf{F}_1:=(F_{11}, F_{12}, \ldots, F_{1k})^T,\ \mathbf{F}_2:=(F_{21}, F_{22}, \ldots, F_{2k})^T \tag{32}$$

and write (32) as

$$\Delta(k)=\mathbf{F}_1^T\mathbf{F}_1\ \mathbf{F}_2^T\mathbf{F}_2-(\mathbf{F}_1^T\mathbf{F}_2)^2. \tag{33}$$

It is easy to check that $\Delta(k)$ vanishes if and only if there are numbers $a_1\neq 0$ and $a_2\neq 0$ such that

$$a_1\mathbf{F}_1+a_2\mathbf{F}_2=0 \tag{34}$$

holds, i.e., if and only if $\mathbf{F}_1$ and $\mathbf{F}_2$ are linearly dependent. In this case however, not only y_1 but also y_2 is proportional to F_1 (in the complex system), as follows from (28) and, therefore, the overall behavior of the complete system is linear, including the "nonlinear" element of Fig. 3(*b*).

The coefficients α_{11} and α_{12} can therefore be uniquely determined from (30), (31) if and only if the element of Fig. 3(*b*) is truly nonlinear. In the presence of measurement errors, (29) is not exactly fulfilled for all s and the system (29) would be overdetermined. The determination of α_{11}, α_{12} from (30), (31) in this case corresponds to a linear regression, i.e., a determination of α_{11}, α_{12} using a least square approximation. The experiments can, of course, also be carried out by changing F_1 continuously (slowly, i.e., quasi-statically) and, in this case, all the finite sums would be substituted by integrals. The coefficients α_{21}, α_{22} can be determined in a similar manner.

With known α_{ij} $(i, j=1, 2)$ the nonlinear elastic behavior of the complete system can easily be computed for any nonlinear spring. If, for example, the nonlinear element is of the type

$$F_2(y_2)=-\alpha y_2^3, \tag{35}$$

equations (27), (28) give

$$y_1=\alpha_{11}F_1-\alpha_{12}a\,y_2^3, \tag{36}$$

$$y_2=\alpha_{21}F_1-\alpha_{22}a\,y_2^3, \tag{37}$$

and y_1, y_2 can easily be determined in terms of F_1.

If the support in L_2 is linear, the experiment cannot be carried out as described, but would have to be modified. A first measurement could, for example, be done with the system of Fig. 2, while in a second test the linear spring in L_2 could be substituted by a rigid support. The first test would then result in the equations

$$y_{11}=\alpha_{11}F_1+\alpha_{12}F_{21}, \tag{38}$$

$$y_{21}=\alpha_{21}F_1+\alpha_{22}F_{21}, \tag{39}$$

and the second one in

$$y_{12}=\alpha_{11}F_1+\alpha_{12}F_{22}, \tag{40}$$

$$0=\alpha_{21}F_1+\alpha_{22}F_{22}. \tag{41}$$

The coefficients α_{11}, α_{12} can then be obtained from the equations (38), (40), which are certainly linearly independent. A different solution would be to initially substitute the linear element in L_2 by a nonlinear one, and to proceed as previously described.

4.2 Simulation of a Nonlinear Dynamical System. The approach described in this paper is being used in the simulation of passenger cars, mainly in studies of riding comfort. In this aspect of vehicle dynamics usually almost the whole system is to a large extent linear, the only essential nonlinearities being the dampers and the pneumatic tires. The corresponding mechanical model of Fig. 4 is obviously a dynamic system of the type depicted in Fig. 1. Such a model is being used for measuring the dynamic characteristics of the linear subsystem, without separating physically the nonlinear dampers and tires from the rest of the system. In this case, four shakers act on the four wheels, the accelerations, velocities, and displacements at several points are measured, together with the forces transmitted by the nonlinear elements. The dynamic behavior of the car with different dampers and/or tires can then easily be simulated, as previously described, provided a mathematical model for the nonlinearities is available. The structure of the linear subsystem does not have to be known.

Since the mechanical system of Fig. 4 is relatively complicated, we discuss instead the simpler system of Fig. 5, which contains most of the essential features of the original system. It is formed by two masses and three linear springs and dampers, all of which are supposed to be identical for greater simplicity. In addition, there is a nonlinear element connecting

Downloaded 03 May 2010 to 171.66.16.21. Redistribution subject to ASME license or copyright; see http://www.asme.org/terms/Terms_Use.cfm

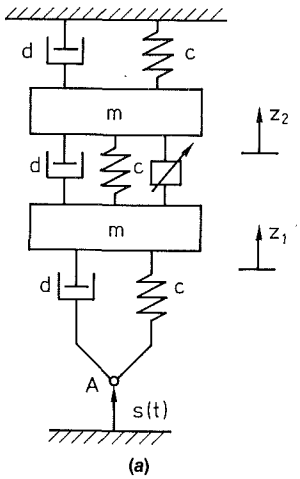

(a)

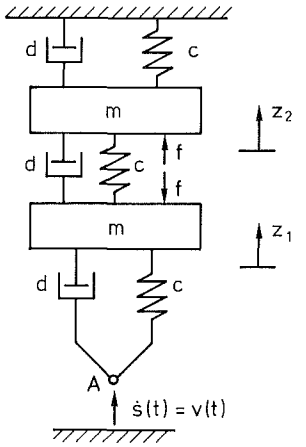

(b)

Fig. 5 Nonlinear system with two-degrees-of-freedom: (a) two-degrees-of-freedom system with nonlinear damper; (b) the linear subsystem

the two point masses which, for simplicity, we assume to be a nonlinear spring with a piecewise constant stiffness, as shown in Fig. 6. The external input into the system is by means of the displacement $s(t)$ of the point A, connected to the lower mass by means of a damper and a spring.

The linear subsystem is shown in Fig. 5(*b*), where the nonlinear spring was substituted by the force f, acting between the two masses. If Fig. 5(*b*) the velocity $v(t)$ of the point A is introduced instead of $s(t)$ as an input variable. The linear subsystem has, therefore, two input variables, namely $v(t)$ and $f(t)$ and two output variables $z_1(t), z_2(t)$, i.e.,

$$\mathbf{x} = (f,\ v)^T, \tag{42}$$

$$\mathbf{y} = (z_1,\ z_2)^T. \tag{43}$$

The dynamics of the linear subsystem is obviously described by the equations of motion

$$m\ddot{z}_1 + c(2z_1 - z_2) + d(2\dot{z}_1 - \dot{z}_2) = -f(t) + c\int_0^t v(\bar{t})d\bar{t} + dv(t), \tag{44}$$

$$m\ddot{z}_2 + c(2z_2 - z_1) + d(2\dot{z}_2 - \dot{z}_1) = f(t). \tag{45}$$

The solution can be written as

$$z_1(t) = \int_0^t h_{11}(\tau)f(t-\tau)d\tau + \int_0^t h_{12}(\tau)v(t-\tau)d\tau, \tag{46}$$

$$z_2(t) = \int_0^t h_{12}(\tau)f(t-\tau)d\tau + \int_0^t h_{22}(\tau)v(t-\tau)d\tau \tag{47}$$

with

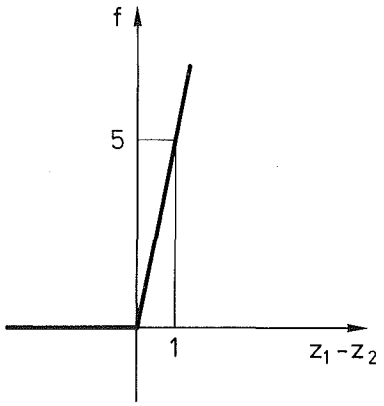

Fig. 6 The characteristics of the nonlinear spring

$$h_{11}(t) = -\frac{1}{m\omega_2}e^{-3\delta t}\sin\ \omega_2 t, \tag{48a}$$

$$h_{12}(t) = \frac{1}{6}\left\{4 - 3e^{-\delta t}\left[\cos\ \omega_1 t - \frac{\delta}{\omega_1}\sin\ \omega_1 t\right] - e^{-3\delta t}\left[\cos\ \omega_2 t - \frac{3\delta}{\omega_2}\sin\ \omega_2 t\right]\right\}, \tag{48b}$$

$$h_{21}(t) = -h_{11}(t), \tag{48c}$$

$$h_{22}(t) = \frac{1}{6}\left\{2 - 3e^{-\delta t}\left[\cos\ \omega_1 t - \frac{\delta}{\omega_1}\sin\ \omega_1 t\right] + e^{-3\delta t}\left[\cos\ \omega_2 t - \frac{3\delta}{\omega_2}\sin\ \omega_2 t\right]\right\}, \tag{48d}$$

$$\delta := d/2m,\ \omega_0^2 := c/m,\ \omega_1^2 := \omega_0^2 - \delta^2,\ \omega_2^2 := 3\omega_0^2 - 9\delta^2. \tag{49}$$

The functions $h_{ij}(t)$, $i, j = 1, 2$ can easily be calculated from the equations of motion (44), (45). Of course, they can also be determined experimentally, as described in Section 3, if a physical model as shown in Fig. 5(*a*) is available.

The dynamic behavior of the composed system, including the nonlinear spring, is now calculated for an input signal of the type

$$s(t) = \begin{cases} \dfrac{h_0}{2}(1 - \cos\ \Omega t)\ , & 0 \le t \le \dfrac{4\pi}{\Omega}\ , \\ 0 & ,\ t<0,\ t> \dfrac{4\pi}{\Omega}\ . \end{cases} \tag{50}$$

This is in a way similar to the passage of a car over two consecutive ramps, and $s(t)$ gives rise to the velocity input

$$v(t) = \begin{cases} \dfrac{h_0\Omega}{2}\sin\ \Omega t, & 0 \le t \le \dfrac{4\pi}{\Omega}\ , \\ 0, & t<0,\ t> \dfrac{4\pi}{\Omega}\ . \end{cases} \tag{51}$$

The system response $z_1(t), z_2(t)$ can now be calculated from (46), (47) with $v(t)$ given by (51) and $f(t-\tau)$ as

$$f(t-\tau) = 2.5\{1 + \mathrm{sgn}[z_1(t-\tau) - z_2(t-\tau)]\}[z,(t-\tau) - z_2(t-\tau)] \tag{52}$$

Figure 7 shows some numerical results obtained in this manner for $m=1$, $d=0.04$, $c=1$, $\Omega=1$, $h_0=1$. The integrations in (46), (47) were performed with the simple approximation (8*a*) for different values of Δt. These results are compared with a

Downloaded 03 May 2010 to 171.66.16.21. Redistribution subject to ASME license or copyright; see http://www.asme.org/terms/Terms_Use.cfm

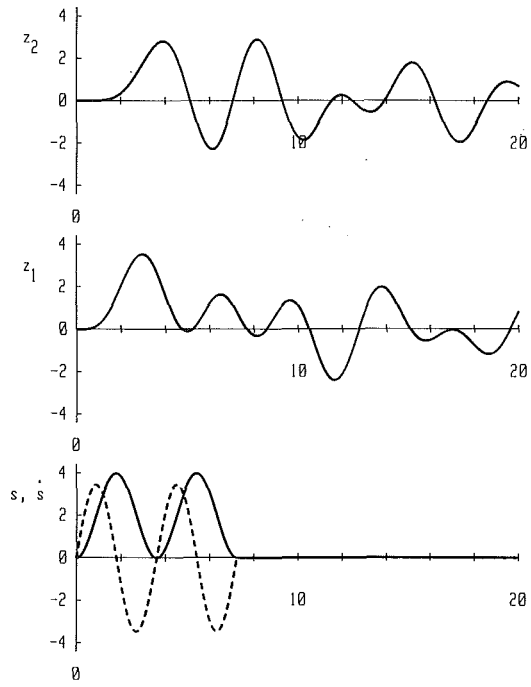

Fig. 7 Numerical results: (*a*) numerically "exact" dynamic response of the linear system (without the nonlinear spring); (*b*) dynamic response of the nonlinear system

"numerically exact" solution of the differential equations (44), (45), obtained via a fourth-order Runge-Kutta method (with $\Delta t = 0.5$). First, the numerically "exact" results are shown in Fig. 7(*a*); obtained with the Runge-Kutta method for $\Delta t = 0.5$. Next, in Fig. 7(*b*) the "exact" dynamic behavior is shown with a dotted line, obtained again by Runge-Kutta integration. If the system response is computed using the simple approximation (8*a*) with $\Delta t = .0125$, the results are for all practical purposes identical to the "exact" ones: Both solutions are indistinguishable in this graphic representation. A solution by (8*a*), using the same step size $\Delta t = .05$ as in the Runge-Kutta integration, gives results (denoted by the solid lines) which differ clearly from the exact ones.

As can be seen, excellent results are obtained for transient oscillations of this nonlinear system using the method with the "convolution" integral. For stationary oscillations involving very large integration intervals, the computation time involved in solving (46), (47), tends to be larger than the direct integration of the equations of motion. This fact does, however, depend very much on the organization of the numerical operations. If vector processors are used, as is sometimes the case for large systems, the convolution can be much faster than a numerical integration of the differential equations. An additional advantage of the proposed method is, of course, that the functions $h_{ij}(t)$, $i, j = 1, 2$ only are needed in (46), (47). They can be obtained by direct measurement in the composed system of Fig. 5, without any knowledge of the structure of the linear subsystem, not even knowing the number of degrees-of-freedom. The proposed procedure gives then an *exact* solution for the composed nonlinear system. The given example is discussed in more detail in Schaarschmidt (1987).

5 Final Remarks

In the present note a description of composed systems, consisting of a linear subsystem and one or more nonlinear elements, is given, which is suitable for simulations and also for measurements. The dynamics of the complex system is represented by an integral equation of the convolution type containing the transfer matrix of the linear subsystem, and by the functional relations describing the nonlinearities.

The problem of measuring this transfer matrix in complex systems, in which only part of the input variables can be changed at will, is also discussed. It is shown that such an experimental determination of the transfer matrix is, in fact, possible, if only all the additional subsystems are completely nonlinear. In these cases, the decomposition of the system into a linear subsystem and other elements, leading to the integral equation, is a useful concept, since it permits an extremely simple representation of the dynamics of the complete system, not involving any parameter identification nor a detailed mathematical model. On the other hand if the subsystem, regarded as linear in the decomposition, contains some substantial nonlinearities, this fact can be identified from the measurements, for example, by means of the coherence matrices.

A simple elastostatic analogy is used to illustrate the ideas. The authors have used the described model for numerical simulation in several cases, particularly in vehicle dynamics, and have obtained good results. Additional experience has to be gained in solving numerically the integral equations (6) for very large and poorly damped systems before the merits of the method can be definitely judged. This will be the subject of further research.

References

Papoulis, A., 1985, *Signal Analysis*, McGraw-Hill, Singapore.

Schaarschmidt, M., 1987, *Numerische Untersuchungen zur Fahrdynamik* (Numerical simulations in vehicle dynamics), Thesis, TH Darmstadt.

Törnig, W., 1979, *Numerische Mathematik für Ingenieure und Physiker* (Numerical Mathematics for Engineers and Physicists), 2 Volumes, Springer, Berlin.

Downloaded 03 May 2010 to 171.66.16.21. Redistribution subject to ASME license or copyright; see http://www.asme.org/terms/Terms_Use.cfm

S. W. Shaw
Department of Mechanical Engineering,
Michigan State University,
East Lansing, MI 48824
Assoc. Mem. ASME

S. Wiggins
Applied Mechanics,
California Institute of Technology,
Pasadena, CA 91125

Chaotic Motions of a Torsional Vibration Absorber

We consider large amplitude motions of a pendulum-type centrifugal vibration absorber which is used for the reduction of torsional oscillations in rotating machinery. The basic two degree-of-freedom model is shown to possess chaotic dynamics for certain ranges of parameter values. The method used is a variation of Melnikov's method (cf., Guckenheimer and Holmes, (1983), Chapter 4) developed for slowly varying oscillators (Wiggins and Holmes (1987), Wiggins and Shaw (1988)).

1 Introduction

The centrifugal pendulum vibration absorber is capable of reducing variations in rotational speeds of machinery which arise from disturbances that are harmonics of the nominal speed (i.e., proportional to it). A basic two degree-of-freedom model for such a system is depicted in Fig. 1. The carrier represents a shaft which is, in an ideal steady-state operating mode, rotating at a constant angular frequency Ω. However, due to unbalances, combustion forces in reciprocating engines, etc., there are disturbances which cause variations in Ω. These disturbances typically arise as excitations at frequencies proportional to Ω. The pendulum represents the absorber; it is often employed in a bifilar configuration (Thompson (1981), page 179). When properly tuned, such an absorber can reduce the Ω variations caused by the type of disturbances mentioned above. See Den Hartog (1938), Newland (1964), and Crossley (1952) for earlier works on this system. We shall consider certain aspects of the large amplitude motions of such a device and prove that chaotic motions are possible.

The paper is outlined as follows. We first derive the equations of motion for the system with applied torques and dissipation included. We then present a brief review of the linearized analysis which demonstrates the utility of the pendulum absorber. To analyze the full nonlinear equations, we begin with an analysis of the (completely integrable) system which has the applied torques and dissipation, collectively referred to as the "perturbations" hereafter, removed. For small perturbations we demonstrate that the system is essentially a single degree-of-freedom oscillator with a parameter which varies slowly in time according to a first order differential equation, i.e., a slowly varying oscillator. The necessary version of Melnikov's method for this situation is then applied to the present system (see Wiggins and Holmes (1987) or Wiggins and Shaw (1988)). It is shown where in parameter space chaotic motions exist and discuss the physical implications of these motions.

Melnikov's method is an asymptotic method for predicting the existence of chaos in the form of *Smale horseshoes*. Such chaos is not necessarily *attractive* and thus Melnikov's method cannot predict the existence of *strange attractors*. However, horseshoes certainly exist in strange attractors and their existence is known to be a good indicator of strange attractors, i.e., *steady-state chaos*. This has been verified in simulation studies and, more importantly, in physical experiments. The works of Moon et al. (1987), Leven et al. (1985), Moore and Shaw (1988), and Moon (1987) provide evidence of this.

The system considered here is a version of a parametrically excited pendulum with a nonideal source. In a limiting case, in which the carrier *speed* is specified as a known function of time (as opposed to specifying the applied torque), this system reduces to a parametrically excited, single degree-of-freedom pendulum. The details for this have been worked out by the authors for another system; see Shaw and Wiggins (1988). The single degree-of-freedom, parametrically excited pendulum has been the source of many investigations including those by Cusumano et al. (1987), Gwinn and Westerveld (1985), Leven et al. (1985), and Koch and Leven (1985). These works include analytical, simulation, and experimental studies.

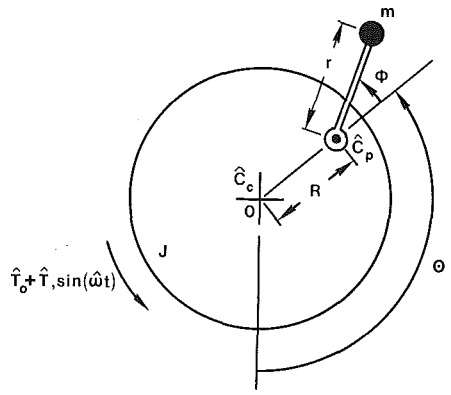

Fig. 1 The basic model of a centrifugal torsional vibration absorber

Contributed by the Applied Mechanics Division for publication in the JOURNAL OF APPLIED MECHANICS.

Discussion on this paper should be addressed to the Editorial Department, ASME, United Engineering Center, 345 East 47th Street, New York, NY 10017, and will be accepted until two months after final publication of the paper itself in the JOURNAL OF APPLIED MECHANICS. Manuscript received by ASME Applied Mechanics Division, October 29, 1986; final revision, February 10, 1988.

Copyright © 1988 by ASME
Downloaded 03 May 2010 to 171.66.16.21. Redistribution subject to ASME license or copyright; see http://www.asme.org/terms/Terms_Use.cfm

2 Equations of Motion and the Linearized System

The results of this section are straightforward; we include them for reference purposes. Considering the sum of the moments about point 0 in Fig. 1, and equating this to the time rate of change of angular momentum about point 0, we obtain

$$(J+mR^2+mr^2+2mRr\cos\phi)\ddot{\theta}+m(r^2+rR\cos\phi)\ddot{\phi} - mRr\dot{\phi}\sin\phi(2\dot{\theta}+\dot{\phi})=-\hat{c}_c\dot{\theta}+\hat{T}_o+\hat{T}_1\sin(\hat{\omega}t). \quad (2.1)$$

Note that we assume $\dot{\theta}$ is large so that gravitational forces are negligible. A free body diagram of the massless rigid rod AB and the mass at B yields a second equation of motion by considering moments about A:

$$m(r^2+rR\cos\phi)\ddot{\theta}+mr^2\ddot{\phi}+mRr\dot{\theta}\sin\phi=-\hat{c}_p\dot{\phi}. \quad (2.2)$$

In order to linearize this system we assume that $\dot{\theta}$ is nearly constant, i.e., $\theta=\Omega t+\psi$, $|\psi|\ll 1$, and that the pendulum angle ϕ is small, $|\phi|\ll 1$. Utilization of these assumptions in equations (2.1) and (2.2) and keeping only first order terms in ϕ, ψ and their time derivatives leads to

$$(J+m(R+r)^2)\ddot{\psi}+mr(r+R)\ddot{\phi}=-\hat{c}_c\dot{\theta}+\hat{T}_o+\hat{T}_1\sin(\hat{\omega}t) \quad (2.3)$$

$$mr(r+R)\ddot{\psi}+mr^2\ddot{\phi}+mRr\Omega^2\phi=-\hat{c}_p\dot{\phi}. \quad (2.4)$$

For simplicity of analysis we take the constant torque $\hat{T}_o$ and the damping constants $\hat{c}_p$ and $\hat{c}_c$ to be zero. In fact, the constant base torque $\hat{T}_o$ and the carrier dissipation $\hat{c}_c$ set the base speed Ω by $\hat{T}_o=\Omega\hat{c}_c$. The amplitudes of steady-state oscillation are determined to be:

$$|\psi|=\hat{T}_1[(R/r)\Omega^2-\omega^2]/\Delta(\omega) \quad (2.5)$$

$$|\phi|=\hat{T}_1\omega^2(1+R/r)/\Delta(\omega) \quad (2.6)$$

where $\Delta(\omega)=\omega^2[J\omega^2-\Omega^2(R/r)(J+m(R+r)^2)]$.

Now, $|\psi|=0$ when $\omega=\Omega\sqrt{R/r}$, thus, if the disturbing frequency is a harmonic of Ω, i.e., $\omega=n\Omega$ (n is an integer), setting $n^2=R/r$ will tune the pendulum to eliminate the effect of that harmonic on the carrier.

We show in the following that the dynamics of this system can be very complicated if large amplitude motions are considered.

3 The Unperturbed System

Without applied torques and dissipation (i.e., $\hat{T}_o=\hat{T}_1=0$ and $\hat{c}_p=\hat{c}_c=0$) this system is completely integrable. A Hamiltonian formulation is used in this section and will be used to guide our analysis in the next section where the effects of the non-Hamiltonian disturbances are considered.

The potential energy for the system is zero and the kinetic energy is given by

$$\hat{T}=\frac{1}{2}(J+mR^2+mr^2+2mrR\cos\phi)\dot{\theta}^2 + m(r^2+Rr\cos\phi)\dot{\theta}\dot{\phi}+\frac{1}{2}mr^2\dot{\phi}^2 \quad (3.1)$$

(a circumflex indicates quantities in terms of original unscaled parameters). At this point we rescale to reduce the number of parameters and put the equations in dimensionless form. Dividing $\hat{T}$ by mr^2 and rescaling time by defining the dimensionless time $\tau=(\hat{p}_{\theta o}/mr^2)t$ (where $\hat{p}_{\theta o}$ is yet to be defined) we obtain the rescaled kinetic energy

$$T=\frac{mr^2\hat{T}}{\hat{p}_{\theta o}^2}=\frac{1}{2}(\mu l^2+1+l^2+2l\cos\phi)\theta'^2 + (1+l\cos\phi)\theta'\phi'+\frac{1}{2}\phi'^2 \quad (3.1)$$

where $(\,)'=d(\,)/d\tau$, $l=R/r$ and $\mu=J/mR^2$. The conjugate momenta are thus given by

$$p_\theta=\frac{\partial T}{\partial\theta'}=(\mu l^2+1+l^2+2l\cos\phi)\theta'+(1+l\cos\phi)\phi' \quad (3.2a)$$

and

$$p_\phi=\frac{\partial T}{\partial\phi'}=(1+l\cos\phi)\theta'+\phi'. \quad (3.2b)$$

Now p_θ is the rescaled angular momentum of the entire system about point 0 and will be constant in this unperturbed case, this will be an immediate consequence in the Hamiltonian formulation below. In fact, $p_\theta=p_{\theta o}=1$ if we take $\hat{p}_{\theta o}$ to be the initial value of $\hat{p}_\theta$. Also, $p_\phi=p_\phi/\hat{p}_{\theta o}$ is the rescaled angular momentum of the mass at B about point A.

To form the Hamiltonian we invert (3.2) to obtain θ' and ϕ' as functions of (ϕ, p_ϕ, p_θ) and then, as is usual, construct $H(\phi, p_\phi, p_\theta)$. Note that the potential energy here is zero and thus the Lagrangian L, is simply equal to T. Forming H:

$$H=\hat{H}mr^2/\hat{p}_{\theta o}^2=\theta' p_\theta+\phi' p_\phi-L(\phi,\phi',\theta') = \left[\frac{1}{2}p_\theta^2-(1+l\cos\phi)p_\theta p_\phi+\frac{1}{2}(\mu l^2+l^2+1+2l\cos\phi)p_\phi^2\right] /D(\phi)$$

where $D(\phi)=l^2(1+\mu-\cos^2\phi)$. The equations of motion can then be obtained via Hamilton's equations:

$$\theta'=\frac{\partial H}{\partial p_\theta}=[p_\theta-(1+l\cos\phi)p_\phi]/D(\phi) \quad (3.4a)$$

$$p_\theta'=-\frac{\partial H}{\partial\theta}=0 \quad (3.4b)$$

$$\phi'=\frac{\partial H}{\partial p_\phi}=[-(1+l\cos\phi)p_\theta+(\mu l^2+1+l^2+2l\cos\phi)p_\phi] /D(\phi) \quad (3.4c)$$

$$p_\phi'=-\frac{\partial H}{\partial\phi}=l\sin\phi[\{l\cos\phi\}p_\theta^2+\{2(1+l\cos\phi) -(1+l\cos\phi)^2-(\mu l^2+1+l^2+2l\cos\phi)\}p_\theta p_\phi + \{(1+l\cos\phi)(\mu l^2+l\cos\phi)\}p_\phi^2]/D^2(\phi). \quad (3.4d)$$

Remarks:

1. Equations (3.4a) and (3.4c) are simply the inversion of equations (3.2) required in the formation of H.
2. Equations (3.4b) immediately yields the fact that $p_\theta=$ constant. In fact $p_\theta=\hat{p}_\theta/\hat{p}_{\theta o}=1$ by choosing the scaling constant $\hat{p}_{\theta o}$ to be the constant value of $\hat{p}_\theta$.
3. Since $p_\theta(=1)$ is constant, equations (3.4c) and (3.4d) uncouple, they represent a planar (single d.o.f.) conservative system with Hamiltonian H. Here p_θ plays no essential role, it simply sets a time scale. In the perturbed system p_θ will be a slowly varying parameter.
4. The system is completely integrable with p_θ and H as constants of the motion.

The uncoupled system (3.4c) and (3.4d) requires consideration, it describes the motion of the pendulum in the centrifugal field and allows for the dynamic coupling between it and the carrier. There exist two "dynamic equilibrium" points in which the carrier rotates at a constant speed $\bar{\theta}'$ and the pendulum remains at a fixed value of ϕ, $\bar{\phi}$, with $\phi'=\bar{\phi}'=0$. These conditions lead to the following:

$$\bar{\phi}=0,\quad \bar{p}_\phi=(1+l)/[\mu l^2+(1+l)^2],\quad \bar{\theta}'=1/[\mu l^2+(1+l)^2] \quad (3.5a)$$

$$\bar{\phi}=\pm\pi,\quad \bar{p}_\phi=(1-l)/[\mu l^2+(1-l)^2],\quad \bar{\theta}'=1/[\mu l^2+(1-l)^2]. \quad (3.5b)$$

Of course, $\bar{p}_\theta=p_\theta=1$. The point $\bar{\phi}=0$ is a center with

Downloaded 03 May 2010 to 171.66.16.21. Redistribution subject to ASME license or copyright; see http://www.asme.org/terms/Terms_Use.cfm

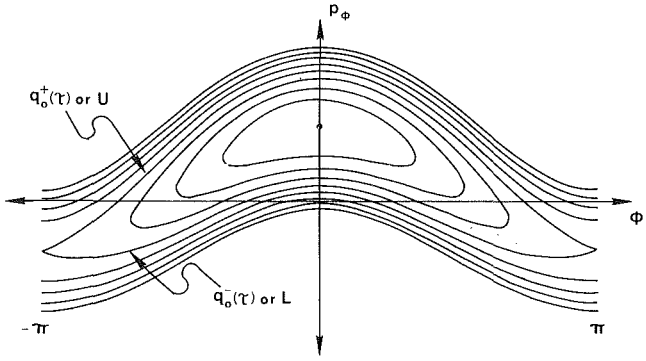

Fig. 2 The phase portrait for equations 3.4(c) and 3.4(d), i.e., the level curves of H given by equation 3.6. Parameter values: $l = 4.0$, $\mu = 10.0$.

linearized frequency $\{\mu l[\mu l^2 + (1+l)^2]\}^{-1/2}$. The values of the Hamiltonian at $\tilde{\phi} = 0, \pm\pi$ are given by $h_c = l^2/2[\mu l^2 + (1+l)^2]$ and $h_s = l^2/2[\mu l^2 + (1-l)^2]$, respectively.

Phase portraits are easily constructed by solving for p_ϕ as a function of ϕ from the equation $H = h =$ constant. Using equation (3.3) with $p_\theta = 1$, this parametarization leads to

$$p_\phi = \frac{(1+l\cos\phi) \pm [D(\phi)\,(2h(\mu l^2 + 1 + l^2 + 2l\cos\phi) - 1)]^{1/2}}{(\mu l^2 + 1 + l^2 + 2l\cos\phi)} . \tag{3.6}$$

A sample phase portrait is shown in Fig. 2. The phase portraits for all l,μ ($\neq 0$) are topologically equivalent to that of the simple pendulum. There exists a center, $\tilde{\phi} = 0$, surrounded by a family of periodic motions, the librations, which limit on a pair of homoclinic motions $q_o^{\pm}(\tau)$ connecting the unstable point $\tilde{\phi} = \pm\pi$ to itself (we assume ϕ lives on the cylinder so that $\pm\pi$ represent the same point). Outside the homoclinic motions is another family of periodic motions, the rotations, which also limit onto the homoclinic motions. An interesting difference between this system and the pendulum is that here the homoclinic motions are not symmetric with respect to p_ϕ. This will affect the types of chaotic motions which can occur in this system.

4 The Perturbed System

In this section we reformulate the full nonlinear equations with the applied torques and dissipation included, equations (2.1) and (2.2), into first order equations in the variables (ϕ, θ, p_ϕ, p_θ). Our desire to use a Hamiltonian-type setting for this non-Hamiltonian system is due to the fact that when the perturbations are small p_θ will be a slowly varying parameter. This is immediately obvious using the Hamiltonian-type variables.

A general set of equations of the motion can be written in Lagrangian form as

$$\frac{d}{dt}\left(\frac{\partial L}{\partial \dot{\underset{\sim}{q}}}\right) - \frac{\partial L}{\partial \underset{\sim}{q}} = \underset{\sim}{Q} \tag{4.1}$$

where $L = L(\underset{\sim}{q}, \dot{\underset{\sim}{q}}, t) = T(\underset{\sim}{q}, \dot{\underset{\sim}{q}}, t) - V(\underset{\sim}{q}, t)$ is the Lagrangian, and T and V are the kinetic energy and potential function, respectively. $\underset{\sim}{Q}$ represents all forces not derivable from V.

In first order form these equations can be written as

$$\dot{\underset{\sim}{q}} = \frac{\partial H}{\partial \underset{\sim}{p}}$$
$$\dot{\underset{\sim}{p}} = -\frac{\partial H}{\partial \underset{\sim}{p}} + \underset{\sim}{Q} \tag{4.2}$$

where $H = H(\underset{\sim}{q}, \underset{\sim}{p}, t)$ is the usual Hamiltonian and $\underset{\sim}{p} = \partial L/\partial \dot{\underset{\sim}{q}}$ are the conjugate momenta. The construction of (4.2) from (4.1) can be found in D'Souza and Garg (1984).

Applying the above to the present system one obtains, after rescaling,

$$\theta' = \frac{\partial H}{\partial p_\theta} , \tag{4.3a}$$

$$p_\theta' = \epsilon Q_\theta , \tag{4.3b}$$

$$\phi' = \frac{\partial H}{\partial p_\phi} , \tag{4.3c}$$

$$p_\phi' = -\frac{\partial H}{\partial \phi} + \epsilon Q_\phi , \tag{4.3d}$$

where

$$Q_\theta = -c_c \frac{\partial H}{\partial p_\theta} + T_o + T_1 \sin(\omega\tau),$$

$$Q_\phi = -c_p \frac{\partial H}{\partial p_\phi} ,$$

$$\epsilon c_{c,p} = \hat{c}_{c,p}/\hat{p}_{\theta o}$$

$$\epsilon T_{o,1} = \hat{T}_{o,1} mr^2/\hat{p}_{\theta o}^2, \text{ and}$$

$$\omega = \hat{\omega} mr^2/\hat{p}_{\theta o}.$$

Remarks:

1 Equations (4.3) represent the equations of motion for the perturbed system and reduce to equations (3.4) when $\epsilon = 0$.
2 The variable θ does not appear in the right-hand side of equations (4.3) and, thus, (4.3*a*) remains uncoupled from the other three. The solution of θ requires direct integration of (4.3*a*) after (4.3*b*), (4.3*c*), and (4.3*d*) have been solved for (ϕ, p_ϕ, p_θ) as functions of time.
3 The system (4.3*b*), (4.3*c*), and (4.3*d*) represents a slowly varying oscillator (2, 3). Equations (4.3*c*) and (4.3*d*) form the oscillator in (ϕ, p_ϕ) with p_θ as a parameter which varies slowly in time according to (4.3*b*).
4 The unperturbed system was reducible to a conservative planar system and was essentially two-dimensional in nature. The perturbed system is four-dimensional, (ϕ, p_ϕ, p_θ, τ), perturbations not only add in an explicit time dependence but they perturb the p_θ integral.

5 Application of Melnikov's Method

Our proof of the existence of chaos in this system will be based on showing that the stable and unstable manifolds of a saddle-type periodic motion intersect transversally. A motion will grow out of the saddle point at $\phi = \pi$ as ϵ becomes nonzero, but will be periodic only under certain conditions obtained from considering the perturbation on p_θ. In Wiggins and Holmes (1987) and in Wiggins and Shaw (1988) averaging was used to find these periodic motions, our approach here is equivalent. Expanding about the unperturbed saddle point at $(\phi, p_\phi, p_\theta) = (\pi, (1-l)/[\mu l^2 + (1-l)^2], 1)$, call it γ_o, we take

$$\phi = \pi + \epsilon\nu$$
$$p_\phi = (1-l)/[\mu l^2 + (1-l)^2] + \epsilon\rho_\phi$$
$$p_\theta = 1 + \epsilon\rho_\theta$$

so that (ν, ρ_ϕ, ρ_θ) represent the deviations from γ_o and are desired to be periodic functions of time. Carrying out the expansion in ϵ yields

$$\begin{pmatrix} \nu' \\ \rho_\phi' \\ \rho_\theta' \end{pmatrix} = \begin{pmatrix} 0 \\ 0 \\ -c_c\theta'(\pi) + T_0 + T_1\sin(\omega\tau) \end{pmatrix} + \mathbf{A}\begin{pmatrix} \nu' \\ \rho_\phi' \\ \rho_\theta' \end{pmatrix} + 0(\epsilon) \tag{5.1}$$

Downloaded 03 May 2010 to 171.66.16.21. Redistribution subject to ASME license or copyright; see http://www.asme.org/terms/Terms_Use.cfm

where $\mathbf{A}$ is a constant matrix depending on μ, l and c_c, and $\theta'(\pi) = 1/[\mu l^2 + (1-l)^2]$. The constant term in the ρ_θ' equation must be set to zero in order for $(\nu, \rho_\phi, \rho_\theta)$ to have a time periodic solution. This results in the following constraint on the perturbation parameters:

$$T_o = c_c \theta'(\pi). \tag{5.2}$$

This simply says that to first order the constant torque must balance the dissipative torque on the carrier at $\phi = \pi$. The periodic motion is within $0(\epsilon)$ of $\phi = \pi$ and, hence, to leading order that dissipative torque is given by $c_c\theta'(\pi)$.

The perturbed saddle type motion is represented by a fixed point, $\tilde{\gamma}_\epsilon = \gamma_o + 0(\epsilon)$, for the three-dimensional time $T = 2\pi/\omega$ Poincaré map defined as

$$\underset{\sim}{P}(\phi(\tau_o),\ p_\phi(\tau_o),\ p_\theta(\tau_o)) \to (\phi(\tau_o+T),\ p_\phi(\tau_o+T),\ p_\theta(\tau_o+T)) \tag{5.3}$$

which samples the $(\phi, p_\phi, p_\theta, \tau)$ extended phase space once every period of the forcing, T, and returns values of (ϕ, p_ϕ, p_θ) at each iterate. When $\epsilon = 0$ the saddle point $\tilde{\gamma}_o$ has one stable, one unstable, and one neutral (p_θ) direction. For $0 < \epsilon \ll 1$ the stable and unstable directions for the fixed point $\tilde{\gamma}_\epsilon$ maintain their stability type while in the p_θ-direction the stability will be of $0(\epsilon)$ and is determined to be (weakly) stable by computing the derivative of the averaged p_θ perturbation, $\bar{Q}_\theta$, with respect to p_θ:

$$\bar{Q}_\theta \overset{\text{def}}{=} \frac{1}{T}\int_0^T Q_\theta d\tau \quad \text{and} \quad \frac{\partial \bar{Q}_\theta}{\partial p_\theta} = \frac{-c_c}{\mu l^2} < 0. \tag{5.4}$$

This makes physical sense, it simply says that the carrier dissipation and the torque T_o draw the system toward $\tilde{\gamma}_\epsilon$ in the p_θ-direction. Also, we now have the following information regarding the stable and unstable manifolds of $\tilde{\gamma}_\epsilon$:

$$\dim(W^S(\tilde{\gamma}_\epsilon)) = 2, \quad \dim(W^u(\tilde{\gamma}_\epsilon)) = 1.$$

We are now able to set up and solve the Melnikov integrals in order to measure the separation of $W^S(\tilde{\gamma}_\epsilon)$ and $W^u(\tilde{\gamma}_\epsilon)$. From Wiggins and Shaw (1988) the Melnikov integral is

$$M(\alpha) = \int_{-\infty}^{\infty} \{\nabla H \cdot \mathbf{Q}\}(q_o(\tau),\ \tau+\alpha)d\tau - \frac{\partial H}{\partial p_\theta}(\gamma_o)\int_{-\infty}^{\infty}\{\mathbf{Q}\}(q_o(\tau),\ \tau+\alpha)d\tau \tag{5.5}$$

where $\mathbf{Q}$ represents our perturbation vector and $q_o(\tau)$ is an unperturbed homoclinic motion. Specifically, for the present system we have

$$M(\alpha) = \int_{-\infty}^{\infty}\left\{-c_p\left(\frac{\partial H}{\partial p_\phi}\right)^2 - c_c\left(\frac{\partial H}{\partial p_\theta}\right)^2 + T_o\left(\frac{\partial H}{\partial p_\theta}\right) + T_1\sin(\omega(\tau+\alpha))\left(\frac{\partial H}{\partial p_\theta}\right)\right\}(q_o(\tau))d\tau - \frac{\partial H}{\partial p_\theta}(\gamma_o)$$

$$\int_{-\infty}^{\infty}\left\{-c_p\frac{\partial H}{\partial p_\theta} + T_o + T_1\sin(\omega(\tau+\alpha))\right\}(q_o(\tau))d\tau \tag{5.6}$$

We take several steps to simplify this expression.

The first term in the first integral is

$$c_c I_2 = c_c\int_{-\infty}^{\infty}\left\{\left(\frac{\partial H}{\partial p_\phi}\right)^2\right\}(q_o(\tau))d\tau \tag{5.7}$$

and is well behaved, $\phi' = \partial H/\partial p_\phi$ is everywhere finite and approaches zero exponentially as $\tau \to \pm\infty$ along either of $q_o^{\pm}(\tau)$. The next two terms of the first integral and the first two of the second combine by virtue of $\partial H/\partial p_\theta\ (\gamma_o) = \theta'(\pi) = T_o/c_c$ to give

$$c_p I_1 = c_p\int_{-\infty}^{\infty}\left(\frac{\partial H}{\partial p_\phi} - \theta'(\pi)\right)^2(q_o(\tau))d\tau. \tag{5.8}$$

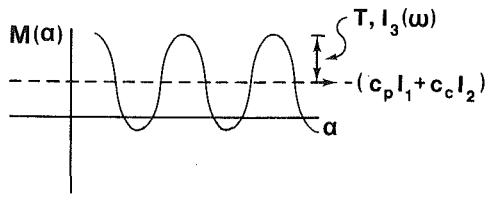

Fig. 3 The Melnikov function

As $\tau \to \pm\infty$, $\theta' = \partial H/\partial p_\theta \to \theta'(\pi)$ exponentially and this integral is thus also well defined. Note that without condition (5.2) this integral would not exist since the integrand would approach a nonzero constant as $\tau \to \pm\infty$. It is interesting to note that T_o and $c_c\theta'$ cancel only at the endpoints and that c_c and T_o contribute to the overall variation.

The final term in the first integral is simplified in two steps. First, note that $\theta' = \partial H/\partial p_\theta$ is an even function of τ along $q_o^{\pm}(\tau)$, then expanding $\sin(\omega(\tau+\alpha))$ and eliminating the terms odd in τ (which integrate to zero) we reduce this term to

$$T_1\sin(\omega\alpha)I_3(\omega) = T_1\sin(\omega\alpha)\int_{-\infty}^{\infty}\left\{\cos(\omega\tau)\left(\frac{\partial H}{\partial p_\theta}\right)\right\}(q_o(\tau))d\tau. \tag{5.9}$$

The integral $I_3(\omega)$ is not absolutely convergent since $\partial H/\partial p_\theta \to \theta'(\pi) \neq 0$ as $\tau \to \pm\infty$. This situation is remedied by writing

$$I_3(\omega) = \lim_{\tau_i\to\infty}\int_{-\tau_i}^{\tau_i}\{\cos(\omega\tau)\theta'\}(q_o(\tau))d\tau$$

and integrating once by parts to obtain

$$I_3(\omega) = \lim_{\tau_i\to\infty}\left[\frac{\theta'\sin(\omega\tau)}{\omega}\Big|_{-\tau_i}^{\tau_i} - \frac{1}{\omega}\int_{-\tau_i}^{\tau_i}\{\sin(\omega\tau)\theta''\}(q_o(\tau))d\tau\right].$$

Taking lim $\tau_i \to \infty$ by choosing a sequence of times $\tau_i = 2\pi i$ and letting $i(=\text{integers}) \to \infty$ yields the well defined and absolutely convergent integral

$$I_3(\omega) = -\frac{1}{\omega}\int_{-\infty}^{\infty}\{\sin(\omega\tau)\theta''\}(q_o(\tau))d\tau$$

$$= \frac{1}{\omega}\int_{-\infty}^{\infty}\left\{\sin(\omega\tau)l\sin\phi\left[\left(\frac{\partial H}{\partial p_\phi}\right)^2 + 2\left(\frac{\partial H}{\partial p_\phi}\right)\left(\frac{\partial H}{\partial p_\theta}\right) + (1+l\cos\phi)\left(\frac{\partial H}{\partial p_\theta}\right)^2\right]/D(\phi)\right\}(q_o(\tau))d\tau. \tag{5.10}$$

The last term of the second integral yields zero by the same procedure that simplified $I_3(\omega)$.

We now have

$$M(\alpha) = -c_p I_1 - c_c I_2 + T_1\sin(\omega\alpha)I_3(\omega)$$

where I_1, I_2 and $I_3(\omega)$ are given by equations (5.7), (5.8), and (5.10), respectively. The bifurcation results in the next section follow from Wiggins and Shaw (1988) applied to $M(\alpha)$ above.

6 Global Bifurcations and Chaos

A schematic representation of $M(\alpha)$ is shown in Fig. 3. $M(\alpha)$ oscillates about a mean value of $-(c_pI_1 + c_cI_2)$ with peak-to-peak amplitude $T_1I_3(\omega)$. We first discuss the case for $T_1 = 0$, i.e., an autonomous perturbation, and then consider $T_1 \neq 0$.

For $T_1 = 0$, define

$$\left(\frac{c_p}{c_c}\right)^* = \left(-\frac{I_2}{I_I}\right), \tag{6.1}$$

Downloaded 03 May 2010 to 171.66.16.21. Redistribution subject to ASME license or copyright; see http://www.asme.org/terms/Terms_Use.cfm

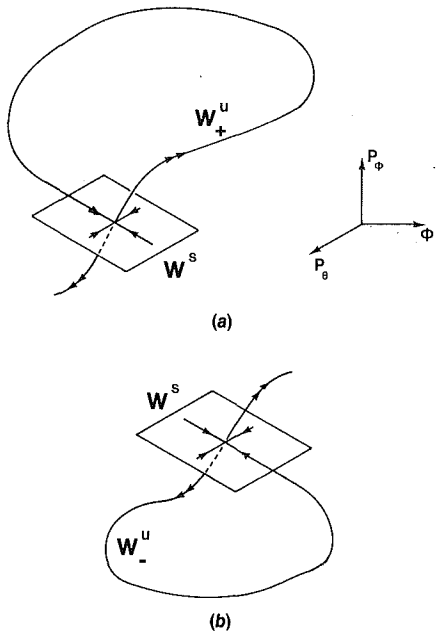

Fig. 4 The homoclinic orbits for autonomous perturbations ($T_1 = 0$), (a) upper at $(c_p/c_c) = (c_p/c_c)^*_+$ (to $0(\epsilon)$) (b) lower at $(c_p/c_c) = (c_p/c_c)^*_-$ (to $0(\epsilon)$)

Table 1

Reference to Fig. 5(*b*)
(+, −) indicates $M(\alpha)$ is strictly (positive, negative)
Z indicates $M(\alpha)$ has simple zeros

Region	$M_+(\alpha)$	$M_-(\alpha)$	Comments
A	+	+	no chaos, (cw) and (ccw) rotations possible
B	+	Z	(cw) chaos and (ccw) rotations possible
C	Z	Z	"full chaos" possible
D	+	−	no chaos, (ccw) rotations possible
E	Z	−	(ccw) chaos possible
F	−	−	no chaos
G	Z	+	(ccw) chaos and (cw) rotations possible

then we have the following cases:

$$\left(\frac{c_p}{c_c}\right) \lessgtr \left(\frac{c_p}{c_c}\right)^* \Rightarrow M(\alpha) \lessgtr 0, \text{ respectively.}$$

Here $M(\alpha) = M$ is independent of α and cannot have simple zeros, when $M = 0$ the system possesses a homoclinic orbit for nearby ($0(\epsilon)$) parameter values. In this case, the Poincaré map is not needed and we simply consider the solution trajectories in the phase space (ϕ, p_ϕ, p_θ). Figure 4 depicts this situation for both the upper and the lower homoclinic motions. As M passes through zero a global bifurcation occurs. The consequences of such homoclinic bifurcations in three-dimensional systems are not completely understood. For our system we can conjecture that as M approaches zero from above and passes through zero, a periodic rotating motion of the pendulum comes near the saddle point, touches it, and is then destroyed. This is analogous to what occurs in planar systems and agrees with physical intuition for this device. For $\theta' > 0$, i.e., counter-clockwise rotation of the carrier, those rotational motions are clockwise (cw) for the pendulum on the lower homoclinic bifurcation and counter clockwise (ccw) for the upper one.

For $T_1 \neq 0$ results are summarized in Fig. 5 and Table 1. Figure 5(*a*) shows a bifurcation diagram of (T_1/c_c) versus (c_p/c_c) and Fig. 5(*b*) indicates the behavior of the stable and unstable manifolds of $\tilde{\gamma}_\epsilon$ in the various parameter regions. In

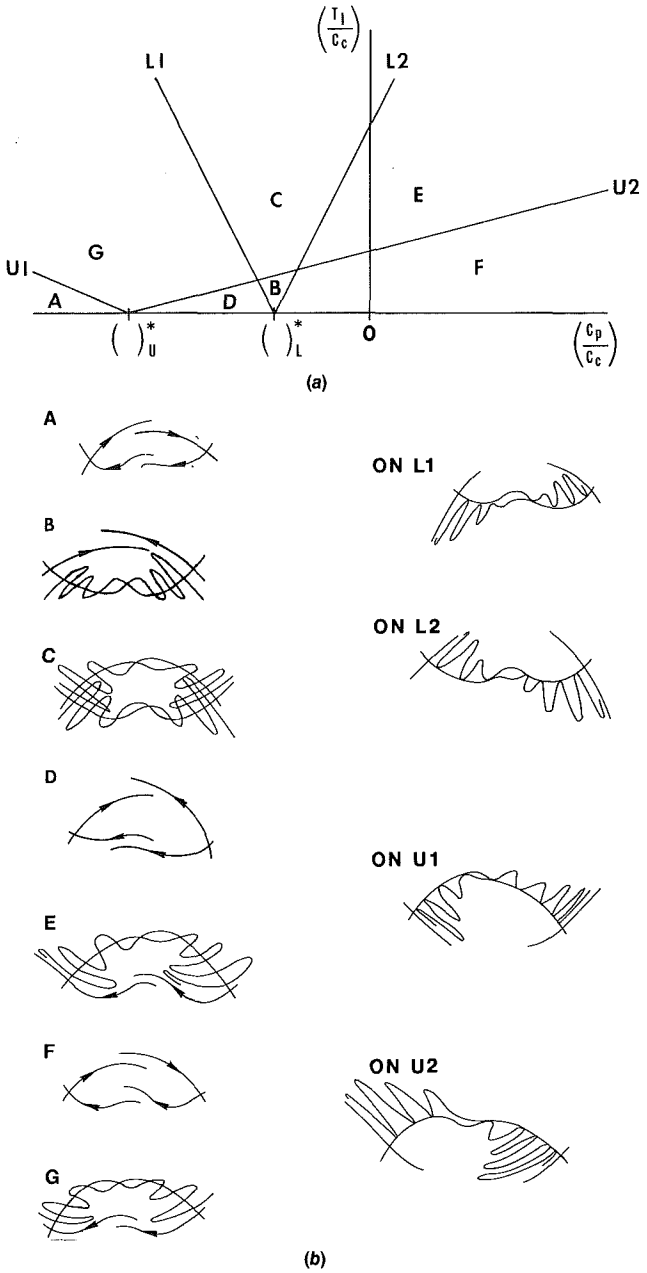

Fig. 5 (*a*) The bifurcation diagram, $I = 4.0$, $\mu = 10.0$, $\omega \simeq 2/177$ (*b*) The various situations possible from (*a*), recall that dim (W^S) = 2

Fig. 5(*b*), $W^S(\tilde{\gamma}_\epsilon)$ is shown as one-dimensional for clarity in the diagrams, it is, of course, a two-dimensional manifold.

The homoclinic tangles in Regions B, D, and G exist for only one direction (clockwise or counter clockwise rotations) and thus the type of chaos one may observe is "uni-directional," i.e., it involves the pendulum going around in the same direction, but in an irregular manner. The direction is the same as that of the original unperturbed homoclinic motion which becomes tangled in the perturbed system. Thus, if θ' is counter clockwise then the chaotic motions in regions G and D involve $q_o^+(\tau)$ and the pendulum also moving counter-clockwise while in region B the pendulum moves clockwise, roughly along $q_o^-(\tau)$.

The dynamics are most interesting in region C where both $q_o^+(\tau)$ and $q_o^-(\tau)$ become tangled. There motions exist in which the pendulum goes through $\phi = \pi$ in (cw) and (ccw) rotation in *any* prescribed order. This is now demonstrated by construc-

Downloaded 03 May 2010 to 171.66.16.21. Redistribution subject to ASME license or copyright; see http://www.asme.org/terms/Terms_Use.cfm

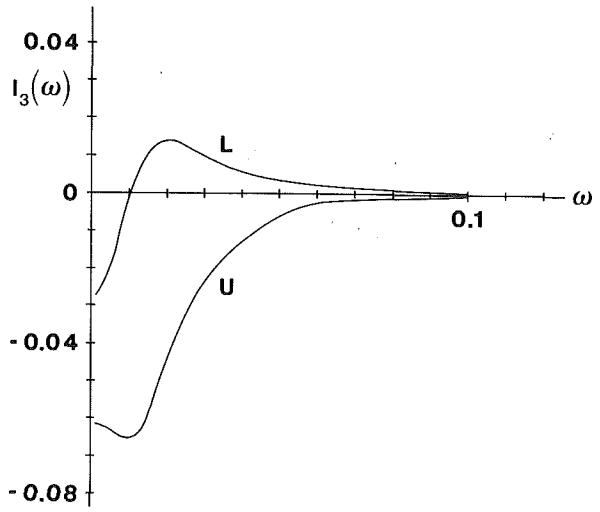

Fig. 6 $I_3(\omega)$ versus ω, $l = 4.0$, $\mu = 10.0$

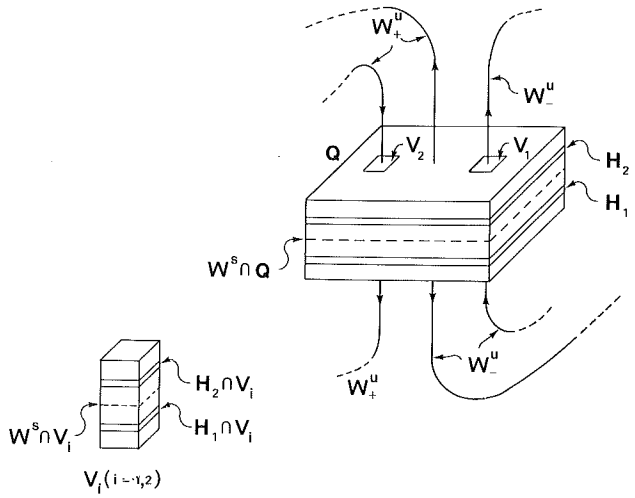

Fig. 7 Construction of the three dimensional horseshoe

ting a simple map near $\tilde{\gamma}_\epsilon$ and using symbolic dynamics as described in Wiggins and Shaw (1988).

Figure 7 shows a rectangular box Q which surrounds $\tilde{\gamma}_\epsilon$. It is chosen such that the sides are roughly parallel with $W^S(\tilde{\gamma}_\epsilon)$ and $W^u(\tilde{\gamma}_\epsilon)$. The image of this box under iterates of $\underset{\sim}{P}$ will shrink along $W^S(\tilde{\gamma}_\epsilon)$ and stretch out along $W^u(\tilde{\gamma}_\epsilon)$. Since these manifolds intersect transversally, $W^u(\tilde{\gamma}_\epsilon)$ must come back and pierce Q. Following the images of Q under $\underset{\sim}{P}$ we consider the places where $W^u(\tilde{\gamma}_\epsilon)$ first comes back and pierces Q after n (n is large) iterates of $\underset{\sim}{P}$. The intersection of $\underset{\sim}{P}^n(Q)$ with Q, $\underset{\sim}{P}^n(Q) \cap Q$, is made up of the two rectangles V_1 and V_2. The preimages of the V_i are the horizontal slabs $H_i \epsilon Q$, $i = 1, 2$. Since $\underset{\sim}{P}^n(H_i) = V_i$ and each H_i intersects each V_i for $i = 1, 2$, we see a topological horseshoe exists. Since $W^S(\tilde{\gamma}_\epsilon)$ and $W^u(\tilde{\gamma}_\epsilon)$ intersect transversally this horseshoe can be constructed to be hyperbolic by a judicious choice of Q. The invariant set of $\underset{\sim}{P}$ restricted to V_1 and V_2 is given by

$$\Lambda_{12} = \left[\bigcap_{k=-\infty}^{\infty} P^{n \cdot k}(H_1 \cup H_2) \right] \cap [V_1 \cup V_2] \tag{6.2}$$

and consists of a Cantor set of finite horizontal planes (roughly parallel to $W^S(\tilde{\gamma}_\epsilon)$ at $\tilde{\gamma}_\epsilon$) intersected with a Cantor set of line segments (roughly parallel to $W^u(\tilde{\gamma}_\epsilon)$ at $\tilde{\gamma}_\epsilon$). This set is itself a Cantor set and represents (some of) the dynamics of the system when the pendulum comes near $\phi = \pi$. We now indicate how (cw) and (ccw) passages past $\phi = \pi$ can occur in any order.

Two-symbol symbol sequences will be used here. We take our symbol sequence as follows

$$\underline{a}(x) = \{a_j(x)\}_{j=-\infty}^{\infty} \tag{6.1}$$

where $x = (\phi, p_\phi, p_\theta)$ and the $a_j(x)$ are defined as

$$a_j(x) = \begin{cases} 1 & \text{if } P^j(x) \epsilon H_1 \\ 2 & \text{if } P^j(x) \epsilon H_2 \end{cases}.$$

Since the horseshoe can be constructed to be hyperbolic, there exists a one-to-one correspondence between points in the invariant set Λ_{12} and symbol sequences $\underline{a}(x)$ (Wiggins and Shaw (1988)). Hence, the result regarding (cw) and (ccw) passages near $\phi = \pi$ follows immediately.

The set Λ_{12} contains points which represent chaotic trajectories, namely the nonrepeating sequences, as well as subharmonic motions. These subharmonics are of period $k \cdot n \cdot (2\pi/\omega)$ for all $k = 1, 2, 3, \ldots$ and are unstable. In fact, all points in Λ_{12} are unstable due to the stretching along $W^u(\tilde{\gamma}_\epsilon)$. Hence, the dynamics represented by points in Λ_{12} do not represent physical steady-state motions. However, sets similar to Λ_{12} are the source of nearly all strange attractor type motions observed in simulations and experiments. If the set Λ_{12} co-exists with a stable periodic motion then irregular transients, or transient chaos, can occur if initial conditions are such that the dynamics come into the vicinity of $\tilde{\gamma}_\epsilon$. In fact, infinitely many sets similar to Λ_{12} exist near $\tilde{\gamma}_\epsilon$ and these transient irregular motions can persist for arbitrarily long times.

7 An Example

An absorber tuned to eliminate second order harmonics of the carrier has $l = 4$. Typically the inertia of the absorber system is significantly less than that of the carrier so we take $\mu = 10$. The unperturbed phase portrait is given in Fig. 2.

The value of the Hamiltonian on the homoclinic motions is $h_s = 1/338$. To determine $q_o^{\pm}(\tau)$ we start on the level curve $h = h_s$ at $\phi = 0$ and run forward in time. This was done using a fourth-order Runge-Kutta integration routine for both $q_o^+(\tau)$ and $q_o^-(\tau)$. The integration is truncated at some large time where the trajectory was sufficiently close to the saddle point so that the (exponentially small) tails of the integrals would be negligible. This procedure gives half of each homoclinic motion, the other half is easily obtained by using the symmetry about $\phi = 0$.

Having $q_o^{\pm}(\tau)$ we can easily evaluate the integrals I_1, I_2, and $I_3(\omega)$ numerically. This was done using Simpson's rule and the results for I_1 and I_2 are:

along $q_o^+(\tau)$ $\quad I_1^+ = 0.0948 \quad I_2^+ = 0.000116$

along $q_o^-(\tau)$ $\quad I_1^- = 0.0948 \quad I_2^- = 0.000005.$

The results for $I_3(\omega)$ are shown in Fig. 6.

Note that $I_3(\omega)$ is extremely small even at moderate ω values, this is due to the rescaling. Recalling that $\omega = \hat{\omega} m r^2 / \hat{p}_{\theta o}$ where $\hat{\omega}$ is the unscaled driving frequency and $\hat{p}_{\theta o}$ is the unscaled initial θ momentum. A nominal value of $\hat{p}_\theta$ which can be used for $\hat{p}_{\theta o}$ is given by $\hat{p}_{\theta o} = mr^2 (\mu l^2 + 1 + l^2)\Omega$ where Ω is again taken to be the nominal angular speed of the carrier. (We have simply neglected the values of ϕ and $\dot{\phi}$ which fluctuate around zero.) In this example, then, $\omega = (\hat{\omega}/\Omega)/(\mu l^2 + 1 + l^2)$. For second order harmonics $\hat{\omega} = 2\Omega$ and, thus, $\omega = 2/(\mu l^2 + 1 + l^2) = 2/177 \ll 1$. In fact the results in Fig. 5 are for $l = 4$, $\mu = 10$ and $\omega \simeq 2/177$.

For $T_1 \neq 0$ only those behaviors indicated in Fig. 5 for positive damping will occur for the device, the negative damping results are presented to demonstrate the complete structure

Downloaded 03 May 2010 to 171.66.16.21. Redistribution subject to ASME license or copyright; see http://www.asme.org/terms/Terms_Use.cfm

of the bifurcation conditions for the mathematical equations. Due to the relative sizes of I_1 and I_2 for the + and − cases the "wedge" in which chaos occurs (cf. Fig. 5) is much broader for + than for −. Thus, (ccw) chaotic motions are more likely to be observed although both are possible.

8 Discussion

The chaotic motions described in this paper involve large amplitude excursions of the pendulum. Actual absorber devices are prevented from achieving such amplitudes by motion limiting stops or other means. In fact, first order nonlinearities due to the softening effects of the pendulum render the pendulum absorber practically useless even for moderate amplitudes (Borowski et al. (1987)). Typically this deficiency is corrected by implementation of a bifilar device (see Tompson (1981)) in which the absorber mass moves on a noncircular path (Borowski et al. (1987)). Investigations are under way which consider these first order nonlinear effects, moderate amplitude subharmonic resonances, and the effects of stops (Sharif-Bakhtiar and Shaw (1987)).

A more realistic model of the disturbances for rotational systems such as the present one is to take a θ-dependent torque, such as $T_1 \sin(n\theta)$, in place of the time-dependent oscillating torque considered here. This more accurately models typical disturbances which occur. Shaw and Wiggins (1987) provide a formulation to handle these spatially periodic terms using a change of independent coordinate. However, for $\dot{\theta}$ large, i.e., Ω large, we have $\theta = \Omega t + \psi$ with ψ relatively small, even for the large ϕ amplitudes considered in this paper. Hence, $\sin(n\theta) \simeq \sin(n\Omega t)$ to first order and the differences will be of higher order.

The effects of gravity, which are small for large $\dot{\theta}$ (i.e., large $\hat{p}_{\theta o}$), also result in θ-dependent terms in the equations of motion. The addition of these, at $O(\epsilon)$, will provide a periodic disturbance in addition to the applied torque. This can be handled using the methods developed in Wiggins (1987). The Melnikov formulation is identical to that presented here; the underlying dynamics, however, require a different interpretation since the transverse homoclinic orbits predicted are homoclinic to a quasiperiodic motion, i.e., a two-torus. The parameter conditions for the onset of chaos will, in that case, correspond to smaller T_1 values (Wiggins, 1987).

Lastly, it should be noted that the methods presented in this and the previous paper are applicable to any system with an unperturbed Hamiltonian of the form $H(q_1, p_1, p_2)$ which is then perturbed by small disturbances which are independent of q_2(θ in the present system). See Shaw and Wiggins (1987) for methods to handle q_2 dependent perturbations.

Acknowledgments

The first author is grateful to the TBPA group at Ford Motor Company for stimulating discussions. This work was supported in part by NSF grants MEA 8421248 and MSM 8613294 and by DARPA.

References

Borowski, V., Denman, H., Shaw, S., Hanisko, C., Brooks, L., Cronin, D., 1987, unpublished notes, Ford Motor Co., Dearborn, MI.

Crossley, F. R. E., 1952, "The Free Oscillation of the Centrifugal Pendulum with Wide Angles," ASME JOURNAL OF APPLIED MECHANICS, Vol. 74, pp. 315–319.

Crossley, F. R. E., 1953, "The Forced Oscillation of the Centrifugal Pendulum with Wide Angles," ASME JOURNAL OF APPLIED MECHANICS, Vol. 75, pp. 41–47.

Den Hartog, J. P., 1938, "Tuned Pendulums as Torsional Vibration Eliminators," *S. Timoshenko 60th Anniversary Volume*, MacMillan Co., New York, pp. 17–26.

D'Souza, A. F., and Garg, V. K., 1984, *Advanced Dynamics: Modeling and Analysis*, Prentice-Hall, Englewood Cliffs, NJ.

Guckenheimer, J., and Holmes, P., 1983, *Nonlinear Oscillations, Dynamical Systems and Bifurcations of Vector Fields*, Springer-Verlag, New York.

Gwinn, E. G., and Westerveld, R. M., 1985, *Physical Review Letters*, Vol. 54, pp. 1613–1616.

Koch, B. P., and Leven, R. W., 1985, "Subharmonic and Homoclinic Bifurcations in a Parmetrically Forced Pendulum," *Physica 16D*, pp. 1–13.

Leven, R. W., Pompe, B., Wilke, K., and Koch, B. P., 1985, "Experiments on Periodic and Chaotic Motions of a Parametrically Forced Pendulum," *Physica 16D*, pp. 371–384.

Moon, F., 1987, *Chaotic Vibrations*, Wiley, New York.

Moon, F., Cusumano, J., and Holmes, P., 1987, "Evidence for Homoclinic Orbits as a Precursor to Chaos in a Magnetic Pendulum," *Physica 24D*, pp. 383–390.

Moore, D., and Shaw, S. W., 1988, "Experiments on the Dynamic Response of an Impacting Pendulum System," preprint.

Newland, D. E., 1964, "Nonlinear Aspects of the Performance of Centrifugal Pendulum Vibration Absorbers," ASME *Journal of Engineering for Industry*, Vol. 86, pp. 257–263.

Sharif-Bakhtiar, M., and Shaw, S. W., 1987, "The Dynamic Analysis of a Centrifugal Pendulum Vibration Absorber with Motion Limiting Stops," *Developments in Mechanics*, Vol. 14(b), pp. 845–850.

Shaw, S. W., and Wiggins, S., 1988, "Chaotic Dynamics of a Whirling Pendulum," *Physica D*, to appear.

Thomson, W. T., 1981, *Theory of Vibration with Applications*, Prentice-Hall, Englewood Cliffs, NJ.

Wiggins, S., and Holmes, P., 1987, "Homoclinic Orbits in Slowly Varying Oscillators," *SIAM J. Math. Anal.*, Vol. 18, pp. 612–629.

Wiggins, S., and Shaw, S. W., 1988, "Chaos and Three-Dimensional Horseshoes in Slowly Varying Oscillators," ASME JOURNAL OF APPLIED MECHANICS, Vol. 55, pp. 959–968.

Wiggins, S., 1987, "On the Detection and Dynamical Consequences of Orbits Homoclinic to Hyperbolic Periodic Orbits and Normally Hyperbolic Invariant Tori in a Class of Ordinary Differential Equations," *SIAM Journal on Applied Mathematics*, Vol. 48, pp. 262–285.

Downloaded 03 May 2010 to 171.66.16.21. Redistribution subject to ASME license or copyright; see http://www.asme.org/terms/Terms_Use.cfm

Stephen Wiggins
Applied Mechanics 104-44,
California Institute of Technology,
Pasadena, CA 91125

Steven W. Shaw
Dept. of Mechanical Engineering,
Michigan State University,
East Lansing, MI 48824
Assoc. Mem. ASME

Chaos and Three-Dimensional Horseshoes in Slowly Varying Oscillators

We present general results pertaining to chaotic motions in a class of systems termed slowly varying oscillators *which consist of weakly perturbed single-degree-of-freedom systems in which parameters vary slowly in time according to an additional equation of motion. Our results include an analytical method for detecting transversal intersections of stable and unstable manifolds (typically a necessary condition for chaotic motions to exist) and a detailed description of the chaotic dynamics that occur when this situation exists.*

1 Introduction

In this paper we will study systems of the form

$$\dot{x} = \frac{\partial}{\partial y} H(x,y,z) + \epsilon g_1(x,y,z,t;\mu)$$

$$\dot{y} = \frac{-\partial}{\partial x} H(x,y,z) + \epsilon g_2(x,y,z,t;\mu)$$

$$\dot{z} = \epsilon g_3(x,y,z,t;\mu) \tag{1.1}$$

where ϵ is small, $H(x,y,z)$ is a scalar-valued function which can be thought of as a one-parameter family of Hamiltonians, $\mu \in \mathbf{R}^P$ is a vector of parameters, and the g_i, $i=1,2,3$, are periodic in t with fixed period T. We will refer to (1.1) as *slowly varying oscillators.* These arise in at least three general classes of physical systems: (1) nonlinear single-degree-of-freedom oscillators in which a parameter varies slowly in time according to a governing differential equation, (2) two-degree-of-freedom, nonlinear, autonomous, weakly coupled systems, and (3) strongly coupled two-degree-of-freedom nonlinear systems with an ignorable coordinate, often referred to as systems with "one and half" degrees-of-freedom. In the following paper (Shaw and Wiggins (1988)) we present specific results for a system from Category (3) above.

Specifically, we will be interested in explicitly computing under what conditions (1.1) displays chaotic motion. Our criteria for chaos will be the existence of a three-dimensional version of the Smale Horseshoe map. We will show that the incredibly complicated dynamics of the horseshoe (e.g., existence of a countable infinity of periodic motions of arbitrarily high period, existence of an uncountable infinity of bounded, non-periodic chaotic motions, etc.) is present when the stable and unstable manifolds of a fixed point of the associated period T Poincaré map of (1.1) intersect transversely. The point of intersection is called a *transverse homoclinic point* and implies the existence of Smale horseshoe via the Smale-Birkhoff homoclinic theorem. We will utilize a version of the perturbation technique of Melnikov (1963) due to Wiggins and Holmes (1987) to detect transverse homoclinic points. We remark that the two-dimensional Smale horseshoe map has been found to lie at the heart of the numerically observed strange attractors found in the Henon map (Devany an Nitecki (1979)) and the forced Duffing oscillator (Holmes (1979)). However, the three-dimensional horseshoe map has received little attention.

This paper is organized as follows: In Section 2 we state our assumptions on (1.1) and develop the version of Melnikov's method which enables us to detect transverse homoclinic points in (1.1). In Section 3 we decribe a simplified model of the three-dimensional Smale horseshoe and motivate a description of the dynamics via the technique of symbolic dynamics, here we explicitly define what we mean by the term "chaos." In Section 3 we describe how the Smale horseshoe is present whenever a map possesses a transverse homoclinic point and we argue that the dynamics in the neighborhood of a transverse homoclinic point is exactly the same as our simplied map given in Section 2.

There is currently much activity in research regarding chaotic motions of physical systems, much of it consisting of observations drawn from digital simulations. Here we present one of the few analytical techniques available for predicting the onset of chaos and present a detailed description of what we mean by "chaos." The results presented here are extensions of these which have been well developed for periodically forced one-degree-of-freedom oscillators (cf. Guckenheimer and Holmes (1983)). Our results may appear to be quite abstract, but as is shown in Shaw and Wiggins (1988), they have direct applicability to physical systems and provide rigorous results on chaotic motions for such systems.

Contributed by the Applied Mechanics Division for publication in the JOURNAL OF APPLIED MECHANICS.

Discussion on this paper should be addressed to the Editorial Department, ASME, United Engineering Center, 345 East 47th Street, New York, N.Y. 10017, and will be accepted until two months after final publication of the paper itself in the JOURNAL OF APPLIED MECHANICS. Manuscript received by ASME Applied Mechanics Division, October 29, 1986; final revision, Feburary 10, 1988.

Copyright © 1988 by ASME
Downloaded 03 May 2010 to 171.66.16.21. Redistribution subject to ASME license or copyright; see http://www.asme.org/terms/Terms_Use.cfm

2 Melnikov's Method

Following Wiggins and Holmes (1987), we consider systems of the form given in (1.1) where $0<\epsilon<<1$, the right-hand side of the equation is assumed to be sufficiently differentiable (C^r, $r\geq 2$ is adequate), g_1, g_2, and g_3 are periodic in t with fixed period T, and $\mu\in\mathbf{R}^p$ is a vector of parameters. We will refer to the system obtained by setting $\epsilon=0$ as the unperturbed system

$$\begin{aligned}\dot{x}&=\frac{\partial}{\partial y}H(x,y,z)\\ \dot{y}&=\frac{-\partial}{\partial x}H(x,y,z)\\ \dot{z}&=0.\end{aligned}\tag{2.1}$$

Thus, the unperturbed system has the structure of a one-parameter (the parameter being the z variable) family of planar Hamiltonian systems. We make the following assumption concerning the unperturbed system.

Assumption. There exists an open interval $J\subset R$ such that for every $z\in J$ the associated planar system has a hyperbolic fixed point $p(z)$ with a homoclinic solution $q^z(t)$ connecting p to itself, i.e.,

$$\lim_{t\to\pm\infty} q^z(t)=p(z).$$

We note that the condition for the fixed point to be hyperbolic is that the eigenvalues of the vector field linearized about the fixed point must have nonzero real part. An easy calculation shows that the condition is equivalent to

$$\frac{\partial}{\partial x}\left(\frac{\partial H}{\partial y}\right)\frac{\partial}{\partial y}\left(\frac{-\partial H}{\partial x}\right)-\frac{\partial}{\partial y}\left(\frac{\partial H}{\partial y}\right)\frac{\partial}{\partial x}\left(\frac{-\partial H}{\partial x}\right)<0.\tag{2.2}$$

Now, since the fixed points are found as solutions of

$$\begin{aligned}\frac{\partial}{\partial y}H(x,y,z)&=0\\ \frac{-\partial}{\partial x}H(x,y,z)&=0\end{aligned}\tag{2.3}$$

using (2.3), the implicit function theorem tell us that in the x-y-z phase space this curve of fixed points can be written as a smooth function of z. We will call this curve $\mathfrak{M}$ and denote it as follows

$$\mathfrak{M}=\left\{(x(z),y(z),z)\equiv\gamma(z)\;\middle|\;\begin{aligned}&\frac{\partial}{\partial y}H(x,y,z)=0\\ &\frac{-\partial}{\partial x}H(x,y,z)=0\end{aligned}\right.$$

with

$$\frac{\partial}{\partial x}\left(\frac{\partial H}{\partial y}\right)\frac{\partial}{\partial y}\left(\frac{-\partial H}{\partial x}\right)-\frac{\partial}{\partial y}\left(\frac{\partial H}{\partial y}\right)\frac{\partial}{\partial x}\left(\frac{-\partial H}{\partial x}\right)<0\;\forall z\in J\Big\}.\tag{2.4}$$

So, the unperturbed phase space of (2.1) appears as in Fig. 1.

We see that the homoclinic solutions form a two-dimensional surface which connect $\mathfrak{M}$ to itself, we refer to this surface as the homoclinic manifold Γ and note that Γ is the intersection of the set of trajectories which are both forward and backward asymptotic to $\mathfrak{M}$ in time, or in other words, Γ is the intersection of the stable and unstable manifolds of $\mathfrak{M}$, i.e., $\Gamma=W^s(\mathfrak{M})\cap W^u(\mathfrak{M})$.

(Recall that the stable manifold of an invariant set is the set of points which approach the set asymptotically in forward time and the unstable manifold of an invariant set is the set of points which approach the set asymptotically in backward time, see Guckenheimer and Holmes (1983) for details and examples.) Now we want to determine what becomes of this structure for $\epsilon\neq 0$.

Recall that we required the fixed points which make up $\mathfrak{M}$ to have eigenvalues with nonzero real part. This property is a sufficient condition for $\mathfrak{M}$ to be a *normally hyperbolic invariant manifold* (see Fenichel (1971)). Roughly speaking, this means that vectors normal to $\mathfrak{M}$ are stretched or contracted much more rapidly than vectors tangent to $\mathfrak{M}$ under the action of the linearized flow. (Note: In our case this property is more or less obvious since $\mathfrak{M}$ consists of fixed points and hence there is no motion at all on $\mathfrak{M}$.) Now normal hyperbolicity is a desirable property since it allows us to make several immediate conclusins concerning the perturbed system regardless of the specific form of the perturbation. Specifically, $\mathfrak{M}$ persists along with its stable and unstable manifolds in the perturbed system. We state this is the form of the following theorem.

Theorem 2.1. There exists $\epsilon_o>0$ such that for $0<\epsilon<\epsilon_o<<1$ the perturbed system has a normally hyperbolic invariant one-dimensional manifold

$$\mathfrak{M}_\epsilon=\{\tilde{\gamma}(z,t;\epsilon)=\gamma(z)+\mathcal{O}(\epsilon)\,|\,z\in J\}\tag{2.5}$$

where $\tilde{\gamma}(z,t;\epsilon)$ is T periodic in t and as smooth as $\gamma(z)$. Moreover, $\mathfrak{M}_\epsilon$ has local stable and unstable manifolds, denoted $W^s_{\text{loc}}(\mathfrak{M}_\epsilon)$, and $W^u_{\text{loc}}(\mathfrak{M}_\epsilon)$, respectively, which are $C^r\epsilon$-close to $W^s_{\text{loc}}(\mathfrak{M})$ and $W^u_{\text{loc}}(\mathfrak{M})$, respectively.

Proof. See Fenichel (1971).

(Note: $C^r\epsilon$-close means that the manifold along with their first r derivatives are ϵ-close.)

This theorem gives us a great deal of information concerning the structure of the perturbed system. In particular, it tells us that the local stable and unstable manifolds of the perturbed system remains close to the unperturbed manifolds, though since the perturbation is T-periodic in time they may wiggle around periodically, but they nevertheless remain close. This fact gives us information concerning perturbed solutions on *semi-infinite time intervals* and is one of the many practical uses of the persistence theory of normally hyperbolic invariant manifolds.

Next, we want to get some information concerning the dynamics on $\mathfrak{M}_\epsilon$. The unperturbed manifold, $\mathfrak{M}$, consisted entirely of fixed points and we would not expect this very degenerate situation to persist under perturbations. Using the expression for the perturbed manifold given in (2.5), we can derive an expression for the perturbed vector field restricted to $\mathfrak{M}$. This is given by

$$\dot{z}=\epsilon g_3(\gamma(z),t)+\mathcal{O}(\epsilon^2).\tag{2.6}$$

Note that this equation is in the standard form where the method of averaging can be applied (see Guckenheimer and Holmes (1983)). Consider the averaged system

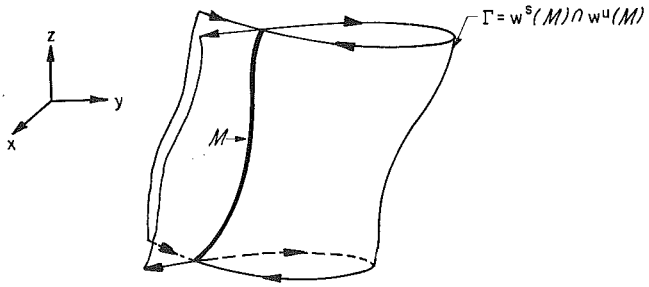

Fig. 1 Unperturbed phase space

Downloaded 03 May 2010 to 171.66.16.21. Redistribution subject to ASME license or copyright; see http://www.asme.org/terms/Terms_Use.cfm

$\dot{z} = \epsilon \overline{g_3(\gamma(z))}$, where $\overline{g_3(\gamma(z))} = \frac{1}{T}\int_0^T g_3(\gamma(z),t)dt$, (2.7)

then, we have the following theorem.

Theorem 2.2. Suppose there exists $z_o \in J$ such that

$$(1) \qquad \overline{g_3(\gamma(z_o))} = 0 \tag{2.8}$$

$$(2) \qquad \frac{d}{dz}\overline{g_3(\gamma(z_o))} \neq 0 \tag{2.9}$$

then $\gamma(z_o,t;\epsilon) = \gamma(z_o) + \mathcal{O}(\epsilon)$ is a hyperbolic periodic orbit on $\mathfrak{M}_\epsilon$ with period T. Furthermore, the oribt, restricted to $\mathfrak{M}_\epsilon$ is stable for $d/dz\ g_3(e(z_o)) < 0$ and unstable for $d/dz\ g_3(\gamma(z_o)) > 0$.

Proof. This is an immediate consequence of the averaging theorem.

(Note: recall that a hyperbolic periodic orbit is one with Floquet Multipliers not on the unit circle.)

Now we want to apply Theorems (2.1) and (2.2) to detecting transverse homoclinic oribits in the perturbed system. Since the perturbed system is nonautonomous it will be convenient to work with an associated discrete system, the so called Poincaré map which is formed by taking initial conditions and letting them evolve in time for one period of the forcing function and then plotting these new points in x–y–z space. It should be clear that a fixed point of the Poincaré map, i.e., a point which returns to where it started from after time T, corresponds to a periodic orbit of period T for the perturbed differential equation. For more information concerning Poincaré maps see Guckenheimer and Holmes (1983). We make this construction more precise by introducing time as a new dependent variable in the equations of motion

$$\begin{aligned}
\dot{x} &= \frac{\partial}{\partial y} H(x,y,z) + \epsilon g_1(x,y,z,t) \\
\dot{y} &= \frac{-\partial}{\partial x} H(x,y,z) + \epsilon g_2(x,y,z,t) \\
\dot{z} &= \epsilon g_3(x,y,z,t) \\
\dot{t} &= 1.
\end{aligned} \tag{2.10}$$

Now our equation is autonomous with a phase space $R^3 \times S^1$ where S^1 is the circle of length T and represents the periodic time dependence of the forcing function. We define the following cross section to be unperturbed vector field

$$\Sigma = \{(x,y,z,t) \mid t = t_o \in (0,T]\} \tag{2.11}$$

and the Poincaré map of Σ into itself

$$P: \Sigma \to \Sigma, \text{ or}$$

$$(x(t_o),y(t_o),z(t_o)) \to (x(t_o+T),y(t_o+T),z(t_o+T)). \tag{2.12}$$

Note that since the unperturbed system is autonomous the Poincaré map associated with the unperturbed system is trivial and $\mathfrak{M}$ and Γ appear in Σ exactly as in Fig. 1. For the perturbed system we know that $\mathfrak{M}$, along with its stable and unstable manifold persist and might appear as in Fig. 2. Now let us suppose we have found $z_o \in J$ satifying Theroem 2.2.

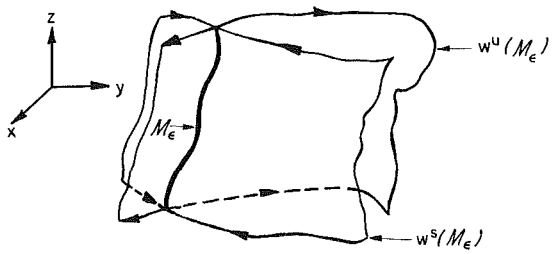

Fig. 2 Perturbed manifolds

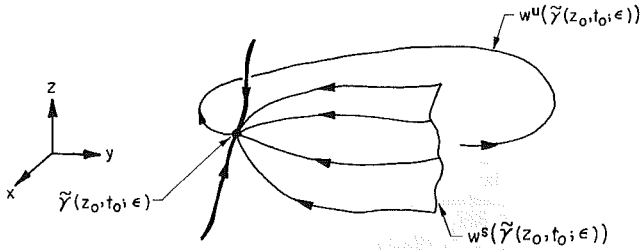

Fig. 3 Stable and unstable manifolds of $\tilde{\gamma}(z_o,t_o;\epsilon)$

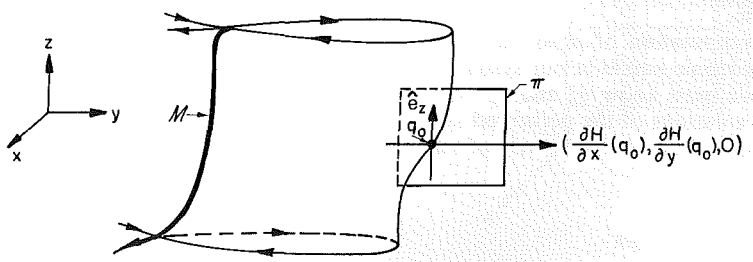

Fig. 4 Unperturbed geometry of the Melnikov Function

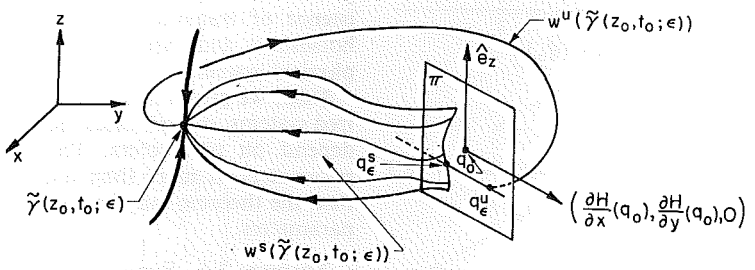

Fig. 5 Perturbed geometry of the Melnikov Function

Downloaded 03 May 2010 to 171.66.16.21. Redistribution subject to ASME license or copyright; see http://www.asme.org/terms/Terms_Use.cfm

Then $\gamma(z_o,t,\epsilon)=\gamma(z_o)+o(\epsilon)$ is a hyberolic periodic orbit on $\mathfrak{M}_\epsilon$ for the system (2.1). (For definiteness we suppose d/dz $(g_3(\gamma(z_o))<0$, the arguments go through precisely the same in the other case, this just saves us from having to draw two sets of diagrams.) Thus it appears as a hyperbolic fxed point, $\tilde{\gamma}_\epsilon(z_o,t_o;\epsilon)$, for the Poincaré map having a two-dimensional stable manifold and a one-dimensional unstable manifold denoted $W^s(\tilde{\gamma}(z_o,t_o;\epsilon))$ and $W^u(\tilde{\gamma}(z_o,t_o;\epsilon))$, respectively, see Fig. 3. Thus, if we an establish that $W^s(\tilde{\gamma}(z_o,t_o;\epsilon))$ and $W^u(\tilde{\gamma}(z_o,t_o;\epsilon))$ intersect transversely, then we will have demonstrated the existence of transverse homoclinic points which we will show in Section 3 are the *mechanisms for chaos.* In order to accomplish this we use our knowledge of the global unperturbed structure on which to develop a measurement of the distance between the perturbed manifolds.

First, let us consider the unperturbed structure. Choose a point, q_o, having z component z_o, on the homoclinic manifold Γ and consider the plane Π passing through this point which is spanned by the vectors $(\partial H/\partial x\ (q_o),\ \partial H/\partial y\ (q_o),\ 0)$ and $\hat{\mathbf{e}}_z$ where $\hat{\mathbf{e}}_z$ is a unit vector in the z direction, see Fig. 4. Note that the coincident two-dimensional stable and unstable manifolds of $\mathfrak{M}$ intersect Π along a one-dimensional curve.

Next, we consider the perturbed system and suppose that z_o is chosen via Theorem (2.2) so that $\tilde{\gamma}(z_o,t_o;\epsilon)$ is a hyberbolic fixed point on $\mathfrak{M}_\epsilon$ for the Poincaré map. Then, since the manifolds vary smoothly with ϵ, for ϵ small the perturbed manifolds might appear as in Fig. 5 with $W^u(\tilde{\gamma}(z_o,t_o;\epsilon))$ intersecting Π in a point and $W^s(\tilde{\gamma}(z_o,t_o;\epsilon))$ intersecting Π in a curve. We define the distance between $W^u(\tilde{\gamma}(z_o,t_o;\epsilon))$ and $W^s(\tilde{\gamma}(z_o,t_o;\epsilon))$ in the following manner: let q_ϵ^u denote $W^u(\tilde{\gamma}(z_o,t_o;\epsilon))\ \cap\Pi$ and let q_ϵ^s denote the point on $W^s(\tilde{\gamma}(z_o,t_o;\epsilon))\cap\Pi$ having the same z value as q_ϵ^u. Then the distance between $W^s(\tilde{\gamma}(z_o,t_o;\epsilon))$ and $W^u(\tilde{\gamma}(z_o,t_o;\epsilon))$ is defined as follows:

$$d(q_o;\epsilon)=\frac{\left(\frac{\partial H}{\partial x}(q),\ \frac{\partial H}{\partial y}(q),0\right)\cdot(q_\epsilon^u-q_\epsilon^s)}{\sqrt{\left(\frac{\partial H}{\partial x}(q_o)\right)^2+\left(\frac{\partial H}{\partial y}(q_o)\right)^2}} \tag{2.13}$$

Note that $d=0$ if and only if $q_\epsilon^u=q_\epsilon^s$. We choose this form of a distance measurement for two reasons: (1) the sign of d tells us the relative orientation of the manifolds and, (2) it lends itself to a computable expression.

Next we consider the computation of d so that we may verify the existence of homoclinic points in our system. Note that from the form of d we must know q_ϵ^s and q_ϵ^u which is equivalent to knowing the solutions of the perturbed system. In order to get around this, we expand d in powers of ϵ about $\epsilon=0$

$$\begin{aligned} d(q_o;\epsilon) &= \epsilon\frac{\left(\frac{\partial H}{\partial x}(q_o),\frac{\partial H}{\partial y}(q_o),0\right)\cdot\left(\frac{\partial q_\epsilon^u}{\partial\epsilon}\Big|_{\epsilon=0}-\frac{\partial q_\epsilon^s}{\partial\epsilon}\Big|_{\epsilon=0}\right)}{\sqrt{\left(\frac{\partial H}{\partial x}(q_o)\right)^2+\left(\frac{\partial H}{\partial y}(q_o)\right)^2}} \\ &\quad+\mathcal{O}(\epsilon^2) \\ &= \epsilon\frac{M(q_o)}{\sqrt{\left(\frac{\partial H}{\partial x}(q_o)\right)^2+\left(\frac{\partial H}{\partial y}(q_o)\right)^2}}+\mathcal{O}(\epsilon^2) \end{aligned} \tag{2.14}$$

where $M(q_o)$ is defined to be the Melnikov function. Thus since

$$\sqrt{\left(\frac{\partial H}{\partial x}(q_o)\right)^2+\left(\frac{\partial H}{\partial y}(q_o)\right)^2}$$

is not zero on the homoclinic manifold (it's only zero on $\mathfrak{M}$), we see that $M(q_o)$ gives a measure of the distance between the perturbed manifolds. The reason $M(q_o)$ bears the name of Melnikov is that through a trick due to Melnikov it can actually be explicitly computed without solving the perturbed equations of motion, we state the result here:

$$\begin{aligned} M(t_o) &= \int_{-\infty}^{\infty}\nabla H(q_o^{z_o}(t_o))\cdot g(q_o^{z_o}(t),t+t_o)dt \\ &\quad-\frac{\partial H}{\partial z}(\gamma(z_o))\int_{-\infty}^{\infty}g_3(q_o^{z_o}(t),t+t_o)dt \end{aligned} \tag{2.13}$$

where

$$\nabla H=\left(\frac{\partial H}{\partial x},\frac{\partial H}{\partial y},\frac{\partial H}{\partial z}\right),$$

$g=(g_1,g_2,g_3)$, z_o is chosen via Theroem (2.2) in order that $\tilde{\gamma}(z_o,t_o;\epsilon)$ is a hyperbolic fixed point for the Poincaré map of the perturbed system and $q_o^{z_o}(t)$ is the homoclinic orbit in the unperturbed system connecting $p(z_o)$ to itself. (Note: Wiggins and Holmes (1987) show that the improper integral (2.15) converges conditionally. In theory this causes no problems, however, numerical computations of (2.15) can be tricky since the integral may exist only for certain sequences of times which approach plus and minus infinity. This issue is dealt with directly in the following paper, Shaw and Wiggins (1988).) Note the functional dependence of the Melnikov function. In our abstract derivation of the Melnikov function we defined the distance between the stable and unstable manifolds at a specific point q_o, since the manifolds are two-dimensional they can be parameterized by two variables, in our case t_o and z_o, but we fix z_o when we find a hyperbolic fixed point on $\mathfrak{M}_\epsilon$ via Theorem (2.2). This leaves the Melnikov function as a function of just one scalar parameter which we call t_o. Geometrically, varying t_o corresponds to moving Π around the homoclinic manifold, (see Wiggins and Holmes (1987) for a more thorough explanation of the geometry), however, we remark that their paper contains an incorrect final form for the Melnikov function which has been corrected here.

We now state our main theorems.

Theorem 2.3. Suppose there exits a point $\bar{t}_o$ such that

(1) $M(\bar{t}_o)=0$

(2) $\dfrac{\partial M}{\partial t_o}(\bar{t}_o)\neq 0$

then for ϵ sufficiently small, near this point $W^s(\tilde{\nu}(z_o,t_o,\epsilon))$ and $W^u(\tilde{\gamma}(z_o,t_o;\epsilon))$ intersect transversely.

We remark that the importance of this theorem is that it gives us an explicit computational way of verifying the existence of transverse homoclinic points and hence, Smale horseshoes and their attendant chaotic dynamics in specific physical systems.

Next, we give a thoerem which is applicable to parameterized systems, in such cases the Melnikov function will likewise depend on parameters. The theorem is stated for scalar parameters, if more than one parameter occurs in a system then the theorem may be applied by fixing all but one of the parameters.

Theorem 2.4 Suppose the perturbed system (2.1) depends on a scalar parameter $\mu\in R$ and that there exists a point $(\bar{t}_o,\bar{\mu})$

Downloaded 03 May 2010 to 171.66.16.21. Redistribution subject to ASME license or copyright; see http://www.asme.org/terms/Terms_Use.cfm

such that

$$(1)\qquad M(\bar{t}_o,\bar{\mu})=0$$

$$(2)\qquad \frac{\partial M}{\partial t_o}(\bar{t}_o,\bar{\mu})=0$$

$$(3)\qquad \frac{\partial^2 M}{\partial t_o^2}(\bar{t}_o,\bar{\mu})\neq 0$$

$$(4)\qquad \frac{\partial M}{\partial \mu}(\bar{t}_o,\bar{\mu})\neq 0$$

then for ϵ sufficiently small, near $\bar{\mu}$ there is a bifurcation value at which quadratic homoclinic tangencies occur.

The proofs of Theorems (2.3) and (2.4) consist of simple applications of the implicit function theorem and can be found in Wiggins and Holmes (1987).

3 The 3-*d* Smale Horseshoe and Transverse Homoclinic Points

Here we describe a three-dimensional mapping which has an amazingly complicated structure on which the dynamics of the map is chaotic. Though this map may appear somewhat artifical, we will see that it contains the same dynamics as that exhibited by our system and thus by physical systems such as the one considered in the following paper, Shaw and Wiggins (1988).

We give a combination geometrical-analytical definition of our map. Consider a map f from the unit cube C in R^3 into R^3

$$f: C\rightarrow R^3 \tag{3.1}$$

where

$$C=\{(x,y,z)\in R^3 \mid 0\leq x\leq 1,0\leq y\leq 1,0\leq z\leq 1\}$$

We assume that f contracts the x and y directions uniformly, stretches the z direction uniformly, and folds the cube over, laying it back on itself in the manner shown in Fig. 6. In particular, let us consider the "horizontal" slabs

$$H_o=\left\{(x,y,z)\in R^3 \mid 0\leq x\leq 1,0\leq y\leq 1,0\leq z\leq \frac{1}{\gamma}\right\}.$$

$$H_1=\left\{(x,y,z)\in R^3 \mid 0\leq x\leq 1,0\leq y\leq 1,1-\frac{1}{\gamma}\leq z\leq 1\right\} \tag{3.2}$$

where γ is a constant greater then 2. We assume that f acts affinely (i.e., linear plus a translation) on H_o and H_1 with the form given below

on H_o:
$$f=\begin{pmatrix}\lambda & 0 & 0\\ 0 & \mu & 0\\ 0 & 0 & \gamma\end{pmatrix}+\begin{pmatrix}\frac{1-\lambda}{2}\\ 0\\ 0\end{pmatrix}$$

with
$$\lambda,\mu<\frac{1}{2},\gamma>2 \tag{3.3}$$

on H_1:
$$f=\begin{pmatrix}\lambda & 0 & 0\\ 0 & -\mu & 0\\ 0 & 0 & -\gamma\end{pmatrix}+\begin{pmatrix}\frac{1-\lambda}{2}\\ 1\\ \gamma\end{pmatrix}$$

which take H_o and H_1 to the "vertical" slabs V_o and V_1 defined below

$$V_o=f(H_o)=\left\{(x,y,z)\in R^3 \mid \frac{1-\lambda}{2}\leq x\leq \frac{1+\lambda}{2},\right.$$

$$\left.0\leq y\leq \mu,0\leq z\leq 1\right\}$$

$$V_1=f(H_1)=\left\{(x,y,z)\in R^3 \mid \frac{1-\lambda}{2}\leq x\leq \frac{1+\lambda}{2},\right.$$

$$\left.1-\mu\leq y\leq 1,0\leq z\leq 1\right\}. \tag{3.4}$$

Also, $f^{-1}(C)\cap C$ will appear as in Fig. 7.

Now considering f as a dynamical system defined on C, we wish to understand the nature of the iterates of f, in particular, we would like to determine the nature of the points which remain in C under all iterations of f, this set will be called the nonwandering set of f(see Guckenheimer and Holmes (1983)) and is denoted by the symbol Λ. By definition, Λ is given by

$$\Lambda=\ldots\cap f^{-n}(C)\cap\ldots\cap f^{-1}(C)\cap C\cap f(C)\cap\ldots$$

$$\cap f^n(C)\cap\ldots=\bigcap_{j=-\infty}^{\infty} f^j(C). \tag{3.5}$$

(Note: The following is standard notation for iterates of maps; $f^n(x)\equiv(n$ applications of $f)=f(f(\ldots(f(x))\ldots))$.

We want to give a geometrical description of this set. This is most easily accomplished by describing separately the two "halves" of Λ, i.e.,

$$\Lambda=\Lambda_+\cap\Lambda_-$$

$$=\left(\bigcap_{j=-\infty}^{o} f^j(C)\right)\cap\left(\bigcap_{j=0}^{+\infty} f^j(C)\right) \tag{3.6}$$

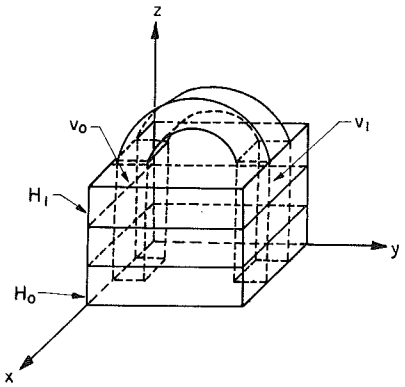

Fig. 6 $f(C)\cap C$

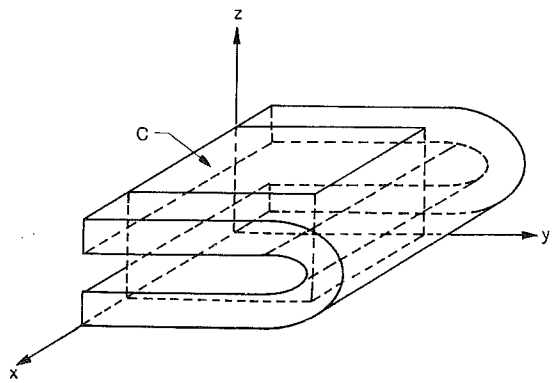

Fig. 7 $f^{-1}(C)\cap C$

Downloaded 03 May 2010 to 171.66.16.21. Redistribution subject to ASME license or copyright; see http://www.asme.org/terms/Terms_Use.cfm

where Λ_+ is the set of points which remain in C under all forward iterations by f and Λ_-, is the set of points remaining in C under all backwards iterations by f.

Before beginning our construction of Λ, we want to firmly emphasize the key geometric and analytic features of the definition of f which are directly responsible for the results to follow.

Observation: Since $f(H_i)=V_i$, $i=0$, 1, with horizontal (resp. vertical) boundaries of H_i mapping to horizontal (resp. vertical) boundaries of V_i under f, it follows that given any vertical slab V contained in V_o or V_1, since V intersects both horizontal boundaries of H_o and H_1, $f(V)\cap C$ consists of precisely two vertical slabs, one in V_o and the other in V_1 and furthermore, the x and y widths of the sides of V are decreased by factors λ and μ, respectively, under the mapping of f. Similary, let H by any horizontal slab in H_o of H_1, then H intersects the vertical boundaries both V_o and V_1 and consequently $f^{-1}(H)\cap C$ consists of precisely two horizontal slabs, one in H_o and the other in H_1. Moreover, the z width of H is decreased by a factor $1/\gamma$ under the mapping by f^{-1}.

Now we begin by constructing $\Lambda_-=\bigcap_{j=0}^{\infty} f^j(C)$ inductively. We will do this by constructing $\Lambda^n_-=\bigcap_{j=0}^{n} f^j(C)$ and then determining the nature of the limit as $n\to\infty$.

$\Lambda^1_- = C\cap f(C)$: By the definition of f, this consists of the two disjoint vertical slabs, V_o and V_1, with sides having x widths and y widths of λ and μ, respectively. This set can be given a more detailed labelling (which is useful later) as follows:

$$\Lambda^1_- = C\cap f(C) = \bigcup_{a_{-1}=0,1} V_{a_{-1}}$$

where $$V_{a_{-1}} = \{p\in C \mid p\in V_{a_{-1}}\}$$

Also, we make the (at present apparently trivial) remark that each point in Λ^1_- can be labelled by a sequence of 0's and 1's of length one using the criteria that a point is labelled 0 if it is in V_o and 1 if it is in V_1.

$\Lambda^2_- = C\cap f(\Lambda^1) = C\cap f(C)\cap f^2(C)$: Note from the observation made previously, since Λ^1_- consists of two vertical slabs then $f(\Lambda^1_-)\cap C$ consists of four vertical slabs, two in V_o and two in V_1. Moreover, the x widths and y widths of the four vertical slabs are given by λ^2 and μ^2, respectively. Thus set is denoted as follows:

$$\Lambda^2_- = C\cap f(C)\cap f^2(C) = \bigcup_{a_{-1}a_{-2}=0,1} f(V_{a_{-2}})\cap V_{a_{-1}}$$

$$= \bigcup_{a_{-1}a_{-2}=0,1} V_{a_{-1}a_{-2}} \tag{3.7}$$

where

$$V_{a_{-1}a_{-2}} = \{p\in C \mid p\in V_{a_{-1}}, f^{-1}(p)\in V_{a_{-2}}\}$$

Each point in Λ^2_- can be labelled by a sequence of 0's and 1's of length 2 according to the rule $p\to a_{-1}a_{-2}$ where $p\in V_{a_{-1}}$, $f^{-1}(p)\in V_{a_{-2}}$ with a_{-i}, $i=1,2$ taking values 0 and 1. Continuing the construction in this manner, at the nth step we obtain 2^n vertical slabs, 2^{n-1} in V_o and 2^{n-1} in V_1, each having x width and y width of λ^n and μ^n, respectively. This set is denoted as follows.

$$\Lambda^n_- = C\cap f(C)\cap \ldots \cap f(C)$$

$$= \bigcup_{\substack{a_{-i}=0,1\\ i=1,\ldots,n}} f(V_{a_{-2}\ldots a_{-n}})\cap V_{a_{-1}}$$

$$= \bigcup_{\substack{a_{-i}=0,1\\ i=1,\ldots,n}} V_{a_{-1}\ldots a_{-n}} \tag{3.8}$$

where

$$V_{a_{-1}\ldots a_{-n}} = \{p\in C \mid f^{-i+1}(p)\in V_{a_{-i}},\quad i=1,\ldots n\}.$$

Similar to the previous cases, each point in this set can be labelled by a sequence of 0's and 1's of length n according to the rule $p\to a_{-1}\ldots a_{-n}$ where $a_{-i}=0$ or 1 and each element of the sequence is chosen according to the rule, a_{-i} if

$$f^{-i+1}(p)\in V_{a_{-i}}, i=1,\ldots,n.$$

Now in the limit as $n\to\infty$, $2^n\to\infty$ and since λ,μ, $<1/2$, $\lambda^n\to 0$ and $\mu^n\to 0$. Thus we see the Λ_- consists of an infinite number of vertical lines in V_o and V_1, the set is denoted as follows

$$\Lambda_- = \bigcap_{j=0}^{\infty} f^j(C) = \bigcup_{\substack{a_{-i}=0,1\\ i=1,\ldots}} f(V_{a_{-2}\ldots a_{-n}\ldots})\cap V_{a_{-1}}$$

$$\bigcup_{\substack{a_{-i}=0,1\\ i=1,\ldots}} V_{a_{-1}\ldots a_{-n}\ldots} \tag{3.9}$$

where

$$V_{a_{-1}\ldots a_{-n}\ldots} = \{p\in C \mid f^{-i+1}(p)\in V_{a_{-i}}, i=1,\ldots\}.$$

Also, to each point in Λ_- we can now associate an infinite sequence of 0's and 1's according to our usual rule, however, it will be important later to utilize the following fact. Since $f(H_j)=V_j$, $j=0,1$, it then follows that $f^{-i+1}(p)\in V_{a_{-i}}$, implies $f^{-j}(p)\in H_{a_{-i}}$, thus, Λ_- can be written equivalently as

$$\Lambda_- = \{p\in C \mid f^{-i}(p)\in H_{a_{-i}}, i=1,\ldots; a_{-i}=0 \text{ and } 1\} \tag{3.10}$$

In this case, the ith entry in the infinite sequence of 0's and 1's associated to any point $p\in\Lambda_-$ tells us that $f^{-i}(p)\in H_{a_{-i}}$ for $i=1,\ldots$.

Next, we construct $\Lambda_+=\bigcap_{j=-\infty}^{o} f^j(C)$ in the same manner. We have $\Lambda^1_+ = C\cap f^{-1}(C)$ consisting of the two horizontal slabs H_o and H_1, each having width $1/\gamma$, $\gamma>2$. Using the previous observation and continuing the construction inductively, at the nth step we obtain $\Lambda^n_+ = C\cap f^{-1}(C)\cap \ldots \cap f^{-n}(C)$ which consists of 2^n horizontal slabs with 2^{n-1} in H_o and 2^{n-1} in H_1 each having width $1/\gamma^n$. Also each point in Λ^n_+ can be labelled a sequence of symbols of 0's and 1's of length n by the same rule as given in the construction on Λ_-. Thus, passing to the limit as $n\to\infty$ we see that Λ_+ consists of an infinite number of horizontal "slices" in $H_o\cup H_1$ each having zero width. Λ_+ can be written as follow:

$$\Lambda_+ = \bigcap_{j=-\infty}^{o} f^j(C) = \bigcup_{\substack{a_i=0,1\\ i=0,1,\ldots}} f(H_{a_1\ldots a_n\ldots})\cap H_{a_o}$$

$$= \bigcup_{\substack{a_i=0,1\\ i=0,1,\ldots}} H_{a_o\ldots a_n\ldots} \tag{3.11}$$

where

$$H_{a_o\ldots a_n\ldots} = \{p\in C \mid f^i(p)\in H_{a_i}, i=0,1,\ldots\}.$$

Therefore, the nonwandering set $\Lambda=\Lambda_+\cap\Lambda_-$ consists of the

Downloaded 03 May 2010 to 171.66.16.21. Redistribution subject to ASME license or copyright; see http://www.asme.org/terms/Terms_Use.cfm

intersection of an infinite number of horizontal slices with an infinite number of vertical lines. Since a given vertical line intersects a given horizontal slice in a unique point, we see that Λ consists of an infinte set of points contained in $[H_o \cup H_1] \cap [V_o \cup V_1]$. Recall that every point in Λ_+ and Λ_- could be associated with an infinite sequence of 0's and 1's and that this sequence contained information concerning the location of any iterate of this point. Now since $\Lambda = \Lambda_+ \cap \Lambda_-$, we can label any point p in Λ by a *bi-infinite* sequence of 0's and 1's using the following rule

$$p \in \Lambda, p \rightarrow \{ \ldots a_{-n} \ldots a_{-1} \bullet a_o a_1 \ldots a_n \ldots \} \tag{3.12}$$

where the ith element of the sequence is given by a_i corresponding to $f^i(p) \in H_{a_i}, a_i = 0$ and 1. Thus, we see that since every point $p \in \Lambda$ is given by the intersection of a vertical line and a horizontal slice, the bi-infinite sequence of 0's and 1's associated with p is given by concatenating the infinite sequences associated to the particular vertical line and horizontal slice of which it arises through their intersection. Furthermore, since the intersection of an element in Λ_+ and an element in Λ_- results in a unique point (which is due to the fact that H_o and H_1 are disjoint) there is only one way to associate a bi-infinite sequence of 0's and 1's to any point in Λ by our rule.

Now that we have constructed the nonwandering set of f and shown that it contains an infinite number of points (indeed, actually an *uncountable* infinity of points, see Devaney (1986)) we want to obtain more detailed information concerning the iterates (or orbits) of f on Λ. Specifically, are there periodic orbits, quasiperiodic orbits, etc?. In order to accomplish this task we will use the very clever technique known as *symbolic dynamics* (see Moser (1973) for a history of the method) which will give the justification for our labelling of points in Λ by bi-infinite sequences of 0's and 1's via our chosen rule. But first, we must make a short abstract digression and give a brief description of the "space" of symbol sequences.

We will consider the collection of bi-infinite sequences of 0's and 1's which we will call E. We want to introduce some structure on this space in the form of a metric in order to make precise the notion of closeness of elements of E. Let

$$a = \{ \ldots a_{-n} \ldots a_{-1} \bullet a_o \ldots a_n \ldots \},$$

$$b = \{ \ldots b_{-n} \ldots b_{-1} \bullet b_o \ldots b_n \ldots \} \in E. \tag{3.13}$$

We define the distance between a and b as follows

$$d(a,d) = \sum_{i=-\infty}^{\infty} \frac{\delta_i}{2|i|} \text{ where } \delta_i = \begin{pmatrix} 0 \text{ if } a_i = b_i \\ 1 \text{ if } a_i \neq b_i \end{pmatrix}. \tag{3.14}$$

Next we define a mapping G, called the shift mapping, of E into to itself as follows

$$G\{ \ldots a_{-n} \ldots a_{-1} \bullet a_o \ldots a_n \ldots \}$$
$$= \{ \ldots a_{-n} \ldots a_{-1} \ldots a_o \bullet a_1 \ldots a_n \ldots \} \tag{3.15}$$

thus for a given symbol sequence, G merely has the effect of shifting the decimal point one place to the right. Now the orbit structure of G acting on E is particularly simple, it is not hard to see that G has precisely two fixed points, namely the sequences $\{ \ldots 0000.0000 \ldots \}$ and $\{ \ldots 11111.11111 \ldots \}$ (Notation: Sequences which periodically repeat will be denoted by the finite repeating block both before and after the decimal point with an overbar, e.g., the sequence consisting of the periodically repeating block 10, i.e., $\{ \ldots 101010.101010 \ldots \}$, is denoted $\{\overline{10.10}\}$). Also G has precisely one orbit of period two given by the orbit of $\{\overline{10.10}\}$ (or $\{\overline{01.01}\}$) since

$$G\{\overline{10.10}\} = \{\overline{01.01}\}$$

and

$$G\{\overline{01.01}\} = \{\overline{10.10}\}$$

therefore,

$$G^2\{\overline{10.10}\} = \{\overline{10.10}\}.$$

Continuing arguing in this manner, it is not difficult to see that G has a countable infinity of periodic orbits of arbitrarily high period and that these are the orbits of periodic sequences. Another fact is that G has an uncountable infinity of nonperiodic oribts. This can be seen as follows: any given bi-infinite sequence of 0's and 1's can be written as a one-sided infinite sequence as follows

$$\{ \ldots a_{-n} \ldots a_{-1} \bullet a_o a_1 \ldots a_n \ldots \}$$
$$\rightarrow \{ \bullet a_0 a_{-1} a_1 a_{-2} a_2 a_{-3} a_3 \ldots \}. \tag{3.16}$$

We will take as a known fact that the set of irrational numbers in the closed unit interval [0,1] is uncountable. Now every number in [0,1] can be presesented in base two as a binary expansion of 0's and 1's with the irrationals corresponding to those sequences which never repeat. Thus, we have an uncountable infinity of infinite sequences of 0's and 1's and by (3.16) above, an uncountable infinity of bi-infinite sequences of 0's and 1's and the orbits of these sequences are nonperiodic. One last fact concerning the dynamics of G and E is that we can find a point $p \in E$ whose orbit is dense in E, this means that given any other point $p' \in E$, some iterate of p is arbitrarily close to p'. We collect these facts together in the following theorem.

Theorem 3.1. The shift map G acting on E has

(1) A countable infinity of periodic oribts of arbitrarily high period.
(2) An uncountable infinity of nonperiodic orbits.
(3) A dense orbit.

For a proof of Theorem 3.1, we refer the reader to Devaney (1986).

So we see that we have a large amount of knowledge concerning the dynamics of G on E. Now we want to relate this to the dynamics of the horseshoe map f on its invariant set Λ.

Recall that we have a well-defined map, which we now call ϕ, from Λ into E

$$\phi : \Lambda \rightarrow E$$
$$p \rightarrow \phi(p) = \{ \ldots a_{-n} \ldots a_{-1} \bullet a_o a_1 \ldots a_n \ldots \}$$
$$\text{where } f^i(p) \in H_{a_i} \text{ with } a_i = 0 \text{ or } 1. \tag{3.17}$$

Note in particular that by the definition of ϕ we have $\phi(f(p)) = \{ \ldots a_{-n} \ldots a_{-1} a_o \bullet a_1 \ldots a_n \ldots \}$ so that we have the following relation

$$G \bullet \phi(p) = \phi \bullet f(p) \tag{3.18}$$

Now suppose that ϕ is a continuous invertible map having a continuous inverse, then we can write

$$\phi^{-1} \bullet G \bullet \phi(p) = f(p) \tag{3.19}$$

and, thus, for any n

$$f^n(p) = \frac{(\phi^{-1} \bullet G \bullet \phi) \bullet (\phi^{-1} \bullet G \bullet \phi) \bullet \ldots \bullet (\phi^{-1} \bullet G \bullet \phi(p))}{(n \text{ factors})}$$
$$= \phi^{-1} \bullet G^n \bullet \phi(p). \tag{3.20}$$

Now given any point $p \in \Lambda$ the orbit of p under f is given by

$$\{ \ldots f^{-n}(p), \ldots, f^{-1}(p), p, f(p), \ldots f^n(p), \ldots \}. \tag{3.21}$$

Downloaded 03 May 2010 to 171.66.16.21. Redistribution subject to ASME license or copyright; see http://www.asme.org/terms/Terms_Use.cfm

So by (3.20), given any orbit in Λ, there is a corresponding orbit in E under the shift map. In particular, Theorem 3.1 goes over directly to f restricted to Λ. Now, all of this is true provided ϕ is continuous and invertible with continuous inverse. We will state, without proof, that this is indeed the case (for a proof see Guckenheimer and Holmes (1983)).

Theorem 3.2. ϕ is a continuous invertible map having a continuous inverse of Λ onto E.

So we can state the following theorem concerning the dynamics of the horseshoe map.

Theorem 3.3. f restricted to Λ (written $f|\Lambda$) has

(1) A countable infinity of periodic oribts of arbitrarily high period with the periodic points being dense in Λ.
(2) An uncountable infinity of nonperiodic orbits.
(3) A dense orbit.

Λ is a *chaotic invariant set* as defined by Davaney (1986). Devaney defines an invariant set to be chaotic if it satisfies properties (1) and (3) of Theorem 3.3 and also displays the property of *sensitive dependence on initial conditions* which we now describe.

Let $p\in\Lambda$ with corresponding symbol sequence $\phi(p)=\{\ldots a_{-n}\ldots a_{-1}\bullet a_o\ldots a_n\ldots\}$. We want to consider points close to p and how they behave under iteration by f compared to p. Let $\epsilon>0$ be given, then we consider an ϵ neighborhood of p determined by the usual topology of the plane. In E, this neighborhood goes over to a neighborhood of $\phi(p)$ via the homeomorphism ϕ. More precisely, there exists an integer $N=N(\epsilon)$ such that the corresponding neighborhood of $\phi(p)$ is given by the set of sequences $a'=\{\ldots a'_{-n}\ldots a'_{-1}\bullet a'_0\ldots a'_n\ldots\}\in E$ such that $a_i=-a'_i$, $|i|\le N$. Now suppose the $N+1$ entry in the sequence corresponding to $\phi(p)$ is 0 and in the $N+1$ sequence corresponding to a' is 1. Thus, after N iterations, no matter how small ϵ, the point p is in H_o and the point, say p', corresponding to a'_1 under ϕ^{-1}, is in H_1. Therefore for any point $p\in\Lambda$, no matter how small a neighborhood of p which we consider, there is at least one point in this neighborhood, say p', such that after a finite number of iterations, p and p' have separated by some fixed distance. A system displaying such behavior is said to exhibit *sensitive dependence on initial conditions*. Note: In the companion to this paper (Shaw and Wiggins (1988)) we will give a very graphic illustration of this property for a specific physical system.

We want to point out that the orbits in Λ are not so-called steady states of the system since in terms of stability they are all of saddle type (Note: This can be ascertained from the form of f given in (3.3)). However, since Λ is nonlocal and occurs in an extended region of space its presence has a striking effect on the dynamics of the system. Indeed, the property of sensitive dependence on initial conditions extends by continuity to nearby initial conditions which can result in arbitrarily close initial conditions ending up in final states arbitrarily far apart. Also, numerical evidence indicates that horseshoes are often the heart of the "strange attractors" which have been observed in many systems (see Guckenheimer and Holmes (1983) for examples). In fact, a working definition of a strange attractor is that a strange attractor is an attractor which contains a horseshoe (Guckenheimer and Holmes (1983)). Therefore an understanding of the mechanisms for the creation of horseshoe in systems is necessary for the understanding of the more complex phenomena of strange attractors.

Now we want to show how the complicated dynamics of the Smale horseshoe map can be present in any smooth map which has a *transverse homoclinic point*.

Note that the crucial elements in the definition of f which resulted in the existence of the chaotic invariant set Λ were the following:

(1) There existed horizontal slabs H_o and H_1 which were mapped to the vertical slabs V_o and V_1 under f with V_o and V_1 each intersecting both H_o and H_1.
(2) The horizontal directions were stronly uniformly contracted and the vertical directions were strongly uniformly expanded.

Condition (1) allowed us to inductively construct the nonwandering set of f by constructing $\bigcap_{j=0}^{n} f^j(C)$ and $\bigcap_{j=-n}^{0} f^j(C)$, taking the limit as $n\to\infty$, and then taking the intersection of the resulting two sets. At each step of the induction process we were able to label each element of the set by a sequence of 0's and 1's according to whether or not it was in H_o or H_1 for a corresponding iterate. By conditions (2), in the limit as $n\to\infty$, $\bigcap_{j=0}^{\infty} f^j(C)$ consisted of an infinite number of vertical lines and $\bigcap_{j=-\infty}^{0} f^j(C)$ consisted of an infinite number of horizontal slices and since each slice intersected each line in a unique point our rule for labelling points in $\Lambda=\bigcap_{j=-\infty}^{0} f^j(C)\cap\bigcap_{j=0}^{\infty} f^j(C)$ by bi-infinite sequences of 0's and 1's led to a unique labelling for each point in Λ. Thus, we ended up with a mapping from Λ to the space of bi-infinite sequences of 0's and 1's. This mapping was continuous and invertible with continuous inverse and this, coupled with our rule for constructing the mapping, resulted in the dynamics of f restricted to Λ being identical to the shift map acting on the space of bi-infinite sequences of 0's and 1's.

Now it is certainly not necessary for the mapping to be affine and for H_o and H_1 to be rectangles in order for the map to exhibit the dynamics of the horseshoe. Conley and Moser developed general conditions for maps to possess chaotic invariant sets (see Moser (1973)). We will briefly decribe these conditions. Let D be a region of R^3 and we consider a smooth map of D into R^3. First we need to weaken our notion of horizontal and vertical slabs. Let x, y denote the horizontal (contacting) directions and z the vertical (expanding) directions. Then we define horizontal slices (resp. vertical slices) as graphs of functions over the horizontal (resp. vertical) variables with a uniform condition of their derivatives such that a horizontal slice may be only intersect a vertical slice in a unique point. We then define horizontal (resp. vertical) slabs bv taking unions of horizontal (resp. vertical) slices in order to give them width. With horizontal and vertical slabs defined, we then postulate that conditions (1) and (2) hold for f and then Moser (1973) shows that this is sufficient for the map to contain a chaotic invariant set with precisely the same properties of Λ. We refer to reader to Moser's monograph for the details.

Now let us suppose that we have a smooth map f of R^3 and

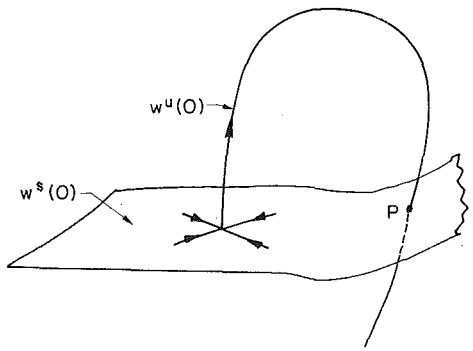

Fig. 8 Stable and unstable manifolds of the origin

Downloaded 03 May 2010 to 171.66.16.21. Redistribution subject to ASME license or copyright; see http://www.asme.org/terms/Terms_Use.cfm

into R^3 which has a fixed point at the origin. Let us further suppose that (in some appropriate coordinate system) the Jacobian of f at the origin takes the form

$$Df(0) = \begin{pmatrix} \lambda & 0 & 0 \\ 0 & \mu & 0 \\ 0 & 0 & \gamma \end{pmatrix} \tag{3.22}$$

where $|\lambda|, |\mu| < 1, |\gamma| > 1$. Then by the invariant manifold theorem (see Fenichel (1971) or Hirsch, Pugh, and Shub (1977)) we know that there exists a two-dimensional stable manifold, $W^s(0)$, defined to be the set of points which approach the origin under forward iteration by f, and a one-dimensional unstable manifold, $W^u(0)$, defined to be the set of points which approach the origin under backward iterations by f. (Note: A fixed point of a map whose Jacobian has no eigenvalues on the unit circle is called *hyperbolic*).

Now suppose we have a situation where the stable manifold of the origin intersects the unstable manifold of the origin transversely (i.e., they pass through each other with nonzero speed) at a point p as shown in Fig. 8. Now let us iterate p by f. Since $W^u(0)$ and $W^s(0)$ are invariant manifolds then p must remain on both manifolds simultaneously under all possible iterations by f, as the diagram shows in Fig. 9.

We have only drawn part of the picture in Fig. 9 since the manifolds continue to intertwine and accumulate on each other. The point p is called a *transvere homoclinic point* and we will now show that the homoclinic points arising from transverse interactions of hyperbolic fixed points of maps give rise to Smale horseshoes.

We consider a neighborhood $\mathfrak{N}$ of the origin in which the behavior of the map is essentially decribed by the linearized map given in (3.22). Then, since $p \in W^s(0) \cap W^u(0)$, there must exist integers n_o and n_1 such that $f^{n_o}(p) \equiv p_o \in \mathfrak{N}$ and $f^{-n_1}(p) \equiv p_1 \in \mathfrak{N}$ (see Fig. 10). We choose two horizontal slabs H_o and H_1 near p_o. Then there must exist some integer N such that f^N maps H_o and H_1 into a neighborhood of p_1 as shown in Fig. 10. (Note: N can be adjusted by taking $\mathfrak{N}$ smaller, points closer to the stable manifold take longer to reach a neighborhood of p_1). Since f is described by its linearization for $\mathfrak{N}$ sufficiently small, we see that the x and y directions are contracted by factors λ^N, μ^N, and the z direction is expanded by a factor γ^N. Thus, by taking H_o and H_1 closer to $W^s(0)$, we can make the contraction and expansion rates arbitrarily large. Next we consider the map $f^{n_o+n_1}$ which takes the point p_1 to p_o and hence a sufficiently small neighborhood of p_1 to a neighborhood of p_o. Since $f^N(H_o)$ and $f^N(H_1)$ are essentially "parallel" to $W^u(O)$ (Note: They can actually be made as parallel to $W^u(0)$ as we wish by taking H_o and H_1 closer to $W^s(0)$) then $f^{N+n_o+n_1}(H_o)$ and $f^{N+n_o+n_1}(H_1)$ intersect H_o and H_1 as shown in Fig. 10. Thus, the map $f^{N+n_o+n_1}$ defined in a sufficiently small neighborhood of p_o has two horizontal slabs which are mapped back over themselves with their horizontal directions contracted and their vertical directions expanded by an arbitrarily large amount. Therefore, just as in our simple affine model of the three-dimensional Smale horseshoe, $f^{N+n_o+n_1}$ has a complicated invariant set on which the dynamics are precisely the same as the shift map acting on the space of bi-infinite sequences of 0's and 1's. We refer the reader to Moser (1973) for an indication of how to make these last remarks mathematically rigorous.

Actually, our result here is a special case of a more general result known as the Smale-Birkhoff homoclinic theorem (see Guckenheimer and Holmes (1983)). This theorem states that given any smooth mapping of R^n into itself (n arbitrary) having a hyperbolic fixed point whose stable and unstable manifolds intersect transversely, the map possesses an invariant set on which the dynamics is the same as the dynamics of the shift map acting on the space of bi-infinite sequences of 0's and 1's (actually, the theorem can be generalized to an infinite number of symbols, see Moser (1973)).

Acknowledgment

This work was partially supported by grants from NSF(MSM-8613294) and DARPA.

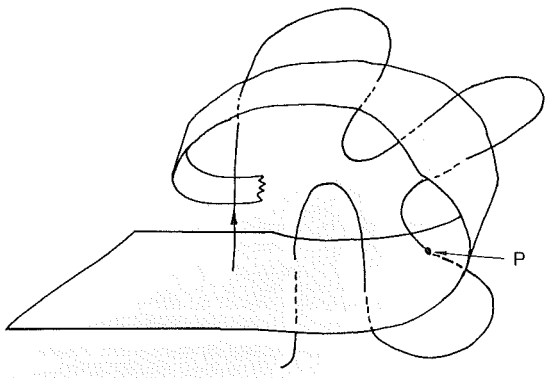

Fig. 9 Intersections of stable and unstable manifolds of the origin

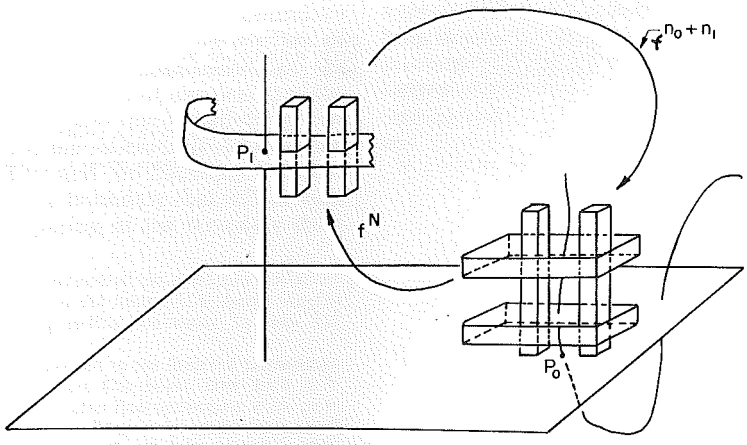

Fig. 10 Construction of horseshoe near a homoclinic point

Downloaded 03 May 2010 to 171.66.16.21. Redistribution subject to ASME license or copyright; see http://www.asme.org/terms/Terms_Use.cfm

References

Devaney, R., 1986, *An Introduction to Chaotic Dynamical Systems*, Benjamin-Cummings, Menlo Park, CA.

Devaney, R., and Nitecki, Z., 1979, "Shift Automorphisms in the Henon Mapping," *Comm. Math. Phys.*, Vol. 67, pp. 137–178.

Fenichel, N., 1971, "Persistence of Smoothness of Invariant Manifolds for Flows," *Ind. Univ. Math. J.*, Vol. 21, pp. 193–225.

Guckenheimer, J., and Holmes, P. J., 1983, *Nonlinear Oscillations, Dynamical Systems, and Bifurcations of Vector Fields*, Springer-Verlag, New York.

Hirsch, M. W., Pugh, C. C., and Shub, M., 1977, *Invariant Manifolds*. (*Springer Lecture Notes in Mathematics*), Vol. 583, Springer-Verlag, New York.

Holmes, P. J., 1979, "A Nonlinear Oscillator with a Strange Attractor," *Phil. Trans. Roy. Soc.*, Series A, Vol. 202, pp. 419–448.

Melnikov, V. K., 1963, "On the Stability of the Center for Time Periodic Perturbations," *Trans. Moscow Math. Soc.*, Vol. 12, pp. 1–57.

Moser, J., 1973, *Stable and Random Motions in Dynamical Systems*, Princeton University Press, Princeton.

Shaw, S. W., and Wiggins, S., 1988, "Chaotic Motions of a Torsional Vibration Absorber," ASME JOURNAL OF APPLIED MECHANICS, Vol. 55, pp. 952–958.

Wiggins, S., and Holmes, P. J., 1987, "Homoclinic Orbits in Slowly Varying Oscillators," *SIAM J. Math. Anal.*, Vol. 18, pp. 612–629.

Downloaded 03 May 2010 to 171.66.16.21. Redistribution subject to ASME license or copyright; see http://www.asme.org/terms/Terms_Use.cfm

D. M. Hanes
Rosenstiel School of Marine and Atmospheric Science, University of Miami, Miami, FL 33149

J. T. Jenkins
Department of Theoretical and Applied Mechanics, Cornell University, Ithaca, NY 14853
Mem. ASME

M. W. Richman
Department of Mechanical Engineering, Worcester Polytechnic Institute, Worcester, MA 01609
Mem. ASME

The Thickness of Steady Plane Shear Flows of Circular Disks Driven by Identical Boundaries

We employ balance laws and constitutive relations for rapid, dense, plane flows of identical circular disks together with boundary conditions at a bumpy wall to analyse steady shearing flows maintained by the relative motion of two identical, parallel walls. The disks and the walls are assumed to be frictionless and nearly elastic. Given the properties of the flowing disks, those of the boundary, and the ratio of the tangential and normal tractions applied to the boundary, we determine what the distance between the walls must be for a steady solution to be possible. For these steady solutions we relate the velocity of the walls to the normal and tangential tractions applied to them. We find that in certain circumstances steady motions may be maintained even when the ratio of tangential to normal traction is much less than its value in a homogeneous simple shear. In the Appendix, the corresponding results for spheres are outlined.

I Introduction

Recent experimental observations (Hanes and Inman (1985); Savage and Sayed (1984); Craig, Buckholtz, and Domoto (1986)) and numerical simulations (Brennen and Campbell (1985); Campbell and Gong (1987)) of rapidly flowing granular materials have indicated that the geometry and material of the boundaries have a significant effect upon the dynamics of the flow.

Jenkins and Richman (1986) have analyzed specific effects of boundaries within the context of the kinetic theory. Implicit in their analysis is the prediction that, because of their dissipative nature, steady flows of inelastic grains are generally limited in extent and that the overall thickness of such a flow can be calculated by considering the energy and momentum balances within the flow and at the boundaries.

In this work we will extend the analysis of Jenkins and Richman to describe explicitly how the boundary characteristics influence the flow thickness for a shear flow of smooth, nearly elastic, circular disks maintained, in the absence of gravity, by the relative motion of identical, parallel boundaries composed of like, regularly spaced half-disks. For such a flow, we also determine the relationship between the tractions applied to a boundary and the boundary velocity. The specific characteristics of the boundary that will be considered are the diameter and spacing of the boundary disks and the coefficient of restitution of a collision between a flow disk and a boundary disk. Figure 1 illustrates the boundary configuration.

The calculation of the steady shear thickness between identical boundaries in the absence of gravity is relevant to the determination of the depth of flow in a half-infinite medium driven by a single horizontal boundary, provided that the normal traction required to maintain the flow is much greater than the weight of the flowing material and that, at the interface between the flowing material and the material at rest, the rates at which momentum and energy are supplied to the flow are the same as those at the upper boundary. The determination of the relation between the boundary velocity and the boundary tractions is relevant to the motion of a granular heap down an incline. From this relation we may obtain a first approximation to the shear stress applied to the bottom of a heap that is supported on a relatively thin, steady shear layer, provided that the weight of the heap is large compared to the weight of the material being sheared and that the top and bottom boundaries of the sheared layer may be idealized as rigid and identical.

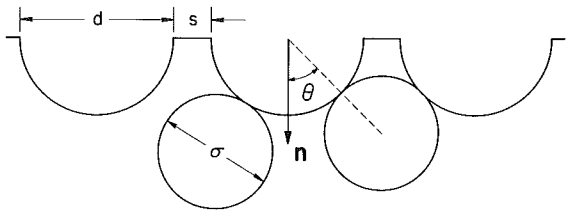

Fig. 1 The boundary geometry

Contributed by the Applied Mechanics Division of THE AMERICAN SOCIETY OF MECHANICAL ENGINEERS for presentation at the Joint ASCE/ASME Applied Mechanics, Biomechanics, and Fluids Engineering Conference, La Jolla, CA, July 9–12, 1989.

Discussion on this paper should be addressed to the Editorial Department, ASME, United Engineering Center, 345 East 47th Street, New York, N.Y. 10017, and will be accepted until two months after final publication of the paper itself in the JOURNAL OF APPLIED MECHANICS. Manuscript received by ASME Applied Mechanics Division, February 12, 1987; final revision, April 8, 1988.

Paper No. 89-APM-8

Copyright © 1988 by ASME
Downloaded 03 May 2010 to 171.66.16.21. Redistribution subject to ASME license or copyright; see http://www.asme.org/terms/Terms_Use.cfm

II Theoretical Formulation

We are concerned here with plane flows of identical, smooth, nearly elastic circular disks of mass m and diameter σ. The coefficient of restitution e characterizes the energy lost when two disks collide. We employ a kinetic theory developed by Jenkins and Richman (1985) for these flows. In this theory, a velocity distribution function is used to define certain mean quantities and to calculate, in terms of these means and their spatial gradients, the rates at which momentum and energy are transferred throughout the flow. The mean fields of interest are the mass density ρ, which is the product of m and the mean number n of disks per unit area; the mean velocity $\underline{u}$, about which the actual particle velocities fluctuate; and the granular temperature T, which measures the kinetic energy per unit mass associated with the fluctuations.

The equation expressing the balance of mass has the familiar form

$$\dot{\rho}+\rho\nabla\cdot\underline{u}=0, \tag{1}$$

where an overdot indicates the time derivative following the mean motion. The balance of linear momentum is

$$\rho\dot{\underline{u}}=-\nabla\cdot\underline{\underline{P}}+n\underline{F}, \tag{2}$$

where $\underline{\underline{P}}$ is the symmetric pressure tensor and $\underline{F}$ is the external force on a particle. The energy balance is

$$\rho\dot{T}=-\nabla\cdot\underline{Q}-tr(\underline{\underline{P}}\cdot\nabla\underline{u})-\gamma, \tag{3}$$

where $\underline{Q}$ is the flux of fluctuation energy and γ its rate of dissipation in inelastic collisions. With appropriate initial and boundary conditions, equations (1) through (3) determine ρ, $\underline{u}$, and T.

At a boundary, the velocity of the flow will not, in general, be the same as velocity of the boundary. The slip velocity $\underline{v}$ is the latter less the former. Boundaries supply momentum to the flow at a rate $\underline{M}$ per unit length and, because the collisions are inelastic, they absorb energy at a rate D. The balance of momentum at a point on the boundary with unit inward normal $\underline{n}$ requires that

$$\underline{M}=\underline{\underline{P}}\cdot\underline{n}; \tag{4}$$

while the balance of energy requires that

$$\underline{M}\cdot\underline{v}-D=\underline{Q}\cdot\underline{n}. \tag{5}$$

Expressions for $\underline{M}$ and D may be obtained by averaging the change of momentum or energy in a collision over the probable frequency of collisions. The resulting expressions depend upon both the geometry and the coefficient of restitution of the boundary.

We focus attention on steady rectilinear flows in the x-y plane that are contained between identical, parallel, bumpy boundaries located at $y = L/2$ and $y = -L/2$. The upper boundary moves in the x-direction with a velocity U while the lower boundary moves with the same speed the opposite direction. Each consists of a flat wall to which identical half-disks of diameter d are attached and evenly spaced a distance s apart. When a flow disk collides with the top of a wall disk, its center is a distance $\bar{\sigma} \equiv (\sigma+d)/2$ from the wall.

In this simple flow, the x-component u of the velocity, the density ρ, and the granular temperature T depend on y only. Equation (1) is satisfied identically and, in the absence of gravity, the x and y-components of equation (2) may be integrated to show that the shear stress $S \equiv -P_{xy}$ and the normal stress $N \equiv P_{yy}$ are constants. With $Q \equiv Q_y$, equation (3) reduces to

$$Q'-Su'+\gamma=0, \tag{6}$$

where a prime denotes differentiation with respect to y.

We employ the specialization to smooth disks of the constitutive theory developed by Jenkins and Richman (1985) for slightly rough disks. We simplify the theory by retaining in the constitutive relations only those terms that dominate in the dense limit. In this limit, the contributions from particle transport to the transfer of momentum and energy are negligible. In addition, the dependence of the collisional contributions on the density is simplified. The stresses in the resulting theory are given by

$$N=\sqrt{\pi}\kappa\sqrt{T}/\sigma, \tag{7}$$

where

$$\kappa=(2/\sqrt{\pi})\rho\sigma\sqrt{T}G, \tag{8}$$

in which G is a function of the area fraction $\nu \equiv \pi n\sigma^2/4$ given by $G(\nu) = \nu(16-7\nu)/16(1-\nu)^2$;

and

$$S=(J/2)\kappa u', \tag{9}$$

where $J \equiv 1+\pi/8$. When κ is eliminated between equations (7) and (9), we obtain the simple relation

$$u'=(2\sqrt{\pi}/J)(\sqrt{T}/\sigma)(S/N), \tag{10}$$

between the velocity gradient and the granular temperature. The energy flux is given by

$$Q=-M\kappa T', \tag{11}$$

where $M \equiv 1+9\pi/16$; and the dissipation rate is

$$\gamma=4(1-e)\kappa T/\sigma^2. \tag{12}$$

This theory applies when $(1-e)$, $\sigma(lnT)'$, $\sigma[ln(\nu G)]'$, and $(\sigma u')^2/T$ are of order σ/L.

The energy equation may be rewritten by employing equations (10), (11), and (12) in it and by recognizing from (7) that κ may be replaced by $\sigma N/\sqrt{\pi T}$ wherever it occurs. When cast in terms of $w \equiv \sqrt{T}$, the result is

$$L^2w''-(\beta k)^2w=0, \tag{13}$$

where $\beta^2 \equiv L^2/\sigma^2$ and

$$k^2\equiv[2(1-e)-(\pi/J)(S/N)^2]/M. \tag{14}$$

The variation of w with y is therefore

$$w=w_1\cosh(\beta ky/L)/\cosh(\beta k/2), \tag{15}$$

in which we have defined $w_1 \equiv w(L/2)$ and have ensured that $w'(0) = 0$.

Expressions for the rates $\underline{M}$ and D that are consistent with the constitutive theory (7) through (12) are the dense limits of those obtained by Richman and Chou (1988). For the boundary at $y = L/2$, the Cartesian components of $\underline{M}$ are

$$M_y=-\rho\chi w^2, \tag{16}$$

where χ is a function of the solid fraction that accounts for the effects of particle shielding and excluded area on the frequency of boundary collisions; and

$$M_x=(2/\pi)^{1/2}\rho\chi w[(v-\bar{\sigma}u')(\theta\csc\theta-\cos\theta)+(2\bar{\sigma}u'/3)(1+\sigma\pi/\bar{\sigma}8\sqrt{2})\sin^2\theta], \tag{17}$$

where v is the slip velocity, $U-u(L/2)$, and $\sin\theta \equiv (d+s)/(d+\sigma)$. The corresponding expression for D is

$$D=(2/\pi)^{1/2}\rho\chi w^3(1-\epsilon)\theta\csc\theta, \tag{18}$$

in which ϵ is the coefficient of restitution of a collision between a wall disk and a flow disk. Equations (16) through (18) apply to circumstances in which $(v/w_1)^2$ and $(1-\epsilon)$ are of order σ/L.

The normal component of the boundary condition (4) $-M_y=N$, now yields

$$N=\rho\chi w_1^2. \tag{19}$$

The tangential component, $M_x=S$, may be rewritten by employing equations (19) and (10) to eliminate, respectively, χ and u' from expression (17) for M_x. Upon solving for v/w_1, we obtain

Downloaded 03 May 2010 to 171.66.16.21. Redistribution subject to ASME license or copyright; see http://www.asme.org/terms/Terms_Use.cfm

$$v/w_1 = (\pi/2)^{1/2}(S/N)f, \tag{20}$$

where

$$f \equiv \frac{\{1-(4\sqrt{2}/3J)\,(\bar{\sigma}/\sigma)[1+(\pi/8\sqrt{2})(\sigma/\bar{\sigma})]\sin^2\theta\}}{\theta\csc\theta-\cos\theta} + (2\sqrt{2}/J)\,(\bar{\sigma}/\sigma). \tag{21}$$

From (5), the energy flux condition is $Sv-D = Q$. In this we use constitutive relation (11) for Q and equation (20) for v/w_1. When κ is replaced by $\sigma N/\sqrt{\pi}\, w_1$ we have, at $L/2$,

$$\sigma w'/w_1 = B, \tag{22}$$

in which

$$B \equiv -[(1-\epsilon)\theta\csc\theta - (\pi f/2)(S/N)^2]/M\sqrt{2}. \tag{23}$$

Finally, with the explicit expression (15) for w employed in (22), the energy flux boundary condition yields the relation

$$\tanh(\beta k/2) = B/k. \tag{24}$$

This equation determines β, the thickness in disk diameters, provided that $0 \le B \le k$ and $k^2 \ge 0$.

If $k^2 < 0$, then the solution for $w(y)$ is trigonometric and the relation analogous to (24) is

$$\tan(\beta K/2) = -B/K, \tag{25}$$

where

$$K^2 \equiv [(\pi/J)\,(S/N)^2 - 2(1-e)]/M. \tag{26}$$

A nonnegative thickness requires that $B \le 0$. Also, solutions for other than the principal value of the argument lead to negative temperatures in the flow and must be discarded.

For a given set of boundaries, six physical constants characterize the flow, L, S, N, ρ_1, U, and v. Jenkins and Richman (1986) adopted the view that if any two of these constants are specified, the remaining four may be chosen to satisfy both stress boundary conditions (19) and (20), the appropriate energy flux condition (24) or (25), and the remaining symmetry condition $u(0) = 0$. The temperature profile is then fixed by (15), the velocity profile is determined by the integration of (10), and the solid fraction profile is obtained by inverting (7). However, this approach leads to uniqueness of steady solutions when it is not expected and nonexistence of steady solutions when they should occur. Here, based on additional information regarding the influence of the boundaries on nearby grains, we relax this procedure somewhat and, essentially, give up one of the boundary conditions.

Numerical simulations of the isothermal equilibrium of perfectly elastic disks or spheres near a flat, perfectly elastic wall carried out, for example, by Snook and Henderson (1978) and Henderson and van Swol (1984), show a layer of relatively high density at the wall and rapid oscillatory decay normal to the wall to the density of the interior. This rapid variation in the density near a boundary cannot be described in the context of the present theory. Here, in order to provide a first approximation to the results of the numerical simulations, we regard the boundary condition (19), used with (7) and (8), as determining χ in terms of the solid fraction ν_1 near the boundary (rather than at the boundary). Then $\chi = 2G_1$, where $G_1 \equiv G(\nu_1)$, and the relative high density of the boundary layer is given in terms of the density ρ_1 near the boundary by $\rho_1\chi$. The density ρ_1 remains as a free parameter. In contrast, Jenkins and Richman (1986), when treating this boundary condition, ignored the possibility of rapid variations in density near the boundary, identified the density near the boundary with that at the boundary, and used the boundary condition to determine its unique value.

The solutions given here are eventually parameterized in terms of N, U, and ρ_1. However, we first suppose that S/N is specified and focus attention on how L/σ varies with S/N for boundaries with different roughness and dissipation.

III The Thickness

That part of the solution presented in the previous section may be examined with respect to the energetics of the flow. By combining equations (9), (10), and (12), we form the ratio of the production of fluctuation energy by the mean shear to the dissipation of fluctuation energy in inelastic collisions:

$$\frac{Su'}{\gamma} = \frac{(S/N)^2}{2(1-e)J/\pi}. \tag{27}$$

This ratio is proportional to the stress ratio and, consequently, is constant at all locations within the flow. Under the rather special condition that production equals dissipation everywhere, $(S/N)^2 = 2(1-e)J/\pi$, and the flow is homogeneous with constant shear rate, temperature, and area fraction. If $(S/N)^2 < 2(1-e)J/\pi$, then the production is less than the dissipation and fluctuation energy must be supplied to the flow through the boundaries. This corresponds to the hyperbolic solutions of the previous section. If $(S/N)^2 > 2(1-e)J/\pi$, production exceeds dissipation and fluctuation energy must be removed through the boundaries. This corresponds to the trigonometric solutions.

The flux of energy to the flow at the boundaries has the sign of B and is proportional to it. In a steady solution, this energy flux must account for the total energy excess or deficit of the flow. Consequently, given S/N, the flux of energy at the boundary determines the thickness of the steady flow.

By examining equations (14) and (23), we find that range of S/N for which the hyperbolic energy conditions $0 \le B \le k$ are both satisfied to be

$$2(1-\epsilon)\theta\csc\theta/\pi f \le (S/N)^2 \le [2(1-\epsilon)\theta\csc\theta/\pi f] + (4M/\pi Jf^2)[-1+\{1+(Jf^2/M)[(1-e)J - (1-\epsilon)\theta\csc\theta/f]\}^{1/2}], \tag{28}$$

provided that

$$(1-\epsilon)\theta\csc\theta/f \le (1-e)J. \tag{29}$$

When the bounds are distinct, as S/N increases from its lower bound, L/σ increases monotonically from zero. As the upper bound is approached, B goes to k and the argument of the hyperbolic tangent diverges as $-\ln(1-B/k)$. Here, as the thickness increases, the temperature approaches zero in a region about the centerline that grows to include all but the immediate neighborhood of the boundary. In order to maintain constant shear and normal stresses, this decrease in temperature must be balanced by an increase in area fraction. Eventually, an area fraction is reached at which the assumptions of molecular chaos and instantaneous, binary collisions upon which the theory is based begin to break down and ordering of particles, multiple collisions, and, finally, enduring contracts become progressively more important. Using the fact that N is constant, the constitutive relations (7) and (8), and the solution (15) for w, the area fraction ν_1 near the wall may be related to its value ν_0 at the center:

$$\nu_1 G_1 \cosh^2(\beta k/2) = \nu_0 G_0. \tag{30}$$

Values of thickness that limit the domain of the theory may be obtained from (30) by taking $\nu_0 = 0.665$, the area fraction at which a phase change to a solid takes place in the equilibrium simulations of elastic disks by Hoover and Adler (1967), and solving for β over the range of k for several values of ν_1.

When k and B are both zero, the bounds collapse in (28) and the equality must hold in (29). The flow is homogeneous and its thickness is unbounded.

In the trigonometric regime, the conditions $K \ge 0$ and $B \le 0$ in equations (25) and (26) must both be satisfied, giving

$$2(1-e)J/\pi \le (S/N)^2 \le 2(1-\epsilon)\theta\csc\theta/\pi f. \tag{31}$$

As S/N decreases from its upper bound, L/σ increases

Downloaded 03 May 2010 to 171.66.16.21. Redistribution subject to ASME license or copyright; see http://www.asme.org/terms/Terms_Use.cfm

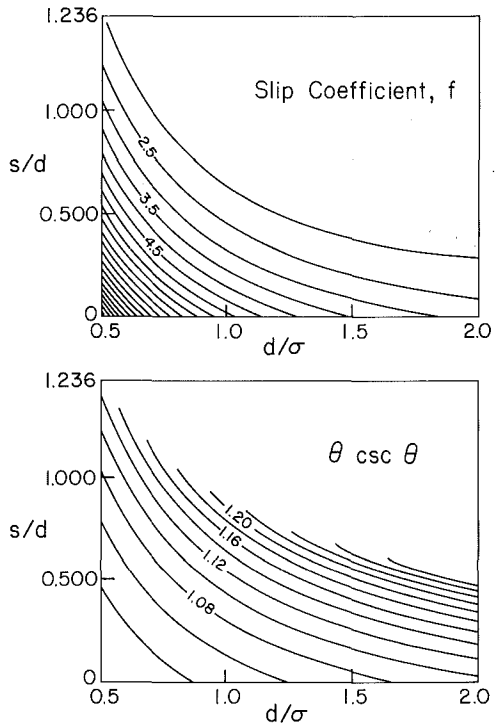

Fig. 2 Contours of the slip coefficient f and the quantity $\theta\csc\theta$ as functions of the nondimensional diameter d/σ and spacing s/d of the wall disk

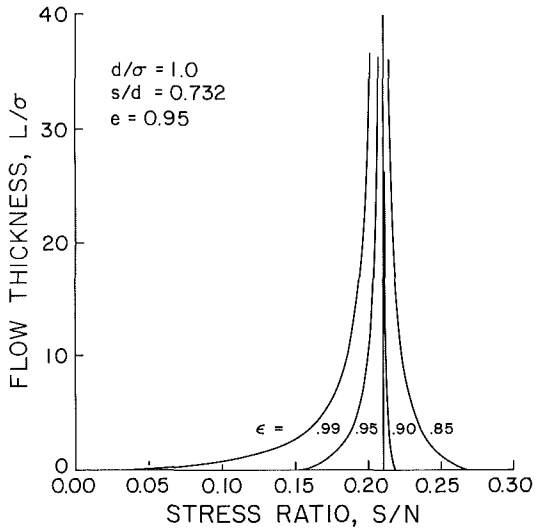

Fig. 3 Steady flow thickness for various values of the coefficient of restitution of the boundary. The boundary roughness is fixed and e = 0.95.

monotonically and, as the lower bound is approached and the flow becomes homogeneous, it diverges as $1/K$.

Clearly, solutions will exist in either the hyperbolic or trigonometric regimes according to whether $(1-\epsilon)\theta\csc\theta/f$ is, respectively, less than or greater than $(1-e)J$.

The solutions for flow thickness depend upon the coefficients of restitution, the size of the wall disks relative to the flow disks, and their spacing. In order to facilitate the calculation of the steady shear thickness for given flow disks and boundaries, in Fig. 2 we plot contours of f and $\theta\csc\theta$ as s/d and d/σ are varied. We next provide example solutions of the flow thickness that illustrate the influence of the boundary

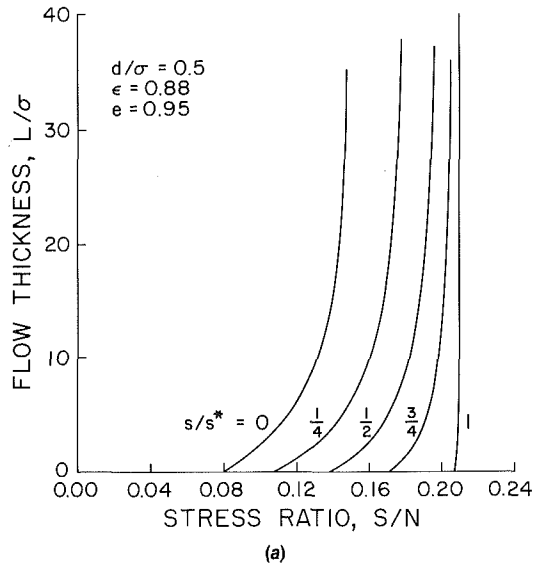

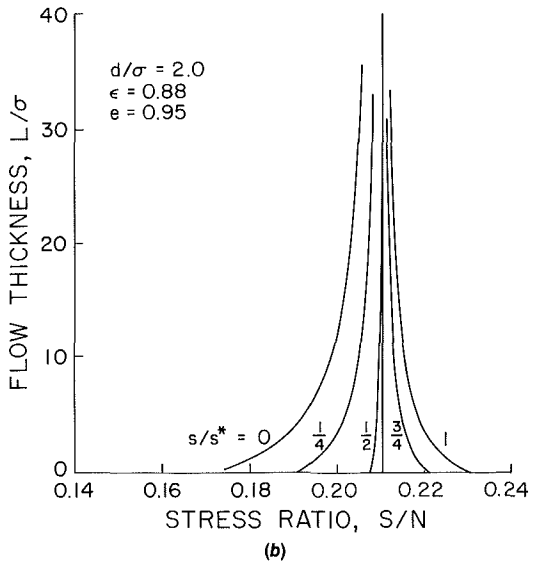

Fig. 4 Steady flow thickness for different boundary roughness. The spacing s is normalized by its largest permitted value $s^* = (d^2 + 2\sigma d)^{1/2} - d$; *a*) $d/\sigma = 0.5$, *b*) $d/\sigma = 2.0$.

parameters. In all examples the coefficient of restitution of the flow disks is kept at 0.95.

The influence of the coefficient of restitution ϵ is illustrated in Fig. 3. As ϵ increases, the boundary is more effective at transferring fluctuation energy into the flow, so the solutions undergo a transition from the trigonometric to the hyperbolic regime. The thickness of the flow is generally less than 20, but rapidly increases near the values of S/N corresponding to either the homogeneous flow or the hyperbolic divergence. For a fixed value of S/N, the thickness is extremely sensitive to ϵ.

The influence of boundary roughness is illustrated in Fig. 4. An increase in d/σ or an increase in s/d both result in a rougher boundary. For a constant value of S/N, an increased roughness decreases the slip working $\underline{M}\cdot\underline{v}$ and, consequently, inhibits the production of fluctuation energy at the boundaries. This results in thinner flows in the hyperbolic regime and thicker flows in the trigonometric regime. Alternatively, for a fixed thickness, an increase in roughness results in higher values of S/N.

Downloaded 03 May 2010 to 171.66.16.21. Redistribution subject to ASME license or copyright; see http://www.asme.org/terms/Terms_Use.cfm

For values of ν_1 less than 0.65, equation (30) indicates that the curves shown in Figs. 3 and 4 for the hyperbolic solutions all fall within the domain of the theory.

IV The Velocity

We employ the solution (15) in the differential equation (10) for the velocity, integrate the resulting expression, require that the velocity vanish on the centerline, and find that

$$\frac{u}{w_1}=\frac{2\sqrt{\pi}}{J}\frac{S}{N}\frac{\sinh(\beta k y/L)}{k\cosh(\beta k/2)}. \tag{32}$$

Upon evaluating this at $L/2$ and using the definition of slip velocity, equation (20), and equation (24), we obtain the relationship between the boundary velocity, boundary temperature, and the stress ratio:

$$U/w_1=(\pi/2)^{1/2}(f+2\sqrt{2}B/Jk^2)(S/N), \tag{33}$$

or, with (14) and (23),

$$\frac{U}{w_1}=\left(\frac{\pi}{2}\right)^{1/2}\frac{[(1-e)Jf-(1-\epsilon)\theta\csc\theta]}{[(1-e)J-(\pi/2)(S/N)^2]}\frac{S}{N}. \tag{34}$$

Next, we use (8) in (7) and determine w_1 in terms of N and ρ_1:

$$w_1=(N/2\rho_1 G_1)^{1/2}. \tag{35}$$

If desired, the density profile may be obtained by inverting (7). Consequently, when N, U, and ρ_1 are given, the solution is completely determined, at least in those situations in which (24) applies.

Finally, if (34) is regarded as a quadratic equation for the stress ratio, it may be solved to yield

$$(\pi/2)^{1/2}(S/N)=-b+[b^2+(1-e)J]^{1/2} \tag{36}$$

where

$$b\equiv[(1-e)Jf-(1-\epsilon)\theta\csc\theta](w_1/2U), \tag{37}$$

and, with (35),

$$w_1/2U=(N/8\rho_1 G_1 U^2)^{1/2}. \tag{38}$$

The range of variation of the stress ratio for typical disks and boundaries can be seen in Figs. 3 and 4. Boundaries with the smallest dissipation give the greatest reduction over homogeneous shear ($b=0$) and, if the slip is high, it is easy to obtain a reduction of one half. It should be possible to test this behavior of the stress ratio using air-table experiments and numerical simulations.

Acknowledgments

D. M. Hanes acknowledges the support of the National Science Foundation, grant CEE-8504419. J. T. Jenkins was supported by the U.S. Army Research Office through the Mathematical Sciences Institute at Cornell University. M. W. Richman acknowledges the support of the National Science Foundation, grant MSM-8707911, in the latter stages of this work.

References

Campbell, C. S., and Brennen, C. E., 1985, "Computer Simulations of Granular Shear Flow," *Journal of Fluid Mechanics*, Vol. 151, pp. 167–188.

Campbell, C. S., and Gong, A., 1987, "Boundary Conditions for Two-Dimensional Granular Flows," *Proceedings of the Sino-U.S. Symposium on Multiphase Flows*, Vol. 1, Hangzhou, China, pp. 278–283.

Craig, K., Buckholz, R. H., and Domoto, G., 1987, "The Effects of Shear Surface Boundaries on Stresses for the Rapid Shearing of Dry Metal Powders – An Experimental Study," ASME *Journal of Tribology*, Vol. 109, pp. 232–237.

Hanes, D. M., and Inman, D. L., 1985, "Observations of Rapidly Flowing Granular-Fluid Materials," *Journal of Fluid Mechanics*, Vol. 150, pp. 357–380.

Henderson, J. R., and van Swol, F., 1984, "On the Interface Between a Fluid and a Planar Wall. Theory and Simulations of a Hard Sphere Fluid at a Hard Wall," *Molecular Physics*, Vol. 51, pp. 991–1010.

Hoover, W. G., and Adler, B. J., 1967, "Studies in Molecular Dynamics, IV. The Pressure, Collision Rate, and Their Number Dependence for Hard Disks," *Journal of Chemical Physics*, Vol. 46, pp. 686–691.

Jenkins, J. T., 1987, "Rapid Flows of Granular Materials," *Non-Classical Continuum Mechanics*, R. J. Knops and A. A. Lacey, eds., Cambridge University Press, pp. 213–225.

Jenkins, J. T., and Richman, M. W., 1985, "Kinetic Theory for Plane Flows of a Dense Gas of Identical, Rough, Inelastic, Circular Disks," *Physics of Fluids*, Vol. 28, pp. 3485–3495.

Jenkins, J. T., and Richman, M. W., 1986, "Boundary Conditions for Plane Flows of Smooth, Nearly Elastic, Circular Disks," *Journal of Fluid Mechanics*, Vol. 171, pp. 53–69.

Richman, M. W., "Boundary Conditions Based Upon a Modified Maxwellion Distribution for Flows of Identical, Smooth, Nearly Elastic Spheres," *Acta Mechanica*, in press.

Richman, M. W., and Chou, C. S., "Boundary Effects on Granular Shear Flows of Smooth Disks," *Journal of Applied Mathematics and Physics (Z.A.M.P.)*, in press.

Savage, S. B., and Sayed, M., 1984, "Stresses Developed by Dry Cohesionless Granular Materials Sheared in an Annular Shear Cell," *Journal of Fluid Mechanics*, Vol. 42, pp. 391–430.

Snook, I. K., and Henderson, D., 1978, "Monte Carlo Study of Hard-Sphere Fluid Near a Hard Wall," *Journal of Chemical Physics*, Vol. 68, pp. 2134–2139.

APPENDIX

Using the balance laws, constitutive relations, and boundary conditions for spheres provided by Jenkins (1987) and Richman (1988), we outline the calculations leading to the corresponding results for spheres.

In this case, $G=\nu(2-\nu)/(1-\nu)^3$, where the volume fraction $\nu\equiv\pi n\sigma^3/6$. The normal stress N is given by (7) with

$$\kappa=(4/\sqrt{\pi})\rho\sigma\sqrt{T}G; \tag{A.1}$$

the shear stress S is

$$S=(2J/5)\kappa u', \tag{A.2}$$

where $J\equiv 1+\pi/12$. Then

$$u'=(5\sqrt{\pi}/2J)(\sqrt{T}/\sigma)(S/N). \tag{A.3}$$

The energy flux Q is given by (11) with $M\equiv 1+9\pi/32$ and the dissipation rate γ is

$$\gamma=6\kappa(1-e)T/\sigma^2. \tag{A.4}$$

Then w is a solution of (13) with

$$k^2\equiv[3(1-e)-(5\pi/4J)(S/N)^2]/M. \tag{A.5}$$

For randomly positioned hemispherical particles, θ is related to the torus of mean nearest neighbors seen in cross-section in Fig. 1 and is defined in terms of d, s, and σ in the same way as for disks. At the boundary M_y is given by (16), M_x is

$$M_x=(2/\pi)^{1/2}\rho\chi w\{[2(2-3\cos\theta+\cos^3\theta)(v-\bar{\sigma}u')/3\sin^2\theta] + (\bar{\sigma}u'/2)(1+\sigma\pi/\bar{\sigma}12\sqrt{2})\sin^2\theta\}, \tag{A.6}$$

and the rate of dissipation D is

$$D=(2/\pi)^{1/2}2\rho\chi(1-\epsilon)w^3(1-\cos\theta)\csc^2\theta. \tag{A.7}$$

Consequently, the slip velocity v satisfies (20) with

$$f\equiv\frac{3\sin^2\theta\{1-(5\sqrt{2}/4J)(\bar{\sigma}/\sigma)[1+(\pi/12\sqrt{2})(\sigma/\bar{\sigma})]\sin^2\theta\}}{2(2-3\cos\theta+\cos^3\theta)} + (5/J\sqrt{2})(\bar{\sigma}/\sigma) \tag{A.8}$$

and, at the wall, w' is specified by (22) with

$$B\equiv-[2(1-\epsilon)(1-\cos\theta)\csc^2\theta-(\pi f/2)(S/N)^2]/M\sqrt{2}. \tag{A.9}$$

Then (24) determines the thickness.

The solution for the velocity that corresponds to (32) is

$$\frac{u}{w_1}=\frac{5\sqrt{\pi}}{2J}\frac{S}{N}\frac{\sinh(\beta k y/L)}{k\cosh(\beta k/2)}, \tag{A.10}$$

so (33) is

Downloaded 03 May 2010 to 171.66.16.21. Redistribution subject to ASME license or copyright; see http://www.asme.org/terms/Terms_Use.cfm

$$U/w_1 = (\pi/2)^{1/2}(f + 5\sqrt{2}B/2Jk^2)(S/N), \quad \text{(A.11)}$$

and (34) becomes

$$\frac{U}{w_1} = \left(\frac{\pi}{2}\right)^{1/2} \frac{[(6/5)(1-e)Jf - 2(1-\epsilon)(1-\cos\theta)\csc^2\theta]}{[(6/5)(1-e)J - (\pi/2)(S/N)^2]} \frac{S}{N}. \quad \text{(A.12)}$$

Consequently, the stress ratio is given by

$$(\pi/2)^{1/2}(S/N) = -b + [b^2 + (6/5)(1-e)J]^{1/2}, \quad \text{(A.13)}$$

where

$$b \equiv [(6/5)(1-e)Jf - 2(1-\epsilon)(1-\cos\theta)\csc^2\theta](w_1/2U), \quad \text{(A.14)}$$

and $w_1/2U = (N/16\rho_1 G_1 U^2)^{1/2}$.

Equation (A.13) provides a first approximation to a bottom boundary condition for a granular heap moving down a rough incline, provided that it is supported on a layer of rapidly sheared material and that it is being supplied with energy at its boundaries. The fact that the stress ratio can be reduced significantly from its value in a homogeneous simple shear may help us to understand long run-out avalanches and landslides.

Downloaded 03 May 2010 to 171.66.16.21. Redistribution subject to ASME license or copyright; see http://www.asme.org/terms/Terms_Use.cfm

H. Koguchi
Research Associate.

M. Okada
Research Associate.

K. Tamura
Graduate Student.

Department of Mechanical Engineering,
Nagaoka University of Technology,
Kamitomioka, Nagaoka, 940-21, Japan

The Meniscus Instability of a Thin Liquid Film

This paper reports on the instability for the meniscus of a thin film of a very viscous liquid between two tilted plates, which are separated at a constant speed with a tilt angle in the normal direction of the plates. The disturbances on the meniscus moving with movement of the plates are examined experimentally and theoretically. The disturbances are started when the velocity of movement of the plates exceeds a critical one. The wavelength of the disturbances is measured by using a VTR. The instability of the meniscus is studied theoretically using the linearized perturbation method. A simple and complete analytical solution yields both a stability criterion and the wave number for a linear thickness geometry. These results compared with experiments for the instability show the validity of the stability criterion and the best agreement is obtained with the wave number of maximum amplification.

1 Introduction

Striated or finger patterns can be seen in: the fibrillar breakup of a mastic in the peeling of pressure sensitive adhesive tape (McEwan and Taylor, 1966); rupturing of the flow viscous lubricant within a journal bearing (Savage, 1977a). Similar patterns can be often observed on the fracture surfaces of polymers and glassy metals. These patterns are considered to be the result of an unstable flow of substance at the free surface. The phenomena arising at the free surface are called meniscus instability and are attracting a lot of interests (Pearson (1960); Savage (1984c)).

There have been several investigations concerning the meniscus instability, such as the rupture of viscous lubricant between counter-rotating cylinders (Pitt and Greiller, 1961) and the flow within a Hele-Shaw cell (Saffman and Taylor, 1959). Most of them deal with the cases where a liquid flows in the same direction of movement of boundaries. There seem to be no reports on the instability of a meniscus moving perpendicularly against the direction of movement of boundaries. The present study treats the instability of the meniscus of a thin film just in this case. A viscous fluid is confined in a very closely defined space between two tilted plates, and then, the plates are moved with respect to each other in the normal direction of the plane of the gap and the instability of the meniscus moving with movement of the plates is investigated. The meniscus is disturbed when the plates are moved faster than a certain velocity. The wavelength of the disturbances of the meniscus is measured under various ranges of velocity and of tilt angle to the plates.

The instability of meniscus is studied theoretically using the linearized perturbation method. A simple and complete analytical solution yields both a stability criterion and the wave number of perturbation. In the present analysis, the authors propose a local capillary number which is a function of the ratio of viscous force to surface tension, the size of the plate, and the thickness of the liquid film. The analytical results are compared with the experimental ones for the local capillary number. The best agreement of both results is obtained in the most unstable mode.

2 Experimental

Figure 1 shows a schematic view of the experimental apparatus used in the present study. In this figure, the plates confining liquids are composed of two pieces of commercial flat-plate glass (5 mm in thickness) bonded with a steel plate (5 mm in thickness). Length L of the plate is 60 mm and width B is 100 mm.

The experimental procedure is as follows. Two plates are set

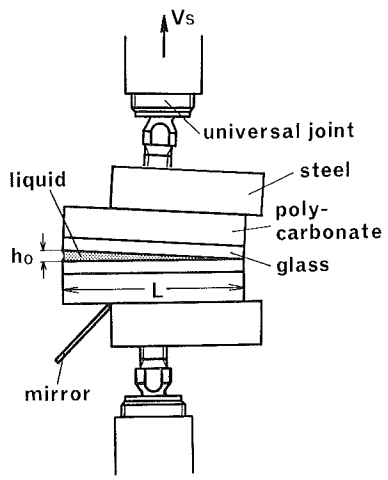

Fig. 1 Schematic illustration of the experimental apparatus

Contributed by the Applied Mechanics Division for publication in the JOURNAL OF APPLIED MECHANICS.

Discussion on this paper should be addressed to the Editorial Department, ASME, United Engineering Center, 345 East 47th Street, New York, N.Y. 10017, and will be accepted until two months after final publication of the paper itself in the JOURNAL OF APPLIED MECHANICS. Manuscript received by ASME Applied Mechanics Division, August 13, 1987; final revision, June 7, 1988.

Copyright © 1988 by ASME
Downloaded 03 May 2010 to 171.66.16.21. Redistribution subject to ASME license or copyright; see http://www.asme.org/terms/Terms_Use.cfm

Table 1 Viscosity and surface tension of sample liquids

Fluid	Viscosity [Pa·s]	Surface tension [mN/m]
Glycerine	1.156	63.4
Silicone oil	1.02	21.2
	3.20	21.2
	10.7	21.2

up close facing each of the glass sides. A viscous fluid is confined between the plates and then a pair of their long edges is allowed to come into contact whereas the other pair is set so as to have a certain gap h_0 by inserting a clearance gauge between the plates. The former edges are called side B and the latter ones side A.

Subsequently, each plate is pulled using a tension tester in the reverse direction at a certain constant velocity. Experiments are conducted at ambient temperature and for tension velocities V_s varying between 0.5 and 100 mm/min and for initial thickness h_0 varying between 0.3 and 1.05 mm. Tests are run three times for each experimental condition. Glycerine and silicone oils with different viscosity are used to examine the effect of viscosity and surface tension on the meniscus instability. The values of viscosity and surface tension of sample liquids are shown in Table 1. The growth process of the disturbance occurring at side A was recorded by using a VTR. Then, the x-coordinate of the meniscus and the wavelength of disturbances was measured with the VTR.

3 Theoretical Analysis of a Meniscus Instability

3.1 Unperturbed Flow of a Thin Liquid Film. Navier-Stokes equation omitting inertial terms and the equation of continuity for an incompressible fluid are

$$-\frac{\partial p}{\partial x}+\mu\left(\frac{\partial^2 u}{\partial x^2}+\frac{\partial^2 u}{\partial y^2}+\frac{\partial^2 u}{\partial z^2}\right)=0$$

$$-\frac{\partial p}{\partial y}+\mu\left(\frac{\partial^2 v}{\partial x^2}+\frac{\partial^2 v}{\partial y^2}+\frac{\partial^2 v}{\partial z^2}\right)=0 \tag{1}$$

$$-\frac{\partial p}{\partial z}+\mu\left(\frac{\partial^2 w}{\partial x^2}+\frac{\partial^2 w}{\partial y^2}+\frac{\partial^2 w}{\partial z^2}\right)=0$$

$$\frac{\partial u}{\partial x}+\frac{\partial v}{\partial y}+\frac{\partial w}{\partial z}=0 \tag{2}$$

where u, v, w are the components of velocity in the direction of x, y, and z axes, p is the pressure and μ is the viscosity.

Figure 2 illustrates the simplified model of an unperturbed meniscus and the coordinate system for analysis. The origin of the coordinate system is placed at the middle point of the gap width and the position of the meniscus at side A at the beginning of the experiments. Rectangular axes are chosen such that z measures distance across the gap width while the x and y axes are along the direction of fluid motion, that is, the direction decreasing flim thickness (from side A to side B) and across the width of the plates, respectively. Taking into account the sizes of the plates (length L and width B), and the initial thickness of the liquid film h_0, (1) is reduced to

$$-\frac{\partial p}{\partial x}+\mu\frac{\partial^2 u}{\partial z^2}=0$$

$$-\frac{\partial p}{\partial y}+\mu\frac{\partial^2 y}{\partial z^2}=0 \tag{3}$$

$$-\frac{\partial p}{\partial z}=0.$$

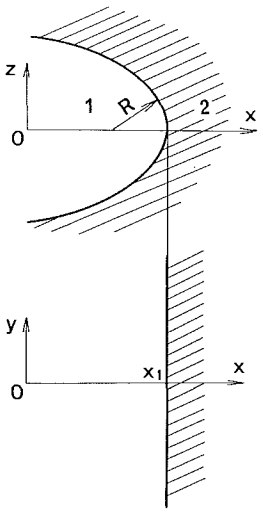

Fig. 2 Meniscus with a straight free surface along the y-axis

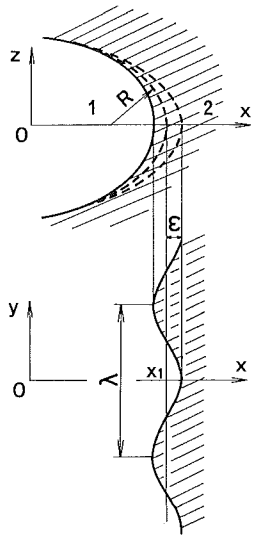

Fig. 3 Perturbed meniscus varying harmonically along the y-axis for the instability analysis

Integrating the first and the second ones of equations (3) with respect to z, and determining the constants of the integration with the boundary conditions $u=v=0$ (at $z=\pm h/2$), yields velocities u and v as follows:

$$u=\frac{1}{2\mu}\frac{\partial p}{\partial x}\left(z^2-\frac{h^2}{4}\right)$$

$$v=\frac{1}{2\mu}\frac{\partial p}{\partial y}\left(z^2-\frac{h^2}{4}\right) \tag{4}$$

where h is a thickness of the liquid film. The thickness h is completely specified in terms of h_0, V_s and t as $h=h_0(1+\alpha-x/L)$, where $\alpha=V_s\,t/h_0$ and t is the time elapsed from the beginning of experiment.

Then, substituting (4) into the continuity equation (2) yields the following equation.

$$\frac{\partial}{\partial x}\left(h^3\frac{\partial p}{\partial x}\right)+\frac{\partial}{\partial y}\left(h^3\frac{\partial p}{\partial y}\right)=12\mu V_s. \tag{5}$$

This equation (5) is exactly the Reynolds equation for lubrication within a journal bearing with a shaft in squeeze motion without rotation.

For simplicity, a system of infinite width with a straight free

Downloaded 03 May 2010 to 171.66.16.21. Redistribution subject to ASME license or copyright; see http://www.asme.org/terms/Terms_Use.cfm

surface along the y-axis, as shown in Fig. 3, is first analyzed. The pressure P_0 in the system is uniformly distributed along the y-axis. Thus, (5) can be simplified as

$$\frac{d}{dx}\left(h^3\frac{dP_0}{dx}\right)=12\mu V_s. \tag{6}$$

The boundary conditions of the present P_0 are obtained by the force balance across the interface of air-fluid. The characteristic of the present phenomenon is that pressure, viscous, and surface tension forces is rather dominant than the inertial force. In an equilibrium flow, the force balance at the interface of the two fluids is generally written as (Landau and Lifshitz, 1975)

$$(p_1-p_2)\mathbf{n}_i=(\sigma'_{1ik}-\sigma'_{2ik})\mathbf{n}_k+T(1/R_1+1/R_2)\mathbf{n}_i \tag{7}$$

where p_1 and p_2 are the pressure of respective fluids at the interface, σ'_{1ik} and σ'_{2ik} the deviatric stress, R_1 and R_2 the principal radius of curvature of the interface, T is a surface tension (constant), and $\mathbf{n}_i$, $\mathbf{n}_k$ the unit normal vector for the free surface of fluid 1($i,k=1,2,3$ or x, y, z).

The authors now neglect all viscous components of stress in the same way as G. I. Taylor (1959), and thus, consider only the surface tension. Putting $1/R_1=2/h$ (h is the thickness of the liquid film), $1/R_2=0$, $p_1=P_a$ (P_a is the atmospheric pressure) and $p_2=P_0$ into (7), the boundary condition of the pressure at sides A and B is written as

$$\begin{aligned}P_0(x_1)&=P_a-\frac{2T}{h_1}\\ P_0(x_2)&=P_a-\frac{2T}{h_2}\end{aligned} \tag{8}$$

where x_1 and x_2 are the positions of the meniscus at sides A and B, and h_1 and h_2 the film thickness at x_1 and x_2, respectively. Hence

$$\begin{aligned}h_1&=h_0\left(1+\alpha-\frac{x_1}{L}\right)\\ h_2&=h_0\left(1+\alpha-\frac{x_2}{L}\right).\end{aligned} \tag{9}$$

Consequently, solving (6) together with (8) and (9) yields the pressure P_0 as follows:

$$P_0(x)=\frac{6\mu V_sL^2(1+\alpha)}{h_0h^2}-\frac{12\mu V_sL^2}{h_0h^2}+\frac{C_1L}{2h_0h^2}+C_2 \tag{10}$$

where the constants C_1 and C_2 are given by

$$C_1=-\frac{4Th_0h_1h_2}{L(h_1+h_2)}-12\mu V_sL(1+\alpha)+\frac{24\mu V_sLh_1h_2}{h_0(h_1+h_2)}$$

$$C_2=P_a-\frac{2T}{h_1+h_2}+\frac{12\mu V_sL^2}{h_0^2(h_1+h_2)}. \tag{11}$$

On the other hand, the average velocity U of the fluid in the direction of the x-axis is obtained by integrating the first of equations (4) with respect to z and then being divided by h

$$U=-\frac{V_s}{h}x-\frac{C_1}{12\mu h}. \tag{12}$$

Then, the equation of motion for the meniscus at sides A and B is obtained as follows:

$$\begin{aligned}\frac{dx_1}{dt}&=-\frac{V_s}{h_1}x_1-\frac{C_1}{12\mu h_1}\\ \frac{dx_2}{dt}&=-\frac{V_s}{h_2}x_2-\frac{C_1}{12\mu h_2}.\end{aligned} \tag{13}$$

3.2 Perturbation Analysis for a Meniscus. The basic solution of the flow with the straight free surface along the y-axis was derived in the preceding section. This section gives an analysis for the growth of perturbations arising at the free surface. It is assumed that the perturbations varying harmonically with wavelength λ and amplitude ϵ arises at the leading edge of the meniscus along the y-axis as shown in Fig. 3. In this case, the position s_1 of the meniscus at side A in the x,y plane can be described as

$$s_1(x_1,y,t)=x_1(t)+\epsilon e^{\omega t}\cos ky \tag{14}$$

where x_1 is the position of the straight free surface, t time, k the wave number of the perturbation ($k=2\pi/\lambda$), and ω the amplification factor. Then, it is assumed that the pressure at the vicinity of the perturbed meniscus is distributed as follows:

$$p(x,y)=P_0(x)+\epsilon G(x)e^{\omega t}\cos ky \tag{15}$$

in which the range of x is $s_1\leqq x\leqq s_2$ (s_2 is the position of the meniscus at side B).

Substituting (15) into (4) yields the velocity u and v in the direction of the x and y axes as follows:

$$\begin{aligned}u(x,y,z,t)&=\frac{1}{2\mu}\left(\frac{dP_0}{dx}+\epsilon\frac{dG(x)}{dx}e^{\omega t}\cos ky\right)\left(z^2-\frac{h^2}{4}\right)\\ v(x,y,z,t)&=\frac{\epsilon}{2\mu}G(x)ke^{\omega t}\sin ky\left(z^2-\frac{h^2}{4}\right).\end{aligned} \tag{16}$$

The ordinary differential equation for $G(x)$ is derived by substituting (15) into (5) and linearizing such that terms of order ϵ yields

$$\frac{d^2G}{dx^2}+\frac{3dh/dx}{h}\frac{dG}{dx}-k^2G=0. \tag{17}$$

Letting $\xi=x-L(1+\alpha)$ and solving (17), $G(x)$ is obtained as follows:

$$G(x)=a_0\sum_{m=0}^{\infty}\frac{k^{2m}\xi^{2m}}{4^m(m+1)!m!}+\frac{a_1}{\xi}\sum_{m=1}^{\infty}\frac{k^{2m}\xi^{2m+1}}{4^m(m+1)!m!}. \tag{18}$$

This equation is rearranged by letting $a_c=a_0+a_1$ as follows:

$$G(x)=a_c\sum_{m=0}^{\infty}\frac{k^{2m}\xi^{2m}}{4^m(m+1)!m!}. \tag{19}$$

This function $G(x)$ is appropriate for the present analysis because it has the characteristic of approaching zero with increasing $|x-x_1|$: the variation of the pressure by the perturbation decays with increasing distance from the meniscus at side A.[1]

The constant a_c can be determined by the boundary condition of pressure on the perturbed surface. Putting $1/R_1=2/h_1(s_1)$, $1/R_2=\epsilon k^2e^{\omega t}\cos ky$, $P_1=P_a$, $P_2=P_0+\epsilon G(s_1)e^{\omega t}\cos ky$, $\sigma'_{1ik}=0$, $\sigma'_{2ik}=0$, $n_1=1$, $n_2=0$, $n_3=0$ into (7), equation (7) yields the boundary condition of pressure at side A.

$$P_a-P_0(s_1)-\epsilon G(s_1)e^{\omega t}\cos ky=-T\left(\frac{2}{h(s_1)}-\epsilon k^2e^{\omega t}\cos ky\right). \tag{20}$$

Rearranging this equation (20) by the Taylor development, linearizing and equating terms of order ϵ yields the relationship

[1] In our experiment, even if the meniscus at side A is disturbed, no disturbance is observed at side B.

Downloaded 03 May 2010 to 171.66.16.21. Redistribution subject to ASME license or copyright; see http://www.asme.org/terms/Terms_Use.cfm

$$G(x_1) = -\frac{dP_0}{dx}\bigg|_{x=x_1} - T\left(\frac{2}{h^2(x_1)} + k^2\right). \tag{21}$$

The constant a_c in (19) is obtained by (21) as follows:

$$a_c = \frac{1}{I_1(x_1)}\left(\frac{12\mu V_s L}{{h_1}^2 h_0}\frac{h_1 - h_2}{h_1 + h_2} - \frac{2h_0 T}{{h_1}^2 L} - k^2 T\right) \tag{22}$$

where

$$I_1(x_1) = \sum_{m=0}^{\infty} \frac{k^{2m}{\xi_1}^{2m}}{4^m(m+1)!m!}$$
$$\xi_1 = x_1 - L(1+\alpha). \tag{23}$$

Subsequently, the stability criterion of perturbations which arise at the leading edge of the meniscus is studied by following Pearson, 1960; Savage, 1984c; Carter and Savage, 1987. The growth or decay of perturbations determines whether the sign of ω in (14) is plus or minus. The expression for ω is derived from the kinematic condition for the perturbed meniscus. The average moving velocity of the meniscus at side A from (4) is given by

$$\frac{ds_1}{dt} = -\frac{h^2}{12\mu}\frac{dp}{dx}\bigg|_{x=s_1} \tag{24}$$

Substituting (15) into (24) yields the following equation

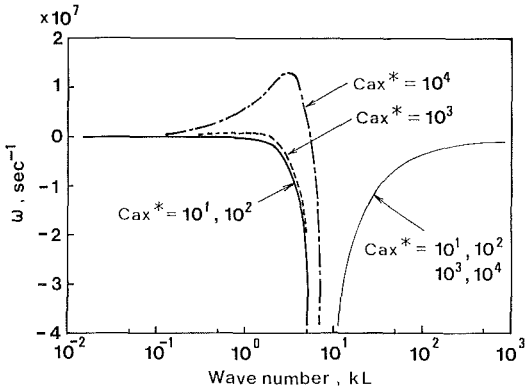

Fig. 4 The variation of amplification factor ω versus dimensionless wave number kL for various Ca_x^* at $x_1 = 3.0$mm in the conditions $V_s = 1.0$mm, $h_0 = 1.05$mm, $\mu = 1.156$Pa•s and $T = 63.4$mN/m

$$\frac{dx_1}{dt} + \epsilon\omega e^{\omega t}\cos ky$$
$$= -\frac{h^2}{12\mu}\bigg|_{x=x_1} + \epsilon e^{\omega t}\cos ky\left(\frac{dP_0}{dx} + \epsilon\frac{dG}{dx}e^{\omega t}\cos ky\right). \tag{25}$$

Equating terms of order ϵ of this equation yields the following relationship

$$\omega = -\frac{1}{12\mu}\left[{h_1}^2\frac{dG}{dx}\bigg|_{x=x_1} + \frac{d}{dx}\left(h^2\frac{dP_0}{dx}\right)\bigg|_{x=x_1}\right]. \tag{26}$$

Thus, substituting (10), (19), and (22) into (26) gives the equation

$$\omega = -\frac{{h_1}^2 T}{12\mu L^3}\left[\frac{24\mathrm{Ca}_x^* h_0 h_2}{h_1(h_1+h_2)} - \frac{4L{h_0}^2 h_2}{{h_1}^3(h_1+h_2)} - \frac{I_2(x_1)L}{I_1(x_1)}\left(12\mathrm{Ca}_x^* - \frac{2Lh_0}{{h_1}^2} - k^2L^2\right)\right] \tag{27}$$

where Ca_x^*, a local capillary number, is a new dimensionless number proposed by the authors and defined as

$$\mathrm{Ca}_x^* = \frac{\mu V_s}{T}\frac{L^3}{h_0{h_1}^2}\frac{h_1 - h_2}{h_1 + h_2} = \frac{\mu V_s}{T}\frac{L^2}{h_1^2}\frac{x_2 - x_1}{h_1 + h_2} \tag{28}$$

and

$$I_2(x_1) = \sum_{m=1}^{\infty} \frac{k^{2m}{\xi_1}^{2m-1}}{2^{2m-1}(m+1)!(m-1)!}.$$

The variation of ω versus kL is shown for various values of Ca_x^* in Fig. 4. The curves plotted in this figure are the ones obtained for $Ca_x^* = 10$, 100, 1000, and 10,000 at $x_1 = 3.0$mm. The thickness (h_1 and h_2) and the position (x_1 and x_2) of the meniscus used in the calculation is obtained by solving (13) with the Runge-Kutta method in the conditions $h_0 = 1.05$mm, $V_s = 1.0$mm/min, $L = 60$mm, and $T = 63.4$mN/m and $\mu = 1.156$Pa•s. The value of ω is always minus in the case of $Ca_x^* = 10$, though the plus region of ω extends with increasing Ca_x^*. The perturbation grows as time elapses in the case of $\omega > 0$. The demarcation between stable ($\omega < 0$) and unstable

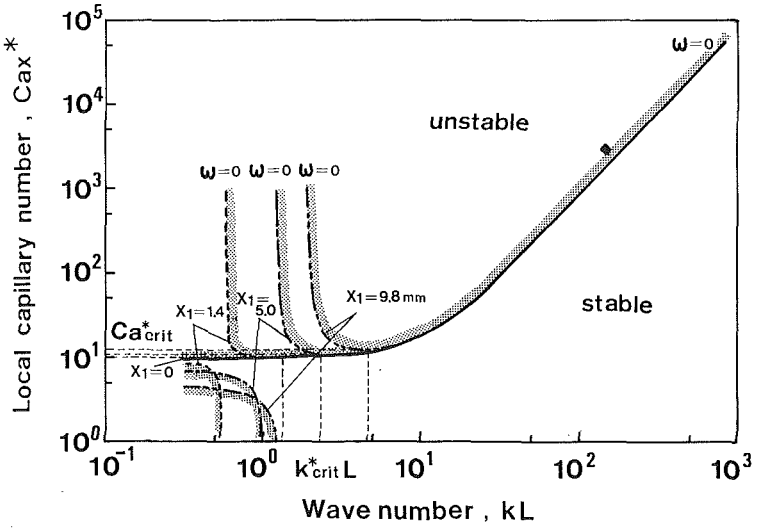

Fig. 5 The variation of neutral stability curves versus dimensionless wave number kL for various positions of the meniscus at side A in the conditions $V_s = 1.0$mm, $h_0 = 1.05$mm, $\mu = 1.07$Pa•s and $T = 21.2$mN/m

Downloaded 03 May 2010 to 171.66.16.21. Redistribution subject to ASME license or copyright; see http://www.asme.org/terms/Terms_Use.cfm

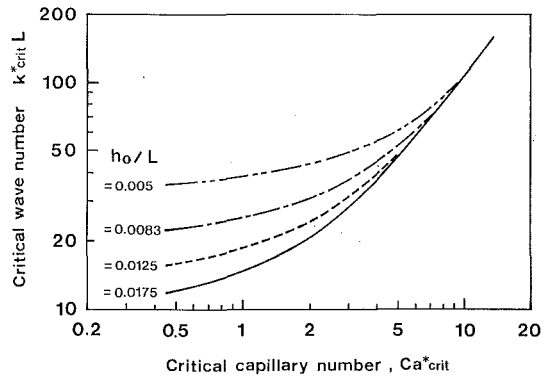

Fig. 6 The variation of critical capillary number Ca^*_{crit} versus dimensionless wave number $k^*_{crit}L$ for various values of h_0/L in the conditions $V_s = 1.0$mm, $h_0 = 1.05$mm, $\mu = 1.07$Pa•s and $T = 21.2$mN/m

($\omega > 0$) situations is given by $\omega = 0$. Thus, a neutral stability condition is obtained by arranging (27) with $\omega = 0$ and it is given by the following relationship:

$$Ca_x^* = Ca^*_{stab} \tag{29}$$

where Ca^*_{stab} is defined as

$$Ca^*_{stab} = \frac{\left(\frac{2Lh_0}{h_1^2} + k^2L^2\right)\frac{I_2(x_1)L}{I_1(x_1)} + \frac{4Lh_0^2h_2}{h_1^3(h_1+h_2)}}{12\left[\frac{I_2(x_1)L}{I_1(x_1)} + \frac{2h_0h2}{h_1(h_1-h_2)}\right]}. \tag{30}$$

Equation (29) gives neutral stability curves for any values of h_0, h_1, h_2, L, k, x_1, and x_2. For $Ca_x^* > Ca^*_{stab}$ the flow is unstable. Figure 5 is a numerical result of the neutral stability curves varying with movement of the meniscus in the conditions $h_0 = 1.05$mm, $V_s = 1.0$mm/min, $L = 60$mm, and $T = 21.2$mN/m and $\mu = 1.07$Pa•s. These curves are the ones for different x-coordinate of the meniscus at side A. It is found that the unstable region varies with movement of the meniscus. The graph of Ca^*_{stab} against kL, Fig. 5, consists of two branches with an asymptote where

$$\frac{I_2(x_1)L}{I_1(x_1)} + \frac{2h_0h_2}{h_1(h_1-h_2)} = 0. \tag{31}$$

The left-hand branch exhibits a maximum and is of no physical interest. The critical capillary number, Ca^*_{crit}, for the right-hand branch is such that for $Ca_x^* < Ca^*_{crit}$ the flow is stable with no perturbations appearing on the meniscus. Both stationary points are found by solving $\partial Ca^*_{stab}/\partial k = 0$ together with (30) to yield the following nonlinear equation with respect to k

$$\frac{d}{dk}\left(\frac{I_2L}{I_1}\right)\left[\frac{2h_0h_2}{h_1(h_1-h_2)}\left(\frac{2Lh_0}{h_1^2} + k^2L^2\right) - \frac{4Lh_0^2h_2}{h_1^3(h_1+h_2)}\right]$$
$$+ 2kL^3\frac{I_2}{I_1}\left(\frac{I_2L}{I_1} + \frac{2h_0h_2}{h_1(h_1-h_2)}\right) = 0. \tag{32}$$

The equation is solved together with (13) as a result of which Ca^*_{crit} and the critical wave number k^*_{crit} are determined for any L, h_0, V_s, h_1, or h_2. Figure 6 illustrates the variation of $k^*_{crit}L$ and Ca^*_{crit} for the moving meniscus in the conditions $V_s = 1.0$mm/min, $L = 60$mm, and $T = 22.1$mN/m and $\mu = 1.07$Pa•s. It should be noted at the beginning of movement of the meniscus ($h_2 = 0$) that the critical wave number equals zero; the wavelength equals infinite, though the critical capillary number is finite [$= L/(6h_0)$].

Of all perturbations, the one that dominates the break-up of the monolithic meniscus will have a wave number that maximizes ω and lies within the range of instability. The authors assume that this is the value of k that would be observed in practice. The relationship between the wave number and the local capillary number Ca_x^* is derived by differentiating (27) with respect to k.

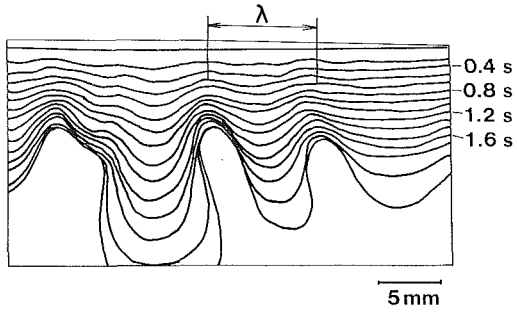

Fig. 7 The sketch of development of perturbations for glycerine at every 1/15 seconds in the experimental conditions $h_0 = 0.5$mm and $V_s = 50$mm/min

$$Ca_x^* = \frac{1}{12}\left[k^2L^2 + \frac{2Lh_0}{h_1^2} + \frac{2kL^2}{\frac{d}{dk}\left\{\ln\frac{I_2(x_1)}{I_1(x_1)}\right\}}\right] \tag{33}$$

This equation gives the local capillary number by substituting k, L, h_0, h_1, and x_1 or (V_s and time t) into (33), if the viscosity and the surface tension of the fluid is known. On the contrary, when the local capillary number, x_1, L, h_0, and h_1 are given, the wavelength can be easily obtained.

4 Application to Experimental Results

Experimental results obtained by the apparatus shown in Fig. 1 can be analyzed in the light of the previous analysis.

First, the movement of the meniscus at side A was recorded by using a VTR and growth of the disturbances was precisely examined. In range of lower V_s (tension velocity), no disturbance on the meniscus within the area of observation ($B \times L = 100 \times 30$mm) can be seen. Increasing V_s or decreasing the initial thickness h_0 causes the meniscus to be disturbed rapidly and the liquid to remain like fingers on the surface of the plates. Such a pattern of the liquid formed on the plates is called a finger pattern. The growth of the disturbances was examined by tracing the movement of the meniscus at side A with elapsed time. Figure 7 is an example of the sketches for glycerine in the experimental condition $h_0 = 0.5$mm and $V_s = 50$mm/min at every 1/15 seconds. The meniscus is almost straight along the y-axis at the early time of the experiment, though it is beginning to be harmonically distorted as time elapses. The wavelength of visible small disturbances was measured from these sketches. All values measured is presented as the experimental ones.

Second, the experimental results are shown together with (29) and (33) in Fig. 8. This figure illustrates the relation between the local capillary number and the wave number for liquids with various viscosities and surface tensions. Solid and dotted lines in the figure is plotted by theoretical equations (29) and (33), respectively. It is found that there are no disturbances for the local capillary number above the neutral stability curve and the experimental values of wave number is nearly on the curve for (33) which corresponds to the most unstable mode. Theoretical lines in this figure vary little within the variation of the position of measurement of the wavelength in our experiments.

Finally, the lines are almost straight in the range of larger wave number because the calculated value of $I_2(x_1)L/I_1(x_1)$, which falls between 1 and 2 for $L = 60$mm, is nearly equal to 1

Downloaded 03 May 2010 to 171.66.16.21. Redistribution subject to ASME license or copyright; see http://www.asme.org/terms/Terms_Use.cfm

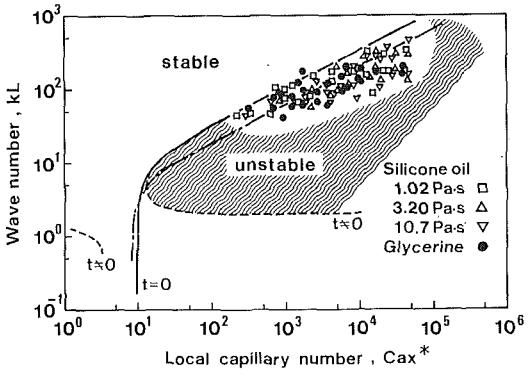

Fig. 8 The relation between the local capillary number Ca_x^* and the wave number kL for various viscosities μ and surface tensions T. Solid and dotted lines are the neutral stability curves at elapsed time $t=0$ and $t\neq 0$, respectively. A dash-dotted line in the figure shows (33)

in the range, and also $2Lh_0/h_1^2$ and $4Lh_0^2h_2/h_1^3/(h_1+h_2)$ is negligibly small against k^2L^2. Thus, (29) and (33) can be simplified as follows

for (29)

$$k_{\text{stab}}L = 2\sqrt{3\text{Ca}_x^*} \tag{34}$$

for (33)

$$k_mL = 2\sqrt{\text{Ca}_x^*} \tag{35}$$

where k_{stab} and k_m is the wave number in (29) and (33), respectively. By eliminating Ca_x^* from (34) and (35), a simple relationship between k_m and k_{stab} is derived as follows:

$$k_{\text{stab}} = \sqrt{3k_m}. \tag{36}$$

These relations enable us to calculate Ca_x^* and λ_{stab} $(=2\pi/k_{\text{stab}})$ from the observed wave number or wavelength.

In spite of the many simplifying assumptions, it is clear that the mathematical model considered in the present study provides reasonably accurate predictions for the wave number.

5 Conclusion

The instability of the meniscus of a thin liquid film are observed in various fields of industry and nature. In the present paper the meniscus instability of a thin liquid film confined between two tilted plates, which is separated perpendicularly to the plates, was studied theoretically and experimentally with several viscous liquids. An analysis of the instability of the meniscus is proposed using the linearized perturbation method. An analytical solution for the stability criterion and the wave number is derived in a closed form for the local capillary number, which is a function of the ratio of surface tension to viscous force, the dimension of the plate, and the thickness of liquid film. The application of this analysis to the experiments is done for various experimental conditions. These results show the validity of the stability criterion. Better agreement of both results is obtained with the wave number corresponds to the most unstable mode.

Acknowledgment

The authors were favored with the assistance of Mr. M. Obata who contributed his effort to the experimental work.

References

Carter, G. C., and Savage, M. D., 1987, "Ribbing in a Variable Speed Two-roll Coater," *Mathematical Engineering Industry*, Vol. 1, pp. 83–95.

Landau, L. D., and Lifshitz, E. M., 1975, *Fluids Mechanics*, Pergamon Press, New York, pp. 230–234.

McEvan, A. D., and Taylor, G. I., 1966, "The Peeling of a Flexible Strip Attached by a Viscous Adhesive," *Journal of Fluid Mechanics*, Vol. 26, pp. 1–15.

Pearson, J., 1960, "The Instability of Uniform Viscous Flow Under Roller and Spreaders," *Journal of Fluid Mechanics*, Vol. 7, pp. 481–500.

Pitt, E., and Greiller, J., 1961, "The Flow of Thin Liquid Films Between Rollers," *Journal of Fluid Mechanics*, Vol. 11, pp. 33–50.

Saffman, P. G., and Taylor, G. I., 1959, "The Penetration of a Fluid into a Porous Medium or Hele-Shaw Cell Containing a More Viscous Liquid," *Journal of Fluid Mechanics*, Vol. 245A, pp. 312–329.

Savage, M. D., 1977a, "Cavitation in Lubrication. Part 1: On Boundary Conditions and Cavity-Fluid Interfaces. Part 2: Analysis of Wavy Interfaces," *Journal of Fluid Mechanics*, Vol. 80, pp. 743–767.

Savage, M. D., 1982b, "Mathematical Models for Coating Processes," *Journal of Fluid Mechanics*, Vol. 117, pp. 443–455.

Savage, M. D., 1984c, "Mathematical Model for the Onset of Ribbing," *American Institute of Chemical Engineers Journal*, Vol. 30, pp. 999–1002.

Downloaded 03 May 2010 to 171.66.16.21. Redistribution subject to ASME license or copyright; see http://www.asme.org/terms/Terms_Use.cfm

An Exact Periodic Solution of a Hydromagnetic Flow in a Horizontal Channel

K. Vajravelu
Department of Mathematics,
University of Central Florida,
Orlando, Fla. 32816

An exact periodic solution for the hydromagnetic unsteady flow of an incompressible fluid with constant properties is obtained. The hydrodynamic (HD) and the hydromagnetic (HM) cases are studied. The flow field here is a generalization of the well-known Couette flow, in which one wall is at rest and the other wall oscillates in its own plane about a constant mean velocity. In order to have some suggestions about the approximate solutions, the exact solution is compared with its own approximate form.

1 Introduction

After the initiation by Lighthill (1954) there has been much work on the subject of laminar boundary layers which have a regular fluctuating flow superimposed on the mean flow. Owing to the mathematical difficulties, most of them include restrictions on an oscillation amplitude or a frequency in the course of their theoretical developments. One of the exact solutions of the Navier-Stokes equation in which no restriction is placed on the amplitude and frequency was obtained by Stuart (1955) for the flow past a flat plate with free stream oscillations.

Although much work has been published (see, Soundalgekar, 1973a, 1973b; Vajravelu and Sastri, 1977, 1978a, 1978b) on the theory of laminar boundary layers in unsteady flow, it appears to have confined to problems of the boundary layer with free stream oscillations. The interesting and important problem of how a fluid confined between two horizontal walls responds to oscillations in the boundary wall has apparently remained untreated.

The main purpose of this paper is to study the hydromagnetic flow in a horizontal channel. The governing equation of the problem is solved exactly, subject to the relevant boundary conditions, for both hydromagnetic and hydrodynamic cases. A comparison is made between the hydromagnetic and hydrodynamic solutions. The contributions of the Hartmann number M and the frequency parameter ω to the flow characteristics are found to be quite significant.

2 Formulation and Solution of the Problem

We consider the two-dimensional flow of an electrically conducting incompressible fluid between two parallel flat walls, one of which is at rest, the other oscillating in its own plane with a constant mean velocity. We restrict our attention to the case in which the flow is independent of the distance along the wall and the velocity component normal to the wall is zero. Then the Navier-Stokes equation is written, in a coordinate system fixed with the wall oscillating with the velocity $U(t)$, as

$$\frac{\partial u}{\partial t} = \frac{\partial U}{\partial t} + \nu \frac{\partial^2 u}{\partial y^2} - \frac{\sigma B_0^2}{\rho}(u-U), \tag{1}$$

where σ the electric conductivity, B_0 an imposed uniform magnetic field, y the normal distance, u the velocity along the wall, t the time, ν the Kinematic viscosity, and ρ the density. Here the induced magnetic field is neglected (which is justified for small magnetic Reynolds number flow; see, Shercliff 1965). The boundary conditions for the velocity field are

$$\left.\begin{aligned} u &= 0 \quad \text{at } y = 0, \\ u &= U(t) \quad \text{at } y = d, \end{aligned}\right\} \tag{2}$$

where d is distance between the walls.

We consider the case in which the unsteady velocity is given by

$$U(t) = U_d\left\{1 + \frac{1}{2}\epsilon(e^{i\omega^* t} + e^{-i\omega^* t})\right\}, \tag{3}$$

where ω^* is the frequency and U_d, ϵ are constants. We then look for a solution of the form

$$u = U_d\left\{F_0(\eta) + \frac{1}{2}\epsilon(F_1(\eta)e^{i\omega^* t} + \tilde{F}_1(\eta)e^{-i\omega^* t})\right\}, \tag{4}$$

in which $\eta = y/d$ and the tilde denotes a complex conjugate. Substituting (3) and (4) into (1) and (2) and equating steady and periodic terms separately to zero, we get

$$F_0'' - M F_0 = -M, \tag{5}$$

$$F_1'' - (i\omega + M)F_1 = -(i\omega + M), \tag{6}$$

$$\left.\begin{aligned} F_0 &= 0 \quad \text{at } \eta = 0, \\ F_0 &= 1 \quad \text{at } \eta = 1, \end{aligned}\right\} \tag{7}$$

Contributed by the Applied Mechanics Division for publication in the JOURNAL OF APPLIED MECHANICS.

Discussion on this paper should be addressed to the Editorial Department, ASME, United Engineering Center, 345 East 47th Street, New York, N.Y. 10017, and will be accepted until two months after final publication of the paper itself in the JOURNAL OF APPLIED MECHANICS. Manuscript received by ASME Applied Mechanics Division, October 21, 1987; final revision, May 15, 1988.

Copyright © 1988 by ASME
Downloaded 03 May 2010 to 171.66.16.21. Redistribution subject to ASME license or copyright; see http://www.asme.org/terms/Terms_Use.cfm

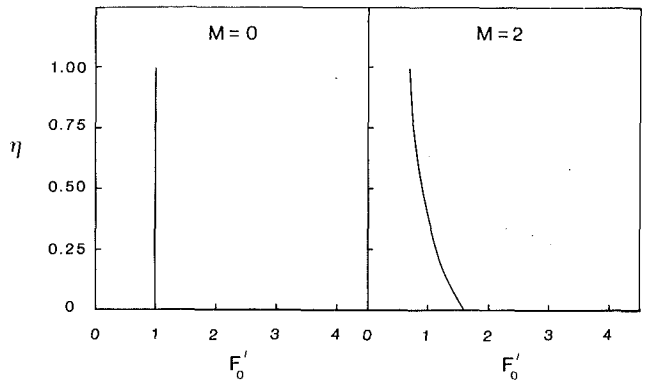

Fig. 1 Profiles of mean velocity gradient

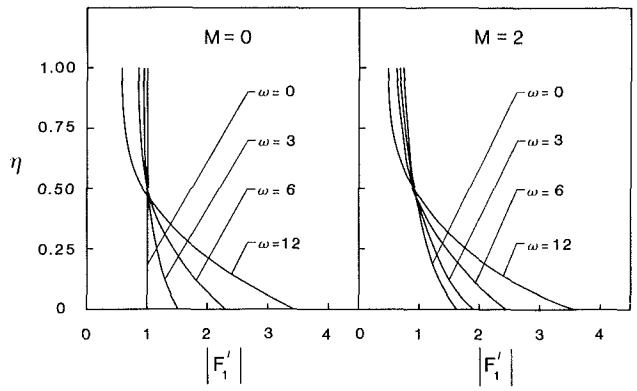

Fig. 2 Profiles of the magnitude of fluctuating velocity gradient

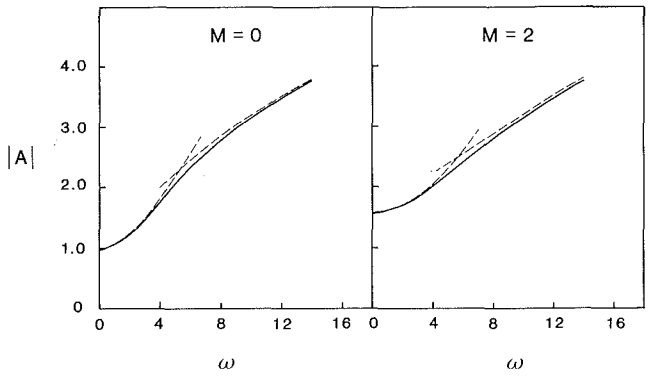

Fig. 3 Skin friction amplitude

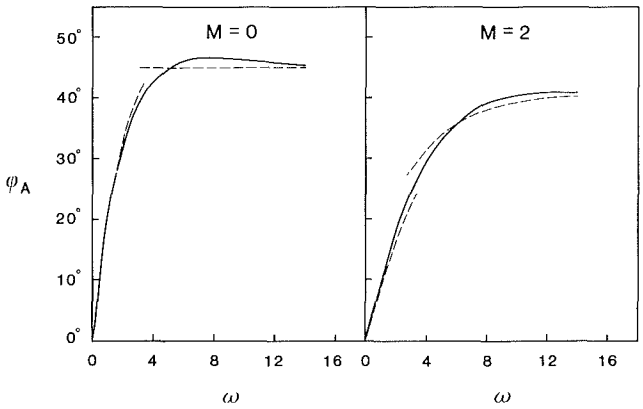

Fig. 4 Phase angle

$$\left.\begin{aligned} F_1 &= 0 \quad \text{at } \eta = 0, \\ F_1 &= 1 \quad \text{at } \eta = 1, \end{aligned}\right\} \tag{8}$$

where $\omega = \omega^* d^2/\nu$ the frequency parameter, $M = d^2\,\sigma B_0^2/\rho\nu$ the Hartmann number and primes denote differentiation with respect to η.

Solving (5) and (6), respectively, with conditions (7) and (8), we get

$$F_0(\eta) = 1 - \cosh(M)^{1/2}\eta + \coth(M)^{1/2}\sinh(M)^{1/2}\eta, \tag{9}$$

$$F_1(\eta) = 1 - \cosh(i\omega + M)^{1/2}\eta + \coth(i\omega + M)^{1/2}\sinh(i\omega + M)^{1/2}\eta. \tag{10}$$

The shear stress at $y = 0$, $\tau_w = \mu(\partial u/\partial y)_{y=0}$, is found to be

$$\tau_w = (\mu U_d/d)\left\{(M)^{1/2}\coth(M)^{1/2} + \frac{1}{2}\epsilon(Ae^{i\omega^* t} + \tilde{A}e^{-i\omega^* t})\right\}, \tag{11}$$

where

$$A = (i\omega + M)^{1/2}\coth(i\omega + M)^{1/2}, \tag{12}$$

and

$$\phi_A = \tan^{-1}(A_i/A_r), \tag{13}$$

the phase advance. The amplitude A can be written in its own approximate form as

$$A = \begin{cases} 1 + \dfrac{1}{3}(i\omega + M) - \dfrac{1}{45}(i\omega + M)^2 + \ldots \text{for small } (\omega \& M), \\ (i\omega + M)^{1/2} + \ldots\ldots\ldots\ldots\ldots\ldots \text{for large } (\omega \& M). \end{cases} \tag{14}$$

The exact solution will be compared with limiting approximations in the discussion of results. The expressions for F_0', $|F_1'|$, $|A|$ and ϕ_A are evaluated numerically for several values of M and ω. The numerical results thus obtained are presented in Figs. 1-4.

3 Discussion of the Results

For both hydrodynamic and hydromagnetic cases, the distribution of the mean velocity gradient F_0', which is related directly to the generation of frictional heat, is shown in Fig. 1. From Fig. 1, it is clear that F_0' is a constant function in the hydrodynamic case whereas it is a decreasing function of η in the hydromagnetic case. That is, the graph of F'_0 is a straight line (linear function) making an angle of 45° with η axis in the hydrodynamic case while its graph is (not a straight line) concave down in the hydromagnetic case. Furthermore, the magnetic field not only changes the shape of the graph of F_0' but also increases it value. This qualitatively agrees with expectations, since the magnetic field exerts an aiding force on the flow field.

For several values of ω, the distribution of the magnitude of the fluctuating velocity gradient $|F_1'|$ is shown in Fig. 2, for both hydrodynamic and hydromagnetic cases. From Fig. 2, we notice that $|F_1'|$ increases with ω in the first half of the channel width and decreases in the other half. This phenomenon is qualitatively true in both hydrodynamic and hydromagnetic cases. Also, the effect of the magnetic field is to increase $|F_1'|$ in the lower half of the channel width and to decrease it in the upper half.

For both hydrodynamic and hydromagnetic cases, the comparison between the exact expression and the combination of low and high frequency approximations (by fixing Hartmann

Downloaded 03 May 2010 to 171.66.16.21. Redistribution subject to ASME license or copyright; see http://www.asme.org/terms/Terms_Use.cfm

number) is shown in Figs. 3 and 4, respectively, for the amplitude and phase angle of the fluctuating shear stress at $y=0$. For all values of the frequency parameter ω, Fig. 3 shows that the effect of Hartmann number M is to increase the amplitude.

From Fig. 4, it can be found that the phase advance $\phi_A = \tan^{-1}(A_i/A_r)$, which is asymptotically given to be 45 deg, slightly overshoots at the intermediate value of ω in the hydrodynamic case. This type of behavior is not present in the hydromagnetic case. This is due to the fact that the magnetic field acting normal to the plate not only reduces ϕ_A but also changes the shape of the curve. However, in the hydromagnetic case ϕ_A, which is given to be 36 deg, slightly overshoots at the intermediate value of ω. This overshooting occurs when $\omega = 5$ in the hydrodynamic case and when $\omega = 6$ in the hydromagnetic case. Further, the effect of the Hartmann number M is to decrease the value of ϕ_A. This phenomenon is true for all values of the frequency parameter ω.

Acknowledgments

The author is greatly indebted to one of the referees for constructive criticisms which led to definite improvements in the paper.

References

Lighthill, M. J., 1954, "The response of Laminar skin friction and heat transfer to fluctuations in the stream velocity," *Proc. R. Soc. Lond.*, Vol. A224, pp. 1-23.

Shercliff, J. A., 1965, *A Textbook of Magnetohydrodynamics*, Pergamon Press, Oxford.

Soundalgekar, V. M., 1973a, "Free Convection on the Oscillatory Flow Past an Infinite, Vertical, Porous Plate With Constant Suction-I," *Proc. R. Soc. Lond.*, Vol. A333, pp. 25-36.

Soundalgekar, V. M., 1973b, "Free Convection Effects on the Oscillatory Flow Past an Infinite, Vertical, Porous Plate with Constant Suction-II," *Proc. R. Soc. Lond.*, Vol. A333, pp. 37-50.

Stuart, J. T., 1955, "A Solution of the Navier-Stokes and Energy Equations Illustrating the Response of Skin Friction and Temperature of an Infinite Plate Thermometer to Fluctuations in the Stream Velocity," *Proc. R. Soc. Lond.*, Vol. A231, pp. 116-130.

Vajravelu, K., and Sastri, K. S., 1977, "Correction to Free Convection Effects on the Oscillatory Flow Past an Infinite, Vertical, Porous Plate with Constant Suction-I," *Proc. R. Soc. Lond.*, Vol. A353, pp. 221-223.

Vajravelu, K., and Sastri, K. S., 1978a, "Laminar Free Convection Heat Transfer of a Viscous Incompressible Heat Generating Fluid Flow Past a Vertical Porous Plate in the Presence of Free Stream Oscillations—I," *Acta Mechanica*, Vol. 31, pp. 71-87.

Vajravelu, K., and Sastri, K. S., 1978b, "Laminar Free Convection Heat Transfer of a Viscous Incompressible Heat Generating Fluid Flow Past a Vertical Porous Plate in the Presence of Free Stream Oscillations-II," *Acta Mechanica*, Vol. 31, pp. 89-100.

Downloaded 03 May 2010 to 171.66.16.21. Redistribution subject to ASME license or copyright; see http://www.asme.org/terms/Terms_Use.cfm

Journal of Applied Mechanics

Brief Notes

A Brief Note is a short paper that presents a specific solution of technical interest in mechanics but which does not necessarily contain new general methods or results. A Brief Note should not exceed 1500 words *or equivalent* (a typical one-column figure or table is equivalent to 250 words; a one line equation to 30 words). Brief Notes will be subject to the usual review procedures prior to publication. After approval such Notes will be published as soon as possible. The Notes should be submitted to the Technical Editor of the JOURNAL OF APPLIED MECHANICS. Discussions on the Brief Notes should be addressed to the Editorial Department, ASME, United Engineering Center, 345 East 47th Street, New York, N. Y. 10017, or to the Technical Editor of the JOURNAL OF APPLIED MECHANICS. Discussions on Brief Notes appearing in this issue will be accepted until two months after publication. Readers who need more time to prepare a Discussion should request an extension of the deadline from the Editorial Department.

Axisymmetric Divergence of Ring-Stiffened Composite Cylindrical Shells Subject to Axial Compression

Victor Birman[1]

Static aeroelastic instability of structures, which is also called divergence, represents an important theoretical and practical problem. Divergence of composite structures has been intensively studied due to increasing utilization of composite materials in the aerospace industry (Librescu and Simovich, 1986).

In this Note, axisymmetric divergence of simply supported, internally ring-reinforced composite shells is considered. The shell is subject to an air flow, directed parallel to the shell axis, and to static axial loading. The analytical coniditions of divergence are obtained both for discrete ring stiffeners and based on the smeared stiffeners technique.

Analysis

Consider an angle-ply cylindrical shell reinforced by internal ring stiffeners. The length of the shell is L, the radius of the middle surface is R and the total thickness is h. The shell is subject to aerodynamic loading of intensity q due to the external gas flow and to the static axial stresses with the resultant N_x. The ends of the shell are simply supported.

If the number of layers is large, which is typical in practical applications, the bending-stretching coupling is negligible even if the layers are not symmetric about the middle surface. Then the equations of equilibrium of the shell experiencing an axisymmetric deformation can be obtained from the equations of Block (1968) or Bogdanovich and Koshkina (1983):

$$A_{11}u_{,xx}+(A_{12}/R)w_{,x}=0$$

$$(A_{12}/R)u_{,x}+D_{11}w_{,xxxx}+(A_{22}/R^2)w-N_xw_{,xx}+\sum_{r=1}^{s}\delta(x-x_r)E_rA_rw/R^2=q \tag{1}$$

where u and w are the axial and radial displacements, respectively, A_{ij} and D_{11} are extensional and bending stiffnesses, E_r is the modulus of elasticity of the rth stiffener in the circumferential direction, and A_r is the cross-sectional area of the same stiffener, $\delta(x-x_r)$ is the Dirac-delta function, x_r is the coordinate of the rth stiffener and s is the total number of stiffeners.

The aerodynamic load is described by quasistatic piston theory:

$$q=-\rho_0c^2M^2(M^2-1)^{-1/2}w_{,x} \tag{2}$$

where ρ_0 is the air density, c is the velocity of sound and M is the Mach number.

The axisymmetric deformations of the simply-supported shell with the ends unrestricted in the axial direction can be represented by two-term series typically used in aeroelastic studies:

$$\begin{aligned} u &= U_m\cos(m\pi\, x/L)+U_{m+1}\cos[(m+1)\pi\, x/L] \\ w &= W_m\sin(m\pi\, x/L)+W_{m+1}\sin[(m+1)\pi\, x/L] \end{aligned} \tag{3}$$

The substitution of (2) and (3) into (1), and use of the Galerkin procedure and some transformations to eliminate U_m, U_{m+1}, yield:

$$\begin{aligned} k_{m1}W_m+(k_{m2}+k_{m3}\bar{M})W_{m+1} &= 0 \\ (k_{m2}+k_{m4}\bar{M})W_m+k_{m5}W_{m+1} &= 0 \end{aligned} \tag{4}$$

where

$$\begin{aligned} k_{m1} &= (m\pi\,\bar{h})^4\bar{D}_{11}+(\lambda\bar{h})^2(\bar{A}_{22}-\bar{A}_{12}{}^2/\bar{A}_{11}) \\ &\quad +(m\,\pi\,\bar{h})^2\bar{N}_x+2\bar{h}\sum_r\bar{E}_r\bar{A}_r\sin^2m\pi\,\bar{x}_r \\ k_{m2} &= 2\bar{h}\sum_r\bar{E}_r\bar{A}_r\sin m\pi\,\bar{x}_r\sin(m+1)\pi\,\bar{x}_r \\ k_{m3} &= (m+1)\pi\,\bar{\rho}\bar{h}f_2(m) \\ k_{m4} &= m\,\pi\,\bar{\rho}\bar{h}f_1(m) \\ k_{m5} &= [(m+1)\pi\,\bar{h}]^4\bar{D}_{11}+(\lambda\bar{h})^2(\bar{A}_{22}-\bar{A}_{12}{}^2/\bar{A}_{11}) \\ &\quad +[(m+1)\pi\,\bar{h})]^2\bar{N}_x+2\bar{h}\Sigma\bar{E}_r\bar{A}_r\sin^2(m+1)\pi\,\bar{x}_r \end{aligned} \tag{5}$$

In (5),

[1]School of Naval Architecture and Marine Engineering, University of New Orleans, New Orleans, LA 70148. Mem. ASME.

Manuscript received by ASME Applied Mechanics Division, February 1, 1988; final revision, May 23, 1988.

Copyright © 1988 by ASME
Downloaded 03 May 2010 to 171.66.16.21. Redistribution subject to ASME license or copyright; see http://www.asme.org/terms/Terms_Use.cfm

$$\bar{h}=h/L \qquad \lambda=L/R \qquad \bar{x}_r=x_r/L$$
$$\bar{A}_{ij}=A_{ij}/E_T h \qquad \bar{D}_{ij}=D_{ij}/E_T h^3$$
$$\bar{E}_r=E_r/E_T \qquad \bar{A}_r=A_r/R^2$$
$$\bar{N}_x=N_x/E_T h \qquad \bar{\rho}=\rho_0 c^2/E_T$$
$$\bar{M}=M^2(M^2-1)^{-1/2}$$
$$f_1(m) = [2+2/(2m+1)]\pi$$
$$f_2(m) = -[2-2/(2m+1)]/\pi \tag{6}$$

where E_T is the modulus of elasticity of the shell material in the transverse direction.

The requirement of the existence of a nonzero solution of (4), used together with the observation that $k_{m3}+k_{m4}=0$, results in the following condition for axisymmetric divergence:

$$\bar{M}=[(k_{m1}k_{m5}-k_{m2}^2)/k_{m3}k_{m4}]^{1/2} \tag{7}$$

The necessary condition of the aeroelastic instability follows from (7):

$$k_{m1}k_{m5}<4\bar{h}^2[\Sigma_r \bar{E}_r\bar{A}_r \sin m\pi\,\bar{x}_r \sin(m+1)\pi\,\bar{x}_r]^2 \tag{8}$$

The product in the left part of the inequality (8) includes the term

$$4\bar{h}^2[\Sigma\,\bar{E}_r\bar{A}_r \sin^2 m\pi\,\bar{x}_r][\Sigma\,\bar{E}_r\bar{A}_r \sin^2(m+1)\pi\,\bar{x}_r]$$

which is larger than the right part of (8) as follows from the Cauchy's inequality. Note also that due to positive-definitiveness of the constitutive matrix, $\bar{A}_{22}-\bar{A}_{12}^2/\bar{A}_{11}>0$. Therefore, the condition (8) can be satisfied only if the shell is subject to compressive axial loads.

Moreover, if the term in the right part of (8) approaches zero, which is typical for aerospace structures, or if the shell is unreinforced, the condition of divergence becomes

$$\bar{N}_{xm}{}^{cr}<\bar{N}_x<\bar{N}_{x(m+1)}{}^{cr} \text{ if } \bar{N}_{xm}{}^{cr}<\bar{N}_{x(m+1)}{}^{cr} \tag{9}$$

or

$$\bar{N}_{x(m+1)}{}^{cr}<\bar{N}_x<\bar{N}_{xm}{}^{cr} \text{ if } \bar{N}_{x(m+1)}{}^{cr}<\bar{N}_{xm}{}^{cr} \tag{10}$$

In (9) and (10) $\bar{N}_{xi}{}^{cr}$ $(i=m,\ m+1)$ are nondimensional axial stress resultants corresponding to axisymmetric buckling with i halfwaves along the shell axis:

$$\bar{N}_{xi}{}^{cr}=-[(i\pi\,\bar{h})^4\bar{D}_{11}+(\lambda\,\bar{h})^2(\bar{A}_{22}-\bar{A}_{12}^2/\bar{A}_{11}) + 2\bar{h}\Sigma_r\bar{E}_r\bar{A}_r \sin i\pi\,\bar{x}_r]/(i\pi\,\bar{h})^2 \tag{11}$$

If the shell is reinforced by a large number of closely spaced identical ring stiffeners, the analysis can be performed using the smeared stiffeners technique. Following this technique the last term in the left part of the second equation (1) must be replaced by $E_r A_r w/R^2 l$, l being the stiffener spacing. Equations (4) become

$$\tilde{k}_{m1}W_m+k_{m3}\bar{M}W_{m+1} = 0$$
$$k_{m4}\bar{M}\,W_m+\tilde{k}_{m5}W_{m+1} = 0 \tag{12}$$

where $\tilde{k}_{m1}$ and $\tilde{k}_{m5}$ can be obtained from k_{m1} and k_{m5}, respectively, if the last terms of these coefficients are replaced by $\bar{E}_r\bar{A}_r/\bar{l}$ where $\bar{l}=l/h$.

Axisymmetric divergence occurs at

$$\bar{M}=(\tilde{k}_{m1}\tilde{k}_{m5}/k_3k_{m4})^{1/2} \tag{13}$$

The condition of axisymmetric divergence which follows from (13) is given by (9) and (10) where

$$\bar{N}_{xi}{}^{cr}=-[(i\pi\,\bar{h})^4\bar{D}_{11}+(\lambda\,\bar{h})^2(\bar{A}_{22}-\bar{A}_{12}^2/\bar{A}_{11}) + \bar{E}_r\bar{A}_r/\bar{l}]/(i\pi\,\bar{h})^2 \tag{14}$$

are nondimensional critical stress resultants calculated for the shell with smeared out rings.

Therefore, axisymmetric divergence of composite shells reinforced by closely spaced identical rings can occur only if the shell is subject to considerable compressive loads exceeding the static buckling value. Note that Vol'mir (1967), who obtained similar results for isotropic rectangular plates, concluded that the flow actually "stabilizes" the plates. In reality, the effect of flow depends on the order of application of loads. If the axial load exceeding the static buckling value is applied before a gas flow, the structure becomes unstable. In such a case the deformations of a structure are a result of dynamic aeroelastic and static post-buckling deformations, and the deflections must be considered using the nonlinear theory. If the gas flow is applied first, static forces can be due to aerodynamic heating. In this case the present analysis can be applied but it must employ corrected values of material properties for the actual elevated temperature.

It is interesting to estimate the magnitude of Mach numbers corresponding to divergence. The maximum parameter $\bar{M}$ can be calculated from (7) or (13). The maximum requirement applied to (7) yields the load corresponding to $\bar{M}_{\max}$:

$$\bar{N}_x{}^*=1/2(\bar{N}_{xm}{}^{cr}+\bar{N}_{x(m+1)}^{cr}) \tag{15}$$

and

$$\bar{M}_{\max}=\{[(m\pi\,\bar{h})^2((m+1)\pi\,\bar{h})^2(\bar{N}_{xm}{}^{cr} - \bar{N}_{x(m+1)}{}^{cr})(\bar{N}_{x(m+1)}{}^{cr}-\bar{N}_{xm}{}^{cr})-k_{m2}{}^2]/k_{m3}k_{m4}\}^{1/2} \tag{16}$$

In the case of smeared-out stiffeners $k_{m2}=0$ and the critical stress resultants in (15) and (16) must be calculated using (14).

An evaluation of (7), (13), and (16) indicates that $\bar{M}\sim 1/\bar{\rho}$. The typical values of $\bar{\rho}$ at sea level are of the order 10^{-5} (Boron/Al 7178-T6: $\bar{\rho}=0.11\times10^{-5}$, Kevlar-49/aramid; $\bar{\rho}=2.57\times10^{-5}$). This indicates that the parameters $\bar{M}$ resulting in divergence are very large at all values of compressive loads except for very narrow intervals adjacent to the loads which yield $\bar{M}=0$ in (7) and (13). In the case of smeared-ring stiffeners $\bar{M}=0$ at $\bar{N}_{xi}{}^{cr}$ $(i=m,\ m+1)$. Note that Mach numbers calculated as functions of $\bar{M}$ are real only if $\bar{M}>2$ (then $M>\sqrt{2}$).

In conclusion, it is shown that axisymmetric divergence of shells reinforced by ring stiffeners can occur only if they are subject to axial compression. Even in this case the velocity of the supersonic flow resulting in divergence is too high to represent practical interest except for narrow intervals of compressive loads. If the number of stiffeners is large and they are closely spaced, these intervals are in the close vicinity of the critical compressive loads. Therefore, axisymmetric divergence is unlikely to occur in shells reinforced by closely spaced identical ring stiffeners.

Note that the conclusion obtained for the shells reinforced by closely spaced rings can be immediately extended to the case of unstiffened shells.

Acknowledgment

The author is grateful to Prof. L. Librescu of the Virginia Polytechnic Institute and State University for helpful discussions.

References

Block, D. L., 1968, "Influence of Discrete Ring Stiffeners and Prebuckling Deformations on the Buckling of Eccentrically Stiffened Orthotropic Cylinders," NASA TN D-4283.

Bogdanovich, A. E., and Koshkina, T. B., 1983, "Deformation and Strength of Ring-Reinforced Orthotropic Cylindrical Shells Subject to Dynamic Compressive Loads," *Mechanics of Composite Materials*, No. 3, pp. 476-488. (In Russian.)

Librescu, L., and Simovich, J., 1986, "A General Formulation for the Aeroelastic Divergence of Composite Sweptforward Wing Structures," Paper ICAS-86-4.8.2 at the 15th Congress of the International Council of the Aeronautical Sciences, London, 1986.

Vol'mir, A. S., 1967, *Stability of Deformable Systems*, Nauka Publishers, Moscow. (In Russian.)

Downloaded 03 May 2010 to 171.66.16.21. Redistribution subject to ASME license or copyright; see http://www.asme.org/terms/Terms_Use.cfm

Comments on Rayleigh's Quotient and Perturbation Theory for the Eigenvalue Problem

Christophe Pierre[2]

The connection between Rayleigh's quotient and perturbation theory for the eigenvalue problem is studied. Equivalence of these techniques is proven under certain conditions.

1 Introduction

Both Rayleigh's quotient and perturbation theory for the eigenvalue problem are well-known approximation techniques for evaluating the modes of vibration of structures without requiring solution of the associated eigenvalue problem. Rayleigh's quotient provides an approximation of the natural frequencies based on trial functions that are often the eigenfunctions of a simpler structural system (Rayleigh, 1926; Meirovitch, 1980; Lancaster, 1966). Perturbation theory for the eigenvalue problem computes, from the eigensolution of the unperturbed system, changes in the modes of vibration that result from structural changes in the system (Meirovitch, 1980; Courant and Hilbert, 1953; Morse and Feshbach, 1953; Plaut and Huseyin, 1973; Fox and Kapoor, 1968; Kato, 1966; Friedrichs, 1960). The latter technique, in particular, is widely used to evaluate the sensitivity of structural and control systems to design changes and uncertainties (Ibrahim, 1987). The relationship between the two methods has been speculated in the literature and Morse and Feshbach (1953) have shown that under some conditions the two techniques are equivalent for stiffness perturbations.

This note presents a detailed discussion of the connection between Rayleigh's quotient and perturbation theory. It is shown that if the unperturbed eigenfunctions are chosen as trial functions for Rayleigh's quotient, a first-order perturbation analysis and Rayleigh's quotient are almost equivalent procedures (what is meant by "almost" is explained below). This result is the primary contribution of the note. In the second part, the relationship between the Rayleigh-Ritz method and perturbation theory is briefly discussed.

2 Perturbation Theory

Here, the perturbation theory for the eigenvalue problem is briefly reviewed. The unperturbed (continuous) eigenvalue problem is considered:

$$\begin{cases} L_0 w_0 = \lambda_0 M_0 w_0 & \text{in } \Omega \\ B_{0k} w_0 = 0 \quad k=1, \ldots, p & \text{on } \Gamma \end{cases} \tag{1}$$

where Ω is the open domain with a boundary Γ, and L_0, M_0, and B_{0k} are linear differential operators. L_0 is of order $2p$, while M_0 and B_{0k} are of order $2p-1$ at most, and M_0 is positive definite. L_0 and M_0 are assumed to be self-adjoint and the eigenvalues to be simple. The first r operators B_{0k} correspond to geometric boundary conditions, while the B_{0k}'s for $k=r+1, \ldots, p$ correspond to natural ones. The boundary conditions are independent of the eigenvalues, which can always be achieved by modifying accordingly the operators in the field equation. If the structural parameters are perturbed, the differential operators are consequently perturbed as

$$L = L_0 + l;\ M = M_0 + m;\ B_k = B_{0k} + b_k,\ k = r+1, \ldots, p \tag{2}$$

where the b_k's, l, and m are perturbation operators. Only perturbations of the *natural* boundary operators are considered. The perturbed eigenvalue problem is

$$\begin{cases} (L_0 + l) w = \lambda (M_0 + m) w & \text{in } \Omega \\ B_{0k} w = 0 \quad k=1, \ldots, r & \text{on } \Gamma \\ (B_{0k} + b_k) w = 0 \quad k=r+1, \ldots, p & \text{on } \Gamma. \end{cases} \tag{3}$$

Considering the first-order expansion of the eigensolution, $\lambda_i = \lambda_{0i} + \delta\lambda_i$, $w_i = w_{0i} + \delta w_i$, and retaining only first-order terms in equation (3) yields

$$\begin{cases} (L_0 - \lambda_{0i} M_0)\delta w_i = \delta\lambda_i M_0 w_{0i} - l w_{0i} + \lambda_{0i} m w_{0i} & \text{in } \Omega \\ B_{0k}\delta w_i = 0 \quad k=1, \ldots, r & \text{on } \Gamma \\ B_{0k}\delta w_i = -b_k w_{0i} \quad k=r+1, \ldots, p & \text{on } \Gamma. \end{cases} \tag{4}$$

Galerkin's method provides an approximate solution of equation (4) by expanding δw_i as

$$\delta w_i = \sum_{j=1}^{+\infty} \epsilon_{ij} w_{0j} \tag{5}$$

However, the approximation procedure must account for the *nonhomogeneous* natural boundary conditions of equation (4). Since the w_{0j}'s are only admissible functions for the problem (4), not comparison functions, this requires one to consider the associated weak formulation:

$$(u,v) = 0 \quad \text{for any admissible function } v \tag{6a}$$

where

$$(u,v) = B(u,v) - \lambda_0 <M_0 u, v> - \delta\lambda <M_0 w_0, v> + <l w_0, v> - \lambda_0 <m w_0, v> \tag{6b}$$

where B is a symmetric bilinear form and $<u,v> = \int_\Omega uv d\Omega$, an inner product on Ω. Integrating equation (6b) by parts and taking $u = \delta w_i$ and $v = w_{0j}$ yields

$$<(L_0 - \lambda_{0i} M_0)\delta w_i, w_{0j}> + <(-\delta\lambda_i M_0 + l - \lambda_{0i} m) w_{0i}, w_{0j}> + \sum_{k=r+1}^{p} <B_{0k}\delta w_i + b_k w_{0i}, C_k w_{0j}>_\Gamma = 0 \tag{7}$$

where $<s,t>_\Gamma = \int_\Gamma st d\Gamma$, an inner product on the boundary. C_k is the operator for the geometric boundary condition corresponding to the natural boundary operator B_k (see examples in (Pierre, 1987)). Finally, the expansion (5) is substituted into equation (7), and the M-orthonormality of the w_{0j}'s is used, yielding

- For $i=j$

$$\delta\lambda_i = <l w_{0i}, w_{0i}> - \lambda_{0i} <m w_{0i}, w_{0i}> + \sum_{k=r+1}^{p} <b_k w_{0i}, C_k w_{0i}>_\Gamma \tag{8}$$

- For $i \neq j$

[2] Assistant Professor, Department of Mechanical Engineering and Applied Mechanics, The University of Michigan, Ann Arbor, MI 48109-2125. Mem. ASME.

Manuscript received by ASME Applied Mechanics Division, September 18, 1987; final revision, June 27, 1988.

Copyright © 1988 by ASME
Downloaded 03 May 2010 to 171.66.16.21. Redistribution subject to ASME license or copyright; see http://www.asme.org/terms/Terms_Use.cfm

$$\epsilon_{ij} = \frac{<lw_{0i}, w_{0j}> - \lambda_{0i} <mw_{0i}, w_{0j}> + \Sigma_{k=r+1}^{p} <b_k w_{0i}, C_k w_{0j}>_\Gamma}{\lambda_{0i} - \lambda_{0j}}. \quad (9)$$

Imposing the normalization condition $<M_0 w_{0i}, w_{0i}> = <Mw_i, w_i> = 1$ determines the remaining unknown to be $\epsilon_{ii} = -\frac{1}{2} <mw_{0i}, w_{0i}>$.

Second-order perturbations can be derived in a similar fashion. For instance, for the eigenvalues:

$$\delta^2\lambda_i = -\delta\lambda_i <mw_{0i}, w_{0i}> + <l\delta w_i', w_{0i}> - \lambda_{0i} <m\delta w_i', w_{0i}> + <\sum_{k=r+1}^{p} <b_k \delta w_i', C_k w_{0i}>_\Gamma \quad (10)$$

where $\delta\lambda_i$ is given by equation (8) and $\delta w_i' = \Sigma_{j \neq i} \epsilon_{ij} w_{0j}$. Note that the above development holds for discrete systems as well.

3 Rayleigh's Quotient

Rayleigh's quotient can be defined from the weak formulation of the eigenvalue problem, namely: find admissible functions u such that

$$B(u,v) - \lambda <Mu, v> = 0 \quad \text{for any admissible function } v \quad (11)$$

where B is a symmetric bilinear form that, after integration by parts, can be written as

$$B(u,v) = <Lu, v> + \sum_{k=r+1}^{p} <B_k u, C_k v>_\Gamma \quad (12)$$

The expression for Rayleigh's quotient is

$$R(u) = \frac{B(u,u)}{<Mu, u>} \quad (13)$$

where u is an admissible function. To obtain an approximation of the ith perturbed eigenvalue, λ_i, u is chosen to be the ith unperturbed eigenfunction, w_{0i}, yielding

$$\lambda_i^R = R(w_{0i}) = \frac{<L_0 w_{0i}, w_{0i}> + <lw_{0i}, w_{0i}> + \Sigma_{k=r+1}^{p} <b_k w_{0i}, C_k w_{0i}>_\Gamma}{<M_0 w_{0i}, w_{0i}> + <mw_{0i}, w_{0i}>} \quad (14)$$

where λ_i^R denotes the Rayleigh's quotient approximation of the ith perturbed eigenvalue. Noting that $\lambda_{0i} = <L_0 w_{0i}, w_{0i}> / <M_0 w_{0i}, w_{0i}>$, with $<M_0 w_{0i}, w_{0i}> = 1$, and defining the variation of the ith eigenvalue due to the structural perturbations, $\delta\lambda_i^R = \lambda_i^R - \lambda_{0i}$ one obtains

$$\delta\lambda_i^R = \lambda_{0i}\left[\frac{1}{1 + <mw_{0i}, w_{0i}>} - 1\right] + \frac{<lw_{0i}, w_{0i}> + \Sigma_{k=r+1}^{p} <b_k w_{0i}, C_k w_{0i}>_\Gamma}{1 + <mw_{0i}, w_{0i}>} \quad (15)$$

4 Comparison of the Two Techniques

The results obtained by Rayleigh's quotient (equation (15)) and perturbation theory (equations (8)–(10)) are compared. It is clear from equations (8) and (15) that when there is no mass perturbation ($m \equiv 0$), *Rayleigh's quotient and first-order perturbation theory yield identical results*. This is the primary result of the note.

When the mass perturbation is present, it is also obvious that the first-order eigenvalue perturbation (8) is a first-order approximation of Rayleigh's quotient with respect to the mass perturbation:

$$\delta\lambda_i^R = -\lambda_{0i} <mw_{0i}, w_{0i}> + <lw_{0i}, w_{0i}> + \sum_{k=r+1}^{p} <b_k w_{0i}, C_k w_{0i}>_\Gamma + \mathcal{O}(<mw_{0i}, w_{0i}>^2) = \delta\lambda_i + \mathcal{O}(<mw_{0i}, w_{0i}>^2). \quad (16)$$

Moreover, expanding Rayleigh's quotient result (15) to the second order in $<mw_{0i}, w_{0i}>$ gives

$$\delta\lambda_i^R = \delta\lambda_i - \delta\lambda_i <mw_{0i}, w_{0i}> + \mathcal{O}(<mw_{0i}, w_{0i}>^3). \quad (17)$$

Hence, the first-order terms in Rayleigh's quotient are the first-order eigenvalue perturbation, $\delta\lambda_i$. The second-order terms are not stiffness or boundary perturbations, but *only* mass perturbation terms, $-\delta\lambda_i <mw_{0i}, w_{0i}>$, which appear precisely in the expression (10) of the second-order eigenvalue perturbation. Therefore, the mass perturbation terms that appear in the denominator of Rayleigh's quotient are only present through their first- and second-order approximations in $\delta\lambda_i$ and $\delta^2\lambda_i$, which is expected. One should *not* conclude, however, that Rayleigh's quotient is equivalent to a second-order perturbation procedure for mass perturbations. This can be clearly seen from the expression (10) of $\delta^2\lambda_i$, since $-\lambda_{0i} <m\delta w_i', w_{0i}>$ (an equally important mass perturbation term) is not accounted for in Rayleigh's quotient expression (15). Therefore, Rayleigh's quotient misses important second-order mass perturbation terms, and the only reason some higher-order mass perturbation terms are present is because mass terms appear in the denominator of Rayleigh's quotient. Of course, it is clear that stiffness and boundary perturbation terms are only present to the *first* order in Rayleigh's quotient. Therefore, even though it keeps some higher-order mass perturbation terms, Rayleigh's quotient is in essence a first-order approximation—an expected result.

One concludes by stating that Rayleigh's quotient is almost (to these higher-order mass terms) equivalent to the first-order perturbation theory, provided the trial functions chosen in Rayleigh's quotient are the unperturbed eigenfunctions. Of course, a second-order perturbation analysis always yields better results than Rayleigh's quotient. It also gives approximations for the eigenfunctions, while Rayleigh's quotient does not.

5 Rayleigh–Ritz and Perturbation Theory

As was shown in Section 2, applying perturbation theory directly to the continuous formulation (3) yields the eigensolution perturbations (8)–(10). This procedure is compared with the one described next.

In the first phase, the perturbed continuous system is discretized by a Rayleigh–Ritz procedure, the sequence of admissible functions being the set of unperturbed eigenfunctions. This is obtained by considering the functional

$$J(u) = \frac{1}{2} B(u,u) - \frac{1}{2} \lambda <Mu, u> \quad (18)$$

where B, after integration by parts, is given by equation (12). The Rayleigh-Ritz procedure consists of approximating u by a finite series in the unperturbed eigenfunctions:

$$u \simeq u_N = \sum_{i=1}^{N} c_i w_{0i} \quad (19)$$

Substituting this expansion into the problem functional (18) and looking for the stationary values of $J(c_1, \ldots, c_i, \ldots, c_N)$ yields

Downloaded 03 May 2010 to 171.66.16.21. Redistribution subject to ASME license or copyright; see http://www.asme.org/terms/Terms_Use.cfm

$$\frac{\partial J}{\partial c_i}(c_1, \ldots, c_j, \ldots, c_N) = 0 \quad i = 1, \ldots, N \tag{20}$$

which, using the symmetry and the bilinearity of B and the self-adjointness of M, leads to the discretized perturbed eigenvalue problem

$$[\mathbf{K}]\mathbf{c} = \lambda[\mathbf{M}]\mathbf{c} \tag{21}$$

where $[\mathbf{K}]$ and $[\mathbf{M}]$ are N by N symmetric matrices defined by

$$\begin{cases} [\mathbf{K}]_{ij} = B(w_{0i}, w_{0j}) = <Lw_{0i}, w_{0j}> + \sum_{k=r+1}^{p} <B_k w_{0i}, C_k w_{0j}>_\Gamma \\ [\mathbf{M}]_{ij} = <Mw_{0i}, w_{0j}> \end{cases} \tag{22}$$

and $\mathbf{c} = [c_1, \ldots, c_i, \ldots, c_N]^T$. One can write $[\mathbf{K}] = [\mathbf{K}_0] + [\mathbf{k}]$ and $[\mathbf{M}] = [\mathbf{M}_0] + [\mathbf{m}]$, where

$$\begin{cases} [\mathbf{K}_0]_{ij} = <L_0 w_{0i}, w_{0j}> + \sum_{k=r+1}^{p} <B_{0k} w_{0i}, C_k w_{0j}>_\Gamma = \lambda_{0i}\delta_{ij} \\ [\mathbf{M}_0]_{ij} = <M_0 w_{0i}, w_{0j}> = \delta_{ij} \end{cases} \tag{23}$$

where δ_{ij} is the Kronecker delta, and

$$\begin{cases} [\mathbf{k}]_{ij} = <lw_{0i}, w_{0j}> + \sum_{k=r+1}^{p} <b_k w_{0i}, C_k w_{0j}>_\Gamma \\ [\mathbf{m}]_{ij} = <mw_{0i}, w_{0j}> \end{cases} \tag{24}$$

In the second phase, perturbation theory is applied to the *discrete* eigenvalue problem (21). Since $[\mathbf{K}_0]$ and $[\mathbf{M}_0]$ are diagonal, the unperturbed solution is $(\lambda_{0i}, \mathbf{c}_{0i} = \mathbf{e}_i)_{i=1,\ldots,N}$, where $\mathbf{e}_i$ is the ith canonical vector. Expanding the eigensolution as $\lambda_i = \lambda_{0i} + \delta\lambda_i$ and $\mathbf{c}_i = \mathbf{c}_{0i} + \delta\mathbf{c}_i$ and applying the first-order perturbation theory for discrete systems (Meirovitch, 1980), one obtains

$$\delta\lambda_i = \mathbf{c}_{0i}^T[\mathbf{k}]\mathbf{c}_{0i} - \lambda_{0i}\mathbf{c}_{0i}^T[\mathbf{m}]\mathbf{c}_{0i} = k_{ii} - \lambda_{0i}m_{ii} \tag{25}$$

which, from equation (24), is readily seen to be *identical* to equation (8) obtained by direct perturbation of the continuous system. Similarly, $\delta\mathbf{c}_i$ is given by

$$\delta\mathbf{c}_i = \sum_{j\neq i} \frac{\mathbf{c}_{0j}^T[\mathbf{k}]\mathbf{c}_{0i} - \lambda_{0i}\mathbf{c}_{0j}^T[\mathbf{m}]\mathbf{c}_{0i}}{\lambda_{0i} - \lambda_{0j}}\ \mathbf{c}_{0j} - \frac{1}{2}\,\mathbf{c}_{0i}^T[\mathbf{m}]\mathbf{c}_{0i}\ \mathbf{c}_{0i}. \tag{26}$$

From the expansion (19), the resulting eigenfunction perturbation is found to be

$$\delta w_i = \sum_{j=1}^{N} (\delta\mathbf{c}_i)_j w_{0j} = \sum_{\substack{j=1 \\ j\neq i}}^{N} \frac{k_{ji} - \lambda_{0i}m_{ji}}{\lambda_{0i} - \lambda_{0j}} w_{0j} - \frac{1}{2}m_{ii}w_{0i} \tag{27}$$

which, using equation (24) and the symmetry of $[\mathbf{k}]$ and $[\mathbf{m}]$, is identical to the first-order eigenfunction perturbation given by equations (5) and (9).

Therefore, it has been shown that using perturbation theory for a continuous eigenvalue problem is equivalent to discretizing the system by a Rayleigh-Ritz procedure and then applying perturbation theory to the discretized system, provided the unperturbed eigenfunctions are chosen as the admissible functions for the Rayleigh-Ritz method. Second-order results could be shown to be identical as well. Finally, the extension of these results to nonself-adjoint systems could be explored.

Acknowledgments

This work was supported by National Science Foundation Grant No. MSM-8700820, Dynamic Systems and Control Program, and by a University of Michigan Rackham Faculty Grant.

References

Courant, R., and Hilbert, D., 1953, *Methods of Mathematical Physics*, Volume I, Wiley, Interscience Publishers, Inc., New York.

Fox, R. L., and Kapoor, M. P., 1968, "Rates of Change of Eigenvalues and Eigenvectors," *AIAA Journal*, Vol. 6, No. 12, pp. 2426–2429.

Friedrichs, K. O., 1960, *Perturbation of Spectra in Hilbert Space*, Lectures in Applied Mathematics, Proceedings of the Summer Seminar, Volume III, Boulder, Colorado.

Ibrahim, R. A., 1987, "Structural Dynamics with Parameter Uncertainties," ASME *Applied Mechanics Reviews*, Vol. 40, No. 3, pp. 309–328.

Kato, T., 1966, *Perturbation Theory for Linear Operators*, Springer-Verlag, New York.

Lancaster, P., 1966, *Lambda-Matrices and Vibrating Systems*, Pergamon Press, New York.

Lord Rayleigh, 1926, *The Theory of Sound*, Vol. 1, Macmillan and Co., Limited, London, Section 90–91.

Meirovitch, L., 1980, *Computational Methods in Structural Dynamics*, Sijthoff-Noordhoff Co., The Netherlands.

Morse, P. M., and Feshbach, H., 1953, *Methods of Theoretical Physics*, Part II, McGraw-Hill, New York, Section 9.4.

Pierre, C., 1987, "Eigensolution Perturbation for Systems with Perturbed Boundary Conditions," *Journal of Sound and Vibration*, Vol. 112, No. 1, pp. 167–172.

Plaut, R. H., and Huseyin, K., 1973, "Derivatives of Eigenvalues and Eigenvectors in Non-Self-Adjoint Systems," *AIAA Journal*, Vol. 11, No. 2, pp. 250–251.

Bounds on Harmonically Forced Response of Damped Linear Systems

Z. Liang[3] and T. T. Soong[4]

Introduction

Response bounds for linear mechanical or structural systems have been the subject of several recent publications (Nicholson, 1980; Inman and Andry, 1980; Yae and Inman, 1987; Nicholson, 1987). Since it is generally difficult and time consuming to determine the detailed system response behavior, particularly when the number of degrees-of-freedom is large, it is useful to seek information on response bounds if they can be determined expediently. Our purpose in this paper is to derive generally sharper and easier to calculate response bounds under harmonic excitations. These bounds are obtained by assuming that the maximum response occurs at the first modal resonance and by omitting minor contributions of conservative forces in this resonance region.

The motion of a damped linear mechanical or structural system is governed by

$$M\ddot{\mathbf{x}}(t) + C\dot{\mathbf{x}}(t) + K\mathbf{x}(t) = \mathbf{f}(t) \tag{1}$$

where M, C, and K are positive definite mass, damping, and stiffness matrices, respectively, $\mathbf{x}(t)$ is the displacement vector, and $\mathbf{f}(t)$ is the external excitation. The overdot represents time derivative. Without loss of generality, we can set $M = I$, the identity matrix.

Consider the conservative force

$$\mathbf{Q}(t) = I\ddot{\mathbf{x}}(t) + K\dot{\mathbf{x}}(t) \tag{2}$$

when the system is subjected to an external harmonic excitation with frequency ω, i.e., $\mathbf{f}(t) = \mathbf{f}_0 \exp(j\omega t)$, we shall first prove the following:

Lemma. When the excitation frequency ω is below or at

[3]Research Associate, and [4]Professor, Department of Civil Engineering, State University of New York at Buffalo, Buffalo, NY 14260.

Manuscript received by ASME Applied Mechanics Division, March 10, 1988; final revision, June 15, 1988.

Downloaded 03 May 2010 to 171.66.16.21. Redistribution subject to ASME license or copyright; see http://www.asme.org/terms/Terms_Use.cfm

$$\frac{\partial J}{\partial c_i}(c_1, \ldots, c_j, \ldots, c_N) = 0 \quad i = 1, \ldots, N \tag{20}$$

which, using the symmetry and the bilinearity of B and the self-adjointness of M, leads to the discretized perturbed eigenvalue problem

$$[\mathbf{K}]\mathbf{c} = \lambda[\mathbf{M}]\mathbf{c} \tag{21}$$

where $[\mathbf{K}]$ and $[\mathbf{M}]$ are N by N symmetric matrices defined by

$$\begin{cases} [\mathbf{K}]_{ij} = B(w_{0i}, w_{0j}) = <Lw_{0i}, w_{0j}> + \sum_{k=r+1}^{p} <B_k w_{0i}, C_k w_{0j}>_\Gamma \\ [\mathbf{M}]_{ij} = <Mw_{0i}, w_{0j}> \end{cases} \tag{22}$$

and $\mathbf{c} = [c_1, \ldots, c_i, \ldots, c_N]^T$. One can write $[\mathbf{K}] = [\mathbf{K}_0] + [\mathbf{k}]$ and $[\mathbf{M}] = [\mathbf{M}_0] + [\mathbf{m}]$, where

$$\begin{cases} [\mathbf{K}_0]_{ij} = <L_0 w_{0i}, w_{0j}> + \sum_{k=r+1}^{p} <B_{0k} w_{0i}, C_k w_{0j}>_\Gamma = \lambda_{0i}\delta_{ij} \\ [\mathbf{M}_0]_{ij} = <M_0 w_{0i}, w_{0j}> = \delta_{ij} \end{cases} \tag{23}$$

where δ_{ij} is the Kronecker delta, and

$$\begin{cases} [\mathbf{k}]_{ij} = <lw_{0i}, w_{0j}> + \sum_{k=r+1}^{p} <b_k w_{0i}, C_k w_{0j}>_\Gamma \\ [\mathbf{m}]_{ij} = <mw_{0i}, w_{0j}> \end{cases} \tag{24}$$

In the second phase, perturbation theory is applied to the *discrete* eigenvalue problem (21). Since $[\mathbf{K}_0]$ and $[\mathbf{M}_0]$ are diagonal, the unperturbed solution is $(\lambda_{0i}, \mathbf{c}_{0i} = \mathbf{e}_i)_{i=1,\ldots,N}$, where $\mathbf{e}_i$ is the ith canonical vector. Expanding the eigensolution as $\lambda_i = \lambda_{0i} + \delta\lambda_i$ and $\mathbf{c}_i = \mathbf{c}_{0i} + \delta\mathbf{c}_i$ and applying the first-order perturbation theory for discrete systems (Meirovitch, 1980), one obtains

$$\delta\lambda_i = \mathbf{c}_{0i}^T[\mathbf{k}]\mathbf{c}_{0i} - \lambda_{0i}\mathbf{c}_{0i}^T[\mathbf{m}]\mathbf{c}_{0i} = k_{ii} - \lambda_{0i}m_{ii} \tag{25}$$

which, from equation (24), is readily seen to be *identical* to equation (8) obtained by direct perturbation of the continuous system. Similarly, $\delta\mathbf{c}_i$ is given by

$$\delta\mathbf{c}_i = \sum_{j\neq i} \frac{\mathbf{c}_{0j}^T[\mathbf{k}]\mathbf{c}_{0i} - \lambda_{0i}\mathbf{c}_{0j}^T[\mathbf{m}]\mathbf{c}_{0i}}{\lambda_{0i} - \lambda_{0j}}\ \mathbf{c}_{0j} - \frac{1}{2}\,\mathbf{c}_{0i}^T[\mathbf{m}]\mathbf{c}_{0i}\ \mathbf{c}_{0i}. \tag{26}$$

From the expansion (19), the resulting eigenfunction perturbation is found to be

$$\delta w_i = \sum_{j=1}^{N} (\delta\mathbf{c}_i)_j w_{0j} = \sum_{\substack{j=1 \\ j\neq i}}^{N} \frac{k_{ji} - \lambda_{0i}m_{ji}}{\lambda_{0i} - \lambda_{0j}} w_{0j} - \frac{1}{2}m_{ii}w_{0i} \tag{27}$$

which, using equation (24) and the symmetry of $[\mathbf{k}]$ and $[\mathbf{m}]$, is identical to the first-order eigenfunction perturbation given by equations (5) and (9).

Therefore, it has been shown that using perturbation theory for a continuous eigenvalue problem is equivalent to discretizing the system by a Rayleigh-Ritz procedure and then applying perturbation theory to the discretized system, provided the unperturbed eigenfunctions are chosen as the admissible functions for the Rayleigh-Ritz method. Second-order results could be shown to be identical as well. Finally, the extension of these results to nonself-adjoint systems could be explored.

Acknowledgments

This work was supported by National Science Foundation Grant No. MSM-8700820, Dynamic Systems and Control Program, and by a University of Michigan Rackham Faculty Grant.

References

Courant, R., and Hilbert, D., 1953, *Methods of Mathematical Physics*, Volume I, Wiley, Interscience Publishers, Inc., New York.

Fox, R. L., and Kapoor, M. P., 1968, "Rates of Change of Eigenvalues and Eigenvectors," *AIAA Journal*, Vol. 6, No. 12, pp. 2426–2429.

Friedrichs, K. O., 1960, *Perturbation of Spectra in Hilbert Space*, Lectures in Applied Mathematics, Proceedings of the Summer Seminar, Volume III, Boulder, Colorado.

Ibrahim, R. A., 1987, "Structural Dynamics with Parameter Uncertainties," ASME *Applied Mechanics Reviews*, Vol. 40, No. 3, pp. 309–328.

Kato, T., 1966, *Perturbation Theory for Linear Operators*, Springer-Verlag, New York.

Lancaster, P., 1966, *Lambda-Matrices and Vibrating Systems*, Pergamon Press, New York.

Lord Rayleigh, 1926, *The Theory of Sound*, Vol. 1, Macmillan and Co., Limited, London, Section 90–91.

Meirovitch, L., 1980, *Computational Methods in Structural Dynamics*, Sijthoff-Noordhoff Co., The Netherlands.

Morse, P. M., and Feshbach, H., 1953, *Methods of Theoretical Physics*, Part II, McGraw-Hill, New York, Section 9.4.

Pierre, C., 1987, "Eigensolution Perturbation for Systems with Perturbed Boundary Conditions," *Journal of Sound and Vibration*, Vol. 112, No. 1, pp. 167–172.

Plaut, R. H., and Huseyin, K., 1973, "Derivatives of Eigenvalues and Eigenvectors in Non-Self-Adjoint Systems," *AIAA Journal*, Vol. 11, No. 2, pp. 250–251.

Bounds on Harmonically Forced Response of Damped Linear Systems

Z. Liang[3] and T. T. Soong[4]

Introduction

Response bounds for linear mechanical or structural systems have been the subject of several recent publications (Nicholson, 1980; Inman and Andry, 1980; Yae and Inman, 1987; Nicholson, 1987). Since it is generally difficult and time consuming to determine the detailed system response behavior, particularly when the number of degrees-of-freedom is large, it is useful to seek information on response bounds if they can be determined expediently. Our purpose in this paper is to derive generally sharper and easier to calculate response bounds under harmonic excitations. These bounds are obtained by assuming that the maximum response occurs at the first modal resonance and by omitting minor contributions of conservative forces in this resonance region.

The motion of a damped linear mechanical or structural system is governed by

$$M\ddot{\mathbf{x}}(t) + C\dot{\mathbf{x}}(t) + K\mathbf{x}(t) = \mathbf{f}(t) \tag{1}$$

where M, C, and K are positive definite mass, damping, and stiffness matrices, respectively, $\mathbf{x}(t)$ is the displacement vector, and $\mathbf{f}(t)$ is the external excitation. The overdot represents time derivative. Without loss of generality, we can set $M = I$, the identity matrix.

Consider the conservative force

$$\mathbf{Q}(t) = I\ddot{\mathbf{x}}(t) + K\dot{\mathbf{x}}(t) \tag{2}$$

when the system is subjected to an external harmonic excitation with frequency ω, i.e., $\mathbf{f}(t) = \mathbf{f}_0 \exp(j\omega t)$, we shall first prove the following:

Lemma. When the excitation frequency ω is below or at

[3]Research Associate, and [4]Professor, Department of Civil Engineering, State University of New York at Buffalo, Buffalo, NY 14260.

Manuscript received by ASME Applied Mechanics Division, March 10, 1988; final revision, June 15, 1988.

Copyright © 1988 by ASME
Downloaded 03 May 2010 to 171.66.16.21. Redistribution subject to ASME license or copyright; see http://www.asme.org/terms/Terms_Use.cfm

the first modal frequency ω_1, the conservative force $\mathbf{Q}(t)$ always does negative or zero work against the external force $\mathbf{f}(t)$.

Proof. Without loss of generality, let the work done by the external force be positive, i.e, $\mathbf{x}^H\mathbf{f}>0$. Then, it is to be proved that

$$-\mathbf{x}^H\mathbf{Q}\le 0 \quad \text{or} \quad \mathbf{x}^H\mathbf{Q}\ge 0 \tag{3}$$

where the superscript H denotes Hermitian transpose.

With $\mathbf{f}(t)$ given by (3), the displacement vector $\mathbf{x}(t)$ has the form

$$\mathbf{x}=P[e^{j\omega t+\Theta_1}, e^{j\omega t+\Theta_2}, \ldots]^T=P\boldsymbol{\Theta}e^{j\omega t} \tag{4}$$

where P is the eigenvector matrix of the undamped system and

$$\boldsymbol{\Theta}=[e^{j\Theta_1}, e^{j\Theta_2}, \ldots]^T.$$

From (4) we have

$$\dot{\mathbf{x}}=j\omega P\boldsymbol{\Theta}e^{j\omega t} \quad \text{and} \quad \ddot{\mathbf{x}}=-\omega^2 P\boldsymbol{\Theta}e^{j\omega t} \tag{5}$$

The substitution of (4) and (5) into (2) yields

$$\begin{aligned}\mathbf{x}^H\mathbf{Q}&=[P\boldsymbol{\Theta}e^{j\omega t}]^H[-\omega^2 P\boldsymbol{\Theta}e^{j\omega t}+KP\boldsymbol{\Theta}e^{j\omega t}]\\&=e^{-j\omega t}\boldsymbol{\Theta}^H P^T(-\omega^2 I+K)P\boldsymbol{\Theta}e^{j\omega t}\\&=\boldsymbol{\Theta}^H P^T(-\omega^2 I+K)P\boldsymbol{\Theta}\end{aligned} \tag{6}$$

At the first modal resonance point, $\omega^2\le\omega_1^2$ and the matrix $(-\omega^2 I+K)$ is semipositive definite and so is $\mathbf{x}^H\mathbf{Q}$ as expressed by (6). Hence, (3) is satisfied.

As a consequence of this lemma, it is clear that, when $\omega^2\le\omega_1^2$, the system response bound would be greater without the conservative force $\mathbf{Q}$ acting against the external force. Hence, we have the inequality

$$\|\dot{\mathbf{x}}\|\le\|C^{-1}\mathbf{f}_0\|. \tag{7}$$

Note that

$$\dot{\mathbf{x}}=j\omega\mathbf{x}\cong j\omega_1[1-2\zeta_1^2]^{1/2}\mathbf{x}. \tag{8}$$

Inequality (7) becomes

$$\|j\omega_1[1-2\zeta_1^2]^{1/2}\mathbf{x}\|\le\|C^{-1}\mathbf{f}_0\| \tag{9}$$

In the above, $\|.\|$ denotes a vector norm, which can be any kind of norm. For convenience, the Euclidean norm is taken here. The quantity ζ_1 denotes the first modal damping ratio.

Upon rearranging, (9) gives the bound on $\|\mathbf{x}\|$ in the form

$$\|\mathbf{x}\|\le\|C^{-1}f_0\|/[\omega_1(1-2\zeta_1^2)^{1/2}]. \tag{10}$$

Since work done by the conservative force $\mathbf{Q}(t)$ diminishes as ω approaches ω_1, inequality (10) is expected to give sharp bounds by omitting $\mathbf{Q}(t)$ in the first modal resonance region. It is also seen that (10) requires much less computation when compared with, for example, integration procedures required in Yae and Inman (1987).

Numerical Examples

Example 1. As the first example and following Yae and Inman (1987), consider a two-degree-of-freedom system with

$$K=\begin{bmatrix}5 & -1\\ -1 & 1\end{bmatrix} \quad \text{and} \quad C=(K+I)/2+e\begin{bmatrix}0 & 1\\ 1 & 0\end{bmatrix}$$

where I is the 2×2 identity matrix. As in Yae and Inman (1987), e is a parameter controlling the degree of decoupling; the smaller the e is, the closer the system is to a decouplable system. The decoupling condition $CK=KC$ is satisfied when $e=0$. Many methods of bound estimation are sensitive to the degree of decoupling, becoming worse as e becomes large in general.

Table 1 Response bounds for Example 1

$\underset{\sim}{f}_o$	e	Response Bounds: Exact	This Paper	From [3]
$[1\ 0]^T$	0.5	0.3875	0.8406	2.2556
	0.2	0.3892	0.6460	1.8057
	0.1	0.3949	0.6403	1.6509
	0	—	0.6496	1.4930
	-0.01	0.3955	0.6512	1.5189
	-0.1	0.4092	0.6716	1.7932
	-0.2	0.4710	0.5413	2.2073
	-0.5	0.6805	0.9041	4.9993
$[0\ 1]^T$	0.5	1.3945	2.5639	2.2556
	0.2	1.4290	1.8963	1.8057
	0.1	1.6400	1.8288	1.6509
	0	—	1.7956	1.4930
	-0.01	1.5091	1.7938	1.5189
	-0.1	1.5262	1.7902	1.7932
	-0.2	1.7456	1.8105	2.2073
	-0.5	1.7900	2.0520	4.9993

Table 2 Response bounds for Example 2 with $f_0=[1\ 0\ 0\ 0]^T$

e	Response Bounds: Exact	This Paper	From [3]
0	1.4128	1.6636	17.3160
0.01	1.3700	1.6210	18.3961
0.05	1.2165	1.4790	22.0782
0.1	1.0761	1.3470	26.0176

Table 3 Response bounds for different external forces

e	$\underset{\sim}{f}_o$	Response Bounds: This Paper	From [3]
0	$[1\ 0\ 0\ 0]^T$	1.6636	
	$[0\ 1\ 0\ 0]^T$	8.5541	
	$[0\ 0\ 1\ 0]^T$	10.1860	17.3160
	$[0\ 0\ 0\ 1]^T$	10.8476	
0.01	$[1\ 0\ 0\ 0]^T$	1.6210	
	$[0\ 1\ 0\ 0]^T$	8.4351	
	$[0\ 0\ 1\ 0]^T$	10.0203	18.3960
	$[0\ 0\ 0\ 1]^T$	10.6386	
0.05	$[1\ 0\ 0\ 0]^T$	1.4790	
	$[0\ 1\ 0\ 0]^T$	7.5986	
	$[0\ 0\ 1\ 0]^T$	8.9411	22.0782
	$[0\ 0\ 0\ 1]^T$	9.3778	
0.1	$[1\ 0\ 0\ 0]^T$	1.3470	
	$[0\ 1\ 0\ 0]^T$	6.8121	
	$[0\ 0\ 1\ 0]^T$	7.9220	26.0176
	$[0\ 0\ 0\ 1]^T$	8.1840	

The bounds on $\|\mathbf{x}\|$ using (10) have been calculated for several values of e and for two cases of $\mathbf{f}_0$: $\mathbf{f}_0=[1, 0]^T$ and $\mathbf{f}_0=[0, 1]^T$. These results are compared with the exact values and those obtained using the estimation formula given in Yae and Inman (1987), and these are tabulated in Table 1. It is seen that (10) provides consistently sharp bounds over the range of e considered and it needs much less computing time, about one-third of that required using the procedure in Yae and Inman (1987). Even greater savings can be realized when the system frequencies are known.

Another important observation to be made is that this procedure gives different bounds for different component information of the external force, while the method in Yae and Inman (1987), being only a function of $\|\mathbf{f}_0\|$, is incapable of doing so. This point is further discussed in the second example.

Example 2. Consider now a more heavily damped four-degree-of-freedom system with

$$K=\begin{bmatrix}6 & -1 & 0 & 0\\ -1 & 4 & -3 & 0\\ 0 & -3 & 7 & -4\\ 0 & 0 & -4 & 4\end{bmatrix} \quad \text{and} \quad C=0.5K+e\begin{bmatrix}1 & 0 & 0 & 0\\ 0 & 0 & 0 & 0\\ 0 & 0 & 0 & 0\\ 0 & 0 & 0 & 1\end{bmatrix}$$

The results of this example are shown in Table 2 with

$$\mathbf{f}_0=[1\quad 0\quad 0\quad 0]^T$$

In Table 2, the force vector was chosen to produce a weak system response. However, for methods which are not capable

Downloaded 03 May 2010 to 171.66.16.21. Redistribution subject to ASME license or copyright; see http://www.asme.org/terms/Terms_Use.cfm

of taking into account component properties of the external force, the bounds can be grossly overestimated as those shown in Table 2 using the procedure developed in Yae and Inman (1987). Table 3 gives the estimated bounds for the same system with different force vectors.

Concluding Remarks

It is seen from the examples cited previously that the results derived here can produce sharp bounds for the system response and are sensitive to component information of the external force vector. Another significant advantage is greater savings in computation.

Unlike many other methods, these bounds are not as sensitive to the degree of decoupling, making it suitable for coupled as well as decouplable systems.

Acknowledgment

This work was supported by the National Science Foundation under the auspices of the National Center for Earthquake Engineering Research, Grant No. NCEER-86-3025.

References

Inman, D. J., and Andry, A. N., 1980, "Some Results on the Nature of Eigenvalues of Discrete Damped Linear Systems," ASME JOURNAL OF APPLIED MECHANICS, Vol. 47, pp. 927–930.

Nicholson, D. W., 1980, "Bounds on the Forced Response of Damped Systems," *Mechanics Research Communications*, Vol. 7, pp. 305–308.

Nicholson, D. W., 1987, "Response Bounds for Nonclassically Damped Mechanical Systems Under Transient Loads," ASME JOURNAL OF APPLIED MECHANICS, Vol. 54, pp. 430–433.

Yae, K. H., and Inman, D. J., 1987, "Response Bounds for Linear Underdamped Systems, ASME JOURNAL OF APPLIED MECHANICS, Vol. 54, pp. 419–423.

Wave Propagation in a Rod With a Varying Cross-Section

David L. Clements[5] and Ashley Larsson[5]

1 Introduction

This paper is concerned with one-dimensional wave propagation in an elastic rod with a varying cross-section. The governing equation is a linear first-order hyperbolic partial differential equation with variable coefficients. Equations of this type have been investigated by a number of authors in connection with a variety of problems (see, for example, Eason (1967), Synge (1981), and Webster (1919)). These authors have used various techniques to obtain analytical solutions which are relevant to the particular physical situation under considerations. These solutions can be applied with appropriate minor modifications to wave propagation in rods of varying cross-section. However, in general, the analytical solutions available in these papers are limited to very particular variations in the cross-section of the rod. The purpose of the present paper is to obtain a relatively simple analytical solution for a general variation in the cross-sectional area. This solution is used to consider a particular problem for a finite rod with one end fixed and the other end subjected to a time-dependent load.

[5]Department of Applied Mathematics, University of Adelaide, Adelaide, Australia 5001.

Manuscript received by ASME Applied Mechanics Division, January 27, 1987; final revision, May 18, 1988.

2 Basic Equations and Their Solution

Wave propagation along a homogeneous elastic rod of varying cross-section is considered. The relevant stress-strain relation is

$$\sigma = \mathrm{E}\frac{\partial u}{\partial x}, \tag{1}$$

where x is the space coordinate measured along the rod, σ is the stress, u the displacement, and E denotes Young's modulus. In the absence of body forces, the equation of motion becomes

$$\frac{1}{A(x)}\frac{\partial}{\partial x}[A(x)\sigma] = \rho\frac{\partial^2 u}{\partial t^2}, \tag{2}$$

where $A(x)$ is the variable cross-sectional area, ρ is the density, and t denotes time. Substitution of (2) into (1) provides

$$\frac{1}{A(x)}\frac{\partial}{\partial x}\left[A(x)\frac{\partial u}{\partial x}\right] = \frac{\rho}{\mathrm{E}}\frac{\partial^2 u}{\partial t^2}. \tag{3}$$

The transformation

$$\tau = \sqrt{\frac{\mathrm{E}}{\rho}}\,t \tag{4}$$

yields

$$\frac{1}{A(x)}\frac{\partial}{\partial x}\left[A(x)\frac{\partial u}{\partial x}\right] = \frac{\partial^2 u}{\partial \tau^2}. \tag{5}$$

We set

$$u = A^{-1/2}U \tag{6}$$

so that

$$\Delta U - \Lambda(x)U = 0, \quad \Delta \equiv \frac{\partial^2}{\partial x^2} - \frac{\partial^2}{\partial \tau^2} \tag{7}$$

where

$$\Lambda(x) = [[A']^2/4A]'/A' \tag{8}$$

where the prime denotes the derivative with respect to x. A formal solution to (7) is sought in the form

$$U = \sum_{n=0}^{\infty} h_n(x)F_n(\tau + x) \tag{9}$$

whence, on insertion

$$\sum_{n=0}^{\infty}[(h_n'' - \Lambda h_n)F_n + 2h_{n+1}'F_n'] = 0. \tag{10}$$

If we set

$$F_n' = F_{n-1} \text{ for } n \geq 1 \tag{11}$$

$$2h_{n+1}' + h_n'' - \Lambda h_n = 0 \quad \text{for } n \geq 0,\ h_0 = \text{constant}. \tag{12}$$

it is seen that (10) is satisfied.

In a similar manner it may be shown that (7) admits solutions of the form

$$U = \sum_{n=0}^{\infty} h_n(x)G_n(\tau - x), \tag{13}$$

where

$$G_n' = G_{n-1},\ n \geq 1 \tag{14}$$

and the h_n satisfy (12).

The validity of these solutions to (7) depends on the convergence of the series (9) and (13). Convergence properties of series of this type may be analyzed after the manner of Bergman (1971). Here, we show that in certain cases, the series (9) and (13) truncate after a finite number of terms and in such case the validity of the solution is assured.

Downloaded 03 May 2010 to 171.66.16.21. Redistribution subject to ASME license or copyright; see http://www.asme.org/terms/Terms_Use.cfm

of taking into account component properties of the external force, the bounds can be grossly overestimated as those shown in Table 2 using the procedure developed in Yae and Inman (1987). Table 3 gives the estimated bounds for the same system with different force vectors.

Concluding Remarks

It is seen from the examples cited previously that the results derived here can produce sharp bounds for the system response and are sensitive to component information of the external force vector. Another significant advantage is greater savings in computation.

Unlike many other methods, these bounds are not as sensitive to the degree of decoupling, making it suitable for coupled as well as decouplable systems.

Acknowledgment

This work was supported by the National Science Foundation under the auspices of the National Center for Earthquake Engineering Research, Grant No. NCEER-86-3025.

References

Inman, D. J., and Andry, A. N., 1980, "Some Results on the Nature of Eigenvalues of Discrete Damped Linear Systems," ASME JOURNAL OF APPLIED MECHANICS, Vol. 47, pp. 927–930.

Nicholson, D. W., 1980, "Bounds on the Forced Response of Damped Systems," *Mechanics Research Communications*, Vol. 7, pp. 305–308.

Nicholson, D. W., 1987, "Response Bounds for Nonclassically Damped Mechanical Systems Under Transient Loads," ASME JOURNAL OF APPLIED MECHANICS, Vol. 54, pp. 430–433.

Yae, K. H., and Inman, D. J., 1987, "Response Bounds for Linear Underdamped Systems, ASME JOURNAL OF APPLIED MECHANICS, Vol. 54, pp. 419–423.

Wave Propagation in a Rod With a Varying Cross-Section

David L. Clements[5] and Ashley Larsson[5]

1 Introduction

This paper is concerned with one-dimensional wave propagation in an elastic rod with a varying cross-section. The governing equation is a linear first-order hyperbolic partial differential equation with variable coefficients. Equations of this type have been investigated by a number of authors in connection with a variety of problems (see, for example, Eason (1967), Synge (1981), and Webster (1919)). These authors have used various techniques to obtain analytical solutions which are relevant to the particular physical situation under considerations. These solutions can be applied with appropriate minor modifications to wave propagation in rods of varying cross-section. However, in general, the analytical solutions available in these papers are limited to very particular variations in the cross-section of the rod. The purpose of the present paper is to obtain a relatively simple analytical solution for a general variation in the cross-sectional area. This solution is used to consider a particular problem for a finite rod with one end fixed and the other end subjected to a time-dependent load.

[5]Department of Applied Mathematics, University of Adelaide, Adelaide, Australia 5001.

Manuscript received by ASME Applied Mechanics Division, January 27, 1987; final revision, May 18, 1988.

2 Basic Equations and Their Solution

Wave propagation along a homogeneous elastic rod of varying cross-section is considered. The relevant stress-strain relation is

$$\sigma = \mathrm{E}\frac{\partial u}{\partial x}, \tag{1}$$

where x is the space coordinate measured along the rod, σ is the stress, u the displacement, and E denotes Young's modulus. In the absence of body forces, the equation of motion becomes

$$\frac{1}{A(x)}\frac{\partial}{\partial x}[A(x)\sigma] = \rho\frac{\partial^2 u}{\partial t^2}, \tag{2}$$

where $A(x)$ is the variable cross-sectional area, ρ is the density, and t denotes time. Substitution of (2) into (1) provides

$$\frac{1}{A(x)}\frac{\partial}{\partial x}\left[A(x)\frac{\partial u}{\partial x}\right] = \frac{\rho}{\mathrm{E}}\frac{\partial^2 u}{\partial t^2}. \tag{3}$$

The transformation

$$\tau = \sqrt{\frac{\mathrm{E}}{\rho}}\,t \tag{4}$$

yields

$$\frac{1}{A(x)}\frac{\partial}{\partial x}\left[A(x)\frac{\partial u}{\partial x}\right] = \frac{\partial^2 u}{\partial \tau^2}. \tag{5}$$

We set

$$u = A^{-1/2}U \tag{6}$$

so that

$$\Delta U - \Lambda(x)U = 0, \quad \Delta \equiv \frac{\partial^2}{\partial x^2} - \frac{\partial^2}{\partial \tau^2} \tag{7}$$

where

$$\Lambda(x) = [[A']^2/4A]'/A' \tag{8}$$

where the prime denotes the derivative with respect to x. A formal solution to (7) is sought in the form

$$U = \sum_{n=0}^{\infty} h_n(x)F_n(\tau + x) \tag{9}$$

whence, on insertion

$$\sum_{n=0}^{\infty}[(h_n'' - \Lambda h_n)F_n + 2h_{n+1}'F_n'] = 0. \tag{10}$$

If we set

$$F_n' = F_{n-1} \text{ for } n \geq 1 \tag{11}$$

$$2h_{n+1}' + h_n'' - \Lambda h_n = 0 \quad \text{for } n \geq 0,\ h_0 = \text{constant}. \tag{12}$$

it is seen that (10) is satisfied.

In a similar manner it may be shown that (7) admits solutions of the form

$$U = \sum_{n=0}^{\infty} h_n(x)G_n(\tau - x), \tag{13}$$

where

$$G_n' = G_{n-1},\ n \geq 1 \tag{14}$$

and the h_n satisfy (12).

The validity of these solutions to (7) depends on the convergence of the series (9) and (13). Convergence properties of series of this type may be analyzed after the manner of Bergman (1971). Here, we show that in certain cases, the series (9) and (13) truncate after a finite number of terms and in such case the validity of the solution is assured.

Copyright © 1988 by ASME
Downloaded 03 May 2010 to 171.66.16.21. Redistribution subject to ASME license or copyright; see http://www.asme.org/terms/Terms_Use.cfm

In the simplest case h_0 may be taken to be one and $h_n = 0$ for $n \geq 1$. It follows from (12) that $\Lambda(x) = 0$ and then (8) provides

$$A(x) = (\alpha x + \beta)^2,$$

where α and β are arbitrary constants. The displacement in this case, may be obtained from (6), (9), and (13) in the form

$$u = (\alpha x + \beta)^{-1}[F_0(\tau + x) + G_0(\tau - x)].$$

When there are two terms in the sum in (9) and (13) (so that $h_n = 0$ when $n \geq 2$) it may be readily verified from (8) and (12) that, with $h_0 = 1$,

$$h_1 = \frac{-\beta}{(\beta x + \delta)}, \quad A(x) = (\beta x + \delta)^{-2}$$

where β and δ are arbitrary constants.

More generally, if $A(x)$ has the form

$$A(x) = (\alpha x + \beta)^p,$$

then

$$\Lambda(x) = \frac{p\alpha^2}{4}(p-2)(\alpha x + \beta)^{-2},$$

so that, taking $h_0 = 1$,

$$h_1(x) = \frac{-\alpha}{8} p(p-2)(\alpha x + \beta)^{-1},$$

$$h_2(x) = \frac{\alpha^2}{128} p(p-2)(p+2)(p-4)(\alpha x + \beta)^{-2},$$

$$\cdot$$

$$\cdot$$

$$\cdot$$

$$h_n(x) = \frac{(-1)^n \alpha^n}{2^{3n} n} p(p-2n) \prod_{r=1}^{n-1} [p^2 - (2r)^2](\alpha x + \beta)^{-n}.$$

3 Specific Problem for a Finite Rod

As a specific example, consider an elastic bar of finite length l lying between $x = 0$ and $x = l$. Suppose the bar has a cross-sectional area $A(x)$ which is such that $h_n(x) = 0$ for $n > m$. The end at $x = 0$ is held fixed while the end at $x = l$ is subject to the impulsive load

$$\sigma(l, \tau) = \mathrm{E}\delta(\tau), \tag{15}$$

where $\delta(\tau)$ is the Dirac delta function. Now in the interval $0 < \tau < l$, only left-going waves will propagate so that for this interval, we obtain from (6) and (9), the displacement in the form

$$u = A^{-1/2} \sum_{n=0}^{m} h_n(x) F_n(\tau + x) \tag{16}$$

so that, from (1),

$$\frac{\sigma(x, \tau)}{\mathrm{E}} = \frac{1}{2} A^{-1/2} \left\{ \sum_{n=0}^{m} \left[-\frac{1}{A}\frac{dA}{dx} h_n(x) F_n(\tau + x) + 2h_n'(x) F_n(\tau + x) + 2h_n(x) F_n'(\tau + x) \right] \right\}. \tag{17}$$

Putting $x = l$, using (15) and taking the Laplace transform provides

$$\overline{F_m}(s) = 2[A(l)]^{1/2} e^{-sl} [P(s)]^{-1}, \tag{18}$$

where $\overline{F_m}(s)$ denotes the Laplace Transform of $F_m(\tau)$ and $P(s)$ is a polynomial of degree $m + 1$ in s given by

$$P(s) = \sum_{n=0}^{m} \{[-A'(l)[A(l)]^{-1} h_n(l) + 2h_n'(l) + 2h_n(l)s] s^{m-n}\} \tag{19}$$

where $A'(l) = A'(x)\,|_{x=l}$ and $h_n'(l) = h_n'(x)\,|_{x=l}$. If the zeros of this polynomial are distinct and are denoted by α_n for $n = 0, 1, \ldots, m$, then the transform (18) may be inverted to yield

$$F_m(\lambda) = \sum_{n=0}^{m} C_n \exp[\alpha_n(\lambda - l)] H(\lambda - l), \tag{20}$$

where $H(\lambda)$ denotes the Heavyside step function and the C_n are constants. When $\tau = l$ the disturbance arrives at the fixed end of the rod at $x = 0$. To continue the solution for the interval $l < \tau < 2l$ and to satisfy the boundary condition $u(0, \tau) = 0$, it is necessary to now introduce the terms $G_n(\mu)$ which represent the right-going waves. The displacement for $0 < \tau < 2l$ is, therefore, taken in the form

$$u = A^{-1/2} \left\{ \sum_{n=0}^{m} h_n(x) [F_n(\tau + x) + G_n(\tau - x)] \right\} \tag{21}$$

where $F_n(\tau + x)$ is obtained from (20). If we take

$$G_n(\tau) = -F_n(\tau) \text{ for } n = 0, 1, \ldots, m \tag{22}$$

then the condition $u(0, \tau) = 0$ is satisfied. As a particular variation in $A(x)$, consider the case of a right circular cone with cross-sectional radius a and $x = 0$ and b at $x = l$, so that $A(x) = \pi[al + (b-a)x]^2/l^2$. From the analysis in Section 2 we see that in this case we may take $h_0 = K$ where K is an arbitrary constant and then $h_n = 0$ for $n \geq 1$. Then from (19)

$$P(s) = 2K\left\{s - \frac{(b-a)}{bl}\right\}$$

so that (20) and (22) yield

$$F_0(\lambda) = K^{-1} b\pi^{1/2} \exp[c(\lambda - l)] H(\lambda - l),$$

$$G_0(\mu) = -K^{-1} b\pi^{1/2} \exp[c(\mu - l)] H(\mu - l),$$

where $c = (bl)^{-1}(b-a)$. Using (21) and (1) the displacement and stress for $0 < \tau < 2l$ are thus given by

$$u = K^{-1}(bl)[al + (b-a)x]^{-1} \{\exp[c(\lambda - l)] H(\lambda - l) - \exp[c(\mu - l)] H(\mu - l)\},$$

$$\frac{K}{E}\sigma = K\frac{\partial u}{\partial x} = \frac{bl(b-a)}{[al + (b-a)x]^2} \{\exp[c(\lambda - l)] H(\lambda - l) - \exp[c(\mu - l)] H(\mu - l)\} + \frac{(b-a)}{[al + (b-a)x]} \{\exp[c(\lambda - l)] H(\lambda - l) + \exp[c(\mu - l)] H(\mu - l)\} + \frac{(bl)}{[al + (b-a)x]} \{\delta(\lambda - l) + \delta(\mu - l)\}.$$

Note that if $b = a$ (so that $c = 0$) then the expressions give the displacement and stress for the corresponding problem for a rod with a uniform cross-section. The displacement at the midpoint of the rod is

$$u = K^{-1} \frac{2b}{(a+b)} \left\{ \exp\left[c\left(\tau - \frac{l}{2}\right)\right] H\left(\tau - \frac{l}{2}\right) - \exp\left[c\left(\tau - \frac{3l}{2}\right)\right] H\left(\tau - \frac{3l}{2}\right) \right\}. \tag{23}$$

This may be compared with the corresponding expression for a uniform rod (obtained by putting $b = a$ and $c = 0$ in (23)) in order to examine the effect of the variation in cross-sectional area on the displacement at the midpoint. For example, the displacement at the midpoint for $l/2 < \tau < 3l/2$ for a uniform rod is $u = K^{-1}$ while the displacement for the same interval for the cone is $K^{-1}\ [2b/(a+b)]\exp[c(\tau - l/2)]$ which is greater

Downloaded 03 May 2010 to 171.66.16.21. Redistribution subject to ASME license or copyright; see http://www.asme.org/terms/Terms_Use.cfm

than K^{-1} if $b>a$ and less than K^{-1} if $b<a$. Note that although the expressions for this example have only been developed for $0<\tau<2l$, it is a straightforward procedure to extend the expressions for $\tau>2l$.

References

Bergman, S., 1971, *Integral operators in the theory of linear partial differential equations*, Springer-Verlag, Berlin.

Eason, G., 1967, "Wave propagation in inhomogeneous elastic media," *Bull. Seism. Soc. Amer.*, Vol. 57, pp. 1267–1277.

Synge, J. L., 1981, "On the vibrations of a heterogeneous string," *Quart. Appl. Math.*, Vol. 39, pp. 292–297.

Webster, A. G., 1919, "Acoustical impedance and the theory of horns and of the phonograph," *Proc. Nat. Acad. Sci.*, Vol. 5, pp. 275–282.

Structural Decomposition Approach for the Stability of Uncertain Dynamic Systems

Y. H. Chen[6] and Chieh Hsu[7]

The stability property for a class of dynamic systems with uncertain parameter variation is studied. The uncertainty can be fast time-varying and unpredictable. A new approach for stability study is proposed. The only required information on the uncertain variation is its possible bound *as well as* structure. *That is, no a priori knowledge on the realization of the variation is needed.*

1 Introduction

A class of linear lumped-parameter dynamic systems is under consideration. Past efforts in studying the stability of the systems can essentially be divided into two parts. The first part is concerned with the time-invariant case. Major approaches along this line are eigenvalue approach (e.g., Hann, 1967; Routh, 1955) and Lyapunov approach (e.g., LaSalle and Lefshetz, 1961; Walker and Schmitendorf, 1973; Zubov, 1964). The second part is concerned with the time-varying case (i.e., the system parameters are time-varying). Major approaches along this line are "frozen" system approach (for slow time-varying parameters) (e.g., Barman, 1973; Vidyasagar, 1978) and the Lyapunov approach, including the "circle-criterion" (e.g., Vidyasagar, 1978). If the parameters are unknown, the Lyapunov approach is, however, only dependent on the bound of variations. No structural properties of the uncertain variations are explored and utilized. This may result in a somewhat conservative estimation of the stability condition in practice.

In this article, we study the stability of a class of dynamic systems with *uncertain* (fast) time-varying variations. The main contribution of this article is to propose the structural decomposition approach. This approach is dependent on the *bound* as well as the structure of the uncertain variations. The combined use of the structural decomposition approach and the Lyapunov approach is also proposed.

Norm Definitions: Vector norms are Euclidean. Matrix norms are the corresponding induced ones (Vidyasagar, 1978); thus, $\|\Xi\| = \lambda_M^{1/2}(\Xi^T\Xi)$, where $\lambda_M(\cdot)$ ($\lambda_m(\cdot)$) denotes the maximum (minimum) eigenvalue of the designated matrix (if all its eigenvalues are real).

[6]The George W. Woodruff School of Mechanical Engineering, Georgia Institute of Technology, Atlanta, GA 30332. Mem. ASME. To whom correspondence should be addressed.

[7]Department of Mechanical and Aerospace Engineering, Syracuse University, Syracuse, NY 13244.

Manuscript received by ASME Applied Mechanics Division, November 10, 1987; final revision, June 2, 1988.

2 Dynamic Systems With Fast Time-Varying Uncertainty

Let use consider a class of lumped-parameter, finite-dimensional dynamic systems described by

$$M\ddot{x}(t)+[C+\Delta C(t)]\dot{x}(t)+[K+\Delta K(t)]x(t)=0. \tag{2.1}$$

Here, $x(t)\in\mathbf{R}^n$ is the vector of generalized coordinates, $M=M^T\in\mathbf{R}^{n\times n}$ is the positive definite mass matrix, $C\in\mathbf{R}^{n\times n}$ is the "nominal" damping matrix and $K\in\mathbf{R}^{n\times n}$ is the "nominal" stiffness matrix. The time-dependent matrices $\Delta C(t)$ and $\Delta K(t)$ are the uncertain portions of C and K, respectively. The functions $\Delta C(\cdot)$: $\mathbf{R}\to\mathbf{R}^{n\times n}$ and $\Delta K(\cdot)$: $\mathbf{R}\to\mathbf{R}^{n\times n}$ are *unknown*. Now we reformulate (2.1) as

$$\ddot{x}(t)+[A+\Delta A(t)]\dot{x}(t)+[B+\Delta B(t)]x(t)=0 \tag{2.2}$$

where

$$A=M^{-1}C,\ \Delta A(t)=M^{-1}\Delta C(t),$$
$$B=M^{-1}K,\ \Delta B(t)=M^{-1}\Delta K(t).$$

System (2.1) can then be put in the following form:

$$\dot{z}(t)=\begin{bmatrix}0 & I\\ -B & -A\end{bmatrix}z(t)+\begin{bmatrix}0 & 0\\ -\Delta B(t) & -\Delta A(t)\end{bmatrix}z(t)$$
$$\triangleq\Gamma z(t)+\Delta\Gamma(t)z(t), \tag{2.3}$$

where $z=[x^T\ \dot{x}^T]^T$.

Theorem (2.4): Consider the nominal system $\dot{z}=\Gamma z$ of (2.3). Suppose for any given $Q>0$, there exists $P>0$ of the Lyapunov equation $\Gamma^TP+P\Gamma+Q=0$. Then $z=0$ of the time-varying system (2.3) is asymptotically stable, provided

$$\max_{t\in\mathbf{R}}\|\Delta\Gamma(t)\|\triangleq\rho<\frac{\lambda_m(Q)}{2\lambda_M(P)}. \tag{2.5}$$

Remark (2.6): Results similar to Theorem (2.4) (the Lyapunov appproach) can be found in many places, e.g., LaSalle and Lefshetz (1961). The only required and utilized information on $\Delta\Gamma(t)$ is its possible bound.

3 Structural Decomposition Approach

The major advantage of the Lyapunov approach is its minimum requirement on the information of the variation $\Delta\Gamma(t)$. Only the possible bound of $\Delta\Gamma(t)$ is needed. It is, however, on the other hand, a drawback. This is so since no more information other than the bound of $\Delta\Gamma(t)$ is utilized for studying stability. The result (2.5) is valid for the "worst" possible case of $\Delta\Gamma(t)$. Thus, the sufficient condition (2.5) for stability may be sometimes conservative. In this section we shall explore and utilize more property of $\Delta\Gamma(t)$, namely, its structure. A similar idea was also discussed in Schmitendorf (1987) for feedback control design.

Definition (3.1): A matrix $\Theta(t)\in\mathbf{R}^{n\times n}$ is said to be *structually decomposed* if one can find functions $r_i(\cdot)$: $\mathbf{R}\to\mathbf{R}$, matrices $F_i\in\mathbf{R}^{n\times n}$ and vectors $f_i\in\mathbf{R}^n$ and $g_i\in\mathbf{R}^n$, $i=1, 2, \ldots, l$, such that

$$\Theta(t)=\sum_{i=1}^{l}F_ir_i(t),\ F_i=f_ig_i^T. \tag{3.2}$$

Here (3.2) implies that $\Theta(t)$ is a linear combination of F_i (with time-varying coefficients $r_i(t)$). Moreover, we note that F_i can always be decomposed into f_i and g_i.

For the dynamic system (2.3), suppose $\Delta\Gamma(t)$ is structurally decomposed as in Definition (3.1). Take $V=z^TMz$. Here, $M=M^T>0$ is yet to be decided. The time derivative of V, along with the solution of (2.3), is

$$\dot{V}=z^TM\dot{z}$$
$$=z^T(M\Gamma+\Gamma^TM)z+2z^TM\Delta\Gamma(t)z. \tag{3.3}$$

Downloaded 03 May 2010 to 171.66.16.21. Redistribution subject to ASME license or copyright; see http://www.asme.org/terms/Terms_Use.cfm

than K^{-1} if $b>a$ and less than K^{-1} if $b<a$. Note that although the expressions for this example have only been developed for $0<\tau<2l$, it is a straightforward procedure to extend the expressions for $\tau>2l$.

References

Bergman, S., 1971, *Integral operators in the theory of linear partial differential equations*, Springer-Verlag, Berlin.

Eason, G., 1967, "Wave propagation in inhomogeneous elastic media," *Bull. Seism. Soc. Amer.*, Vol. 57, pp. 1267–1277.

Synge, J. L., 1981, "On the vibrations of a heterogeneous string," *Quart. Appl. Math.*, Vol. 39, pp. 292–297.

Webster, A. G., 1919, "Acoustical impedance and the theory of horns and of the phonograph," *Proc. Nat. Acad. Sci.*, Vol. 5, pp. 275–282.

Structural Decomposition Approach for the Stability of Uncertain Dynamic Systems

Y. H. Chen[6] and Chieh Hsu[7]

The stability property for a class of dynamic systems with uncertain parameter variation is studied. The uncertainty can be fast time-varying and unpredictable. A new approach for stability study is proposed. The only required information on the uncertain variation is its possible bound *as well as* structure. *That is, no a priori knowledge on the realization of the variation is needed.*

1 Introduction

A class of linear lumped-parameter dynamic systems is under consideration. Past efforts in studying the stability of the systems can essentially be divided into two parts. The first part is concerned with the time-invariant case. Major approaches along this line are eigenvalue approach (e.g., Hann, 1967; Routh, 1955) and Lyapunov approach (e.g., LaSalle and Lefshetz, 1961; Walker and Schmitendorf, 1973; Zubov, 1964). The second part is concerned with the time-varying case (i.e., the system parameters are time-varying). Major approaches along this line are "frozen" system approach (for slow time-varying parameters) (e.g., Barman, 1973; Vidyasagar, 1978) and the Lyapunov approach, including the "circle-criterion" (e.g., Vidyasagar, 1978). If the parameters are unknown, the Lyapunov approach is, however, only dependent on the bound of variations. No structural properties of the uncertain variations are explored and utilized. This may result in a somewhat conservative estimation of the stability condition in practice.

In this article, we study the stability of a class of dynamic systems with *uncertain* (fast) time-varying variations. The main contribution of this article is to propose the structural decomposition approach. This approach is dependent on the *bound* as well as the structure of the uncertain variations. The combined use of the structural decomposition approach and the Lyapunov approach is also proposed.

Norm Definitions: Vector norms are Euclidean. Matrix norms are the corresponding induced ones (Vidyasagar, 1978); thus, $\|\Xi\| = \lambda_M^{1/2}(\Xi^T\Xi)$, where $\lambda_M(\cdot)$ ($\lambda_m(\cdot)$) denotes the maximum (minimum) eigenvalue of the designated matrix (if all its eigenvalues are real).

[6]The George W. Woodruff School of Mechanical Engineering, Georgia Institute of Technology, Atlanta, GA 30332. Mem. ASME. To whom correspondence should be addressed.

[7]Department of Mechanical and Aerospace Engineering, Syracuse University, Syracuse, NY 13244.

Manuscript received by ASME Applied Mechanics Division, November 10, 1987; final revision, June 2, 1988.

2 Dynamic Systems With Fast Time-Varying Uncertainty

Let use consider a class of lumped-parameter, finite-dimensional dynamic systems described by

$$M\ddot{x}(t)+[C+\Delta C(t)]\dot{x}(t)+[K+\Delta K(t)]x(t)=0. \tag{2.1}$$

Here, $x(t)\in\mathbf{R}^n$ is the vector of generalized coordinates, $M=M^T\in\mathbf{R}^{n\times n}$ is the positive definite mass matrix, $C\in\mathbf{R}^{n\times n}$ is the "nominal" damping matrix and $K\in\mathbf{R}^{n\times n}$ is the "nominal" stiffness matrix. The time-dependent matrices $\Delta C(t)$ and $\Delta K(t)$ are the uncertain portions of C and K, respectively. The functions $\Delta C(\cdot)$: $\mathbf{R}\to\mathbf{R}^{n\times n}$ and $\Delta K(\cdot)$: $\mathbf{R}\to\mathbf{R}^{n\times n}$ are *unknown*. Now we reformulate (2.1) as

$$\ddot{x}(t)+[A+\Delta A(t)]\dot{x}(t)+[B+\Delta B(t)]x(t)=0 \tag{2.2}$$

where

$$A=M^{-1}C,\ \Delta A(t)=M^{-1}\Delta C(t),$$
$$B=M^{-1}K,\ \Delta B(t)=M^{-1}\Delta K(t).$$

System (2.1) can then be put in the following form:

$$\dot{z}(t)=\begin{bmatrix}0 & I\\ -B & -A\end{bmatrix}z(t)+\begin{bmatrix}0 & 0\\ -\Delta B(t) & -\Delta A(t)\end{bmatrix}z(t)$$
$$\triangleq\Gamma z(t)+\Delta\Gamma(t)z(t), \tag{2.3}$$

where $z=[x^T\ \dot{x}^T]^T$.

Theorem (2.4): Consider the nominal system $\dot{z}=\Gamma z$ of (2.3). Suppose for any given $Q>0$, there exists $P>0$ of the Lyapunov equation $\Gamma^TP+P\Gamma+Q=0$. Then $z=0$ of the time-varying system (2.3) is asymptotically stable, provided

$$\max_{t\in\mathbf{R}}\|\Delta\Gamma(t)\|\triangleq\rho<\frac{\lambda_m(Q)}{2\lambda_M(P)}. \tag{2.5}$$

Remark (2.6): Results similar to Theorem (2.4) (the Lyapunov appproach) can be found in many places, e.g., LaSalle and Lefshetz (1961). The only required and utilized information on $\Delta\Gamma(t)$ is its possible bound.

3 Structural Decomposition Approach

The major advantage of the Lyapunov approach is its minimum requirement on the information of the variation $\Delta\Gamma(t)$. Only the possible bound of $\Delta\Gamma(t)$ is needed. It is, however, on the other hand, a drawback. This is so since no more information other than the bound of $\Delta\Gamma(t)$ is utilized for studying stability. The result (2.5) is valid for the "worst" possible case of $\Delta\Gamma(t)$. Thus, the sufficient condition (2.5) for stability may be sometimes conservative. In this section we shall explore and utilize more property of $\Delta\Gamma(t)$, namely, its structure. A similar idea was also discussed in Schmitendorf (1987) for feedback control design.

Definition (3.1): A matrix $\Theta(t)\in\mathbf{R}^{n\times n}$ is said to be *structually decomposed* if one can find functions $r_i(\cdot)$: $\mathbf{R}\to\mathbf{R}$, matrices $F_i\in\mathbf{R}^{n\times n}$ and vectors $f_i\in\mathbf{R}^n$ and $g_i\in\mathbf{R}^n$, $i=1, 2, \ldots, l$, such that

$$\Theta(t)=\sum_{i=1}^{l}F_ir_i(t),\ F_i=f_ig_i^T. \tag{3.2}$$

Here (3.2) implies that $\Theta(t)$ is a linear combination of F_i (with time-varying coefficients $r_i(t)$). Moreover, we note that F_i can always be decomposed into f_i and g_i.

For the dynamic system (2.3), suppose $\Delta\Gamma(t)$ is structurally decomposed as in Definition (3.1). Take $V=z^TMz$. Here, $M=M^T>0$ is yet to be decided. The time derivative of V, along with the solution of (2.3), is

$$\dot{V}=z^TM\dot{z}$$
$$=z^T(M\Gamma+\Gamma^TM)z+2z^TM\Delta\Gamma(t)z. \tag{3.3}$$

Copyright © 1988 by ASME

Downloaded 03 May 2010 to 171.66.16.21. Redistribution subject to ASME license or copyright; see http://www.asme.org/terms/Terms_Use.cfm

However, in view of (3.2), it can be shown that

$$2z^TM\Delta\Gamma(r)z = 2z^TM\Big[\sum_{i=1}^{l} F_i r_i(t)\Big]z$$

$$= 2z^TM\Big[\sum_i f_i g_i{}^T r_i(t)\Big]z \tag{3.4}$$

Suppose there exists an $\bar{r}\geq 0$ such that $|r_i(t)|\leq \bar{r}$ for all i. Then

$$2z^TM\Big[\sum_i f_i g_i{}^T r_i(t)\Big]z$$

$$\leq 2\bar{r}\sum_i |z^TMf_i g_i{}^T z|$$

$$\leq \bar{r}\sum_i (z^TMf_i)^2 + \bar{r}\sum_i (g_i{}^T z)^2 \tag{3.5}$$

The last inequality is valid by the fact that $2|ab|\leq a^2+b^2$, where $a, b\in\mathbf{R}$. Let matrices $\mathbf{T}$ and $\mathbf{U}$ be defined as

$$\mathbf{T}\triangleq\sum_{i=1}^{l} f_i f_i{}^T, \qquad \mathbf{U}\triangleq\bar{r}\sum_{i=1}^{l} g_i g_i T. \tag{3.6}$$

Then we have, by (3.5),

$$2z^TM\Delta\Gamma(t)z$$

$$\leq \bar{r}z^TM\sum_i f_i f_i{}^TMz + \bar{r}z^T\sum_i g_i g_i{}^T z$$

$$= z^TMTMz + z^TUz. \tag{3.7}$$

Finally, combining (3.3)–(3.7) yields

$$\dot{V}\leq z^T(M\Gamma+\Gamma^TM+MTM+\mathbf{U})z\triangleq -z^TWz. \tag{3.8}$$

The following theorem summarizes the main result in this article.

Theorem (3.9): Suppose $\Delta\Gamma(t)$ in (2.3) is structurally decomposed and there exists an $\bar{r}\geq 0$ such that $|r_i(t)|\leq\bar{r}$ for all i. If, for a given $W>0$, there exists a solution $M>0$ for the matrix equation

$$M\Gamma+\Gamma^TM+MTM+\mathbf{U}+W=0, \tag{3.10}$$

then $z=0$ of (2.3) is asymptotically stable.

Remark (3.11): The matrix equation (3.10) is now dependent on the *bound* as well as the *structure* of $\Delta\Gamma(t)$. It reduces to the Lyapunov equation as $\bar{r}=0$.

4 Structural Decomposition-Lyapunov Approach

The advantage and motivation of the Lyapunov approach is that all nominally asymptotically stable systems are capable of tolerating certain amount of uncertainty. This is so since, as long as we obtain the pair $(P, Q)>0$ from the Lyapunov equation, there always exists an upper bound ρ for (2.5). The combined use of the structural decomposition and Lyapunov approaches is then desirable. Let us rewrite (2.3) as the following (by separating $\Delta\Gamma(t)$):

$$\dot{z}(t) = \Gamma z(t) + \Delta\Gamma(t)z(t)$$

$$\triangleq \Gamma z(t) + [\Delta\Gamma_1(t) + \Delta\Gamma_2(t)]z(t). \tag{4.1}$$

Theorem (4.2): Suppose $\Delta\Gamma_1(t)$ of (4.1) is structurally decomposed and $\bar{r}\geq 0$ exists. If $M>0$ of

$$M\Gamma+\Gamma^TM+MTM+\mathbf{U}+W=0 \tag{4.3}$$

exists for a given $W>0$. Then $z=0$ of (4.1) is asymptotically stable, provided

$$\max_{t\in\mathbf{R}} \|\Delta\Gamma_2(t)\| \triangleq \bar{\rho} < \frac{\lambda_m(W)}{2\lambda_M(M)}. \tag{4.4}$$

5 An Illustrative Example

Consider the system (2.2) with

$$A=\begin{bmatrix}8 & -1.25\\ 1 & 3\end{bmatrix}, \quad B=\begin{bmatrix}5 & -2\\ 0.5 & 3\end{bmatrix},$$

$$\Delta A(t) = \Delta A_1(t) + \Delta A_2(t)$$

$$\triangleq \begin{bmatrix}0 & -a_1(t)\\ -a_2(t) & -a_3(t)\end{bmatrix} + \begin{bmatrix}c(t) & 0\\ 0 & 0\end{bmatrix},$$

$$\Delta B(t) = \Delta B_1(t) + \Delta B_2(t)$$

$$= \begin{bmatrix}0 & -b_1(t)\\ 0 & -b_2(t)\end{bmatrix} + \begin{bmatrix}0 & 0\\ d(t) & 0\end{bmatrix}. \tag{5.1}$$

We notice that

$$\Delta\Gamma_1(t) = \begin{bmatrix}0 & 0\\ -\Delta B_1(t) & -\Delta A_1(t)\end{bmatrix} \tag{5.2}$$

can be structurally decomposed by taking $l=5$, $r_1(t)=a_1(t)$, $r_2(t)=a_2(t)$, $r_3(t)=a_3(t)$, $r_4(t)=b_1(t)$, $r_5(t)=b_2(t)$, and $f_1=f_3=g_4{}^T=[0\ 0\ 1\ 0]^T$, $f_2=f_4=f_5=g_3{}^T=g_5{}^T=[0\ 0\ 0\ 1]^T$, $g_1{}^T=g_2{}^T=[0\ 1\ 0\ 0]$. Moreover, we have

$$\mathbf{T}=\bar{r}\begin{bmatrix}0&0&0&0\\0&0&0&0\\0&0&2&0\\0&0&0&3\end{bmatrix}, \quad \mathbf{U}=\bar{r}\begin{bmatrix}0&0&0&0\\0&2&0&0\\0&0&1&0\\0&0&0&2\end{bmatrix}.$$

If $\bar{r}=0.6$, it can found, by taking $W=I$, that

$$M=\begin{bmatrix}1.376 & 0.014 & 0.103 & -0.014\\ 0.014 & 2.999 & 5.203 & 0.424\\ 0.103 & 5.203 & 0.126 & -0.089\\ -0.014 & 0.424 & -0.089 & 0.689\end{bmatrix}>0, \tag{5.3}$$

and $\lambda(M)=\{3.075, 1.384, 0.629, 0.103\}$. A straightforward calculation shows that

$$\bar{\rho}=\max_t\|\Delta\Gamma_2(t)\|=\max_t \max\{c^2(t), d^2(t)\}. \tag{5.4}$$

Suppose $|c(t)|\leq 0.3$ and $|d(t)|\leq 0.4$. The equilibrium $z=0$ is proved to be asymptotically stable since

$$\lambda_m(W)/2\lambda_M(M)=0.163.$$

The advantage of the combined use of the structural decomposition approach and the Lypaunov approach is the exploration of a larger range of parameter variation for stability.

6 Conclusion

A new approach for studying the stability of a class of dynamic systems with fast time-varying uncertain variation is proposed. This new structural decomposition approach utilizes the possible *bound* as well as the *structure* of the uncertain variation. The combined use of the classical Lyapunov approach and this new approach is suggested.

References

Barman, J., 1973, "Well-Posedness of Feedback Systems and Singular Perturbations," Ph.D. Thesis, Univ. of California, Berkeley, CA.

Hahn, W., 1967, *Stability of Motion*, Berlin, Springer-Verlag.

LaSalle, J., and Lefshetz, S., 1961, *Stability by Lyapunov's Direct Method*, Academic Press, New York.

Routh, E. J., 1955, *Dynamics of a System of Rigid Bodies*, Dover Publications, New York.

Downloaded 03 May 2010 to 171.66.16.21. Redistribution subject to ASME license or copyright; see http://www.asme.org/terms/Terms_Use.cfm

Schmitendorf, W. E., 1987, "Designing Stabilizing Controllers for Uncertian Systems Using the Riccati Equation Approach," *1987 American Control Conference*, Minneapolis, pp. 502–505.

Vidyasagar, M., 1978, *Nonlinear Systems Analysis*, Prentice-Hall, Englewood Cliffs, New Jersey.

Walker, J. A., and Schmnitendorf, W. E., 1973, "A Simple Test for Asymptotic Stability in Partially Dissipative Symmetric Systems," ASME JOURNAL OF APPLIED MECHANICS, Vol. 40, pp. 1120–1121.

Zubov, V. J., 1964, *Methods of A. M. Lyapunov and Their Applications*, Noordhoff, Groningen, The Netherlands.

On Certain Refined Theories for Plate Bending

Kostas P. Soldatos[8]

Introduction

This note presents the derivation of an eighth-order theory for plate bending which decomposes the plate flexure as occurring in two stages. During the basic stage of flexure the plate bends in accordance with the Kirchhoff hypothesis, while during an additional flexural stage the effects of transverse shear deformation are incorporated into the theory. It is shown that this is an alterative version of Reddy's (1984) parabolic transverse shear deformable plate theory in which the role of the occurring higher-order moment and shear force resultants is elucidated, in the sense that those resultants can acquire some physical meaning. Moreover, with the introduction of certain effective middle plane curvatures and twist, the theory derived is reduced to a new sixth-order plate theory which appears very closely connected with the recent sixth-order plate theories due to Reissner (1975) and Levinson (1980). Hence, it is believed that the present note could also contribute towards the clarification of ideas related to certain scientific arguments and comments concerned with the aforementioned recent plate theories (Reddy, 1984; Reissner, 1985; Levinson, 1985, 1987; Rychter, 1987), as well as with Levinson's (1981) and Bickford's (1982) beam theories which are the exact one-dimensional analogues of Levinson's (1980) and Reddy's (1984) plate theories, respectively.

A Two-Stage Bending Plate Theory

Consider the bending problem of a homogeneous orthotropic linearly elastic plate whose material axes of symmetry coincide with the axes of the Cartesian coordinate system. The plate has a constant thickness h and is subjected to an external transverse load $p(x,y)$ applied downwards on its top plane. The plate middle plane coincides with the x-y plane of the coordinate system; the z-axis is directed upwards.

The formulation of the present refined plate theory is based on the superposition

$$\begin{aligned} u_x(x,y,z) &= u_x^c(x,y,z)+u_x^a(x,y,z),\\ u_y(x,y,z) &= u_y^c(x,y,z)+u_y^a(x,y,z),\\ u_z(x,y,z) &= u_z^c(x,y)=w(x,y) \end{aligned} \tag{1}$$

of two different displacement fields. The basic displacement field,

$$u_z^c=w,\ \ (u_x^c,u_y^c)=-z(w_{,x},w_{,y}), \tag{2}$$

is the displacement approximation employed in the classical plate theory. The additional displacement field,

$$(u_x^a,u_y^a)=z(1-4z^2/3h^2)[u_1(x,y),v_1(x,y)], \tag{3}$$

is considered as a disturbance which dismisses the Kirchhoff's hypothesis and, during a second stage of bending, incorporates into the theory the effects of transverse shear deformation.

The kinematic relations are consequently obtained as the superposition of two different strain fields. In the basic strain field

$$\begin{aligned} &(\epsilon_x^c,\epsilon_y^c,\gamma_{xy}^c)=z(k_x^c,k_y^c,k_{xy}^c),\ \ \epsilon_z^c=\gamma_{xz}^c=\gamma_{yz}^c=0,\\ &k_x^c=-w_{,xx},\ \ k_y^c=-w_{,yy},\ \ k_{xy}^c=-2w_{,xy}, \end{aligned} \tag{4}$$

k_x^c, k_y^c, and k_{xy}^c are the well-known curvatures and twist of the deflected middle plane occurred in the classical theory. From the additional strain field

$$\begin{aligned} &(\epsilon_x^a,\epsilon_y^a,\gamma_{xy}^a)=z(1-4z^2/3h^2)(k_x^a,k_y^a,k_{xy}^a),\\ &(\gamma_{xz}^a,\gamma_{yz}^a)=(1-4z^2/h^2)(u_1,v_1),\epsilon_z^a=0,\\ &k_x^a=u_{1,x},k_y^a=v_{1,y},k_{xy}^a=u_{1,y}+v_{1,x}, \end{aligned} \tag{5}$$

it becomes clear that the transverse shear strains vary parabolically through the plate thickness, and this guarantees the satisfaction of the zero shear traction boundary conditions prescribed on the top and bottom planes of the plate. The unknown functions u_1 and v_1 represent the action of transverse shear strains on the plate middle plane. This action, by means of the first partial derivatives of u_1, and v_1, causes some additional curvatures, k_x^a and k_y^a, and twist, k_{xy}^a, on the plate middle plane.

Upon expressing the bending strain energy density, U_0, in terms of the aforementioned curvatures, twists, and shear strains (Soldatos, 1987), the bending moment resultants associated with the basic and additional strain fields are defined according to

$$(M_x^i,M_y^i,M_{xy}^i)=\int_{-h/2}^{h/2}\left(\frac{\partial U_0}{\partial k_x^i},\frac{\partial U_0}{\partial k_y^i},\frac{\partial U_0}{\partial k_{xy}^i}\right)dz, \tag{6a}$$

with $i=c$ and $i=a$, respectively, while transverse shear force resultants are defined as follows

$$(Q_x^a,Q_y^a)=\int_{-h/2}^{h/2}\left(\frac{\partial U_0}{\partial u_1},\frac{\partial U_0}{\partial v_1}\right)dz. \tag{6b}$$

These definitions are equivalent to the following:

$$\begin{aligned} (M_x^c,M_y^c,M_{xy}^c) &= \int_{-h/2}^{h/2}(\sigma_x,\sigma_y,\tau_{xy})z\,dz,\\ (M_x^a,M_y^a,M_{xy}^a) &= \int_{-h/2}^{h/2}(\sigma_x,\sigma_y,\tau_{xy})(1-4z^2/3h^2)z\,dz,\\ (Q_x^a,Q_y^a) &= \int_{-h/2}^{h/2}(\tau_{xz},\tau_{yz})(1-4z^2/h^2)dz. \end{aligned} \tag{7}$$

Employing either equations (6) or (7) one obtains

$$\begin{bmatrix} M_x^c\\ M_y^c \end{bmatrix}=\begin{bmatrix} D_{11} & D_{12}\\ D_{12} & D_{22} \end{bmatrix}\left(\begin{bmatrix} k_x^c\\ k_y^c \end{bmatrix}+\frac{4}{5}\begin{bmatrix} k_x^a\\ k_y^a \end{bmatrix}\right),$$

$$\begin{bmatrix} M_x^a\\ M_y^a \end{bmatrix}=\frac{4}{5}\begin{bmatrix} D_{11} & D_{12}\\ D_{12} & D_{22} \end{bmatrix}\left(\begin{bmatrix} k_x^c\\ k_y^c \end{bmatrix}+\frac{17}{24}\begin{bmatrix} k_x^a\\ k_y^a \end{bmatrix}\right),$$

$$M_{xy}^c=D_{66}\left(k_{xy}^c+\frac{4}{5}k_{xy}^a\right),$$

[8]Department of Mathematics, University of Ioannina, Ioannina, Greece, 451 10.

Manuscript received by ASME Applied Mechanics Division, October 29, 1987; final revision, May 21, 1988.

Downloaded 03 May 2010 to 171.66.16.21. Redistribution subject to ASME license or copyright; see http://www.asme.org/terms/Terms_Use.cfm

Schmitendorf, W. E., 1987, "Designing Stabilizing Controllers for Uncertian Systems Using the Riccati Equation Approach," *1987 American Control Conference*, Minneapolis, pp. 502–505.

Vidyasagar, M., 1978, *Nonlinear Systems Analysis*, Prentice-Hall, Englewood Cliffs, New Jersey.

Walker, J. A., and Schmnitendorf, W. E., 1973, "A Simple Test for Asymptotic Stability in Partially Dissipative Symmetric Systems," ASME JOURNAL OF APPLIED MECHANICS, Vol. 40, pp. 1120–1121.

Zubov, V. J., 1964, *Methods of A. M. Lyapunov and Their Applications*, Noordhoff, Groningen, The Netherlands.

On Certain Refined Theories for Plate Bending

Kostas P. Soldatos[8]

Introduction

This note presents the derivation of an eighth-order theory for plate bending which decomposes the plate flexure as occurring in two stages. During the basic stage of flexure the plate bends in accordance with the Kirchhoff hypothesis, while during an additional flexural stage the effects of transverse shear deformation are incorporated into the theory. It is shown that this is an alterative version of Reddy's (1984) parabolic transverse shear deformable plate theory in which the role of the occurring higher-order moment and shear force resultants is elucidated, in the sense that those resultants can acquire some physical meaning. Moreover, with the introduction of certain effective middle plane curvatures and twist, the theory derived is reduced to a new sixth-order plate theory which appears very closely connected with the recent sixth-order plate theories due to Reissner (1975) and Levinson (1980). Hence, it is believed that the present note could also contribute towards the clarification of ideas related to certain scientific arguments and comments concerned with the aforementioned recent plate theories (Reddy, 1984; Reissner, 1985; Levinson, 1985, 1987; Rychter, 1987), as well as with Levinson's (1981) and Bickford's (1982) beam theories which are the exact one-dimensional analogues of Levinson's (1980) and Reddy's (1984) plate theories, respectively.

A Two-Stage Bending Plate Theory

Consider the bending problem of a homogeneous orthotropic linearly elastic plate whose material axes of symmetry coincide with the axes of the Cartesian coordinate system. The plate has a constant thickness h and is subjected to an external transverse load $p(x,y)$ applied downwards on its top plane. The plate middle plane coincides with the x-y plane of the coordinate system; the z-axis is directed upwards.

The formulation of the present refined plate theory is based on the superposition

$$\begin{aligned} u_x(x,y,z) &= u_x^c(x,y,z)+u_x^a(x,y,z),\\ u_y(x,y,z) &= u_y^c(x,y,z)+u_y^a(x,y,z),\\ u_z(x,y,z) &= u_z^c(x,y)=w(x,y) \end{aligned} \tag{1}$$

of two different displacement fields. The basic displacement field,

$$u_z^c = w,\ \ (u_x^c,u_y^c) = -z(w_{,x},w_{,y}), \tag{2}$$

is the displacement approximation employed in the classical plate theory. The additional displacement field,

$$(u_x^a,u_y^a) = z(1-4z^2/3h^2)[u_1(x,y),v_1(x,y)], \tag{3}$$

is considered as a disturbance which dismisses the Kirchhoff's hypothesis and, during a second stage of bending, incorporates into the theory the effects of transverse shear deformation.

The kinematic relations are consequently obtained as the superposition of two different strain fields. In the basic strain field

$$\begin{aligned} &(\epsilon_x^c,\epsilon_y^c,\gamma_{xy}^c) = z(k_x^c,k_y^c,k_{xy}^c),\ \ \epsilon_z^c=\gamma_{xz}^c=\gamma_{yz}^c=0,\\ &k_x^c=-w_{,xx},\ \ k_y^c=-w_{,yy},\ \ k_{xy}^c=-2w_{,xy}, \end{aligned} \tag{4}$$

k_x^c, k_y^c, and k_{xy}^c are the well-known curvatures and twist of the deflected middle plane occurred in the classical theory. From the additional strain field

$$\begin{aligned} &(\epsilon_x^a,\epsilon_y^a,\gamma_{xy}^a) = z(1-4z^2/3h^2)(k_x^a,k_y^a,k_{xy}^a),\\ &(\gamma_{xz}^a,\gamma_{yz}^a) = (1-4z^2/h^2)(u_1,v_1),\epsilon_z^a=0,\\ &k_x^a=u_{1,x},k_y^a=v_{1,y},k_{xy}^a=u_{1,y}+v_{1,x}, \end{aligned} \tag{5}$$

it becomes clear that the transverse shear strains vary parabolically through the plate thickness, and this guarantees the satisfaction of the zero shear traction boundary conditions prescribed on the top and bottom planes of the plate. The unknown functions u_1 and v_1 represent the action of transverse shear strains on the plate middle plane. This action, by means of the first partial derivatives of u_1, and v_1, causes some additional curvatures, k_x^a and k_y^a, and twist, k_{xy}^a, on the plate middle plane.

Upon expressing the bending strain energy density, U_0, in terms of the aforementioned curvatures, twists, and shear strains (Soldatos, 1987), the bending moment resultants associated with the basic and additional strain fields are defined according to

$$(M_x^i,M_y^i,M_{xy}^i) = \int_{-h/2}^{h/2}\left(\frac{\partial U_0}{\partial k_x^i},\frac{\partial U_0}{\partial k_y^i},\frac{\partial U_0}{\partial k_{xy}^i}\right)dz, \tag{6a}$$

with $i=c$ and $i=a$, respectively, while transverse shear force resultants are defined as follows

$$(Q_x^a,Q_y^a) = \int_{-h/2}^{h/2}\left(\frac{\partial U_0}{\partial u_1},\frac{\partial U_0}{\partial v_1}\right)dz. \tag{6b}$$

These definitions are equivalent to the following:

$$\begin{aligned} (M_x^c,M_y^c,M_{xy}^c) &= \int_{-h/2}^{h/2}(\sigma_x,\sigma_y,\tau_{xy})z\,dz,\\ (M_x^a,M_y^a,M_{xy}^a) &= \int_{-h/2}^{h/2}(\sigma_x,\sigma_y,\tau_{xy})(1-4z^2/3h^2)z\,dz,\\ (Q_x^a,Q_y^a) &= \int_{-h/2}^{h/2}(\tau_{xz},\tau_{yz})(1-4z^2/h^2)dz. \end{aligned} \tag{7}$$

Employing either equations (6) or (7) one obtains

$$\begin{bmatrix} M_x^c\\ M_y^c \end{bmatrix} = \begin{bmatrix} D_{11} & D_{12}\\ D_{12} & D_{22} \end{bmatrix}\left(\begin{bmatrix} k_x^c\\ k_y^c \end{bmatrix}+\frac{4}{5}\begin{bmatrix} k_x^a\\ k_y^a \end{bmatrix}\right),$$

$$\begin{bmatrix} M_x^a\\ M_y^a \end{bmatrix} = \frac{4}{5}\begin{bmatrix} D_{11} & D_{12}\\ D_{12} & D_{22} \end{bmatrix}\left(\begin{bmatrix} k_x^c\\ k_y^c \end{bmatrix}+\frac{17}{24}\begin{bmatrix} k_x^a\\ k_y^a \end{bmatrix}\right),$$

$$M_{xy}^c = D_{66}\left(k_{xy}^c+\frac{4}{5}k_{xy}^a\right),$$

[8]Department of Mathematics, University of Ioannina, Ioannina, Greece, 451 10.

Manuscript received by ASME Applied Mechanics Division, October 29, 1987; final revision, May 21, 1988.

Copyright © 1988 by ASME
Downloaded 03 May 2010 to 171.66.16.21. Redistribution subject to ASME license or copyright; see http://www.asme.org/terms/Terms_Use.cfm

$$M^a_{xy} = \frac{4}{5} D_{66}\left(k^c_{xy} + \frac{17}{21} k^a_{xy}\right),$$

$$(Q^a_x, Q^a_y) = \frac{4}{5} (A_{55}u_1, A_{44}v_1). \tag{8}$$

The bending and transverse shear rigidities appearing here are, respectively, given according to

$$(D_{11}, D_{12}, D_{22}, D_{66}) = \frac{h^3}{12} (Q_{11}, Q_{12}, Q_{22}, Q_{66}),$$

$$(A_{44}, A_{55}) = \frac{2h}{3} (Q_{44}, Q_{55}), \tag{9}$$

where Q_{ij} $(i,j = 1,2, \ldots, 6)$ are the well-known reduced stiffnesses.

Upon employing the total potential energy principle the following governing equations are obtained

$$\begin{aligned} &M^c_{x,xx} + 2M^c_{xy,xy} + M^c_{y,yy} = P, \\ &M^a_{x,x} + M^a_{xy,y} - Q^a_x = 0, \\ &M^a_{y,y} + M^a_{xy,x} - Q^a_y = 0, \end{aligned} \tag{10}$$

together with the following edge boundary conditions

$$w = \bar{w} \text{ or } [(M^c_{x,x} + M^c_{xy,y})n_x + (M^c_{y,y} + M^c_{xy,x})n_y] + M^c_{s,s} = \bar{Q}_n,$$

$$\begin{aligned} w_{,n} &= \bar{w}_{,n} \text{ or } M^c_n = \bar{M}^c_n, \\ u_{1n} &= \bar{u}_{1n} \text{ or } M^a_n = \bar{M}^a_n, \\ u_{1s} &= \bar{u}_{1s} \text{ or } M^a_{ns} = \bar{M}^a_{ns}. \end{aligned} \tag{11}$$

Here, n and s are the normal and the tangential parameters, respectively, of the plane curve formed by the intersection of the middle plane and the cylindrical edge surface of the plate; n_x and n_y denote the direction cosines of the n-direction with respect to the x and y directions, respectively. Moreover, all barred symbols denote prescribed quantities on the edge boundary.

Apparently, equation (10*a*), which relates the action of the external loading with second-order partial derivatives of the conventional moment resultants, occurs in the form of the governing equation of the classical theory. On the other hand, one should notice an obvious similarity of equations (10*b*,*c*) with corresponding equations known from other sixth-order theories (Reissner, 1945; Mindlin, 1951); the only apparent difference is that, here, additional instead of conventional quantities are involved. Moreover, similar observations can be made with regard to the boundary conditions (11). (It can be shown (Soldatos, 1987) that the second part of the condition (11*a*) can be transformed into the Kirchhoff free-edge boundary condition.)

It can further be shown (Soldatos, 1987) that the Navier-type equations of the present two stage bending plate theory form an eighth-order system of simultaneous partial differential equations. Using the transformations

$$u_1 = \psi_x + w_{,x}, \quad v_1 = \psi_y + w_{,y}, \tag{12}$$

that eighth-order system is directly reduced into the corresponding Navier-type equations of Reddy's (1984) plate theory.

Reduction to a Sixth-Order Plate Theory

Upon observing that the arithmetic values of the fractions 4/5 (= 0.8) and 17/21 (≃ 0.809) appearing in equations (8) are very close to each other, the following effective middle plane curvatures and twist are defined

$$(k^e_x, k^e_y, k^e_{xy}) = (k^c_x, k^c_y, k^c_{xy}) + \alpha(k^a_x, k^a_y, k^a_{xy}), \tag{13}$$

where $4/5 \le \alpha \le 17/21$. With these definitions, both conventional and additional bending moment resultants are approximated according to

$$\begin{bmatrix} M^c_x \\ M^c_y \end{bmatrix} \simeq \frac{5}{4} \begin{bmatrix} M^a_x \\ M^a_y \end{bmatrix} \simeq \begin{bmatrix} D_{11} & D_{12} \\ D_{12} & D_{22} \end{bmatrix} \begin{bmatrix} k^e_x \\ k^e_y \end{bmatrix},$$

$$M^c_{xy} \simeq \frac{5}{4} M^a_{xy} \simeq D_{66} k^e_{xy}. \tag{14}$$

Using these approximations together with expressions (8*b*), equations (10) can be reduced in the form

$$\begin{aligned} &Q^c_{x,x} + Q^c_{y,y} = p, \\ &M^c_{x,x} + M^c_{xy,y} - Q^c_x = 0, \\ &M^c_{y,y} + M^c_{xy,x} - Q^c_y = 0, \end{aligned} \tag{15}$$

where

$$(Q^c_x, Q^c_y) = \int_{-h/2}^{h/2} (\tau_{xz}, \tau_{yz}) dz = (A_{55}u_1, A_{44}v_1) \tag{16}$$

are the conventional transverse shear force resultants.

Equations (15) are well known from other sixth-order plate theories (Reissner, 1945; Mindlin, 1951) and have been considered as governing equations in both refined plate theories due to Reissner (1975) and Levinson (1980), which are also of the sixth order. In accordance with these observations, it can be shown that the present reduced theory is also of the sixth order (Soldatos, 1987). This is achieved upon inserting expressions (13) and (14) into equations (15). The Navier-type equations thus obtained, in terms of the unknown function u_1, v_1 and w, form a sixth-order set of simultaneous partial differential equations in which the constant α is involved.

Upon choosing $\alpha = 4/5$ and restricting attention to the case of an isotropic plate, the following results can be further achieved (Soldatos, 1987): (1) with the transformation (12), the Navier-type equations of the present sixth-order theory can be directly transformed into the corresponding equations of Levinson's (1980) theory, and (2) with $p = 0$, the constitutive equations (14) can be reduced in exactly the same form given in the corresponding expressions (15) of Reissner (1975).

Hence, it is concluded that Reissner's (1975) theory occurs as a particular case of Levinson's (1980) plate theory, for $p = 0$.

References

Bickford, W. B., 1982, "A Consistent Higher Order Beam Theory," *Develop. Theor. Appl. Mech.*, Vol. 11, pp. 137–142.

Levinson, M., 1980, "An Accurate Simple Theory of the Statics and Dynamics of Elastic Plates," *Mech. Res. Commun.*, Vol. 7, pp. 343–350.

Levinson, M., 1981, "A New Rectangular Beam Theory," *J. Sound Vibr.*, Vol. 73, pp. 81–87.

Levinson, M., 1985, "On Bickford's Consistent Higher Order Beam Theory," *Mech. Res. Commun.*, Vol. 12, pp. 1–9.

Levinson, M., 1987, "On Higher Order Beam and Plate Theories," *Mech. Res. Commun.*, Vol. 14, pp. 421–424.

Mindlin, R. D., 1951, "Influence of Rotatory Inertia and Shear on Flexural Vibrations of Isotropic Elastic Plates," ASME Journal of Applied Mechanics, Vol. 18, pp. 31–38.

Reddy, J. N., 1984, "A Simple Higher-Order Theory for Laminated Composite Plates," ASME Journal of Applied Mechanics, Vol. 51, pp. 745–752.

Reissner, E., 1945, "The Effect of Transverse Shear Deformation on the Bending of Elastic Plates," ASME Journal of Applied Mechanics, Vol. 12, pp. A69–A77.

Reissner, E., 1975, "On Transverse Bending of Plates, Including the Effect of Transverse Shear Deformation," *Int. J. Solids Struct.*, Vol. 11, pp. 569–573.

Reissner, E., 1985, "Reflections on the Theory of Elastic Plates," ASME *Appl. Mech. Rev.*, Vol. 38, pp. 1453–1464.

Rychter, Z., 1987, "A Sixth-Order Plate Theory—Derivation and Error Estimates," ASME Journal of Applied Mechanics, Vol. 54, pp. 275–279.

Soldatos, K. P., 1987, "An Eighth-Order, Two-Stage-Bending Plate Theory. Derivation of Governing Equations and Reduction to a New Sixth-Order Theory for Plate Bending," Tech. Report No. 146, Dept. of Mathematics, University of Ioannina, Greece.

Downloaded 03 May 2010 to 171.66.16.21. Redistribution subject to ASME license or copyright; see http://www.asme.org/terms/Terms_Use.cfm

Journal of Applied Mechanics

Book Reviews

Thermal Stresses II, edited by R. B. Hetnarski. Volume 2 of the second series "Thermal Stresses—A Series of Handbooks in Mechanics and Mathematical Methods," North Holland, Amsterdam, 1987, 441 Pages.

REVIEWED BY L. Y. BAHAR[1]

This text represents a continuing effort on the part of the publisher, under the general editorship of J. D. Achenbach, to bring the knowledge of interested engineering scientists to the level of current research by creating an awareness of topical coverage and technical level of accomplishment in the field of thermal stresses. This is not a simple task, as it necessitates bridging the gap between the concise style of the research paper and the extremely detailed exposition of textbook writing.

Thermal Stresses II is the second volume in the handbook series pertaining to that subject. The series is edited by Richard B. Hetnarski, the founder and Editor-in-Chief of the *Journal of Thermal Stresses*, and a researcher in the field of thermal stresses for almost three decades.

The second volume of the series has received the same attention as the first, and reflects the care that the publisher and the editor have devoted to their aims. Again, the editor R. B. Hetnarski was assisted by the same two reviewers who helped with the first volume, Professors Theodore R. Tauchert of the University of Kentucky and Joseph Padovan of the University of Akron. Both of these reviewers are well recognized for their research contributions to the field of thermal stresses as well as other areas of the mechanics of solids. They serve on the editorial board of the *Journal of Thermal Stresses*, and have published regularly in that Journal as well as in *Thermal Stresses I*, the volume whose sequel is under review here.

The text consists of six chapters. The first chapter discusses dynamical problems in thermal stresses in plates, and provides solutions for coupled and uncoupled problems. The chapter concludes with the treatment of anisotropic and heterogeneous plates. In chapter 2, thermal stress singularities are considered. These include dislocations, concentrated forces, cracks, inclusions, and stiffeners. In chapter 3 Maysel's formula is used to develop thermoelastic deformations in thin shells, and its extension to nonlinear and viscoelastic problems. Of particular interest is the connection of Maysel's formula with structural applications such as Castigliano's theorem. Chapter 4 considers probabilistic approaches to thermal stresses including a reliability study of brittle materials. Chapter 5 encompasses thermoelasticity with microstructure including micropolar effects. Chapter 6 treats low-cycle thermal fatigue.

This text continues the tradition set forth by the previous volume which gave a balanced presentation between theory and applications. The printing, format, and visual impact of the graphs and figures is excellent.

The state-of-the-art review contained at the end of each chapter followed by an extensive list of references, will give the reader the opportunity to pursue any particular topic treated in that chapter in more depth. Along with the previous volume, this text is strongly recommended to researchers interested in the theoretical and practical aspects of thermal stresses including industrial applications.

Numerical Modelling in Science and Engineering, by Myron B. Allen, III, Ismael Herrera, and George F. Pinder. John Wiley and Sons, Inc., New York, 1988. 418 pages, Price: $39.95.

REVIEWED BY WING KAM LIU[2]

Unlike most applied mathematics textbooks, this book presents an alternative approach to the teaching of applied mathematics. Traditionally, continuum mechanics, approximation methods to differential equations, and numerical analysis, are taught as three distinct disciplines. As the authors explain, "this book is an effort to meld all three aspects of the numerical modeler's task into a unified treatment."

The book begins with the derivation of the governing equations for a continuum. The various approximation methods to differential equations are then discussed, followed by the numerical solution procedures. Given the space limitations, the authors have presented applied mathematics from a truly broad perspectve: continuum physics, differential equations, including boundary value problems and initial value problems, the discrete counterparts of these problems and algorithms for their solution. This book is intended as an advanced text for applied mathematicias and engineering science students.

A representative list of topics treated in this book follows.

Chapter 1: "Basic Equations of Macroscopic Systems" considers kinematics, material derivatives, balance laws, constitutive laws, mixture mechanics, and some examples.

Chapter 2: "Introduction to Numerical Methods" is a self-contained chapter. It deals with Lagrange and Hermite polynomial approximations, tensor-product rules for higher dimensions, triangular and isoparametric elements, and finite difference approximations. The convergence criteria, such as consistency and stability are introduced along with methods of weighted residuals, which include Galerkin and collocation finite element methods. Error bounds for the methods are also given.

Chapter 3: "Steady-State Systems" includes such topics as Laplace's equation, principle of superposition, variational

[1]Professor, Department of Mechanical Engineering and Mechanics, Drexel University, Philadelphia, PA 19104.

[2]Professor and P.E., Department of Mechanical Engineering, Northwestern University, Evanston, IL 60208. Mem. ASME.

Copyright © 1988 by ASME
Downloaded 03 May 2010 to 171.66.16.21. Redistribution subject to ASME license or copyright; see http://www.asme.org/terms/Terms_Use.cfm

principles, invariance under translation and fundamental solutions, integral representation theorem, finite difference methods, finite element methods, Petrov-Galerkin finite element methods and boundary element methods. Various special iterative methods for the finite difference equations are also discussed.

Chapter 4: "Dissipative Systems". The numerical methods considered in Chapter 3 are revised to deal with the advection-diffusion type equations. Nonstandard methods such as upstream weighting, solution pathology at sharp fronts, and alternating direction methods are also introduced in this chapter.

Chapter 5: "Nondissipative Systems" deals with transport equations such as the Euler equations, the Burger's equation, and the wave equation. Methods of characteristic, conservative finite-difference schemes, and nonstandard Galerkin finite element methods are considered.

Chapter 6: "High-Order, Nonlinear, and Coupled Systems," considers special problems such as the biharmonic equation, nonlinear diffusion equations and compositional flows in porous media. The oil reservoir modeling is discussed at great length.

The above list is not complete, merely representative of the topics covered in the book.

Boundary Element Methods in Mechanics, by D. E. Beskos, Vol. 3 of "Computational Methods in Mechanics," Elsevier Science Publishing Co., New York, 1987, 598 pages.

REVIEWED BY U. HEISE[3]

The Boundary Element Method (BEM) has undergone rapid developments during the past 15 years and represents now one of the most useful tools for engineers. The aim of this textbook is to describe the present state of the theory and the possibilities of efficient application of the method. The book consists of 12 chapters each of which is written by a most outstanding active specialist in the research in his field.

In a brief introductory chapter, the historical development of the BEM, its philosophy and context with other techniques, are outlined. The basic principles of the BEM, i.e., formulation of the physics as integral equations, discretization, and numerical treatment are explained by the examples of the classical problems of potential- and elasticity-theory in chapters 2 and 3. These chapters are particularly suited for those wishing to learn about the BEM. The remaining chapters deal with more sophisticated problems and aim at an audience of researchers and practicing engineers already somewhat familar with the subjects. Chapters 4 and 5 are devoted to elasto-dynamics and deal with integral equations in the time-space domain and the transformed domain. Chapter 6 addresses the solution of nonlinear problems in solid mechanics. Integral equations are successfully applied to deal with large strains and with elasto-plastic and viscoplastic materials. Fracture mechanics represents a field of most fruitful application of the BEM. T. A. Cruse, a pioneer in the subject, points out in chapter 7 the mathematical modeling of the problems and the solution strategy. Chapter 8 examines integral formulations for various fluid mechanics problems, e.g., porous media flow, free surface flow, and water waves. Application of the BEM for the solution of accoustic problems is presented concisely in chapter 9. Integral equations for the thermoelastic problem of the consolidation process are treated in chapter 10. The last two chapters of the book are devoted to the interaction of structures with soil and fluid.

In the individual chapters, two- as well as three-dimensional problems are investigated. The book is devoted mostly to the direct BEM but emphasis is placed on the fact that the indirect BEM has certain advantages for particular problems.

The individual contributions are self-contained and present their particular topics sufficiently detailed for engineers to be able to apply the theory to practical problems. The understanding is made relatively easy by a number of carefully chosen illustrating examples of technical interest. The reader is supposed to have knowledge of general engineering mathematics and physics but not necessarily of the BEM. The introductions of each individual chapter will be valuable for potential users of the BEM since not only the advantages of the BEM are appraised, but also their restrictions are emphasized, and possibilities of application of the BEM are critically compared with those of other methods. Such information as well as presentation of numerical accuracy are very helpful in choosing the method most suited for the solution of a particular problem. A successful feature of the book is the presentation of an extensive list of references at the end of each chapter making easily accessable the BEM literature which has grown to such an extent that it is hard to keep up with the developments.

Although the book was written by several authors, the selection of the topics and the arrangement of the material make it a unit.

The book can be highly recommended to technical libraries and to any person who is concerned with the BEM.

Chaotic Vibrations: An Introduction for Applied Scientists and Engineers, by Francis C. Moon. John Wiley and Sons, Inc., New York, 1987. 309 pages.

REVIEWED BY EARL DOWELL[4] **AND CHARLES PEZESHKI**[5]

This book fills a void in the technical literature concerning chaotic vibrations. Until this text, there was a large gap between very elementary texts on chaotic vibrations, such as the one written by Abraham and Shaw, and the more mathematical analyses described in tomes such as the one by Guckenheimer and Holmes. The book descriptively covers such topics as identification of chaotic vibrations, experimental methods, heuristic criteria for chaos to occur, and fractal concepts in chaos. All these very complex topics are presented to the reader in an accessible form. As might be expected of any introductory text, depth in each of these areas is limited; however, the author provides an excellent bibliography on the forefront of chaotic dynamic research for those interested in pursuing particular topics further.

The book is full of illustrations and physical examples – a significant help in terms of understanding the types of systems that can possess chaotic behavior. Also, since the impetus in present dynamical systems research is geometric, the pictures accurately depict current techniques used in chaotic system analysis. An extensive glossary is also included in the book for those unfamiliar with the jargon associated with the field.

Those looking for an in-depth, step-by-step description of the mathematical methods used to analyze chaos will not find this book to their liking. There is virtually no mathematics in the book, save for the system models, i.e., differential and difference equations, a brief description of the Melnikov method, and a short development on Lyapunov exponents. However, one needs also to realize that this not a book on nonlinear analysis per se, and most chaotic vibrations

[3]Professor, Lehr-Und Forschungsgebiet Mechanik, Techniche Hoschsdwle Aachen, Aachen, West Germany.

[4]School of Engineering, Duke University, Durham, NC 27706

[5]Presently at Washington State University.

Copyright © 1988 by ASME
Downloaded 03 May 2010 to 171.66.16.21. Redistribution subject to ASME license or copyright; see http://www.asme.org/terms/Terms_Use.cfm